Vishal S. Sharma · Uday S. Dixit ·
Knut Sørby · Arvind Bhardwaj ·
Rajeev Trehan   *Editors*

Manufacturing Engineering

Select Proceedings of CPIE 2019

Lecture Notes on Multidisciplinary Industrial Engineering

Series Editor

J. Paulo Davim, Department of Mechanical Engineering, University of Aveiro, Aveiro, Portugal

"Lecture Notes on Multidisciplinary Industrial Engineering" publishes special volumes of conferences, workshops and symposia in interdisciplinary topics of interest. Disciplines such as materials science, nanosciences, sustainability science, management sciences, computational sciences, mechanical engineering, industrial engineering, manufacturing, mechatronics, electrical engineering, environmental and civil engineering, chemical engineering, systems engineering and biomedical engineering are covered. Selected and peer-reviewed papers from events in these fields can be considered for publication in this series.

More information about this series at http://www.springer.com/series/15734

Vishal S. Sharma · Uday S. Dixit ·
Knut Sørby · Arvind Bhardwaj ·
Rajeev Trehan
Editors

Manufacturing Engineering

Select Proceedings of CPIE 2019

Springer

Editors
Vishal S. Sharma
School of Mechanical, Industrial
and Aeronautical Engineering
University of Witwatersrand
Johannesburg, Gauteng, South Africa

Knut Sørby
Department of Mechanical and Industrial
Engineering
Norwegian University of Science
and Technology
Trondheim, Norway

Rajeev Trehan
Department of Industrial and Production
Engineering
Dr. B. R. Ambedkar National Institute
of Technology
Jalandhar, Punjab, India

Uday S. Dixit
Department of Mechanical Engineering
Indian Institute of Technology Guwahati
Guwahati, Assam, India

Arvind Bhardwaj
Department of Industrial and Production
Engineering
Dr. B. R. Ambedkar National Institute
of Technology
Jalandhar, Punjab, India

Contents

About the Editors

Dr. Vishal S. Sharma is currently working as Associate Professor at School of Mechanical, Industrial and Aeronautical Engineering at University of Witwatersrand, Johannesburg, South Africa. Prior to his joining at WITS University he was Professor at the Department of Industrial and Production Engineering at Dr. B. R. Ambedkar National Institute of Technology, Jalandhar. He obtained his bachelor's degree (Production Engineering) from Shivaji University, Kolhapur in the year 1992; Masters in Mechanical (Production) Engineering from Punjab University Chandigarh in 1998; and his Ph.D. in Mechanical Engineering from Kurukshetra University in the year 2005. He also received a postdoctoral fellowship from ENSAM Cluny, France in 2010. He has three years of industrial exposure and 23 years of teaching experience at Dr B R Ambedkar National Institute of Technology Jalandhar, India. He has published more than 70 scientific papers in international journals and conferences, and edited more than 10 books and proceedings. His current research interests include additive manufacturing and machining, condition monitoring and industrial IOT/Industry 4.0.

Dr. Uday S. Dixit is a Professor at the Department of Mechanical Engineering at IIT Guwahati. He received his bachelor's degree (Mechanical Engineering) from IIT Roorkee in 1987; and his masters and Ph.D. (Mechanical Engineering) from IIT Kanpur in 1993 and 1998, respectively. He has published over 200 scientific papers in international journals and conferences and edited more than 12 books and proceedings. He has also undertaken 19 research and consultancy projects. In addition to developing course material on mechatronics for IGNOU, and on engineering mechanics for NPTEL, he has produced QIP course material in the area of "Finite Element Method in Engineering and its applications in manufacturing", and "Introduction to Micro-manufacturing Technologies". His research interests include plasticity, metal forming, laser-based manufacturing, finite element modeling, and optimization. He has authored/edited more than 15 books and proceedings.

Dr. Knut Sørby is a Professor at Department of Mechanical & Industrial Engineering at Norwegian University of Science and Technology (NTNU), Trondhiem, Norway. He completed PhD and Post-doc fellowship from NTNU, Norway. He is Research Adviser at Sandvik Teeness. Prof. Sørby is having keen interest in machining processes. He has worked on preparation of control programs for multi-axis machines, kinematics for multi-axis machines, efficient processing of complex shaped products, tool life modelling, machining cost models, optimization of machining efficiency, and milling and turning of nickel based alloys with ceramic cutting tools. He has developed vibration absorbers for cutting tools: design and optimization of damping systems for machining processes, modeling and design of damping systems for multiple modes of vibration in boring bars, theoretical and experimental modal analysis, numerical methods for simulation of time response, instrumentation and vibration monitoring, and systems for active vibration suppression. He is Board member of the Norwegian association for machining technology - Technical expert for Norwegian Accreditation in laboratory accreditation.

Dr. Arvind Bhardwaj received his Bachelor in Mechanical Engineering from the Punjab University, India in 1988, and PhD from the Kurukshetra University, India in 2006. He is working as a Professor in the Department of Industrial and Production Engineering at Dr. B.R. Ambedkar National Institute of Technology, Jalandhar (An Institute of National Repute established by Government of India), Punjab, India. He is also looking after the responsibility of Dean Research and Consultancy. He has one years of industrial and more than 27 years of teaching experience. His areas of research are supply chain management, operations management, optimisation of production systems and ergonomics. He has published more than 100 articles in various international journals and conferences.

Dr. Rajeev Trehan is working as an Associate Professor in the Department of Industrial and Production Engineering at Dr. B.R. Ambedkar National Institute of Technology, Jalandhar. He holds a PhD degree in Industrial Engineering. He has more than three years' experience in industry and 17 years' experience of teaching UG and PG students. He has guided 20 MTech thesis and having three PhD students. His area of interest is quality management, advanced manufacturing and has published more than 15 articles on these topics in different journals and conferences.

Chapter 1
Investigations on the Development of Heated Build Platform for Additive Manufacturing of Large-Size Parts

Sagar Kailas Gawali, Narendra Kumar, and Prashant K. Jain

Abstract Extrusion-based additive manufacturing (AM) is a process that fabricates the parts by extruding and depositing material through extruder in a layer-by-layer manner on a build platform. Build platform provides a foundation to fabricate parts and also provides an appropriate heat to bottom layer required for adequate adhesion. In extrusion-based AM, adhesion between the first deposited layer and the surface of build platform is crucial. Long and wide roads are deposited during the large-size part fabrication from a nozzle which leads to large temperature gradient between deposited roads. Therefore, a large-size platform having uniform temperature distribution is needed in order to fabricate large-size parts. This paper presents a study on the development of a heated build platform for enabling large-size part fabrication through a CNC-assisted extrusion-based AM system. The set-up consists of a screw-driven extrusion system and heated large-size build platform. Build platform consists of aluminium plate, silicon pad heater, levelling screw and PID temperature controller as the main components. The build platform is tested for temperature distribution using a Fluke IR camera. Results show that uniform temperature is distributed across the build platform, and it can be used for additive manufacturing of large-size parts.

Keywords Additive manufacturing · Build platform · Large-size parts · Pellet · ABS · Retrofitment · CNC-assisted extrusion-based AM system

1.1 Introduction

With the arrival of new technologies, designing products have become much easier. A large number of computer-aided design (CAD) software packages are available in the market, which has eased the design process as a whole, and the designers are experimenting much more with design and development of new products than

S. K. Gawali · N. Kumar (✉) · P. K. Jain
Mechanical Engineering Discipline, PDPM Indian Institute of Information Technology,
Design & Manufacturing, Jabalpur, Madhya Pradesh 482005, India
e-mail: nyiiitj@gmail.com
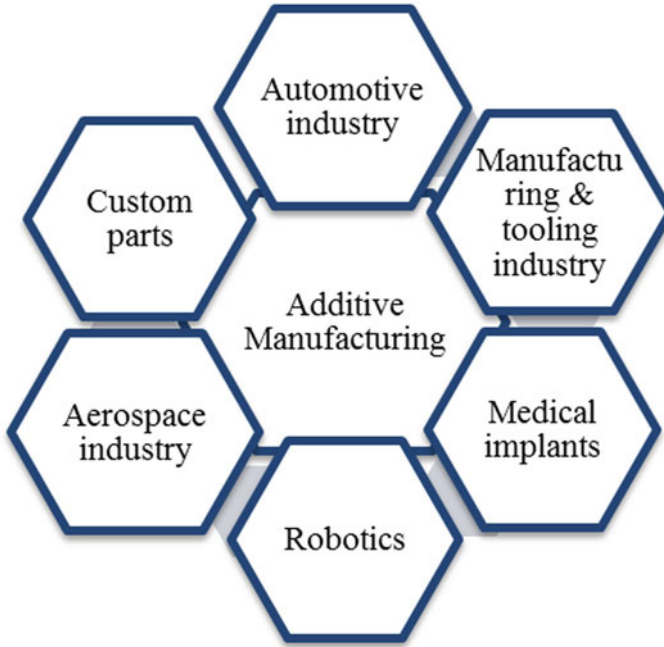
Fig. 1.1 Application domains of AM

ever before. In today's competitive world of manufacturing industries, competition has been increased rapidly for new product development as early as possible. Additive manufacturing (AM) process works as a flexible and quick manufacturing process that is used by manufacturers globally for product development due to various benefits.

In last decades, additive manufacturing (AM) emerges as the fastest growing technology, which is formerly known as rapid prototyping (RP), and it is also known as 3D printing. AM is the process that manufactures parts with resources efficiently in quick time. AM offering fabricated complex-shaped parts increases its popularity in application fields such as automotive, aerospace, biomedical, robotics, manufacturing industry and fashion and research. Figure 1.1 shows applications of AM in various industrial fields.

1.1.1 Additive Manufacturing

Additive manufacturing (AM) is a process of fabricating 3D parts from CAD model directly. It simply built the parts by adding material in a layer-by-layer manner. On comparing with traditional manufacturing processes, there is no requirement of specific tools and fixtures to fabricate parts. According to 'ASTM F42–Additive
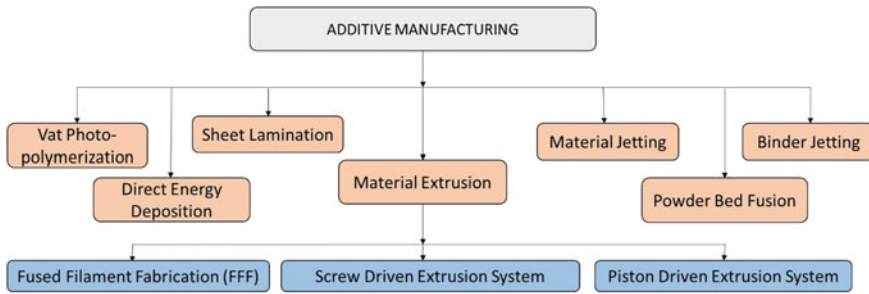
Fig. 1.2 Categorization of AM processes

Manufacturing' standard, AM processes can be classified into seven categories based on different working principles, i.e., material extrusion, direct energy deposition, powder bed fusion, binder jetting, vat photo-polymerization, material jetting, sheet lamination, etc. [1] (Fig. 1.2).

Among these processes, material extrusion-based AM process has grown as viable and economical manufacturing technology. Material extrusion is a process that consists of mainly a material extrusion tool and build platform. Either of the material extrusion tool or build platform is moved in usually *z*-direction that helps to deposit material on top of layer previously deposited on build platform. After fabrication, parts have to perform some post-processing, that is essential for functional use. The AM system manufactures parts at reasonable cost with good quality in the shortest time, which helps to compete with others in the current manufacturing world. Manufacturing world witnessed evolution of new process since last three decades, and earlier, AM process is only used for prototyping purpose, popularly known as rapid prototyping (RP). Nowadays, many industries adopted AM to make functional products of parts to minimize the product development cycle time [2–5].

1.1.2 Fused Filament Fabrication (FFF)

Fused filament fabrication (FFF) is a one of the most popular material extrusion-based AM processes which is used to fabricate prototypes and small end-use functional products [6–8]. FFF is a process in which material in the filament form is processed through extrusion principle to fabricate plastic parts, as shown in Fig. 1.3. FFF is the most commonly used process for fabrication of parts among other AM processes with ease, minimum wastage of material and easy material change. FFF is a typical RP process that fabricates prototypes for visualization and validation of designs. FFF process need not require a tooling for fabrication of parts and has design freedom with no geometrical restriction [9–11].
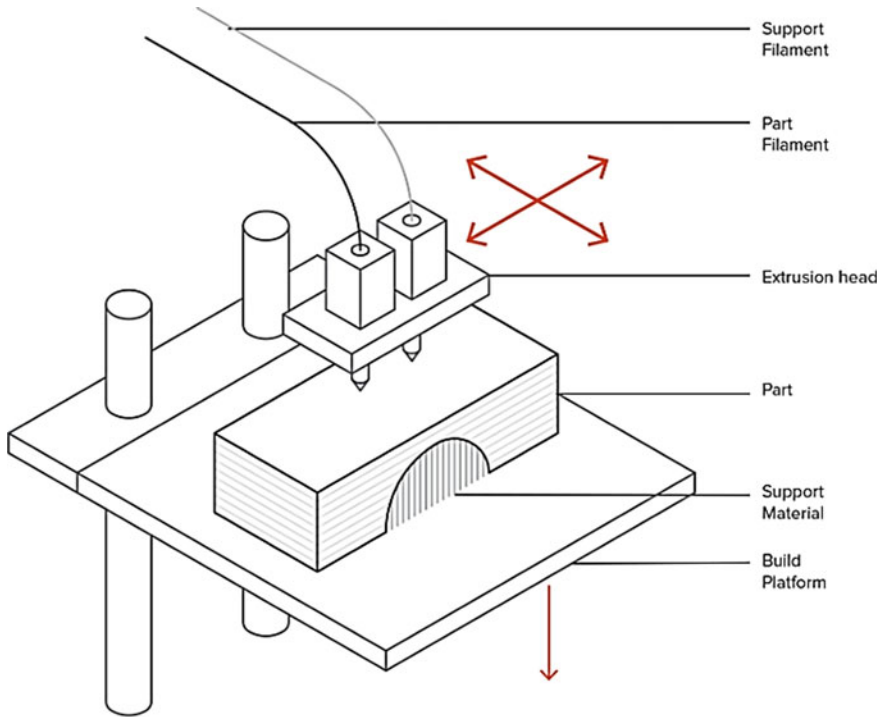
Fig. 1.3 Schematic diagram of the FFF system. *Source* 3D Hubs

1.1.3 Need of Build Platform and Issues with FFF

There are various parameters in extrusion-based AM process which affect the quality of fabricated parts, as shown in Fig. 1.4.

In these processes, the material is heated until it reaches to semi-molten state and then extruded through a nozzle on the build platform. During the material deposition, heat is transferred from the part to the environment due to temperature difference which leads to the formation of defects, i.e., warpage, deformation [12, 13]. In commercial material extrusion system, two discrete methods are used to prevent or limit warpage, one is the incorporation of the heated build platform and another one is closed build chamber [14].

Despite the wide use, FFF can make parts with limited dimensions due to the small size workspace of build platform. As dimension of workspace increases, capital cost of machine increases for large-size parts and due to slow rate of material supply effects on build rate which is very slow for high volume manufacturing [15, 16]. The size of the part can be increased by enhancing the dimensions of the build platform. The modifications in the size of build platform would lead to change in the dimensions of gantry system of machine. Machines with large build platform are costly as compared to small ones as large gantry system is added. Large-size parts
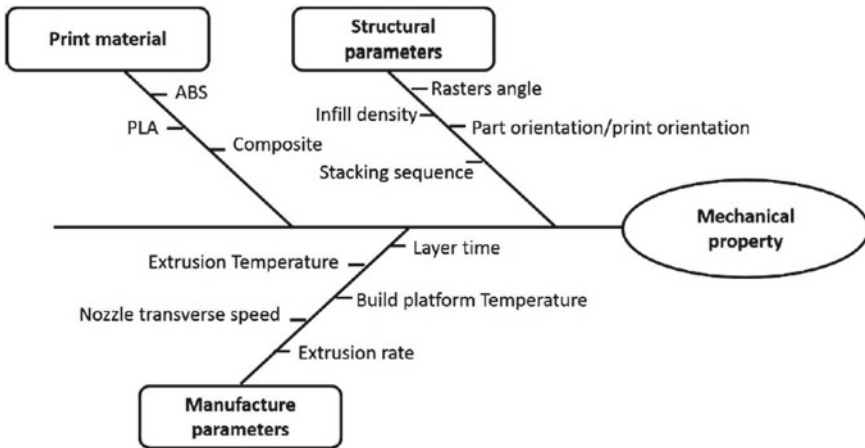
Fig. 1.4 Cause and effect diagram of extrusion-based AM process

fabrication can be accomplished with a large gantry system and large-size heated build platform. Therefore, the present paper aims to develop a heated build platform for additive manufacturing of large-size parts. However, available CNC machining centre has been used as a gantry system which helps in material deposition at required coordinates. Development of build platform depends greatly on the material being processed, nature of the build platform surface and heating mechanism.

1.2 Development of Heated Build Platform

Heated build platform is vital element of system which plays a major role during part fabrication. It is well-known that warpage may occur within the fabricated parts due to induced thermal stresses. When surface area increases with an increase in part size, it may lead to rapid heat transfer which results into warpage. Due to this warpage, part fabrication may be failed as bottom layers of the part may get curled and peeled off from the build platform as shown in Fig. 1.5.

Build platform provides the essential temperature to the part during fabrication in order to avoid any possible warpage by keeping your part warm during the whole process which keeps the material at or above the glass transition temperature to prevent any possible damage to part induced due to uneven heat transfer. Moreover, build platform helps in the increase adhesion with the surface and to improve part quality [17].
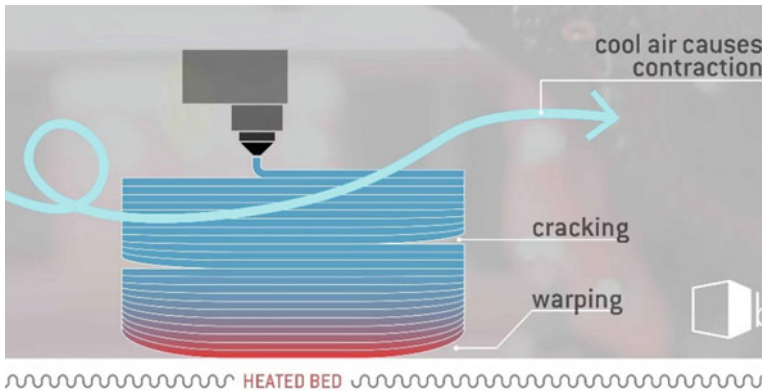
Fig. 1.5 Issues due to build platform. *Source* https://box3d.eu

1.2.1 Design Methodology

The purpose to develop the build platform is to improve the adhesion of base layer with heated surface and to help in bonding of successive layers. Deposition of the first layer on the build platform is most vital to the successful fabrication of the part, and it acts as a base to other layers. Improper build platform may cause warpage or separation of the deposited layer from the platform during processing. It may lead to part failure and process interruption. Purpose of build platform is to provide heat to fabricated parts during the process to raise the temperature of part up to or more than the glass transition temperature of a material, and efficient heat transfer is vital.

Selection of platform material is important to adhere the layers, especially for large-size and complex parts and high-shrinkage materials. In the current research, aluminium material has also been selected as a build platform surface for developing uniform heating in a simple and cost-effective manner. Aluminium was selected due to high thermal conductivity which provides uniform heating and high durability. Also, ease in removal of fabricated part with aluminium builds up over time after each fabrication. Also to maintain uniform heating of build platform, there should be different heating systems that have been used to avoid cold spots on the surface. For the large surface area of platform capacity of the heating build platform, the controlled silicon heating pad may be a good choice of preference. Silicone heater under an aluminium build platform will heat evenly. Also, it is easy to choose heater power with a silicone heater. Silicon pad heaters are selected as a heating element because of its advantages such as light in weight, fast heating and reliable. Silicon pad heaters are easy to install with aluminium plate due to good adhesion quality (Fig. 1.6). These heaters are relatively inexpensive and long life span as compared to other types of heaters. The need of AC supply to operate these heaters is the biggest limitation as circuit needs ground connection with AC.
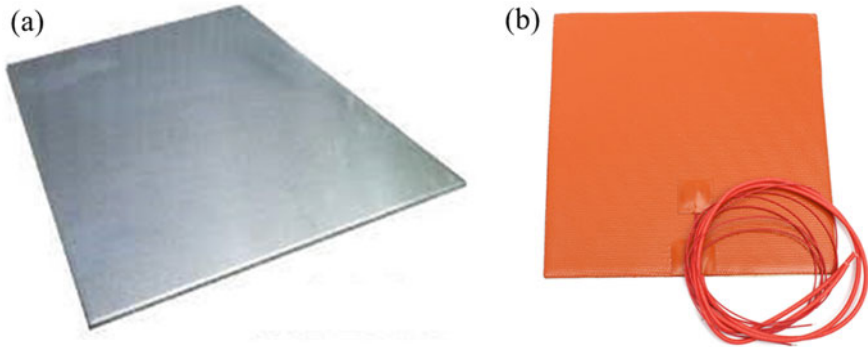
Fig. 1.6 a Aluminium plate, **b** silicon pad heater

1.2.2 Development of Build Platform

Build platform has been developed using components, namely (a) aluminium plate (5 mm thick), (b) silicon pad heater (AC supply 230 W), (c) wooden board, (d) PID temperature controller, type-K thermocouple and (e) levelling screw. Aluminium plate of dimension $600 \times 450 \, \text{mm}^2$ is used (Fig. 1.7). Aluminium plate is kept fixed over the wooden board using levelling screw, and four silicon pad heaters are attached to the bottom side of plate in order to provide uniform heating. A type-K thermocouple is attached to the centre of the plate to measure the temperature and to provide feedback to the controller.

1.2.2.1 Proposed Circuit of Build Plate Design

A circuit has been proposed to connect all the heating mechanism components together. Figure 1.8 shows a proposed circuit diagram prepared to provide heat to the
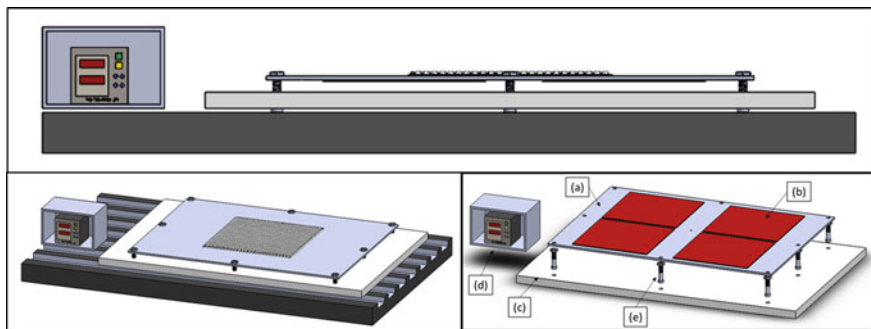
Fig. 1.7 Proposed CAD design of build platform
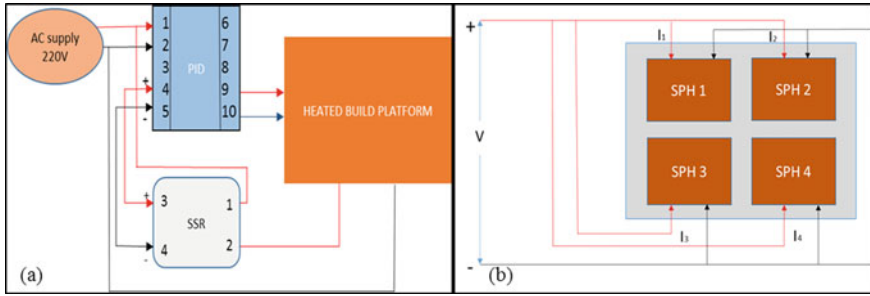
Fig. 1.8 **a** Proposed circuit diagram, **b** parallel connection of four SPH

developed build platform. The proposed circuit is an assembly of components such as silicon pad heaters, proportional–integral–derivative (PID) temperature controller, solid-state relay (SSR), type-K thermocouple (Table 1.1).

The temperature controller takes an input from the thermocouple and has output of PID temperature controller maintained the temperature of system at set value temperature. PID controller accurately control process temperature without the involvement of operator, a control system relies upon a PID controller feedback data, and it compares the actual temperature to the desired control temperature, or set value

Table 1.1 Build platform components

PID temperature controller		• Control unit that easier to implement • Act as feedback unit • More robust to tuning mismatches • Easier to tune by simple trial and error • Better response to unmeasured disturbances
Solid-state relay (SSR)		• Electronic switching device • Very fast response usually about 1 μs ON and 0.5 μs OFF • Life span is much higher • Low power consumption, highly durable
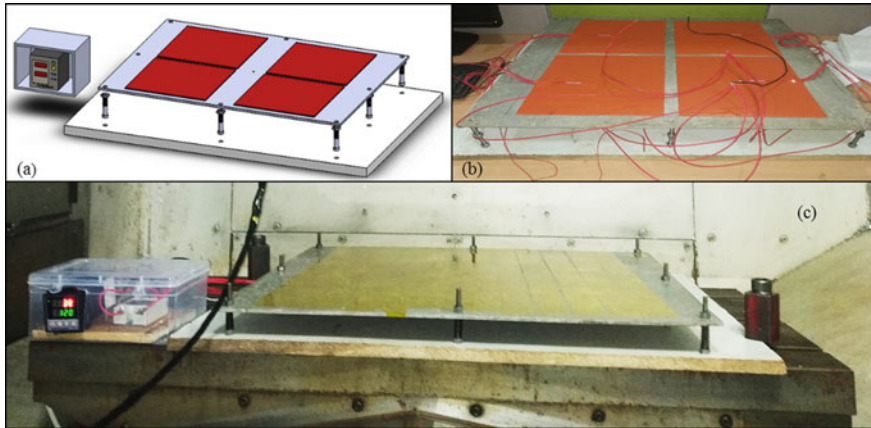
Fig. 1.9 **a** CAD model of a proposed design, **b** assembly of SPH on the plate, **c** developed set-up of build platform

temperature. Solid-state relay (SSR) plays the role of a switching device which maintained the actual value of temperature to set value temperature. SSR is a device that responds to correct input, and it acts as an electronic switching device which enabled and disabled the power supply to load circuitry. This circuit assembly shown in Fig. 1.9 is attached bottom side of the aluminium plate to develop a build platform.

1.2.2.2 Time Taken to Heat Build Plate-Calculation

• SPH—Silicon pad heater	• Heat required to plate
Specifications: Voltage 220 V Current 1A • Plate material: Aluminium Thickness: 5 mm Dimension: 600 × 450 mm Weight: 4.5 kg Specific heat capacity: 900 J/kg K • Bed temperature: 110 °C • Room temperature: 25 °C	$Q = m \times Cp \times (T_1 - T_0)$ $\quad = 4.5 \times 900 \times (110 - 25)$ $\quad = 344.25 \text{ KJ}$ • Power supplied to circuit $P = V \times I_T$ $\quad = 220 \times 4 = 880 \text{ W}$ • Time taken to heat 5 mm plate $t = Q \div P$ $\quad = 344{,}250/880$ $\quad = 391.1931 \text{ s} = 6.51 \text{min}$

Similar to commercial AM machines, threaded bolts with spring and adjustable nuts are provided to fix and level the platform on CNC machining centre. The gap between nozzle and build platform can also be adjusted. This developed build platform is placed over the CNC machine workspace and fixed with jigs and fixtures. The maximum travel range of CNC machine workspace was $750 \times 450 \times 400\,\text{mm}^3$. In order to utilize the space for additive manufacturing purpose, a build platform with the size of $600 \times 450 \times 400\,\text{mm}^3$ was developed.

1.3   Characterization of Developed Build Platform

Developed build platform was characterized in order to assess its temperature and heat distribution capability.

1.3.1   Temperature Distribution Testing

Thermal IR camera was used to check temperature distribution across the build platform surface. Captured thermal images show the uniform distribution of heat across the surface of the build platform. It also shows that developed build platform can attain appropriate temperature within a short time of span. Build platform heated using four silicon pad heaters that stick to the bottom side provides a uniform heat distribution on the total surface of platform. It helps to reduce warpage during and after process. The heated build platform has been developed based on the parameters required for the printing of ABS material. It is known that 110 °C build platform temperature is need to build parts of ABS material [18]. Figure 1.10 shows temperature distribution from the initial time (t_0) to time (t_{10}) at an interval of 1 min till platform reaches a temperature 110 °C. It can be seen that temperature has been attained within 10 min.
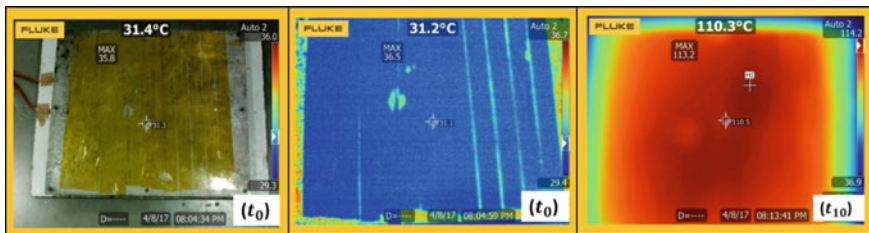
Fig. 1.10 Temperature distribution on build platform
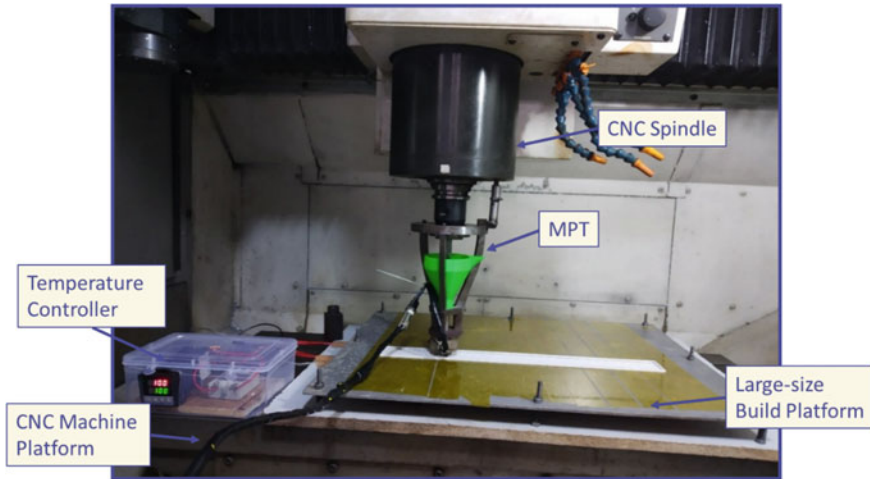
Fig. 1.11 Developed experimental set-up

1.3.2 Experimental Testing

The developed build platform was tested experimentally in order to see its feasibility for additive manufacturing of large-size parts. Therefore, it was tested with the already available CNC-assisted extrusion-based AM system developed Kumar et al. [19]. The available AM system uses CNC machining centre as a gantry system along with a material processing tool (MPT). Material processing tool (MPT) is a vital element which is accountable for continuous and uniform extrusion of the material. MPT works on screw-driven extrusion principle to process the material in pellet form. In the current study, processing tool was modified which was developed by Kumar et al. In this version, hopper, barrel and nozzle assembly is modified to fabricate large-size parts relatively faster rate. The developed experimental set-up of the MPT and build platform on three-axes CNC machining centre is depicted in Fig. 1.11 [20–23].

1.3.2.1 Material

Acrylonitrile butadiene styrene (ABS) grade M204 was taken as a raw material in pellet form due to easy availability at low cost (Fig. 1.12). The robust rheological behaviour of ABS provides material extrusion at constant rate which may help in robust part fabrication. Moreover, ABS has established itself as the standard material in commercial additive manufacturing. This is the reason why the ABS is selected in the current study.

Fig. 1.12 ABS material used in the current study

1.3.2.2 Feasibility Study

For feasibility analysis of set-up, nozzle of 2.5 mm diameter was used in the current study. For part fabrication at initial level, process parameters were chosen based on the literature as build platform temperature (100 °C), screw speed (60 RPM), extrusion temperature (220 °C) and deposition speed (700 mm/min). Using these process parameters, experiments were conducted and fabrication of different primitive shapes of large-size was attempted in order to analyse the feasibility of developed system. The considered geometries are presented along with their dimensions in Fig. 1.13.

Figure 1.14 illustrates the successful fabrication of parts with straight and curvy edges through developed set-up, Furthermore, internal contour features in the parts were combined which shows the capability of system.
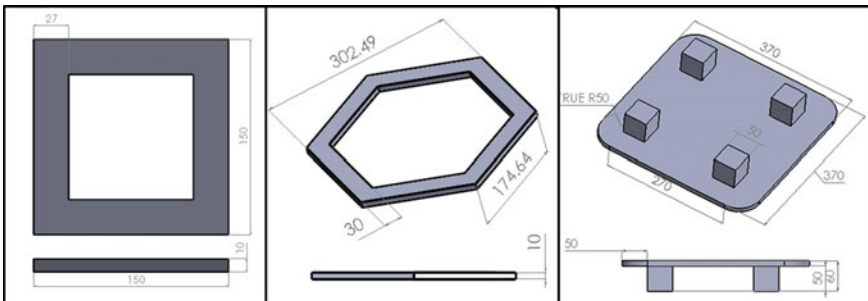
Fig. 1.13 Primitive shapes
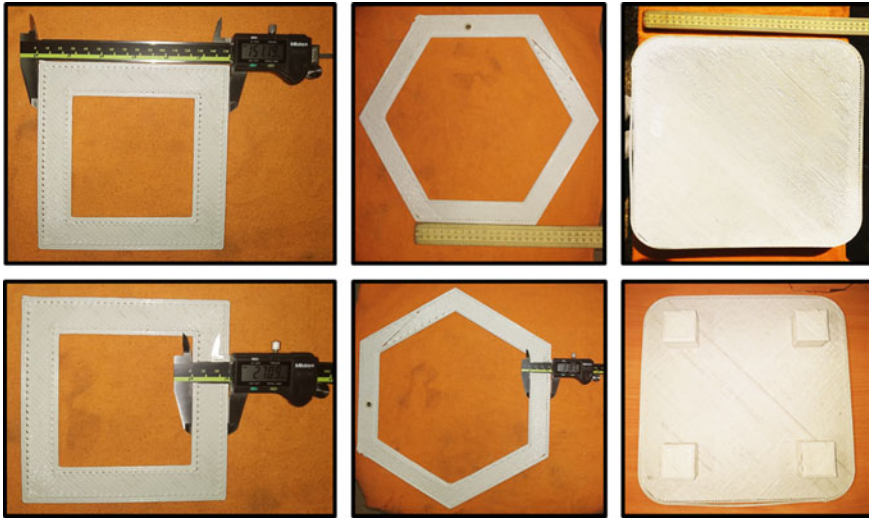
Fig. 1.14 Fabricated parts
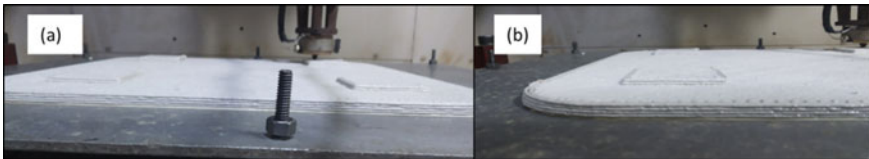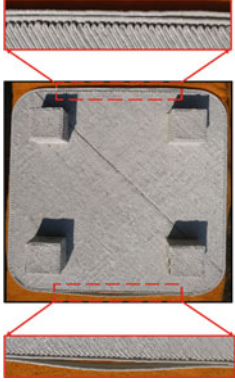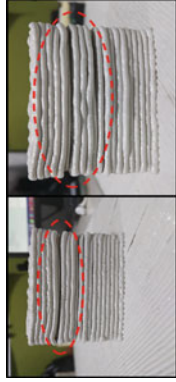
Fig. 1.15 **a** Adequate adhesion, **b** no warpage

Also, obtained results show that build platform is capable to generate heat uniformly across the surface during part fabrication. There was no warpage and deformation induced within the fabricated parts. Moreover, adequate adhesion between the roads and layers was found which indicates the capability of developed heated build platform (Fig. 1.15). The fabricated parts were characterized in order to see the structure and quality.

1.3.2.3 Parts Characterization

The fabricated parts were characterized to analyze their quality as the presented approach is different in comparison with commercial extrusion-based AM process. The differences are in the material processing technique, size of nozzle and build platform. In additive manufacturing, the quality of the fabricated parts depends on various factors. The changes in processing technique, size of nozzle and build platform may lead to change in the quality of fabricated parts. Therefore, it was important to assess the quality of parts for validating the process and presented approach. In

Table 1.2 Observations during characterization of parts

Gaps between infill and internal–external contours	• Infill percentage, deposition speed and raster angle • Due to higher deposition speed, road does not get enough time to bond with contour, which leads to creation of voids of irregular shapes	
Layer separation/delamination	• Layer thickness, barrel temperature and deposition speed • Variation in deposition speed leads layer separate	
Warpage	• High heat transfer rate • Deposited roads cool and solidify fast • ABS has tendency of warpage during cooling	

(continued)

Table 1.2 (continued)

Under-extrusion/over-extrusion	• MPT which do not have feedback unit to control the flow through nozzle • Screw speed, deposition speed • Under-extrusion gaps between the contours and layers • Over-extrusion creates overlapping of layers	
Holes on the top layers	• Pellet form ABS material contains an some moisture and entrapped air • Intra-bead porosity manifests as small circular voids in beads	

order to observe part quality, characterization was done by capturing the images of fabricated parts structure. The characterization results are enlisted in Table 1.2.

1.4   Conclusions

Commercial additive manufacturing (AM) systems with large build volume are relatively costly as compared to small AM machines. However, the use of existing CNC machining centres could provide alternate solution for large-size parts fabrication at a nominal cost. Therefore, a detailed study on the development of cost-effective build platform was presented. A large build platform was developed that was retrofitted on three-axis CNC machining centre for the fabrication of large-size parts. The characterization of the developed build platform was done in order to see its capability for additive manufacturing of large-size parts. Results showed the satisfactory performance of developed build platform. It can be concluded that the developed build platform set-up has potential and could be utilized to fabricate large-size parts in future under the industrial environment.

References

1. Turner, B.N., Strong, R., Gold, S.A.: A review of melt extrusion additive manufacturing processes: I. Process design and modeling. Rapid Prototyp. J. **20**(3), 192–204 (2014)
2. Newell, C., Palas, S., Duty, C., Love, L., Kunc, V., Lind, R., et al.: Out of bounds additive manufacturing. Adv. Mater. Process. 15–17 (2013)
3. Biswas, K., Lind, R., Jackson, R., Post, B., Love, L., Obendorf, A., et al.: Big area additive manufacturing applied to buildings (2016)
4. Post, B.K., Lind, R.F., Lloyd, P.D., Kunc, V., Linhal, J.M., Love, L.J.: The economics of big area additive manufacturing. 1176–1182 (2016)
5. Li, L., Tirado, A., Nlebedim, I.C., Rios, O., Post, B., Kunc, V., Lowden, R.R., Lara-Curzio, E., Fredette, R., Ormerod, J., Lograsso, T.A., Paranthaman, M.P.: Big area additive manufacturing of high performance bonded NdFeB magnets. Sci. Rep. **6**(October), 1–7 (2016)
6. Taufik, M., Jain, P.K.: Estimation and simulation of shape deviation for additive manufacturing prototypes. V004T05A018 (2016)
7. Taufik, M., Jain, P.K.: Computer aided visualization tool for part quality analysis of additive manufacturing process. V02AT03A034 (2016)
8. Brenken, B., Barocio, E., Favaloro, A., Pipes, R.B., Kunc, V.: Fused filament fabrication of fiber-reinforced polymers: a review. Addit. Manuf. **21**, 1–16 (2018). https://doi.org/10.1016/j.addma.2018.01.002
9. Sun, Q.: Effect of processing conditions on the bonding quality of FDM polymer filaments. Rapid Prototyp. J. **2008**(2), 72–80 (2007)
10. Qattawi, A., Alrawi, B., Guzman, A.: Experimental optimization of fused deposition modelling processing parameters: a design-for-manufacturing approach. Procedia Manuf. **10**, 791–803 (2017). https://doi.org/10.1016/j.promfg.2017.07.079
11. Kumar, N., Jain, P.K., Tandon, P., Mohan, P.: Investigation on the effects of process parameters in CNC assisted pellet based fused layer modeling process. J. Manuf. Process. **35**, 428–436 (2018). https://doi.org/10.1016/j.jmapro.2018.08.029

12. Messimer, S.L., Patterson, A.E., Muna, N., Deshpande, A.P., Rocha, Pereira T.: Characterization and processing behavior of heated aluminum-polycarbonate composite build plates for the FDM additive manufacturing process. J. Manuf. Mater. Process. **2**(1), 12 (2018)
13. Spoerk, M., Gonzalez-Gutierrez, J., Sapkota, J., Schuschnigg, S., Holzer, C.: Effect of the printing bed temperature on the adhesion of parts produced by fused filament fabrication. Plast. Rubber Compos. **47**(1), 17–24 (2018)
14. Rictor, A., Riley, B.: Optimization of a heated platform based on statistical annealing of critical design parameters in a 3D printing application. Procedia Comput. Sci. **83**, 712–716 (2016)
15. Love, L., Kunc, V.: Thermal analysis of additive manufacturing of large-scale thermoplastic polymer composites. Addit. Manuf. (2017). https://doi.org/10.1016/j.addma.2017.07.006
16. Duty, C.E., Kunc, V., Compton, B., Post, B., Erdman, D., Smith, R., et al.: Article information: to cite this document: structure and mechanical behavior of big area additive manufacturing (BAAM) materials. Rapid Prototyp. J. (2017)
17. Zhen, C.: An improved fused deposition modeling process for forming. J. Mater. Process. Tech. (2016). https://doi.org/10.1016/j.jmatprotec.2016.04.005
18. Kumar, N., Jain, P.K., Tandon, P., Mohan, Pandey P.: Experimental investigations on suitability of polypropylene (PP) and ethylene vinyl acetate (EVA) in additive manufacturing. Mater. Today: Proc. **5**(2), 4118–4127 (2018)
19. Kumar, N., Jain, P.K., Tandon, P., Pandey, P.M.: Extrusion-based additive manufacturing process for producing flexible parts. J. Braz. Soc. Mech. Sci. Eng. **40**(3), 1–12 (2018)
20. Kunc, V., Hassen, A.A., Lindahl, J., Kim, S., Post, B.: Large scale additively manufactured (2017)
21. Felsch, T., Klaeger, U., Steuer, J., Schmidt, L., Schilling, M.: Robotic system for additive manufacturing of large and complex parts. 3–6 (2017)
22. Wang, Z., Liu, R., Sparks, T., Liou, F.: Large-scale deposition system by an industrial robot (I): design of fused pellet modeling system and extrusion process analysis. 3D Print. Addit. Manuf. **3**(1), 39–47 (2016)
23. Liu, X., Chi, B., Jiao, Z., Tan, J., Liu, F., Yang, W.: A large-scale double-stage-screw 3D printer for fused deposition of plastic pellets. J. Appl. Polym. Sci. 45147:1–45147:9 (2017)

Chapter 2
On the Numerical Investigation of Material Deposition in Fused Filament Fabrication

Anand Singh Yadav, Narendra Kumar, and Prashant K. Jain

Abstract Fused filament fabrication (FFF) is a widely used additive manufacturing process in which part is fabricated by depositing material in the form of strand through a nozzle. Material deposition with different processing conditions may influence the part quality, namely surface finish, mechanical strength and dimensional accuracy. The part quality largely depends on the cross-sectional shape of deposited strand which gets affected by the stand-off gap between nozzle tip and bed surface and moving velocity of bed. Thus, it would be important to study the effect of these parameters on the cross-sectional shape of deposited strand numerically prior to actual part fabrication. It may provide optimum process conditions for part fabrication without any material wastage. In this paper, a numerical investigation has been carried out to study the effect of stand-off gap between the nozzle tip and bed surface with moving velocity of bed on the cross-sectional shape of deposited strand. ANSYS Fluent along with computational fluid dynamics (CFD) has been used in order to carry out the investigation. Material has been deposited at different process conditions, and then, the cross-sectional shape of deposited strand is obtained using extraction of point cloud data in MATLAB. Results show the variation in cross section of the deposited strand. In most of the cases, elliptical and rectangular with rounded corners shapes have been observed.

Keywords Additive manufacturing · Fused deposition modeling · Fused filament fabrication · 3D printing · Numerical simulation · Strand deposition

2.1 Introduction

Additive manufacturing (AM) is an advanced manufacturing process, which comprises processing of digital data of geometrical model for fabricating part by adding material in layers. There are various types of AM processes available which work on

A. S. Yadav · N. Kumar (✉) · P. K. Jain
Mechanical Engineering Discipline, PDPM Indian Institute of Information Technology,
Design and Manufacturing, Jabalpur, Madhya Pradesh 482005, India
e-mail: nyiiitj@gmail.com

different material processing principles to fabricate parts. Fused filament fabrication (FFF) is one of the AM processes in which semi-molten thermoplastic material is extruded and deposited in the form of a strand on the bed [1]. Various materials are available in the material library of FFF in which acrylonitrile butadiene styrene (ABS) is most commonly used. In FFF, part quality largely depends on the processing conditions used in fabrication. It may differ with different processing conditions. The temperature of molten material, gap between nozzle tip and bed, inner and outer diameter of the nozzle, velocity of material flow through nozzle and velocity of bed, tool path and raster angle are some of the influential parameters for part quality [2, 3]. These parameters, directly and indirectly, influence the final part quality. In literature, various studies have been reported on the process optimization of FFF process in order to improve the part quality [4–6]. Reported literature reveals that stand-off gap between the nozzle tip and bed surface and moving velocity of bed are the crucial parameters affecting the cross-sectional shape of deposited strand. Deposited strand having unpredicted cross-sectional shape depends on density and viscosity of molten polymeric material at different temperatures [7, 8]. Part quality is directly or indirectly linked with the shape of deposited strand. Thermal models have additionally been coupled to a sintering model with capillary action and healing models with intermolecular diffusion [9], to detect the neighbourhood bond arrangement between connecting strands [10]. Global thermo-mechanical simulation of the whole part has additionally been used to figure out the temperature-initiated distortions (shrinkage and warpage), crystallinity [11] and the potential areas of crack inception [12]. In these models, the material expulsion is normally imitated by finite volume method. The geometry of the strand is typically improved to rectangular voxels, in the global simulations, and to a cylinder with circular, elliptical or octagonal cross-sectional areas, in the nearby models. In any case, the shape of the strands is a vital parameter in the heat balance: the strands transfer heat by conduction through their contact surfaces, while their free surfaces by convection and radiation [13]. In this manner, the precision of the thermal models could be upgraded if the geometry of the strands was really determined with CFD simulation. The cross-sectional shape of the strands and their overlap interim are key parameters in the mathematical model of surface roughness [14]. These parameters are utilized as fitting parameters of the model, almost difficult to calculation, without CFD simulation. Additionally, CFD simulation of the material deposition could be utilized to anticipate the interstitial void thickness between the strands, which can legitimately into the models of the mechanical properties of the created part [15]. Non-isothermal flow of molten polymeric material follows power law of Newtonian fluids. CFD simulation of extrusion of these thermo-fluids through nozzle has been done in [16]. Therefore, a numerical investigation on finding the optimized shape of deposited strand might be useful in FFF for obtaining superior part quality without performing actual experiments. Hence, the present paper aims to investigate the effect of aforementioned parameters on the cross-sectional shape of deposited strand numerically. ABS material has been considered in this study. The surface of deposited strand is extracted in the form of point cloud data. Computational geometry is implemented to get a bounding region

of point cloud data by using MATLAB, and then, the cross-sectional shape of the deposited strand is captured.

2.2 Description of the Model

2.2.1 Physics and Numerical Model

The model described in this paper deals with the deposition of semi-molten polymeric material having high viscosity (μ) value. In other way, a controlled shear deformation of extruded material is occurred in gap between nozzle tip and bed. This physical process takes place in the region between the nozzle tip and bed. The velocity of material flow through a nozzle (U) and moving velocity of bed (V), both simultaneously affect the shape of deposited strands. The assumptions are made about the physics of flow to reduce complexity during the simulation. The fluid is considered incompressible, which means density (ρ) remains constant. Hence, the mass conservation equation is simplified into volume conservation. Here, the advective inertial force is comparatively smaller then viscous force, so creeping flow is under the assumption. Newtonian fluid flow is assumed isothermal due to negligible temperature change across the gap between nozzle tip and bed. However, simulation is performed by taking specific temperature values of molten material and bed. The domain is filled by air and polymer material. Reynolds number is very less for small diameter; hence, laminar flow will take place at deposition region. The geometry of model considered and its meshing is shown in Figs. 2.1 and 2.2, respectively.
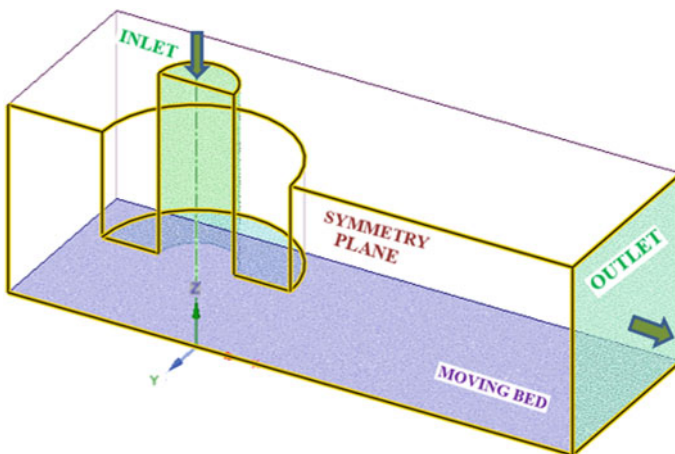
Fig. 2.1 Model geometry
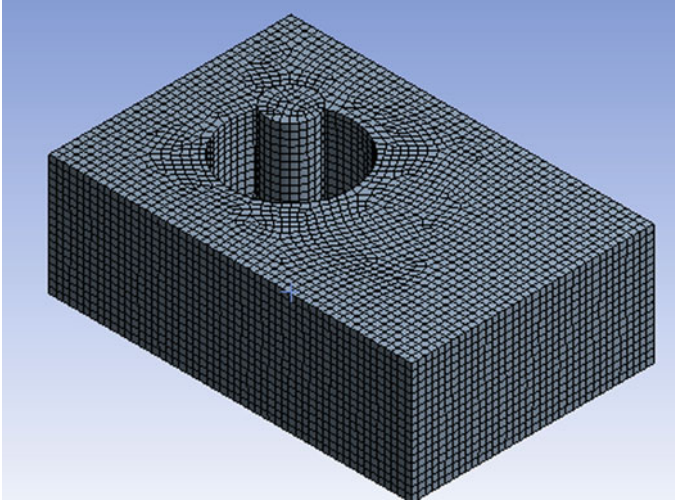
Fig. 2.2 Meshing details

Governing equations for physics of extrusion and deposition through nozzle have been solved on control volumes prescribed in meshing. Governing equations for physics of extrusion and deposition flow through the nozzle are conservation of mass $\frac{\partial u_i}{\partial z} = 0$ and the conservation of momentum $\rho \frac{\partial P}{\partial t} = -\frac{\partial p}{\partial z} + \mu \frac{\partial^2 u_i}{\partial z \partial z} + \rho g_0$. where u_i is flow velocity in z-direction, P is momentum per unit mass, p is pressure and g_0 is gravitational acceleration.

Deposition of material between a moving bed and nozzle is physically a laminar flow with viscous heating up to nozzle tip; then, material comes with the contact of moving bed and sticks on it due to wall roughness. No slip condition is considered; it means no flow velocity of deposited bottom layer adhered to bed. Therefore, bottom layer is moved with bed velocity. Flow velocity of upper surface is vectorized resultant of velocity of moving bed and flow velocity of material through nozzle. Consequently, velocity gradient of fluid flow occurs between the adhered surface and upper surface, which further generates internal shear stress. Therefore, controllable shear deformation of extruded material can be developed in the gap between nozzle tip and bed. Numerical values of parameters and material properties chosen for numerical simulation are provided in Table 2.1. The material deposition is held along a prescribed deposition path or contour. Nozzle tip and printing platform or bed are commonly made of aluminium material. Nozzle of printer works as inlet point of fluid domain. The cross section of nozzle affects shape of strand. However, in case of polymeric materials like ABS, "Barus effect", also known as extrudate swell, causes shape memory effect in extrusion of material. This diminishes effect of cross-sectional shape of nozzle to control cross-sectional shape of strand extruded through nozzle head (Tables 2.2 and 2.3).

Table 2.1   Parameters used in the numerical simulations

Parameters	Nomenclature	Values	Units
G	Gap distance	{0.16, 0.2, 0.24, 0.28, 0.32, 0.4}	mm
D	Inner diameter of the nozzle	0.4	mm
g	Normalized gap ratio (G/D)	{0.4, 0.5, 0.6, 0.7, 0.8, 0.9, 1, 1.1}	
V	Bed velocity	{10, 15, 20, 25, 30, 40}	mm/s
U	Average velocity inside the nozzle	20	mm/s
u	Normalized velocity ratio (V/U)	{0.5, 0.75, 1, 1.25, 1.5, 1, 2}	
ρ	Density of the molten material (ABS)	1040	kg/m^3
μ	Viscosity of the molten material	980	Pa s
g_0	Standard gravity acceleration	9.81	m/s^2

Table 2.2   Properties of ABS material

Properties	Value
Young's modulus	2.4×10^9 MPa
Poisson's ratio	0.35
Thermal expansion coefficient	0.1 W/m K
Density	1040 kg/m^3
Viscosity	980 kg m/s

Table 2.3   Properties of air

Properties	Value
Density	1.23 kg/m^3
Viscosity	0.35

Strands with idealized shapes like ellipse, oblong and cuboid have analytical relations between road width (W) and gap G can be derived by volume conservation equation. Flat-shaped printed strand is better to bind with strands near to it. It can be obtained by reduction in gap and printing speed. An idealized relationship strand width (W) = G is derived to obtain flat cuboid with rounded edge which is $G \leq D\sqrt{(U/V)}$. Calculation of area and road width of idealized cross-sectional shapes (ellipse, oblong, cuboid, etc.) of strands assuming that the strand thickness (H) equals the gap G.

- For oblong shape, ($G < D$)

$$\text{Area} = \left(\pi(G/2)^2 + (W - G)G\right)$$

From conservation of volume of flow,
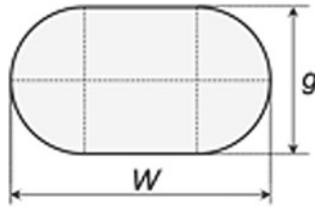
$$\text{Volume}_{\text{cylinder}} = \text{Volume}_{\text{oblong}}$$

$$W = (\pi/4)(U/V)(D^2/G) + G(1 - (\pi/4))$$

$$(W/G) = 0.785(U/V)(D/G)^2 + 0.215$$

For idealized linear relationship $W = G$,

$$G \leq D\sqrt{\left(\frac{U}{V}\right)}$$

In a gap value beyond that limit, the material would be extruded without contact with the cap of the extruder, leading to a smooth deposition on the bed without secondary flows. In that case, the strand thickness would become independent of the gap distance.

- For ellipse shape $(G > D)$,
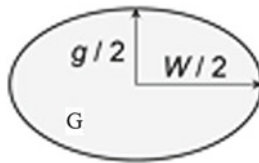
$$\text{Volume}_{\text{cylinder}} = \text{Volume}_{\text{ellipse}}$$

$$(\pi/4)D^2U = (\pi/4)GWV$$

$$W = (U/V)(D^2/G)$$

- For cuboid shape $(G < D)$
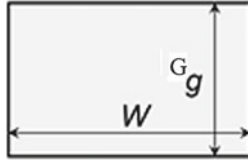
$$\text{Volume}_{\text{cylinder}} = \text{Volume}_{\text{cuboid}}$$

$$\left(\frac{\pi}{4}\right)D^2 U = WGV$$

$$W = 0.215(U/V)\left(D^2/G\right)$$

Analytically, area of cross section does not depend on gap but on velocity ratio (u). However, the shape of strand cross section is influenced by gap ratio (g) and velocity ratio.

2.2.2 Numerical Simulation

CFD deals with fluid flow and heat transfer-related problems. ANSYS Fluent solver is based on the finite volume method (FVM). Discretization of partial differential equation to get a solution in continuous form is the primary objective of FVM. Partial differential equations are discretized into a system of algebraic equations. All algebraic equations are then solved numerically to render the solution field. Domain, a region where the physical process occurs, is discretized into cell-centred control volumes [16]. Meshing is discrete representation of the geometry that is involved in the problem. Mesh generation includes various algorithms. The most challenging task is to create a mesh which comprises high-quality cells with almost least number. Higher number of cells in meshing causes redundancy in calculation and requires more computation time. Mesh convergence and independency provide optimized mesh. The selection of mesh type is based on physics involved in process. Tetrahedron mesh type is preferable in complex geometry but requires a greater number of elements and nodes in case of three-dimensional problem. In this fluid deposition simulation, hexahedral mesh type is preferred because of simple geometry problem and its own features such as low skewness, minimized numerical diffusion and better computational time due to lesser number of elements and nodes require for solution. Hexahedral meshing is generated with higher element quality. Element size is taken 0.05 mm with default growth rate 1.2 (Figs. 2.3 and 2.4).

Pressure-based transient solver is used with absolute velocity formulation. Multiphase-volume of fluid (VOF) solver model adopted with coupled level set model is taken under consideration with implicit volume fraction parameters [17].
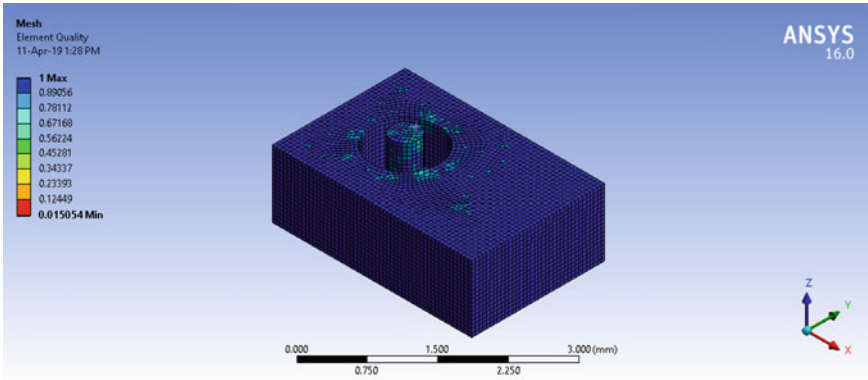
Fig. 2.3 Model with hexahedral meshing

Nozzle Head | Velocity Inlet | Stationary Wall

Moving Bed | Pressure Outlet | Final Model
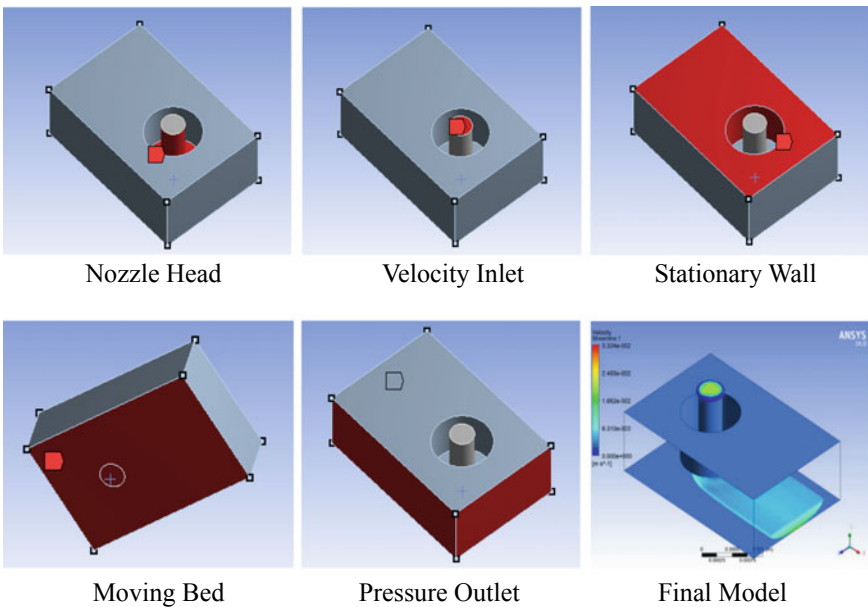
Fig. 2.4 Boundary conditions

Viscous-laminar model is included with viscous heating. Cell zone and boundary conditions with appropriate parametric values and directions are provided. Second-order implicit transient formulation with coupled pressure–velocity scheme is used to solve a discretized governing equation with assured stability. Green–Gauss node-based gradients and Presto pressure discretization for the volume fraction is used to control solution. The second-order implicit transient formulation and implicit formulation for the multiphase volume of fluid model have been executed. Flow and

```
┌─────────────────────────────────────────────┐
│          Generation of 3D model             │
└─────────────────────────────────────────────┘
                      │
                      ▼
┌─────────────────────────────────────────────┐
│        CFD analysis using ANSYS Fluent       │
└─────────────────────────────────────────────┘
                      │
                      ▼
┌─────────────────────────────────────────────┐
│       Point Cloud Extraction using MATLAB    │
└─────────────────────────────────────────────┘
                      │
                      ▼
┌─────────────────────────────────────────────┐
│  Cross-sectional shape of deposited strand   │
│  captured by using point cloud data and      │
│  CFD-Post                                     │
└─────────────────────────────────────────────┘
                      │
                      ▼
┌─────────────────────────────────────────────┐
│      Strand thickness and width as a          │
│      function of the printing parameters      │
└─────────────────────────────────────────────┘
```
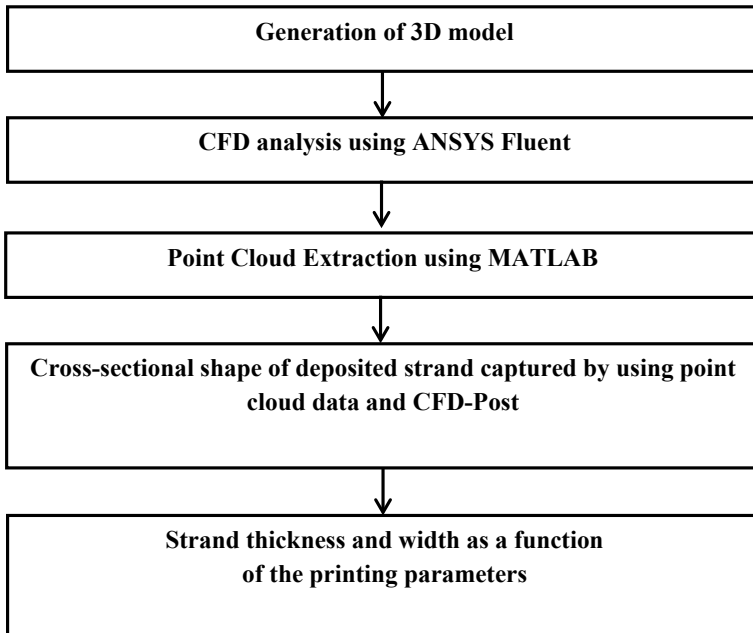
Fig. 2.5 Methodology process flow

volume fraction courant number should have appropriate minimum value to control solution. The courant number should be low up to 0.25 with specified about max 20 iterations per time step 0.01, with the default convergence criteria. Convergence can be improved by tuning the relaxation factor for the pressure and momentum between 0.8 and 0.5. Cross sections of deposited fluid can also be captured in CFD-post by generation of streamlines of fluid flow. The velocities, pressure, local temperature and positions with point cloud are saved in a comma-separated value file to transfer this calculated data into MATLAB for further numerical analysis. The methodology adopted to conduct the study is shown in (Figs. 2.5 and 2.6).

2.3 Results and Discussions

2.3.1 Morphology of Deposited Strands

The information of shape is evaluated in MATLAB for surface generation using point cloud. Volumetric conversation causes the equal volumetric flow rate of the material deposited on the bed and flowed through a cylindrical nozzle, $A_s = A_n(U/V)$ (Fig. 2.7).

Geometrical Modelling

Streamlines of flow

**Extraction of point cloud
Data and surface generation**

Generation of Point Clouds
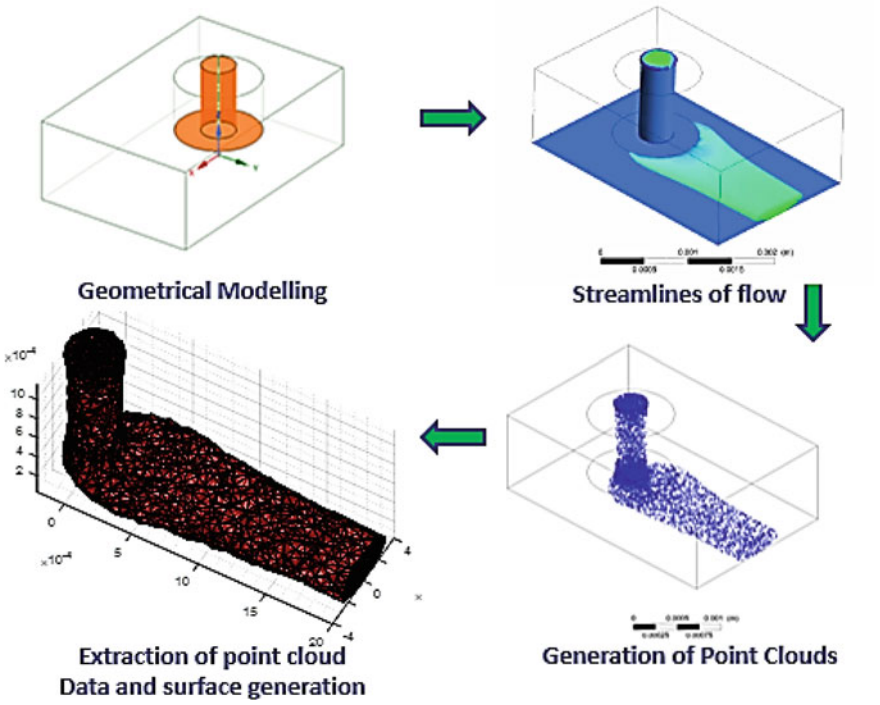
Fig. 2.6 Methodology
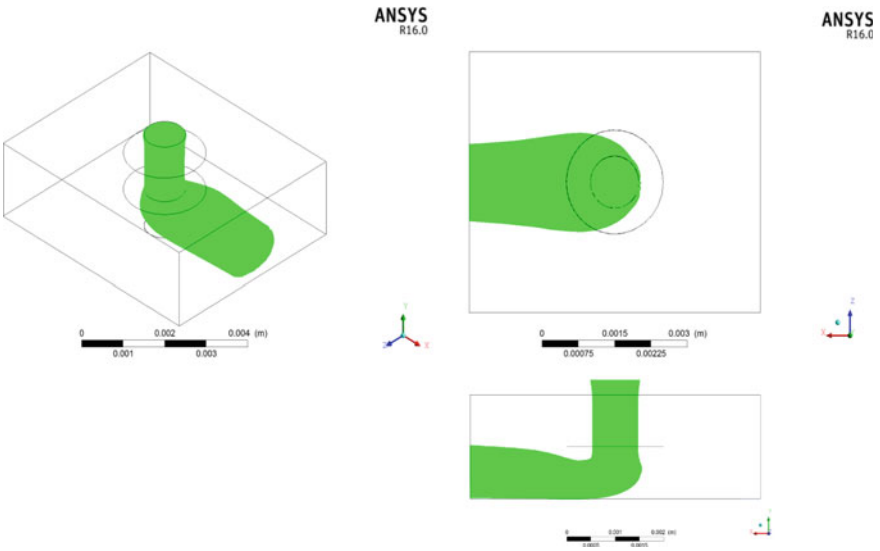
Fig. 2.7 Streamlines generation of thermo-plastic material flow

Streamline of flow is generated in CFD-post. CFD-post comprises various plots with user location. Streamline generation has been done to visualize flow behaviour and to accomplish further post-processing. Point cloud data has been extracted by using streamline as location plot to transfer result into computational geometry domain. Computational geometry encompasses various algorithmic approaches, like triangulation, bounding regions, Voronoi diagrams, etc., which can be specified in terms of geometry. These streamlines are drawn by considering velocity variable in such way that it started from inlet velocity boundary condition to all domains with equally spaced sampling method. The number of preview seed points is 3000, and velocity is considered as variable to draw streamline (Fig. 2.8).

After exporting the ANSYS Fluent results from CFD-post in comma-separated value file format (.csv), this file was imported with spatial coordinates into a MATLAB script. Maximum number of point cloud to be generated can be controlled in CFD-Post by different sampling methods provided. Vertex sampling method has been applied with reduction factor 1, so that point cloud generation can be uniform and global. Point cloud was generated in ANSYS and plotted in MATLAB through above methodology are shown in Figs. 2.9 and 2.10.

A program has been developed for converting point clouds into respective triangular surfaces which are given in figure. As described above, point clouds got from previous stage are imported into a MATLAB script using comma-separated value file. Point cloud is evaluated using Bounding regions, and value of shrink factor is
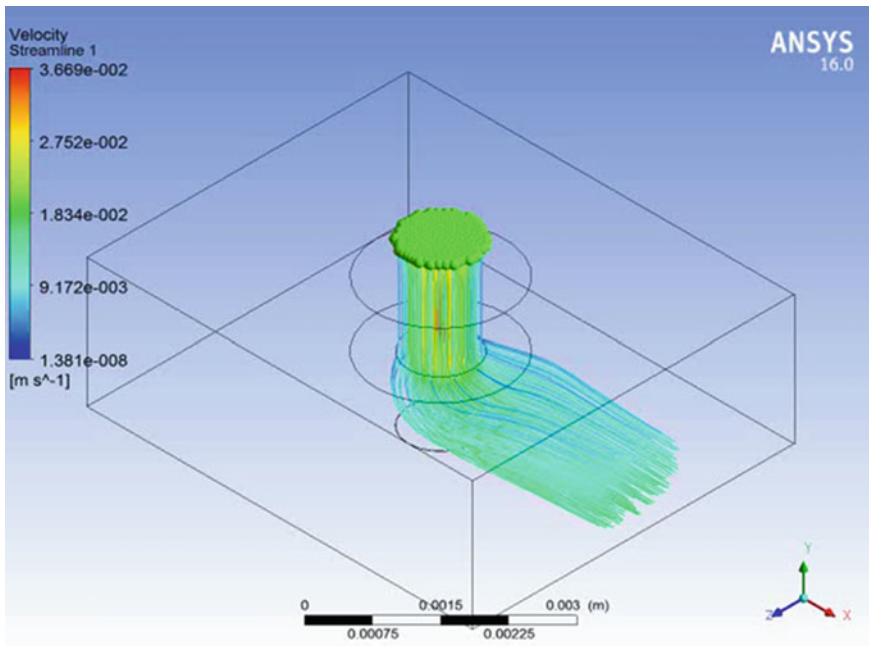
Fig. 2.8 Streamlines of material deposition flow
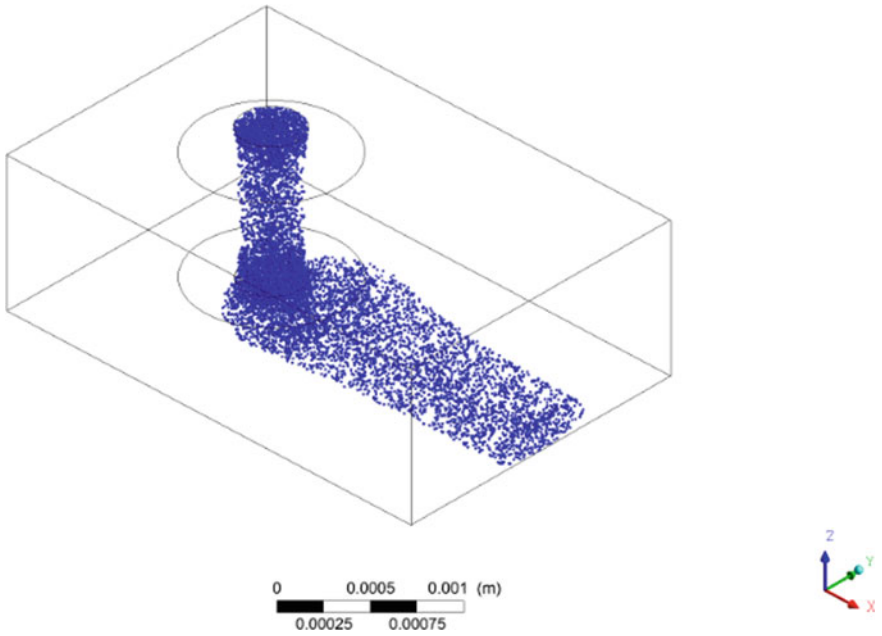
Fig. 2.9 Point cloud in ANSYS fluent
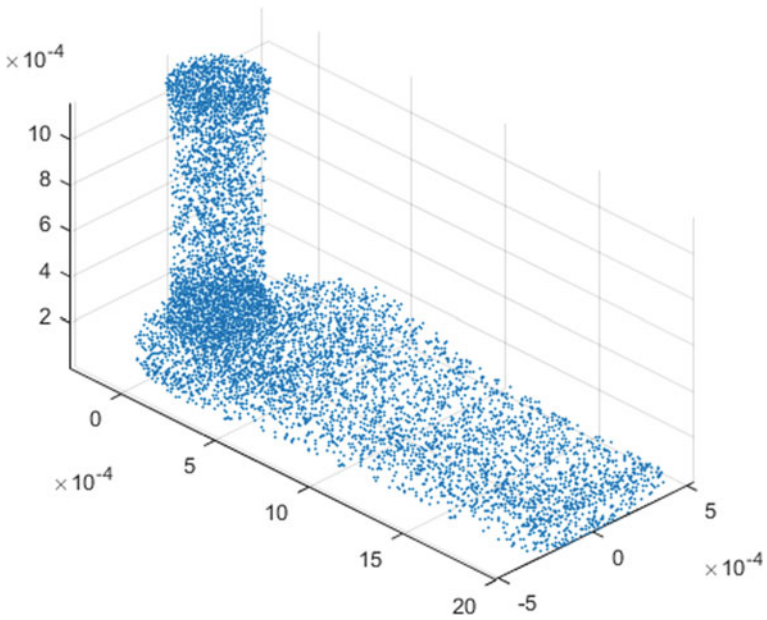
Fig. 2.10 Plotting of point cloud in MATLAB

entered. Shrink factor pretrains the concavity and its value ranges form 0 to 1. Shrink factor value zero corresponds to convex shape and as the value is increased shape transformed from convex to concave. After entering the suitable value of shrink factor, mesh is generated using Delaunay triangulation (DT).

Flat-shaped strand is desirable to get bonding with adjacent strands which can be obtained by a reduction in gap and deposition speed. Different shapes obtained at different process conditions are shown in Fig. 2.8.

2.3.2 Functional Relationship

The normalized width ratio (*W/D*) and normalized thickness ratio (*H/D*) of a deposited strand are plotted with gap ratio (*G/D*) as a function of fabrication parameters. The strand aspect ratio (*W/H*) of cross-sectional shape is also evaluated with gap ratio. Same parameters for idealized shapes like ellipse, cuboid and oblong are also presented with deposited strand cross-sectional shapes in order to perform the comparison. The obtained results are presented in Figs. 2.9, 2.10 and 2.11 (Figs. 2.12 and 2.13).

In this graph, different velocity ratio values are considered that are of obtained shape and of idealized shape like ellipse, oblong and rectangular shapes with rounded corner. Then, various gap ratios have been involved with velocity ratios, for drawing graph for strand dimensions. In Fig. 2.14, strand width as a function of the printing parameters has been plotted and with every idealized cross-sectional shape, thickness is taken as equal to gap. For this reason, in graph for strand thickness and normalized
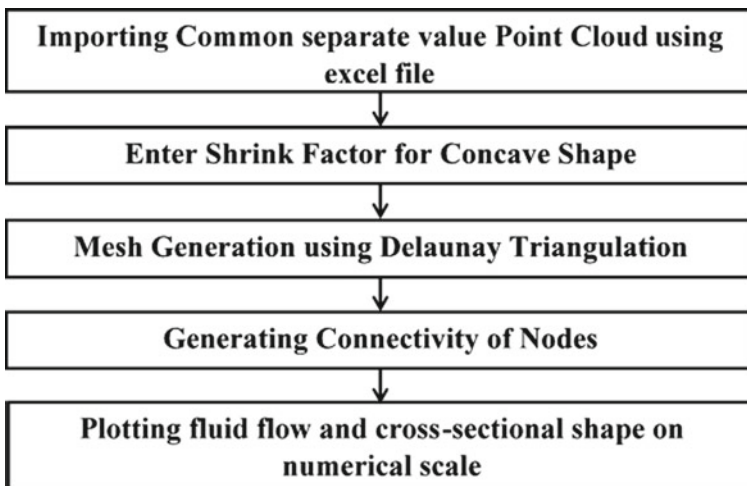
Fig. 2.11 Methodology for point cloud to surface generation
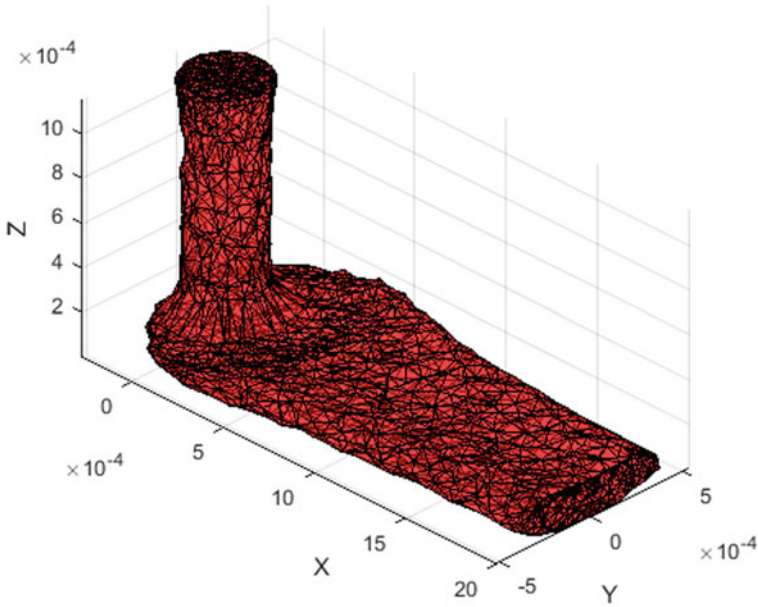
Fig. 2.12 Surface generation of material deposition flow using bounding region

gap ratio, line for idealized shapes is a straight line. In Fig. 2.16, aspect ratio of the strand as a function of the printing parameters has been drawn (Fig. 2.15).

2.4 Conclusion

Numerical investigation on material deposition was performed in fused filament fabrication using computational fluid dynamics. The shape of deposited strands was evaluated under different processing conditions as it can affect the part quality in terms of surface roughness and strength. Strand width, thickness and aspect ratios were plotted as a function of fabrication parameters. Strands having aspect ratio nearly 1 had flatness, nearly oblong and rectangular shape with rounded corner. High normalized velocity and gap ratios caused a reduction in strand width and thickness. Low deposition speed and low gap ratio led to side flow and increased strand width and thickness. The cylindrical cross section was obtained for high deposition speed with large gap ratio, whereas a flat cuboid with rounded corner for low deposition speed and less gap ratio.
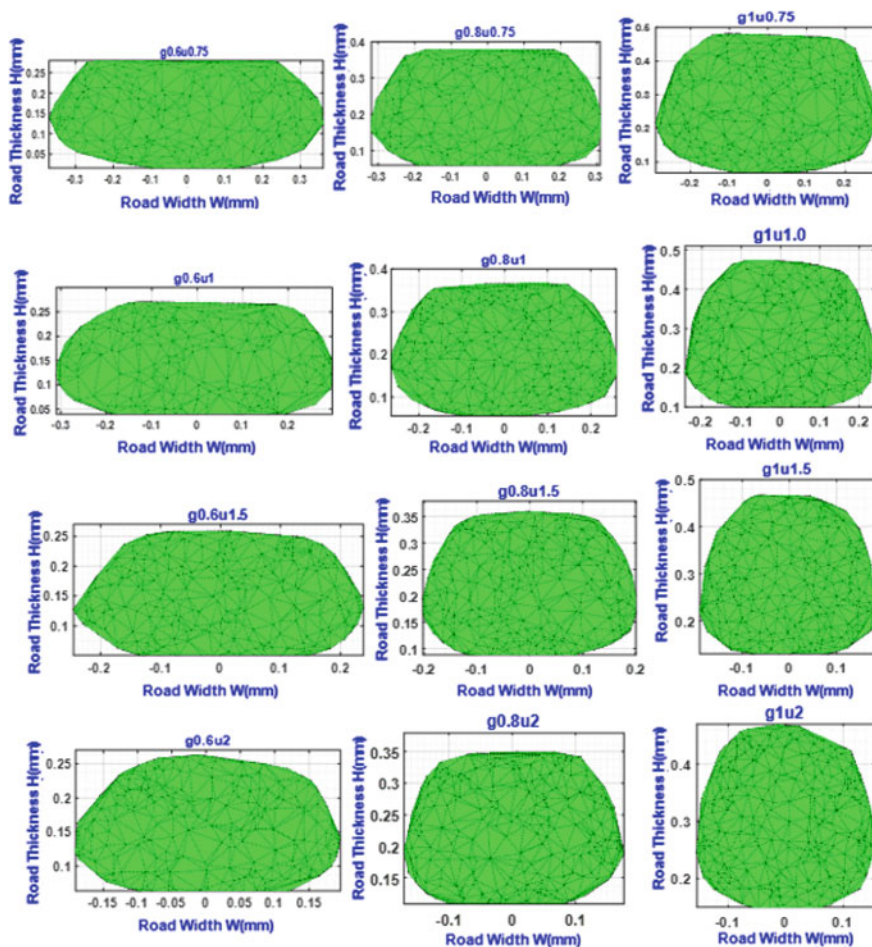
Fig. 2.13 Cross sections of the strands for various printing parameters
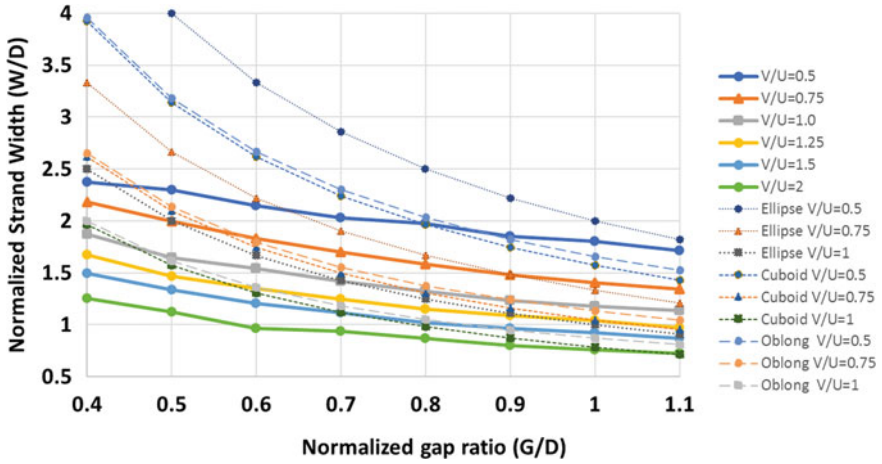
Fig. 2.14 Strand width as a function of printing parameters
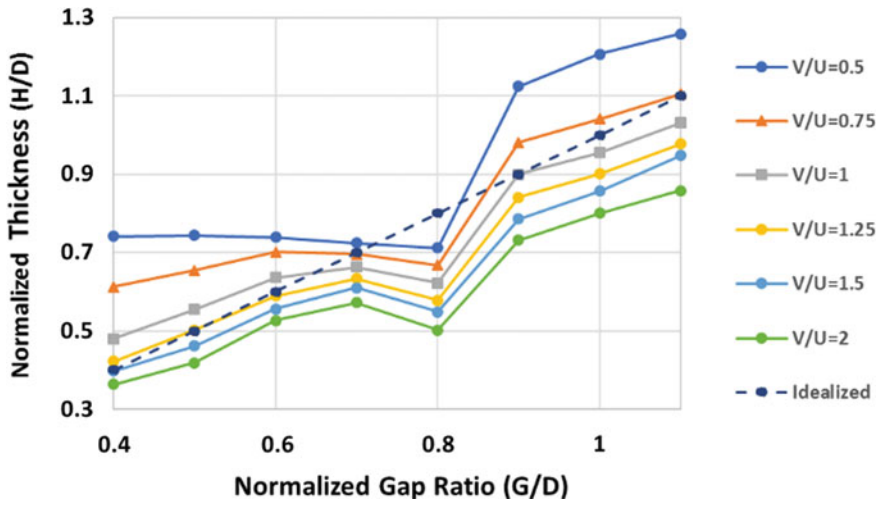
Fig. 2.15 Strand thickness as a function of printing parameters
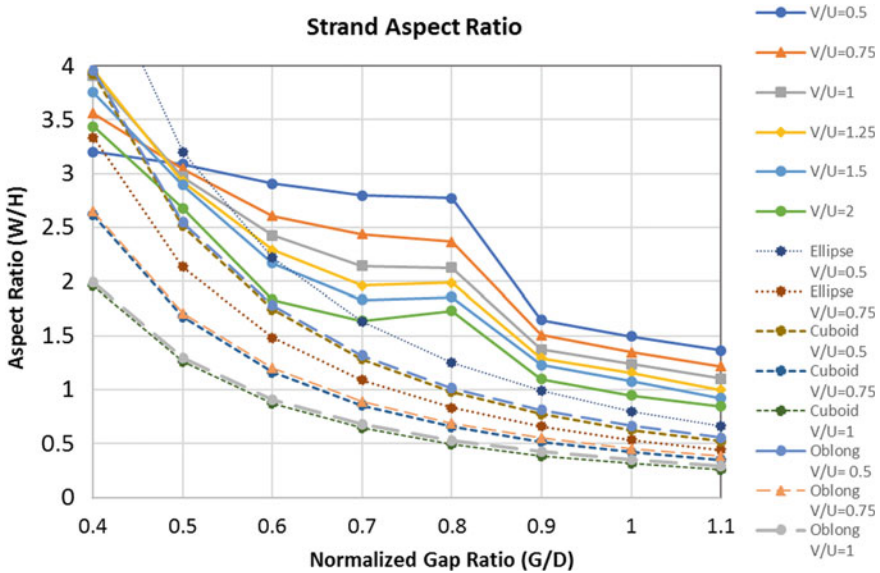
Fig. 2.16 Strand aspect ratio as a function of printing parameters

References

1. Turner, B.N., Strong, R., Gold, S.A.: A review of melt extrusion additive manufacturing processes: I. Process design and modeling. Rapid Prototyp. J. **20**, 192–204 (2014). https://doi.org/10.1108/rpj-01-2013-0012

2. Kumar, N., Jain, P.K., Tandon, P., Pandey, P.M.: Investigation on the effects of process parameters in CNC assisted pellet based fused layer modeling process. J. Manuf. Process. **35**, 428–436 (2018). https://doi.org/10.1016/j.jmapro.2018.08.029

3. Kumar, N., Jain, P.K., Tandon, P., Pandey, P.M.: The effect of process parameters on tensile behavior of 3D printed flexible parts of ethylene vinyl acetate (EVA). J. Manuf. Process. **35**, 317–326 (2018). https://doi.org/10.1016/j.jmapro.2018.08.013

4. Sun, Q., Rizvi, G.M., Bellehumeur, C.T., Gu, P.: Effect of processing conditions on the bonding quality of FDM polymer filaments. Rapid Prototyp. J. **14**, 72–80 (2008). https://doi.org/10.1108/13552540810862028

5. Fernandez-Vicente, M., Calle, W., Ferrandiz, S., Conejero, A.: Effect of infill parameters on tensile mechanical behavior in desktop 3D printing. 3D Print. Addit. Manuf. **3**, 183–192 (2016). https://doi.org/10.1089/3dp.2015.0036

6. Taufik, M., Jain, P.K.: A study of build edge profile for prediction of surface roughness in fused deposition modeling. J. Manuf. Sci. Eng. **138**, 1–11 (2016). https://doi.org/10.1115/1.4032193

7. Yardimci, M.A., Guceri, S.I., Agarwala, M., Danforth, S.C.: Part quality prediction tools for fused deposition processing. Proc. Solid Free. Fabr. Symp. **7**, 539–548 (1996)

8. Bellehumeur, C., Li, L., Sun, Q., Gu, P.: Modeling of bond formation between polymer filaments in the fused deposition modeling process. J. Manuf. Process. **6**(2), 170–178 (2004)

9. McIlroy, C., Olmsted, P.D.: Disentanglement effects on welding behaviour of polymer melts during the fused-filament-fabrication method for additive manufacturing. Polymer (Guildf) **123**, 376–391 (2017)

10. Favaloro, A.J., Brenken, B., Barocio, E., Pipes, R.B.: Simulation of polymeric composites additive manufacturing using Abaqus. Sci. Age Exp. 103–114 (2017)

11. Rodríguez, J.F., Thomas, J.P., Renaud, J.E.: Mechanical behavior of acrylonitrile butadiene styrene fused deposition materials modeling. Rapid Prototyp. J. **9**(4), 219–230 (2003)
12. Costa, S.F., Duarte, F.M., Covas, J.A.: Thermal conditions affecting heat transfer in FDM/FFE: a contribution towards the numerical modelling of the process: This paper investigates convection, conduction and radiation phenomena in the filament deposition process. Virtual Phys. Prototyp. **10**(1), 35–46 (2015)
13. Ahn, D.K., Kwon, S.M., Lee, S.H.: Expression for surface roughness distribution of FDM processed parts. In: ICSMA 2008—International Conference on Smart Manufacturing Application, Dec, pp. 490–493 (2008)
14. Li, L., Sun, Q., Bellehumeur, C., Gu, P.: 25. Composite modeling and analysis of FDM prototypes for design and fabrication of functionally graded parts. Solid Free. Fabr. Proc. 187–194 (2001)
15. Bellini, A.: Fused deposition of ceramics: a comprehensive experimental, analytical and computational study of material behavior, fabrication process and equipment design. In: Ph.D. thesis, Drexel University, 2002., vol. 427, no. 1–2 (1999)
16. Zhang, J., Wang, X.Z., Yu, W.W., Deng, Y.H.: Numerical investigation of the influence of process conditions on the temperature variation in fused deposition modeling. Mater. Des. **130**, 59–68 (2017). https://doi.org/10.1016/j.matdes.2017.05.040
17. Sussman, M., Puckett, E.G.: A coupled level set and volume-of-fluid method for computing 3D and axisymmetric incompressible two-phase flows. J. Comput. Phys. **162**(2), 301–337 (2000)

Chapter 3
An Experimental Investigation on Fabricating Objects for Origami Applications Through Fused Filament Fabrication (FFF)

Check for updates

Jitesh Katre and Prashant K. Jain

Abstract The current paper explores the potential of FFF process to fabricate objects for origami applications. Origami is a Japanese art in which a paper is converted into 3D object with the help of folding pattern. The foldability of any object depends on the material used at the joint. Object made with rigid materials completely cannot be folded. Therefore, flexible material can be introduced at the joints to be folded along with the hard plastic for rigid panel. In order to make a high-quality foldable structure, junction of flexible and rigid materials should have enough strength. In this paper, some structures have been fabricated with different joining profiles, and then, their mechanical strength is tested using ultimate tensile testing apparatus. PLA and TPU materials have been used as rigid and flexible materials, respectively. Based on the obtained results, a foldable object has been prepared in order to show the application of FFF process in origami.

Keywords Fused filament fabrication (FFF) · Origami · Polylactic acid (PLA) · Thermoplastic polyurethane (TPU)

3.1 Introduction

Among the various types of additive manufacturing (AM) processes, FFF is a widely used process due to its capabilities of complex parts fabrication in short time without using any specific tooling and fixtures [1]. It is an extrusion-based AM process, in which the semi-molten material is deposited on a build platform in the form of thin roads. The road deposition process continues till the final part is fabricated. A variety of materials are available for this process, i.e., PLA, TPU, acrylonitrile butadiene styrene (ABS), and nylon which are used in different applications [2]. The major applications include biomedical, electronics, shoe, aerospace, and automobile in which the potential of FFF has been explored. In order to utilize parts in these

---

J. Katre (✉) · P. K. Jain

Mechanical Engineering Discipline, PDPM Indian Institute of Information Technology, Design and Manufacturing, Jabalpur 482005, India

e-mail: jkatre001@gmail.com

applications, part quality has been traded off using parametric optimization. Most of the studies have been reported on the optimization of process parameters in which single material was considered such as PLA, ABS, and nylon depending on the targeted applications [3]. Lanzotti et al. considered the impact of layer thickness, raster angle, and number of shells on the rigidity of 3D printer printed PLA part [4]. They found that rigidity decreases with an addition in raster angle toward 90°, while higher rigidity at a lower estimation of layer thickness has been obtained. Huang et al. built an analytical model for elastic stress, strain, and moduli for FDM-printed part utilizing plane stress approach [5]. They found that tensile strength decreases with increasing raster angle, least tensile strength accomplished at 70° to 90° raster angle. For PLA parts maximum rigidity occurs at 0° raster angle followed by 45°, and 90° raster angle [6]. They additionally observed that crack way is subjected to the directionality of the raster and strength of individual layers. Kumar et al. studied the effect of process parameter on fabrication of flexible parts using CNC-assisted pellet-based extrusion machine [7, 8]. They observed that as raster angle increases, tensile strength decreases and increases with the increase in barrel temperature.

Reported literature shows that most of the studies were focused on tensile strength of specimen fabricated using single material. Nowadays, research on dynamic origami is in trend in which a thin sheet is converted into 3D structure without using any external tool. Origami structures can be made using the combination of flexible and relatively rigid materials. Flexible materials can be used at joints as it can enable folding of different panels presented in origami. However, panel can be made using relatively rigid materials. It means that strength at the junction of flexible and rigid parts should be enough to sustain its shape for long time. FFF can be utilized to fabricate origami as it can deal with the range of different materials. Nowadays, the range of flexible and relative rigid materials is available for use in FFF process, which may enable the fabrication of origami. Therefore, the current study explores the origami fabrication through FFF in which PLA and TPU materials are used for fabrication of rigid and flexible portions of origami. Before origami fabrication, the study analyzes the strength of four different types of joints. On the basis of strength criteria, process parameters and design of joint have been selected for origami fabrication.

3.2 Experimental Details

3.2.1 Materials

Two different materials have been incorporated for the specimen fabrication, i.e., TPU and PLA. Compared to PLA, TPU is more flexible, so it can be used at joints, and PLA is a relatively rigid material, and hence, it can be used for panel fabrication.
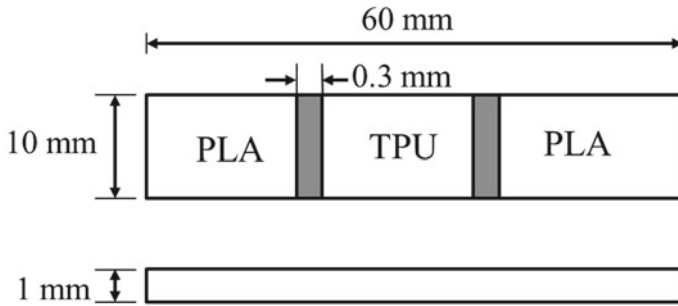
Fig. 3.1 Drawing of joint for preliminary experimentation

3.2.2   Printing Method

AM does not provide any specific tool for the joining of two dissimilar materials; in the case of similar materials, they join because both of them possess similar properties. Nowadays, dissimilar materials can be joined with the help of overlapping provided between materials. At the time of solid modeling, it has been considered that two dissimilar materials should overlap at 0.3 mm. In this type, TPU is used for flexible joints and PLA is used for rigid panel. Figure 3.1 shows the drawing of joint for preliminary experimentation.

3.2.3   Preliminary Experimentation

Some preliminary experimentation has been performed on the joining of two dissimilar materials, i.e., TPU and PLA. Figure 3.1 shows the drawing of joint which can be used for initial experimentation. TPU is incorporated between PLAs, to provide flexibility at joint. Figure 3.2 shows the fabricated specimen with the help of FFF,

Fig. 3.2 Fabricated part joins with dissimilar material

Table 3.1 Standard process parameters for PLA and TPU

S. No.	Parameters	TPU	ABS
1	Extrusion temperature (°C)	220	220
2	Bed temperature (°C)	80	105
3	Infill percentage (%)	25	20
4	Layer height (mm)	0.15	0.15
5	Travel speed (mm/s)	50	80

and Table 3.1 shows the standard printing process parameters for PLA and TPU.

It is observed that the joining of two dissimilar materials is accomplished but strength is poor. FFF does not provide any specific tool for the joining of two dissimilar materials. For proper joining, selection of printing process parameters plays a key role.

3.2.4 Experimental Design for Specimen Fabrication

The primary target of the present work is to study the tensile properties of the multi-material FFF-printed specimens for possible applications in origami structures. In order to fabricate specimen, a rectangular strip made of two different materials is considered, as appeared in Fig. 3.3.

The raster angle and layer thickness have been varied along with the design of joints as given in Table 3.2, and their effects have been observed on the tensile strength of joints printed with two dissimilar materials. The raster angle and layer thickness have been changed at three levels, and the design of joints has been shifted
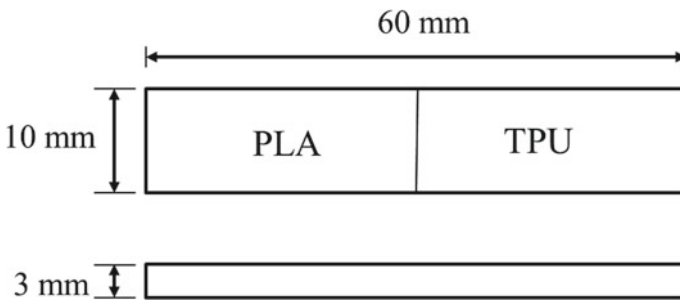
Fig. 3.3 Rectangular strip for tensile testing

Table 3.2 Process parameters and their levels

Parameters	Unit	Levels
Raster angle	Degree (°)	0, 45, 90
Layer height	Mm	100, 200, 300

Table 3.3 Constant process parameters

Parameters	Value
Nozzle temperature	PLA—210 °C, TPU—220 °C
Platform temperature	60 °C
Print speed	60 mm/s
Raster width	0.4 mm
No. of shells	1
Infill percentage	100%
Material	PLA, TPU

Table 3.4 All possible combinations for single joint

S. No.	Raster angle (°)	Layer thickness (mm)
1	0	0.1
2	0	0.2
3	0	0.3
4	45	0.1
5	45	0.2
6	45	0.3
7	90	0.1
8	90	0.2
9	90	0.3

at four levels. After taking all possible mix of process parameters, complete 36 trials have been performed and the whole arrangement of trials have been performed twice. Table 3.4 shows all possible combinations of single specimen. CAD model of specimen has been created in SolidWorks 2012 and saved as STL file. This STL file is exported in FlashPrint 3.25.1, which is dedicated slicing software for FlashForge CreatorPro to find the tool path and selection of all suitable printing process parameters; it converts STL file into .x3g. Utilizing PLA and TPU filament, all specimens were printed using constant process parameters as appeared in Table 3.3 with Flash-Forge CreatorPro Dual Extruder FFF printer. It has a volume chamber of 227 × 148 × 150 mm with nozzle diameter of 0.4 mm (Figs. 3.4 and 3.5).

3.2.5   Tensile Testing

To observe tensile properties, test has been performed by using Tinius Olsen H25KS universal testing machine as shown in Fig. 3.6. The machine has a capacity of 25 KN. A dedicated software Horizon programming permits to control, screen, and record estimation information. The crosshead speed has been kept up at 1 mm/min
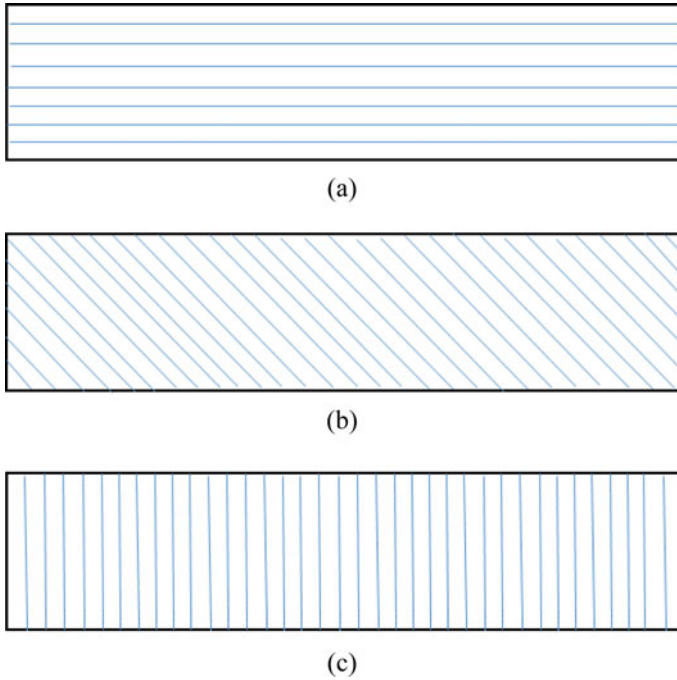
Fig. 3.4 Schematic representation of raster angles: **a** 0°; **b** 45°; **c** 90°

for specimen, and gauge length is taken as 30 mm [9]. The crosshead movement proceeds until the part breaks from joint while running out the test.

3.3   Results and Discussion

Figure 3.7 shows the effect of raster angle and layer thickness on type 1 joint. It is shown that maximum tensile strength 7.01 MPa is observed at 0° raster angle at 0.10-mm layer thickness. Minimum tensile strength 4.98 MPa occurs at 90° raster angle with layer thickness of 0.3 mm. From this result, it is observed that as layer thickness increases, tensile strength reduces.

From Fig. 3.8, it is shown that 0° raster angle with layer thickness of 0.1 mm has maximum tensile of 7.99 MPa, while minimum tensile strength occurs at 90° raster angle with layer thickness of 0.1 mm, i.e., 6.86 MPa. It is observed that as raster angle decreases from 90° to 0°, tensile strength increases [5].

Similarly, Fig. 3.9 shows the effect of raster angle on tensile strength of type 3 sample. It is seen that 10.1 MPa maximum tensile strength occurs at 0° raster angle with 0.1-mm layer thickness; on the other hand, minimum tensile strength 8.23 MPa occurs at 90° raster angle with 0.3-mm layer thickness. It is observed
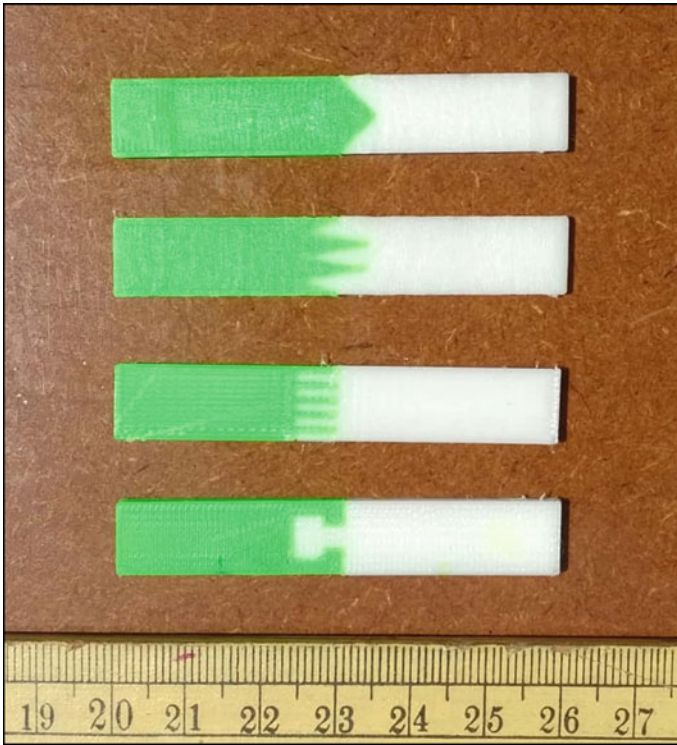
Fig. 3.5 3D printed specimens with different types of joints

that as surface contact area between two material increases, tensile strength also increases. Increasing surface contact area is the key to design the samples [10].

In Fig. 3.10, tensile strength of type 4 sample is calculated. Minimum tensile strength is observed at 45° raster angle with layer thickness of 0.3 mm, i.e., 6.8 MPa, while maximum tensile strength 8.9 MPa is observed at 0° raster angle with layer thickness of 0.1 mm. It is concluded that due to its design, minimum tensile strength is observed at 45° [11].

From Figs. 3.7, 3.8 and 3.9, it can be expressed that 0° raster angle shows maximum tensile strength in all types of joints. In most of the cases, tensile strength decreases for all values of layer thickness as raster angle decreases from 90° to 0°. It might be seen that parts with 0° raster angle have all layers parallel to the loading direction. As raster was kept parallel to loading direction, then each raster takes equal load; it minimizes the failure rate of the fabricated part; hence, maximum tensile occurs at 0° raster angle. On the other hand, rasters with 90° angle align perpendicular to the loading direction. Failure occurs due to adhesion bonding between rasters [3]. When tensile load is applied on specimen printed with 90° raster angle, the stress concentration in the narrow place of intra-layer bond location causing into the delamination of layers from bonded place. That is why, minimum tensile strength

Fig. 3.6 Tinius Olsen H25KS universal tensile testing machine
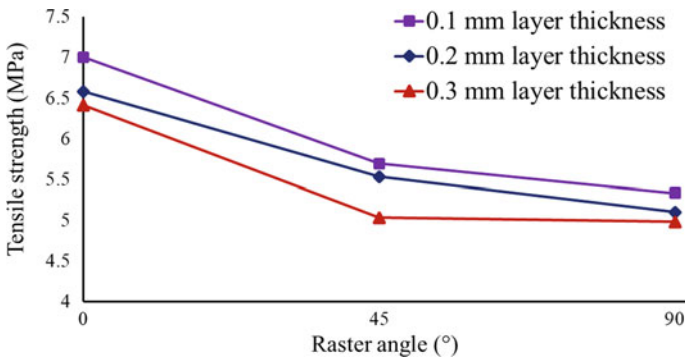
Fig. 3.7 Effect of raster angle on tensile strength of type 1 sample

occurs for 90° raster angle, while in the case of 45°, failure occurs due to shear failure between rasters [12] and along the direction of raster. Table 3.5 shows the obtained maximum and minimum values of tensile strength of each type of joint. It might be seen that maximum tensile strength is observed at 0.1-mm layer thickness. At 0.1-mm layer thickness, maximum bonding area is observed between rasters [13]. As layer thickness is minimized, extruder applies pressure on that layer; due to that bonding,
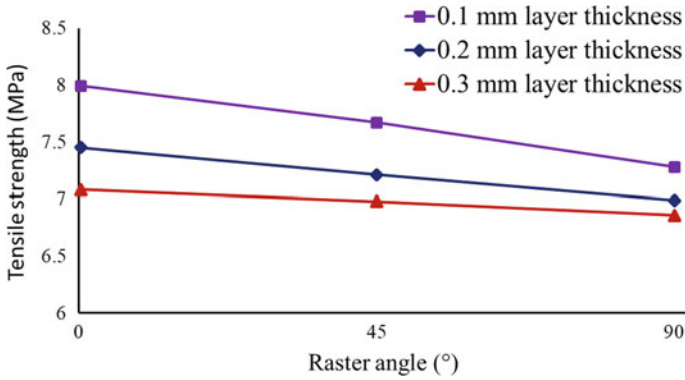
Fig. 3.8   Effect of raster angle on tensile strength of type 2 sample
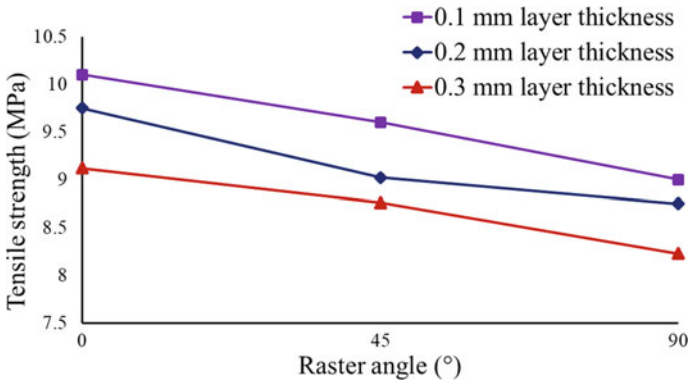
Fig. 3.9   Effect of raster angle on tensile strength of type 3 sample
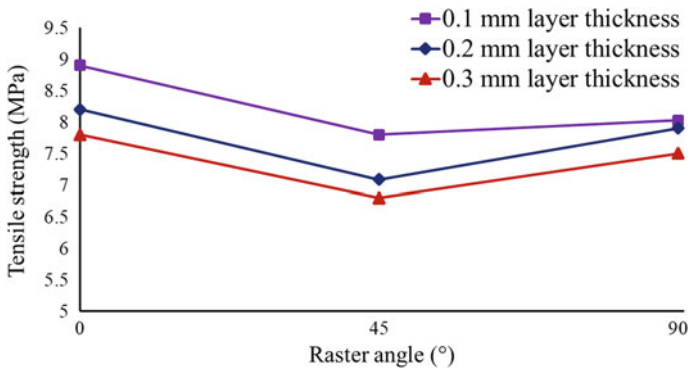
Fig. 3.10   Effect of raster angle on tensile strength of type 4 sample

Table 3.5 Maximum and minimum tensile strength of joints at different parameters

Type		Tensile strength (MPa)	Raster angle (°)	Layer thickness (mm)
Type 1	Max	7.01	0	0.1
	Min	4.98	90	0.3
Type 2	Max	7.99	0	0.1
	Min	6.86	90	0.3
Type 3	Max	10.1	0	0.1
	Min	8.23	90	0.3
Type 4	Max	8.9	0	0.1
	Min	6.8	45	0.3

strength between layers has been maximized; it results in higher tensile strength. All joints are designed in such a way to increase surface contact area between two materials, and it results in maximizing the tensile strength.

From the experimentation, it is observed that type 1–3 joints break from the region of the joining of two dissimilar materials, but in type 4 joint, breaking has not occurred at the joining region. Due to loading elongation is occurred at TPU side and due to that necking is occurred and it is breaking as shown in Fig. 3.11. Type 4 joint is the
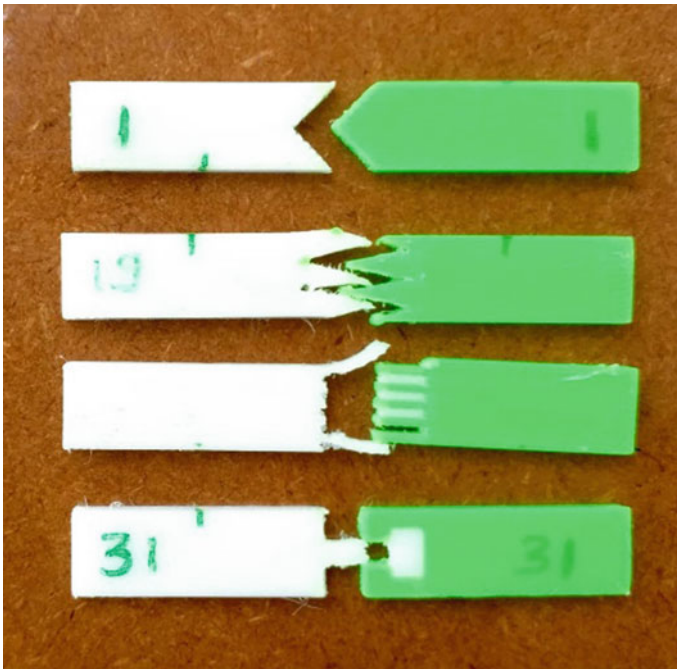
Fig. 3.11 Fractured 3D printed specimen

most successful joint among four, but it differs in tensile strength. That is why, type 3 joint is used for fabrication of origami in the future.

3.4   Additive Manufacturing of Origami

On the basis of above parameters, origami structure has been fabricated with the help of FlashForge CreatorPro 3D printer.

3.4.1   Cube

From the above results, it is shown that raster angle 0° with layer thickness 0.1 mm in type 3 joint shows maximum tensile strength. Therefore, test specimen of origami structure is fabricated using these parameters. Developed faces of cube were considered as specimen and were printed using PLA, whereas TPU was used to join two faces together. Later on, the printed specimen was converted into 3D cube. The application of these kinds of structures can be in the fabrication of high-frequency antenna sensors [14] (Fig. 3.12).

(a)   (b)
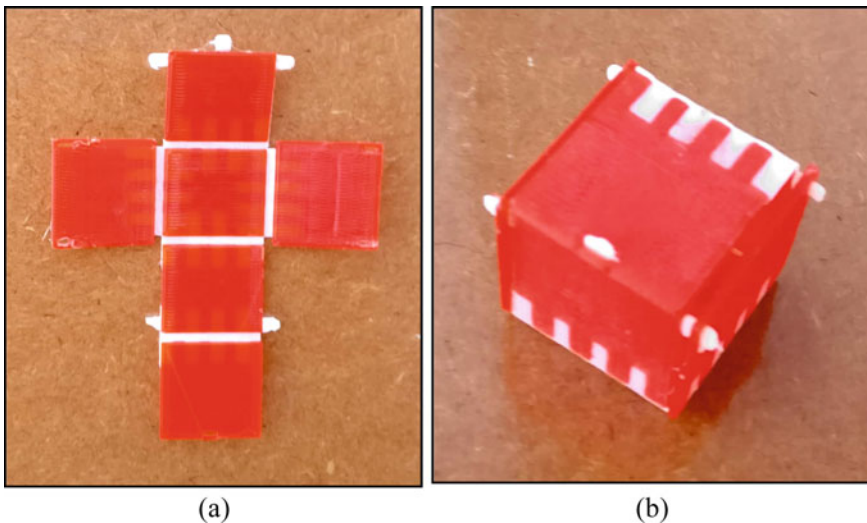
Fig. 3.12   a Fabricated part with best suitable process parameters and **b** final shape of fabricated part
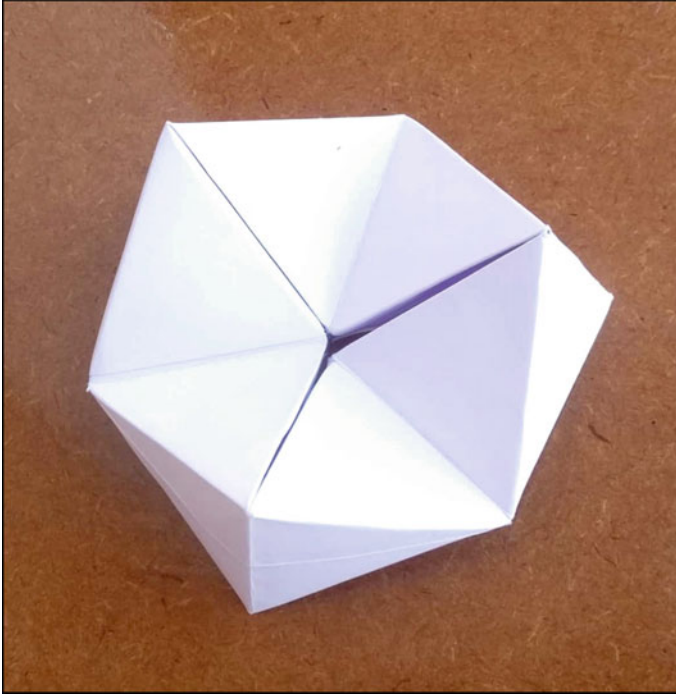
Fig. 3.13 Flexagon made from paper

3.4.2 Flexagon

Initially, Arthur H. Stone fabricates flexagon using paper, by folding strips of paper. Flexagon is a flat model that can be folded in such a way to reveal faces besides that were originally on the front and rear [15]. Flexagons has sometimes square or rectangular (tetraflexagons) or hexagonal (hexaflexagons). A prefix can be added to the name to indicate the number of faces that the model can display, including the two faces (back and front) that are visible before folding. For example, a flexagon with a six number of faces is named a hexaflexagon. Figure 3.13 shows a flexagon made from paper. This flexagon has six tetrahedrons; to fulfill that a CAD model of body of flexagon has been developed as appeared [16], hinges of TPU have been provided for proper folding. Figure 3.14 shows fabricated flexagon by FFF.

3.5 Conclusions

From the above experimentation, it is concluded that the highest tensile strength of multi-material printed part is dependent upon mainly layer thickness and raster
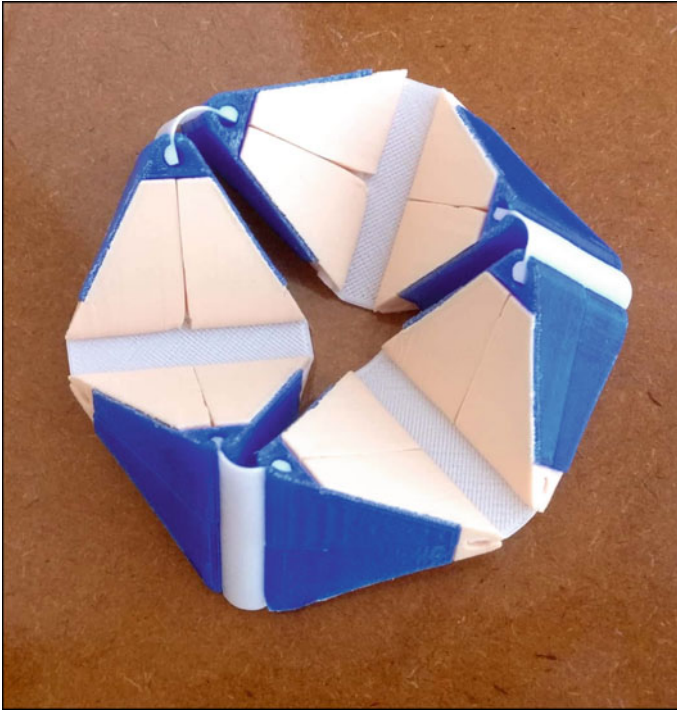
Fig. 3.14 Flexagon made from 3D printing

angle. Maximum tensile strength is obtained at 0° raster angle, while minimum tensile strength occurs at 90° raster angle in most of the cases. As layer thickness increases, then bonding area between rasters decreases; hence, the lower tensile occurs at 0.3-mm layer thickness; in lower layer, thickness bonding area is larger as compared to higher layer thickness, so maximum tensile strength occurs at 0.1-mm layer thickness. As surface contact area between two materials increases, then tensile strength also increases. The result of current study may be used to fabricate self-deployable structures for space exploration.

References

1. Shaikh, S., Kumar, N., Jain, P.K., Tandon, P.: Hilbert curve based toolpath for FDM process. CAD/CAM. Robotics A 751–759 (2016). https://doi.org/10.1007/978-81-322-2740-3_72
2. Song, Z., Ma, T., Tang, R., Cheng, Q., Wang, X., Krishnaraju, D., Panat, R., Chan, C.K., Yu, H., Jiang, H.: Origami lithium-ion batteries. Nat. Commun. **5**, 1–6 (2014). https://doi.org/10.1038/ncomms4140

3. Chacón, J.M., Caminero, M.A., García-plaza, E., Núñez, P.J.: Additive manufacturing of PLA structures using fused deposition modelling: effect of process parameters on mechanical properties and their optimal selection. Mater. Des. **124**, 143–157 (2017). https://doi.org/10.1016/j.matdes.2017.03.065

4. Lanzotti, A., Grasso, M., Staiano, G., Martorelli, M.: The impact of process parameters on mechanical properties of parts fabricated in PLA with an open-source 3-D printer. Rapid Prototyp. J. **21**, 604–617 (2015). https://doi.org/10.1108/RPJ-09-2014-0135

5. Huang, B., Singamneni, S.: Raster angle mechanics in fused deposition modelling. J. Compos. Mater. **49**, 363–383 (2014). https://doi.org/10.1177/0021998313519153

6. Ziemian, S., Okwara, M., Ziemian, C.W., Ziemian, S., Okwara, M., Ziemian, C.W.: Tensile and fatigue behavior of layered acrylonitrile butadiene styrene. Rapid Prototyp. J. **21**, 270–278 (2015). https://doi.org/10.1108/RPJ-09-2013-0086

7. Kumar, N., Jain, P.K., Tandon, P., Mohan, P.: The effect of process parameters on tensile behavior of 3D printed flexible parts of ethylene vinyl acetate (EVA). J. Manuf. Process. **35**, 317–326 (2018). https://doi.org/10.1016/j.jmapro.2018.08.013

8. Kumar, N., Jain, P.K., Tandon, P., Pandey, P.M.: 3D printing of flexible parts using EVA material. Mater. Phys. Mech. **37**, 124–132 (2018). https://doi.org/10.18720/MPM.3722018-3

9. Rajpurohit, S.R., Dave, H.K.: Effect of process parameters on tensile strength of FDM printed PLA part. Rapid Prototyp. J. **24**, 1317–1324 (2018). https://doi.org/10.1108/RPJ-06-2017-0134

10. Durgun, I., Ertan, R.: Experimental investigation of FDM process for improvement of mechanical properties and production cost. Rapid Prototyp. J. **20**, 228–235 (2014). https://doi.org/10.1108/RPJ-10-2012-0091

11. Onwubolu, G.C., Rayegani, F.: Characterization and optimization of mechanical properties of ABS parts manufactured by the fused deposition modelling process. Int. J. Manuf. Eng. **2014**, 1–13 (2014). https://doi.org/10.1155/2014/598531

12. Uddin, M.S., Sidek, M.F.R., Faizal, M.A., Ghomashchi, R., Pramanik, A.: Evaluating mechanical properties and failure mechanisms of fused deposition modeling acrylonitrile butadiene styrene parts. J. Manuf. Sci. Eng. **139**, 081018 (2017). https://doi.org/10.1115/1.4036713

13. Vega, V., Clements, J., Lam, T., Abad, A., Fritz, B., Ula, N., Es-Said, O.S.: The effect of layer orientation on the mechanical properties and microstructure of a polymer. J. Mater. Eng. Perform. **20**, 978–988 (2011). https://doi.org/10.1007/s11665-010-9740-z

14. Kimionis, J., Isakov, M., Koh, B.S., Georgiadis, A., Tentzeris, M.M.: 3D-printed origami packaging with inkjet-printed antennas for RF harvesting sensors. IEEE Trans. Microw. Theory Tech. **63**, 4521–4532 (2015). https://doi.org/10.1109/TMTT.2015.2494580

15. Teoh, J.E.M., An, J., Feng, X., Zhao, Y., Chua, C.K., Liu, Y.: Design and 4D printing of cross-folded origami structures: a preliminary investigation. Materials (Basel). **11** (2018). https://doi.org/10.3390/ma11030376

16. Pei, E., Loh, G.H.: Technological considerations for 4D printing: an overview. Prog. Addit. Manuf. **3**, 95–107 (2018). https://doi.org/10.1007/s40964-018-0047-1

Chapter 4
Study of Microstructure, Hardness and Dimensional Accuracy in Al-6061 Centrifugally Cast Pipe

Abdul Rouf Ganai and Balbir Singh

Abstract Centrifugal casting method is most widely used for producing cylindrical components. In order to produce quality casting products, there comes a lot of challenges in the way to achieve defect-free casting. Various defects such as geometrical defects in appearance, microsegregation, blowholes, raining and shrinkage porosities, etc. are likely to occur, owing to poor casting practices and improper setting of process parameters. The process parameters like mould rotational speed, pouring temperature and pouring rate significantly affect the quality of the casting. In the present work, a centrifugal casting machine has been designed and fabricated. The casting of Al-6061 pipe has been carried out in the fabricated setup. This paper studies microstructure, hardness throughout the axial length and dimensional accuracy of Al-6061 pipe centrifugally cast in the fabricated centrifugal casting machine.

Keywords Centrifugal force · Microstructure · Pouring speed · Solidification · Hardness

4.1 Introduction

In the centrifugal casting process, molten metal is poured into a rotating mould and is rotated till the molten metal gets solidified inside the mould. In this process, the mould holds the molten metal and provides the desired shape and size to the casting. Centrifugal casting machines mainly consist of a high-speed motor, a mould and a transmission system either gear or belt and pulley, shaft, pouring spout, bearings and bed of the machine [1]. In centrifugal casting, there is no need for runners and risers. Centrifugal forces exert the compressive pressure on the poured metal inside the mould and give it the desired shape. Centrifugal casting process is also called a liquid-phase process. Centrifugal casting machines are categorized into three basic types based on the direction of the spinning axis: horizontal, vertical, or inclined. Centrifugal casting processes can be categorized as follows:

A. R. Ganai · B. Singh (✉)
School of Mechanical Engineering, Shri Mata Vaishno Devi University, Katra 182320, India
e-mail: Balbir.isst@gmail.com
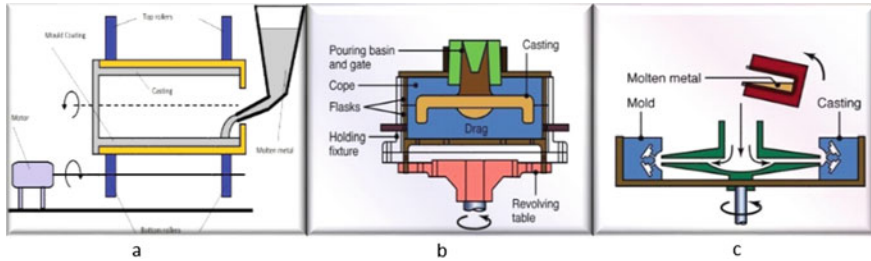
Fig. 4.1 Types of centrifugal casting machines [2]

- True centrifugal casting (horizontal, vertical, or inclined)
- Semi centrifugal (centrifugal mould) casting (Fig. 4.1)

Harshil Bhatt et al. studied the simulation of the casting process to optimize the design for the pouring and feeding system by using Computer-Aided Engineering (CAE) package AUTO Cast X a various parameters were optimized. The research was concluded by optimizing the feeding system and reduction in the hotspots in a component [3]. Huijun Feng et al. studied the various optimization techniques used for solidification during heat transfer of continuous slab casting. It was observed that there was a lot of heat loss in this system due to which this problem was taken into consideration for further research. For efficient cooling rate and solidification of slab component, numerical simulations tools were used. [4]. Hassan Jafari et al. studied the lost foam casting process where process parameters were taken into consideration for manufacturing Al–Si–Cu alloy. The evaluation of these significant parameters was conducted using Design of Experiment (DOE) as the tool where a full factorial model of the system was formed. The properties of casting were affected due to significant manufacturing factors which indicated pouring temperature played an important role in the quality of the castings. It was found that higher pouring temperature resulted in the better surface finish in the components [5]. Radhika and Raghu studied the mechanical and tribological properties of functionally graded aluminum/zirconia metal matrix composite synthesized by centrifugal casting and found that functionally graded aluminum/zirconia metal matrix composite has been fabricated successfully through a liquid metallurgy route followed by centrifugal casting. The outer surface of the composite reveals a particle-rich region and the particle segregation was found to decrease when moving towards the inner periphery of the casting. The maximum hardness was found at the outer layer of the composite and it decreased as the radial distance from the outer periphery increased, and also the tensile strength was found to be highest at the upper section. The abrasion wear rate was increased with an increase in load [6]. S. Pandey et al. studied the effect of the rotational speed of mould on the quality of bimetallic pipe produced by the centrifugal casting process and it was found that pure metal bonding region, metal oxides exist in interface shrinkage voids during the evaluation of aluminum–copper cast product and also intermetallic compounds create at the interface between two metals. If the temperature is too high and metal oxides glues cool the second melt

and no bond is formed if the temperature is too low [7]. On the basis of the present survey, a horizontal centrifugal casting machine has been designed and an Al-6061 pipe has been fabricated in order to study microstructure, hardness and dimensional accuracy in centrifugally cast pipe.

4.2   Design and Fabrication

The design and fabrication of a centrifugal casting setup were successfully carried out. The operation of the machine is based on the principle of centrifugal force. Suitable design theory, analysis and calculation were carried out. The mould is bolted to the base plate which can rotate at moderate speeds thereby forcing the molten metal against the inner walls of the mould. This machine as shown in Fig. 4.2 could be used to cast small engineering components. The centrifugal force on the machine was determined to be 1161.3 N, while the required power on the machine was 256 W. A test was carried out on the fabricated centrifugal casting machine with aluminum alloy and the machine was able to cast 2.5 kg of aluminum alloy successful.

Various parts of the centrifugal casting machine have been designed as follows.
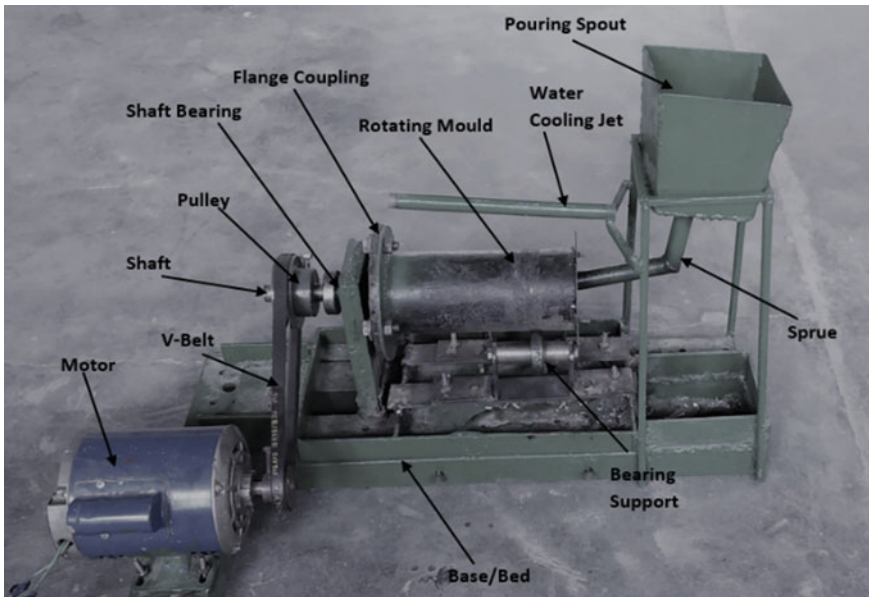
Fig. 4.2   Fabricated horizontal centrifugal casting machine

4.2.1 Angular Velocity of the Mould

The angular velocity 'ω_n' (m/s) of the turntable mould is determined by,

$$\omega_n = \frac{\pi D N}{60}$$

where: D = Diameter of the turntable (mm), N = RPM of the mould.

4.2.2 Centrifugal Force on the Machine

The centrifugal force 'F' (N) on the machine is given by,

$$F = M\omega_n r^2$$

where: M = Total mass of the rotating disc (kg), r = Radius of the disc (mm)
ω_n = angular speed of rotating mould (rpm).

4.2.3 Diameter of the Shaft

The shaft diameter 'd' (mm) is designed on the basis of the following data

$$M_b = 0.3855 \quad M_t = 0.057 \quad K_t = 1.5 \quad K_b = 2.0$$

$$d^3 = \frac{16}{\pi T}\sqrt{(K_b M_b)^2 + (K_t M_t)^2}$$

where: M_t = belt torque moment (Nm), M_b = Bending moment (Nm)
K_b, K_t = Shock and fatigue factor applied to bending and torsional moment resp.
[8].

4.2.4 Speed of Driven Pulley

The speed of the driven pulley 'N_1' is determined by,

$$N_2 = \frac{N_1 \times d_1}{d_2}$$

where: N_2 = Speed of the driven pulley (rpm);
d_1, d_2 = Sheave diameter of motor and driven pulley (mm) resp.

4.2.5   Belt Speed

The speed of the belt 'B_S' is determined by the relation,

$$B_S = \frac{\pi d_1 d_2}{1000}$$

4.2.6   Belt Length

The length of the belt 'L' of the centrifugal casting machine is determined by

$$L = 2C + \frac{\pi}{2}(d_1 + d_2) + \frac{(d_1 - d_2)^2}{4C}$$

where: C = Distance between the two pulleys (mm) [9].

4.2.7   Flow Rate and Pouring Speed of Molten Metal

For the design of flow rate and pouring speed three pouring sprouts with different sprue diameter as 12.5, 25 and 38 mm have been designed to provide a variable flow of the molten metal as shown in Fig. 4.3 (Fig. 4.4).

4.3   Experimentation

An Al-6061 pipe is made by using the horizontal centrifugal casting setup as shown in Fig. 4.2. The molten metal is being poured inside the mould through a 12.5 mm sprue

Fig. 4.3   Pouring spouts of different sprue diameter

Fig. 4.4 Actual view of pouring spout
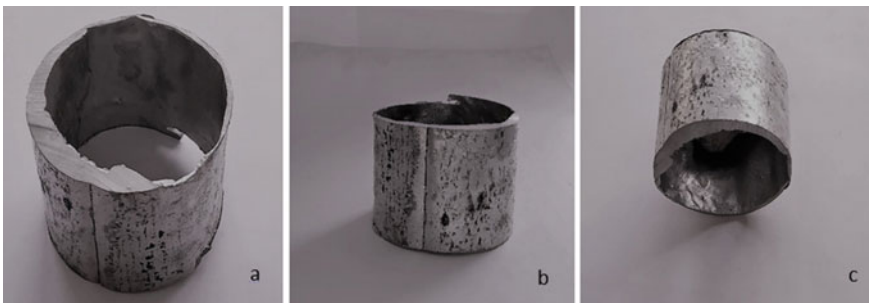
Fig. 4.5 Al-6061 centrifugally casted pipe at different angles

diameter pouring sprout with the mass flow rate as 1.21 kg/s. The density of Al-6061 in molten state is 2375 kg/m^3. Mould is rotated at 700 rpm by a belt connected with motor. After the solidification of molten Al-6061, the pipe is drawn out by pushing it from the other side and three samples are being taken axially from the pipe as shown in Fig. 4.6 and are being tested for microstructure by optical microscope, hardness by Vickers micro-hardness tester and dimensional accuracy by dimension gauges in the form circularity, cylindricity, concentricity and uniformity in the pipe (Fig. 4.5).

4.4 Results and Discussion

Horizontal centrifugal casting machine is designed for the mould to rotate at different speeds. The "*V*" belt drive attachment is used to change the speed. The rotation of the mould helps to generate a centrifugal force that acts on the metal and solidifies it within the mould. Three samples viz. at the inlet, center, and other end of pipe were taken for the tests as shown in Fig. 4.6.

After performing the experiment, geometrical errors were studied in the pipe and studies were made about to get remedies, and also it is found that at 700 rpm and
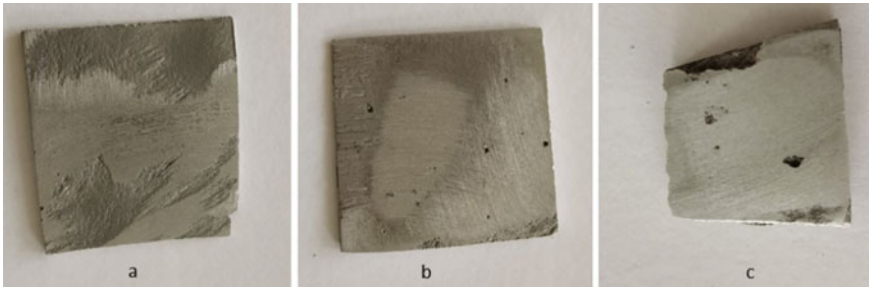
Fig. 4.6 Three samples of pipe at entry, center and end as **a**, **b** and **c** respectively

590 °C pouring temperature the maximum hardness is found at the entry end of casting then there is a small decrease in hardness at center and shows a maximum of 10% decrease at the other end of casting. The difference was observed in the microstructure and the surface closed porosity when analyzed through the optical microscope.

4.4.1 Geometrical Errors

Parameters like Cylindricity, Circularity, Concentricity and Position from center were studied in an open experiment with the help of GD&T basics by using dimension gauges (Fig. 4.7).

The geometrical errors define the overall geometric appearance under the given tolerances (Table 4.1).
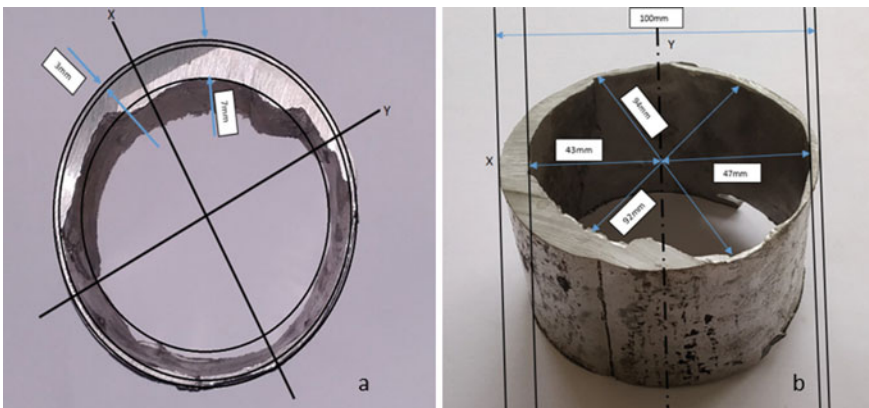
Fig. 4.7 Geometrical dimensions while calculating geometrical errors

Table 4.1 Results of geometrical errors in an open experiment

S. No.	Parameter	Tolerances	Results
1	Cylindricity	±0.04	$X = +93.96, Y = +91.96$
2	Circularity	±0.02	$X = -3.98, Y = ±0.0$
3	Concentricity	±0.04	$X = +3.02, Y = -3.98$
4	Position	±0.08	$X = +38.92, Y = +42.92$
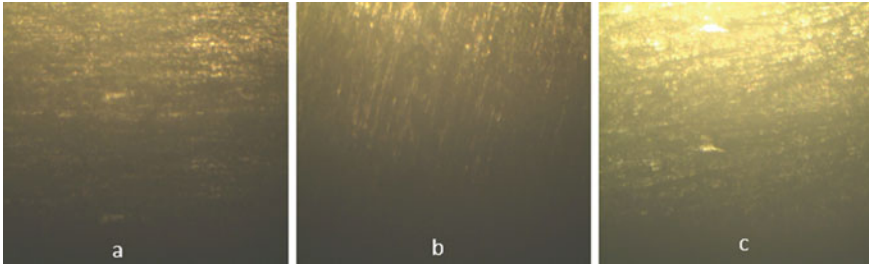
Fig. 4.8 Optical microscope images

4.4.2 Microstructure Test

The microstructure of the Al-6061 pipe was characterized by an optical microscope. The specimens were initially polished with silicon carbide paper up to a 1200 grit paper finish followed by the automatic finisher. The optical microscopic images as shown in figure reveals the close porosity and surface properties at the entry, center and other end of the pipe as shown in Fig. 4.8a–c. At the starting side of pipe, less defects were depicted and blackish in colour shown by Fig. 4.8a. Some blow holes, raining and also less microsegregation defects were seen at the center as shown by Fig. 4.8b. At the other end of the pipe white grey structure and some blow holes defects were found as shown in Fig. 4.8c.

4.4.3 Hardness Test

Static indentation method is the most method widely used to determine the hardness of metals. It involves the formation of permanent indentation on the surface of metals to be examined. Load and size of the indentation are the two parameters that determine the hardness of metals. The width or depth of the resulting scratch is used to examine the hardness, the harder the metal, smaller is the scratch. Vickers hardness tester is being used to examine this scratch and hardness is being evaluated [10].

Hardness test was performed on Vickers micro-hardness tester on all the three samples taken axially at start, center and other end of the pipe.

Fig. 4.9 Hardness along axial direction of centrifugally cast Al-6061 pipe
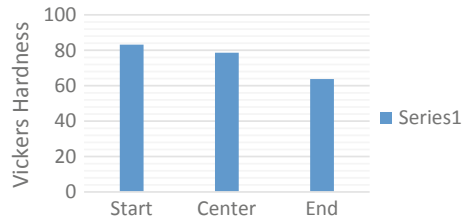
Figure 4.9 shows the hardness as 83.23, 78.67 and 63.78 HV at the start, center and other end respectively of the centrifugally cast Al-6061 pipe. It was observed that the hardness decrease along the axial length of the pipe. It is found that at 700 rpm and 590 °C pouring temperature, the maximum hardness is found at the entry of casting then there is a small decrease in hardness at center and shows a maximum of 10% decrease at the other end of casting. This variation in hardness is to the improper mould filling and pouring rate of the molten metal. The molten metal imparts greater centrifugal force at the start and center of mould and less impact at the other end of mould.

4.5 Conclusions

- The mould rotational speed has a great influence on the quality of the casting. The mould rotational speed must not be kept as high that it renders the proper solidification process.
- The variation of the hardness is due to the improper flow manner of molten metal.
- The dimensional errors are caused due to the improper centering of the mould.

References

1. Ebhota, W.S., Karun, A.S., Inambao, F.L.: Centrifugal casting technique baseline knowledge, applications, and processing parameters. Int. J. Mater. Res. (formerly Z. Metallkd.) **107**(10), 960–969 (2016)
2. ASM Handbook: Casting ASM Handbook Committee, vol. 15, p 667–673 (2008). https://doi.org/10.1361/asmhba00052579
3. Bhatt, H., Barot, R., Bhatt, K., Beravala, H., Shah, J.: Design optimization of feeding system and solidification simulation for cast Iron. In: 2nd International Conference on Innovations in Automation and Mechatronics Engineering, ICIAME 2014, Procedia Technology, vol. 14, pp. 357–364 (2014)
4. Feng, H., Chen, L., Xie, Z., Ding, Z., Sun, F.: Generalized constructal optimization for solidification heat transfer process of slab continuous casting based on heat loss rate. Energy **66**, 991–998 (2014)

5. Jafari, H., Idris, M.H., Amirreza, S.: Evaluation of significant manufacturing parameters in lost foam casting of thin-wall Al–Si–Cu alloy using full factorial design of experiment. Trans. Nonferrous Met. Soc. China **23**, 2843–2851 (2013)
6. Radhika, N., Raghu, R.: Mechanical and tribological properties of functionally graded aluminium/zirconia MMC synthesized by centrifugal casting. Int. J. Mater. Res. (formerly Z. Metallkd.) **106**, 1–8 (2015). https://doi.org/10.3139/146.111293
7. Pandey, S., Parhi, S., Jha, S.K.: Effect of the mould rotational speed on the quality of bimetallic pipe fabricated by centrifugal casting process. Int. J. Emerg. Res. Manag. Technol. **6**(7), 2278–9359 (2017)
8. Rattan, S.S.: Theory of Machine, 4th edn. McGraw Hill, New York (2014)
9. Oyewole, A., Sunday, A.M.: Design and fabrication of acentrifugal casting machine. Int. J. Eng. Sci. Technol. (IJEST) **3**(11), 8204–8210 (2011). ISSN: 0975-5462
10. Tabor, D.: The Hardness of Metals. Oxford University Press, Oxford (1951)

Chapter 5
Micro-hardness Study of Ni–P, Ni–W–P, and Ni–P/Ni–W–P Electroless Coating

Rishav Kumar Baranwal, Arghya Mukherjee, Souparna Banerjee, Subhasish Sarkar, and Gautam Majumdar

Abstract This paper compares the micro-hardness of a binary (Ni–P), ternary (Ni–W–P), and a duplex coating (Ni–P/Ni–W–P) over the copper substrate. Vickers Hardness Test is taken for determining the hardness of the coating due to its compatibility of the indenter with the electroless coating. Scanning Electron Microscopy (SEM) of the images of the Ni–W–P coating shows the porous nature while Ni–P coating shows very less porosity compared to Ni–W–P. Hence, the Ni–P/Ni–W–P coating shows very less porosity since it has Ni–P layer as the inner layer. The hardness of duplex layer is greater than the ternary coating which in turn is better than the binary coating. The efficiency of the Ni–P is 57.33%, Ni–W–P is 75.81%, and of duplex is 80.71%.

Keywords Electroless · Vickers hardness test · Scanning electron microscope

5.1 Introduction

Electroless coating is an autocatalytic process in which the material is deposited from the solution onto a certain substrate without any external source of electricity. The process is carried out in an electroless bath which comprises of the metal ions source, a reducing agent, a complexing agent, a buffering agent, and surfactants. The deposition of the alloy over the surface of the catalytic substrate is carried out by the metallic ions reduced through the oxidation of the reducing agent present in the solution [1, 2]. These metallic ions from the solution are reduced by the electrons from the catalytic metal substrate initiating the deposition, which are in turn obtained over the substrate by the oxidation of the reducing agent. Along with the great quality of the deposit, electroless coatings have unique physical, chemical, and mechanical properties which have led to their rapid increase of use in the areas of surface engineering and metal finishing in industries such as automotive, petrochemical, electronics, marine, mining [3, 4]. Some of the properties which make them good

R. K. Baranwal (✉) · A. Mukherjee · S. Banerjee · S. Sarkar · G. Majumdar
Department of Mechanical Engineering, Jadavpur University, Kolkata 700032, India
e-mail: rishavbaranwal22@gmail.com

enough to be used in the industries are homogeneity, high corrosion resistance, wear, and abrasion resistance, solderability, high hardness, low friction coefficient, high reflectivity, resistivity, and ductility. Among the aforesaid properties, wear, and abrasion resistance is the one on which most of the applications of electroless coatings are based [5]. For example, in internal combustion engines, the piston moves up and down in a cylinder, and is quite prone to surface wear caused by the flat rubbing contact with the cylinder, transmitting its motion through a connecting rod to the crankshaft which drives the vehicle. Thus the piston has to be coated with a material that provides good resistance to such kinds of surface wear. This is the point where wear and abrasion resistance of the material comes into action.

Electroless Nickel (EN) coating is by far the most common and important catalytic coating used nowadays. The predominant reasons for this being such widespread are found in the exclusive properties (improved corrosion resistance, wear, and abrasion resistance, etc.) of the EN deposits over the catalytic substrate. The electroless coatings can be broadly classified into four categories, viz. pure nickel coatings, alloy, and poly-alloy coatings, composite coatings, and electroless nanocoatings [3]. The alloy and poly-alloy can be further classified into unary, binary, ternary, and quaternary coatings. In binary alloys, there are two elements in the deposited coating, for example, Ni–P, Ni–B, etc. Similarly, ternary and quaternary alloys have three and four elements respectively. For example, Ni–W–P, Ni–Cu–P, Ni–Co–P for ternary alloys and Ni–W–Cu–P for quaternary alloys [6, 7]. Electroless Ni–P Coatings can be divided into three main types viz. low phosphorus (1–4 wt% P), mid phosphorus (4–10 wt% P), and high phosphorus (>10.5 wt% P). The high content of phosphorous offers great anti-corrosion properties whereas the medium and low content of phosphorous offers better hardness. Although a lot of materials can be electrolessly coated over the substrate, Ni–P has been preferred due to the superior properties possessed by it over other alloys such as higher hardness and better wear and abrasion resistance [8]. This coating of Ni–P acts as a sacrificial barrier thereby protecting the substrate from the corrosive environments [8]. Among the mentioned binary alloys, Ni–P and Ni–B are found to have better tribological properties as compared to the other ones. This study is normally based on the characterization of the hardness, wear, and friction, abrasion resistance of the coating [9–11]. However, in this era, which is in constant demand for unique and better inventions, coatings with better tribological, mechanical, and chemical properties are always preferred over the others. Studies have revealed that with the addition of an extra element/complex (the third one) in the binary alloy coating, better tribological properties can be observed. These include Co, TiO_2, W, Cu, Fe, ZrO_2, Al_2O_3, PTFE, Mo, Pd, Zn [12–17]. In 1963, Pearlstein became the first to prepare a Ni–W–P alloy via electroless plating. The Ni–W–P coating was found to have better properties viz. hardness, heat resistance, wear, and abrasion resistance compared to that of Ni–P alloy. Tungsten has unique properties such as high hardness, high melting point, low coefficient of thermal expansion, high tensile strength which has led to the vast development of Ni–W–P ternary alloys [18]. The deposition of tungsten along with the Ni–P coating affects the deposition rate and improves the hardness and tribological properties such as wear and abrasion resistance, coefficient of friction. As compared to the atomic

radii of Ni and P, tungsten as a greater one. Hence, as it is deposited in the voids of Ni–P coatings, the Ni and P atoms try to pull themselves towards the tungsten atom thereby increasing the compactness and compressive stress of the coating [19]. This internal compressive stress is not a major problem as it can be easily removed by annealing of the coated substrate [15]. By comparing the phase transformations of the binary Ni–P coating with the ternary Ni–W–P coating, it was observed that Ni–W–P has higher thermal stability and re-crystallization temperature and hence possesses higher hardness at a specified temperature [20, 21]. The duplex coating is a special coating which comprises of two alloys deposited over the substrate. This involves combined surface treatment which is done to improve the tribological, mechanical, and chemical properties of the catalytic substrate. The resultant coating is a combination of two layers thereby combining all the properties of the two alloys resulting in a better one [15, 22]. In most cases, the alloy with comparatively superior properties (better corrosion resistance, wear, and tear resistance) as compared to the other alloy is chosen to be the topmost layer, but theoretically, the position of the layers should be chosen according to the desired properties. For example, Ni–W–P alloy has superior properties than Ni–P alloy as mentioned earlier, hence in a duplex coating of Ni–W–P and Ni–P, Ni–W–P is chosen to be the topmost layer to obtain a final coating with better hardness and wear and abrasion resistance along with minimized chances of corrosion [23].

The aim of this research is to improve the hardness of copper substrate by electrolessly coating it with binary, ternary and duplex alloys. Vickers Hardness Test was performed to calculate the Vickers Hardness Number and hence, the coating efficiency of each coated sample and to find out which coating provides the maximum hardness to the copper substrate. Scanning Electron Microscope was used to find the surface morphology of the coated substrates and Energy dispersive X-Ray Spectroscopy (EDAX) was done to find out the percentage of each element in the coating.

5.2 Experimental Details

5.2.1 Preparation of the Substrate and Coating

5.2.1.1 Substrate Activation/Cleaning

The substrate on which the coating is supposed to be done is chosen to be copper. Copper, one of the most electrochemically active and very common and important material in our daily lives, needs to be provided a physical barrier from corrosion attack since it gets corroded easily in the presence of air or moisture [24]. The copper substrate was cut from a foil (99% pure, LobaChemie) present in the rolled form. The dimensions of the copper substrate are 2×1.5 cm^2 in area and 0.1 mm in thickness. At first, the copper substrate is rinsed in distilled water for 5 min; then it

is dipped in 25% HCl solution for 10 min to remove oxide layers and other metal impurities. After that, the surfaces of the copper substrates are activated by dipping them into Palladium Chloride ($PdCl_2$) solution (which was pre-heated to 55 °C) for 5–10 s. $PdCl_2$ acts as an adsorbing agent thereby initiating the reaction by forming a layer over the substrate [25]. Finally, the substrate is ready to be dipped in the electroless bath.

5.2.1.2 Bath Preparation

The bath consists of Nickel Sulfate ($NiSO_4$), Sodium Tungstate (Na_2WO_4), Trisodium Citrate Dihydrate (TCD), Sodium Acetate (CH_3COONa), and Sodium Hypophosphite (NaH_2PO_4). $NiSO_4$ is the source of nickel ions in the electroless bath. Nickel Acetate and Nickel Chloride are not chosen because they are not so suitable for the reduction process as compared to Nickel Sulfate [26]. TCD is the complexing agent that forms metastable nickel complexes thereby slowing down the rate of the reaction to reach a beneficial and suitable state. NaH_2PO_4 is the reducing agent which helps in reducing the nickel ions provided by the Nickel Sulfate solution. CH_3COONa is the buffering agent which maintains the pH of the bath to around 5. Na_2WO_4 is the source of the tungstate ions which will be used in the preparation of Ni–W–P and Ni–P/Ni–W–P duplex coatings. In one beaker, the nickel ions source and the reducing agent are mixed and in the other beaker, the rest of the components are mixed with 250 ml of distilled water distributed among them, hence forming two separate solutions. Both the solutions are heated to around 60 °C and then mixed together to form the electroless bath. The activated copper substrate is then dipped into the electroless bath and is heated till 85–90 °C until a bright layer of the desired coating is obtained after around 40 min. The electroless bath's compositions are provided in Tables 5.1 and 5.2. Duplex coating was made using the compositions as stated in Tables 5.1 and 5.2.

Table 5.1 Bath composition of Ni–P coating

Ni–P	
Reagents	Concentration
$NiSO_4$	25 g/L
NaH_2PO_4	20 g/L
TCD	15 g/L
CH_3COONa	5 g/L

Table 5.2 Bath composition of Ni–W–P coating

Ni–W–P	
Reagents	Concentration
$NiSO_4$	36 g/L
NaH_2PO_4	28 g/L
TCD	30 g/L
CH_3COONa	4 g/L
Na_2WO_4	16 g/L

5.2.2 Hardness Testing

For measuring the hardness of the coated sample, we use Vickers Hardness Test (VHT). It is an optical method and is carried out with the help of a pyramidal shaped diamond indenter (Fig. 5.1).

The depth of the indentation left by the indenter is measured. The larger the indent left by the indenter at a defined test force in the surface of the coated sample, the softer the tested specimen. VHT is done with less force and more accuracy than the Brinell Hardness Test (BHT) and Rockwell Hardness Test (RHT). The BHT makes use of a round-shaped indenter which is an important reason why it is not preferred as a suitable test to measure the hardness of the coated sample. In the case of a round-shaped indenter, the surface area in contact with the coated sample will be more and hence the results will not be accurate enough, whereas, for a pyramidal shaped indenter, the surface area in contact will be the least, thereby making a point impact, it will produce the most accurate results for the hardness test. By magnifying the surface of the specimen, VHT can target specific microstructural constituents, or assess the quality of the heat treating and surface hardening options. Non-destructive testing is possible in VHT unlike BHT and RHT, hence the test specimen can be used for other purposes. This is only possible due to the minimized surface contact of the
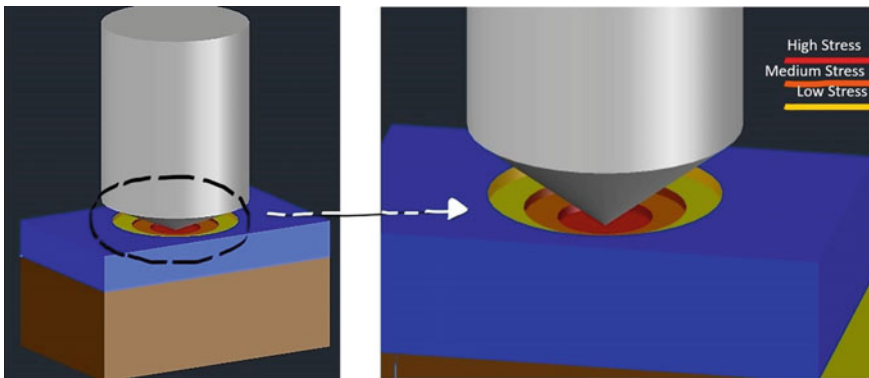
Fig. 5.1 Vickers hardness test

indenter with the test specimen. Due to this, VHT has to be performed quite a few number of times in different regions of the coated specimen in order to get perfectly accurate results.

5.2.3 Surface Study and Characterization of the Coating

The coating's surface morphology was done using Scanning Electron Microscopy (SEM). In order to find the percentage composition of each of the elements present in the coating, Energy Dispersive X-ray Analysis (EDAX) was done.

5.3 Results and Discussions

5.3.1 Hardness Study

The hardness of the coated samples prepared goes in the following order: Ni–P/Ni–W–P > Ni–W–P > Ni–P > Cu substrate. The duplex layer has a thicker layer as compared to the binary and ternary layer. As we have mentioned in Sect. 5.2.2, VHT is based on the principle of higher the indent left by the indenter, softer the tested specimen. Ni–P coated sample has a higher hardness than Cu substrate because of the higher hardness properties of Ni–P predominant over Cu. This can be also explained by VHT; due to the lower indent left by the indenter in the case of Ni–P coated sample because of an extra sacrificial layer, the hardness value of Ni–P coated sample is more than that of the Cu substrate. Again Ni–W–P coated sample has high hardness as compared to Ni–P. This is only due to the extra tungsten ion in the ternary alloy which improves properties such as hardness to a great extent. The reason for the higher hardness of the duplex coated substrate than the other samples is already mentioned in this section itself. Due to an extra layer of ternary coating over the binary coating, there is a low indent left by the indenter in VHT resulting in higher hardness. The micro-hardness was measured using a 10 g diamond indenter having an apex angle of 136°. The efficiency of the coating is defined as $\eta = \frac{\text{VHN}_{\text{Coating}} - \text{VHN}_{\text{Substrate}}}{\text{VHN}_{\text{Coating}}}$. Higher the efficiency of the coating, better is its hardness. Hence, from Table 5.3, we can conclude that the hardness of Ni–P/Ni–W–P > Ni–W–P > Ni–P.

5.3.2 SEM Study

Figure 5.2 shows the SEM image of Ni–W–P ternary coating over the copper substrate. The SEM analysis reveals the presence of compact, non-uniform granular structures that do not seem to have definite shapes. The white spots represent holes

Table 5.3 VHN and efficiencies of Ni–P, Ni–W–P, Ni–P/Ni–W–P coatings

Position	Cu substrate (VHN)	Ni–P (VHN)	Ni–W–P (VHN)	Ni–P/Ni–W–P (VHN)	(Ni–P)	(Ni–W–P)	(Ni–P/Ni–W–P)
1.	162	378	672	846	57.14	75.89	80.85
2.	164	385	678	850	57.40	75.81	80.70
3.	165	388	680	850	57.47	75.73	80.58
AVG:	164	384	677	849	57.33	75.81	80.71

Fig. 5.2 SEM image of Ni–W–P coating
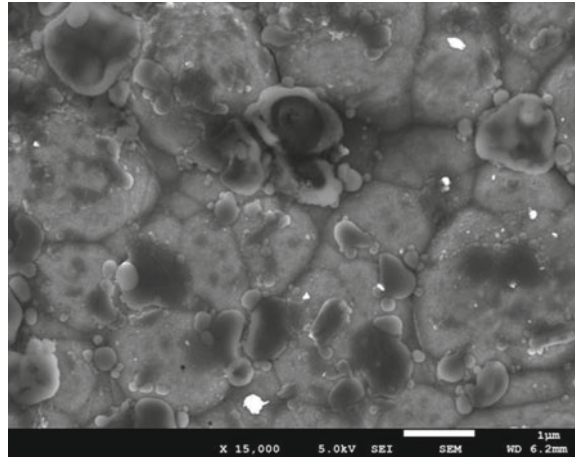
that signify the porosity of the medium. Visual defects are not observed as such. Grain boundaries are not visible to that extent.

Figure 5.3 shows the SEM image of Ni–P binary coating over the copper substrate. This SEM image depicts coarse nodular structures with grain boundaries very well marked. Fine nodules are scattered which run low in number as well as size. No holes are observed in this image which signifies the low porosity of the medium. Visual defects are also not observed in this image.

Figure 5.4 shows the SEM image of the duplex Ni–P/Ni–W–P coating over the copper substrate. This image depicts a very clear view of the deposition of the ternary (Ni–W–P) layer over the binary (Ni–P) layer. As seen in Fig. 5.3, the coating had well-defined grain boundaries, this image obtained with 15,000× more zoom than Fig. 5.3 has an enlarged view of the binary layer of coating. The ternary layer can be well observed to be deposited over the binary layer with dense and compact, non-uniform (mostly circular) granular structures. The white dots represent holes as observed in Fig. 5.2 depicting the porosity of the medium. No cracks are observed which depicts that the coating has been well intact all over the surface of the substrate.

Fig. 5.3 SEM image of
Ni–P coating
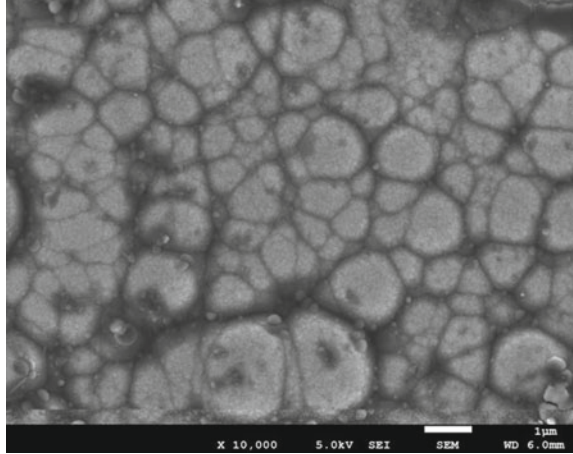
Fig. 5.4 SEM image of
duplex Ni–P/Ni–W–P
coating
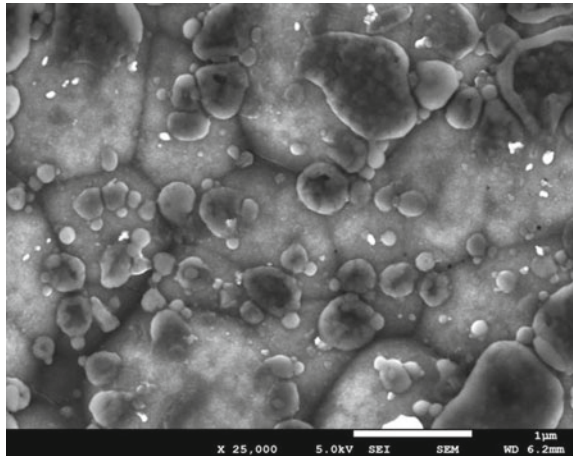
5.3.3 EDAX Study

Figure 5.5 shows the EDAX patterns observed on the ternary, binary, and duplex coatings respectively. The percentage of every single element which is coated over the copper substrate is given in Table 5.4.

From the table, we can notice that the percentage of phosphorous varies between 2 and 7% which signifies that the phosphorous content of the coating is medium indicating high hardness. In the duplex coating, the percentage of tungsten is 2.87% which is quite significant hence it has the highest hardness amongst the three coatings. Tungsten plays an important role in increasing the hardness of the specimen. The tungsten content in the ternary coating (1.33%) is less than the duplex one, hence the ternary coating is next to the duplex coating on the basis of hardness. As mentioned
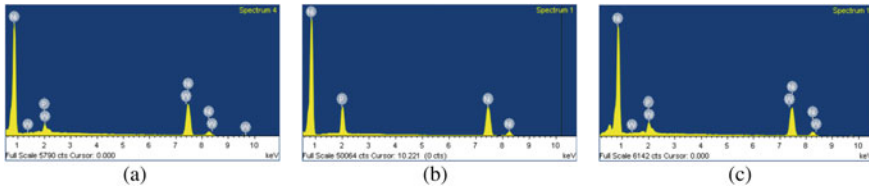
Fig. 5.5 EDAX pattern of deposition on Cu substrate **a** Ni–W–P, **b** Ni–P, **c** Ni–P/Ni–W–P

Table 5.4 Percentage composition of components

Ni–W–P		
Component	wt%	Atomic wt%
P	2.87	5.35
Ni	95.80	94.23
W	1.33	0.42
Ni–P		
Component	wt%	
Ni	93.86	
P	6.14	
Ni–P/Ni–W–P		
Component	wt%	
Ni	93.70	
P	3.43	
W	2.87	

earlier, medium phosphorous content in any coating increases its hardness, hence Ni–P has a higher hardness than the original copper substrate, but lower hardness than Ni–W–P due to the presence of tungsten in the ternary coating.

5.4 Conclusion

The conclusions can be drawn as follows:

- The binary, ternary, and duplex coatings were successfully deposited over the copper substrate.
- The hardness of the coated sample was in the following order:
  Ni–P/Ni–W–P > Ni–W–P > Ni–P > Cu substrate according to the VHN: 849, 677, 384, respectively.
- The coating efficiencies for Ni–P, Ni–W–P, and Ni–P/Ni–W–P are 57.33%, 75.81%, 80.71%, respectively.

- EDAX results show higher percentage of tungsten in the duplex coating which attributes to amoleriation of the hardness.
- From the SEM images of Ni–P, Ni–W–P, and Ni–P/Ni–W–P, it is revealed that the porosity of Ni–P/Ni–W–P coating is less due to the presence of Ni–P coating as the inner layer.

References

1. Ploof, L.: Electroless nickel composite coatings. Adv. Mater. Processes **166**(5), 36 (2008)
2. Sudagar, J., Lian, J., Sha, W.: Electroless nickel, alloy, composite andnano coatings—a critical review. J. Alloy. Compd. **15**(571), 183–204 (2013)
3. Sarkar, S., Baranwal, R.K., Biswas, C., Majumdar, G., Haider, J.: Optimization of process parameters for electroless Ni-Co-P coating deposition to maximize micro-hardness. Mater. Res. Express. (2019)
4. Tamilarasan, T.R., Rajendran, R., Sanjith, U., Rajagopal, G., Sudagar, J.: Wear and scratch behaviour of electroless Ni-P-nano-TiO$_2$: effect of surfactants. Wear **15**(346), 148–157 (2016)
5. Agarwala, R.C., Agarwala, V.: Electroless alloy/composite coatings: a review. Sadhana **28**(3–4), 475–493 (2003)
6. Narayanan, T.S., Krishnaveni, K., Seshadri, S.K.: Electroless Ni–P/Ni–B duplex coatings: preparation and evaluation of microhardness, wear and corrosion resistance. Mater. Chem. Phys. **82**(3), 771–779 (2003)
7. Balaraju, J.N., Narayanan, T.S., Seshadri, S.K.: Electroless Ni–P composite coatings. J. Appl. Electrochem. **33**(9), 807–816 (2003)
8. Narayanan, T.S., Baskaran, I., Krishnaveni, K., Parthiban, S.: Deposition of electroless Ni–P graded coatings and evaluation of their corrosion resistance. Surf. Coat. Technol. **200**(11), 3438–3445 (2006)
9. Pal, S., Jayaram, V.: Effect of microstructure on the hardness and dry sliding behavior of electroless Ni–B coating. Materialia **1**(4), 47–64 (2018)
10. Zhang, W.X., Jiang, Z.H., Li, G.Y., Jiang, Q., Lian, J.S.: Electroless Ni-P/Ni-B duplex coatings for improving the hardness and the corrosion resistance of AZ91D magnesium alloy. Appl. Surf. Sci. **254**(16), 4949–4955 (2008)
11. Vitry, V., Bonin, L., Malet, L.: Chemical, morphological and structural characterisation of electroless duplex NiP/NiB coatings on steel. Surf. Eng. **34**(6), 475–484 (2018)
12. Wang, Y., Shu, X., Wei, S., Liu, C., Gao, W., Shakoor, R.A., Kahraman, R.: Duplex Ni–P–ZrO$_2$/Ni–P electroless coating on stainless steel. J. Alloy. Compd. **5**(630), 189–194 (2015)
13. Chen, X.M., Li, G.Y., Lian, J.S.: Deposition of electroless Ni-P/Ni-WP duplex coatings on AZ91D magnesium alloy. Trans. Nonferr. Met. Soc. China **1**(18), s323–s328 (2008)
14. Omidvar, H., Sajjadnejad, M., Stremsdoerfer, G., Meas, Y., Mozafari, A.: Manufacturing ternary alloy NiBP-PTFE composite coatings by dynamic chemical plating process. Mater. Manuf. Processes **31**(1), 31–36 (2016)
15. Balaraju, J.N., Rajam, K.S.: Electroless ternary Ni–W–P alloys containing micron size Al$_2$O$_3$ particles. Surf. Coat. Technol. **205**(2), 575–581 (2010)
16. Ranganatha, S., Venkatesha, T.V., Vathsala, K.: Development of electroless Ni–Zn–P/nanoTiO$_2$ composite coatings and their properties. Appl. Surf. Sci. **256**(24), 7377–7383 (2010)
17. Hu, X., Jiang, P., Wan, J., Xu, Y., Sun, X.: Study of corrosion and friction reduction of electroless Ni–P coating with molybdenum disulfide nanoparticles. J. Coat. Technol. Res. **6**(2), 275–281 (2009)
18. Nishijima, D., Baldwin, M.J., Doerner RP, Yu JH. Sputtering properties of tungsten 'fuzzy' surfaces. J. Nucl. Mater. **415**(1), S96–S99 (2011)

19. Callister Jr., W.D., Rethwisch, D.G.: Fundamentals of materials science and engineering: an integrated approach. Wiley, New York (2012)
20. Lee, H.B., Wu, M.Y.: A study on the corrosion and wear behavior of electrodeposited Ni-WP coating. Metall. Mater. Trans. A **48**(10), 466780 (2017)
21. Balaraju, J.N., Selvi, V.E., Grips, V.W., Rajam, K.S.: Electrochemical studies on electroless ternary and quaternary Ni–P based alloys. Electrochim. Acta **52**(3), 1064–1074 (2006)
22. Biswas, N., Baranwal, R.K., Majumdar, G., Brabazon, D.: Review of duplex electroless coatings and their properties. Adv. Mater. Process. Technol. **4**(3), 448–465 (2018)
23. Selvi, V.E., Chatterji, P., Subramanian, S., Balaraju, J.N.: Autocatalytic duplex Ni–P/Ni–W–P coatings on AZ31B magnesium alloy. Surf. Coat. Technol. **15**(240), 103–109 (2014)
24. Kreislova, K., Geiplova, H.: Prediction of the long-term corrosion rate of copper alloy objects. Mater. Corros. **67**(2), 152–159 (2016)
25. Sarkar, S., Baranwal, R.K., Lamichaney, S., De, J., Majumdar, G.: Optimization of electroless Ni-Co-P coating with hardness as response parameter: a computational approach. J. Tribol. **1**(18), 81–96 (2018)
26. Mallory, G.O., Hajdu, J.B.: Electroless plating: fundamentals and applications. William Andrew, Norwich (1990)

Chapter 6
Mechanical Stability of Fabricated Superhydrophobic Aluminium Alloy and Enhancement of Its Oleophobic Characteristics

Rishabh Raj, Saurabh Kango, and Sarbjot S. Sandhu

Abstract The main objective of the present work is to check the durability of super-hydrophobic aluminium alloy by using an adhesive peel, sandpaper abrasion and water impact test. Chemical etching and dip-coating methods are used to fabricate the superhydrophobic aluminium surfaces. It is observed that the water contact angle decreases with the increase in number of cycles in adhesive peel, sand abrasion test and with an increase in time in a water impact test. It is also observed that the fabricated superhydrophobic samples sustained its characteristics up to 20 cycles in adhesive peel test, 15 cycles in sand abrasion test and 4 min in water impact test. Further, in order to enhance the oleophobic characteristics, the surface formed after the treatment by immersing in boiling water shows oleophobic characteristics as well. It is found that the contact angle formed by glycerol and water droplet on the surface is $110.56°$ and $150.13°$, respectively.

Keywords Hydrophilic · Hydrophobic · Superhydrophobic · Chemical etching · Water contact angle · Oleophobic

6.1 Introduction

Aluminium and its alloys play a vital role in people's daily lives and industrial applications. It is one of the most widely used metallic materials. It has a series of excellent properties such as excellent thermal conductivity, flexibility, high strength, good machinability properties and corrosion resistance. It can be widely used in aircraft and aerospace materials, building materials, automotive, home appliances, food packaging, cooking supplies, industrial machinery, etc.

However, since aluminium itself is active and the surface free energy is relatively high and therefore they are more likely to be contaminated. Their long-term stability in a corrosive environment and in an acidic or basic solution is still lacking. Therefore,

R. Raj (✉) · S. Kango · S. S. Sandhu
Department of Mechanical Engineering, Dr B R Ambedkar National Institute of Technology, Jalandhar 144011, India
e-mail: rishabh.raj199514@gmail.com

to explore how stronger, more stable long-term protection of a new aluminium alloy method can be obtained has always been an important issue for the protection of this metal [1]. There are a number of methods [2–4] to increase the stability and long-term durability in harsh environments like heat treatment [2], modifying chemical composition [3] and by surface coating [4]. Surface coating is one of the simple and economically efficient methods, the superhydrophobic coatings are widely used in self-cleaning [5], antifouling [6], antifogging [7], anti-icing [8] and corrosion resistance [9]. Therefore, if the superhydrophobic coated metal material surfaces are prepared the metal surface may be made self-cleaning, anti-contamination and anticorrosion properties, so as to achieve long-term protection of the substrate metal.

To prepare superhydrophobic coating on the substrate, two-step procedures have been adopted; first creating micro-level roughness by using different methods and second is the deposition of low surface energy material on the substrate. The methods to create roughness on a substrate are electrochemical etching [10], laser surface texturing [11], chemical etching [12] and photolithography [13]. There are a number of processes like electrospinning [14], dip-coating [15], spray coating [16], etc. which are used for deposition of low surface energy materials such as fatty acids [17], synthetic polymers [18], etc.

The fabricated superhydrophobic surface has the ability to repel water droplets and the contact angle formed on the surface is greater than in 150°. However, the practicality of theses surfaces is affected due to its poor mechanical stability, even weak friction forces are sufficient to destroy its superhydrophobic ability. Therefore, it is important to calculate the mechanical durability of the prepared superhydrophobic surfaces. Some of the researchers used different types of wear tests such as adhesive peel test [19], sand paper abrasion test [20] and by water impact test [21] to check the mechanical stability of the fabricated superhydrophobic surfaces.

Oleophobic surfaces are those types of surfaces that can also repel oil of low surface tensions along with water droplets. To create this type of surface, micro-nano scale roughness is required. Micro-level roughness is created by the chemical etching method and for the fabrication of nano-platelets structure boiling immersion method is used to obtain dual-scale roughness [22]. Further low surface energy materials such as fluoropolymers, silane, collide [23] are coated on the surface.

In our previous work ref. [24], the hydrophobic and superhydrophobic surfaces have been fabricated on aluminium alloy (Series 8000) by using chemical etching and dip-coating method. It has been concluded that the hydrophilic aluminium alloy surface was converted to superhydrophobic surface after 15 min of etching which is followed by dip-coating technique. However, the influence of mechanical forces such as action of friction has not been investigated in previous work.

Therefore, the current work focuses on the calculation of the mechanical stability of the fabricated superhydrophobic surfaces by different test. Further, try to improve the oleophobic characteristic of the surfaces.

6.2   Experimentation

6.2.1   *Material*

The raw material selected for the present work is aluminium alloy (8000 series) as shown in Fig. 6.1a. The SEM image and energy dispersive X-Ray spectroscopy (EDS or EDX) of the sample are shown in Fig. 6.1b, c. The chemical composition of the sample is87.04% Al, 0.74% Fe, 2.43% O and 9.79% of C.
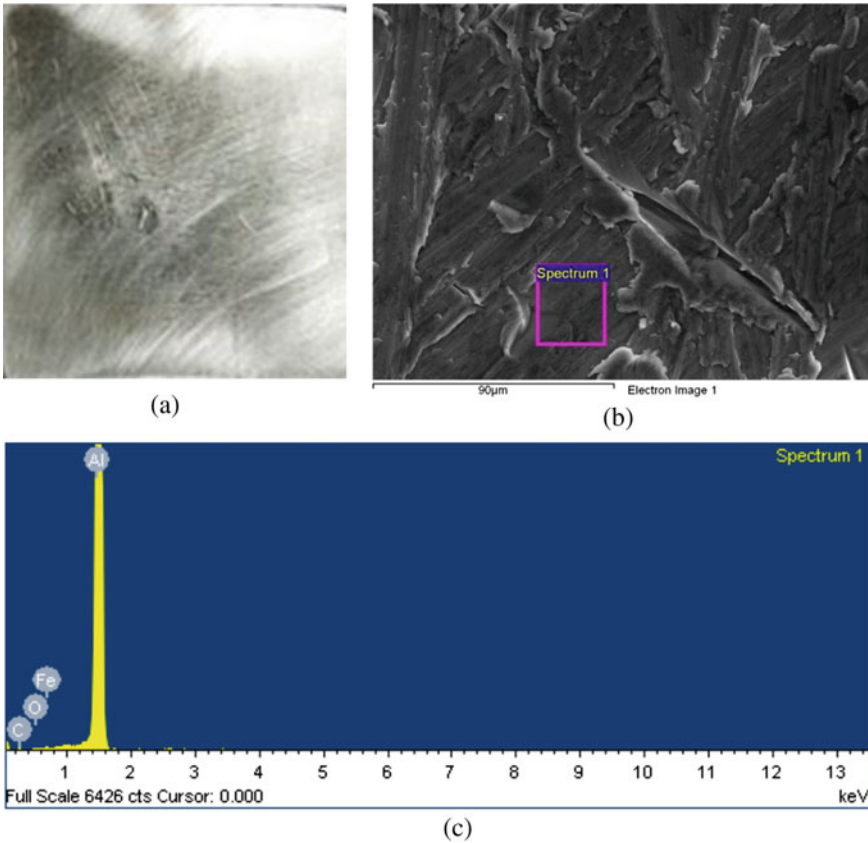
Fig. 6.1   a Aluminium alloy (8000 Series), **b** SEM image of the sample, **b** Energy spectrum graph of the sample using EDS

(a)

(b)

(c)

(d)
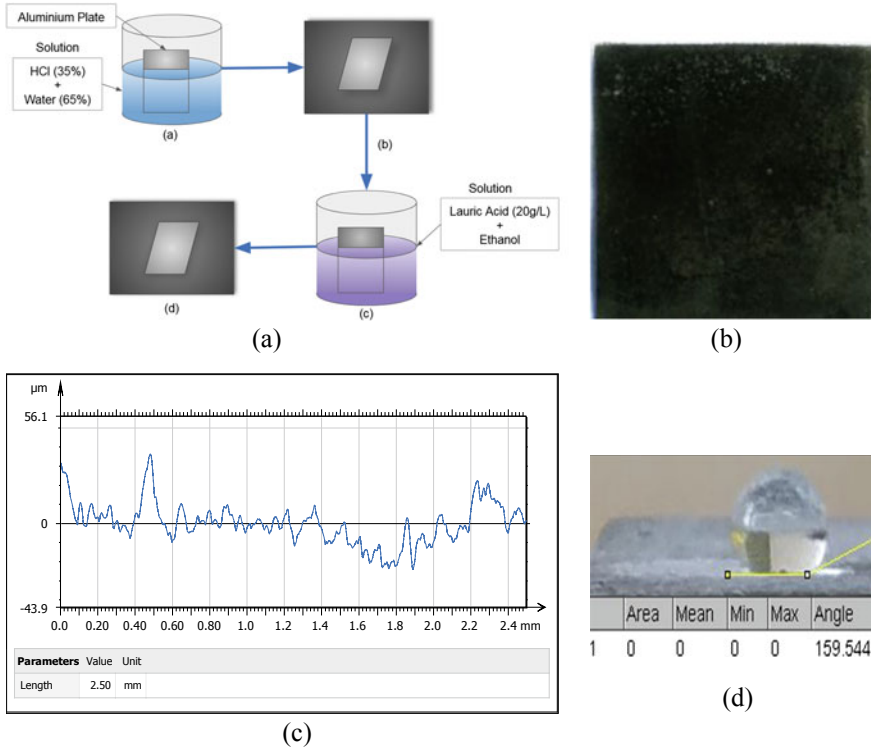
Fig. 6.2 **a** Steps to prepare superhydrophobic surfaces, **b** etched sample, **c** surface profile, **d** water contact angle [24]

6.2.2 Specimen Preparation

In our previous work Ref. [24], the fabrication details of superhydrophobic surfaces on aluminium alloy (Series 8000) and measurement of water contact angles for different samples are presented as shown in Fig. 6.2a–d. Water contact angle on the fabricated superhydrophobic surface was observed to be 159.54°.

6.2.3 Mechanical Stability of Prepared Samples

The following methods are adopted to check the mechanical stability of the superhydrophobic samples in the present study.
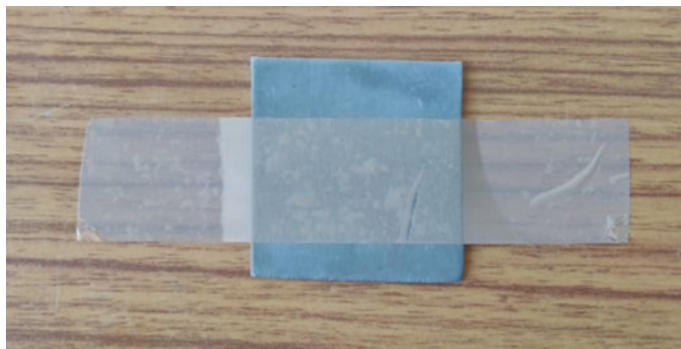
Fig. 6.3   Adhesive peel tests

6.2.3.1   Adhesive Peel Test

Adhesive tape (Cello fix) is used for repeated peeling on the fabricated superhydrophobic surfaces. The substrate is fixed on the table, then the adhesive tape is glued to it and a weight of 100 gm is applied over it for uniform sticking as shown in Fig. 6.3. Then, the adhesive tape is peeled off at an angle of 180° from the surface. This process of peeling is repeated 20 times. After a cycle of 5 peelings, water droplet is dropped by using micropipette (7 μl) on the substrate surface and the contact angle is measured using ImageJ software.

6.2.3.2   Sand Paper Abrasion Test

For the abrasion test, the coated sample is placed faced down to sandpaper (Grit No. 1000) and dragged for 10 cm along a ruler under a weight of 100 gm by the application of external drawing force as shown in Fig. 6.4. This process is also repeated for 20 times and after every 5 cycles, the contact angle of water droplet was measured.

6.2.3.3   Water Impact Test

In this test, the coated sample is placed vertically in the direction of flow and a constant velocity of about 2.5 m/s with the help of a container of diameter 25 cm and height 36 cm. After an interval of 2 min contact angle of water droplet was measured.
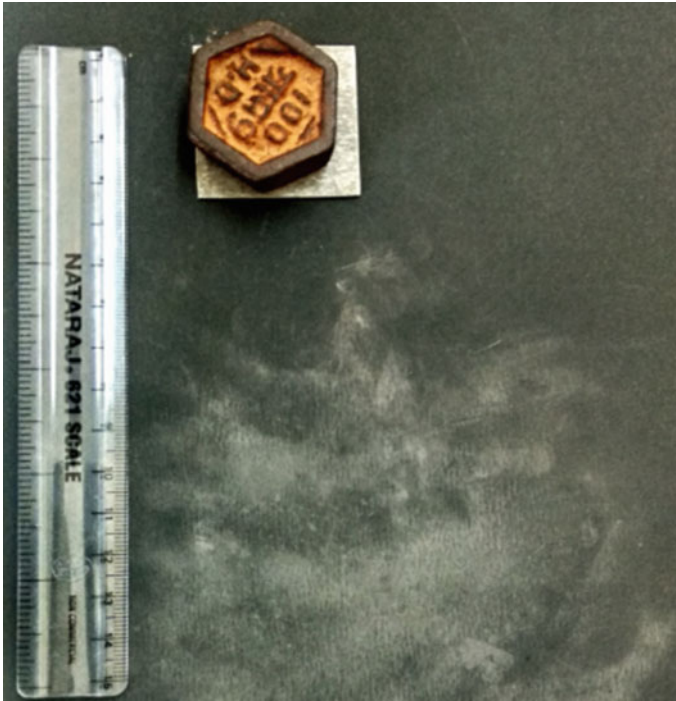
Fig. 6.4 Sand paper abrasion tests

6.3 Results and Discussions

Figure 6.5 shows the SEM images of cleaned aluminium sample (untreated), surface-treated sample, and tested sample after 20 cycles in adhesion peel test.

In present work, the surface grinder (1200 grit), deionized water and acetone are used for removing the oxide layer formed on the surface of aluminium and after cleaning process the SEM image of cleaned sample is shown in Fig. 6.5a. Thereafter, chemical etching and dip-coating methods are used to fabricate the superhydrophobic aluminium sample as shown in Fig. 6.5b.

Figure 6.5b shows the SEM image of surface-treated sample. It is depicted from Fig. 6.5b that after the deposition of low surface energy material on etched sample, the small cavities and low surface energy particles are shown in the samples. The air is trapped in between these cavities due to this, the water is not able to sink inside and make the higher contact angle, which is caused to convert the hydrophilic surface to superhydrophobic. Figure 6.5c shows SEM image of the surface after adhesion peel test. It is observed from the figure that after mechanical testing, microstructures get eroded from the surface and size of cavities increases. Due to this the water contact angle decreases and the treated surface becomes hydrophobic in nature.
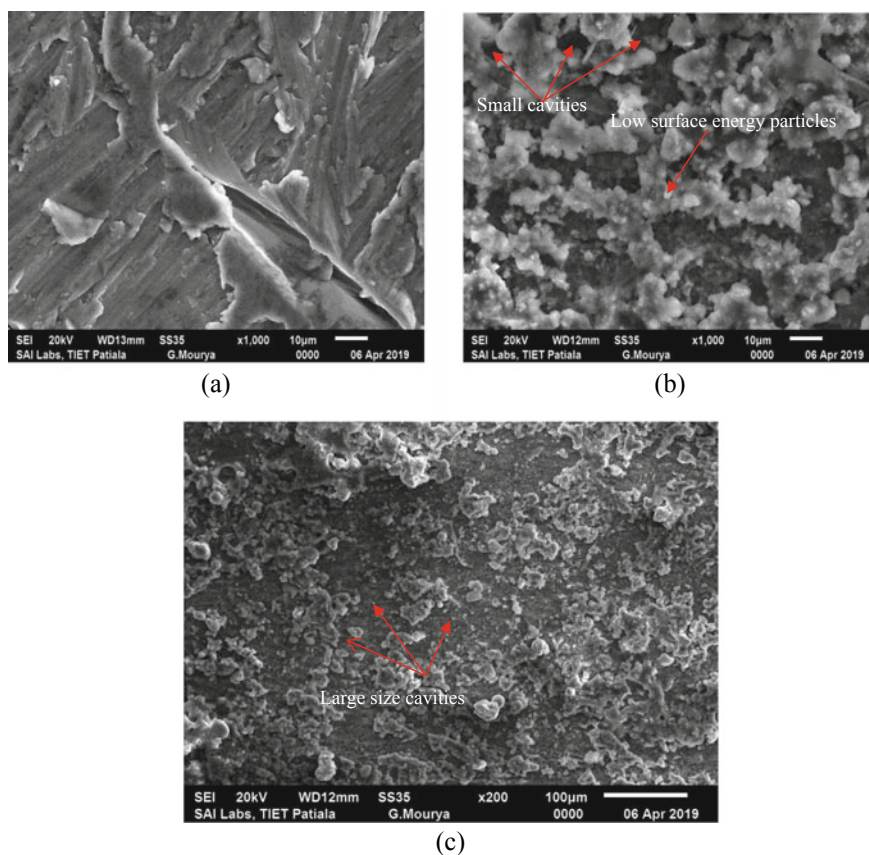
Fig. 6.5 SEM images for different samples, **a** aluminium sample, **b** surface-treated aluminium sample, **c** surface-treated sample after adhesion peel test

To check the mechanical durability of the fabricated superhydrophobic aluminium surfaces, the adhesive tape peeling, sand abrasion test and water impact test are used. Figure 6.6a, b shows the results of the adhesion peel test, sand abrasion test and water impact test. As shown in Fig. 6.6a, the coating remained unaffected for up to 20 cycles of peeling, as the water droplets fall off the surface. To check abrasive strength, sand paper is used. As shown in Fig. 6.6a, the coating remained unaffected for up to 15 cycles of abrasion. Figure 6.6b shows the result of water impact test. It reveals that the coated Al surface prevents water from spreading, and it bounces off the water jet in the opposite direction. This is because of the superhydrophobic nature of the coating. The presence of air pockets and the lower surface energy on the surface do not allow the impacting water jet to enter into the rough structure of
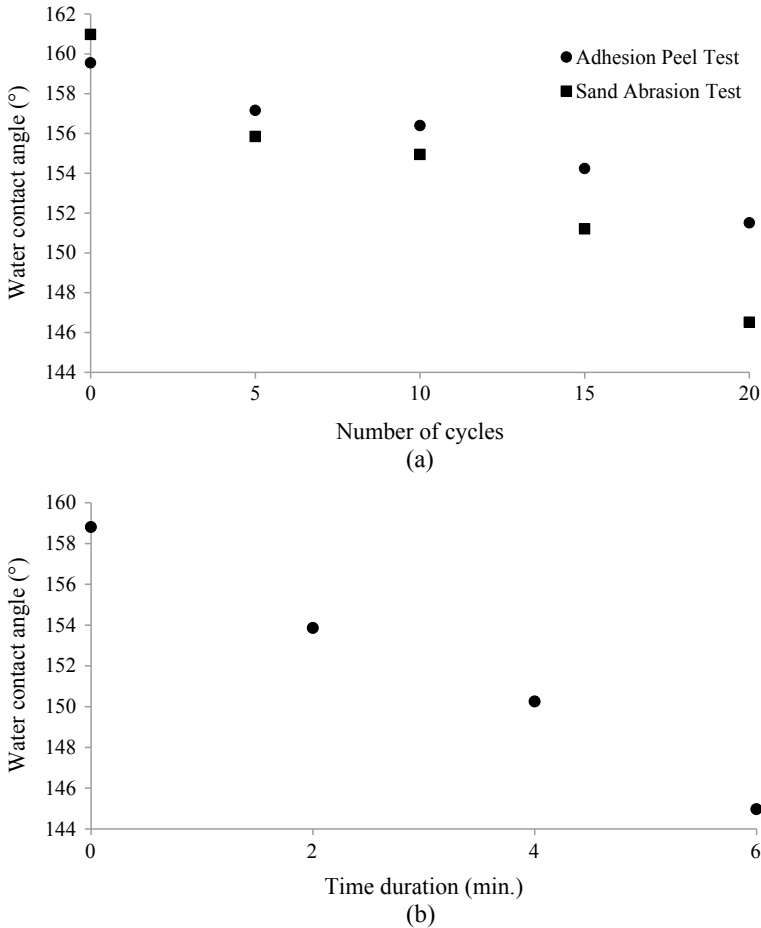
Fig. 6.6 Effect of number of cycles and time duration on water contact angle, **a** adhesion peel and Sand abrasion test, **b** water impact test

the surface, and it leads to the jet bouncing off from the surface. It is observed that the coating remained unaffected up to 4 min of water impingement.

Some of the etched samples after chemical etching are cleaned with deionized water and acetone. Then they are immersed in boiling water for about 20 min as shown in Fig. 6.7. After this heat treatment process of the samples, they are again coated with the low surface energy materials by dip-coating method. By combing the simple chemical etching and boiling of the etched aluminium surface, the dual structures including micro and nano-platelets are successfully built on the Al surface. They play a significant role in enhancing oleophobic characteristics of the resultant surface that could repel liquids with the surface tension ranged from 63 to 73.1 mN/m.

Fig. 6.7 Boiling of etched samples by immersing in water

The formation of the large-scale nano-platelets is due to the physical attack of H2 and air bubbles at the boiling water/Al interface. Thus by combining the above-mentioned preparation steps acid etching followed by boiling water immersion, MNS-surface is obtained. Figure 6.8a, b shows the SEM image of the aluminium sample after heat treatment and coating.

The surface formed after the treatment shows oleophobic characteristics as well. The contact angle formed by glycerol droplet having surface tension 63 mN/m on the surface is 110.56° as compared to water droplet having surface tension 73.1 mN/m shows water contact angle of 150.133° as shown in Fig. 6.9. This is due to macro and nanoscale roughness formed on the surface by combing chemical etching and boiling as shown in Fig. 6.8a, b.

6.4   Conclusions

The mechanical durability of surface-treated aluminium samples is investigated in the present study. The broad outcomes of the present work:

- Water contact angle decreases from 159.54° to 151.51° in adhesive peel test and from 160.97° to 146.51° in sand abrasion test for 20 number of cycles.
- Water contact angle decreases from 158.81° to 144.97° in water impact test for 6 min of water impingement.
- Fabricated superhydrophobic samples show its non-wettability characteristics up to 20 cycles in adhesive peel test, 15 cycles in sand abrasion test and 4 min in water impact test.

SEI   20kV   WD11mm   SS35   x1,000   10µm
SAI Labs, TIET Patiala   G.Mourya   0000   06 Apr 2019

(a)

SEI   20kV   WD11mm   SS35   x100   100µm
SAI Labs, TIET Patiala   G.Mourya   0000   06 Apr 2019
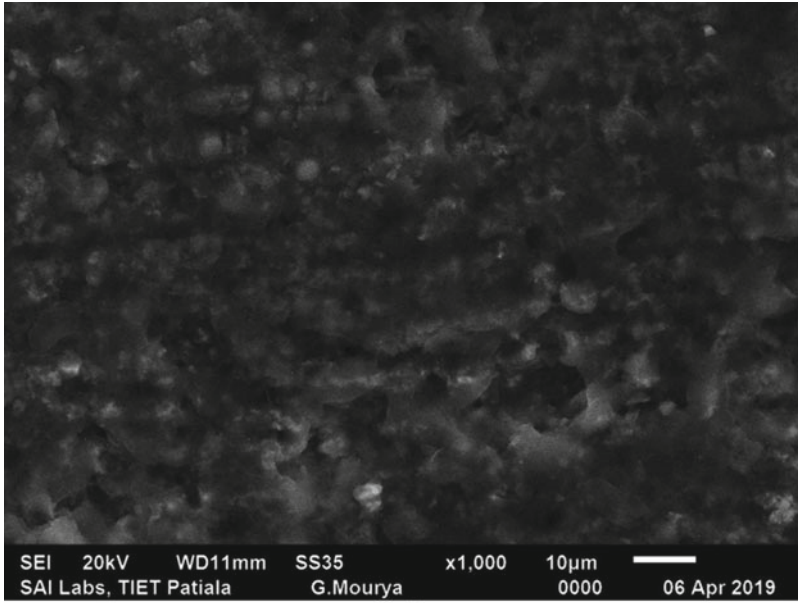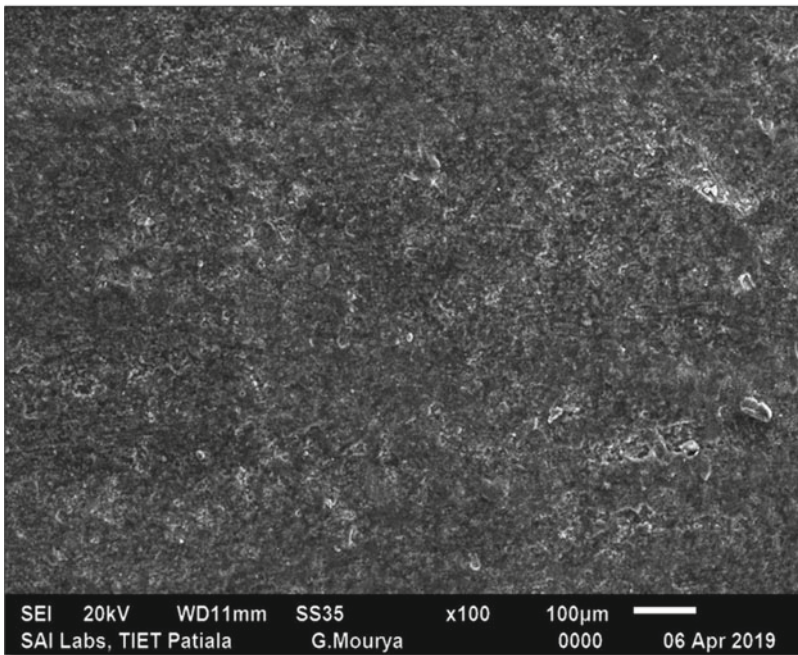
(b)

Fig. 6.8   a, **b** SEM image of the aluminium sample after heat treatment and coating

Fig. 6.9 Measurement of water contact angle of glycerol and water droplet of volume 7 µl by using ImageJ
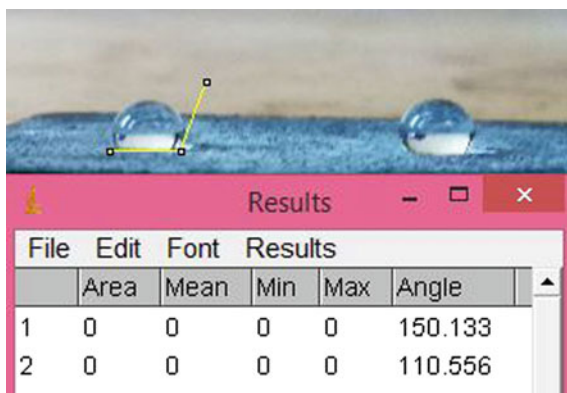
- The contact angle formed by glycerol droplet having surface tension 63mN/m on the surface is 110.56° as compared to water droplet having surface tension 73.1 mN/m shows water contact angle of 150.13°.

It is observed that the microstructures get eroded from the surface-treated samples after each test. Due to this the water contact angle decreases and the surface becomes hydrophobic in nature.

References

1. Tudu, B.K., Kumar, A., Bhushan, B.: Facile approach to develop anti-corrosive superhydropho-bic aluminium with high mechanical, chemical and thermal durability. Philos. Trans. R. Soc. A **377**(2138), 20180272 (2018)
2. da Silva, R.G., Vieira, M.R., Malta, M.I., da Silva, C.H., de Oliveira, S. H., Severino Filho, L.U.: Effect of initial surface treatment on obtaining a superhydrophobic surface on 5052 aluminum alloy with enhanced anticorrosion properties. Surf. Coat. Technol. 5074–5078 (2019)
3. Chi, Y., Gu, G., Yu, H., Chen, C.: Laser surface alloying on aluminum and its alloys: a review. Opt. Lasers Eng. **100**, 23–37 (2018)
4. Yang, H., He, Y., Wu, Z., Miao, J., Yang, F., Lu, Z.: Fabrication of a superhydrophobic and high-glossy copper coating on aluminum substrates. Appl. Surf. Sci. **433**, 1192–1196 (2018)
5. Zhao, Q., Tang, T., Wang, F.: Fabrication of superhydrophobic AA5052 aluminum alloy surface with improved corrosion resistance and self-cleaning property. Surf. Coat. Technol. **8**(11), 390 (2018)
6. Feng, L., Che, Y., Liu, Y., Qiang, X., Wang, Y.: Fabrication of superhydrophobic aluminium alloy surface with excellent corrosion resistance by a facile and environment-friendly method. Appl. Surf. Sci. **283**, 367–374 (2013)
7. Nanda, D., Varshney, P., Satapathy, M., Mohapatra, S.S., Bhushan, B., Kumar, A.: Single step method to fabricate durable superliquiphobic coating on aluminum surface with self-cleaning and anti-fogging properties. J. Colloid Interface Sci. **507**, 397–409 (2017)
8. Vazirinasab, E., Jafari, R., Momen, G.: Application of superhydrophobic coatings as a corrosion barrier: a review. Surf. Coat. Technol. **341**, 40–56 (2018)

9. Sun, Y., Zhao, D., Song, J., Wang, C., Zhang, Z., Huang, L., Liu, Z.: Rapid fabrication of super-hydrophobic high-silicon aluminum alloy surfaces with corrosion resistance. Results Phys. **12**, 1082–1088 (2019)

10. Kamaraj, A.B., Shaw, V., Sundaram, M.M.: Novel fabrication of un-coated super-hydrophobic aluminum via pulsed electrochemical surface modification. Procedia Manuf. **1**, 892–903 (2015)

11. Li, J., Fan, F., Zhao, Y., Zhou, Y., Li, H., Yu, H.: Influence of laser surface texturing on a low-adhesion and superhydrophobic aluminium alloy surface. Micro Nano Letters **13**(3), 389–392 (2018)

12. Zhang, X., Zhao, J., Mo, J., Sun, R., Li, Z., Guo, Z.: Fabrication of superhydrophobic aluminum surface by droplet etching and chemical modification. Colloids Surf., A **567**, 205–212 (2019)

13. Liu, B., He, Y., Fan, Y., Wang, X.: Fabricating super-hydrophobic lotus-leaf like surfaces through soft-lithographic imprinting. Macromol. Rapid Commun. **27**(21), 1859–1864 (2006)

14. Cui, M., Xu, C., Shen, Y., Tian, H., Feng, H., Li, J.: Electrospinning superhydrophobic nanofibrous poly (vinylidene fluoride)/stearic acid coatings with excellent corrosion resistance. Thin Solid Films **657**, 88–94 (2018)

15. Zhang, H., Hou, C., Song, L., Ma, Y., Ali, Z., Gu, J., Zhang, Q.: A stable 3D sol-gel network with dangling fluoroalkyl chains and rapid self-healing ability as a long-lived superhydrophobic fabric coating. Chem. Eng. J. **334**, 598–610 (2018)

16. Polizos, G., Jang, G.G., Smith, D.B., List, F.A., Lassiter, M.G., Park, J., Datskos, P.G.: Transparent superhydrophobic surfaces using a spray coating process. Sol. Energy Mater. Sol. Cells **176**, 405–410 (2018)

17. Varshney, P., Lomga, J., Gupta, P.K., Mohapatra, S.S., Kumar, A.: Durable and re-generable superhydrophobic coatings for aluminum surfaces with excellent self-cleaning and anti-fogging properties. Tribol. Int. **119**, 38–44 (2018)

18. Das, S., Kumar, S., Samal, S.K., Mohanty, S., Nayak, S.K.: A review on superhydrophobic polymer nano coatings: recent development and applications. Ind. Eng. Chem. Res. **57**(8), 2727–2745 (2018)

19. Li, X., Zhao, S., Hu, W., Zhang, X., Pei, L., Wang, Z.: Robust superhydrophobic surface with excellent adhesive properties based on benzoxazine/epoxy/mesoporous SiO_2. Appl. Surf. Sci. **481**, 374–378 (2019)

20. Darband, G.B., Aliofkhazraei, M., Khorsand, S., Sokhanvar, S., Kaboli, A.: Science and engineering of superhydrophobic surfaces: review of corrosion resistance, chemical and mechanical stability. Arab Chem. **52**(11), 3709–3713 (2018)

21. Ding, B., Wang, H., Zhu, X., Chen, R., Liao, Q.: How super cooled superhydrophobic surfaces affect dynamic behaviours of impacting water droplets? Int. J. Heat Mass Transfer **124**, 1025–1032 (2018)

22. Peng, S., Yang, X., Tian, D., Deng, W.: Chemically stable and mechanically durable super-amphiphobic aluminum surface with a micro/nanoscale binary structure. ACS Appl. Mater. Interfaces **6**, 15188–15197 (2014)

23. Deng, X., Mammen, L., Butt, H.J., Vollmer, D.: Candle soot as a template for a transparent robust superamphiphobic coating. Science **337**, 67–70 (2012)

24. Raj, R., Kango, S., Sandhu, S.S.: Fabrication of hydrophobic and superhydrophobic aluminum surfaces. In: Presented in 1st International Conference on Material Science & Engineering (ICMSE-2019), (Paper ID-27) at Dr B R Ambedkar National Institute of Technology, Jalandhar, 11–12 June 2019

Chapter 7
Design and Development of High-Velocity Submerged Water Jet Cavitation Erosion Test Rig

Anuj Bansal, Jonny Singla, Shivam Pandey, and Prem Raj

Abstract Several hydro-machinery components such as impellers of submersible pump, draft tubes and turbine blades generally suffer from cavitation erosion (CE) during their operation, and due to this, service life and capability of such parts are reduced. During the design and development of these components, test rigs are usually required to evaluate their performance. In the present research work, keeping in view the economic aspects, out of different test rigs available, it is proposed to use high-velocity submerged water jet cavitation erosion test rig. The test rig was designed with flexibility in cavitation erosion parameters (velocity, angle of attack, stand-off distance, nozzle diameter) and fabricated with an aim to test the cavitation erosion of hydro-machinery steel under different cavitation erosion parameters. Calibration of the test rig was done for jet velocity, stand-off distance (SOD) and angle of attack. The CE rate of steel SS410 was evaluated using the fabricated test rig under different operating parameters consists of 3 velocities and 3 stand-off distance, keeping the other parameters like angle of attack as 90° and nozzle diameter as 3 mm. The test rig was capable of producing CE as observed from the specimen microstructure. From the microstructure analysis, the pits produced during the CE are clearly visible. The CE rate was found to be maximum for a parametric combination consist of maximum velocity (35 m/sec) and stand-off distance (10 cm). With an increase in velocity, the amount of water bubbles increases in the cavitation cloud, which contributes to maximum erosion. The cavitation erosion rate is enhanced by increasing the stand-off distance from 5 cm to 10 cm, followed by a decrement when moving from 10 to 15 cm.

Keywords Cavitation erosion test rig · Stand-off distance · Cavitation erosion · SS410 · Velocity

A. Bansal (✉) · J. Singla · S. Pandey · P. Raj
Department of Mechanical Engineering, Sant Longowal Institute of Engineering and Technology, Longowal 148106, India
e-mail: anujbansalsliet@gmail.com

Nomenclature

CE   Cavitation erosion
SS   Stainless steel
SOD   Stand-off distance
ASTM   American Society for Testing and Materials

7.1 Introduction

In the present-day scenario, water handling equipments like heat exchangers, hydro-turbines and submersible pumps become the basic need of life. Out of many problems encountered by the hydro-machinery components, cavitation becomes the major issue for the erosion of material in draft tube, penstock, impellers of turbine and pump, submarine, etc. [1–7]. Cavitation erosion is majorly seen in reaction turbines such as Francis and Kaplan turbines, and in Francis turbine, the defects due to cavitation erosion can be seen at five places, i.e. leading edge, trailing edge, draft tube swirl and inter-blade vortex, wickets gates, and in Kaplan turbine, these defects can be seen on blades and guide vanes [5–8]. Cavitation erosion (CE) is a usual damage phenomenon, in which due to pressure difference, the water bubbles get generated and collapsed at the surface which leads to the generation of shockwave, which travels with an enormous force of impact (≥ 1500 MPa) towards the surface and deteriorates the material [1, 2, 6–9]. Depending upon the working environment, sometimes, the effect caused by cavitation erosion may be severe enough to render the components from its future functionality. The above-said fact may contribute to huge economic losses to the industries. The CE rate mainly depends upon the operating conditions, such as velocity of flowing fluid, angle of attack and distance of components from the low-pressure region. Further, the CE also depends upon the properties of the target material of the component. The erosion of material due to cavitation cannot be eliminated but can be controlled by proper surface modification of the material [5, 10, 11]. Researchers [5, 8, 10–12] explored the possibilities of epoxy coating, different heat treatments, hard facing, etc. of hydro-machinery steels with an aim to enhance their cavitation erosion resistance. In actual, cavitation erosion occurs slowly during the operation and mechanism involved in it is complex. To evaluate the performance of such materials under the action of cavitation before actual implementation, test rig cable of enhancing the cavitation erosion is required. The extensive literature survey has been done in accordance with the test rigs associated with the cavitation erosion. From the literature survey, it was concluded that a few test rigs were used for cavitation erosion testing. However out of available test rigs, a lot of work has been done on the ultrasonic/vibrating cavitation erosion test rig, rotary disc type test rig and experimental set-up with Venturi geometry for analysing the cavitation erosion of hydro-machinery steels [3–5, 13, 14]. Further, the submerged high-velocity water jet is also capable of producing cavitation erosion [9, 15–18] which will be

a cheaper potential solution as compared to the conventionally available cavitation test rigs. But the cavitation erosion through high-velocity submerged water jet was still not fully explored. So, keeping the above facts into consideration, in this project work, the high-velocity water jet cavitation erosion test rig will be designed and fabricated with the flexibility in cavitation erosion parameters (velocity, angle of attack, stand-off distance, nozzle diameter). In the designed test rig, the effect of fluid jet is negligible as the target material was submerged under the fluid during cavitation erosion. Martensitic grade SS 410 is selected for the present study because of its enormous use in the field of hydro-machinery components. The cavitation erosion of the said steel was tested using the designed high-velocity water jet cavitation erosion test rig under different operating parameters. Further, the variation in the cavitation erosion parameters during the test may be helpful to set standards for optimizing the working conditions and designing of hydro-machinery components. The velocity plays a crucial role during the cavitation erosion of hydro-machinery component as it affects the pressure of the flowing fluid, which in turn increases the number of bubbles in the flow [15–18]. Further, the stand-off distance also had a great importance in CE. So, the three levels each for velocity and stand-off distance are taken during the study. Moreover, the other parameters like angle of attack and nozzle diameter were kept constant. The results obtained may be useful for designing and fabrication of hydro-machinery components exposed to cavitation erosion conditions.

7.2 Review of Different CE Test Rigs

Extensive study regarding the used test rigs associated with the cavitation erosion was carried out. Some of the major test rigs used are discussed in this section. Osterman et al. in 2009 [13] had used rotating disc test rig as shown in Fig. 7.1 to analyse the time-dependent measurements of cavitation damage. It consists of a closed water loop system and rotational disc having diameter 500 mm with four holes where cavitation
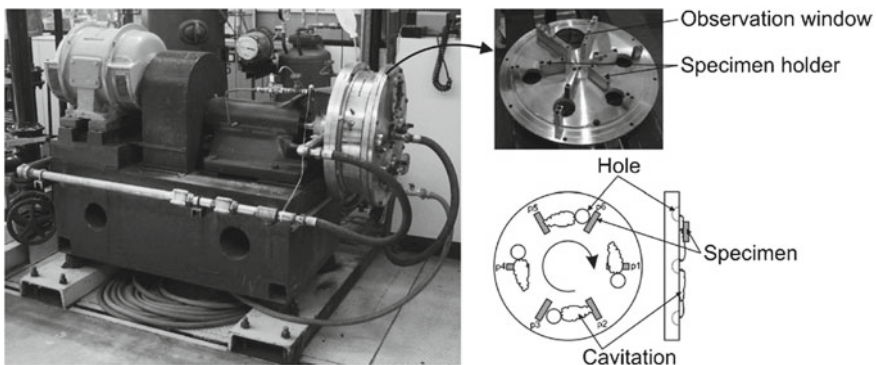
Fig. 7.1 Rotational disc-type test rig used by Osterman et al. [13]
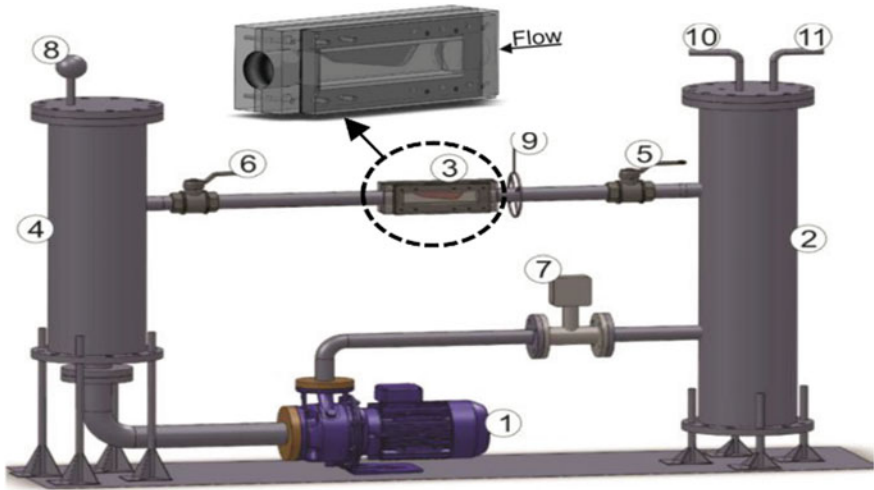
Fig. 7.2 Experimental set-up with Venturi geometry used by Dular et al. [14]

occurs and is driven by 35 kW motor, which is controlled by the frequency controller
to vary the rotational frequency.

Dular et al. in 2015 [14] used the experimental set-up as shown in Fig. 7.2 with Venturi geometry for analysing the cavitation erosion. The designed Venturi decreases
the flow area which further helps in producing the bubbles. These bubbles collapse
at the nearby targeted material, which contributes to CE.

Sato et al. in 2013 [17] studied the periodic behaviour of cavitation cloud through
the convergent–divergent nozzle as shown in Fig. 7.3 for water jet at different pressure. They concluded that the cavitation cloud mainly consists of two portions, one
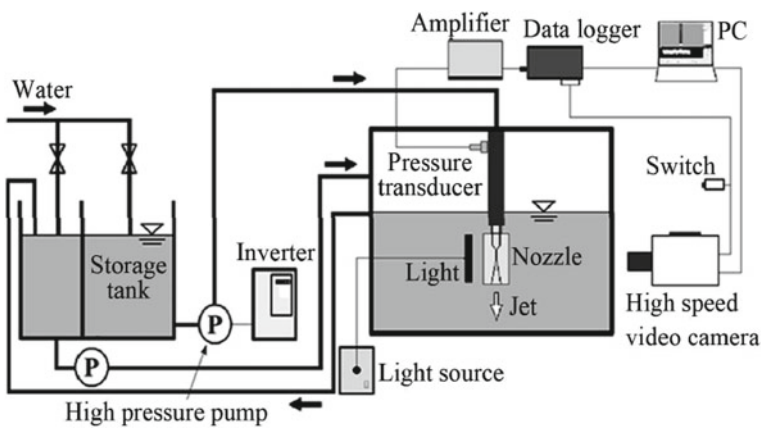
Fig. 7.3 Convergent–divergent nozzle set-up used by Sato et al. [17]
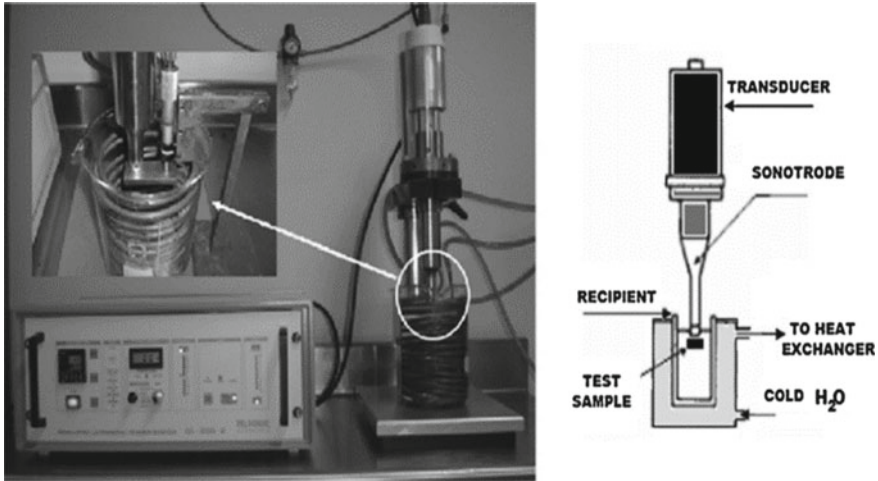
Fig. 7.4   Ultrasonic/vibrating cavitation erosion test rig. Used by Santa et al. [5]

contributes by upstream pressure fluctuation and other may be caused by shorter periodic oscillation of cavity length.

Researchers like Liu et al. [3], Lin et al. [4], Santa et al. [5], Chi et al. [11] and Qiu et al. [12] had used the conventionally available ultrasonic/vibrating cavitation erosion test rig as shown in the Fig.7.4, which uses ASTM G32 method. The test rig consists of a vibrating horn with variability in diameter which is capable of producing bubbles.

Further, some researchers explored the high-velocity underwater jet, which can produce CE [1, 9, 15, 16, 18, 19]. Test rig consisting of the submerged water jet is easy to construct, and further, it is also a cheaper solution as compared to the above-said test rigs. In this type of test rig, the pressurized water is supposed to be passed through the submerged nozzle, where the bubbles get generated, due to decrease in the area at the tip of the nozzle. These bubbles will be carried along with the flow to a distance, where the targeted sample is placed. The bursting of such bubbles causes the CE at the surface of the target sample. As the sample is fully submerged in the water, the effect of the direct water jet is negligible. As per the discussed features of the above-said test rig, in this research work, the cavitation erosion test rig was designed and fabricated for the analyses.

7.3   Design and Development of Test Rig

The block diagram of the designed high-velocity submerged water jet test rig is shown in Fig. 7.5a. The water from the tank is pumped using a 1.5 kW, 3-phase motor to nozzle through the delivery pipe. The valves are used to control the discharge of water
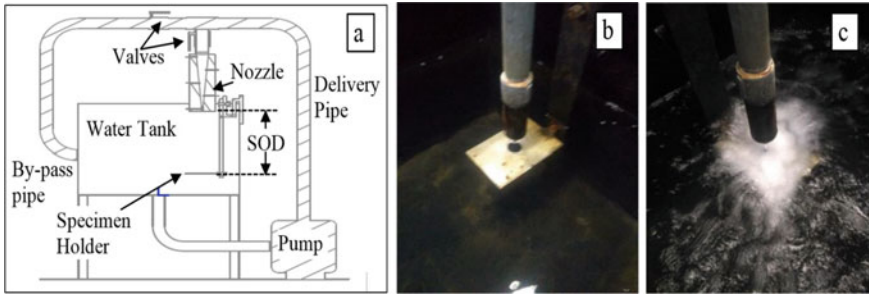
Fig. 7.5 **a** Block diagram of the designed test rig, **b** specimen holder with flexibility in movements and **c** actual cavitation cloud

to the inlet of nozzle. The specimen holder is attached with the flexibility in stand-off distance and angle of attack as shown in Fig. 7.5b. Both specimen holder and the nozzle are completely submerged in the water. With an increase in velocity at the tip of the nozzle, the pressure decreases even below the saturated vapour pressure, the upshot to the generation of bubbles and the cavitation cloud as shown in Fig. 7.5c.

This cavitation cloud is basically responsible for the CE of the target material. The calibration of the test rig with respect to the angle of attack, velocity and stand-off distance was done before the actual experimentation.

7.4 Cavitation Erosion of SS 410

The SS410 was procured in the form forged road having diameter 25 mm. The spectroscopy test was conducted to validate the chemical composition of the material, and the results found to be in accordance with the standard limits. The specimens having diameter 25 mm and thickness 4 mm were prepared. The density and microhardness of the said steel were found to be 7.9 g/cc and 151 HV, respectively. The CE of the said samples was carried out using the test rig under the variation in CE parameters like velocity of jet and SOD. As discussed earlier, velocity is one of the major contributors to the CE, so three levels of velocity (35, 30 and 25 m/s) were taken during the analysis. Further, the three SOD (5, 10 and 15 cm) were taken to analyse the effect of SOD on the CE. For experimentation, nine combinations of the said parameters as per full factorial technique were used as shown in Table 7.1. Angle of attack as 90° and nozzle diameter 3 mm were kept constant throughout the study. The samples were polished and cleaned with the help of acetone before subjected to the CE conditions. Specimens were exposed to the CE condition for 10 h each.

CE erosion can be measure by two ways either by calculating the number of pits or by measuring the Mass loss. But, the measurement of Mass loss is more accurate because with an increase in time the pits can be overlapped. So, in the present research work, the CE was measured in terms of mass loss. Mass loss in gm

Table 7.1 Parametric combinations as per full factorial and mass loss of samples

S. No.	Experimental run	Velocity (m/s)	SOD (cm)	Mass loss $\times 10^{-3}$ (gm)
1	Run 1	25	5	5.6
2	Run 2	25	10	6.3
3	Run 3	25	15	4.8
4	Run 4	30	5	8.3
5	Run 5	30	10	8.5
6	Run 6	30	15	6.1
7	Run 7	35	5	9.2
8	Run 8	35	10	11.9
9	Run 9	35	15	7.6

obtained for the said set of samples is also represented in Table 7.1. Further, the mass loss was compared using a line graph as represented in Fig. 7.6.

It was concluded that with an increase in velocity of the jet, mass loss increases, which may be due to the increase in bubble density in the cavitation cloud. It was also observed that the mass loss during the CE firstly increases with increase in SOD from 5 to 10 cm, followed by a decrement, when moving from 10 to 15 cm. In case of 5 cm, SOD, the bubbles are not able to grow properly while striking the target material, whereas in case of 15 cm, SOD, some of the bubbles were collapsed in the fluid itself before reaching the target specimen. This may be the possible reason behind the CE peak obtained at 10 cm, SOD. The results obtained are in accordance with the researchers [15–19]. The microstructural images of a sample subjected to the CE condition of run number 8 (velocity: 35 m/s and SOD: 10 cm) before and after CE are shown in Fig. 7.7.

From the microstructural images, the pits are clearly visible on the surface of the specimen after CE as shown in Fig. 7.7b. Material was removed from the surface as
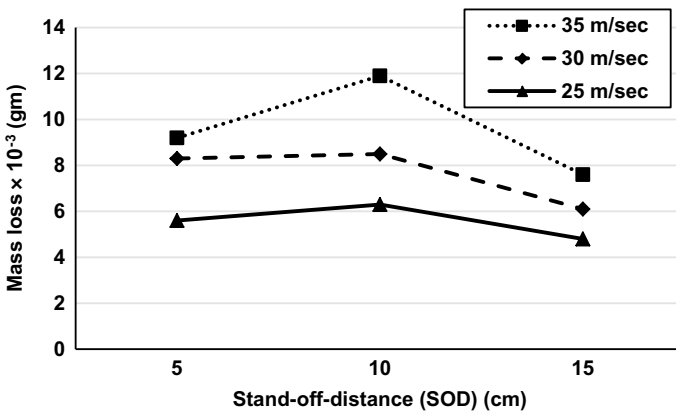
Fig. 7.6 Mass loss due to cavitation erosion under the action of variable velocity and SOD
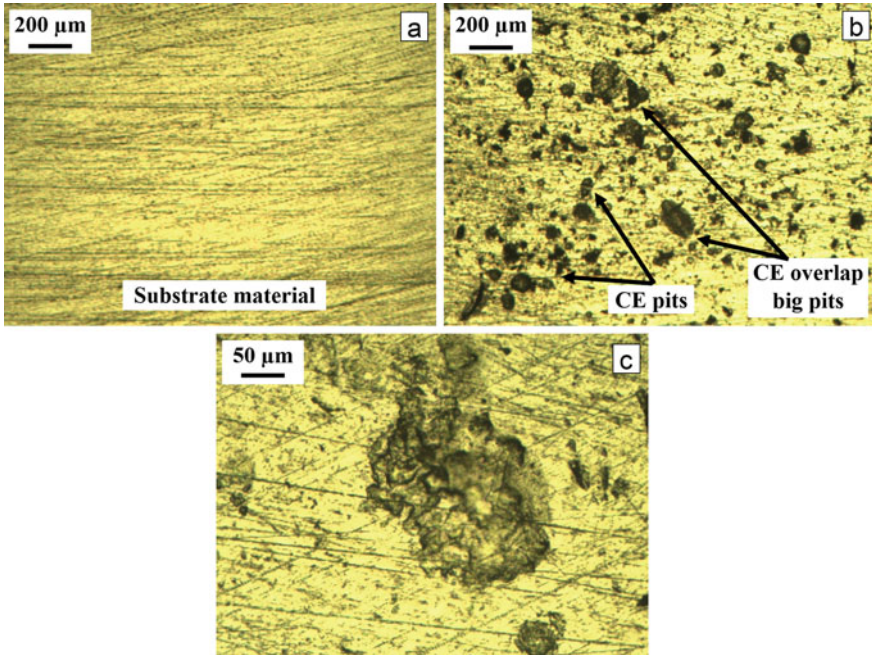
Fig. 7.7 Microstructural images of **a** Substrate material, **b** CE pits and **c** enlarged view of the pit

shown in Fig. 7.7c, as a result of impact drawn by the shock wave produced during the bursting of bubble.

7.5 Conclusion

The main aim of the study is to design and development high-velocity submerged water jet cavitation erosion test rig. Further, SS410 was tested under different cavitation erosion parameters on the designed test rig. The conclusion drawn is stated below.

- The developed test rig was capable of producing the cavitation erosion of the target material in the stipulated time, hence proven to be a cheaper potential solution in this regard. Flexibility in CE parameters was also successfully achieved.
- It was also reported that the mass loss due to CE has a maximum value at intermediate SOD and for the maximum velocity. As with the increase in velocity, the amount of bubbles increases. Whereas, most of these bubbles collapse at a particular distance from where they are generated.
- The CE pits are clearly visible from the microstructure images. The overlapping of the pits was also reported in the images. Further, from the microstructural analysis,

it was found that the material was removed as an action of impact produced by the shock wave on the targeted surface.

References

1. Kang, C., Liu, H., Zhang, T., Li, Q.: Investigation of submerged waterjet cavitation through surface property and flow information in ambient water. Appl. Surf. Sci. **425**, 915–922 (2017)
2. Hu, H.X., Zheng, Y.G., Qin, C.P.: Comparison of Inconel 625 and Inconel 600 in resistance to cavitation erosion and jet impingement erosion. Nucl. Eng. Des. **240**, 2721–2730 (2010)
3. Liu, W., Zheng, Y.G., Liu, C.S., Yao, Z.M., Kea, W.: Cavitation erosion behavior of Cr–Mn–N stainless steels in comparison with 0Cr13Ni5Mo stainless steel. Wear **254**, 713–722 (2003)
4. Lin, C.J., Chen, K.C., He, J.L.: The cavitation erosion behavior of electroless Ni–P–SiC composite coating. Wear **261**, 1390–1396 (2006)
5. Santa, J.F., Blanco, J.A., Giraldo, J.E., Toroa, A.: Cavitation erosion of martensitic and austenitic stainless steel welded coatings. Wear **271**, 1445–1453 (2011)
6. Bansal, A., Singh, J., Singh, H.: Slurry erosion behavior of HVOF-sprayed WC-10Co-4Cr coated SS 316 steel with and without PTFE modification. J. Therm. Spray Tech. (2019). https://doi.org/10.1007/s11666-019-00903-y
7. Upadhyay, J., Bansal, A., Singh, J.: Effect on mechanical and metallurgical properties of cryogenically treated material SS316. In: Sharma, V., Dixit, U., Alba-Baena, N. (eds.) Manufacturing Engineering. Lecture Notes on Multidisciplinary Industrial Engineering. Springer, Singapore, pp. 97–107 (2019)
8. Singh, P., Bansal, A., Goyal, D.K.: Erosion wear evaluation of HVOF sprayed WC-12Co coating on some pipeline materials using Taguchi approach. Kovove Mater. **57**, 113–120 (2019)
9. Hutli, E., Nedeljkovic, S.M., Bonyár, A., Légrády, D.: Experimental study on the influence of geometrical parameters on the cavitation erosion characteristics of high-speed submerged jets. Exp. Therm. Fluid Sci. **80**, 281–292 (2017)
10. Wang, Y., Stella, J., Darut, G., Poirier, T., Liao, H., Planche, P.M.: APS prepared NiCrBSi-YSZ composite coatings for protection against cavitation erosion. J. Alloys Compounds **699**, 1095–1103 (2017)
11. Chi, S., Park, J., Shon, M.: Study on cavitation erosion resistance and surface topologies of various coating materials used in shipbuilding industry. J. Ind. Eng. Chem. **26**, 384–389 (2015)
12. Qiu, N., Wang, L., Wub, S., Likhachev, S.D.: Research on cavitation erosion and wear resistance performance of coatings. Eng. Failure Anal. **55**, 208–223 (2015)
13. Osterman, A., Bachert, B., Sirok, B., Dular, M.: Time dependant measurements of cavitation damage. Wear **266**, 945–951 (2009)
14. Dular, M., Petkovsek, M.: On the mechanisms of cavitation erosion—coupling high speed videos to damage patterns. Exp. Therm. Fluid Sci. **68**, 359–370 (2015)
15. Sun, Z., Kang, X.Q., Wang, X.H.: Experimental system of cavitation erosion with water-jet. Mater. Des. **26**, 59–63 (2005)
16. Hutli, F.A.E., Nedeljkovic, S.M., Radovic, A.N.: Mechanics of submerged jet cavitating action: material properties, exposure time and temperature effects on erosion. Arch. Appl. Mech. **78**, 329–341 (2008)
17. Sato, K., Taguchi, Y., Hayashi, S.: High speed observation of periodic cavity behavior in a convergent-divergent nozzle for cavitating water jet. J. Flow Control Meas. Visualization **1**, 102–107 (2013)
18. Li, D., Kang, Y., Wang, X., Ding, X., Fang, Z.: Effects of nozzle inner surface roughness on the cavitation erosion characteristics of high speed submerged jets. Exp. Therm. Fluid Sci. **74**, 444–452 (2016)
19. Cheng, F., Ji, W., Qian, C., Xu, J.: Cavitation bubbles dynamics and cavitation erosion in water jet. Results Phys. **9**, 1585–1593 (2018)

Chapter 8
Development of Durable Super-Hydrophobic Surface on WC–Co–Cr Coated ASTM A988 Stainless Steel Substrate

Check for updates

Vijay Kumar and Rajeev Verma

Abstract Graphic Abstract
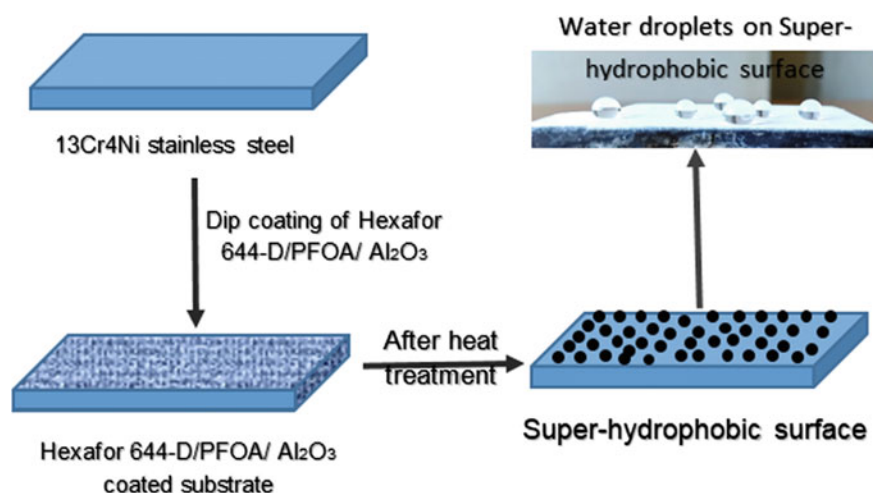
Abstract Super-hydrophobic surfaces were fabricated at low cost using a simple dip coating method. Super-hydrophobic surfaces on metal and alloys play an important role in industries because of its numerous advantages are anti-pollutant ability and water repellence. In this work, Hexafor 644-D/PFOA/Al_2O_3 aqueous solution was used for dip coating on ASTM A988 stainless steel. The water contact angle of approximately 161° was obtained by deposition of Hexafor 644-D/PFOA/Al_2O_3 solution on the WC–Co–Cr coated substrate. To investigate mechanical stability of

V. Kumar · R. Verma (✉)
Department of Industrial and Production Engineering, Dr. B. R. Ambedkar National Institute of Technology, Jalandhar 144011, India
e-mail: vermar@nitj.ac.in

V. Kumar
e-mail: vknitj94@gmail.com

coated surface, four consecutive testings were used like sandpaper test, water impact test, tape peeling test and water contact angle measurement test with time. The surface characterization and elemental composition of coated surface were observed by the scanning electron microscopy (SEM) and energy-dispersive X-ray spectroscopy (EDS) analysis, respectively. The obtained surface showed the non-wetting phenomena for water droplets with time and rolled off easily with a small inclination of the surface.

Keywords Super-hydrophobic surfaces · Fabrication · Hexafor 644-D/PFOA/al$_2$o$_3$ · ASTM A988

8.1   Introduction

ASTM A988steel is a versatile and the most widely used material in the hydro-turbine industry. Its chemical composition, weldability, heat resistance and mechanical properties provide the best performance to use in hydro-turbine industry. However, cavitation erosion and slurry erosion are reportedly the problems for its use in hydro-turbine in the mountain region [1–3]. To overcome cavitation erosion and slurry erosion of turbine materials, wear-resistant coatings have been commonly used before its use in hydro-turbines [4]. These coatings also improve oxidation and corrosion resistance, both of which prove advantageous in such application. In general, super-hydrophobic surfaces required an amalgamation of low surface tension and the surface features of the substrate, however, due to thick coating on the materials/substrate leads to loss of the colour and its transparency [5].

It is obvious that from the published article, a work has been shown on WC–10Co–4Cr thermal spray coatings, which were deposited on hydro turbine materials by the detonation–gun spray process and the method reduced the slurry erosion of the steels compared to bare substrates [1, 6, 7]. The adapted surface treatment process was implemented on the substrate with the help of laser surface texturing and which is used to enhance the interface energy and improve adhesion strength [8–14]. However, still hydro-turbine components face problems which may be attributed to wettability and self-cleaning. A strategy is adopted to fabricate super-hydrophobic coating on different substrates or substrates independent with a fluorinated agent, which helps for achieving self-repairable, self-cleaning and anti-wetting properties [15].

Super-hydrophobic surfaces have in recent times drawn an important consideration from both the necessary and applied points of view. Super-hydrophobic property of specimens was improved through the surface roughness improvement by a coating of nanoparticles. It was first addressed theoretically in the 1930s. After that, a lot of research has been done to implement it in industrial application. There have been significant advantages of super-hydrophobic surfaces to use it in industry and daily life. The basic design principles to the fabrication of super-hydrophobic surfaces categorized in three different approaches: (1) roughening of the surfaces, (2) develops rough topographic features on substrates followed by the use of super-hydrophobic

surface modification method and (3) depositing super-hydrophobic materials with bumpy surface textures.

In this work, fabrication of super-hydrophobic coatings on turbine materials or substrate was done by dipping the substrate into the aqueous solution containing Hexafor 644-D/Al_2O_3/PFOA. Before super-hydrophobic coating, a series of circular and triangular micro-texturing was done on the substrate in order to enhance the bond strength of the ceramic coating. Later, on WC–10Co–4Cr thermal spray coatings were done by high-velocity oxygen fuel (HVOF) method. The fabricated super-hydrophobic surfaces proved to be excellent for anti-wetting, anti-erosion and self-cleaning. These developed coatings have the potential to increasing economic spending and decrease pollutants as well as increase in the durability of turbo-machine components which are susceptible to water damage.

8.1.1 Selection of Material

The first and essential step towards effective utilization of any materials is the determination of the best possible materials for its relevant application. Stainless steels consist of an enormous number of standard models; however, these types vary essentially from each other in physical properties, corrosion resistance, composition and choice of the best kind for a particular use which is the key to acceptable performance at a comparatively low cost. The list as shown below is a proposed for the selection of the best materials for a particular application.

- Quality and flexibility at service and ambient temperatures
- Suitability for intended cleaning strategies
- Property permanence in service
- Durability
- Corrosion resistance
- Erosion and abrasion resistance
- Magnetic properties
- Thermal conductivity
- Thermal expansion
- Electrical resistively
- Stiffness.

Corrosion resistance is regularly the prime characteristic for a heat resistance or stainless steel. In any case, it is frequently likewise the hardest to evaluate for a particular application. Mechanical properties at operating temperature are a noticeable consideration, and however in some cases, ignored is the need for agreeable properties at particular temperatures, which are probably going to be experienced.

8.1.2 Literature Review

The literature review comprised of three sections. The first section reported the recent works published related to thermal barrier coating and super-hydrophobic coating and the concept of super-hydrophobic coating to use in industry. In the second section of the literature is about the investigations pertaining to the various substrates, low surface materials, surfactant and its application. The third section explains a suitable method for fabricating super-hydrophobic coating on stainless steel material. Review of the recent literature was important because it would allow us to design more efficient and durable coatings eliminating the complicated fabrication methods and experiment.

Ozbek et al. (2016) in their studies proposed that 88%WC–12%Co were utilized to deposited coatings on substrates by HVOF thermal spray method [16]. A mixture of WC-Co powder is commonly used as a tribological coating aggregate providing of very hard surface and good bond strength. The coated substrates were characterized by utilizing stereomicroscope, optical micrograph, SEM, X-ray diffractometry and micro-hardness tests. Additionally, the wear execution of the thermal spray coatings (TSC) was explored. From the surface investigation, it was observed that the coated surface shows comparatively higher micro-hardness and preferable abrasive wear resistance over the ordinary counterpart and low co-efficient of friction.

Lavigne et al. (2017) performed a study on thermal spray coating, and it is a common process for a group of coating used to the deposited metallic or non-metallic powder on the substrate. Thermal spray coatings are grouped into three groups: electric arc spray, flame spray and plasma arc spray. Coating materials are heated using energy sources (in wire, powder or rod form) to a molten or semi-molten stage. Result of that, heated particles are accelerated and propelled towards a prepared substrate by either gases or atomization jets. The significant advantage of thermal spray technology is the use of a wide variety of nanomaterials to produce a required surface. Thermal spray coating techniques have replaced the conventional welding technique in creating protective weld overlays [4].

Qiao et al. (2018) deposited WC–Co–Cr nanoparticles on metallic substrates by (HVOF) which are the existence application for components which are susceptible to critical slurry erosion. In this experiment, the HVOF coating was applied to polycrystalline diamond compact (PDC) bits [17]. The WC–Co–Cr coated substrates were textured by laser surface texturing machine with different structural characteristics. The surface morphology of the untextured and textured coated substrates was investigated by SEM. The angle between the solid surface and different fluid on the coated substrates was examined by goniometer. The untextured coated substrates show a contact angle of 81.5° with water droplets and 69.1° with mud droplets. However, the contact angle of water droplets is 136.6° and that of mud droplets is 112.1° on the textured substrates. The contact angle remains slightly increase with decreasing the texturing spacing compatible with increasing coating deposition rate (R). Surface texturing with two consecutive grid distance of 100 μm results in the highest contact angle on the WC–Co–Cr thermal spray coated substrates due to the co-action

of surface morphology and interface chemical enactments. However, the durability of the hydrophobic coating on the textured surface is not enough, which may result from the fluctuation of the trapped air inside the textured pattern.

Liu et al. (2018) reported that non-inorganic solvents are used to disperse or dissolve organic bonding agent and modifiers on fabricated super-hydrophobic surfaces to increase mechanical strength. An aqueous spraying solution was prepared for the fabrication of super-hydrophobic surface, which include ZnO nanoparticles, polytetrafluoroethylene with low surface energy and aluminium phosphate as an inorganic adhesive. An aqueous spraying solution was appreciated for a low price and comparatively less pollution. Significantly, the super-hydrophobic surfaces were durable to the different harsh situation and physical destruction. The developed interfacial materials exhibit excellent results for practical applications such as oil–water separation, anti-icing and ZnO nanoparticles which replace the chemical etching [18].

Ma et al. (2018) during their studies proposed that manufacturing super-hydrophobic surface has been considered to be a proposed methodology for metallic surface corrosion protection [19]. A simple and facile nanosecond laser texturing pattern was proposed for the constructing super-hydrophobic surfaces on steel substrates. During the texturing procedure, a progression of circular pattern with a various pitch-to-diameter ratio was straightforwardly manufactured on steel surfaces by nanosecond laser texturing machine. After laser texturing, all substrates were chemically modified, and it progressed towards becoming super-hydrophobic surfaces. With increasing pitch-to-diameter ratio from 1.0 to 1.85, the super-hydrophobicity of laser texturing substrates reduces constantly because of the increased undesirable flat surfaces. Moreover, the textured super-hydrophobic steel additionally showed excellent mechanical strength against erosion and abrasive damaged. In addition, the textured super-hydrophobic steels also promise desirable chemical stability and better heal ability after it lost its super-hydrophobicity.

8.1.3 Application of Super-Hydrophobic Surfaces

There is a lot of application of super-hydrophobic surfaces in day-to-day life, due to its amazing surface behaviour. One of the most important uses of super-hydrophobic surfaces is to repel liquid or water droplets with aggregates present on surfaces. The water-repellent behaviour of surfaces can be used to fabricate a water-proofing coat for electronic equipments. When heavy liquid-like mud and a mixture of water-aggregates drop continuously on the surface then super-hydrophobic behaviour of the surface change to hydrophilic condition. In the little stain obstruction, super-hydrophobic surfaces have one important aspect of their self-cleaning properties like lotus leaf. Another aspect of super-hydrophobic properties is that dust particles easily pick up and remove from the super-hydrophobic surfaces by rolling liquid; this property shows the excellent performance to remove dust particles and liquid from any surface to save from corrosion. Aside from self-cleaning and liquid-repellent

properties, super-hydrophobic surfaces have several applications, for example, anti-corrosion resistance, drag reduction behaviour, anti-bacterial properties, water–oil separation behaviour and anti-icing properties.

8.2 Experimentation

8.2.1 Specimen Preparation

(See Fig. 8.1).

8.2.2 Material

Hexafor 644-D was procured from Ecokem Technologies Private Limited Vashi, Navi Mumbai, Maharashtra, India [20]. Pentadecafluorooctanoic acid (PFOA), organic solvent and deionized water were purchased from Chemical Corporation, Gokal Road, Ludhiana, Punjab, India [15]. Aluminium oxide nanoparticles of size 50–80 nm were procured from Nanopar Tech, Chandigarh, Punjab, India [21]. WC–10Co–4Cr powder purchased from Metallizing Equipment Co. Pvt. Jodhpur (Raj.) India [1].

Heat treatment	Heat treatment		
Dip coating (Hexafor 644-D/ PFOA/ Al$_2$O$_3$)	Dip coating (Hexafor 644-D/ PFOA/ Al$_2$O$_3$)	Heat treatment	
WC-Co-Cr powder coating	WC-Co-Cr powder coating	Dip coating (Hexafor 644-D/ PFOA/ Al$_2$O$_3$)	Heat treatment
Laser texturing (Circular pattern)	Triangular pattern	WC-Co-Cr powder coating	Dip coating (Hexafor 644-D/ PFOA/ Al$_2$O$_3$)
Stainless steel (Grade TP-201) sample of size (55X36X5.6)mm (Specimen-1)	Stainless steel (Grade TP-201) sample of size (55X36X5.6)mm (Specimen-2)	Stainless steel (Grade TP-201) sample of size (55X36X5.6)mm (Specimen-3)	Stainless steel (Grade TP-201) sample of size (55X36X5.6)mm (Specimen-4)

Fig. 8.1 Configurations of fabricating super-hydrophobic coating

All chemicals and nanoparticles were laboratory grade and used without any further refinement. Commercially available ASTM A988 was used as based materials.

8.2.3   Fabrication of Laser Textured and Coated Surfaces

Specimen of required size was sectioned by low-speed diamond saw, and subsequently, the specimen removed the uneven surface grind to achieve flatness of 10.50 μm. After section, the surface was polished by emery paper of grit size 1200. Before WC–Co–Cr thermal spray coating, circular and triangular texturing on specimen 1 and 2, respectively, by laser texturing. The circular pattern texturing was made with diameter and pitch 140 μm and 200 μm, respectively, on specimen-1 (Fig. 8.1). The triangular pattern texturing was done with side and pitch 140 μm and 200 μm, respectively, on specimen-2. These laser textured patterns enhanced bond strength of WC–Co–Cr thermal spray coating. For fabrication of the coating configurations as per Fig. 8.1, HVOF thermal spray coating was used as shown in Fig. 8.2.

Aluminium grit blasting of size 80 was done on the samples to developed surface roughness (Ra) for proper coating. After aluminium blasting, the HVOF coating
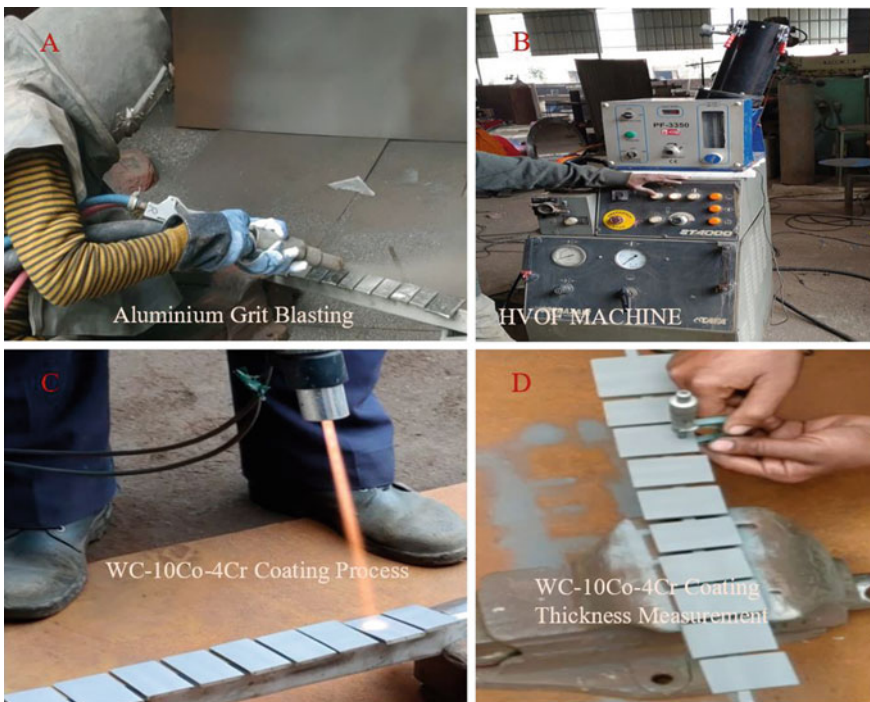
Fig. 8.2   Steps of HVOF coating

machine set at its required conditions. RPM of the container 5.18, the pressure of oxygen gas 17 bar, the pressure of nitrogen gas 7.5 bar, at current 50 amp and voltage were 220 V. The thickness of WC–Co–Cr powder coating was obtained within the range of 200–220 micron.

8.2.4 Super-Hydrophobic Surface by Dip Coating

The primary experimental process is presented in Fig. 8.3. In the experimental process, ASTM A988 steel of a size of $5.5 \times 3.6 \times 0.56$ cm^3 sectioned, washed with deionised water and ethanol. Next, the cleaned samples were dried in a hot wire oven at 70 °C for 25 min to remove the moisture contained. In order to prepare aqueous solution, (1.0) gm pentadecafluorooctanoic acid (PFOA) was added in (40 ml) water and sonicated for 20 min. Later, (4) ml Hexafor 644-D and (3.0) g aluminium oxide (Al$_2$O$_3$) were added in sonicated solution which was magnetically stirred at 800 RPM for the next 30 min as shown in Fig. 8.4.

The substrates were subsequently dipped into the solution for the next 30 min. After 30 min, all the substrates were removed from the solution and placed in an atmospheric condition to allow drying of the liquid from coated surfaces. After
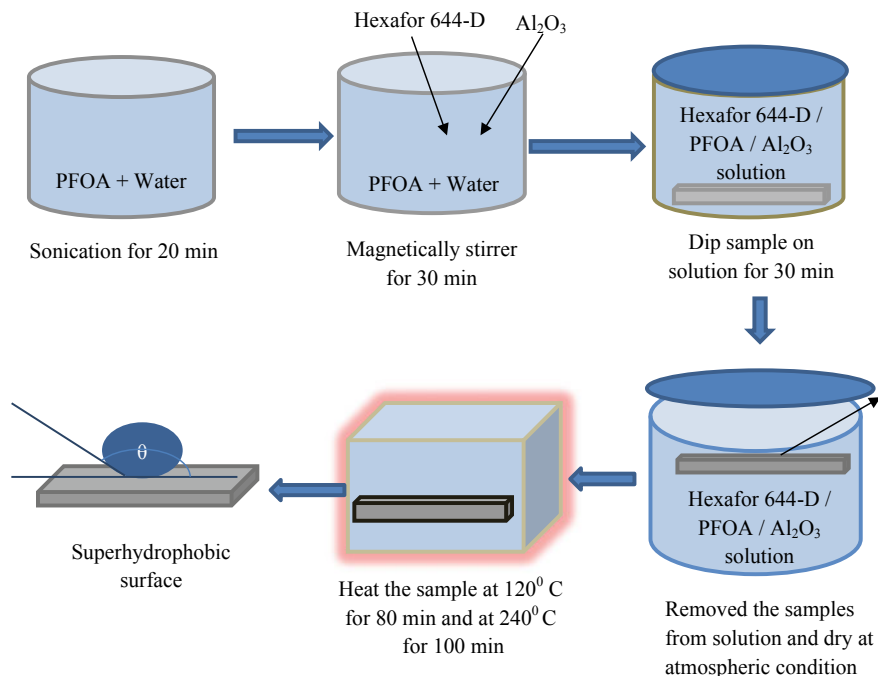
Fig. 8.3 Principal scheme of experimental process

Fig. 8.4 Solution preparation for dip coating **a** Sonication for 20 min and **b** magnetically stirred for 30 min

dried, coated substrates put into the electric oven and heated at 120 °C for 80 min and 240 °C for the next 100 min consecutively. The obtained coated surface showed a super-hydrophobic nature as shown in Fig. 8.3.

8.2.5 Characterization

The surface morphology and structure of the substrates were analysed using the scanning electron microscopy (SEM) at the operating voltage 15 kV. The elemental composition was observed via energy-dispersive X-ray spectroscopy (EDS). The water contact angle and sliding angle were measured using Image J software, and images of water droplets were taken using a high-resolution camera in normal atmospheric condition. The volume of each water droplets used for water contact angle measurement was 8–12 μL. Water contact angle value was measured at different positions of coated samples. For abrasion test, the coated surface was placed face down to sandpaper (Grit No. 1200) and dragged for 5.5 cm along a ruler under a weight of 200 g by the application of external drawing force. This process was repeated for 45 times, and after every five cycle, water contact angle of a water droplet was measured using Image J software. For tape peel test, adhesive tape (Cellofix) was used for repeated peeling on the fabricated super-hydrophobic surfaces. Firstly, the coated substrate was fixed then the adhesive tape was glued to it and a weight of 100 g applied over it for uniform sticking. Then, the adhesive tape was peeled off at an angle of 180° from the surface. This process of peeling repeated for 45 times. After a cycle of five peeling, water droplet dropped on the substrate surface, and the contact angle formed by this water droplet was absorbed and was measured using Image J application. For water impact test, the fabricated surface was placed horizontally in the direction of flow and constant discharge of 74.9 cm^3/s with the help of a container of diameter 25 cm and height 36 cm. After 5 min contact angle of a water droplet

was measured using Image J application on the surface of the substrate. The water impact test conducted for 15 min.

8.3 Results and Discussions

The textured surface investigated by scanning electron microscopy (SEM). In Fig. 8.5a, b, SEM micrographs show that corner of all texturing area has irregular shapes due to sticking of melted materials at the upper edge. The distribution of pores and nanoparticles is also shown on the surfaces due to cleaning with a wire brush before SEM, which is more in circular texturing.

The morphology and elemental composition of WC-Co-Cr coated surface were examined by SEM and EDS, respectively. The coated substrate has a similar surface structure except for the texturing features. In texturing areas, some cracks appeared due to the mismatch of thermal expansion coefficients of WC-Co-Cr coating and ASTM A988 steel substrate. The optical micrographs of sample 1 and 2 are shown in Fig. 8.6a, b, which shows that coated surfaces have a systematically distributed lamellar structure and nanoparticles with a different orientation. Figure 8.6c, d shows the scanning area and its elemental composition, respectively.

The surface structure of super-hydrophobic coatings investigated by SEM images is shown in Fig. 8.7. A lot of micro-nano-holes appeared on the surface, which trapped the air and not permitted liquid to enter, inside the hole, results of that liquid takes spherical shapes and rolled off with small inclination. A fibre-like structure constructed on the surface which helps the fabrication of super-hydrophobic surfaces. For investigating of coating strength, three tests conducted on three different specimens, namely specimen 1, 2 and 3. Investigation of anti-wetting characterization of water droplets with time was performed on sample 4. During the abrasion test, the water contact angle was decreased from 161° to 143° after 45 cycles of abrasion as shown in Fig. 8.8a. However, water droplets still get rolled off easily with a small inclination of the surfaces. During the adhesive peel test, the water contact angle
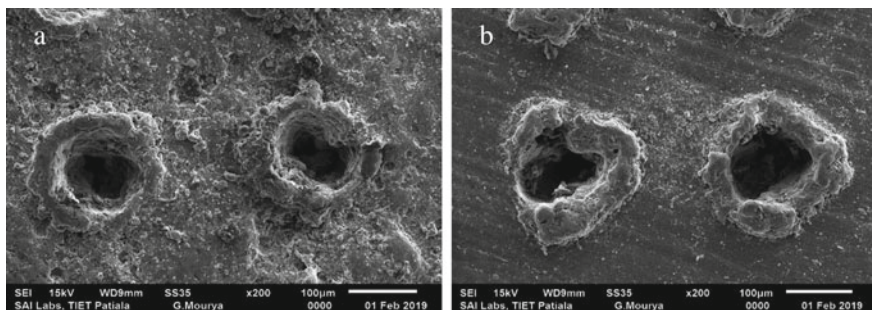
Fig. 8.5 SEM image of **a** Circular texturing specimen-1 **b** triangular texturing specimen-2
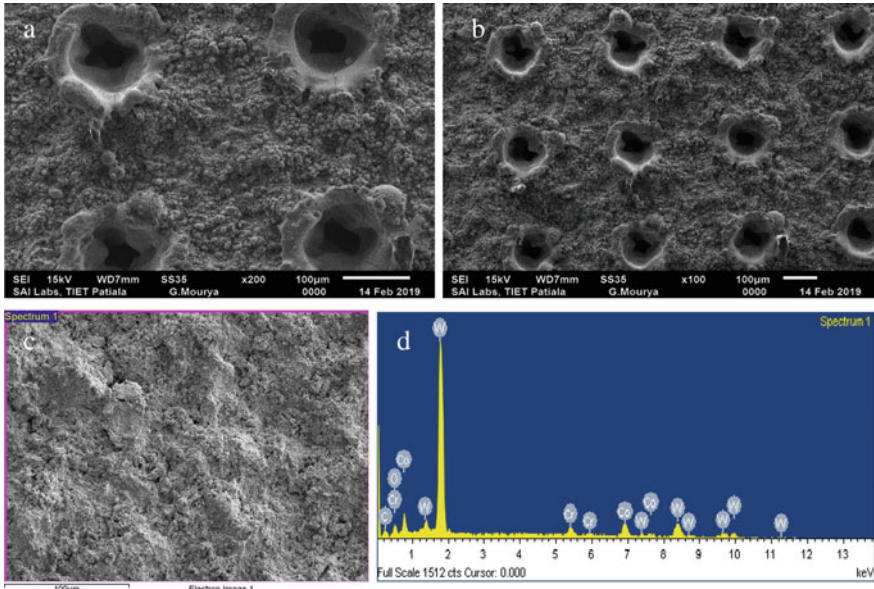
All elements analysed (normalized) and Number of iterations = 3

Spectrum	C	O	Cr	Co	W	Total
Spectrum 1	4.53	4.58	4.33	13.14	73.42	100

Fig. 8.6 SEM images of WC-10Co-4Cr powder coating on **a** Sample 1, **b** sample 2, **c** scanning area for EDS analysis and **d** the pictorial image of EDS analysis
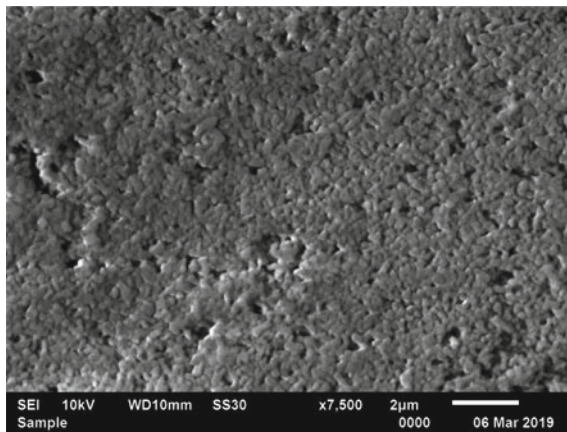
Fig. 8.7 SEM images of super-hydrophobic coating
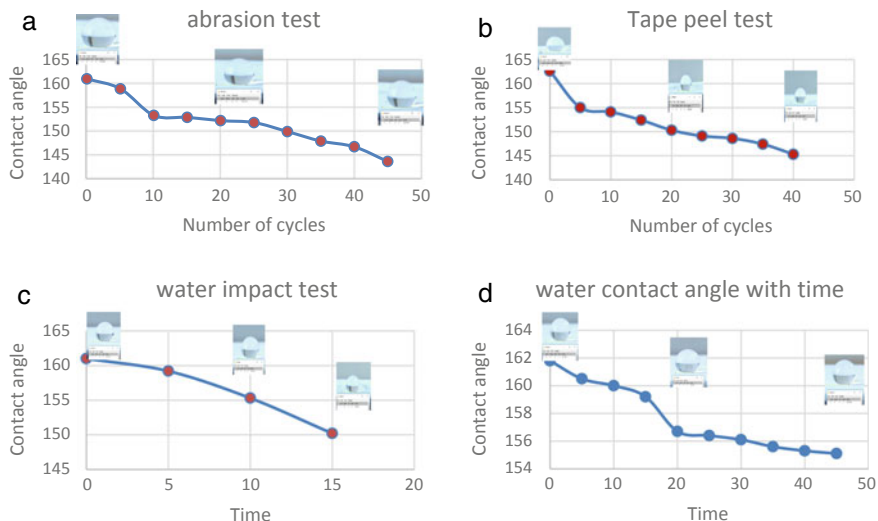
Fig. 8.8 Testing graphs with image of **a** Abrasion test, **b** tape peel test, **c** water impact test and **d** water contact angle with time

decreased from 162° to 145° after 45 cycles of tape peeling as shown in Fig. 8.8b. For water impact testing, the contact angle was reduced from 159° to 150° in 15 min of water jet impact as shown in Fig. 8.8c, however heating at 130 °C water contact angle again achieved 158° (approx.) [15]. For non-wetting characterization of liquid, we observed a single water droplet for 45 min and measured the water contact angle at every 5-min interval. The water contact angle decreased marginally from 161.7° to 155° in 45 min of observations as shown in Fig. 8.8d.

8.4 Conclusions

The super-hydrophobic surfaces on WC–Co–Cr coated ASTM A988 steel were successfully fabricated by simple dip coating in the aqueous solution containing Hexafor 644-D/PFOA/Al_2O_3.

a. The self-cleaning, non-wettability and anti-erosion of the substrates increased remarkably for the developed surface.
b. Obtained super-hydrophobic coating can remain stable for different liquid droplets like ball pen ink, a mixture of ink–water and water.
c. This method is time-saving and quite simple.
d. The obtained super-hydrophobic surfaces can extend their application to the numerous relevant industrial fields.

References

1. Grewal, H.S., Bhandari, S., Singh, H.: Parametric study of slurry-erosion of hydroturbine steels with and without detonation gun spray coatings using Taguchi technique. Metall. Mater. Trans. A Phys. Metall. Mater. Sci. **43**, 3387–3401 (2012). https://doi.org/10.1007/s11661-012-1148-y

2. Ding, H., Qiu, Y.: Combined Slurry and Cavitation Erosion Resistance of HVOF Spray Coated SS 410 Steel Combined Slurry and Cavitation Erosion Resistance of HVOF Spray Coated SS 410 Steel (2016). https://doi.org/10.1088/1757-899x/149/1/012053

3. Singh, R., Kumar, D., Mishra, S.K., Tiwari, S.K.: Surface & coatings technology laser cladding of stellite 6 on stainless steel to enhance solid particle erosion and cavitation resistance. Surf. Coat. Technol. **251**, 87–97 (2014). https://doi.org/10.1016/j.surfcoat.2014.04.008

4. Lavigne, S., Pougoum, F., Savoie, S., Martinu, L., Klemberg-sapieha, J.E., Schulz, R.: Cavitation erosion behavior of HVOF CaviTec coatings. **387**, 90–98 (2017). https://doi.org/10.1016/j.wear.2017.06.003

5. Kobina Sam, E., Kobina Sam, D., Lv, X., Liu, B., Xiao, X., Gong, S., Yu, W., Chen, J., Liu, J.: Recent development in the fabrication of self-healing superhydrophobic surfaces. Chem. Eng. J. **373**, 531–546 (2019). https://doi.org/10.1016/j.cej.2019.05.077

6. Li, C.J., Yang, G.J., Gao, P.H., Ma, J., Wang, Y.Y., Li, C.X.: Characterization of nanostructured WC-Co deposited by cold spraying. J. Therm. Spray Technol. **16**, 1011–1020 (2007). https://doi.org/10.1007/s11666-007-9096-6

7. Ali, O., Ahmed, R., Faisal, N.H., Alanazi, N.M., Berger, L.M., Kaiser, A., Toma, F.L., Polychroniadis, E.K., Sall, M., Elakwah, Y.O., Goosen, M.F.A.: Influence of post-treatment on the microstructural and tribomechanical properties of suspension thermally sprayed WC–12 wt%Co nanocomposite coatings. Tribol. Lett. **65**, 1–27 (2017). https://doi.org/10.1007/s11249-017-0815-y

8. Aditya, S.V, Duraiselvam, M.: Key Knowledge Generation Laser Surface Texturing of Nickel Superalloy to Improve Adhesion Bond Strength of Thermal Barrier Coating

9. Boinovich, L.B., Emelyanenko, K.A., Domantovsky, A.G., Emelyanenko, A.M.: Laser Tailoring the Surface Chemistry and Morphology for Wear, Scale and Corrosion Resistant Superhydrophobic Coatings (2018). https://doi.org/10.1021/acs.langmuir.8b01317

10. Conradi, M., Drnovšek, A., Gregorčič, P.: Wettability and Friction Control of a Stainless Steel Surface by Combining Nanosecond Laser Texturing and Adsorption of Superhydrophobic Nanosilica Particles, pp. 2–10 (2018). https://doi.org/10.1038/s41598-018-25850-6

11. Courapied, D.: Laser Adhesion Test for Thermal Sprayed Coatings on Textured Surface by Laser, 022509 (2016). https://doi.org/10.2351/1.4944451

12. Kromer, R., Costil, S., Cormier, J., Berthe, L., Peyre, P., Courapied, D.: Laser patterning pretreatment before thermal spraying: a technique to adapt and control the surface topography to thermomechanical loading and materials. J. Therm. Spray Technol. **25**, 401–410 (2017). https://doi.org/10.1007/s11666-015-0352-x

13. Kromer, R., Costil, S., Verdy, C., Gojon, S., Liao, H.: Surface & coatings technology laser surface texturing to enhance adhesion bond strength of spray coatings—cold spraying, wirearc spraying, and atmospheric plasma spraying. Surf. Coat. Technol. (2017). https://doi.org/10.1016/j.surfcoat.2017.05.007

14. Costil, S., Kromer, R., Gojon, S., Aubignat, E., Verdy, C., Liao, H., Langlade, C.: Laser-induced surface texturing of metal or organic substrates for structural adhesive bonding. **879**, 390–395 (2017). doi:10.4028/www.scientific.net/MSF.879.390

15. Liu, M., Hou, Y., Li, J., Tie, L., Guo, Z.: Robust and self-repairing superamphiphobic coating from all-water-based spray. Colloids Surf. A **553**, 645–651 (2018). https://doi.org/10.1016/j.colsurfa.2018.06.010

16. Özbek, Y.Y., Canikoğlu, N., Ipek, M.: The mechanical properties and wear resistance of HVOF sprayed WC-Co coatings. Acta Phys. Pol., A **129**, 600–603 (2016). https://doi.org/10.12693/APhysPolA.129.600

17. Qiao, J., Zhu, L., Yue, W., Fu, Z., Kang, J., Wang, C.: Surface & coatings technology the effect of attributes of micro-shapes of laser surface texture on the wettability of WC-CrCo metal ceramic coatings. Surf. Coat. Technol. **334**, 429–437 (2018). https://doi.org/10.1016/j.surfcoat.2017.12.001

18. Liu, M., Hou, Y., Li, J., Tie, L., Guo, Z.: An all-water-based system for robust superhydrophobic surfaces. J. Colloid Interface Sci. **519**, 130–136 (2018). https://doi.org/10.1016/j.jcis.2018.02.055

19. Ma, Q., Tong, Z., Wang, W., Dong, G.: Applied surface science fabricating robust and repairable superhydrophobic surface on carbon steel by nanosecond laser texturing for corrosion protection. Appl. Surf. Sci. **455**, 748–757 (2018). https://doi.org/10.1016/j.apsusc.2018.06.033

20. Td, O.D.: TDS—Technical Data Sheet, 2–5 (2010)

21. Ding, B., Wang, H., Zhu, X., Chen, R., Liao, Q.: How supercooled superhydrophobic surfaces affect dynamic behaviors of impacting water droplets? Int. J. Heat Mass Transf. **124**, 1025–1032 (2018). https://doi.org/10.1016/j.ijheatmasstransfer.2018.03.112

Chapter 9
Experimental Validation of Thermal Properties on Composite Thermal Barrier Coating

Muhammed Naseem O and Rajeev Verma

Abstract The composites are the artificially made materials by combining two or more distinct inhomogeneous class of materials for improving the properties. These coatings have been used as a protective layer in diesel engines, and the important material property required for the temperature reduction is low thermal conductivity, which can be achieved by using ceramic materials as a protective coating layer. In this paper, the thermal properties of the multi-layered composite thermal barrier coating (TBC) have been compared using experimentation and mean-field micro-mechanics model, which is a prediction method for determining material properties of composites. Based on the comparison, a comparison curve of theoretical and experimental thermal conductivity, specific heat capacity and thermal diffusivity have been plotted and the final mean percentage deviation was coming 5.705%, 8.06% and 7.60, respectively.

Keywords Thermal barrier coating · Composite · Mullite · Mean-field micro-mechanics model · Thermal conductivity

9.1 Introduction

Thermal barrier coatings (TBCs) are generally used for improving high-temperature stability of the gas turbines and aircraft engine, and this method was widely used since the early 1960s [1]. In power generation sectors, it is beneficial to increase the working temperature by using a protective layer termed TBC, which increases the efficiency by increasing the life of the turbine blade as well as the boundary surface. The same technique could be used as a protective layer in same sector as well as in diesel engines, and here, the TBC layer acts as a thermal insulating medium in which that will reduce the heat loss and enhance the efficiency of the system [2]. There are mainly three basic layers for a coating system (Fig. 9.1) named as, a ceramic

M. Naseem O (✉) · R. Verma
Department of Industrial and Production Engineering, Dr. B. R. Ambedkar National Institute of Technology, Jalandhar 144011, India
e-mail: mnonaseem@gmail.com

Fig. 9.1 TBC structure
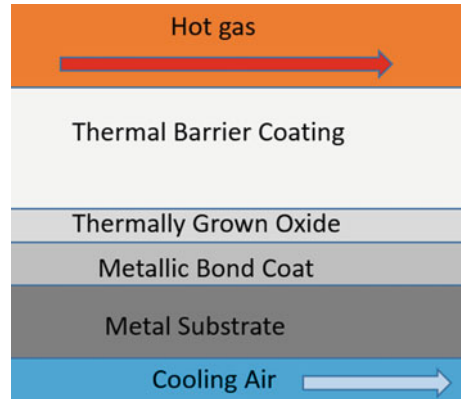
topcoat which acts as the temperature reduction medium because of its low thermal conductivity and high stability, and there is one another layer called metallic bond coat for attaining the structural link with the substrate or superalloy. Because of the oxidation occurs in topcoat and bond coat interface on a high working temperature medium, a thermally grown oxide (TGO) layer is induced at the interface and which acts as a coating layer because of its properties like ceramics.

Literature survey suggests some techniques which may be used to predict the material properties of composites such as mean-field micro-mechanics model [3], unified micro-mechanics approach [4] and rule of mixtures (RoM) [5]. The prediction method was used to determine the different thermo-mechanical properties on a given temperature range for analysing and plotting the variation curves. The effective thermal properties of different layers were calculated using the Fourier law [6] and the inverse rule of mixture.

Functionally graded coatings (FGC) are an improved coating structure used for achieving better thermal properties by continuously changing the composition from substrate to outermost layer. The major cause of failure in TBCs was large thermal stress generated during thermal cycling on interfaces because of mismatch between thermal expansions. To overcome this problem, the introduction of FGC improves the resistance of TBCs to thermal fatigue cracking by multi-layer ceramic coating system [7]. The advantages of FGCs over conventional monolithic coating systems are: improved toughness, improved wear resistance, a significant reduction in residual stress level and improved thermal properties [8].

The thickness of the coatings generally varies from 5 μm to 2 mm with good insulating properties [1, 9], but in some studies, it has been proven that the optimum effective thickness of ceramic coatings comes in a range of 100 μm to 450 μm [10]. So it is evident that increasing coating thickness after attaining the optimal values will cause only the crack initiations and which will affect the life of the coated systems. For addressing this problem, here multi-layered coating system has been considered which have higher adhesive strength than thicker mono-layered coatings and have
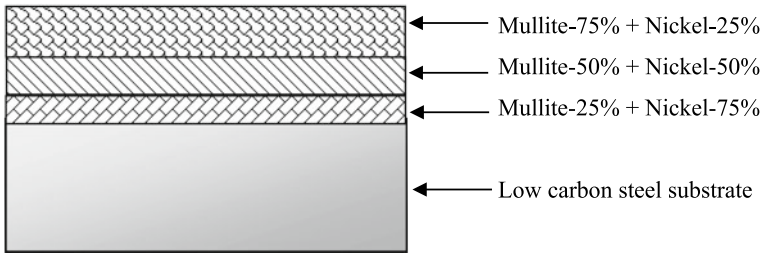
Fig. 9.2 Multi-layered TBC [11]

less residual stress initiation also. The composition of different layers is varying and which is shown in Fig. 9.2.

Mullite ($3SiO_2 + 2Al_2O_3$) is itself a composite material and which is one of the important and efficient ceramic coating material because of its favourable properties and stability on high-temperature working medium. It is a composite of alumina and silicon oxide in the composition of 3:2 and which can work on a high temperature at the range of up to 1500 °C [1]. Mullite is widely used because of its low thermal conductivity, low density, creep behaviour, favourable strength and higher chemical and structural thermal stability [12].

In previous experimental studies [1, 13], it has been shown that adding nickel powder to mullite coatings at different compositions can reduce the mismatch between the coefficient of thermal expansion (CTE). Addition of the nickel powder in mullite coatings is benefited for reducing the thermal stresses experienced in the substrate–coating interface. Here, the nickel powder used was nickel 200 with compositions of 99% nickel, 0.15% carbon, 0.25% copper, 0.35% silicon and up to 0.4% iron.

In this paper, the effort has been made to compare the theoretical thermal properties like thermal conductivity, specific heat capacity and thermal diffusivity values to those predicted using mean-field micro-mechanics model and finding out the percentage deviation with the actual value. The mullite and nickel-coated ASTM 1018 steel were tested by using a TPS 500S Thermal Constants Analyser [14, 15]. The deviation could be because of the accuracy error in experimentation or the assumptions considered while calculating the thermo-mechanical properties using mean-field analysis and rule of mixtures. The mean percentage deviation of experimental value with the theoretically predicted value was found to be 5.705% with the highest percentage deviation of 12.24% for thermal conductivity, 8.06% with the highest percentage deviation of 21.55% for specific heat capacity and 7.60% with a larger value of 11.67% for thermal diffusivity.

9.2   Experimentation

The TBC layer is used primarily for reducing the thermal conductivity of the substrate surface for achieving the high thermal load capacity and high-temperature stability, which can be done by coating low thermal conductivity materials such as ceramic coatings. Here, the composite material has three different coating layers with different compositions coated on an ASTM 1018 steel, which is the substrate material. The transient plane source (TPS) technique is an important tool for testing the thermal properties because of its robustness and the ability to measure the properties of complex materials as well as nanomaterials [16]. The experimental set-up of TPS 500S thermal property analyser is shown in Fig. 9.3.

It is a rapid and flexible analyser where one test will take only 60 s, and the solid, high viscous liquid, powder and nanomaterials can be tested using parent equipment by changing the sensors only. Here, the sensor used was Kapton 2.001 mm [17] which was sandwiched between a pair of the workpiece of dimension 50 mm*25 mm*5 mm, and the system was kept inside two standard stainless steel plate which was fitted to a load cell. The testing rig was connected to a computer for plotting and analysing the results. The sensor has an inner circular heating area as well as outer sensing areas which sense the rapid temperature changes in the given time. The schematic view of the workpiece holder is shown in Fig. 9.4.
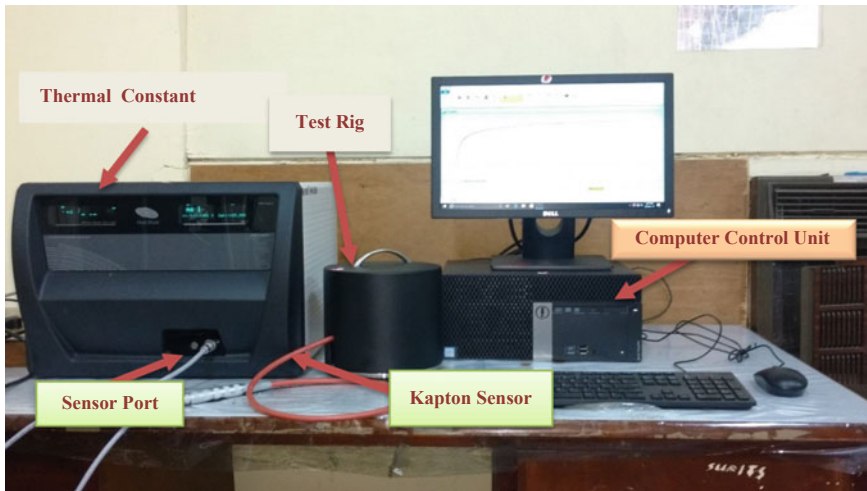
Fig. 9.3 Experimental set-up of TPS 500S thermal property analyser
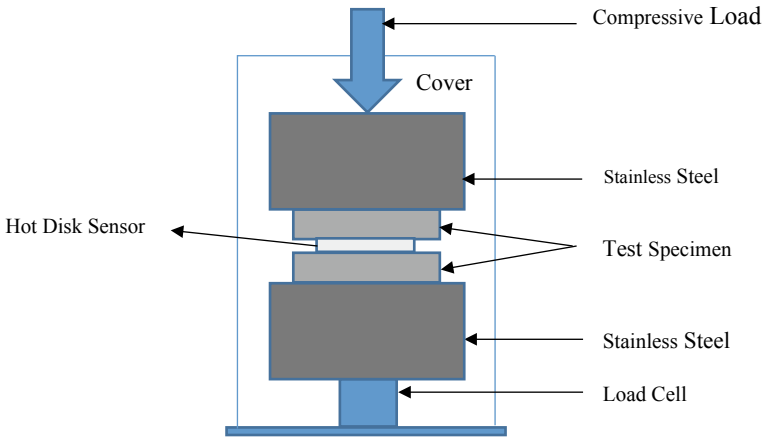
Fig. 9.4 Schematic view of the workpiece holder

9.3 Thermal Conductivity Calculation

Mean-Field Micro-Mechanics Model for Composite

Two or more monolithic materials are combined to form a new material called composite for attaining the effective ideal properties. Apart from the traditional classification, namely ceramics, polymers or metals, this new class of materials comes in the composite category which can be a composition of different traditional classification, or in another word the composite material can be made using the combination of any of the materials [3]. Here, in this study the coating material contains mullite and nickel as the primary coating materials and titanium oxide powder as an additive in different compositions. So, the material properties were defined using a mean-field micro-mechanics approach and rule of the mixture with the properties taken from CRC Material Science and Engineering Handbook [18, 19]. The weight percentage of mullite and nickel powder in different layers are defined as 25% mullite and 75% nickel in the bottom layer, 50% mullite and 50% nickel in the middle layer and 75% mullite and 25% nickel in the top layer with 1% of the total weight fraction of titanium oxide powder [13].

The assumptions considered for calculating the thermo-mechanical properties were: the fibres on the composite matrices are uniformly distributed, perfect bonding between matrices and fibres, the matrix is free of voids and stress-free at initial state. From this prediction method, the generalised equation for finding the effective thermal conductivity of the N number of composites [4] is given below,

Elastic compliance tensor, $\overline{M} = \sum_{r=0}^{N} f_r M_r B_r$.

Where f_r is the fraction of monolithic components in the given composite material and B_r is the phase stress concentration factor with, $\sum f_r B_r = 1$.

The thermal conductivity of the work sample can be calculated using Fourier's Law [20] after measuring the steady-state temperature difference [20].

$$Q = -\frac{KA(dT)}{dx}$$

Where K is thermal conductivity in W/m K, Q is the thermal energy in Watt, dT is the temperature difference in Kelvin scale and dx is the gauge difference in the metre.

For a simple binary system with spherical composite reinforcement and unidirectional fibrous composite with uniform and circular cross section, the equivalent thermal conductivity $\overline{K}$ is derived as

$$\frac{\overline{K} - K_0}{K_1 - K_0} = \frac{f_1 K_0}{K_0 + \frac{1}{3}(1 - f_1)(K_1 - K_0)}$$

where K_0, K_1 are the thermal conductivity of first and second monolithic material, respectively, and f_1 is the mass fraction of second material [4].

The overall heat capacity per unit volume $\overline{C^p}$ is obtained from equation,

$$\overline{C^p} = (1 - f_1)C_0^p + f_1 C_1^p + f_1 \frac{12 K_1 \mu_0}{3K_1 + 4\mu_0}(\alpha_1 - \overline{\alpha})(\alpha_1 - \alpha_0)T_R$$

where $\overline{C^p}$ is the overall heat capacity, C_0^p is the heat capacity of the monolithic base material, C_1^p is the heat capacity of additive monolithic material and T_R is the room temperature.

Thermal diffusivity means, how quickly or how easily heat can penetrate a substance and which is a dependent property of thermal conductivity, specific heat and density. In a material with larger thermal diffusivity, heat moves quickly through it because the material conducts heat rapidly with respect to its volumetric heat capacity. The relation of thermal diffusivity α is given below,

$$\alpha = \frac{k}{\rho C^p}$$

where k is the thermal conductivity, C^p is the specific heat capacity on constant pressure, ρ is the density at a particular instant of time.

In the absence of heat loss, at any area the heat flux is constant. So the overall thermal conductivity can be calculated by using the inverse rule of mixture relation [5], $\frac{l_O}{K_O} = \frac{l_S}{K_S} + \frac{l_C}{K_C}$, where K_O, K_S and K_C are the overall, substrate and coating thermal conductivity on respective thicknesses with $l_O = l_S + l_C$.

9.4 Results and Discussions

The mean-field analysis was used to find out the various thermal properties of each layer named as substrate, top layer, middle layer and bottom layer. The overall thermal properties were later calculated using the rule of mixtures and inverse rule of mixture relation. The weight percentage of the slurry mixture used is shown in Table 9.1, and the weight percentage is calculated for total 125 g mixture. The mean coating thickens and trial samples considered for experimentation based on the Taguchi method is shown in Table 9.2.

Variation of Thermal Conductivity
It is evident that from Table 9.3, the thermal conductivity of the layer is changing according to the material composition as well as the thickness of the coating layer. When the percentage of metal content increases such as nickel and titanium oxide, the thermal conductivity of the coating layer also increases. The percentage of nickel is changing from 25% to 75%, while the percentage of mullite is decreasing from 75% to 25%, respectively, when it goes from top layer to bottom layer, then the thermal conductivity values are also changing from 10 to 28 W/m K. The composition of slurry mixture used in the triple coating of 1% TiO_2 are shown in Table 9.1 which was taken from the past experimentation work [11].

Table 9.1 Composition of slurry mixture used (125 g) TiO_2: 1 wt%; fly ash: 1 wt% [11]

Ceramic to metal	Mullite (49%)	Fly-ash (1%)	Nickel (50%)	Additive: TiO_2	Binder	Dispersant	Mixing agent
	44%			1%	2.5%	0.5%	52%
75–25	40.837	0.412	13.75	1.25	3.125	0.625	65
50–50	27.225	0.275	27.5	1.25	3.125	0.625	65
25–75	13.612	0.137	41.25	1.25	3.125	0.625	65

Table 9.2 Composition of samples and mean coating thickness [11]

	Sample 1 (Trial 2 + Trial 11)	Sample 2 (Trial 5 + Trial 14)	Sample 3 (Trial 15 + Trial 18)	Sample 4 (Trial 13 + Trial 16)	Sample 5 (Trial 4 + Trial 10)	Sample 6 (Trial 6 + Trial 12)
Composition of coating (excluding 44% mullite and nickel) of 125 g	3% TiO_2	3% TiO_2	5% TiO_2	1% TiO_2	1% TiO_2	5% TiO_2
Mean coating thickness in μm	172.0	209.5	179.5	156	130.5	176

Table 9.3 Thermal conductivity by mean-field micro-mechanics model in W/m^{2}K

Thermal conductivity	Sample 1	Sample 2	Sample 3	Sample 4	Sample 5	Sample 6
Substrate	51.89	51.89	51.89	51.89	51.89	51.89
Top layer (75:25)	10.124	10.124	9.942	10.308	10.125	10.033
Middle layer (50:50)	16.549	16.549	15.975	17.135	16.556	16.262
Bottom layer (25:75)	28.176	28.176	27.351	30.124	28.737	28.034
Overall coating	18.463	18.463	17.756	19.189	18.473	18.109
Coated substrate	48.952	48.377	48.657	49.357	49.616	48.806

After finding out the overall thermal conductivity using the prediction method as well as the experimentation work, a comparison graph is plotted using the six set of readings. The experiment was repeated for four times for getting an accurate result, and the mean of all readings is considered for plotting the curve. From Fig. 9.5, it is shown that the theoretical and experimental values are overlapping at three different points and the deflection is shown in the curve. The trial samples, mean coating thickness and weight percentage of TiO$_2$ based on previous experimentation work are shown in Table 9.3, and the TiO$_2$ composition and mean coating thickness is varying.

The comparison between theoretical and experimental values is plotted in Table 9.4. The percentage deviations of all the samples were calculated by comparing the experimental and theoretical values. The percentage of deviations was in the range lesser than 12.5% with a lower value of 1.38% and an upper value of 12.24%. The average percentage deviation in thermal conductivity is coming at 5.705%. The results confirm the validity of the theoretically predicted with experimental values.

Variation of Specific Heat Capacity
The specific heat capacity of the coating layer is changing according to the material composition as well as the thickness of the coating layer. The property value is
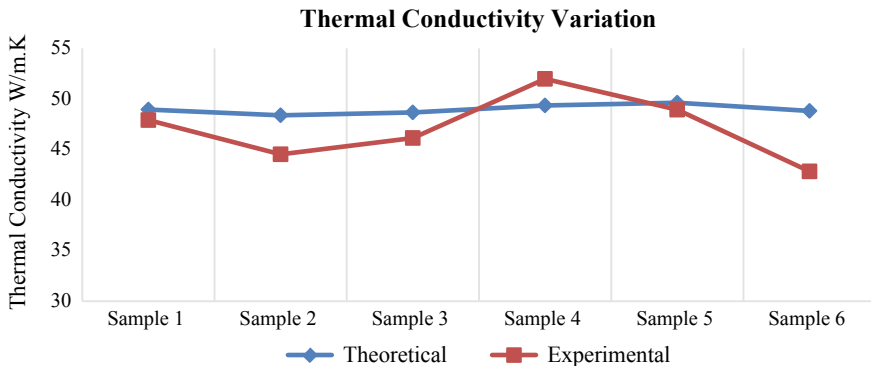
Fig. 9.5 Variation in theoretical and experimental thermal conductivity of samples

Table 9.4 Comparison table of thermal conductivity

	Sample 1	Sample 2	Sample 3	Sample 4	Sample 5	Sample 6
Theoretical value	48.952	48.377	48.657	49.357	49.616	48.806
Experimental value	47.90	44.52	46.13	51.98	48.93	42.83
Difference	1.052	3.857	2.527	2.622	0.686	5.976
Percentage deviation	2.14%	7.97%	5.19%	5.31%	1.38%	12.24%

varying with respect to the variation of coating thickness and compositions, and the predicted values for various layers are shown in Table 9.5.

After finding out the overall specific heat capacity using the prediction method as well as the experimentation work, a comparison graph was plotted using the six set of readings. The experiment was repeated for four times for getting an accurate result, and the mean of all readings are considered for plotting the curve. From Fig. 9.6, it is shown that the theoretical and experimental values are overlapping at three different points, and the deflection is shown in the curve. The percentage deviations of all the samples were calculated by comparing the experimental and theoretical values, which is shown in Table 9.6. The average percentage deviation in

Table 9.5 Predicted specific heat capacity (KJ/Kg-K)

Heat capacity	Sample 1	Sample 2	Sample 3	Sample 4	Sample 5	Sample 6
Substrate	0.486	0.486	0.486	0.486	0.486	0.486
Top layer (75:25)	0.816	0.816	0.800	0.832	0.816	0.808
Middle layer (50:50)	0.702	0.702	0.691	0.713	0.702	0.697
Bottom layer (25:75)	0.588	0.588	0.583	0.594	0.588	0.586
Overall coating	0.702	0.702	0.691	0.713	0.702	0.697
Coated substrate	0.491	0.492	0.491	0.491	0.490	0.491
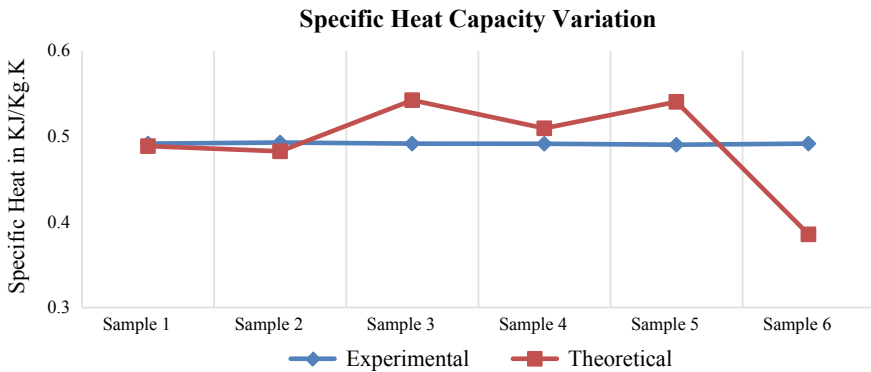
Fig. 9.6 Variation of specific heat capacity

Table 9.6 Comparison of specific heat capacity (kJ/kg K)

Heat capacity	Sample 1	Sample 2	Sample 3	Sample 4	Sample 5	Sample 6
Theoretical value	0.491	0.492	0.491	0.491	0.490	0.491
Experimental value	0.488	0.482	0.542	0.509	0.540	0.385
Deviation	0.0028	0.0101	0.0507	0.0181	0.0501	0.1059
Percentage deviation	0.57	2.05	10.32	3.67	10.22	21.55

thermal conductivity is coming at 8.06% with a lower value of 0.57% and an upper value of 21.55%. The results confirm the validity of the theoretically predicted with experimental values. The large variation may because of the assumptions considered while predicting the thermo-mechanical properties or non-uniform distribution of materials in coating layers.

Validation of Thermal Diffusivity

Thermal diffusivity is a dependent property of thermal conductivity and volume heat capacity [16]. Here, the thermal diffusivity of the triple coated composite material was compared with the predicted thermal diffusivity values which were calculated using equation and mean-field micro-mechanics approach. After finding out the thermal diffusivity of the coated substrate using experimentation and the equations, a comparison graph was plotted (Fig. 9.7) and which was shown the deviation of experimental values with the predicted values. From the comparison curve, the experimental values were overlapping the predicted values in some points, and the mean deviation of the curve was coming 7.60% with the lowest value of 1.57% and the highest value of 11.87%, which was in the acceptable range. The comparison table and the percentage difference of specific heat capacity are shown in Table 9.7.

The deviation was reported on both sides of the theoretical curve, and the transient temperature increment taken for doing the thermal conductivity test is 1.5–4.5 K [17] and which is shown in Fig. 9.8.
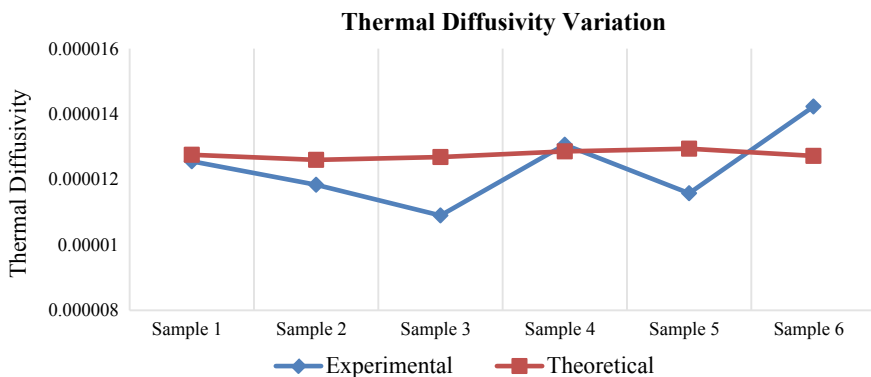
Fig. 9.7 Variation of thermal diffusivity

Table 9.7 Comparison of thermal diffusivity

Thermal diffusivity	Sample 1	Sample 2	Sample 3	Sample 4	Sample 5	Sample 6
Theoretical value	1.27E − 05	1.25E − 05	1.26E − 05	1.28E − 05	1.29E − 05	1.27E − 05
Experimental value	1.25E − 05	1.18E − 05	1.09E − 05	1.30E − 05	1.15E − 05	1.42E − 05
Deviation	2.01E − 07	7.61E − 07	1.78E − 06	2.02E − 07	1.36E − 06	1.51E − 06
Percentage deviation	1.58	6.04	14.06	1.57	10.52	11.87
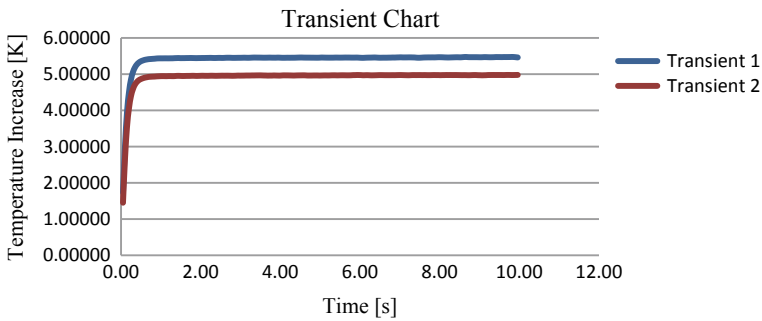
Fig. 9.8 Transient temperature increment of mullite-based TBC from the experiment

9.5 Conclusions

It is validated that the deviation of various material properties obtained using theoretical and experimental works was acceptable with a mean percentage deviation of less than 10%. It is useful to use the mean-field micro-mechanics approach on composite materials when it comes to finding the ideal material properties to find the best result. No single material can give the desired properties. However, by using composite materials, the best material properties and results may be achieved. The same approach could be used for predicting more thermo-mechanical properties like the coefficient of thermal expansion, heat capacity, bulk modulus, shear modulus, Young's modulus, Poisson's ratio and density.

References

1. Nguyen, P., Harding, S., Ho, S.-Y.: Experimental studies on slurry based thermal barrier coatings. In: 5th Australas. Congr. Appl. Mech. (ACAM 2007), vol. 1, pp. 545–550 (2007)

2. Zhou, D., Guillon, O., Vaßen, R.: Development of YSZ thermal barrier coatings using axial suspension plasma spraying. Coatings **7**, 120 (2017). https://doi.org/10.3390/coatings7080120

3. Wakashima, K., Tsukamoto, H.: Mean-field micromechanics model and its application to the analysis of thermomechanical behaviour of composite materials. Mater. Sci. Eng., A **146**, 291–316 (1991). https://doi.org/10.1016/0921-5093(91)90284-T

4. Tsukamoto, H.: Rev. Micromech. Approach Toward Thermomech Metal Matrix Compos. **32**, 883–892 (1992)

5. Liu, G.R.: A step-by-step method of rule-of-mixture of fiber- and particle-reinforced composite materials. Compos. Struct. **40**, 313–322 (1997). https://doi.org/10.1016/S0263-8223(98)00033-6

6. Wang, L., Zhong, X.H., Zhao, Y.X., Yang, J.S., Tao, S.Y., Zhang, W., Wang, Y., Sun, X.G.: Effect of interface on the thermal conductivity of thermal barrier coatings: A numerical simulation study. Int. J. Heat Mass Transf. **79**, 954–967 (2014). https://doi.org/10.1016/j.ijheatmasstransfer.2014.08.088

7. Pasupuleti, K.T., Dsouza, S., Thejaraju, R., Venkataraman, S., Ramaswamy, P., Murty, N.: Performance and steady state heat transfer analysis of functionally graded thermal barrier coatings systems. Mater. Today Proc. **5**, 27936–27945 (2018). https://doi.org/10.1016/j.matpr.2018.10.033

8. Wang, L., Shao, F., Zhong, X.H., Ni, J.X., Yang, K., Tao, S.Y., Wang, Y.: Tailoring of self-healing thermal barrier coatings via finite element method. Appl. Surf. Sci. **431**, 60–74 (2018). https://doi.org/10.1016/j.apsusc.2017.06.025

9. Wang, L., Li, D.C., Yang, J.S., Shao, F., Zhong, X.H., Zhao, H.Y., Yang, K., Tao, S.Y., Wang, Y.: Modeling of thermal properties and failure of thermal barrier coatings with the use of finite element methods: a review. J. Eur. Ceram. Soc. **36**, 1313–1331 (2016). https://doi.org/10.1016/j.jeurceramsoc.2015.12.038

10. Shrestha, R., Kim, W.: Evaluation of coating thickness by thermal wave imaging: a comparative study of pulsed and lock-in infrared thermography—Part II: experimental investigation. Infrared Phys. Technol. **92**, 24–29 (2018). https://doi.org/10.1016/j.infrared.2018.05.001

11. Verma, R., Randhawa, J.S., Kant, S., Suri, N.M.: Characterization studies of slurry-sprayed Mullite-Nickel coatings on ASTM 1018 Steel. Arab. J. Sci. Eng. (2019). https://doi.org/10.1007/s13369-019-03753-6

12. Torrecillas, R., Calderón, J.M., Moya, J.S., Reece, M.J., Davies, C.K.L., Olagnon, C., Fantozzi, G.: Suitability of mullite for high temperature applications. J. Eur. Ceram. Soc. **19**, 2519–2527 (2002). https://doi.org/10.1016/s0955-2219(99)00116-8

13. Verma, R., Suri, N.M., Kant, S.: Parametric appraisal of slurry-sprayed Mullite coatings for coating thickness. J. Therm. Spray Technol. **25**, 1289–1301 (2016). https://doi.org/10.1007/s11666-016-0437-1

14. He, Y.: Rapid thermal conductivity measurement with a hot disk sensor: Part 2. Characterization of thermal greases. Thermochim. Acta **436**, 130–134 (2005). https://doi.org/10.1016/j.tca.2005.07.003

15. He, Y.: Heat capacity, thermal conductivity, and thermal expansion of barium titanate-based ceramics. Thermochim. Acta **419**, 135–141 (2004). https://doi.org/10.1016/j.tca.2004.02.008

16. Ajlan, S.A.: Measurements of thermal properties of insulation materials by using transient plane source technique. Appl. Therm. Eng. **26**, 2184–2191 (2006). https://doi.org/10.1016/j.applthermaleng.2006.04.006

17. He, Y.: Rapid thermal conductivity measurement with a hot disk sensor: Part 1. Theoretical considerations. Thermochim. Acta **436**, 122–129 (2005). https://doi.org/10.1016/j.tca.2005.06.026

18. Alexander, J.F.S.: CRC Materials Science and Engineering Databook (2001)

19. Barton, A.F.M.: CRC Handbook of Solubility Parameters and Other Cohesion Parameters, 2nd edn (2017)

20. Heat conduction. Fluid Mech. Appl. **112**, 155–173 (2015). https://doi.org/10.1007/978-3-319-15793-1_9

Chapter 10
Surface Modification of Al–4.5%Cu/MoS$_2$ Composites by Laser Surface Melting

Praveen Kumar Bannaravuri, Anil Kumar Birru, and Uday S. Dixit

Abstract In this research work, aluminum composites were prepared with Al–4.5%Cu alloy as a matrix with 2 and 4 wt% of MoS$_2$ as reinforcement. The composites were prepared using stir casting method. Surfaces of the composites were melted using a CO$_2$ laser beam. Microstructure and micro-hardness of the laser melted surfaces were studied. Results of the composites after laser surface melting (LSM) were compared with the as-cast surface. Grain refinement was observed after LSM, and porosity was minimized. The micro-hardness was improved remarkably by LSM. LSM can be conveniently applied to enhance the surface properties of the aluminum composites.

Keywords Aluminum composites · Molybdenum disulfide · Stir casting · Laser surface melting · Micro-hardness

Note: Praveen Kumar Bannaravuri was at IIT Guwahati, from August 2019 shifted to Karunya Institute of Science and Technology, Coimbatore-641114.

P. K. Bannaravuri (✉) · U. S. Dixit
Department of Mechanical Engineering, Indian Institute of Technology Guwahati, Guwahati, Assam 781039, India
e-mail: banna.mech@gmail.com

U. S. Dixit
e-mail: uday@iitg.ac.in

P. K. Bannaravuri
Department of Mechanical Engineering, Karunya Institute of Science and Technology, Coimbatore 641114, India

A. K. Birru
Department of Mechanical Engineering, National Institute of Technology Manipur, Manipur, Imphal 795004, India
e-mail: anilbirru@gmail.com

10.1   Introduction

Addition of the aluminum metal matrix composites (AMMCs) with the ceramic particles such as SiC, Al_2O_3, TiO_2, B_4C and TiC provides the superior strength and improves the tribological properties of a composite [1]. However, lubricating particles such as graphite (Gr) and MoS_2 are added for improving the tribological behavior of composites by developing a solid lubricating layer [2, 3]. The incorporation of these particles in the composites considerably affects the mechanical behavior of the composites. The surface of composites prepared by stir casting method contains defects such as porosity, particles agglomeration and micro-segregations [4]. Ahmad et al. [5] observed that the porosity of Al–Si composite increased with increase in weight percentage of SiC particles by conventional stir casting method. Razzaq et al. [6] noticed that agglomeration of fly ash particles increased with an increase in the fly ash content in AA6063 alloy.

Often one needs a defect-free surface. Laser surface melting (LSM) is an effective technique to produce the defect-free surface of the composites [7]. However, at low solidification rates (less than the diffusion rate), local equilibrium can be developed, and interface crystals may achieve the same composition as the melt [8, 9]. Therefore, a high cooling rate as in LSM results in a fine solidified microstructure, which may contain non-equilibrium phases, new precipitates and extended solid solubility.

Microstructure of the composites can be refined by LSM due to rapid solidification; it also helps to disperse reinforcement particles uniformly. Hu et al. [10] reported that micro-hardness of $Al2024/Al_{18}B_4O_{33w}$ composite increased after LSM due to fine grain structure. After LSM, the properties of material improved significantly. The corrosion damage of Al 6013 alloy is remarkably lower after LSM than that for the as-received Al 6013 alloy. The enhancement in the pitting corrosion of the LSM Al alloy was observed. Enhancement of corrosion resistance of alloys after LSM in both 10% H_2SO_4 and 10% HNO_3 solutions is observed by Wong et al. [11].

In this present investigation, the Al–4.5Cu alloy reinforced with 2 and 4 wt% of MoS_2 was prepared by stir casting method, and surface of the cast samples was melted by a laser beam. The structural modification and surface hardness were studied after LSM and compared with as-cast material. A clear improvement in properties was obtained.

10.2   Experimental Details

The aluminum alloy Al–4.5wt% Cu was selected as the matrix material. Chemical composition of the alloy obtained by inductively coupled plasma optical emission spectrometry (ICP-OES) is presented in Table 10.1. MoS_2 (average particles size of 35 μm and density of 5.06 g/cm^3) were selected as reinforcements for the synthesis of the composite. The Al–4.5Cu/MoS2 composites are fabricated using stir casting method. After fabrication in a foundry, the testing for material characterization and

Table 10.1 Chemical Composition of Al–4.5wt% Cu alloy

Element	Cu	Mg	Si	Fe	Mn	Ni	Pb	Sn	Ti	Zn	Al
wt%	4.52	0.066	0.538	0.663	0.131	0.075	0.029	0.021	0.013	0.118	Balance

mechanical properties was performed in the laboratory using the required tools and equipment.

10.2.1 Fabrication of AMMCs Using the Stir Casting Method

In producing AMMCs, manufacturers prefer the most cost-effective options, while ensuring that the casting meets the mandated quality requirements [12]. The stir casting method is one such option. In the stir casting method, in order to achieve the optimal properties of metal matrix composites (MMCs) [13], it is needed to distribute the reinforcement particles uniformly in the matrix while improving the wetting between the MoS_2 particles and matrix. The porosity in the cast MMCs should be minimized while also eliminating the unnecessary chemical reaction [14].

The stir casting parameters shown in Fig. 10.1 can influence the microstructure and properties of composites. Rajmohan et al. [15] observed the uniform distribution of the reinforcements particles in the matrix alloy to achieve the uniform mechanical properties of the composite materials with stir casting method. Radhika et al. [16] also fabricated aluminum-based composites reinforced with Al_2O_3 and graphite particles by stir casting method and found that reinforcement particles were distributed uniformly. It was also observed that with addition of reinforcement particles, the hardness and tensile strength of composite increased. In the present work, the Al–4.5wt% Cu alloy was reinforced with MoS_2 (average particles size of 35 μm and density of 5.06 g/cm^3) to produce AMMCs using the stir casting experimental setup as shown in Fig. 10.2. This setup was used for making the alloys of aluminum in the earlier works of first two authors [17].
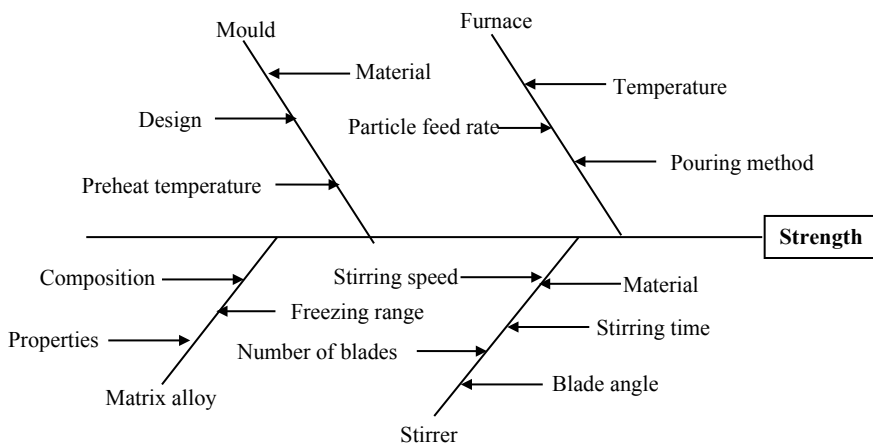
Fig. 10.1 Stir casting parameters affecting the strength of MMCs

Fig. 10.2 Stir casting experimental setup [17]

10.2.1.1   Fabrication Details of AMMCs

The Al–4.5Cu alloy and MoS$_2$ materials are heated at 350 °C to release all the moisture and trapped air between the particles [18]. The Al–4.5wt% Cu alloy was melted in the induction electric resistance furnace. It was melted at 800 °C in a crucible in an argon atmosphere. The temperature of molten metal was brought down to 620–650 °C, which is known as semi-solid state [19]. The solidification range for Al–4.5Cu alloy is 548–660 °C [20]. The MoS$_2$ particles at 0, 2 and 4 wt% were added in the molten Al–4.5wt% Cu alloy. The heated MoS$_2$ particles were injected along with argon gas. Nearly, 0.1 wt% Mg in ingot form is also added to enhance the wettability between the MoS$_2$ particles and molten alloy, while stirring and stirring were continued for 5–6 min.

The semi-solid composite is then superheated to 750 °C to increase its fluidity, and again, stirring was performed by a stainless steel stirrer coated with graphite. The coating of graphite helps to prevent the migration of ferrous ions from the stainless steel stirrer into the melt. The melt was stirred at a speed of 600 rotations per minute (rpm) for 10 min to enhance homogeneous distribution of the MoS$_2$ particles in the Al–4.5wt% Cu alloy. Concurrently, argon gas was used as a shielding veil on the surface of molt. The process was similar to that employed by Prabu et al. [21] and was seen to increase the hardness of composite with uniform distribution

Table 10.2 List of AMMCs fabricated by stir casting

Composite code	Composition	MoS_2 (wt%)
1	Al–4.5Cu alloy	0
2	Al–4.5Cu/2MoS$_2$	2
3	Al–4.5Cu/4MoS$_2$	4

of reinforcement. After completely incorporating the MoS_2 particles into the Al–4.5wt% Cu alloy, the composite was poured into a permanent steel mold which is preheated at 350 °C [17]. The fabricated composite material is fettled at room temperature from the steel mold. The composite ingot was fabricated with 2 and 4 wt% of MoS_2 particles. Samples were prepared for microstructure analysis, density and hardness tests. Table 10.2 lists the fabricated AMMCs by stir casting method.

10.2.2 Density and Porosity Measurement

The density was calculated to estimate the porosity levels in the fabricated composite in the stir casting method and to analyze the effect of the reinforcement weight percent on the density. Porosity may be determined by the difference of the experimental and theoretical densities of each fabricated composite [22]. The experimental density (ρ_{exp}) of the fabricated composites was found out using the water displacement technique (Archimedes' principle) [17, 23] and calculated using

$$\rho_{exp} = \frac{m}{V}, \tag{10.1}$$

where m is the mass of the test sample and V is the volume of the test sample.

Some porosity levels may be normal in the fabricated composites due to increase in the contact area of incorporated particles with air during production. The porosity may play a crucial role in the mechanical properties of the fabricated composites. It can be controlled, but it may not be possible to completely eliminate in a casting process. The porosity of the fabricated composites was determined using

$$\text{Porosity (\%)} = \frac{\rho_{th} - \rho_{exp}}{\rho_{th}} 100, \tag{10.2}$$

where ρ_{th} is the theoretical density and ρ_{ex} is the experimental density. Theoretical density (ρ_{th}) for may be measured using the rule of mixtures [15]. The rule of mixture for particulate composite provides

$$\rho_{th} = \rho_m V_m + \rho_r V_r, \tag{10.3}$$

where ρ_m and ρ_r are the density of matrix and reinforcement, and V_m and V_r are the volume fraction of the matrix and reinforcement, respectively.

10.2.3   Laser Surface Melting by 2.5 kW CO$_2$ Laser

The surface of the cast samples was melted by using 2.5 kW CO$_2$ laser (Model: Orion 3015, Make: LVD, Belgium) as shown in Fig. 10.3, at a wavelength of 10.6 μm. The laser parameters are depicted in Table 10.3. The laser specific energy (LSE) is important parameter that can be calculated as [24]

$$E = \frac{P}{vd},\tag{10.4}$$

where P refers the laser power, v refers the scan speed (constant 400 mm/s) and d refers the laser beam diameter.

Fig. 10.3 Experimental setup of LSM

Table 10.3 Laser parameters used for surface re-melting of composites

Sr. No.	Material	Laser parameters			
		P (kW)	H (mm)	d (mm)	E (J/mm^2)
1	Al–4.5Cu alloy	1.9	35	6.61	43
2	Al–4.5Cu alloy	1.9	40	7.56	38
3	Al–4.5Cu alloy	1.9	45	8.5	34
4	Al–4.5Cu/2MoS$_2$	1.9	35	6.61	43
5	Al–4.5Cu/2MoS$_2$	1.9	40	7.56	38
6	Al–4.5Cu/2MoS$_2$	1.9	45	8.5	34
7	Al–4.5Cu/4MoS$_2$	1.9	35	6.61	43
8	Al–4.5Cu/4MoS$_2$	1.9	40	7.56	38
9	Al–4.5Cu/4MoS$_2$	1.9	45	8.5	34

10.2.4 Material Characterization

The properties of composite may be affected by the microstructure of the composite and interface between reinforcements particles and matrix alloy. Material characterization of the as-cast and after LSM samples is observed using several tools to understand the interface between reinforcement and the matrix alloy. The procedure is described briefly.

10.2.4.1 Morphological Analysis

The metallographic examination of the composites was carried out using an optical microscope (OM) and a scanning electron microscope (SEM). Energy dispersive analysis of X-rays (EDAX) of the composites was examined by FEI Quanta 250 SEM. The samples of fabricated composites were cut in the desired shapes, and the surface was polished. It was etched for microstructure analysis using Keller's reagent (95 ml water, 2.5 ml HNO$_3$, 1.5 ml HCl, 1.0 ml HF). This reagent used for Al and Al alloys widely as an etching agent [25].

Optical microscope was used to analyze the microstructure and measure the grain size of the composites. Grain size of composite was determined using the "linear intercept method" by ImageJ software. In a micrograph of composites, at any straight line, the length of the line divided by the average number of grains intercepted by it gives the average grain size [26]. The average grain size was measured at various locations on every specimen.

10.2.4.2   X-ray Diffraction Analysis

X-ray diffraction patterns of MoS_2 reinforced composite samples were examined using a Bruker D8 advanced eco X-ray diffractometer, with $CuK\alpha$-radiation and Ni filter. Voltage of 40 kV and 25 mA current intensity was used for XRD analysis.

10.2.5   Hardness Test

The samples of the fabricated composites were prepared for the hardness and tensile test as per the standard practice. The sample prepared for the hardness test was of dimension, 15 mm × 15 mm × 15 mm, and was polished to get an smooth and flat surface. The hardness test was exhibited by taking the average of three readings for each sample using micro-Vickers hardness machine as per ASTM E384-11, with a load of 100 gm. The hardness of the sample was calculated by measuring the dimension of indenter mark observed on the surface with dwelling time of 15 s.

10.3   Results and Discussion

Results of XRD analysis are discussed in Sect. 3.1. The microstructures of as-cast and LSM samples were analyzed by optical microscopy and are discussed in Sect. 3.2. The micro-hardness is described in detail in Sect. 3.3.

10.3.1   XRD Analysis of AMMCs

The XRD pattern of the fabricated composite is shown in Fig. 10.4, in which the diffraction peaks of MoS_2 are evidently noticed. This confirms the findings from the EDAX profiles (Fig. 10.8b) about the particles in the composites. In the most of the composites, it was seen that the intensity of Mo peaks increases as MoS_2 content increases in AMMCs. Figure 10.4 confirms that the aluminum peaks are slightly shifted to the lower 2θ in the composite material when compared to the Al–4.5wt.%Cu alloy. The shifting occurs due to the existence of MoS_2 particles in the fabricated composite materials. Peaks of other element, such as alumina (Al_2O_3), ferric oxide (Fe_2O_3) and magnesium oxide (MgO), were also detected. The peaks of the main elements are aluminum and Mo, thus demonstrating that the integrity of MoS_2 particles is preserved during the formation of the composite. Joseph et al. [27] fabricated AlMg0.5Si/MoS_2 composites by stir casting and observed the existence of MoS_2 in the composite with thermal stability. The MoS_2 particles were thermodynamically stable at the casting conditions in the present research; the particles neither decomposed nor interacted with aluminum to form an intermetallic compound. This
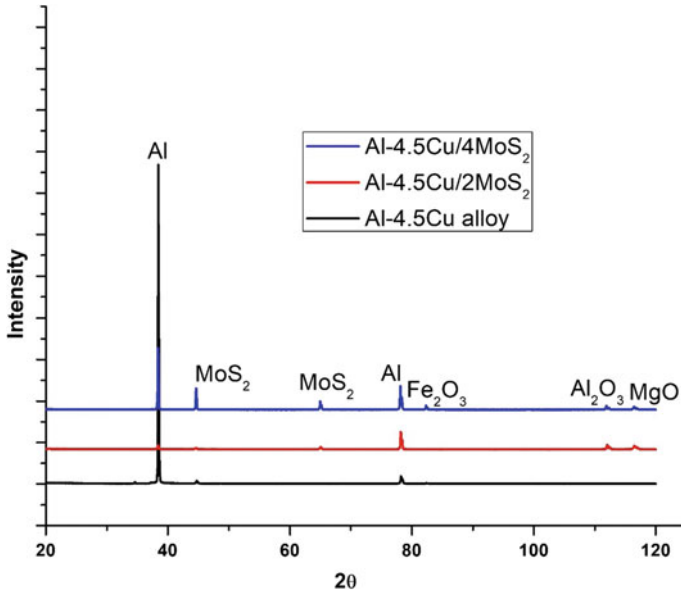
Fig. 10.4 XRD pattern of AMMCs fabricated by stir casting

confirms that the interface between the Al–4.5Cu matrix alloy and MoS_2 particles was clean, which is beneficial, otherwise the reaction products would have accrued at the interface and hampered load transfer mechanism to operate during tensile loading [28].
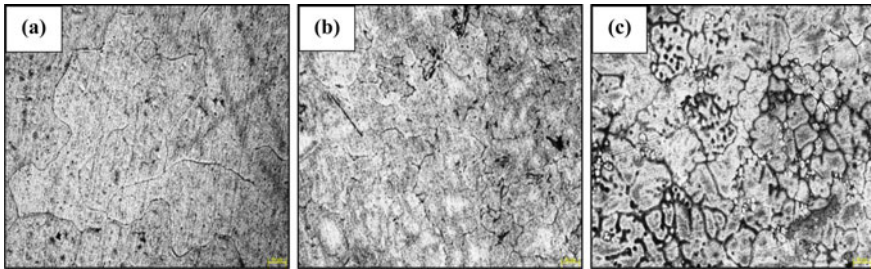
Fig. 10.5 Microstructure (X100) of as-cast **a** Al–4.5Cu alloy, **b** Al–4.5Cu/2MoS_2 and **c** Al–4.5Cu/4MoS_2
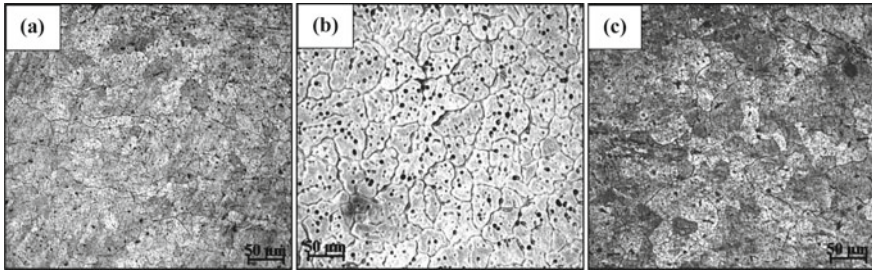
Fig. 10.6 Microstructure (X100) of LSM Al-4.5Cu matrix alloy at LSE of **a** 34 J/mm^2, **b** 38 J/mm^2 and **c** 43 J/mm^2
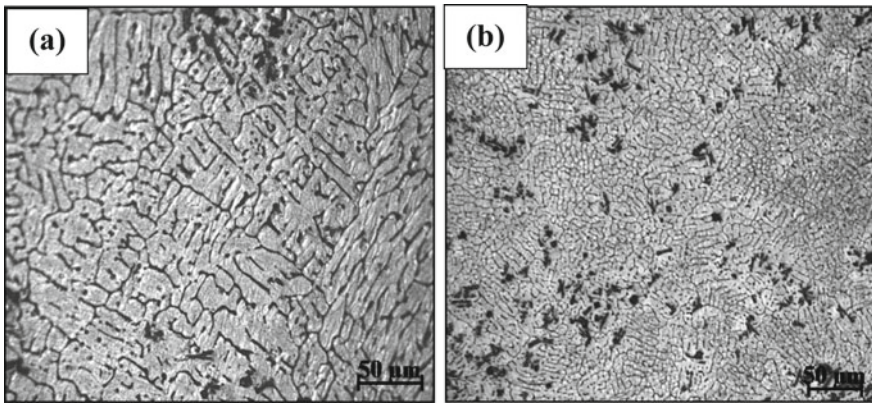
Fig. 10.7 Microstructure (X100) of LSM **a** Al–4.5Cu/2MoS$_2$ and **b** Al–4.5Cu/4MoS$_2$ composite at LSE of 38 J/mm^2
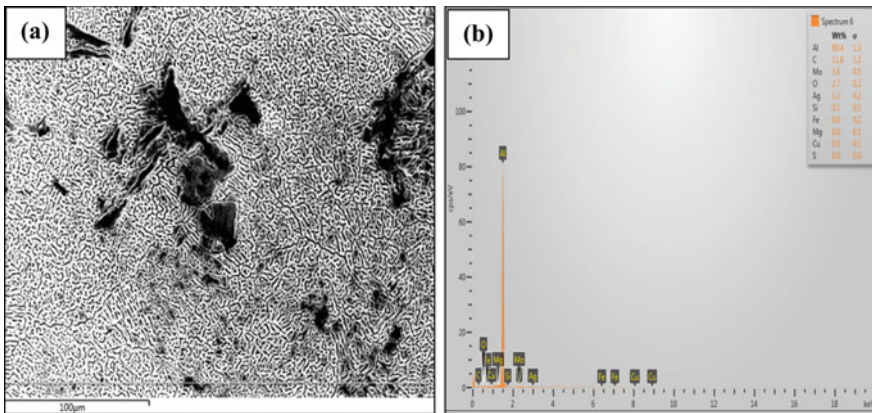
Fig. 10.8 **a** SEM micrograph with **b** EDX profile of Al–4.5Cu/4MoS$_2$ composite

10.3.2 Analysis of Microstructure

The microstructure of the as-cast matrix alloy, Al–4.5Cu/2MoS$_2$ and Al–4.5Cu/4MoS$_2$ was analyzed through optical micrographs as shown in Fig. 10.5. It was observed that the MoS$_2$ particles are reasonably homogeneously distributed in the matrix. The optical micrographs of Al–4.5Cu alloy and Al–4.5Cu/MoS$_2$ composites show sizable amount of blow holes, which were detected due to the drag of air bubbles into the melt during stir casting. The porosity was noticed due to entrapped gases in the molten metal as shown in Fig. 10.5a. In Fig. 10.5b, c, at some places, particle agglomeration was observed. Microstructure of the Al–4.5Cu/4MoS$_2$ is shown in Fig. 10.5c. MoS$_2$ particles tend to agglomerate at aluminum grain boundaries and are trapped by converging dendrites in the intercellular regions. The dispersal of the MoS$_2$ particles can be increased more uniformly as the solidification rate increases [4].

The microstructures of matrix after LSM are shown in Fig. 10.6 at LSEs of 34 J/mm^2, 38 J/mm^2 and 43 J/mm^2, respectively. At LSE of 34 J/mm^2, grain refinement was observed as shown in Fig. 10.6a, but some porosity is also seen. The fine grain refinement of matrix without defects was observed at LSE of 38 J/mm^2 as shown in Fig. 10.6b. In this case, the porosity of surface of matrix alloy was not found after LSM due to appropriate melting and high solidification rate. At LSE of 43 J/mm^2, many micro-pores and micro-cracks were observed in the optical image shown in Fig. 10.3c due to overheating. In LSM, solidification rate is very high. As a result of the fast solidification of the LSM zone, finer grains were formed compared to as-cast material. SEM micrograph as shown in Fig. 10.8a of Al–4.5Cu/4MoS$_2$ shows clear interface between Al–4.5Cu matrix and MoS$_2$ particles confirm the uniform distribution of reinforcement particles. EDX pattern as shown in Fig. 10.8b also confirms the existence of MoS$_2$ particles in the matrix alloy. The intensity of Mo and S peaks increases as MoS$_2$ content increases in AMMCs and other elements peaks also existed (Fig. 10.8).

The microstructures of composite after LSM are shown in Fig. 10.7, at LSE of 38 J/mm^2. The noticable grain refinement of Al–4.5Cu/2MoS$_2$ composite was observed as shown in Fig. 10.7a. The grain size of the Al–4.5Cu/4MoS$_2$ composites reduced as shown in Fig. 10.7b. No micro-cracks were observed around the hard particles after the rapid solidification of the surface.

Surface of composite melted by laser beam has a refined microstructure devoid of the particle agglomeration, thus forming a homogeneous distribution of particles. The average grain size was determined with help of the "mean linear intercept method." Figure 10.9 shows the average graine size of the as-cast and after LSM (at LSE of 38 J/mm^2) matrix and composite materials. Noticeable reduction in average grain size of material after LSM was observed in comparison with as-cast material due to rapid solidification after LSM. Similarly, results were obtained by Pariona et al. [29] on the surface of Al–1.5 wt% Fe alloy after LSM by a high-power Yb-fiber laser (IPG YLR-2000S) equipped with an ytterbium single emitter semiconductor diode.
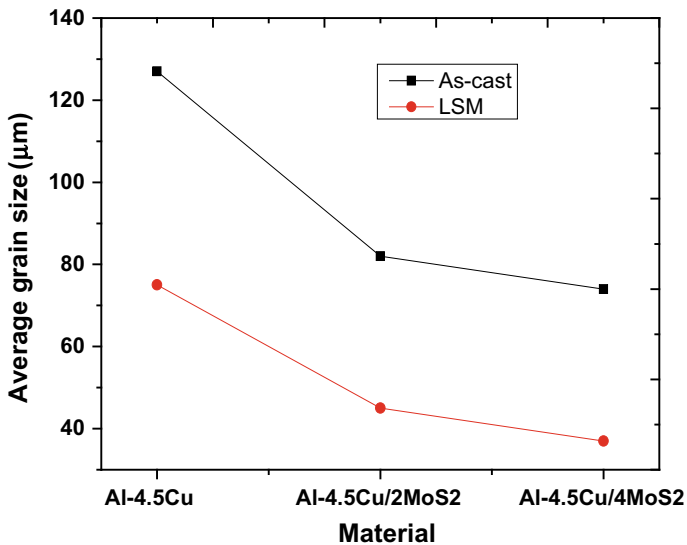
Fig. 10.9 Average grain size of as-cast and LSM composite material at LSE of 38 J/mm^2

10.3.3   Micro-hardness

The micro-hardness and density of as-cast matrix and composites are depicted in Fig. 10.10. Density of the composite was increased with incorporation of reinforcement as the density of MoS$_2$ is higher than that of matrix alloy. The average micro-hardness value of as-cast matrix and composites was observed as 84, 86 and 92
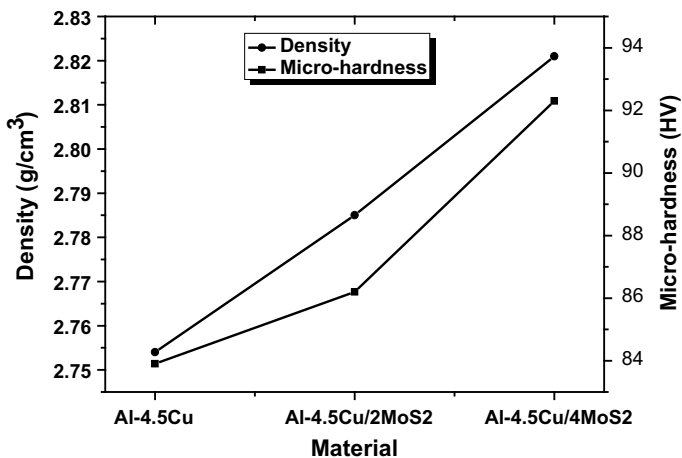
Fig. 10.10 Density and micro-hardness of as-cast material

$HV_{0.1}$ as shown in Fig. 10.10. The hardness got enhanced with the addition of MoS_2 in the composite. Similar results were found for aluminum 5059/SiC/MoS_2 composite fabricated by stir casting method, where the density and hardness of the composite increased with the addition of MoS_2 [30].

The micro-hardness values of laser surface melted matrix and composites are depicted in Fig. 10.11 at LSEs of 34, 38 and 43 J/mm^2. LSM enhanced the micro-hardness significantly in all the cases. For the matrix after LSM, the highest hardness of 102 $HV_{0.1}$ was observed at LSE of 38 J/mm^2. For Al–4.5Cu/2MoS_2 composite after LSM, the highest hardness of 107 $HV_{0.1}$ was observed at LSE of 38 J/mm^2. For Al–4.5Cu/4MoS_2 after LSM, the highest hardness of 116 $HV_{0.1}$ was observed at LSE 38 J/mm^2 was observed. The hardness of matrix and composites after LSM is higher than as-cast material. The highest hardness was observed at LSE of 38 J/mm^2 due to fine grain structure of material and uniformly distribution of reinforcement particles. Yilbas et al. [31] also noticed that micro-hardness of Al/SiC composite increased 50% higher than base material after laser melting.

Figures 10.12 and 10.13 show diamond indenter marks on samples after hardness test. The indentation mark on the surface of as-cast composites as shown in Figs. 10.12a and 10.13a was bigger in size in comparison with composite after LSM as shown in Fig. 10.12b and 10.13b under same load and surface condition. The smaller the indentation mark formed on the surface of composite after LSM, the harder the material.
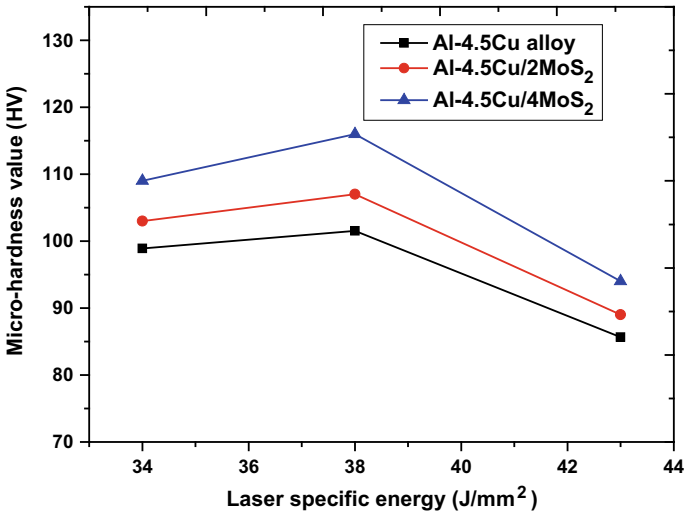
Fig. 10.11 Effect of laser specific energy on micro-hardness of LSM material
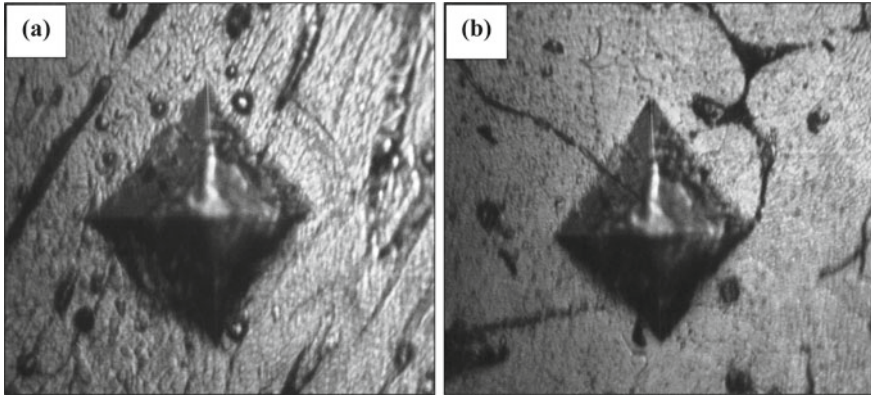
Fig. 10.12 Diamond indenter mark on surface of Al-4.5Cu alloy; **a** As-cast and **b** LSM at LSE of 38 J/mm^2
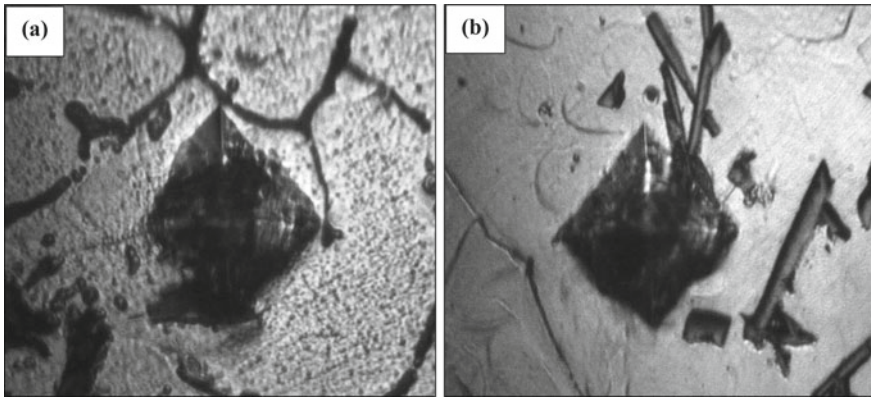
Fig. 10.13 Diamond indenter mark on surface of Al–4.5Cu/4MoS$_2$ composite; **a** As-cast and **b** LSM at LSE of 38 J/mm^2

10.4   Conclusions

Al–4.5Cu alloy composites reinforced with 2 and 4 wt% of MoS$_2$ were fabricated by stir casting method, and surface was remelted by laser. Some concluding remarks drawn are as follows:

1. The dispersal of MoS$_2$ particles in the fabricated composite was nearly uniform by stir casting method, but some particles agglomeration was observed.
2. The density of the composite increased with increase in reinforcement particles. Porosity of the composites increased with increase in reinforcement particles.
3. LSM improved surface properties of composites by eliminating porosity and refining the grains, and particles distribution was uniform.

4. The hardness of composite improved with addition of reinforcement particles, and hardness of the composites improved remarkably after LSM.

References

1. Rebba, B., Ramanaiah, N.: Investigations on mechanical behaviour of B_4C and MoS_2 reinforced AA2024 hybrid composites. J. Manuf. Sci. Prod. **15**(4), 339–343 (2015)
2. Daniel, S.A.A., Sakthivel, M., Gopal, P.M., Sudhagar, S.: Study on tribological behaviour of Al/SiC/MoS_2 hybrid metal matrix composites in high temperature environmental condition. Silicon **10**, 2129–2139 (2018)
3. Sharma, A., Garg, M.: Taguchi optimization of tribological properties of Al/Gr/B4C composite. Ind. Lubrication Tribol. **67**(4), 380–388 (2015)
4. Chen, R., Zhang, G.: Casting defects and properties of cast A356 Aluminium alloy reinforced with SiC particles. Compos. Sci. Technol. **47**, 51–56 (1993)
5. Ahmad, S.N., Hashim, J., Ghazali, M.J.: The effects of porosity on mechanical properties of cast discontinuous reinforced metal-matrix composite. J. Compos. Mater. **39**(5), 451–466 (2005)
6. Razzaq, A.M., Majid, D.L., Ishak, M.R., Uday, M.B.: Effect of fly ash addition on the physical and mechanical properties of AA6063 alloy reinforcement. Metals **7**(11), 477 (2017)
7. Jiru, W.G., Sankar, M.R., Dixit, U.S., Liao, H.: Laser surface melting of Al-12Si-4Cu-1.2Mn alloy. Int. J. Mechatron. Manuf. Syst. **11**, 230–249 (2018)
8. Ion, J.C.: Laser Processing of Engineering Materials, Principles, Procedure and Industrial Application. Elsevier Butterworth-Heinemann, pp. 261–268 (2005)
9. Steen, W.M., Powell, J.: Laser surface treatment. Mater. Des. **2**(3), 157–162 (1981)
10. Hu, J., Kong, L.C., Liu, G.: Structure and hardness of surface of Al18B4O33w/Al composite by laser surface melting. Mater. Sci. Eng., A **486**, 80–84 (2008)
11. Wong, T.T., Liang, G.Y., Tang, C.Y.: The surface character and substructure of aluminum alloys by laser-melting treatment. J. Mater. Process. Technol. **66**, 172–178 (1997)
12. Ezatpour, H.R., Torabi-Parizi, M., Sajjadi, S.A.: Microstructure and mechanical properties of extruded Al/Al_2O_3 composites fabricated by stir-casting process. Trans. Nonferrous Metal Soc. China **23**, 1262–1268 (2013)
13. Moses, J.J., Dinaharan, I., Joseph, S.S.: Prediction of influence of process parameters on tensile strength of AA6061/TiC Aluminum matrix composites produced using stir casting. Trans. Nonferrous Metal Soc. China **26**, 1498–1511 (2016)
14. Anthymidis, K., David, K., Agrianidis, P., Trakali, A.: Production of Al metal matrix composites by the stir-casting method. Key Eng. Mater. **592–593**, 614–617 (2014)
15. Chawla, K.K.: On the applicability of the "rule-of-mixtures" to the strength properties of metal-matrix composites. Rev. Bras. Fis. **4**, 411–418 (1974)
16. Radhika, N., Subramanian, R.: Effect of reinforcement on wear behavior of aluminum hybrid composites. Tribology **7**(1), 36–41 (2014)
17. Kumar, B.P., Birru, A.K.: Microstructure and mechanical properties of aluminium metal matrix composites with addition of bamboo leaf ash by stir casting method. Trans. Nonferrous Metals Soc. China **27**, 2555–2572 (2017)

18. Shueiwan, H., Juang, L.-J.F., Yang, H.P.O.: Influence of preheating temperatures and adding rates on distributions of fly ash in aluminum matrix composites prepared by stir casting. Int. J. Precision Eng. Manuf. **16**(7), 1321–1327 (2015)
19. Geng, L., Zhang H., Li H., Guan, L., Lu-jun, H.U.: Effects of Mg content on microstructure and mechanical properties of SiCp/Al-Mg composites fabricated by semi-solid stirring technique. Trans. Nonferrous Metal Soc. China **20**, 1851–1855 (2010)
20. Choi, S.W., Cho, H.S., Kumai, S.: Effect of the precipitation of secondary phases on the thermal diffusivity and thermal conductivity of Al-4.5Cu alloy. J. Alloys Compounds **688**, 897–907 (2016)
21. Prabu, L., Karumoorthy, S.B., Kathiresan, S, Mohan, B.: Influence of stirring speed and stirring time on distribution of particles in cast metal matrix composite. J. Mater. Process. Technol. **171**, 268–273 (2006)
22. Khosravi, H., Bakhshi, H., Salahinejad, E.: Effects of compo-casting process parameters on microstructural characteristics and tensile properties of A356 − SiCp composites. Trans. Nonferrous Metal Soc. China **24**, 2482–2488 (2014)
23. Gupta, M., Lai, M.O., Sooa, C.Y.: Effect of type of processing on the microstructural features and mechanical properties of Al-Cu/SiC metal matrix composites. Mater. Sci. Eng., A **210**, 114–122 (1996)
24. Kadhim, M.J., Al-rubaiey, S.I., Hammood, A.S.: The influence of laser specific energy on laser sealing of plasma sprayed yttria partially stabilized zirconia coating. Optics Lasers Eng. **51**, 159–166 (2013)
25. Mazahery, A., Shabani, M.O.: Characterization of cast A356 alloy reinforced with nano SiC composites. Trans. Nonferrous Metal Soc. China **22**, 275–280 (2012)
26. Birru, A.K., Karunakar, D.B.: Effects of grain refinement and residual elements on hot tearing of A713 aluminium cast alloy. Trans. Nonferrous Metal Soc. China **26**, 1783–1790 (2016)
27. Joseph, J.S.D., Kumaragururubaran, B., Satish, S.: Effect of MoS$_2$ on the wear behavior of Aluminium (AlMg0.5Si) composite. Silicon (2019). https://doi.org/10.1007/s12633-019-00238-x
28. Rajan, T.P.D., Pillai, R.M., Pai, B.C., Satyanarayana, K.G., Rohatgi, P.K.: Fabrication and characterization of Al–7Si–0.35 Mg/fly ash metal matrix composites processed by different stir casting routes. Compos. Sci. Technol. **67**, 3369–3377 (2007)
29. Pariona, M.M., Teleginski, V., Dos Santos, K., Machado, S., Zara, A.J., Zurba, N.K., Riva, R.: Yb-fiber laser beam effects on the surface modification of Al–Fe aerospace alloy obtaining weld filet structures, low fine porosity and corrosion resistance. Surf. Coatings Technol. **206**, 2293–2301 (2012)
30. Daniel, A.A., Murugesana, S., Manojkumara, Sukkasamy, S.: Dry sliding wear behaviour of Aluminium 5059/SiC/MoS$_2$ hybrid metal matrix composites. Mater. Res. **20**, 1697–1706 (2017)
31. Yilbas, B.S., Toor, I., Malik, J.: Laser surface treatment of aluminum composite: surface characteristics. Sci. Eng. Compos. Mater. **23**(5), 495–503 (2015)

Chapter 11
Configuration Design Development of Internal Bore GTAW Welding

Harsh Radadiya, Ashish Yadav, Jaydeep Joshi, Arun Kumar Chakraborty, and Navneet Khanna

Abstract The cooling water lines operating in vacuum and nuclear environment being a crucial component subjected to high pressure, welding is of utmost importance from the perspective of their through thickness integrity, and therefore, the full penetration butt welding is the mandatory requirement. However, in complex geometries like high-voltage bushing for neutral beam systems for fusion devices, the cooling pipes are so closely spaced that the welding from outside is not feasible by orbital welding technique. For this and similar systems, there is a need to have an alternative tool development, wherein the welding arm goes inside the pipe, reaches to the location of weld edge preparation and produces the arc such that the penetration is produced on the outer circumference of pipe. Such a technique, known as 'Internal Bore Welding' (IBW), is proposed here. IBW torch is being designed to work with the wide range of pipe diameter with varying arm length to weld at different length locations. The minimum pipe size considered for the torch design is 25.4 mm. In order to give the rotation, precision motors have been used, and to avoid the interference on the electric and shielding gas supply connections, non-axial motion transfer has been designed with gear connections.

H. Radadiya (✉) · N. Khanna
Institute of Infrastructure Technology Research and Management, Ahmedabad, Gujarat 380026, India
e-mail: harshradadiya24@gmail.com

N. Khanna
e-mail: navneetkhanna@iitram.ac.in

A. Yadav · J. Joshi · A. K. Chakraborty
ITER-India, Institute for Plasma Research, Ahmedabad, Gujarat 382428, India
e-mail: ashish.yadav@iter-india.org

J. Joshi
e-mail: jaydeep.joshi@iter-india.org

A. K. Chakraborty
e-mail: arunkc@iter-india.org

Nomenclature

GTAW   Gas Tungsten Arc Welding
IBW   Internal Bore Welding
OD   Outer Diameter
DOF   Degree Of Freedom

11.1   Introduction

In recent times, the increased use of robotic systems in place of human labour is an important area of study to assess feasibility of implementation. A significant proportion of robots are present in material handling, spray painting, spot welding and arc welding [1]. Not only do robots and mechanized equipment enhance productivity, weld quality and flexibility but also account for safety in workspace and reduced labour costs [2]. Welding of pipes and tubes is largely based on orbital welding technology [3] with automation techniques which is readily used by industries [1]. For components where multiple cooling pipes are required to be welded in close proximities, the workspace required for orbital welding apparatus is inadequate. Alternate technologies need to be explored to carry out the welding operation. One such technique internal bore welding (IBW) with specifically designed manipulator and welding torch can be implemented for such complex configurations. In this mechanism, a welding torch ensures the current flow to the electrode, holds/grips the electrode firmly and directs the flow of shielding gas to weld pool [4]. However, welding from inside the pipe would require a different design of welding torch so as to equip the torch inside the pipes.

Gas tungsten arc welding (GTAW) has a major advantage in terms of producing cleaner weld compared to other arc welding processes and with adequate heat required to weld even without a filler material [5]. Other advantages are precise control of heat during welding, high-quality welds and minimal residues [6]. Study of Devakumar et al. [7] revealed that GTAW is most suitable to weld thin sections of stainless steel metal which is the material of pipes on which IBW needs to be performed. Argon being a bit heavier than helium and requiring less flow rates is better option for GTAW [8]. US3350537A [9] designed an internal stub tube welding apparatus with extendable arm and electrode holder parallel to the axis of rotation.

As shown in Fig. 11.1, there are numerous pipes that need to be welded with the dish end of high-voltage bushing present at ITER, Institute for Plasma Research, India. Hence, a specific apparatus must be made that undertakes GTAW at the interface of pipes and dish end. The design of this configuration-specific, internal bore welding torch has to be done by taking into consideration the several weld parameters required for welding. In this paper, the design of IBW torch for carrying out welding in stainless steel pipes with diameter as small as 25.4 mm having the provision of motion transfer and system stability is presented.
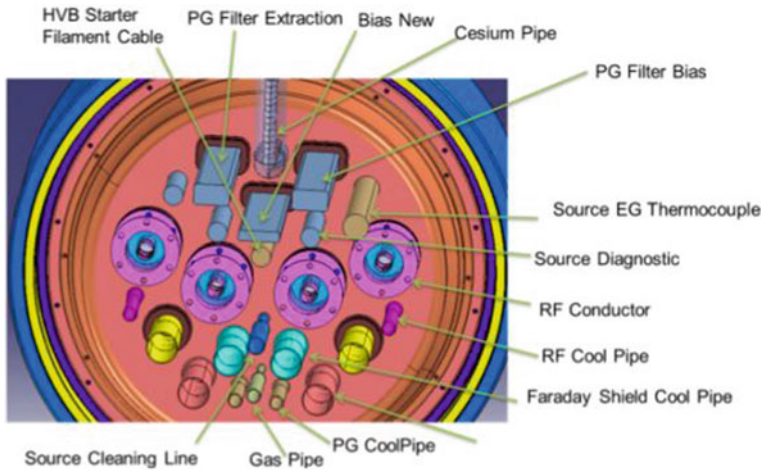
Fig. 11.1 Dish end of high-voltage bushing vessel

11.2 Welding Torch Requirements

300-mm-long stainless steel pipes with OD 25.4 mm and thickness 2.58 mm are supposed to be welded with other stainless steel pipes of similar dimension attached with dish end. Further, the weld current and argon gas flow rate were considered as 50–80 A and 11–15 cfh for IBW operation based on which the components are designed. Rotation shall be required for the welding torch to weld around the pipes. In addition to the rotation, translation is being required for welding along the pipe length at desired locations. Along with it, the basic necessities of shielding gas and electricity supply should be reached to the torch end for welding to take place.

11.2.1 Electric Current and Shielding Gas Supply

If the electric current cable and shielding gas tube are incorporated separately to the torch, different modes of supplies to welding torch tend to increase the size of the apparatus. Instead, fulfilling requirement of confining shield gas, electric supply and electrode holder into a single wand leads in reduced dimensions of welding torch assembly. Figure 11.2 shows the different components of welding torch end where copper rod is used to transfer the current to electrode, while space is provided between copper rod and insulation pipe to allow shielding gas flow, whereas nozzle is provided to concentrate the shielding gas to weld zone and fasteners to hold the electrode. The tungsten electrode is slotted into a groove made in copper rod and then tightened by bolt. The selection for dimensions for copper rod is done by taking into consideration the electric current requirement, and dimensions for insulation tube are

Fig. 11.2 Configuration of welding torch head
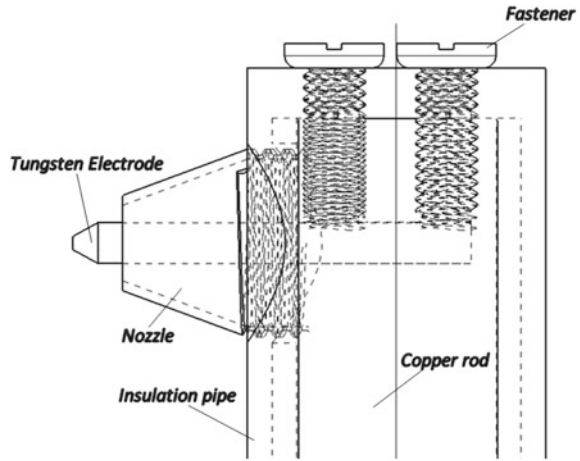
finalized to ensure sufficient flow rate of shielding gas. Due to high heat resistance property of ceramics and electrical isolation property [10], ceramic nozzle is used with threads to tighten the nozzle with insulating tube. Ceramic being potential insulator and demonstrating refractory property [10], material of insulating pipe surrounding copper rod was also considered as ceramic.

The electric supply to the copper rod and supply of shielding gas through the gap between copper rod and insulation tube need to be provided from the other end of this assembly which would be open.

11.3 Motion Transfer and System Stability

For welding of pipes, the torch end needs to have a complete rotation around the periphery of pipe to ensure proper bore welding. Hence, the assembly needs to be provided with rotational motion. The suitability of axial and non-axial rotational movements for the IBW torch is further discussed.

11.3.1 Axial Motion

The physical connection of IBW torch end to the motor for providing rotational motion is emphasized here. As shown in Fig. 11.3, ceramic tube is connected with motor with the help of flange. Electric current and shielding gas are supplied through two distinct cables before the flanged connection. During rotating of the welding torch assembly, both the wires twist around each other and are required to be reversed
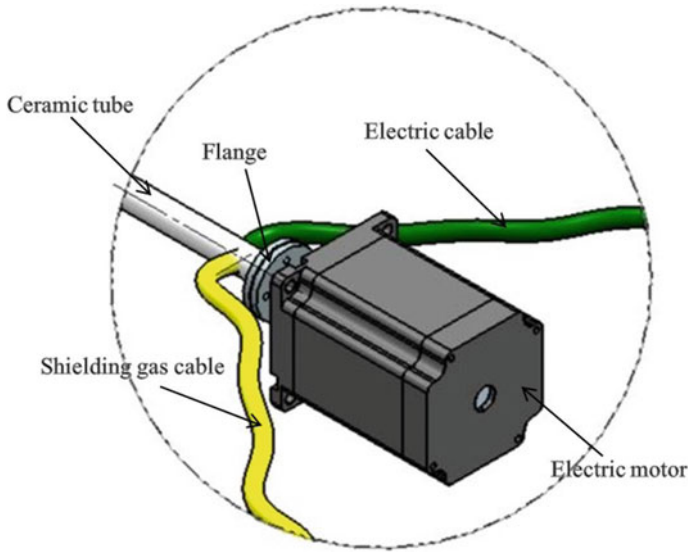
Fig. 11.3 Axial motion transfer through motor

after each rotation of IBW torch. To avoid this complexity, a non-axial connection to provide rotation was thus considered.

11.3.2 Non-axial Motion Transfer

Out of commonly used chain, belt and gear drives, motion transfer through gears consumes least space due to direct contact with each other and typically has very high efficiency [11]. Instead of directly providing electric and shielding gas connections, the connections are now provided through the gears. Figure 11.4 shows exploded view of two copper rods (long one would be attached with tungsten, and other one on the back side of gear for providing current supply) connected by the means of copper collet through threaded connection as depicted by Fig. 11.5.

The main copper rod is tightened with collet, while back end of rod is allowed to have lateral movement. This ensures that during rotation of gear required for welding operation, it would result in the movement of back side of copper only which is freely allowed to move in lateral direction. Hence, cable connection is provided on back copper to deprive twisting of cable as the back copper rod only moves laterally equivalent to the pitch of the collet and does not rotate unlike the copper rod of torch end that is tightened with collet. The collet must not be too thin as it would have low current carrying capacity, while too thick collet increases unnecessary overall dimensions; thus, the size of collet must be considered accordingly.

Fig. 11.4 Connection of
copper rods through gear
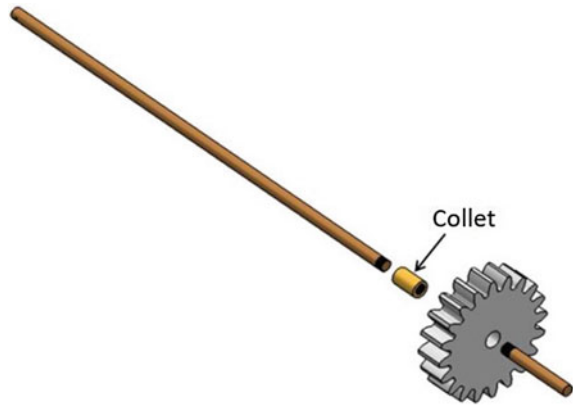
Fig. 11.5 Copper collet with
threads at both ends
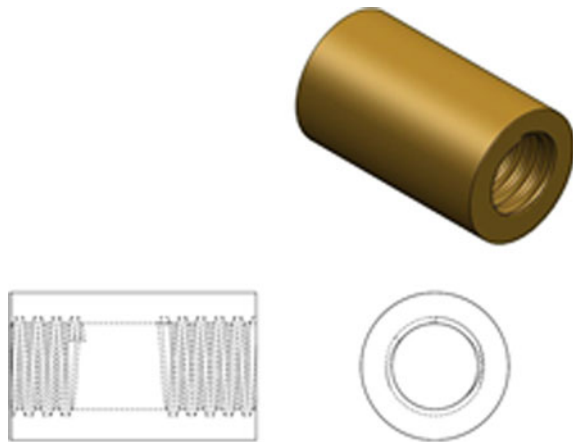
Similarly shielding gas supply is provided from the back end of the gear to resist
twisting of cable during welding operation. Shielding gas is transferred to the torch
end by providing deep holes in the gear to make passage for the shielding gas as
shown in Fig. 11.6.

A cup is attached with ceramic pipe to collect the shielding gases as shown in
Fig. 11.7. Therefore, the shielding gas that is supplied the stationary side of the gear
gets transferred to the torch end through the holes given for shield gas to pass.

An enclosure tube at back end is provided with two opening for electric current
cable and shielding gas cable. As shown in Fig. 11.8, a slot is also provided for
sliding key attached at end of copper rod to restrict copper rod to only single degree
of freedom (DOF) of translation. The tube enclosing shield gas is assembled in a
bearing whose inner ring is stationary and outer ring rotates with gear so that the
entire assembly at the back end of gear remains stationary, while gear and torch end
are having rotation.
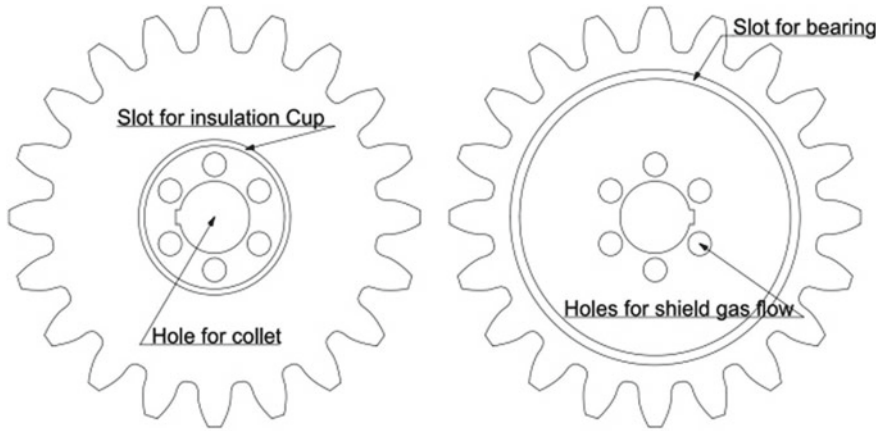
Fig. 11.6 Front and back view of driven gear with passage of shielding gas
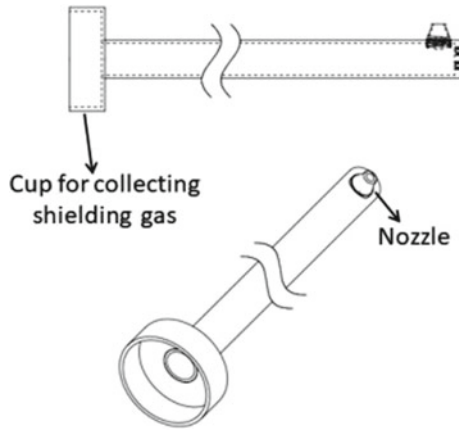
Fig. 11.7 Insulating tube of IBW torch attached with cup

As depicted in Fig. 11.10, the inner ring of bearing is mounted on the insulating tube, while the outer ring is attached with the sleeve which has interference fit with slot made on the gear for mounting of sleeve as shown in Fig. 11.9. A cap at the back of tube prevents leakage of shielding gas. This arrangement turns the welding torch with the rotation of gear allowing internal bore welding operation but holds the supply end stationary to allow static connections of electric cable and shielding gas (Fig. 11.11).

Herewith the issue of transferring the current and shielding gas to the torch end is now fulfilled with this setup. Now another gear of similar dimension is taken as driving gear so as the torque and angular velocity of driven gear are same as that provided by the motor. The welding velocity for the full penetration welding must

Fig. 11.8 Cup fitted into slot on gear to collect shield gas
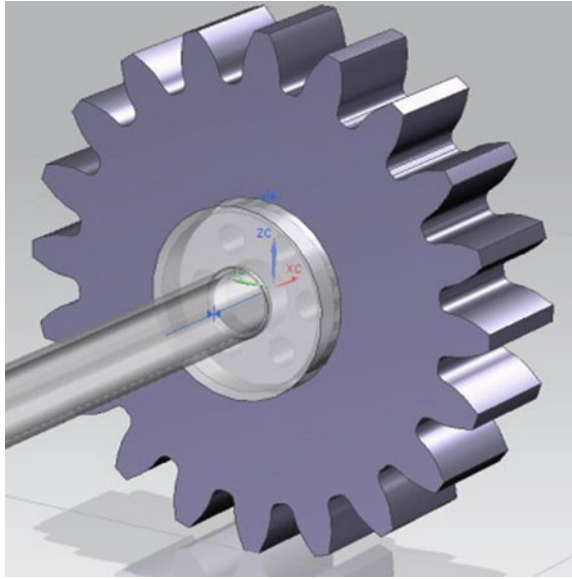
Fig. 11.9 Tube at back part of gear with slot at end face
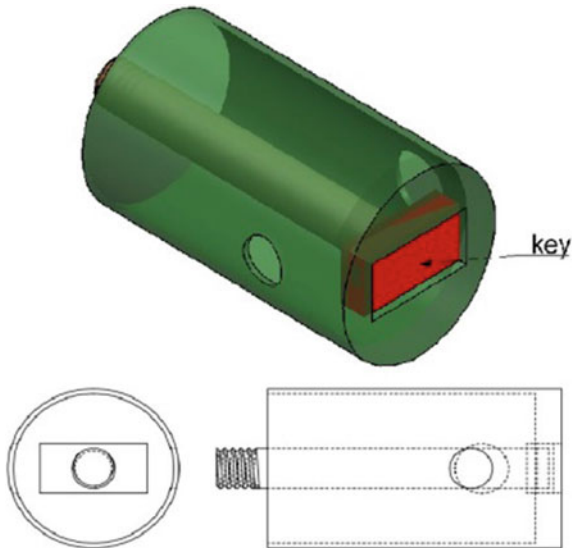
be determined first, and accordingly, the motor must be selected which can deliver such required speeds.

As the gears have motion, it is necessary to enclose them to prevent any harm to humans as well as gears from contaminants present in surrounding environment. The gearbox provides one such function but the requirement of a heavy gearbox which

Fig. 11.10 Assembly of stationary part of gear

Fig. 11.11 Exploded view of assembly components of welding torch
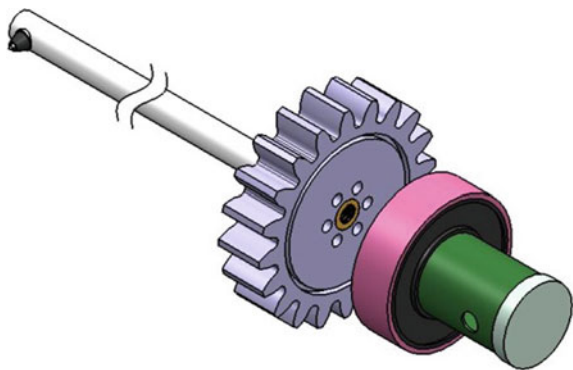
would unnecessarily increase the weight of the system. Instead, a well-supported closed enclosure will perform the function to protect the gears as shown in Fig. 11.12.

11.4 Linear Motion

After providing the rotational motion to the welding equipment, the next task is to provide the entire mechanism a horizontal translational motion. The objective of providing linear motion is to move the welding torch assembly into the pipe and perform the welding operation thereby. An automated linear motion is in contention because of the accuracy and ease offered in inserting the welding equipment effectively and precisely into the pipe at the weld location. The movement of the entire system could be precisely performed with the help of either hydraulics or pneumatics or electrical motors.

Pneumatic-based linear actuators consist of a piston inside a hollow cylinder which is operated by pressurizing air by compressor which makes the movement of the piston to and fro [12]. Force of the end point depends on the pressure supplied

Fig. 11.12 Gears enclosed
in a box
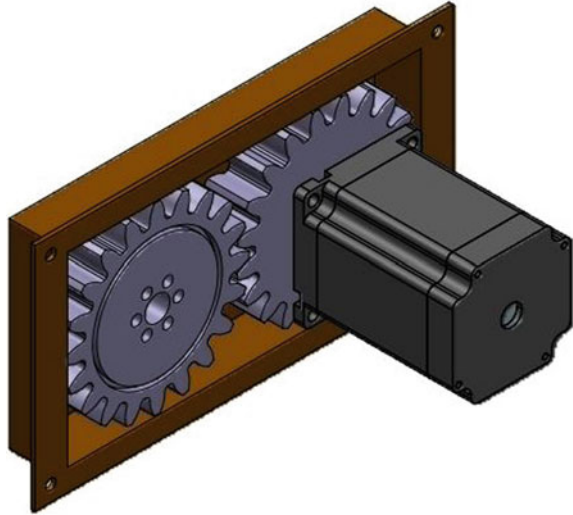
by external compressor. Piston is retractable by changing the direction of direction
control valve, and pressure is supplied in opposite direction to other side of the
piston. They hardly have any effect of magnetism as motors are absent and have
good accuracy.

Loss of pressure and property of compression of air decreases the efficiency as
compared to other linear motion methods [13]. A compressor has to run continuously
even if nothing is moving. If accurate control and efficiency are needed, then pro-
portional regulators and valves are inevitable, but this proliferate the cost and make
system complex. Pneumatic actuator must be made as per the size of the object as
well as the amount of linear shift given to the part.

Hydraulics-based linear actuators have a similar operation as pneumatic actuators,
but an incompressible liquid is used rather than pressurized air to move the cylinder
of actuator. Hydraulic actuators tend to work for very high-force applications. They
produce much higher forces than pneumatic cylinders of equal size. Hydraulic system
has high horsepower-to-weight ratio provided the ability to work with loads in metric
tonnes. In hydraulic system, actuators could be located at considerable distance away
from pump and motor, and connection through pipes is possible.

Hydraulics does also leak fluid which can lead to lower efficiency values [14].
Leakages of hydraulic oil also lead to cleanliness problems and can inflict damage
to surrounding components. A hydraulic system requires an actuator, pump, motor,
oil reservoir, valves and numerous pipes making the system typically complex and
costly [15]. It is generally suited for high load applications which beyond the scope
of electric or pneumatic actuators.

A servomotor is a rotary actuator or linear actuator that allows for precise control
of angular or linear position, velocity and acceleration [16]. The motor has pairing
with encoder in order to provide feedback of position and speed. The output position

Fig. 11.13 Motor assembled feed screw to provide linear motion to the slider
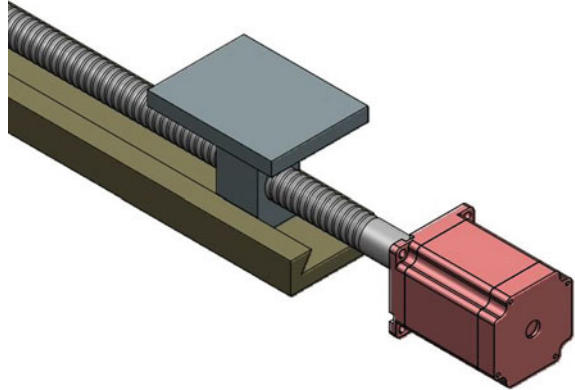
is compared with the required position. If the output position is different than required one, an error signal is generated which is responsible in rotating motor to bring the output shaft to the appropriate position. On approaching the required location, the error signal reduces to zero and the motor stops.

Electrical actuators provide the highest precision-control positioning. The setups are scalable for various purposes and force requirement while moving quietly, smoothly and repeatedly. Electric systems can be connected and reprogrammed easily, and immediate feedback for diagnostics and maintenance is possible.

Given the fact that the entire welding system is lightweight, the need of pneumatics or hydraulics is very little. Using hydraulics or pneumatics may also add the additional complexity, which could be otherwise avoided in the system. The best suitable option, therefore selected was an electric motor which provides translational motion due to feed screw-nut mechanism. This system will also have lower cost and maintenance issues.

As depicted by Fig. 11.13, a feed screw would be connected to a motor at one side that would provide a rotational motion. There would be a nut/collar connected to the entire assembly which would allow linear movement of the system. The feed screw will only rotate, but the assembly constrained to move only in one direction will move forward or backwards based on the rotational direction of the motor.

Support is provided to the box enclosing gears as shown in Fig. 11.14. Now as the enclosure containing entire assembly of IBW torch is rested on dovetail slider and being connected with lead screw, it would have a lateral DOF that could go to the pipe–dish end interface and perform welding operation and retract out of the pipe.

11.5   Apparatus Support

The torch end that would go inside the pipe and perform GTAW operation is quite long and requires a support such that it can have two DOFs. The support should be
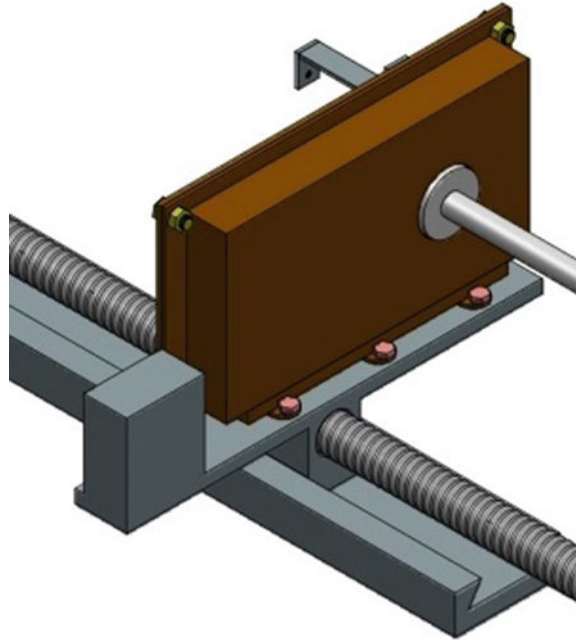
decided such as to allow the torch to rotate and also move to and fro. A bearing
or a slider put for support is not capable to permit both the motions. To fulfil such
requirement, caster wheels could be used which have two DOF. Caster wheels are
effectively used in moving heavy equipment or robotics to ensure dual movement
from a single joint. US1440641A [17] invented a spherical caster that could rotate
in two axes. Three such casters are arranged at 120 degrees to facilitate two motions
of insulating tube as shown in Fig. 11.15.

As depicted in Fig. 11.15, the caster wheels are attached with stationary structure
with two caster wheels being fixed and one retractable with the help of screw joint
provided at the top. This helps in easily removing the ceramic tube by losing the grip
of one caster wheel and then extracting the ceramic tube horizontally.

This assembly is fully capable of going inside the pipe, welding the pipe–dish
end interface and coming back to the original position (Fig. 11.16). However, to
weld multiple pipes on the dish end as shown in Fig. 11.1, this assembly needs to
have movement in both the directions perpendicular to the lateral motion provided
by the slider (Fig. 11.17). Hence, a specific base has to be built that could provide
movement in other two directions.

For the sideways movement of this assembly, a similar concept of feed screw and
sliders is used. As per the weight of the bed and other requirements, an M-V slider is
used to facilitate easy slide with very less coefficient of friction. To enhance stability,
two M-V sliders are used at the ends of the IBW torch bed as shown in Fig. 11.18.
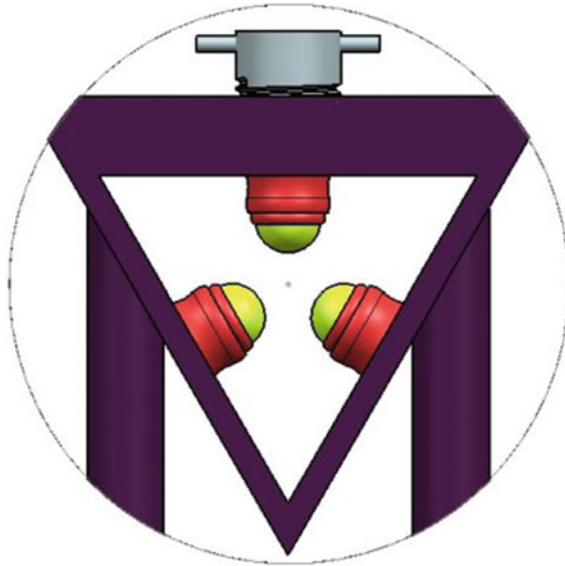
Fig. 11.15 Caster wheels for support of ceramic tube
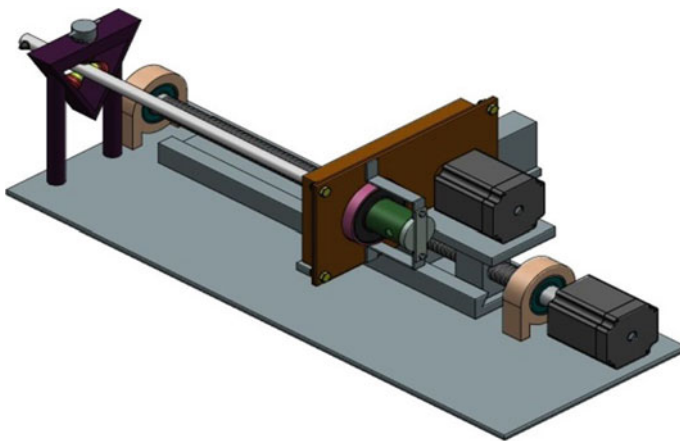
Fig. 11.16 Entire internal bore welding torch assembly bed

Moreover, the threaded hole is provided under the bed itself, through which the feed screw will pass, so as to move the entire bed when the screw is rotated.

Figure 11.19 demonstrates the entire mechanism for the sideways movement of the IBW torch base. The feed screw is controlled manually in this system; however, precision stepper or servo could also be used.
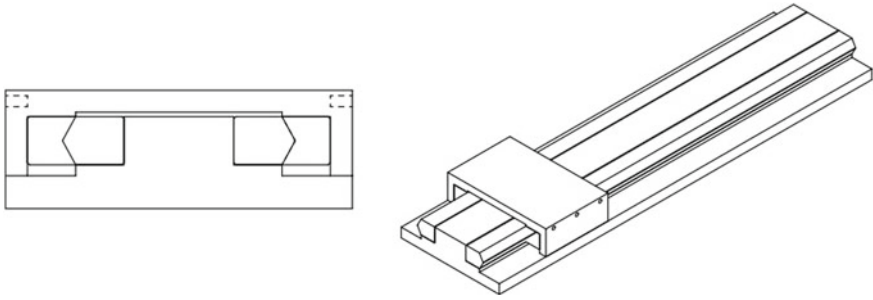
Fig. 11.17 Model of a M-V slider
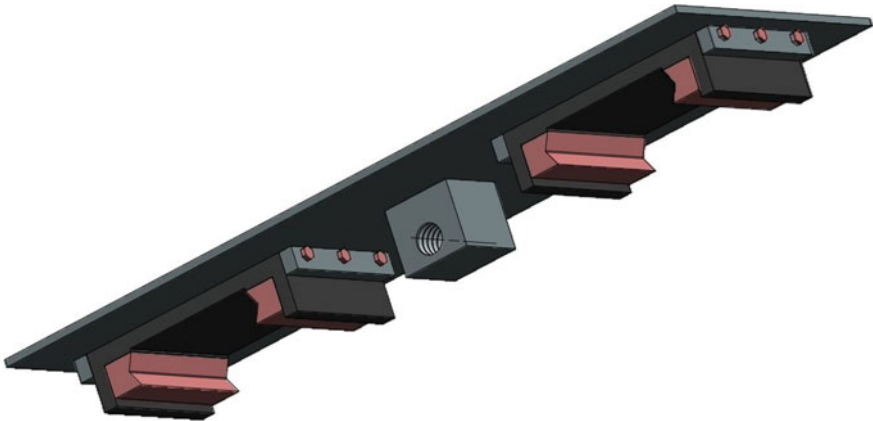
Fig. 11.18 Isometric view of base of welding torch assembly with M slides
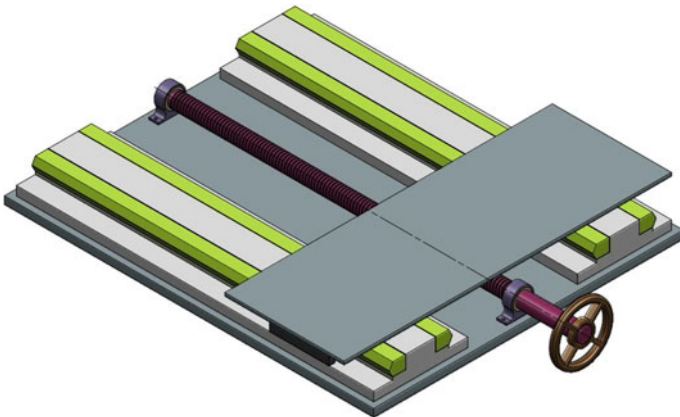
Fig. 11.19 System for providing sideways movement of welding torch assembly

Fig. 11.20 Screw jack for providing vertical lifting of welding torch assembly

The entire assembly must be moved in vertical direction to cover all the welding locations on the dish head. For the same, a screw jack similar to that used in jacks which is used to lift cars and other vehicles is considered here as shown in Fig. 11.20.

The calculation of height achieved by screw jack per rotation of handle is nonlinear, and hence, to understand the relation between distances of screws and height achieved in jack, understanding the geometric layout is of paramount importance (Fig. 11.21).

To measure height $h1$ for the known link length $l1$ and at different locations, Pythagoras theorem can be used (Table 11.1) [18].

$$l_1^2 = w_1^2 + h_1^2 \tag{11.1}$$

$$h_1^2 = l_1^2 - w_1^2 \tag{11.2}$$

Two Important observations from the table

- The increase in height per the revolution of the lead screw is non-uniform.
- It is evident that as the distance between the centre and the nut decreases (nut coming closer to the centre), the movement in vertical direction becomes finer, i.e. the upsurge in height with entire revolution of screw is constantly decreasing.

Hence, due to lack of proper measurements regarding the height increased or decreased, it is not feasible to use similar screw jack for up and down motion.

A jacking system has more than one screw jack operating simultaneously for achieving linear movement. The support comes in the form of four worm gear screw jacks at four corners of the bed. A worm gear screw jack comprises a worm gear (driver) and a worm wheel (driven), wherein the lead screw on which the assembly
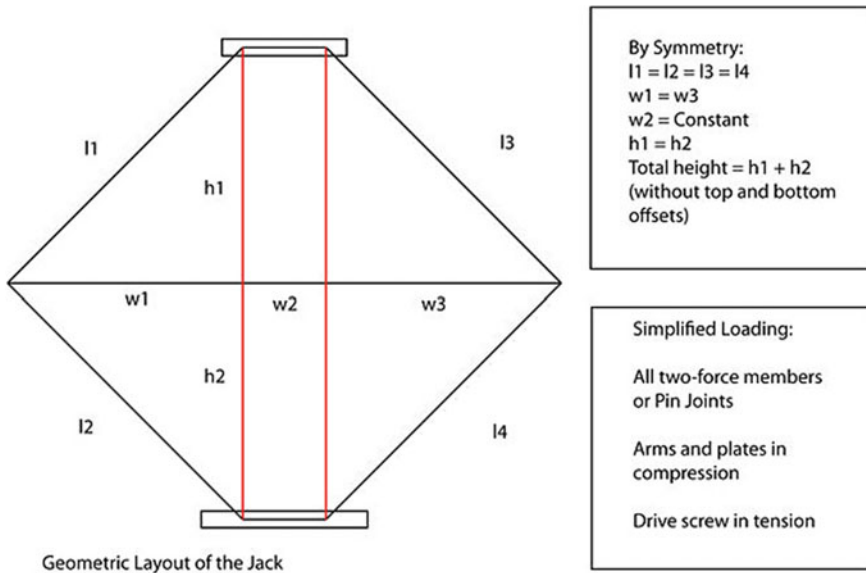
Fig. 11.21 Geometric representation of screw jack

is to be mounted is attached with worm wheel. The synchronization of all the worm gears is of paramount importance in order to maintain stability in the system.

As depicted in Fig. 11.22, the two shafts driving the system are connected with spindles on one end. These spindles are then connected with other spindle attached with a manually driven wheel through a chain, i.e. a chain sprocket mechanism to drive the shafts. The upward or downward movement of the nut on screw jack depends on the rotation of the worm shaft, and hence, the gear ratio for chain sprocket is considered as 1 (both sprockets of equal dimensions) so that the vertical movement of screw jack and with that the entire welding torch assembly, directly depends on the rotation of handle (Fig. 11.23).

11.6 Discussion and Conclusion

This paper presented a customized internal bore welding torch design to facilitate pipe to pipe and flange to pipe welding. The welding torch has tendency to weld typically long pipes with bore diameters as small as 1 inch because of its configuration. Internal bore welding operation could be performed without twisting of electric and shield gas cables by altering axis of rotational motion of welding torch. The assembly arranged on flat bed could be mounted on planar surfaces and multiple angles to assist internal welding at complex places.

Table 11.1 Height values of screw jack calculated for different positions (all dimension in mm)

Link length	Distance between two pins	Distance from centre		Total height	Height with respect to reference	Height difference	Change in height per 1 revolution of handle
l	w_2	$w_1 + (w_2/2)$	w_1	$(h_1 + h_2)$	Total height − initial value	$h_{i+1} - h_i$	Δh/revolution
200	20	190	180	174.3559	0	0	
200	20	180	170	210.7130	36.35711	36.35711	18.17855
200	20	170	160	240	65.64404	29.28692	14.64346
200	20	160	150	264.5751	90.21917	24.57513	12.28756
200	20	150	140	285.6571	111.3011	21.08200	10.54100
200	20	140	130	303.9736	129.6171	18.31654	9.158272
200	20	130	120	320	145.6441	16.02631	8.013158
200	20	120	110	334.0658	159.7099	14.06586	7.032930
200	20	110	100	346.4101	172.0542	12.34429	6.172149
200	20	100	90	357.2114	182.855	10.80126	5.400630
200	20	90	80	366.6060	192.2500	9.394633	4.697316
200	20	80	70	374.6998	200.3439	8.093824	4.046912
200	20	70	60	381.5756	207.2197	6.875800	3.437900
200	20	60	50	387.2983	212.9423	5.722654	2.861327
200	20	50	40	391.9183	217.5624	4.620024	2.310012
200	20	40	30	395.4743	221.1184	3.556039	1.77801
200	20	30	20	397.9949	223.6390	2.520576	1.260288
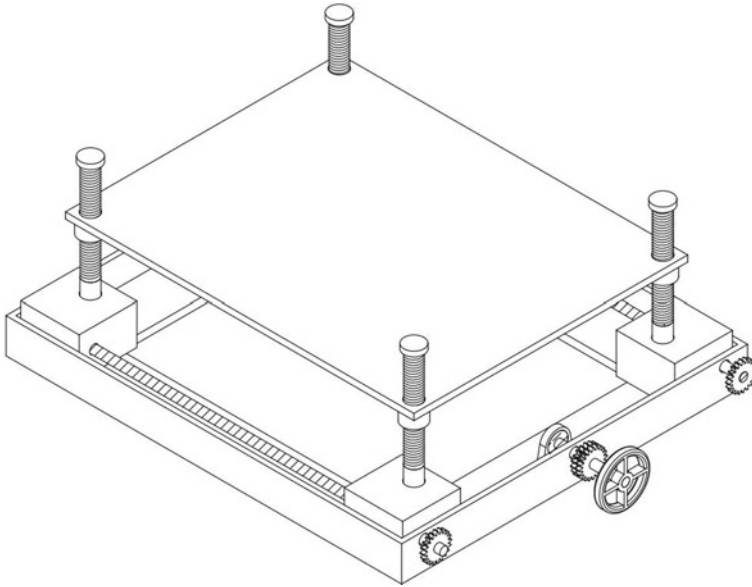
Fig. 11.22 Manually operated worm gear-based jacking system
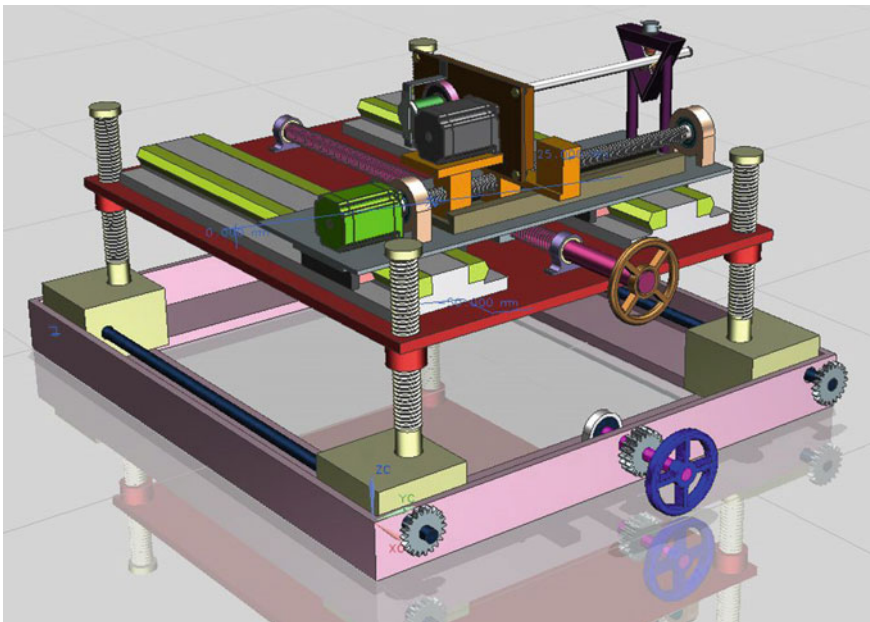
Fig. 11.23 Entire assembly of IBW torch capable to do welding at any location of dish end

References

1. Ryuh, B.S., Pennock, G.R.: Arc welding robot automation systems. In: Industrial Robotics: Programming, Simulation and Applications. IntechOpen, 1 Dec 2006
2. Kah, P., Shrestha, M., Hiltunen, E., Martikainen, J.: Robotic arc welding sensors and programming in industrial applications. Int. J. Mech. Mater. Eng. **10**(1), 13 (2015)
3. Joshi, O., Arunkumar, D.: Design and Analysis of Welding Fixture For Orbital Welding Machine. 2015 On IJPME, 3
4. Pires, J.N., Loureiro, A., Bölmsjo, G.: Welding Robots: Technology, System Issues and Application. Springer Science & Business Media, 21 May 2006
5. Anand, A., Khajuria, A.: Welding processes in marine application: a review. Int. J. Mech. Eng. Robot. Res. **2**(1), 215–225 (2015)
6. Sarolkar, A., Kolhe, K.: A Review of (GTAW) Gas Tungsten Arc Welding and its Parameters for Joining Aluminium Alloy. IJSART **3**(8) (2017)
7. Devakumar, D., Jabaraj, D.B.: Research on gas tungsten arc welding of stainless steel—an overview. Int. J. Sci. Eng. Res. **5**(1), 1612 (2014)
8. Kumar, R., Bharathi, S.: A review study on A-TIG welding of 316 (L) austenitic stainless steel. Int. J. Emerg. Trends Sci. Technol. **2**, 2066–2072 (2015)
9. Charles, L.A., William, G.R.: Inventors; Foster Wheeler Corp, assignee. Internal Stub Tube Welding Apparatus. United States patent US 3,350,537, 31 Oct 1967
10. Jeyaprakash, N., Haile, A., Arunprasath, M.: The parameters and equipments used in TIG welding: a review. Int. J. Eng. Sci. (IJES) **4**(2), 11–20 (2015)
11. Martin, K.F.: The efficiency of involute spur gears. J. Mech. Des. **103**(1), 160–169 (1981)
12. Beater, P.: Pneumatic Drives. Springer, Heidelberg (2007)
13. Oshita, M., Ozawa, M., Hattori, M.: Inventors; Aisin Seiki Co Ltd, assignee. Compressed Air Control Apparatus. United States patent US 5,600,953, 11 Feb 1997
14. Goharrizi, A.Y., Sepehri, N.: Internal leakage detection in hydraulic actuators using empirical mode decomposition and Hilbert spectrum. IEEE Trans. Instrumentation Measurement **61**(2), 368–378 (2011)
15. Bihlmaier, J.A.: Inventor; Bihlmaier John A, assignee. Pneumatic-Hydraulic Actuator System. United States patent US 4,335,867, 22 June 1982
16. Firoozian, R.: Servo Motors and Industrial Control Theory. Springer, Chicago (2014)
17. Sidney, S.: Inventor. Spherical Ball-Bearing Caster. United States patent US 1,440,641, 2 Jan 1923
18. Maor, E.: The Pythagorean Theorem: A 4,000-Year History. Princeton University Press, 19 Nov 2019

Chapter 12
Effect of Tool Rotation on Metal Removal Rate During Electro-Discharge Machining of Hastelloy C-276

Check for updates

Nikhil Jain, Jinesh Kumar Jain, and Bhuvnesh Bhardwaj

Abstract In the present work, two-level full factorial design with Box-Cox transformation has been used to investigate the impact of EDM conditions on metal removal rate during the machining of Hastalloy C-276. The pulse on time, gap voltage, peak current and tool motion has been considered as EDM conditions. It has been revealed that pulse on time is the main influencing EDM condition affecting the metal removal rate. The metal removal rate increases with increase in pulse on time, peak current and with tool rotation but decreases with increase in gap voltage.

Keywords Hastelloy C-276 · EDM · Tool motion · Metal removal rate

12.1 Introduction

In the present era, materials such as die steel, new alloys, superalloys, ceramics and metal matrix composite are extensively employed in different industries such as automotive, aerospace, surgical, die molding [1]. The machining of these materials is very difficult using conventional machining due to high hardness, wear resistance and toughness. These materials can be easily machined using electrical discharge machining (EDM). During the EDM, the molten metal from the surface of workpiece and tool electrode evaporates rapidly. Flushing the eroded material from the machining gap is the major problem during the EDM machining [2]. Due to these reasons, in the past, lot of researches have been carried out to improve flushing in EDM. Wang and Yan [3] investigated the effect of EDM conditions on MRR, surface

N. Jain (✉) · B. Bhardwaj
Department of Mechanical Engineering, Jaipur Engineering College and Research Centre, Jaipur 302022, India
e-mail: 2019rme9056@mnit.ac.in

J. K. Jain
Department of Mechanical Engineering, Malaviya National Institute of Technology, Jaipur 302017, India
e-mail: jineshjain.mech@mnit.ac.in

roughness and tool wear during the machining of Al_2O_3/6061Al composite material. Guu and Hocheng [4] examined the impact of tool rotation on MRR during the EDM machining. Mohan et al. [5] examined the effect of EDM conditions on electrode wear, surface roughness and MRR during the electrode discharge machining of SiCp/6025 composite. Mahapatra and Patnaik [6] used Taguchi methodology to optimize EDM conditions for maximum MRR and minimum SR. Chattopadhyay et al. [7] examined the effect of intensity of induced magnetic field on MRR and electrode wear during the EDM machining of EN-8 steel with rotating tool electrode. Lin and Lee [8] investigated the impact of magnetic field on MRR and SR during the EDM machining. Singh et al. [9] studied the impact of EDM conditions on MRR and electrode wear during the EDM machining of die steel.

The Hastelloy C-276 is a nickel–molybdenum–chromium grade which is widely used by the chemical processing industries. It has excellent stress corrosion cracking resistance with very good resistance to localized attack. The literature reveals that very few efforts have been made to investigate the effect of EDM conditions on metal removal rate during the machining of this material. Accordingly, the main objective of the present work is to examine the effect of EDM conditions on metal removal rate during the machining of Hastelloy C-276. An attempt has also been made to develop MRR prediction model using two-level full factorial design with Box-Cox transformation.

12.2   Machining Condition and Design Matrix

The pulse on time, peak current, gap voltage and tool motion (stationary and rotating) have been selected as EDM conditions. In this analysis, the pulse on time, peak current, gap voltage have been considered as numerical machining conditions, while tool motion has been considered as category machining condition. The speed of rotating tool has been kept constant at 1000 RPM. Table 12.1 shows the selected EDM conditions and various levels of EDM machining conditions according to selected approach, i.e., two-level full factorial design. Table 12.2 shows the design matrix for experimentation.

Table 12.1 EDM conditions and level of condition

Name	Units	Type	Minimum	Maximum	Mean
Pulse on time	Micro sec	Numeric	4	20	12
Gap voltage	V	Numeric	10	40	25
Peak current	A	Numeric	2	12	7
Tool motion		Categoric	Stationary	Rotating	

Table 12.2 Design matrix and measured value of MRR

Std.	A: Pulse on time (Micro sec)	B: Gap voltage (V)	C: Peak current (A)	D: Tool motion	MRR (mg/min)
1	4	10	2	Stationary	13.042
2	20	10	2	Stationary	38.651
3	4	40	2	Stationary	11.519
4	20	40	2	Stationary	30.559
5	4	10	12	Stationary	28.560
6	20	10	12	Stationary	51.122
7	4	40	12	Stationary	19.230
8	20	40	12	Stationary	32.844
9	4	10	2	Rotating	15.673
10	20	10	2	Rotating	46.446
11	4	40	2	Rotating	15.415
12	20	40	2	Rotating	40.895
13	4	10	12	Rotating	37.724
14	20	10	12	Rotating	67.526
15	4	40	12	Rotating	25.771
16	20	40	12	Rotating	44.014
17	12	25	7	Stationary	29.798
18	12	25	7	Rotating	34.355
19	12	25	7	Stationary	27.700
20	12	25	7	Rotating	37.380
21	12	25	7	Stationary	30.202
22	12	25	7	Rotating	36.239
23	12	25	7	Stationary	28.846
24	12	25	7	Rotating	34.193

12.3   Materials and Methods

12.3.1   Experimentation

To achieve the objective of the present research work, all the experiments have been conducted on Hastalloy C-276 plate of dimension 80 mm × 50 mm × 10 mm using EDM die sinking machine (Model C-425), manufactured by Electronica Industries, India. The rotation of tool is given by rotating head through special arrangement. The copper tool having diameter 10 mm, thermal conductivity 412 W/mk and density 9.12 g/cc has been used for all experimentation. To avoid the error during experimentation, turning and facing operation followed by the polishing have been carried

out on the copper tool. The kerosene has been taken as dielectric fluid. The tool electrode is kept at negative polarity, and workpiece is kept at positive polarity for the machining. Table 12.3 shows the chemical composition of Hastalloy C-276.

12.3.2 Measurement

The metal removal rate has been calculated using Eq. (12.1).

$$MRR = \frac{W_i - W_f}{T} \tag{12.1}$$

where W_i is the initial weight, W_f is the final weight and T is the machining time. The measured value of MRR is shown in Table 12.2.

12.4 Results and Discussion

The measured values of MRR along with the design matrix have been fed into the design expert 8.0.4.1 software for the formulation of MRR model and to examine the impact of EDM conditions on MRR.

12.4.1 Development of Prediction Model

The first step for the formulation of models is ANOVA analysis. The ANOVA is based on two assumptions, (i) normal distribution of data and (ii) constant variance [10].

To diagnosis the first assumption of ANOVA, the normal probability plot of residuals for MRR is shown in Fig. 12.1. The plot indicates whether the residuals follow the normal distribution or not. If the residuals follow normal distribution, most of the points should fall on the straight line. From the figures, it has been revealed that some of the residuals are lying outside the straight line; thus, residuals are not completely normally distributed. Therefore, to make the data more normally distributed, some transformation is required.

The Box-Cox transformation is a family of transformations that is used to make data normally distributed by identifying suitable exponent (λ). This transformation simultaneously increases the normality and homogeneity of the data. Figure 12.2 shows the Box-Cox plot for MRR. In this figure, the blue line shows the present value of "λ", while green line indicates the best recommended value of "λ" for transformation. In Fig. 12.3, the present value of "λ" is "1", but the recommended value of "λ" is 0.31. Thus, power transformation is needed to make the data normally

Table 12.3 Chemical composition of Hastalloy C-276

C	Co	Cr	Mo	V	W	Fe	Mn	Si	Ni
0.02	2.5	14.6	16.3	0.35	3.78	6.4	1	0.05	55
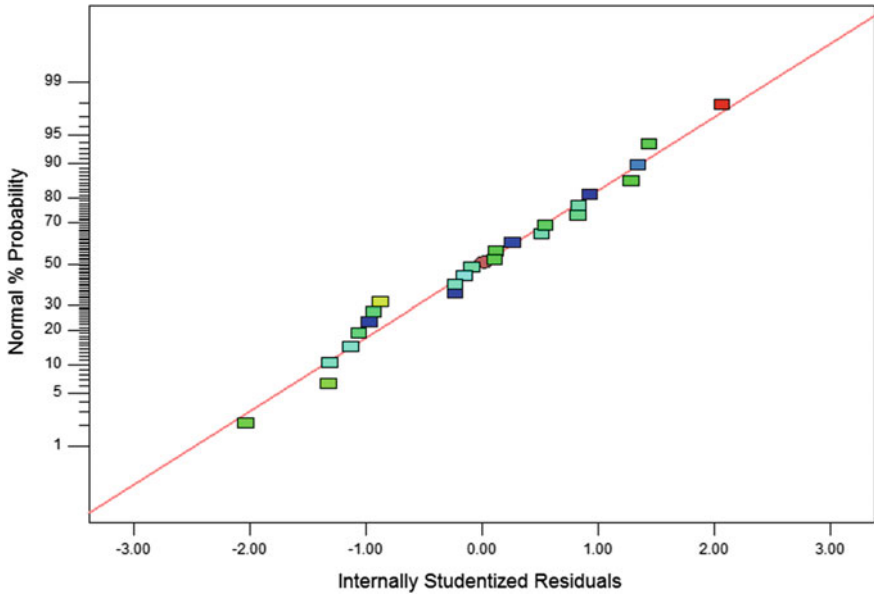
Fig. 12.1 Normal probability plot of residuals for MRR
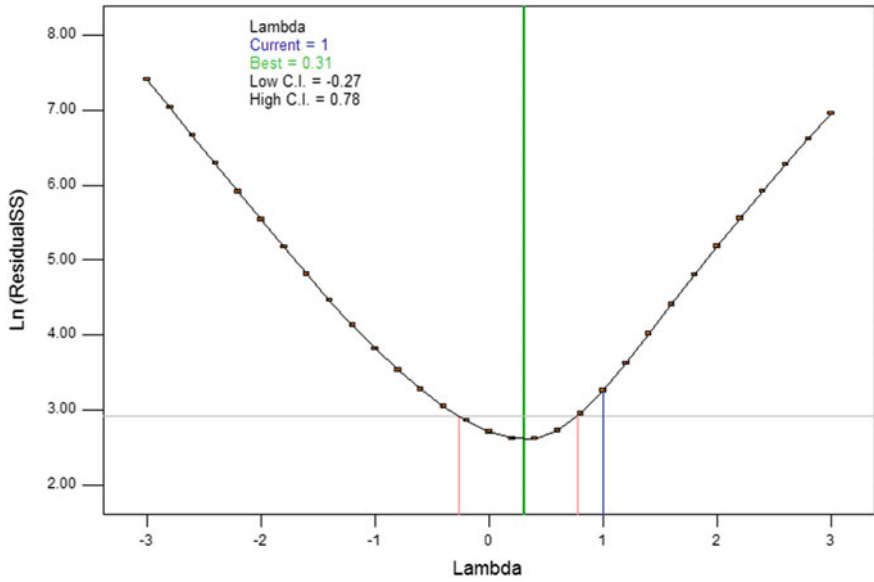
Fig. 12.2 Box-Cox plot of MRR
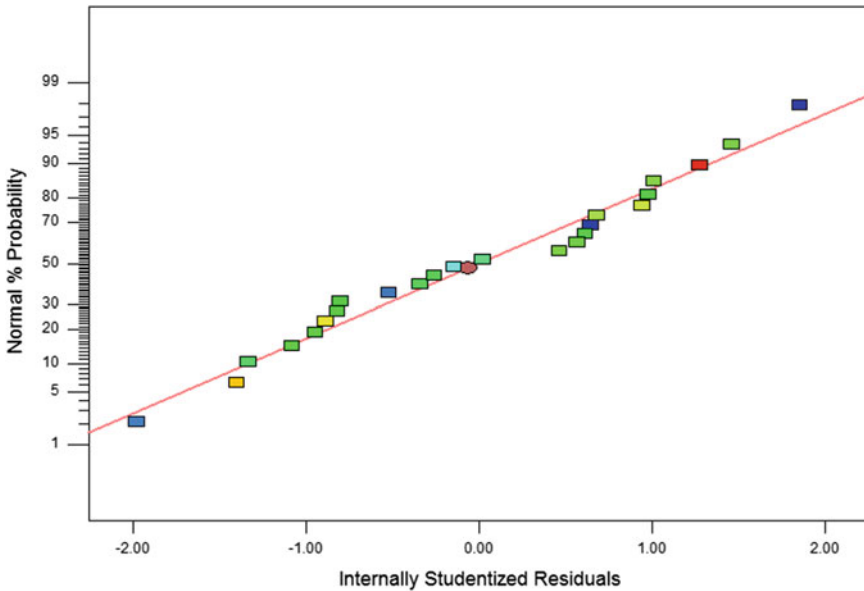
Fig. 12.3 Normal distribution plot after the transformation for the MRR

distributed. Figure 12.3 shows the normal distribution plot after the transformation for the MRR. The figures display that the mostly residuals are falling on a straight line; therefore, now data is normally distributed.

The residuals versus the predicted response plot for MRR are shown in Fig. 12.4. For assumption of constant variance to be true, the plot should be a random scatter. Figure 12.4 reveals no specific pattern and indicates that data is following assumption variance.

Table 12.4 shows the ANOVA table after Box-Cox transformation for MRR. The ANOVA analysis has been conducted at significance level 0.05. Table 12.4 indicates that "Prob. $> F$" for MRR model is 0.001 which is less than 0.05, which indicates that MRR model is significant. In the same way, "Prob. $> F$" for pulse on time, gap voltage, peak current, tool motion and two-level interaction of pulse on time and voltage, pulse on time and peak current, gap voltage and peak current are less than 0.05; therefore, these are significant model terms. The value of "Prob. $> F$" for lack of fit is 0.1073 and indicates that the lack of fit is insignificant. The ordinary R^2 value, which is the measure of the amount of variation around the mean, is equal to 0.985. The adjusted R^2 is equal to 0.979. The result shows that the adjusted R^2 value is very close to the ordinary R^2 value.

The final prediction models for MRR in terms of coded machining conditions are represented in Eq. (12.2). The prediction models in terms of actual machining conditions for MRR are given in Eqs. (12.3) and (12.4),
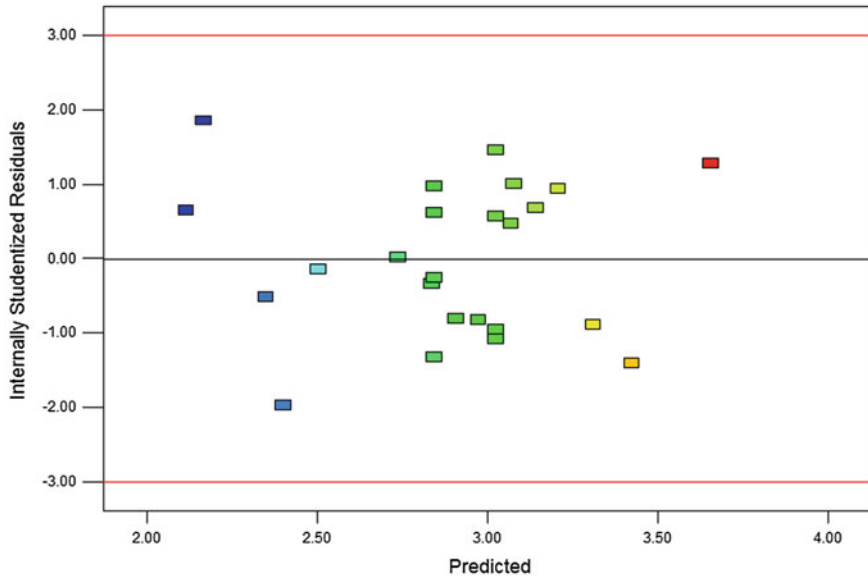
Fig. 12.4 Residuals versus the predicted response plot for MRR

Table 12.4 ANOVA table after Box-Cox transformation for MRR

Source	Sum of squares	Degree of freedom	Mean square	F-value	p-value Prob > F
Model	3.170	7	0.453	151.531	<0.0001
A-Pulse on time	1.904	1	1.904	637.155	<0.0001
B-Gap voltage	0.251	1	0.251	83.908	<0.0001
C-Peak current	0.540	1	0.540	180.552	<0.0001
D-Tool motion	0.279	1	0.279	93.275	<0.0001
AB	0.014	1	0.014	4.670	0.0462
AC	0.104	1	0.104	34.872	<0.0001
BC	0.079	1	0.079	26.287	0.0001
Residual	0.048	16	0.003		
Lack of fit	0.039	10	0.004	2.835	0.1073
Pure error	0.008	6	0.001		
Cor total	3.218	23			
Std. dev.	0.055		R-Squared		0.985
Mean	2.89		Adj R-Squared		0.979
C.V. %	1.89		Pred R-Squared		0.968
PRESS	0.10		Adeq Precision		48.259

$$MRR = +32.40 + 11.57 * A - 4.91 * B + 5.91 * C$$
$$+ 3.90 * D - 2.02 * A * B - 1.04 * A * C$$
$$+ 1.47 * A * D - 2.98 * B * C + 1.16 * C * D \qquad (12.2)$$

For MRR (in actual form)

(1) For stationary tool

$$(MRR)^{0.31} = +1.80913 + 0.063399 * \text{Pulse on time}$$
$$+ 1.14731E - 003 * \text{Gap voltage} + 0.084298 * \text{Peak Current}$$
$$- 2.46117E - 004 * \text{Pulse on time} * \text{Gap voltage}$$
$$- 2.01767E - 003 * \text{Pulse on time} * \text{Peak Current}$$
$$- 9.34292E - 004 * \text{Gap voltage} * \text{Peak Current} \qquad (12.3)$$

(2) For rotating tool

$$(MRR)^{0.31} = +2.02468 + 0.063399 * \text{Pulse on time}$$
$$+ 1.14731E - 003 * \text{Gap voltage}$$
$$+ 0.084298 * \text{Peak Current} - 2.46117E - 004 * \text{Pulse on time}$$
$$* \text{Gap voltage} - 2.01767E - 003 * \text{Pulse on time} * \text{Peak Current}$$
$$- 9.34292E - 004 * \text{Gap voltage} * \text{Peak Current} \qquad (12.4)$$

12.4.2 Effect of EDM Conditions on MRR

In order to examine the impact of EDM conditions on MRR, different plots between EDM conditions and responses have been plotted using prediction models.

12.4.2.1 Impact of EDM Conditions on MRR

Figures 12.5, 12.6, 12.7 and 12.8 show the 3D plot for MRR. Figure 12.5 shows the impact of pulse on time and gap voltage on MRR without tool rotation, while Fig. 12.6 shows the impact of pulse on time and gap voltage on MRR with rotating tool. From both plots, it has been revealed that MRR increases with increase in pulse on time. This upward trend may be attributed due to increase in discharge energy per unit time with increase in pulse on time [11]. On the other hand, inverse effect of gap voltage on MRR has been found. It is due to decrease in sparking frequency with
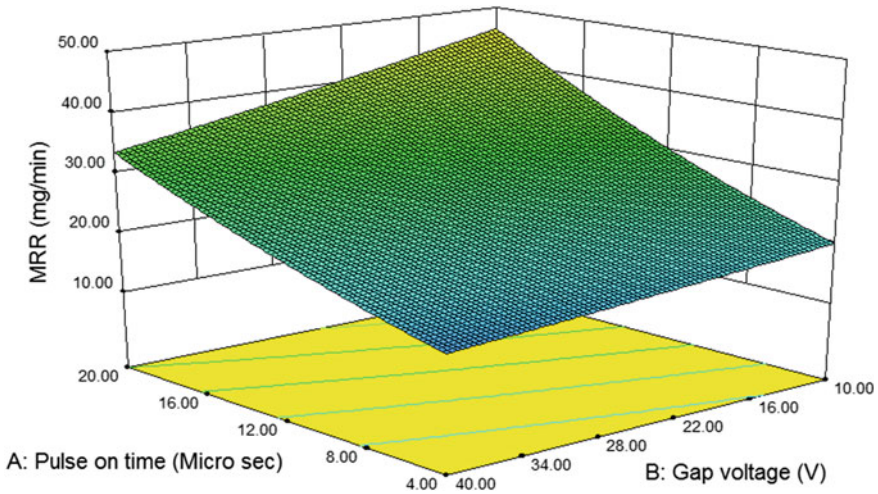
Fig. 12.5 Effect of pulse on time and gap voltage on MRR without tool rotation
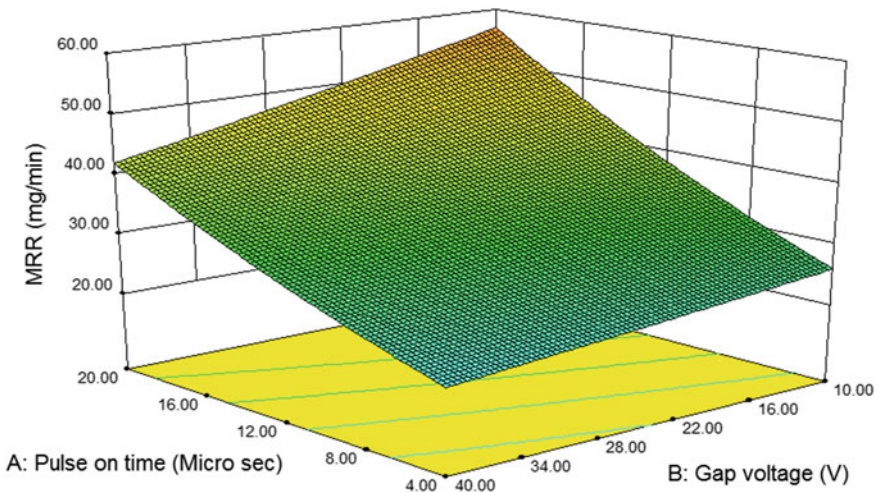
Fig. 12.6 Effect of pulse on time and gap voltage and MRR with tool rotation

increase in gap voltage, and the net outcome is the fall in MRR [12]. The impact of pulse on time and peak current on MRR without tool rotation is shown in Fig. 12.7, while Fig. 12.8 shows the impact of pulse on time and peak current on MRR with rotating tool.

It has been revealed from the Figs. 12.8 and 12.9 that MRR increases with increase in peak current. This upward trend may be attributed due to generation of strong discharge energy at high peak current. The spark with high discharge energy strikes
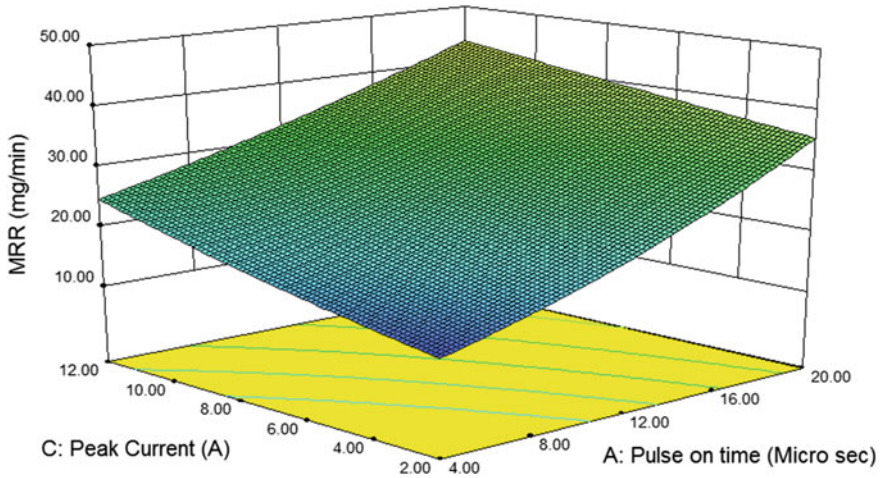
Fig. 12.7 Effect of peak current and pulse on time on MRR without tool rotation
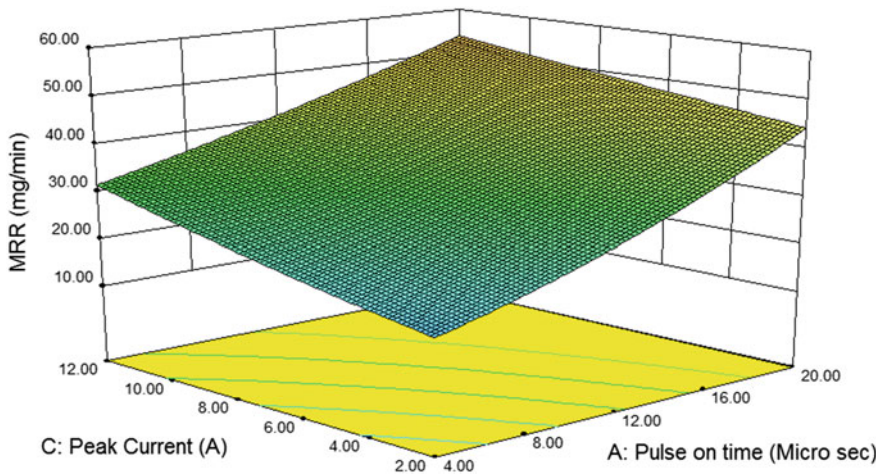
Fig. 12.8 Effect of peak current and pulse on time on MRR with tool rotation

the surface of the material and produces large size of craters on the surface of material and removes the large amount of material [12].

Figure 12.9 shows the impact of tool rotation on MRR. It is clear from the plot that high MRR is achieved with rotating tool as compared to stationary tool for all values of other EDM conditions. It is due to generation of centrifugal force with tool rotation. This centrifugal force frequently cleans the debris from the melt pool, which increases the intensity of discharge energy that increases the melting of more material in the vicinity of the spark and hence increases the MRR [13].
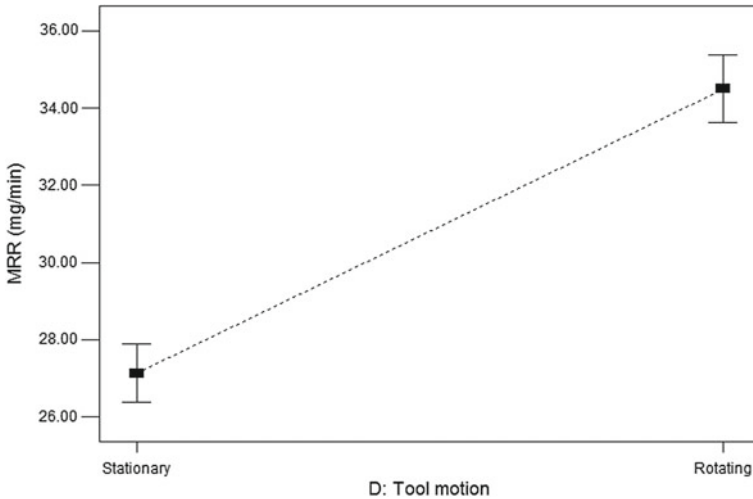
Fig. 12.9 Effect of tool rotation on MRR

12.5   Conclusion

In this paper, two-level full factorial design with Box-Cox transformation has been employed to examine the effect of EDM conditions on MRR during the machining of Hastelloy C-276. The pulse on time, gap voltage, peak current and tool motion have been considered as EDM conditions. The experimental result has led to the following conclusions.

- The pulse on time, gap voltage, peak current and tool motion have been found significant model terms for MRR.
- For MRR, pulse on time has been found most significant EDM condition followed by peak current, tool motion and gap voltage.
- The coefficient of determination (R^2) for MRR has been found to be 0.985 which shows the excellent prediction ability of develop model.
- The results show that MRR increased with increasing the pulse on time, peak current and with tool rotation but decreased with increasing the gap voltage.

References

1. Teimouri, R., Baseri, H.: Study of tool wear and overcut in EDM process with rotary tool and magnetic field. In: Advances in Tribology, pp. 1–8 (2012)
2. Aliakbari, E., Baseri, H.: Optimization of machining parameters in rotary EDM process by using the Taguchi method. Int. J. Adv. Manuf. Technol. **62**, 1041–1053 (2012)
3. Wang, C.C., Yan, B.H.: Blind hole drilling of Al_2O_3/6061Al composite using rotary electro-discharge machining. J. Mater. Process. Technol. **102**, 90–102 (2000)

4. Guu, Y.H., Hocheng, H.: Effects of workpiece rotation on machinability during electric discharge machining. J. Mater. Manuf. Process. **16**(1), 91–101 (2001)
5. Mohan, B., Rajadurai, A., Satyanarayana, K.G.: Electric discharge machining of Al–SiC matrix composites using rotary tube electrode. J. Mater. Process. Technol. **153–154**, 978–985 (2004)
6. Mahapatra, S.S., Patnaik, A.: Optimization of Wire Electrical Discharge Machining (WEDM) process parameters using Taguchi method. Int. J. Adv. Manuf. Technol. **34**, 911–925 (2004)
7. Chattopadhyay, K.D., Satsangi, P.S., Verma, S., Sharma, P.C.: Analysis of rotary electrical discharge machining characteristics in reversal magnetic field for copper-EN 8 steel system. Int. J. Adv. Manuf. Technol. **38**, 925–937 (2008)
8. Lin, Y.C., Lee, H.S.: Machining characteristics of magnetic force-assisted EDM. Int. J. Mach. Tools Manuf **48**(11), 1179–1186 (2008)
9. Singh, N.K., Pandey, P.M., Singh, K.K.: EDM with an air-assisted multi-hole rotating tool. Mater. Manuf. Process. **31**(14), 1–23 (2015)
10. Bhardwaj, B., Kumar, R., Singh, P.: Prediction of Surface roughness in turning of EN 353 using response surface methodology. Trans. Indian Inst. Met. **67**(3), 313 (2014)
11. Jain, N., Pareek, A., Bhardwaj, B.: Effect of Al_2O_3 powder in deionized water on metal removal rate during electro discharge machining of H11 die steel. In: IOP Conference Series: Material Science and Engineering, pp. 1–13 (2018)
12. Lee, S.H., Li, X.P.: Study of the effect of machining parameter on the machining characteristics in electrical discharge machining of tungsten carbide. J. Mater. Process. Technol. **115**, 344–358 (2001)
13. Dwivedi, A.P., Choudhury, S.K.: Increasing the performance of EDM process using tool rotation methodology for machining AISI D3 steel. Proc. CIRP **46**, 131–134 (2016)

Chapter 13
Vibration Analysis of BTA Deep Hole Drilling Machine

Ahmed M. Zakwan and Nilesh Raykar

Abstract In order to drill holes with large length-to-diameter ratio without compromising in surface finish or straightness of the holes, Boring Trepanning Association (BTA) deep hole drilling method was developed. The detrimental effect of vibration amplitude on the surface finish of drilled holes is well known. Present work attempts to provide a simple model to predict vibration amplitude during a typical deep hole drilling operation. The experimentally measured vibration displacement amplitude is used to develop a simple analytical model based on the theory of un-damped vibration for a single degree freedom system. The magnitude of vibration is measured by accelerometers placed at two different locations of machine frame during deep hole drilling operation of high alloy steel using 125 mm diameter BTA cutting tool. An analytical model is used to validate experimental results calculated by using FFT. The experimental data is found to fit satisfactorily with the predictions of the analytical model.

Keywords Drilling operation · Chatter · BTA deep hole drilling

Nomenclature

A	Vibrational displacement in (mm)
A_H	Experimental amplitude in a horizontal direction (mm)
A_{Ha}	Analytical amplitude in an axial direction (mm)
A_v	Experimental amplitude in a vertical direction (mm)
A_{va}	Analytical amplitude in a vertical direction (mm)
F	External excitation force (KN)
F_c	Tangential cutting force (KN)
K	Stiffness of the material (N/m)

A. M. Zakwan (✉) · N. Raykar
Department of Mechanical Engineering, Sardar Patel College of Engineering, Andheri, Mumbai, India
e-mail: ahmedzakwan81@gmail.com

N Spindle speed (RPM)
ω External excitation frequency (rad/sec)
ω_n Natural frequency (rad/sec)
Ø   Tool diameter (mm)

13.1   Introduction

Deep hole drilling methods are specifically developed for producing holes of high length-to- diameter ratio ($L/d > 10$), with excellent surface finish and straightness. For deep hole drilling (depth of hole/bore diameter >20), the boring trepanning association (BTA) technique [1] is available. The schematic of machining process around the BTA tool is shown in Fig. 13.1. Deep hole tools have a non-symmetric cutting edge which provides a radial component of the cutting force; such radial force is negligible for conventional drilling tools. The radial cutting force component along with the guiding pads (Fig. 13.1), provide to a self-guided path for the tool during drilling operation. The self-guidance results in superior straightness of the drilled hole. The high flow rate of cutting fluid during this operation forcibly pushes out metal chips which is an additional advantage of BTA over normal drilling operation. These two aspects of machining process are prerequisites for achieving a good quality of deep hole drilling [2].

The deep hole drilling by its nature necessitates use of slender tooling which has low stiffness both in static and dynamic modes. Such low stiffness tooling leads to undesirable chatter vibrations and spiraling which cause increase in rejected work-pieces due to bad surface quality. Usually, the BTA is the last manufacturing process and any rejection at this stage amounts to huge loss of production time as well as profit margins. Hence, utmost attention is paid to ensure reliability of this process.
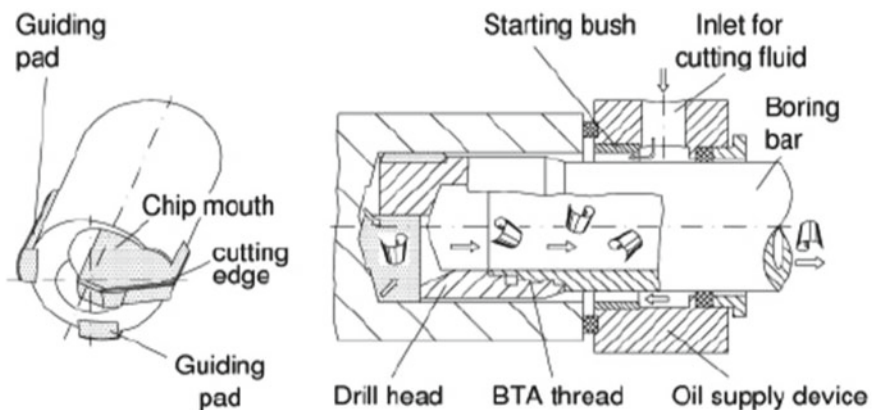
Fig. 13.1   Working principle of BTA deep hole drilling [1]

Such stringent requirements demand in-depth analysis of dynamic behavior of tool and workpiece during machining operation [3].

Studies have shown that the vibrations of deep hole drilling tool structure is challenging to model; it is also an unavoidable part of the fabrication procedure. The analysis of vibrations is crucial in ascertaining quality of deep hole drilling in high-speed machining [4].

This paper covers basic analysis of BTA process for a specific machine with emphasis on predicting its vibration characteristics [5]. During the associated experiment, displacement amplitudes of vibration for different rotational speeds of the tool have been recorded to evaluate the features of dynamic disturbances.

The evaluation is focused on the chatter vibration of the machine frame. The modeling of the machine was carried out without considering damping effects.

13.2 Experimentation Work

13.2.1 Experimental Method

The vibrations in various machining operations are studied by using pressure transducers, audio sensors and accelerometers or displacement sensors. A CNC BTA deep hole drilling machine was employed to conduct the experiments. The machine specifications are as follows: bed length = 9.5 m, maximum spindle speed = 1150 RPM, maximum feed rate = 133 mm/min and a maximum spindle power = 30 KW. The workpiece material used was high alloy steel (annealed) of 225BHN. A commercially available multi-edge BTA robust drilling tool of Ø 125 mm has used. It is equipped with three guiding pads and five cutting inserts and has a nominal external diameter of 125 mm (Fig. 13.2). During the machining operation, the tool is stationary and the workpiece is rotating.

Fig. 13.2 BTA cutting tool

13.2.2 Experimental Measurement of Vibration Amplitude

The displacement values are decisive from vibration amplitude data obtained at two different locations on the machine frame with the aid of fast Fourier transform (FFT) analyzer. This analyzer utilizes an acceleration sensor (Figs. 13.3 and 13.4) and displays the vibration amplitude in waveform with time and the frequency spectrum [6].

The sensor (accelerometer) was seated at one of the two positions (i) along a horizontal plane (Fig. 13.5) and (ii) along a vertical plane (Fig. 13.6).

FFT over time series analysis used because the time series analysis is usually incapable of isolating defect-scattered information from noise in different frequency bands. Therefore, time domain signal must be converted into the frequency domain as spectrum graphs with the help of FFT [7].

Fig. 13.3 Multipurpose accelerometer AC-102-1A

Fig. 13.4 Fast Fourier transformation (FFT)

Fig. 13.5 Accelerometer in horizontal direction
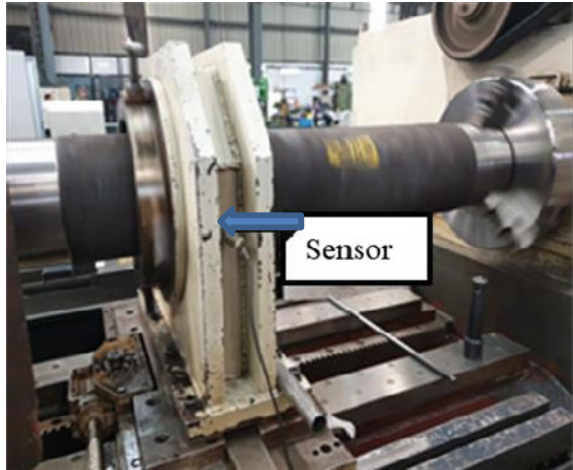
Fig. 13.6 Accelerometer in vertical direction

13.2.3 Analytical Model to Predict Vibration Amplitude

To validate the experimental results, a simple analytical model based on un-damped vibration of single degree of freedom (SDOF) system is recycled. Following assumptions are made,

(a) Workpiece, tool and machine frame behave as an un-damped SDOF system.
(b) The tangential cutting force F_c (Fig. 13.7) which set within the machine during the cutting operation studied as the amplitude of periodic external force acting on the system.
(c) Effect of forces acting along other directions neglected.

Fig. 13.7 Cutting forces on
deep hole drilling tool [8]
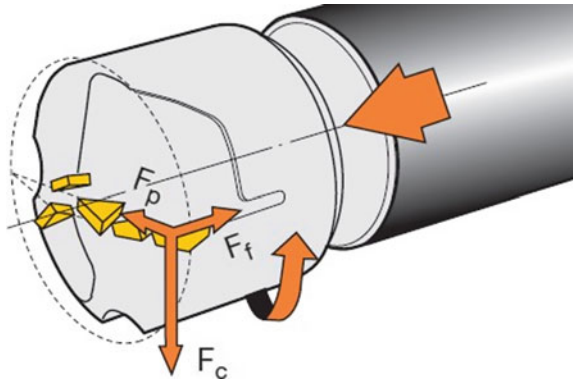
The vibration of a machine frame studied as a case of forced vibration produced
by the excitation provided at the work head by the cutting process. The forcing
frequency (ω) regarded as the same as the spindle rotational speed.

The cutting forces that arise during drilling are illustrated in Fig. 3.7. The axial
force F_f gives rise to an opposite feed force. The tangential cutting force F_c causes the
torque Mc and F_p is the radial force that acts on the guide pad. Present work mainly
focused on effect of transverse vibrations on drilled hole diameter. It is important
to note that the large part of energy dissipation occurs at the tool holder-spindle
interference.

The cutting forces can be determined experimentally. If the specific cutting force
k_c for the material is known, the size of the cutting forces can be calculated,

Tangential force

$$F_c = k_c \times f_n \times \text{ap}$$

The specific cutting force, like the coefficient of friction for support pads, is
difficult to calculate exactly.

The formulas for feed force, torque and power requirement are therefore only
approximate,

Feed force (F_f)

$$F_f = 0.5 \times k_c \times \text{ap} \times f_n$$

- When the drill is rotating and approaching toward workpiece. Forced longitudinal
  vibrations do not exist when drill is approaching toward the workpiece. It is
  because of the fact that as drill is approaching, no force acts on the drill in the
  upward direction. Due to this, the vibrations of the drilling during approaching
  toward the workpiece can be neglected.
- When the drill is rotating and drilling a hole into the workpiece. When drill touches
  the workpiece and starts cutting the material to produce the hole, the upward
  resistive force acts on the drill because of the tensile stress of the workpiece

material. When the material breaks during drilling the hole, its failure in the longitudinal direction can be considered as the compressive failure. The force exerted in the upward longitudinal direction during the failure of the workpiece can be calculated using the above formula,

When the drill is rotating and approaching toward workpiece.

When the drill approaches toward the workpiece, the no external force on the drill except the force of vibration developed by the motor torque, and thus these vibrations can be neglected because there is no restricting force acting on the drill bit in the direction of the transverse vibration of the drill.

When the drill is rotating and drilling a hole into the workpiece.

When drill enters into the workpiece, the force is exerted by the workpiece material on the drill bit in the direction of the transverse motion of the drill, i.e., perpendicular to the axis of the drill. The analysis of this force can be understood from the following.

Present work focuses on the transverse vibrations during the drilling process. It is convenient to characterize the system response by modeling it as a linear system and obtaining its response to a specific sinusoidal input force $f(t)$ representing the cutting forces,

$$f(t) = F \sin(\omega t) \tag{13.1}$$

where t is the time and F is the amplitude of external periodic force The amplitude A of vibration is given by,

$$A = \frac{F/k}{\sqrt{\left(1 - \left(\frac{\omega}{\omega_n}\right)^2\right)^2 + \left(2\xi \frac{\omega}{\omega_n}\right)^2}} \tag{13.2}$$

Since the deep hole drilling system modeled as un-damped SDOF system, external excitation force F is considered proportional to F_C. The damping coefficient, $\xi = 0$. Thus, $F = C_o F_c$ where C_0 is system constant. Therefore,

$$A = \frac{\frac{C_0 F_c}{k}}{1 - \left(\frac{\omega}{\omega_n}\right)^2} \quad \text{or} \quad A = \frac{\overline{C_1 F_c}}{\left(1 - \left(\frac{\omega}{\omega_n}\right)^2\right)} \tag{13.3}$$

where 1= constant

The system constants C_1 and are determined in order to obtain the best fit with the experimental results. The drill and workpiece are considered to be attached with the help of the spring whose stiffness is 'k'. Under equilibrium conditions,

$$k = \sigma * v \tag{13.4}$$

This is because of the fact when the drill transverses with the linear velocity '*v*', the force is exerted on the drill in the direction of the transverse motion due to the stress induced in the material. Force is the resistive force applied by the workpiece in the direction perpendicular to the axis of the drill.

13.3 Results and Discussion

13.3.1 Experimental Results

The experimental data obtained for the amplitude of vibration at different rotational speed in horizontal (A_H) and vertical (A_v) directions are shown in Tables 13.1 and 13.2, respectively. The similar results obtained from the analytical model are shown as (A_{Ha}) and (A_{Va}), respectively in this table.

The system constants for analytical model are determined as follows,
$C_1 = 2.5E-06$ mm/KN, $\omega = 29.1$ rad/sec
$C_1 = 2.9E-06$ mm/KN, ω 41.5 rad/sec

The experimental data and results obtained from the model for vibration amplitude versus spindle speed plotted in Figs. 13.8 and 13.9.

In longitudinal direction accelerometer shown in Table 13.1, attached to find out displacement along the length direction. Vibration produced because of drilling itself, i.e., due to spindle speed and feed cannot be controlled completely when drill is rotating and drilling a hole into workpiece when it touches the workpiece and starts cutting the material to produce the hole, the upward resistive force acts on the drill because of the tensile stress of the workpiece material.

Maximum percentage error between experimental data and analytical values predicted by the model are 4.9% (horizontal direction) and 11.6% (vertical direction).

Table 13.1 Experimental data and results from the model for vibration measured along the horizontal

Case	N (rpm)	ω (rad/sec)	Fc (KN)	A_H (mm)	A_{Ha} (mm)	% error
1	117	12.25	25	0.08	0.076	+4.9
2	130	13.61	30	0.1	0.096	+3.8
3	156	16.38	40	0.14	0.146	−4.6

Table 13.2 Experimental data and results from the model for vibration measured along the vertical

Case	N (rpm)	ω (rad/sec)	F_c (KN)	A_V (mm)	A_{Va} (mm)	% error
1	117	12.25	25	0.09	0.084	+6.6
2	130	13.61	30	0.11	0.103	+6.5
3	156	16.33	40	0.18	0.159	+11.6

Fig. 13.8 Amplitude in horizontal direction versus spindle speed
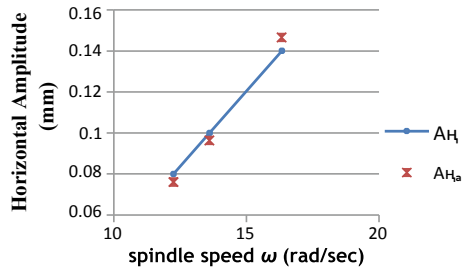
Fig. 13.9 Amplitude in a vertical direction versus spindle speed
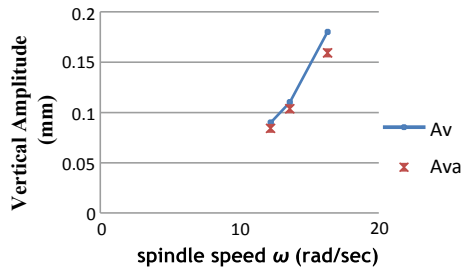
13.4 Conclusions

A simplified approach to predict the vibration produced during the drilling operation on BTA machine is developed. For this purpose, an analytical model based on un-damped forced vibration of Single Degree of Freedom (SDOF) system has been established. The maximum error between the experimentally and analytically obtained vibration amplitude is 4.9% in horizontal and 11.6% in vertical direction. These error magnitudes are reasonable for further evaluation to improve the accuracy of deep hole drilling operation. This model can be adapted to analyze vibrations during deep hole drilling operations with other machines of similar construction.

References

1. N.N.: VDI-Richtlinie 3210: Tiefbohrverfahren. VDI Dusseldorf, Juni1974
2. Quintana, Guillem, Ciurana, Joaquim: Chatter in machining processes: a review. Int. J. Mach. Tools Manuf. **51**, 363–376 (2011)
3. Astakhov, V.P., Osman, M., Al-Ata, M.: Statistical design of experiments in metal cutting—part one & two. J. Testing Eval. **25**(3), 322–335 (1997)

4. Izelu, C.O., Eze, S.C., Oreko, B.U., Edward, B.A., Garba, D.K.: Response surface methodology, in the study of induced machining vibration and work surface roughness in the turning of 41Cr4 alloy steel. Int. J. Emerg. Technol. Adv. Eng. **3**, 13–17 (2013)
5. Dolinšek, S., Kopač, J.: Mechanism and types of tool wear; particularities in advanced cutting materials. J. Achiev. Mater. Manuf. Eng. **19**(1), 11 (2006)
6. Wani, A.S., Sagavkar, G.S.: Vibration analysis pf drilling operation. **2**, 163–175 (2013)
7. Hajra choudhry, S.K., Roy, N.: Workshop technology. **2** (2010)
8. Sandvik Coromant deep hole drillingcatalogue

Chapter 14
Influence of Process Parameters on Tool Wear Rate for Rotary Cu Tool Electrode in Electrical Discharge Drilling

Rakesh Kumar, Anand Pandey, Pooja Sharma, Ashish Goyal, and Satish Namdev

Abstract In this paper, electrical discharge drilling (EDD) of Inconel 718 material with a rotary copper tool electrode by using Taguchi optimization methodology has been reported. Taguchi technique is used to analyze the influence of each parameter on the tool wear rate (TWR), and to compute the optimal choice for each EDD parameter such as tool diameter, peak current, pulse-on time, pulse-off time, tool rotation and hole depth. It is found that hole depth and peak current are the most significant process parameters affecting TWR. ANOVA has been conducted for determining impact of process parameters on TWR. A regression model has been developed for predicting the TWR in terms of machining factors.

Keywords EDM · EDD · TWR · Copper

14.1 Introduction

Electrical discharge machining (EDM) is a machining method used for machining of difficult-to-cut materials. In EDM, machining stability can be improved by rotating the tool electrode because rotation is effective in flushing debris particles from the gap and cooling the tool electrode surface, avoiding repeated occurrence of discharge in one location. The contactless machining method has been continuously evolving from a mere tool and dies making process to a micro-scale application [1, 2]. EDM is based on thermoelectric energy which is used to remove material from tool electrode and workpiece. A spark is produced between the two electrodes and its location is determined by the narrowest gap between the two [3, 4]. Researchers have been compared for cryogenically processed and non-treated tool electrode in

R. Kumar (✉) · S. Namdev
Department of Automobile Engineering, Manipal University Jaipur, Jaipur 303007, India
e-mail: rakesh.kumar@jaipur.manipal.edu

A. Pandey · A. Goyal
Department of Mechanical Engineering, Manipal University Jaipur, Jaipur 303007, India

P. Sharma
Department of Mathematics and Statistics, Manipal University Jaipur, Jaipur 303007, India

EDM. Cryogenic process minimizes residual stress and crystal imperfections cause lesser TWR and better tool lifespan [5]. Influence of cryogenic process on response characteristics, viz. TWR, MRR and SR for Cu–Cr–Zr alloy tool electrodes in EDM of AISI P20 tool steel conducted successfully [6].

The current experimental study is engrossed on the EDD of Inconel 718 alloy with CT copper tool electrode. An effort has been made to attain optimal setting of the process parameters for minimum TWR using Taguchi approach.

14.2   Experimental Setup, Materials and Methods

The experimental research was achieved on a z-axis electro-discharge drilling setup as shown in Fig. 14.1. In all the experiments, kerosene oil is taken as dielectric medium. This experimental setup consists of a mild steel frame, DC motor (speed control by the controller) and RPM indicator and tool.

Solid copper tool electrode with 4 and 6 mm diameter with helical groove was used in the experimental studies of cryogenic treated electro-discharge drilling (EDD) as shown in Fig. 14.2. Helical groove is used to increase machinability [7]. The selected workpiece material in the research work is Inconel 718 plate with 3 mm thickness. Depth of 1, 1.5 and 2 mm holes were drilled in Inconel 718.

TWR (mm^3/min) can be determined from the following formula:

$$\text{TWR} = \left(T_i - T_f\right) * 1000 / \rho_t * T \tag{14.1}$$

Fig. 14.1 EDD experimental setup
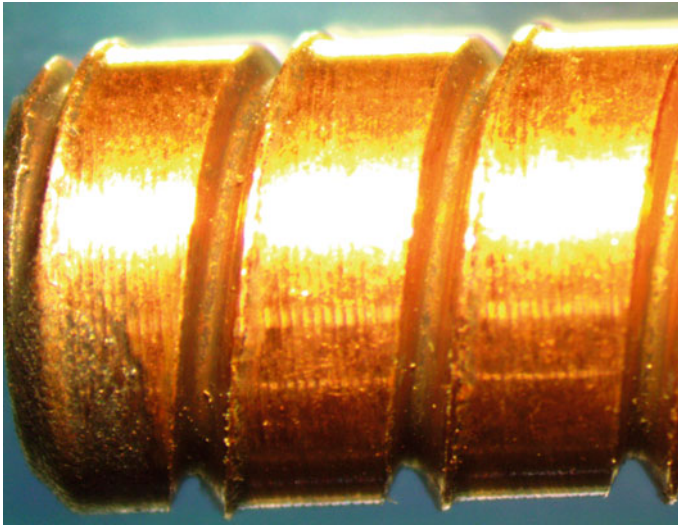
Fig. 14.2 Cu tool electrode

where T_i is the initial weight of tool in gms, T_f is the final weight of tool in gms and ρ_t is the tool material density in gm/cm3. T is the operational time in minutes [8, 9].

In this study, Taguchi's "the smaller-the-better" performance characteristic was considered for TWR, a property which is generally anticipated to be as low as possible. The S/N ratio was computed for each level of process parameters. Then, the optimal combination of the test parameters was determined. The control factors (parameters) and their levels are given in Table 14.1.

Table 14.1 Control factors and their levels

Control factor	Unit	Level		
		1	2	3
Tool diameter (d)	Mm	4	6	–
Peak current (Ip)	Amp	6	10	14
Pulse-on time (T_{on})	µs	20	30	40
Pulse-off time (T_{off})	µs	75	150	225
Tool rotation (Nt)	RPM	30	40	50
Hole depth (h)	Mm	1	1.5	2

14.3 Results and Discussion

Experimental design using L_{18} orthogonal array and obtained TWR value with corresponding S/N ratio has been presented in Table 14.2.

Analysis of the influence of each control parameter on the TWR was performed with signal-to-noise (S/N) response table. S/N ratio response table for TWR with normal rotary Cu tool electrode is presented in Table 14.3. It can be seen in Table 14.3, the strongest influence was exerted by the hole depth followed by peak current, pulse-on-time, pulse-off time, tool diameter and tool rotation for normal rotary Cu tool electrode. Optimal levels for each control factor can be easily determined from this graphs by considering the lowest points in accordance with Taguchi's "smaller-the-better" performance characteristic [10–12].

Based on S/N ratio values, the lower value of the TWR has been attained for optimum parametric conditions at tool diameter: 4 mm (level 1), peak current: 6 A (level 1), pulse-on time: 40 µs (level 3), pulse-off time: 225 µs (level 3), tool rotation: 50 rpm (level 3) and hole depth: 2 mm (level 3) settings. Therefore, the optimal level setting of the respective control factors is A1B1C3D3E3F3.

Table 14.2 Experimental design using L18 orthogonal array and obtained TWR with corresponding S/N ratio

Sr no.	Tool diameter (mm)	Peak current (Amp)	Pulse-on time (µs)	Pulse-off time (µs)	Tool rotation (RPM)	Hole depth (mm)	TWR (mm³/min)	S/N ratio (dB)
1	4	6	20	75	30	1	0.736	2.66
2	4	6	30	150	40	1.5	0.406	7.82
3	4	6	40	225	50	2	0.228	12.84
4	4	10	20	75	40	1.5	0.882	1.09
5	4	10	30	150	50	2	0.492	6.16
6	4	10	40	225	30	1	0.891	1.00
7	4	14	20	150	30	2	0.627	4.05
8	4	14	30	225	40	1	1.218	−1.71
9	4	14	40	75	50	1.5	0.680	3.34
10	6	6	20	225	50	1.5	0.434	7.25
11	6	6	30	75	30	2	0.397	8.02
12	6	6	40	150	40	1	0.513	5.79
13	6	10	20	150	50	1	1.300	−2.27
14	6	10	30	225	30	1.5	0.635	3.94
15	6	10	40	75	40	2	0.418	7.57
16	6	14	20	225	40	2	0.627	4.05
17	6	14	30	75	50	1	1.344	−2.56
18	6	14	40	150	30	1.5	0.578	4.76

Table 14.3 S/N ratio response table of TWR (smaller the better)

Level	Tool diameter (d_t)	Peak current (I_p)	Pulse-on time (T_{ON})	Pulse-off time (T_{OFF})	Tool rotation (N_t)	Hole depth (h)
1	4.142	7.400	2.805	3.355	4.074	0.483
2	4.062	2.916	3.613	4.387	4.106	4.704
3	–	1.989	5.888	4.563	4.125	7.118
Delta	0.0796	5.410	3.082	1.207	0.050	6.634
Rank	5	2	3	4	6	1

Response graphs for means of S/N ratio for TWR of each control factor are shown in Fig. 14.3.

It can be seen from the Fig. 14.3, TWR increases with increase in tool diameter from 4 to 6 mm. It may be due to that at higher diameter of tool electrode (6 mm) discharge energy of single spark increases [13–15]. TWR increases with increasing peak current at all settings (6–14 A). It may be due to more discharge energy creates between electrodes in machining at larger peak current (14 A). [15, 16]. TWR decreases with increase in pulse-on time for all setting (20–40 μs). At small values of pulse-on time (20 μs), more particles attack the Cu tool electrode resulting more TWR. At higher T_{on}, plasma channel forms causes reduction of heat transfer to the Cu tool thus decrease TWR [15]. Further, it has been seen that TWR decreases with an increase of pulse-off time at all settings (75–225 μs). Increasing in T_{off} is
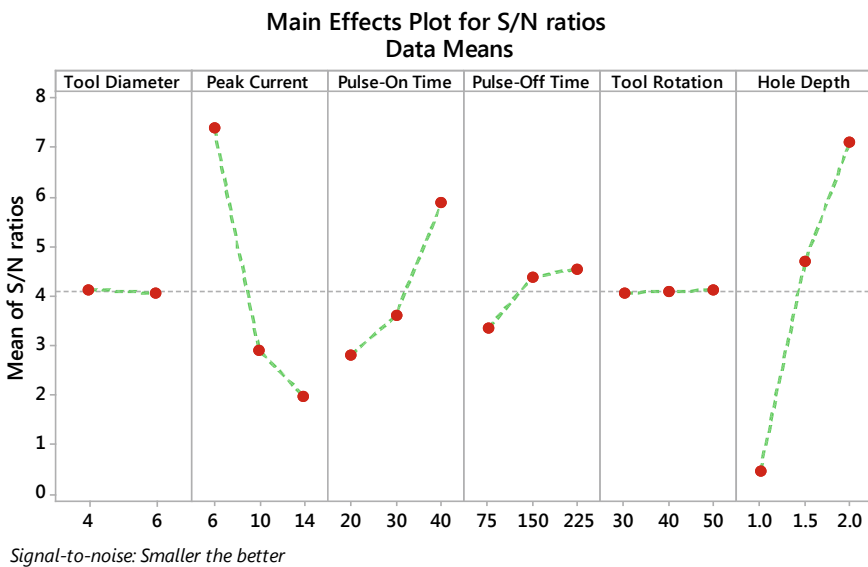
Fig. 14.3 Main effect plots of TWR: S/N ratio for normal rotary Cu tool electrode

responsible for cooling of machining area resulting increasing in machining time, i.e., less TWR [16, 17]. TWR slightly affected for all setting of rotation of Cu tool electrode from 30 to 50 rpm. It is due to the increased spark intensity in the gap leads to melt more materials resulting more TWR [18]. TWR decreases with increase in hole depth from 1 to 2 mm. It may be due to the fact that in blind hole drilling, formation of plasma channel occurs which reduce the secondary discharge resulting less TWR [19].

14.3.1 ANOVA for TWR

ANOVA is used to describe the influence of process parameters on TWR [20]. Table 14.4 shows that ANOVA of process parameters on TWR of Inconel 718 super alloy.

From ANOVA, it is observed that at 95% confidence level ($p < 0.05$), peak current, pulse-on time and hole depth are most significant parameters that affects TWR.

Table 14.4 ANOVA of TWR (S/N ratio) for normal rotary Cu tool electrode

Source	DF	Seq SS	Contribution (%)	SS Adj	Adj MS	F	P
Tool diameter	1	0.00041	0.02	0.000411	0.000411	0.03	0.873
Peak current	2	0.52238	29.49	0.522375	0.261188	17.62	0.003
Pulse-on time	2	0.17220	9.72	0.172203	0.086102	5.81	0.039
Pulse-off time	2	0.02701	1.52	0.027008	0.013504	0.91	0.451
Tool rotation	2	0.03269	1.85	0.032688	0.016344	1.10	0.391
Hole depth	2	0.92797	52.38	0.927967	0.463984	31.31	0.001
Residual error	6	0.08893	5.02	0.088926	0.014821	–	–
Total	17	1.77158	100.00	–	–	–	–
Model Summary	–	–	–	–	–	–	–
$S =$ 0.121742	$R-$sq $=$ 94.98%	$R-$sq (adj) $=$ 85.78%	$R-$sq (pred) $= 54.82\%$	–	–	–	–

Table 14.5 Validation table of TWR for normal rotary Cu tool electrode

Optimum level	TWR (mm³/min)		Difference	% Difference
	Predicted	Experiment		
A1B1C3D3E3F3	0.1276	0.1252	0.0024	1.88

14.3.2 Regression Analysis for TWR

Regression analysis is used to know effect of process parameters on performance characteristics [20, 21]. The regression equation of TWR is presented by Eq. (14.2).

$$\begin{aligned}
TWR = &1.167 + 0.0048\,\text{Tool Diameter} + 0.0492\,\text{Peak Current} \\
&- 0.01082\,\text{Pulse} - \text{on time} - 0.000471\,\text{Pulse} - \text{Off Time} \\
&+ 0.00512\,\text{Tool Rotation} - 0.5355\,\text{Hole Depth}
\end{aligned} \tag{14.2}$$

From Eq. (14.2), the predicted R^2 (94.98%) value and the adjusted R^2 value were found almost coinciding with experimental results. Adjusted R^2 determines the amount of deviation about the mean which is described by the model.

14.3.3 Confirmation of Experiments

Aim of confirmation experiments is to validate conclusions drawn during analysis [21, 22]. It is conducted by setting the process parameters at the optimum level of A1B1C3D3E3F3. Table 14.5 shows validation results of TWR for normal rotary Cu tool electrode.

It is clear from Table 14.5 that the optimal predicted value of TWR (0.1276 mm³/min) is deviated from optimal experimented value (0.1252 mm³/min) by 1.88%.

14.3.4 Interaction Plots of TWR

Figure 14.4 presents interaction plots for S/N ratio of TWR among hole depth and peak current for Cu tool electrode.

Since lines are non-parallel, there is certain interaction among hole depth and peak current. With increase in peak current from level 6 to 14 A, the influence of hole depth on the TWR increases.

The SEM images of Cu tool electrode after machining at resolution of 50 and 100 μm are shown in Figs. 14.5 and 14.6, respectively. It can be seen from Figs. 14.5 and 14.6, some black spots are formed due to machining.
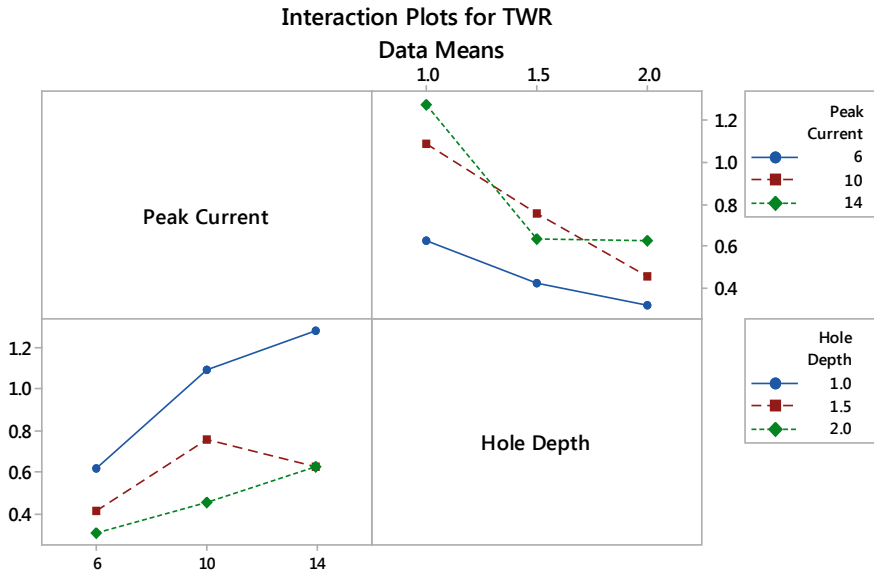
Fig. 14.4 Interaction plots of TWR for normal rotary Cu tool electrode
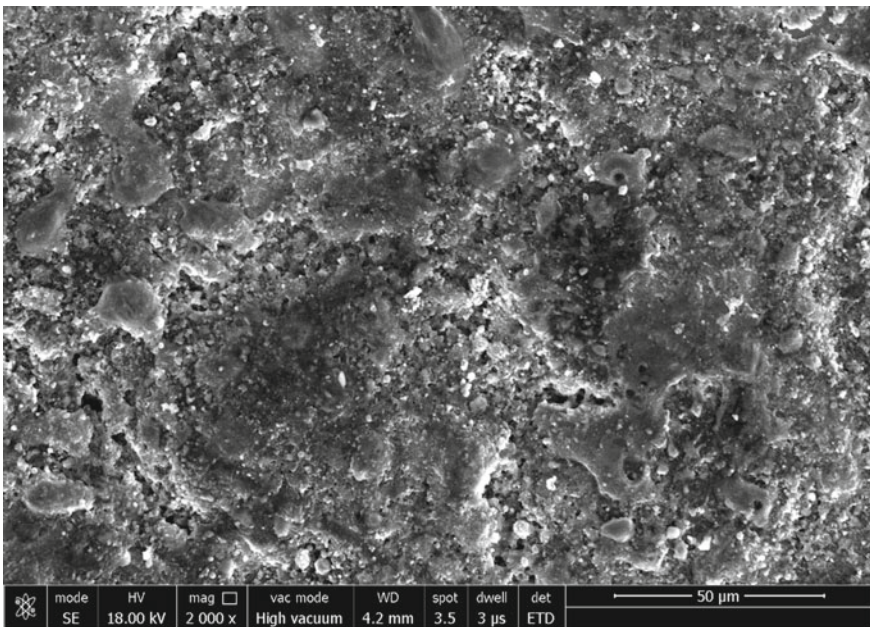
Fig. 14.5 SEM image of Cu tool electrode after machining at resolution of 50 µm
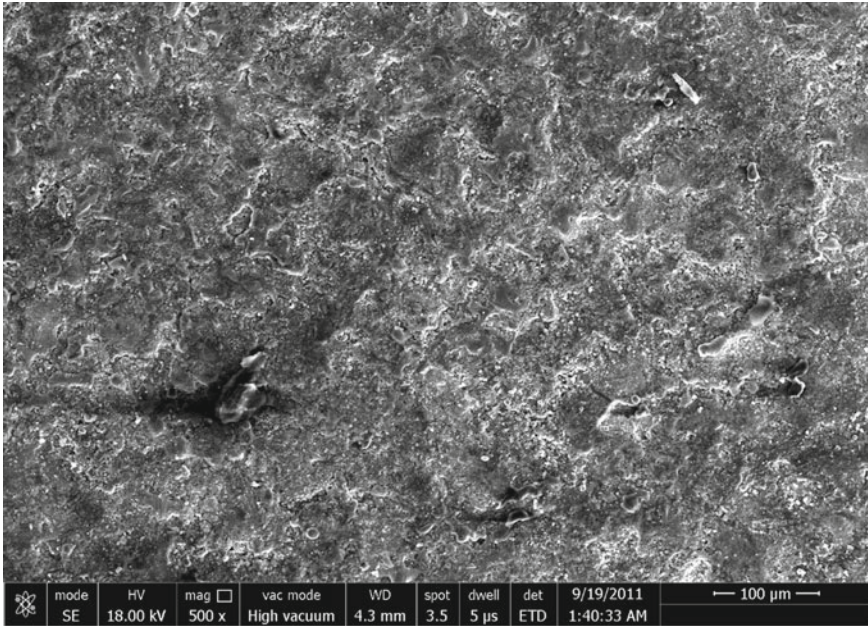
Fig. 14.6 SEM image of Cu tool electrode after machining at resolution of 100 μm

14.4   Conclusions

The following specific conclusions can be drawn from the experimental study

- Combination of tool diameter: 4 mm, peak current: 6 A, pulse-on time: 40 μs, pulse-off time: 225 μs, tool rotation: 50 rpm and hole depth: 2 mm found optimal settings for minimum TWR. Therefore, the optimal level setting of the respective control factors is A1B1C3D3E3F3.
- Hole depth and peak current are the two most affecting process parameters effecting TWR of rotary copper tool electrode.
- Tool rotation is the less significant process parameters effecting TWR of rotary copper tool electrode.
- A regression model has been developed for predict the response output, i.e., TWR confirmation of experiments shows the developed model exist within the limit at 95% confidence level.
- Interaction plots have been drawn successfully between hole depth and peak current which are the most affecting parameters for TWR.

References

1. Soni, J.S., Chakraverti, G.: Performance evaluation of rotary EDM by experimental design technique. Defense Sci. J. **47**(1), 65–73 (1997)
2. Wang, C.C., Yan, B.H.: Blind-hole drilling of Al2O3/6061Al composite using rotary electro-discharge machining. J. Mater. Process. Technol. **102**, 90–102 (2000)
3. Singh, S., Maheshwari, S., Pandey, P.C.: Some investigations into the electric discharge machining of hardened tool steel using different electrode materials. J. Mater. Process. Technol. **149**, 272–277 (2004)
4. Yahagi, Y., Koyano, T., Kunieda, M., Yang, X.: Micro drilling EDM with high rotation speed of tool electrode using the electrostatic induction feeding method. Procedia CIRP. **1**, 162–165 (2012)
5. Rahul Datta, S., Biswal, B. B., Mahapatra, S.S.: Electrical discharge machining of Inconel 825 using cryogenically treated copper electrode: Emphasis on surface integrity and metallurgical characteristics. J. Manuf. Proc. **26**, 188–202 (2017)
6. Cetin, A., Cakir, G., Aslantas, K., Ucak, N., Cicek, A.: Performance of cryogenically treated Cu and CuCrZr electrodes in an EDM process. Metal. Mater. **55**(6), 431–440 (2017)
7. Plaza, S., Sanchez, J.A., Perez, E., Gila, R., Izquierdo, B., Ortegaa, N., Pombo, I.: Experimental study on micro EDM-drilling of Ti6Al4V using helical electrode. Precision Eng. **38**, 821–827 (2014)
8. Singh, A., Kumar, P., Singh, I.: Process optimization for electro-discharge drilling of metal matrix composites. Procedia Eng. **64**, 1157–1165 (2013)
9. Ay, M., Caydaş, U., Hasçalık, A.: Optimization of micro-EDM drilling of Inconel 718 super alloy. Int. J. Adv. Manuf. Technol. **6**, 1015–1023 (2013)
10. Baghlani, V., Mehbudi, P., Akbari, J., Sohrabi, M.: Ultrasonic assisted deep drilling of Inconel 738LC superalloy. Procedia CIRP. **6**, 571–576 (2013)
11. Kumar, J., Ahmad, H.: Parametric analysis of rotary tool electrical discharge machining of metal matrix composite. Int. J. Eng. Res. Technol. **3**(9), 1225–1229 (2014)
12. Gaur, S., Bharti, P.K.: Experimental study with rotating tool electrode of EDM for Ni Alloy. Int. J. Modern Eng. Res. **5**, 15–22 (2015)
13. Liu, Q., Zhang, Q., Zhu, G., Wang, K., Zhang, J., Dong, C.: Effect of electrode size on the performances of micro-EDM. Mater. Manuf. Process. **31**(4), 391–396 (2016)
14. Wang, K., Zhang, Q., Zhu, G., Zhang, J.: Effects of tool electrode size on surface characteristics in micro-EDM. Int. J. Adv. Manuf. Technol. **96**(9–12), 3909–3916 (2018)
15. Habib, S.S.: Study of the parameters in electrical discharge machining through response surface methodology approach. Appl. Math. Model. **33**(12), 4397–4440 (2009)
16. Sultan, T., Kumar, A., Gupta, R. D.: Material removal rate, electrode wear rate, and surface roughness evaluation in die sinking EDM with hollow tool through response surface methodology. Int. J. Manuf. Eng. Article ID 259129, p. 16 (2014)
17. Boopathi, R., Thanigaivelan, R., Prabu, M.: Effects of process parameters on MRR, EWR and Ra in nanoparticles mixed EDM. Res. Dev. Mater. Sci. **4**(3), 3. https://doi.org/10.31031/rdms.2018.04.000586 (2018)
18. Dwivedi, A.P., Choudhary, S.K.: Increasing the performance of EDM process using tool rotation methodology for machining AISI D3 steel. Procedia CIRP. **46**, 131–134 (2016)
19. Karthikeyan, G., Ramkumar, J., Dhamodaran, S., Aravindan, S.: Micro electric discharge milling process performance: an experimental investigation. Int. J. Mach. Tools Manuf. **50**(8), 718–727 (2010)
20. Kumar, R., Pandey, A., Sharma, P.: Comparative study of Tool Wear Rate with conventional and cryogenically treated electrode in electrical discharge drilling. Int. J. Mater. Eng. Innov. **9**(4), 322–344 (2018)
21. Kumar, R., Pandey, A., Sharma, P.: Investigation of surface roughness for Inconel-718 in blind hole drilling with rotary tool electrode. J. Adv. Manuf. Syst. https://doi.org/10.1142/S0219686719500203

22. Goyal, A., Pandey, A., Sharma, P.: An experimental study on MRR and SR of aerospace material during fabrication of V-Groove using WEDM. Int. J. Mech. Prod. Eng. Res. Dev. **7**(3), 249–258 (2017)

Chapter 15
Machinability Study of Zirconia Material by Micro-ECDM

Manoj Kumar, Rahul Omprakash Vaishya, and Narendra Mohan Suri

Abstract The need for zirconia material is increasing nowadays due to excellent properties such as high strength, wear resistance, hot hardness, and chemical stability. Zirconia material is used in dental frameworks such as crowns, refractory material, lab crucible, wear coating, and electroceramics. In the present research study, machining characteristics for drilling the zirconia are studied using developed electrochemical discharge machining (ECDM) setup, which is a hybridization process (ECDM) of electrochemical machining (ECM) and electro-discharge machining (EDM). The effect of input parameter voltage is studied on the surface integrity of the machined surface using one factor at a time (OFAT). From the results, it is evident that at higher levels of voltage, the material removal rate and overcut increase. Moreover, high thermal energy results into the crack propagation in the material due to brittle nature of zirconia which ultimately leads to its fracture.

Keywords ECDM · Zirconia · Machining · MRR · OC · SEM · EDS

Nomenclature

ECDM	Electrochemical discharge machining
MEMS	Microelectromechanical system
MOEMS	Microoptoelectromechanical system
USM	Ultrasonic machining
LBM	Laser beam machining
EDM	Electric discharge machining
ECM	Electrochemical machining
DC	Direct current
AC	Alternative current

M. Kumar (✉) · R. O. Vaishya · N. M. Suri
Department of Production and Industrial Engineering, Punjab Engineering College (Deemed to be University), Chandigarh 160012, India
e-mail: mnjbrd.02@gmail.com

NaOH   Sodium hydroxide
V   Voltage
EC   Electrolyte concentration
IEG   Inter-electrode gap
SS   Stainless steel
WC   Tungsten carbide
MRR   Material removal rate
(W)OC   (width of) overcut
TWR   Tool wear rate
SR   Surface roughness
MSD   Mean square deviation
S/N ratio Signal-to-noise ratio
DF   Duty factor

15.1 Introduction

In recent times, the importance of microfeatures such as micro-hole, counters, channels is increasing due to their special application in the medical, electronics, industries, and defense sector. Zirconia is a white crystalline ceramic widely used in such applications due to excellent properties such as high hot hardness, wear-resistance, and chemical stability. Zirconia being a non-conductive material, emerges as a replacement of earlier existing metal dental frameworks such as crown and bridges. Zirconia existed in three crystalline structures, namely monoclinic, tetragonal, and cubic phase at different temperatures. If the cubic structure of zirconia is restored to room temperature, then it is known as a diamond simulant [1].

Due to the high melting point, hardness, and brittle nature of the complex parts, machining is very difficult through conventional methods owing to the generation of high cutting forces. The zirconia is fabricated through a sintering process; however, complex counters, blind and through holes are very difficult with the desired accuracy. Zirconia plastically deformed during ultrasonic machining with a surface altercation in terms of microcavities and fragments over the machined surface [2]. The pulse laser machining is also possible, but the power consumption and heat-affected zone are the main concerns with the process. The pulse laser machine modifies the machined surface, and its state [3], the problem of cracking in the machined surface also reported [4]. Although some researchers have attempted to machine zirconia material by the EDM process by depositing the layer of conductive material and assisting electrode [5]. Bian et al. [6] conducted the experiments on zirconia by a diamond-coated tool specially designed to machine ceramic material. The results show that the coated tool well suited for 3D micro-structuring applications with a good surface finish.

Jui et al. [7] have studied the electrochemical discharge machining process for machining glass using the tungsten carbide electrode, reported that lower electrolyte concentration improves the overcut of machined holes and surface roughness can be

achieved to 250–300 nm. The electrochemical discharge drilling proceeds in asymmetrical shape during the machining of composites [8]. The performance parameters such as material removal rate, overcut of electrochemical discharge phenomena depend on the governing process parameters. MRR increases with an increase in the voltage, electrolyte concentration, and duty cycle [9]. Chak et al. [9, 10] have machined the alumina ceramic material using the two different tool configuration and claimed that abrasive tool with rotary motion has better performance due to additional features of abrasive grains which helps in maintaining the gap between tool and workpiece. Huang et al. [11] studied the tool wear for drilling of electrochemical machining for stainless steel. They reported that tool wear is inversely proportional to the tool diameter, voltage, and rotational speed. ECDM is a hybrid process using the features of the parent process (EDM and ECM) and is five times faster [12]. Further, it can machine any kind of materials weather metal, alloy, superalloy, composite, and ceramics. ECDM emerges as a cost-effective alternative to earlier existing advanced machining processes [13]. There are certain constraints of the process which needed to be improved for the commercialization of the process [14]. The literature for the ECDM process is summarized in Table 15.1. In the ECDM process, the material is removed by the thermal spark as well as the chemical action of electrolyte. The spark is generated between the tool (cathode) and electrolyte when there is sufficient potential difference between cathode and anode (auxiliary electrode). The potential difference is governed by Eq. 1. The thermal spark generates the high temperature by keeping the workpiece (zirconia) in the vicinity of the thermal spark leads to melting, which further vaporizes the workpiece.

Basak and Ghosh [15, 16] developed the theoretical model to evaluate the critical parameters responsible for material removal. They modeled the process as switching phenomena in an electrical circuit. At higher voltage greater than the critical value, under the electrochemical reaction, the gas bubbles generated at the electrode and due to bubble coalescence, which grows in size analogs to the switching off action. This breaks the contact between tool and electrolyte; once the bubble breaks, the cycle repeats itself. The emf (E) in an electrical circuit is given by:

$$E = -L\frac{dI}{dt} \tag{1}$$

Where L, I, and t are known as inductance, current of the circuit, and time taken during discharge. Later, researchers derived the mathematical equation, which gives agreement with experimental results. Jain and Adhikary [17] observed that reverse polarity machined the ceramics at higher rates, but the surface quality deteriorates compared to direct polarity. Crichton and McGeough [12] studied the mechanism for single discharge stated that process proceeds in four stages, namely the high frequency in phase, high rate ECM, normal ECM, and EDM. Jain et al. [18] explained the spark and discharge occur through gas bubbles intermittently for a short duration as per the valve theory. During bubble coalescence, a high magnitude electric field exists across the tool and electrolyte, resulting in the discharge within gas surrounding the tool [19]. The schematic for the material removal mechanism is shown in Fig. 15.1.

Table 15.1 Summary of the ECDM process parameters

Authors	Cathode and Anode	Electrolyte and W/P	I/P parameters	Response parameters	Inference
Huang et al. [11] 2014	WC (∅0.25–0.4 mm) 304 SS	water 304 SS	V Rotational speed Diameter of tool	Tool wear L16 OA	At high-speed drilling, an empirical mathematical model was developed for tool wear considering the voltage, spindle speed and diameter of the tool as input parameters. It can have concluded that tool wear was affected in the order of voltage, speed and diameter of the tool.
Goud and Sharma [23] 2017	SS (∅0.45 mm) Graphite material	NaOH Quartz glass	V EC Feed rate	MRR WOC L9 OA + GRA	Feed rate is more dominating factor compared to voltage and electrolyte concentration during micromachining of quartz glass. It is also reported that chemical etching has the least effect on material removal, but higher voltage causes overcut on the machined surface

Table 15.1 (continued)

Authors	Cathode and Anode	Electrolyte and W/P	I/P parameters	Response parameters	Inference
Paul et al. [9] 2013	WC ($\emptyset$0.3 mm) Graphite (50 × 30 × 5 mm)	Borosilicate glass ---	V EC DF	MRR OC TWR L9 OA + RSM	Machining capability of borosilicate glass was studied for MRR, TWR and ROC. Due to overheating of top surface and bending of the tool leads to overcut damage for blind holes
Manna and Narang [8] 2012	IS-3748/T35Cr5Mo1V30 ($\emptyset$0.4 mm)	NaOH E-glass fiber epoxy composite	V EC IEG	MRR WOC L16 OA	Simultaneous optimization was done for MRR and spark gap width for micro-drilling operation, which follows in an asymmetrical manner. The burrs were observed across the machined surface. The reinforced epoxy fibers were not properly machined rather burnt under intense heat. The tool gets unevenly wear might be due to improper circulation of electrolyte

(continued)

Table 15.1 (continued)

Authors	Cathode and Anode	Electrolyte and W/P	I/P parameters	Response parameters	Inference
Chak and Rao [24] 2008	Hollow brass tool and cylindrical abrasive tool ($\emptyset$1.5 mm)	NaOH + KOH Alumina (15 × 15 × 7 mm)	V DF Electrolyte conductivity	MRR L20 (CCRD)	Rotary-motioned abrasive tool has more material removal compared to the hollow tool because it provides the extra cutting deed and discharges to enhance material removal
Jui et al. [7] 2013	WC ($\emptyset$0.1–0.3 mm)Steel block (8 mm T)	NaOH Glass (0.2 mm T)	Tool rotation EC	Entrance and exit diameter Taper Tool wear OC Aspect ratio Surface finish	The rotary motion to specially fabricated tool improves the circularity of the micro-hole. The low electrolyte concentration increases the aspect ratio, overcut and tool wear
Zheng et al. [25] 2007	WC ($\emptyset$0.2 mm) Graphite	KOH Pyrex glass	V(pulse) Rotational speed Travel rate	Groove width	Layer-by-layer complex microfeatures were generated on glass for various working depth up to 350 μm. The sidewall taper can be significantly improved from 450 to 250 μm by using a pulse voltage power source

Table 15.1 (continued)

Authors	Cathode and Anode	Electrolyte and W/P	I/P parameters	Response parameters	Inference
Maillard et al. [26] 2007	316L SS (Ø0.4 mm) —	NaOH Soda-lime glass	V Depth	Characterization of micro-holes	The micro-drilling operation was characterized in a different regime called discharge regime for lower depth (100 μm) and hydrodynamic regime for higher depth. Different holes characterized as per different input parameters for machining roundness and standard deviation
Antil et al. [27] 2017	SS (Ø0.4 mm) —	NaOH + HCl Composite	V EC IEG DF	MRR OC Taper	GRA was performed for the optimal combination of input parameters. Inter-electrode gap and voltage were observed as the most significant parameters for MRR, OC and taper
Madhavi and Hiremath [28] 2019	SS (Ø0.37 mm) Graphite (50 × 40 × 5 mm)	KOH Quartz glass (20 × 20 × 4 mm)	V EC DF	MRR TWR Width L9 OA + GRA	45° criss-cross texture was successfully generated on quartz glass using optimized parameters of GRA. At higher penetration of tool during machining, channels become tapered and irregular due to tool wear

K$^+$ ions from electrolyte moving towards cathode to get reduced.

OH$^-$ ions formed at cathode from water and also available from electrolyte moving towards anode to get oxidized forming water and oxygen gas bubbles as a result.

Water molecule reduced to form Hydrogen gas bubbles.

Oxygen gas bubbles evolved at anode

Hydrogen gas bubbles evolved at cathode
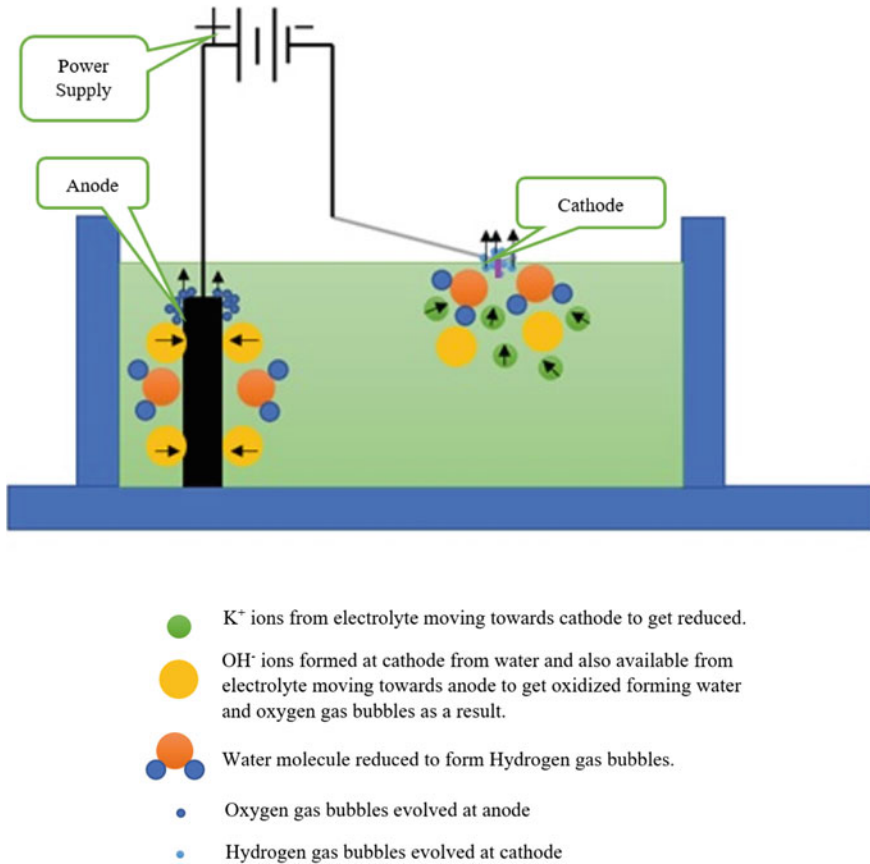
Fig. 15.1 Generation of electrochemical spark

Zirconia is a ceramic material having a melting point 2715 °C, which is the highest among all the material (glass, composite, alumina, etc.) machined earlier by the electrochemical discharge drilling process as shown by Table 15.2. Zirconia is quite hard and brittle. These properties make the machining difficult, and further, very limited literature is available on the machining of Zirconia material. This paper is an attempt to study the ECDD characterization for zirconia material. Further, the voltage parameter was analyzed to find their effect on response parameters.

Table 15.2 Melting point of materials machined by ECDM process

S. No.	Material	Melting point (°C)
1	Borosilicate glass	820
2	Soda-lime glass	573
3	Pyrex glass	820
4	Quartz glass	1683
5	Alumina	2072
6	Brass	900–940
7	Copper	1085
8	E-fiber glass composite	1200

15.2 Materials and Method

The sintered zirconia material is used as a workpiece having a rectangular dimension of 25 × 25 × 3 mm purchased from Hitech ceramics, Chennai, India. The workpiece material is composed of zirconium, oxygen, and yttrium elements. The yttrium element was used as a stabilizing agent to impart desirable properties. The detailed composition and properties are shown in Tables 15.3 and 15.4, respectively.

The stainless steel microtool was used for conducting the experiments. The material selected in such a way that it can withstand high temperature and its properties do not change critically with change in the temperature. The tool material has high electrical conductivity and thermal conductivity for smooth movements of ions across the electrodes. The NaOH electrolyte was preferred over other electrolytes due to high specific conductance. The graphite electrode was used as an auxiliary electrode. The stainless steel tool and graphite rod act as cathode and anode in the electrochemical reaction.

Table 15.3 Composition of Zirconia material

Element	Zirconium	Oxygen	Yttrium	Carbon
Percentage (wt%)	60.68	14.86	7.32	8.46

Table 15.4 Properties of Zirconia material [20, 21]

Properties (unit)	Melting point (°C)	Thermal conductivity (W/mK)	Vicker hardness (H_v)	Toughness (MPa m$^{1/2}$)	Specific heat (J/kg K)	Density (kg/m^3)
Zirconia	2720	2	1200–1300	5.4	400	5680

15.2.1 Experimental Setup

The in-house fabricated setup was developed to conduct the experiments, as shown in Fig. 15.2. The outer structure of the setup was used of a conventional milling machine. The machining chamber was made of Pyrex glass to avoid any splashing of the electrolyte under the action of the thermal spark. The dimensions of the machine chamber were 210 × 100 × 80 mm. The tool and workpiece fixture were made up of nylon material. The vertical movement of the tool is controlled by a gravity feed mechanism. The ohmic-type continuous DC power supply was used for the power requirement of electrochemical discharge phenomena having capacity 0–120 V and current 0–10 amp. The positive output terminal of supply was connected to the auxiliary electrode (anode) and negative terminal to a tool (cathode).

15.3 Methodology

From the past literature, the main governing parameters were identified. It was observed that DC supply is the main influential input parameter. Therefore, an attempt has been made to machine non-conductive zirconia material using one factor at a time (OFAT) approach for DC supply voltage. Table 15.5 represents the fixed parameters that were taken during OFAT experimentations .
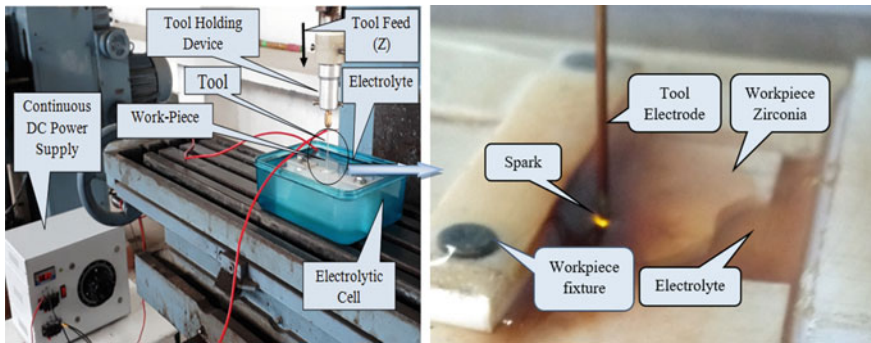
Fig. 15.2 Experimental setup of ECDM [22]

Table 15.5 Fixed parameter for experimental study

Fixed parameters	Machining process	Electrolyte	Machining time (min)	Power input	Workpiece	Tool material
Factors	Micro-ECDM	NaOH	45	DC Power supply	Zirconia (25 × 25 × 3 mm)	Stainless steel (Pointed end cross-section)

15.3.1 Measurements of Response Parameters

The material removal rate (MRR) and overcut (OC) were the response parameters considered for the study. Material removal rate can be calculated by dividing the material removal to the time taken for machining as shown by the Eq. 2, where m_i and m_f are the initial and final weight of the zirconia workpiece before and after machining, respectively, t is the time taken for the machining. The weight was calculated by Denver SI 234 weighing machine for precise measure. In order to avoid the error, the average of three readings was taken as final values. The stereo zoom microscope is used to study machining surface and overcut. The overcut dimensions are measured as the best fit circle obtained by image acquisition; managing and processing ISCapture software comes with a microscope.

$$\text{MRR} = \frac{m_i - m_f}{t} \qquad (2)$$

where

m_i Weight of workpiece before the machining (mg)
m_f Weight of workpiece after machining (mg)
t Time taken during machining (min).

15.4 Results

15.4.1 Effect on MRR

Figure 15.3a shows the effect of DC supply voltage on the material removal rate. The material removal rate increases proportionally with an increase in the DC supply voltage as the material removal is directly related to spark energy available across the machined surface governed by the Eq. 1. Therefore, with an increase in DC supply voltage, the spark intensity increases, which helps in material removal. For fixed
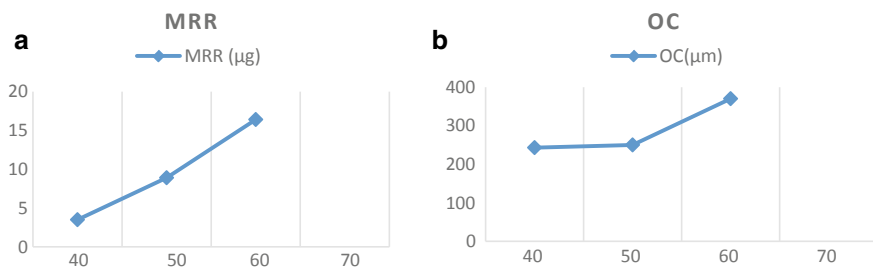
Fig. 15.3 a Effect of voltage on MRR **b** Effect of voltage on overcut

parameters, the spark is observed after 26 volts, and therefore, minimum material removal occurred. The material removal rate increased till 60 volts, and afterthat, the zirconia workpiece got fractured. This might be due to the intensity of thermal sparks that overcome the fractural toughness of the workpiece.

15.4.2 Effect on Overcut

The overcut parameter is governed by spark intensity and discharge area surrounding the tool. It was observed at a lower voltage (30 V), the micro-hole obtained almost circular, due to smooth sparking, but as the voltage is increased, the more overcut can be observed. The surface damage across the circumference is considerably high, as ovality can be easily observed. This might be due to the unstable thermal spark available at a tool which unevenly affects the surface.

15.4.3 Morphology of Machined Surface

The optical microscopic images is used to characterize the machined holes. The result of micro-holes for operating voltage 40 V is shown in Fig. 15.3a. The machined surface shows that at low voltage, the micro-hole obtained is smooth and circular. But as the voltage is increased to 50 V, the slight deviation is observed, as shown in Fig. 15.3b (Fig. 15.4a, b).

In order to study the morphology of the machined surface, an energy dispersive spectroscopy test is performed. It was observed that there is a deposition of
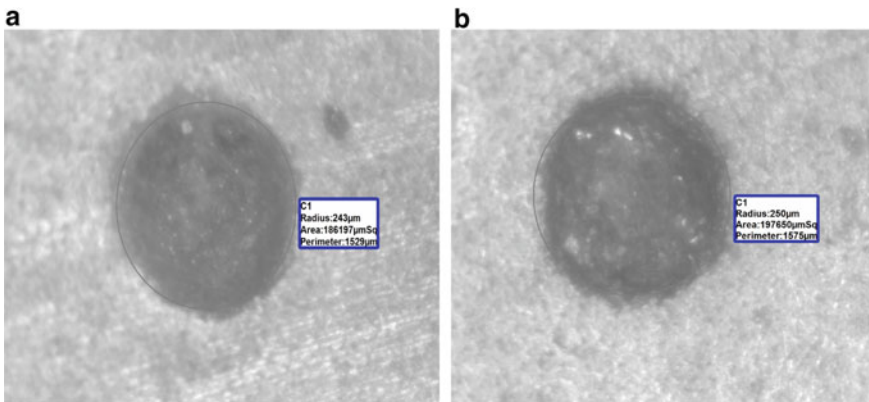
Fig. 15.4 **a** Micro-hole at voltage 40 V **b** Micro-hole at voltage 50 V
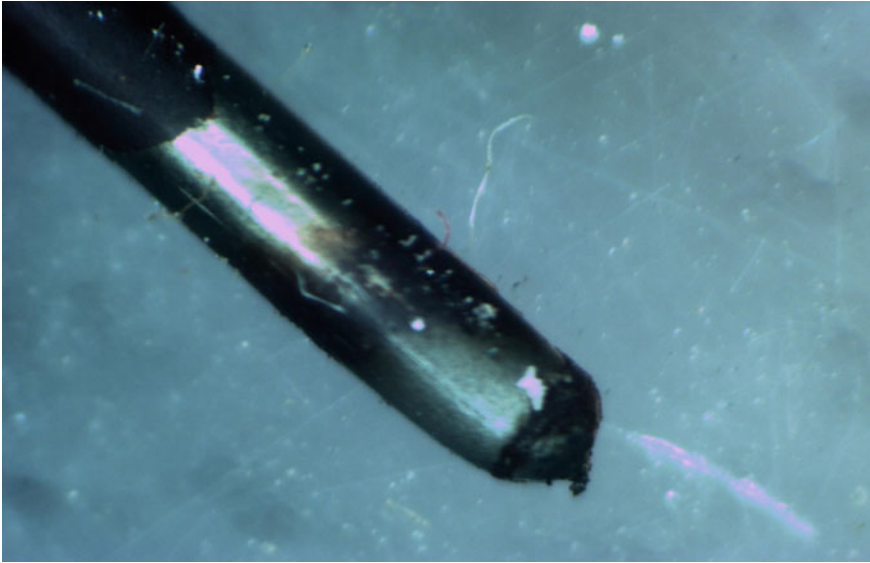
Fig. 15.5   ECDM tool after machining

the oxide layer along with the presence of the iron element. The iron element presented, due to the phenomena of pyrolysis at higher temperatures resulting in oxidation of the machined surface. There might be steel tool material transfer from cathode to anode during discharge. Overall, very minute changes are observed in the composition of parent zirconia material during machining.

15.4.4   Effect on Tool Wear

Figure 15.5 shows the tool conditioning after machining at 60 volts for 45 min. From the tip and circumference of the tool, the black burning effect of electrical discharge can be observed. The tool wear increases with an increase in the DC supply voltage as the intensity of thermal spark increases with an increase in the voltage.

15.5   Conclusion

In the present study, the feasibility of micro-holes on zirconia material is studied using developed electrochemical discharge machining (ECDM) setup. The one factor at a time (OFAT) approach is used to study the effect of voltage parameter on the response of material removal rate and overcut. The following main conclusions are drawn from the study.

1. The in-house fabricated ECDM setup can be successfully used for micro-holes on zirconia material.
2. The material removal rate and overcut increase with an increase in voltage. At higher voltage, the overcut becomes a severe problem.
3. The frequent workpiece fracture was observed for voltage 70 V and above, and this might be due to the brittle nature of the workpiece, which fails to sustain the intensity of the thermal spark.
4. The gas fumes evolve during machining are partially toxic in nature, and the separate mechanism is recommended to dispose the same. The precaution should be taken during the handling of electrolyte as it causes etching effect on the skins.
5. EDX results show the change in machined surface morphology after machining as there is the deposition of carbon and oxide layer. Further, the iron element is transferred from stainless steel to a machined surface during machining.

References

1. Schünemann, F.H., Galárraga-Vinueza, M.E., Magini, R., et al.: Zirconia surface modifications for implant dentistry. Mater. Sci. Eng. C **98**, 1294–1305 (2019). https://doi.org/10.1016/j.msec.2019.01.062
2. Bhosale, S.B., Pawade, R.S., Brahmankar, P.K.: Effect of process parameters on MRR, TWR and surface topography in ultrasonic machining of alumina-zirconia ceramic composite. Ceram. Int. **40**, 12831–12836 (2014). https://doi.org/10.1016/j.ceramint.2014.04.137
3. Kuzin, V.V., Grigoriev, S., Fedorov, M., et al.: Surface modification of Zirconia (Y-TZP) Ceramics induced by pulsed laser machining. Appl. Mech. Mater. **752–753**, 481–484 (2015). https://doi.org/10.4028/www.scientific.net/amm.752-753.481
4. Dear, F.C., Shephard, J.D., Wang, X., et al.: Pulsed laser micromachining of yttria-stabilized zirconia dental ceramic for manufacturing. Int. J. Appl. Ceram. Technol. **5**, 188–197 (2008). https://doi.org/10.1111/j.1744-7402.2008.02203.x
5. Banu, A., Ali, M.Y., Rahman, M.A.: Micro-electro discharge machining of non-conductive zirconia ceramic: investigation of MRR and recast layer hardness. Int. J. Adv. Manuf. Technol. **75**, 257–267 (2014). https://doi.org/10.1007/s00170-014-6124-9
6. Bian, R., Ferraris, E., He, N., Reynaerts, D.: Process investigation on meso-scale hard milling of ZrO_2 by diamond coated tools. Precis. Eng. **38**, 82–91 (2014). https://doi.org/10.1016/j.precisioneng.2013.07.007
7. Jui, S.K., Kamaraj, A.B., Sundaram, M.M.: High aspect ratio micromachining of glass by electrochemical discharge machining (ECDM). J. Manuf. Process. **15**, 460–466 (2013). https://doi.org/10.1016/j.jmapro.2013.05.006
8. Manna, A., Narang, V.: A study on micro machining of e-glass-fibre-epoxy composite by ECSM process. Int. J. Adv. Manuf. Technol. **61**, 1191–1197 (2012). https://doi.org/10.1007/s00170-012-4094-3
9. Paul, L., Hiremath, S.S.: Response surface modelling of micro holes in electrochemical discharge machining process. Procedia Eng. **64**, 1395–1404 (2013). https://doi.org/10.1016/j.proeng.2013.09.221
10. Chak, S.K.: Spark-assisted electrochemical drilling of ceramics. Int. J. Precis. Technol. **6**, 171–189 (2016)
11. Huang, S.F., Liu, Y., Li, J., et al.: Electrochemical discharge machining micro-hole in stainless steel with tool electrode high-speed rotating. Mater. Manuf. Process. **29**, 634–637 (2014). https://doi.org/10.1080/10426914.2014.901523

12. Crichton, I.M., McGeough, J.A.: Studies of the discharge mechanisms in electrochemical arc machining. J. Appl. Electrochem. **15**, 113–119 (1985). https://doi.org/10.1007/BF00617748

13. Singh, J., Vaishya, R., Kumar, M.: Fabrication of micro features on quartz glass using developed wecdm setup. ARPN J. Eng. Appl. Sci. **14**, 725–731 (2019)

14. Dhiman, P., Vaishya, R., Kumar, M.: A review on machining by electrochemical discharge phenomena. Int. J. Tech. Innov. Mod. Eng. Sci. **5**, 71–74 (2019)

15. Basak, I., Ghosh, A.: Mechanism of spark generation during electrochemical discharge machining: a theoretical model and experimental verification. J. Mater. Process. Technol. **62**, 46–53 (1996). https://doi.org/10.1016/0924-0136(95)02202-3

16. Basak, I., Ghosh, A.: Mechanism of material removal in electrochemical discharge machining: a theoretical model and experimental verification. J. Mater. Process. Technol. **71**, 350–359 (1997). https://doi.org/10.1016/S0924-0136(97)00097-6

17. Jain, V.K., Adhikary, S.: On the mechanism of material removal in electrochemical spark machining of quartz under different polarity conditions. J. Mater. Process. Technol. **200**, 460–470 (2008). https://doi.org/10.1016/j.jmatprotec.2007.08.071

18. Jain, V.K., Dixit, P.M., Pandey, P.M.: On the analysis of the electrochemical spark machining process. Int. J. Mach. Tools Manuf. **39**, 165–186 (1999). https://doi.org/10.1016/S0890-6955(98)00010-8

19. Kulkarni, A., Sharan, R., Lal, G.K.: An experimental study of discharge mechanism in electrochemical discharge machining. Int. J. Mach. Tools Manuf. **42**, 1121–1127 (2002). https://doi.org/10.1016/S0890-6955(02)00058-5

20. Kucukturk, G., Cogun, C.: A new method for machining of electrically nonconductive workpieces using electric discharge machining technique. Mach. Sci. Technol. **14**, 189–207 (2010). https://doi.org/10.1080/10910344.2010.500497

21. Mohri, N., Fukuzawa, Y., Tani, T., Sata, T.: Some considerations to machining characteristics of insulating ceramics—towards practical use in industry. CIRP Ann. Manuf. Technol. **51**, 161–164 (2002). https://doi.org/10.1016/S0007-8506(07)61490-5

22. Rajput, V., Goud, M., Suri, N.M.: Experimental investigation to improve the removal rate of material in ECDM process by utilizing different tool electrode shapes. Int. J. Tech. Innov. Mod. Eng. Sci. **5**, 333–341 (2019)

23. Goud, M., Sharma, A.K.: On performance studies during micromachining of quartz glass using electrochemical discharge machining. J. Mech. Sci. Technol. **31**, 1365–1372 (2017). https://doi.org/10.1007/s12206-017-0236-8

24. Chak, S.K., Venkateswara Rao, P.: The drilling of Al_2O_3 using a pulsed DC supply with a rotary abrasive electrode by the electrochemical discharge process. Int. J. Adv. Manuf. Technol. **39**, 633–641 (2008). https://doi.org/10.1007/s00170-007-1263-x

25. Zheng, Z.P., Cheng, W.H., Huang, F.Y., Yan, B.H.: 3D microstructuring of Pyrex glass using the electrochemical discharge machining process. J. Micromechanics Microengineering **17**, 960–966 (2007). https://doi.org/10.1088/0960-1317/17/5/016

26. Maillard, P., Despont, B., Bleuler, H., Wüthrich, R.: Geometrical characterization of microholes drilled in glass by gravity-feed with spark assisted chemical engraving (SACE). J. Micromechanics Microengineering **17**, 1343–1349 (2007). https://doi.org/10.1088/0960-1317/17/7/017

27. Antil, P., Singh, S., Manna, A.: Electrochemical discharge drilling of SiC reinforced polymer matrix composite using Taguchi's Grey relational analysis. Arab J. Sci. Eng. **43**, 1257–1266 (2018). https://doi.org/10.1007/s13369-017-2822-6

28. Madhavi, J.B., Hiremath, S.S.: Machining and characterization of channels and textures on quartz glass using μ-ECDM Process. Silicon (2019). https://doi.org/10.1007/s12633-019-0083-6

Chapter 16
Experimental Investigation on the Effect of Grinding Infeed and Pass Counts on Grindability of Mild Steel

Pranab Kumar Kundu, Bishan Raj Rai, and Manish Mukhopadhyay

Abstract Grinding is an important machining operation, widely used to obtain finished or semi-finished surfaces of different materials. Mild steel, being one of the mostly used materials in practice, also needs grinding in many cases where it is used in the devices with high precision. However, grinding being a complex operation exhibits several adversities while operated on mild steel. In the present experimental investigation, the grindability of mild steel specimens are thoroughly evaluated at different grinding infeed values and also with changes in number of passes. The typical parameters for accessing the grindability, e.g., surface hardness, surface roughness, ground surface quality and volume of material removal are measured and discussed in details. Two grinding infeed values, viz. 10 and 20 μm are conceived while grinding under four sets of pass counts, i.e., 5, 10, 15 and 20. Experimental results reveal that grinding for 15 pass counts at 10 and 20 μm infeed values are the ideal set of parameters in the operating ranges considered herein.

Keywords Dry grinding · Mild steel · Grindability · Alumina wheel

16.1 Introduction

Conventional grinding wheels are manufactured from the abrasive grains of different ceramic materials. These tiny abrasive grains containing micro-edges have the ability to remove material from a workpiece substrate in the order micron or submicron. Hence, it can produce a surface with high accuracy and high surface finish that motivates grinding process to be used largely as finishing operations for many components, and also for sharpening the cutting tool edges of many materials. Nevertheless, grinding is also used for bulk material removal in some instances. Due to random orientations of the abrasive grits in grinding wheel, the exposed cutting edges are mostly having negative rake angles. Furthermore, the grinding wheel rotates at a

P. K. Kundu (✉) · B. R. Rai · M. Mukhopadhyay
Department of Mechanical Engineering, National Institute of Technology Sikkim, Ravangla, South Sikkim 737139, India
e-mail: pranabkundu@gmai.com

very high speed during which a huge number of undefined cutting edges are involved in material removal resulting in high demand of specific energy consumption that makes the process more complex [1, 2].

Mild steel (MS), also known as low carbon steel and plain carbon steel is widely employed metal in various industrial and non-industrial applications due to its low cost, excellent machinability, good strength and other structural properties, easy availability, high ductility and malleability. MS contains very low amount of carbon, approximately ranging from 0.05 to 0.25% that results in a relatively low tensile strength and low surface hardness. However, the surface hardness can be increased subsequently using process like carburizing. There are many MS components used for the devices that need to be machined with high-dimensional accuracy, close tolerances and high surface finish making the grinding process important [3]. Grinding being a complex process becomes more challenging while applied on MS as it has a tendency to adhere in between the grits of the grinding wheel due to its high ductility leading to the phenomena, known as wheel loading [1, 2, 4]. The process escalates due to the generation of high heat flux that results in high temperature at the machining zone [4]. This wheel loading forces the grinding wheel to be dressed more frequently during which the outer layer of the wheel is removed and fresh grits from subsequent layer are exposed with the help of a dressing tool. Moreover, due to the generation of high temperature at the grinding zone, the surface finish, accuracy and the surface quality of the ground substrate are deteriorated [5].

Several researchers have been trying to overcome these challenges by improving the parameters responsible to assess the grindability such as using optimized dressing infeed, applying different cutting fluid via different fluid delivery systems, using scrapper board, using rexine-pasted wheels, varying coolant concentration, etc. [4, 6–13]. Kundu et al. [4] experimented on the grinding of MS using scrapper board to restrict the stiff air layer formation that opposes the grinding fluid to reach into the machining zone. Employing the scrapper board, they observed enhanced grindability in terms of obtaining better ground surface and grinding ratio. Mukhopadhyay and Kundu investigated a simple an economic yet effective delivery setup and termed as restricted quantity lubrication (RQL), which can throw the fluid at a very low rate of 3.5 ml/sec [9]. They observed better grindability while compared with flood cooling and dry grinding environments. Rai et al. [14] studied the change in the surface quality under varying in number of passes while grinding on superalloy, Ti–6Al-4 V and observed better results while 15 number of passes were run. In some different studies, Kundu and his co-researchers investigated the potentiality of several unconventional environment-friendly cutting fluids under different modes of fluid delivery and using both SiC and alumina grinding wheels [11, 12]. They observed propylene glycol to perform better in every aspect.

Grinding of MS exhibits severe wheel loading due to its high affinity to the conventional wheel material and formation of long chips resulted due to its high ductility. Chattopadhyay and his co-researchers [15, 16] experimented using brazed monolayer wheels and found it to be suitable to grind sticky material like MS. However, the brazed diamond wheel is not suitable to grind MS as graphitization occurs at elevated temperature due to the high affinity of carbon to MS [17]. Cubic boron nitride

(cBN) is another option in the formation of monolayer grinding wheel to grind MS. However, due to low carbon and high free iron contents in MS, the tribochemical reaction takes place at an elevated temperature while using monolayer cBN wheel, during which boron nitride diffuses continuously into the flowing iron oxide chips, and subsequently forms compounds like Fe2B [18]. Hence, conventional wheels are widely used to grind MS.

Researchers aimed toward the solution of challenges faced while grinding MS using conventional wheels. In this experimental study, an effort has been made to study the changes in the hardness, roughness and volume of material removal of mild steel, with the change in infeed values and number of pass counts.

16.2 Experimentation

Experiments are performed on a horizontal grinding machine (Bhavya M/C Tools) under dry environments. Rectangular MS plates of dimensions 65 mm × 32 mm × 6 mm and hardness 69 HRB have been considered for the present experimental study. Aluminum oxide wheel of 200 mm diameter has been trued before the starting of the experimentation followed by workpiece truing. First, the wheel is dressed with a 0.75 karat single point diamond dresser with an infeed of 20 µm, which is the optimized dressing infeed for conventional wheels [6, 7]. A constant wheel speed of 2800 rpm is maintained throughout the dressing and experimentations. To eliminate error in dimensional accuracy, spark out process has been performed during each set of experimentations in which the wheel is passed through the workpiece until all the sparks vanish. Two infeed values, e.g., 10 and 20 µm have been employed while grinding MS for four different number of pass counts, viz. 5, 10, 15 and 20. Each pass is comprised of both down and up grinding, and infeed has been applied during both the passes. The height of the workpiece is measured before and after every set of pass count using a Vernier caliper. The hardness of the workpiece is measured using a Rockwell Cum Brinell hardness tester while the average roughness parameters are measured with the help of a mechanical type stylus (Mitutoyo, Japan). The details of experimentation and equipment used are depicted in Table 16.1. The grinding process is shown in Fig. 16.1.

16.3 Problem Solution Results and Discussion

In the present experimental study, the effects of grinding infeed and number of pass counts on grindability of MS has been thoroughly investigated. The changes in hardness, surface roughness and volume of material removal roughness under different experimental parameters, and also the visible surface burns have been observed, recorded and analyzed. Figure 16.2 represents the variations of the hardness, before and after grinding, with the number of pass counts at various infeed values. It can

Table 16.1 Details of experimentation and equipment

Surface grinding machine	Make: Bhavya M/C Tools Model: BSG-225 Maximum spindle speed: 2800 rpm
Grinding wheel	Make: Carborundum Universal Limited; Type: Disk Dimensions: 200 × 31.75 × 13 Specifications: AA46/56 K5 V8
Rockwell and Brinell hardness tester	Make: Blue Star Limited Model: BSHT-250FRB; Load: 60-250 kgf
Wheel dresser	Make: Solar, India Specification: 0.5 karat single point diamond tip Dressing infeed: 20 µm
Surface roughness tester	Make: Mitutoyo, Japan Model: SJ-210; Range: 17.5 × 103 µm; Resolution: 0.001 µm
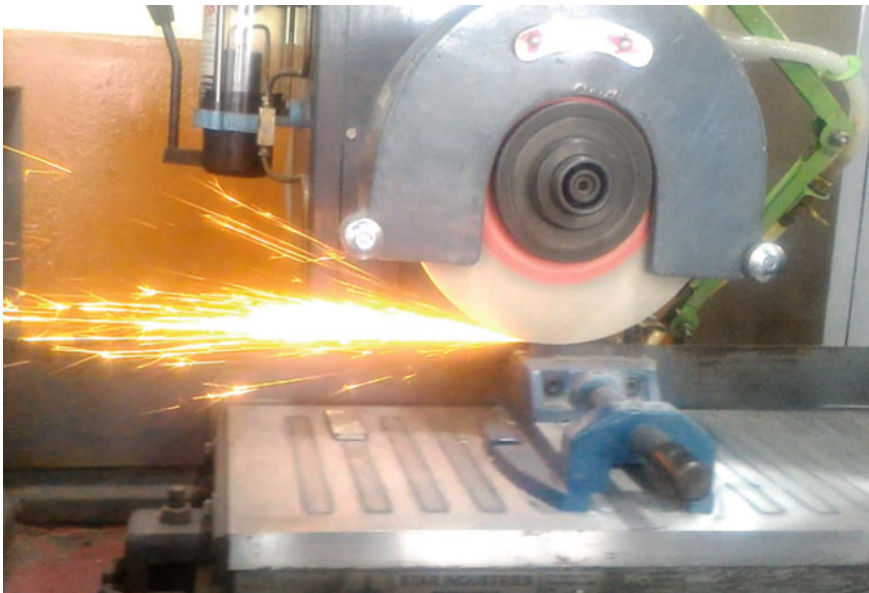
Fig. 16.1 Grinding of mild steel

be observed from these figures that the hardness of mild steel decreases first, and it increases prominently when infeed and number of pass counts are increased. This may be due to the work softening that might have occurred for air cooling in dry grinding processes. The effect of annealing with air cooling is significantly distinguishable that leads to work softening.

Figure 16.3 depicts the variations of average roughness parameters (Ra) of the ground MS surface with the number of passes at different infeed values. The roughness values tend to increase as expected with infeed values and pass counts. However, in some cases, the values are found to be unexpectedly lesser. This may be due to the excess rubbing and glazing during those pass counts.

Figure 16.4 represents the images of the grinding wheel employed during the experimentation at various infeed values and pass counts. From these figures (Fig. 16.4a–e), it is evident that the wheel loading is not prominent while grinding is performed at 10 μm infeed. This is because of the fact that at low infeed small chips are formed, which have lesser tendency to adhere in between the wheel grits. Additionally, as the specific energy requirement is comparatively less, lesser amount of heat is generated. However, the loading has been increased while the grinding is

(a) 5 passes   (b) 10 passes   (c) 15 passes   (d) 20 passes

10 μm infeed for different pass counts

(e) 5 passes   (f) 10 passes   (g) 15 passes   (h) 20 passes

20 μm infeed for different pass counts
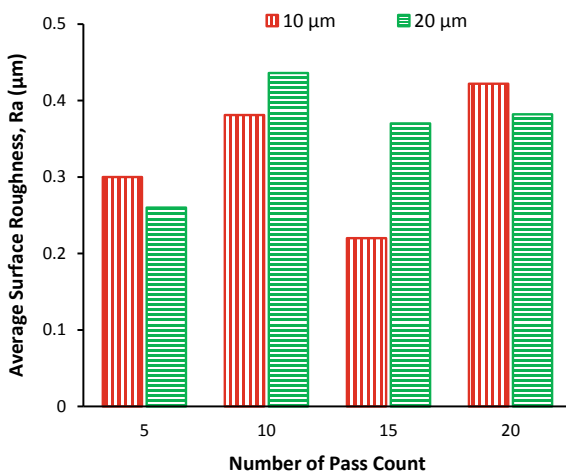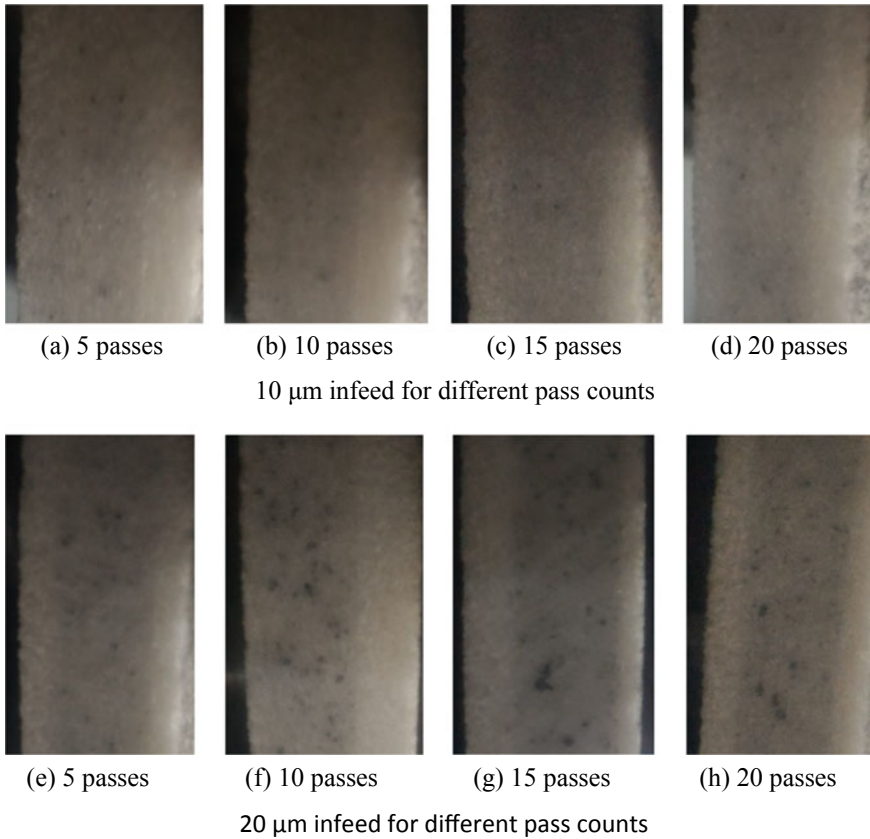
Fig. 16.4 Wheel loading under different pass counts

performed at 20 μm infeed under every pass count as expected due to the formation of long leafy chips. With the increase in number of pass counts, the loading has also increased in every set of experimentations due to the increase in adherence of chips in between the grit spaces with the increase in the number of passes.

Micrographs of the ground MS surfaces have been captured and presented in Fig. 16.5. From these figures, it can be stated that better surfaces have been obtained while grinding with 15 pass counts at both 10 and 20 μm infeed values. In Fig. 16.5g–h, visible burns indicate the generation of high temperature while grinding is performed at 20 μm infeed and at an elevated number of pass counts. No visible burs have been noted during grinding at 10 μm infeed as heat generation is less due to low-specific energy consumptions.

The volume of material removal has been measured after each set of experimentation and presented in Fig. 16.6. From this figure, it can be noticed that the volume of material removal has increased with the increase in infeed and number of passes. It is obvious that when the infeed is increased more an amount of abrasive grits is

(a) 5   (b) 10   (c) 15   (d) 20

10 μm infeed for different pass counts

(e) 5   (f) 10   (g) 15   (h) 20

20 μm infeed for different pass counts
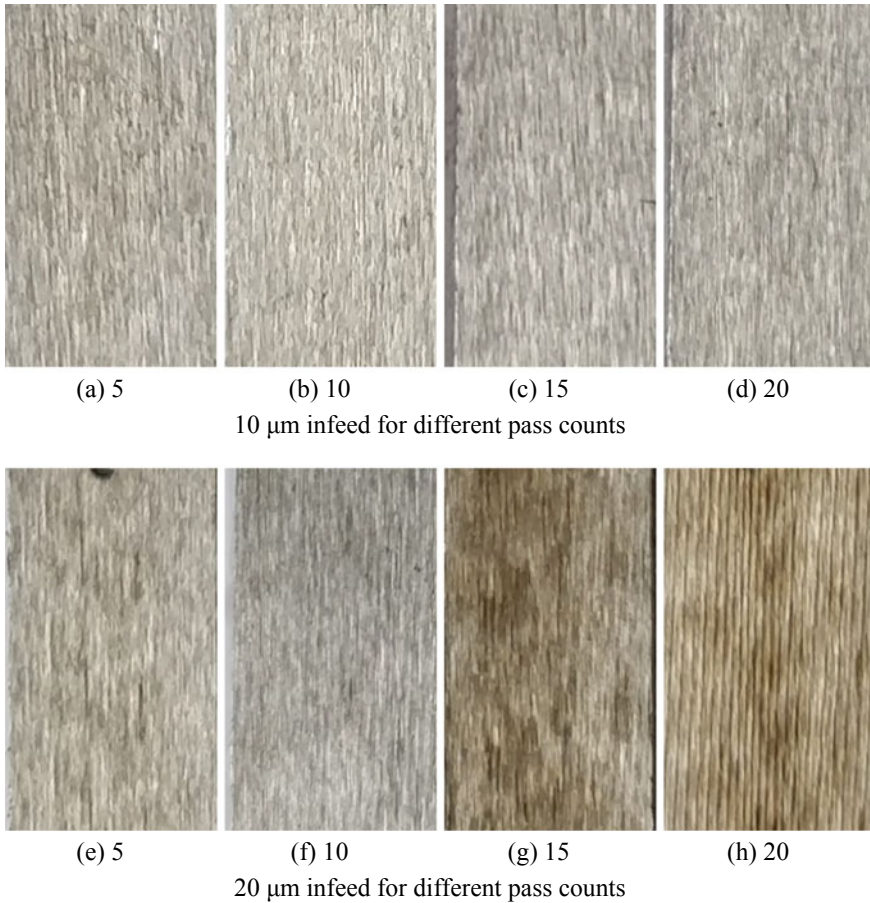
Fig. 16.5 Micrographs of ground surfaces under different infeed values

protruded into the workpiece resulting in higher amount of material removal. Furthermore, with the increase in number of pass counts, the wheel passes through the workpiece for more number of times at a given infeed that leads to the greater volume of material removal.

16.4 Conclusions

In the present experimental study, the effects of grinding infeed and number of pass counts on grindability of MS has been thoroughly investigated. The following major conclusions are drawn from the present study.

Fig. 16.6 Volume of
material removal under
different infeed values
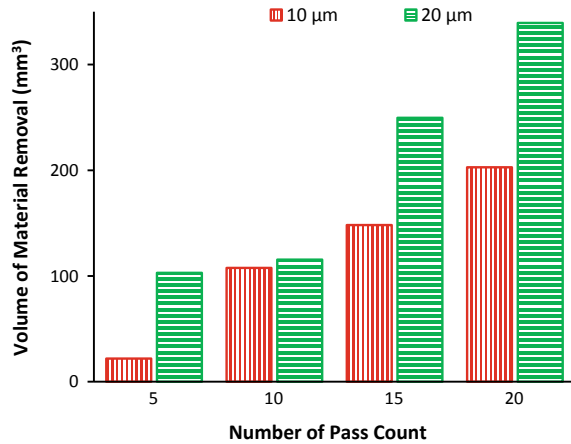
- The work softening due to air cooling during grinding of MS resulted in a decrease in the hardness.
- Grinding for 15 pass counts at both 10 and 20 μm infeed values are found to be better parameters in context of surface quality obtained herein.
- Volume of material removal has increased with the increase in the infeed and number of pass counts.

References

1. Malkin, S., Guo, C.: Grinding technology: theory and application of machining with abrasives. Industrial Press Inc. (2008)
2. Lindsay, R.P.: Principles of grinding. In: Handbook of Modern Grinding Technology. Chapman and Hall Advanced Industrial Technology Series. Springer, Boston, MA (1986)
3. Khan, A.A., Mridha, S., Ali, M.Y.: Cryogenic grinding of mild steel and stainless steel. J. Manu. Sci. Prod. **10**(1), 69–74 (2009)
4. Kundu, P.K., Das, S., Sinha, S., Chowdhury, P.P.: On grinding wheel performance in dry and wet conditions. In: Proceedings of 4th International Conference on Mechanical Engineering, BUET Dhaka, pp. 19–24
5. Mukhopadhyay, M., Kundu, P.K.: Laser assisted conditioning of Aluminium Oxide grinding wheel using Nd: YAG laser: a review. In: Proceedings of National Conference on Advanced Functional Materials Processing & Manufacturing, CMERI Durgapur, pp. 63–66, 2–3 Feb 2017
6. Mukhopadhyay, M., Kundu, P.K.: Optimization of dressing infeed of Alumina wheel for grinding Ti-6Al-4 V. Mater. Manu. Process. **33**(13), 1453–1458 (2018)
7. Mukhopadhyay, M., Kundu, P.K.: Impact of dressing infeed on SiC wheel for grinding Ti-6Al-4 V. Mater. Manu. Process. **34**(1), 54–60 (2019)
8. Mukhopadhyay, M., Kundu, P.K., Das, S.: Experimental investigation on enhancing grindability using alkaline based fluid for grinding Ti-6Al-4 V. Mater. Manu. Proces. **33**(16), 1775–1781 (2018)
9. Mukhopadhyay, M., Kundu, P.K.: Development of a simple and efficient delivery technique for grinding Ti-6Al-4 V. Int. J. Mach. Machina Mater. **20**(4), 345–357 (2018)

10. Mukhopadhyay, M., Kundu, P.K.: Laser dressing of grinding wheels—a review. Int. J. Mech. Manu. Syst. **11**(2/3), 167–181 (2018)
11. Mukhopadhyay, M., Kundu,P.K.: Evaluating application potentiality of unconventional fluids for grinding Ti-6Al-4 V using Alumina wheel. Mater. Manu. Proces. **34**(10), 1151–1159 (2019)
12. Mukhopadhyay, M., Kundu, P.K.: Enhancing grindability of Ti-6Al-4 V applying ecological fluids under SQL using SiC wheel. SN App. Sci. **1**(600) (2019)
13. Mukhopadhyay, M., Kundu, P.K.: Performance evaluation of conventional abrasive wheels for grinding Ti-6Al-4V. IOP Con. Ser. Mater. Sci. Eng. **377**
14. Rai, B.R., Mukhopadhyay, M., Kundu, P.K.: Evaluating the grinding ratio and surface quality of Ti-6Al-4V under varying grinding pass count and depth of cut. In: 2nd International conference on New Frontiers in Engineering, Science and Technology, NIT Kurukshetra, 18–22 Feb 2019
15. Hintermann, H.E., Chattopadhyay, A.K.: New generation superabrasive tool with monolayer configuration. Dia. Rel. Mater. **1**, 1131–1143 (1992)
16. Chattopadhyay, A.K., Chollet, L., Hintermann, H.E.: On performance of brazed bonded monolayer diamond grinding wheel. CIRP Annals Manu. Tech. **40**, 347–350 (1991)
17. Malkin, S.: Current trends in CBN grinding technology. CIRP Ann. **34**(2), 557–563 (1985)
18. Malkin, S., Cook, N.H.: The wear of grinding wheels: part 1—attritious wear. J. Eng. Ind. **93**(4), 1120–1128 (1971)

Chapter 17
Effect of Cryogenic Treatment on Mechanical and Metallurgical Properties of SS410

Amrinder Singh, Anuj Bansal, Jagtar Singh, and Anil Kumar Singla

Abstract Martensitic grade SS410 is used extensively for manufacturing of turbine blades and other hydro-machinery components. During working of such components, due to poor mechanical properties of the material, the components lose its functionality and life of such components decreases. In this regard, the improvement in the material properties is essential, to enhance the life of such components. For improving the mechanical and metallurgical properties of the material, deep cryogenic treatment (DCT) can be effectively used. In this research work, DCT followed by tempering at two temperatures 350 and 250 °C has been performed on SS410. The SS410 specimens with and without DCT were tested for tensile strength, toughness, and micro-hardness. It has been observed that DCT followed by post-tempering at 250 °C has shown better results in terms of ultimate tensile strength (UTS) and micro-hardness as compared to its counterparts. This may correspond to the conversion of retained austenite to martensite and formation of fine secondary carbides.

Keywords Deep cryogenic treatment · Tempering · SS410 · Martensitic

Nomenclature

DCT	Deep cryogenic treatment
HT	Heat treatment
SS	Stainless steel
ASTM	American Society for Testing and Materials
UTS	Ultimate tensile strength
HV	Vickers micro-hardness
YS	Yield strength

A. Singh · A. Bansal (✉) · J. Singh · A. K. Singla
Department of Mechanical Engineering, Sant Longowal Institute of Engineering and Technology, Sangrur 148106, India
e-mail: anujbansalsliet@gmail.com

17.1   Introduction

Martensitic SS410 is a high chromium steel, which has high wear resistance and high corrosion resistance as compared to the other counterparts belong to steels family. Due to its wide expediency, SS410 is used extensively in the hydro-turbine blade, shafts, pumps, and valves, etc. During the functionality, such parts are exposed to the troublous working conditions, which intern degrade the material and component losses its functionality [1–3]. Such problem encountered by the industry, lead to a bigger financial loss. The resistance offered by the material to the severe working conditions, mainly depends upon the mechanical and metallurgical properties of the material. Many researchers tried conventional HT, thermal spray coatings to enhance the mechanical and physical properties of material surface [4–7], which even shows promising results. On the other side, Molinari et al. [9] concluded that DCT with tempering and quenching significantly enhances the mechanical and physical properties of tool steel, the similar results in the favor of DCT were also concluded by some other researchers [8, 10–24]. By keeping the above facts into consideration, the DCT along with the tempering may be a good alternative solution to enhance the mechanical and metallurgical properties of the said steels. So, in the present study, DCT with tempering at two temperatures (350 and 250 °C) was performed on SS410 material. Further, a comparative study of DCT material SS410 tempered at 350 and 250 °C vis-à-vis the substrate material and was also done with respect to mechanical and metallurgical properties.

17.2   Experimental Procedure

17.2.1   Material Selection and Specimen Preparation

Due to wide expediency of the material, high chromium martensitic SS410 was chosen for the present research work. The spectroscopy test of the as received material was carried out and the material was found to have 12.3354% Cr, 0.1342% C, 0.9865% Si, 0.9517% Mn, 0.0381% P, 0.0257% S, and 85.5284% Fe. The material composition was found to be in limits of the standard composition. Further, the specimens were prepared for Charpy impact test from raw material strip according to ASTM A370 standard dimensions, and the notches were prepared using wire EDM. The specimen for tensile test was prepared according to ASTM-E8 standard by using wire EDM from the raw material strip. For testing of micro-hardness, ASTM-E384 standard was used to prepare the specimens [19].
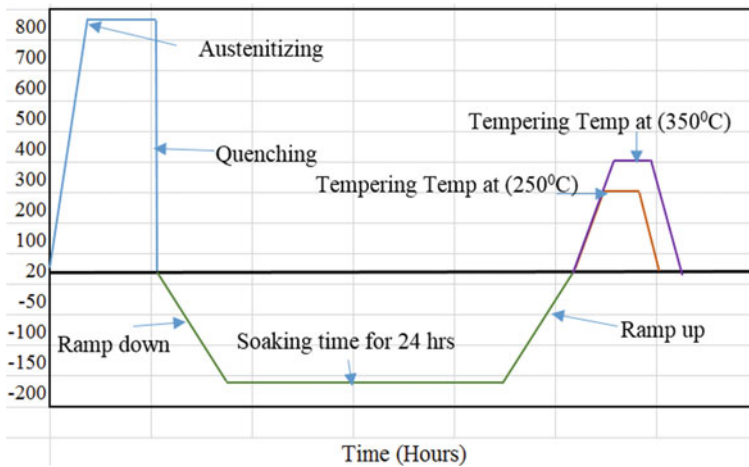
Fig. 17.1 Representation of used DCT cycle with tempering

17.2.2 Deep Cryogenic Treatment (DCT)Cycle

As per Liu et al. [8], DCT converts retained austenite into martensite, due to this, hardness and toughness of steel must be enhanced. DCT is basically a type of heat treatment in which material is kept at low temperature for 24–72 h to enhance the metallurgical and mechanical properties of the material. In the study, DCT on said specimens was performed as per the cycle represented in Fig. 17.1.

To perform DCT on specimens, 12-24-12 cycle was used. In first 12 h, cryogenic chamber temperature was ramp down to −185 °C from the room temperature using controlled supply of liquid nitrogen, for next 24 h, cryogenic chamber temperature was held constant at −185 °C and in next 12 h cryogenic chamber temperature was ramp up to atmospheric temperature. To reduce internal stresses generated during the DCT treatment, post-tempering was performed on SS410 specimens at two different temperatures 350 and 250 °C as represented in the cycle, shown in Fig. 17.1.

17.2.3 Mechanical Properties

Mechanical properties like yield strength (YS), ultimate tensile strength (UTS), Charpy impact toughness, and Vickers micro-hardness (HV) were measured for the untreated and cryogenically treated SS410 specimen tempered at two different temperatures. The tensile strength of the said samples was calculated by using the Tinius Olsen, Model: HK 50 (capacity: 50kN) machine. The specimens as per the ASTM-E8 standard were used for the testing. Stress-strain graph produced during the test are used to analyze the effect of DCT on the strength of SS410. Further,

Vickers diamond pyramid test machine (MVH-II, OMNITECH, India) is used to measure the micro-hardness values. The specimens were prepared as per the ASTM-E384 standard and polished using emery paper size from 100 grits to 2000 grits, to make the surface clear from the scratches, before subjecting to micro-hardness test. Diamond indenter with indent angle 136° between two opposites face was used for making an intent on said specimen's surfaces. The load used during the testing was 1000 gm for a dwell time of 15 s. Impact test measures the amount of energy stored by specimen before its fracture. This stored energy is known as toughness of specimen. Six specimens were prepared from untreated and deep cryogenically treated material followed by tempering at two different temperatures, according to ASTM A370 standards for conducting of Charpy impact test.

17.2.4 Metallurgical Analysis

Microstructural analysis of untreated and DCT specimens tempered at different tempering temperatures was conducted with the help of an inverted trinocular microscope (Qualitech Systems, India). After polishing specimens with abrasive papers size from 150 to 3000 grits, velvet cloth along with the alumina powder was used to achieve finished surface. The Kalling's etchant was used for microstructural analysis. The etchnat was prepared by mixing 5 gm cupric chloride in a mixture of 100 ml ethanol and 100 ml hydrochloric acid. The samples were immersed in the said etchant for 40 s, to get the structure revealed.

17.3 Results and Discussion

17.3.1 Tensile Strength

The average value of YS, UTS, % elongation, and % RA values obtained for specimens corresponding to untreated material along with the cryo-treated material tempered at 250 and 350 °C are shown in Table 17.1 and compared in Fig. 17.2.

Table 17.1 Ultimate strength for DCT treated and untreated specimens

Sample name	Tensile test			
	Average YS (MPa)	Average UTS (MPa)	Average elongation (%)	Average RA (%)
Untreated 410	485	519	27.5	56.8
410 (350 °C)	528	541	24.8	49.1
410 (250 °C)	569	598	21.9	40.3
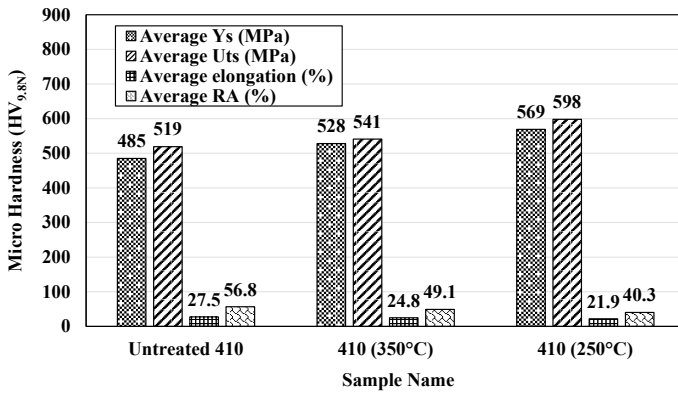
Fig. 17.2 Average value of YS, UTS, % elongation, and % RA values for DCT treated and untreated specimens

As per the literature, with cryogenic treatment, the retained austenite changes into martensite [8–10]. This makes material harder, so tensile strength after cryogenic treatment always increases. This trend was also followed in our experimentation and tensile strength of cryogenically treated material increases by 4.23% in case of tempering temperature 350 °C and by 15.22% in case of tempering temperature 250 °C, as compared to untreated material. Further, the % elongation and % RA reduce with the DCT. Similar results were also observed by Jaswin et al. [13], Upadhyay et al. [7] and Nauman et al. [10] for the En 52, SS316, and 316 L, respectively. Jaswin et al. [13] noticed approximately 7.9% improvement in UTS for En 52 steel.

17.3.2 Micro-Hardness Test

To find the Vickers micro-hardness of untreated and DCT SS410 specimens, the test was performed at five different locations on each specimen. The obtained values are shown in Table 17.2 and the average micro-hardness values for the candidate material are compared in Fig. 17.3.

Table 17.2 Micro-hardness values for DCT treated and untreated specimens

Sample name	Microhardness ($HV_{9.8N}$)					
	$HV_{9.8N}$ 1	$HV_{9.8N}$ 2	$HV_{9.8N}$ 3	$HV_{9.8N}$ 4	$HV_{9.8N}$ 5	Average $HV_{9.8N}$
Untreated 410	152.5	156.9	161.3	147.5	145.2	152.7
410 (350 °C)	168.2	165.3	175.6	179.9	171.5	172.1
410 (250 °C)	188.6	205.5	195.3	201.2	199.9	198.1
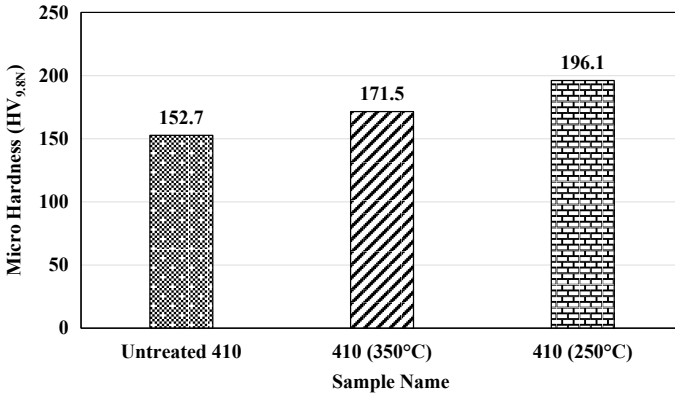
Fig. 17.3 Bar chart compression for average micro-hardness values for DCT treated and untreated specimens

Micro-hardness of cryogenically treated specimen tempered at two different temperatures increases as compared to the untreated SS410, and this may be due to fine distribution of secondary carbide particles and conversion of retained austenite into martensite. Similar results were also obtained by Nauman et al. [10] and Upadhyay et al. [7]. Micro-hardness of cryogenically treated material increases by 12.70% in cases of tempering temperature 350 °C and by 29.73% in cases of tempering temperature 250 °C as compared to untreated material.

17.3.3   Charpy Impact Toughness

To find the toughness of untreated and DCT SS410 specimens, the impact testing machine was used and obtained results shown in Table 17.3 and the average toughness values for the candidate material are compared in Fig. 17.4.

From the results, it can be seen that toughness of both the DCT SS410 material decreases as compared to untreated SS410. From the obtained data, it can be concluded that the micro-hardness and toughness are inversely proportional to each other, which is also seen by Nauman et al. [10] and Upadhyay et al. [7]. The toughness

Table 17.3 Toughness data for DCT treated and untreated specimens

Toughness (J)	
Sample	Average toughness (J)
410 untreated	55
410 T1 (350 °C)	46
410 T2 (250 °C)	35.5
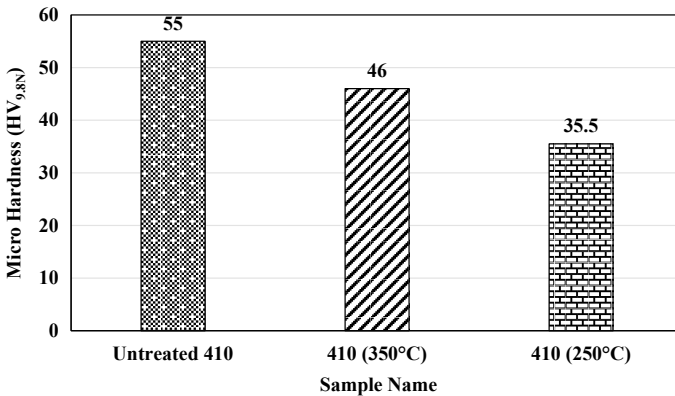
Fig. 17.4 Bar chart compression for toughness of DCT treated and untreated specimens

of cryogenically treated material decreases by 16.36% in case of tempering temperature 350 °C and by 35.45% in case of tempering temperature 250 °C as compared to untreated material.

17.3.4   Microstructure

The microstructure images of untreated and DCT SS 410 specimens tempered at two different temperatures 350 and 250 °C along with the signatures are represented in Fig. 17.5. In Fig. 17.5a, b, retained austenite and un-dissolved carbides are clearly visible in untreated SS410 material. Patil et al. [11] studied the effect of DCT on steel and concludes that retained austenite reduces strength and hardness of the material, due to this life of material reduces.

After DCT, retained austenite converts into martensite, due to this conversion, hardness and strength of material increases. Further, it was also observed that DCT material with tempering temperature of 250 °C shows more refinement of secondary
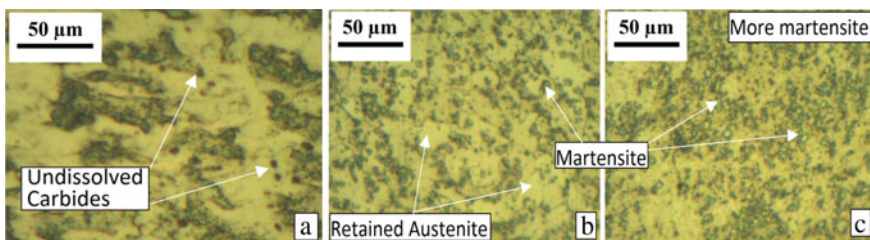
Fig. 17.5 Microstructural images of **a** untreated SS410, **b** DCT tempered at 350 °C, and **c** DCT tempered at 250 °C temperatures taken at 500X

carbide particles, which may the reason behind the better mechanical strength of the same. The similar signatures were also observed by Singh et al. [12, 21–24].

17.4 Conclusions

The main focus of the paper was to study the effect of DCT with tempering at two different temperatures on mechanical and metallurgical properties of SS410. The following are the conclusions which have been drawn from the study:

- Tensile strength was found to be increased by 15.22 and 4.23% in case of cryogenically treated material tempered at 250 and 350 °C, respectively, as compared to untreated material. More refinement of secondary carbide particles may be the potential solution behind the increment.
- Micro-hardness (HV) was found to be increased by 29.73% and 12.70% in case of DCT material tempered at 250 and 350 °C, respectively, as compared to untreated material, this increment may correspond to the conversion of retained austenite into martensite.
- The impact toughness reduces by 35.45% and 16.36% in case of DCT material tempered at 250 and 350 °C, respectively, as compared to untreated material.
- From the microstructural analyses, it was observed that in DCT specimens, retained austenite converts into martensite and the refinement of the grains was also observed, which contribute to the increment in the strength of the discussed material. At last, the tempering of DCT material was found to be optimized for a value of 250 °C.

References

1. Kang, C., Liu, H., Zhang, T., Li, Q.: Investigation of submerged waterjet cavitation through surface property and flow information in ambient water. Appl. Surf. Sci. **425**, 915–922 (2017)
2. Hu, H.X., Zheng, Y.G., Qin, C.P.: Comparison of Inconel 625 and Inconel 600 in resistance to cavitation erosion and jet impingement erosion. Nucl. Eng. Des. **240**, 2721–2730 (2010)
3. Singh, P., Bansal, A., Goyal, D.K.: Erosion wear evaluation of HVOF sprayed WC-12Co coating on some pipeline materials using Taguchi approach. Kovove Mater. **57**, 113–120 (2019)
4. Wang, Y., Stella, J., Darut, G., Poirier, T., Liao, H., Planche, P.M.: APS prepared NiCrBSi-YSZ composite coatings for protection against cavitation erosion. J. Alloy. Compd. **699**, 1095–1103 (2017)
5. Chi, S., Park, J., Shon, M.: Study on cavitation erosion resistance and surface topologies of various coating materials used in shipbuilding industry. J. Ind. Eng. Chem. **26**, 384–389 (2015)
6. Qiu, N., Wang, L., Wub, S., Likhachev, S.D.: Research on cavitation erosion and wear resistance performance of coatings. Eng. Fail. Anal. **55**, 208–223 (2015)
7. Upadhyay, J., Bansal, A. and Singh, J.: Effect on mechanical and metallurgical properties of cryogenically treated material SS316. In: Sharma V., Dixit U., Alba-Baena N. (eds.) Manufacturing Engineering. Lecture Notes on Multidisciplinary Industrial Engineering, pp. 97–107. Springer, Singapore (2019)

8. Liu, H., Wang, J., Shen, B., Yang, H., Gao, S. and Huang, S.: Effects of deep cryogenic treatment on the property of 3Cr13Mo1V1.5 high chromium cast iron. Mater. Des. **28**, 1059–1064 (2007)
9. Molinari, A., Pellizzari, M., Gialanella, S., Straffelini, G., Stiasny, K.H.: Effect of deep cryogenic treatment on the mechanical properties of tool steels. J. Mater. Process. Technol. **118**, 350–355 (2001)
10. Nauman, M.T., Mohideen, S.R., Kaleem, N.: Material characterization of 316 L stainless steel after being subjected to cryogenic treatment. Int. J. Mech Indus. Eng. **2**(1), 44–48 (2012)
11. Patil, P.I., and Tated, R.G.: Comparison of effects of cryogenic treatment on different types of steels: a review. In: International Conference on Computational Intelligence (ICCIA). Proceedings in International Journal of Computer Applications (IJCA). pp. 10–29 (2012)
12. Singh, P.J., Guha, B., Acha, D.R.G.: Fatigue life improvement of AISI 304L cruciform welded joints by cryogenic treatment. Eng. Fail. Anal. **10**, 1–12 (2003)
13. Jaswin, M.A., Lal, D.M.: Effect of cryogenic treatment on the tensile behaviour of En 52 and 21-4 N valve steels at room and elevated temperatures. Mater. Des. **32**, 2429–2437 (2010)
14. Singla, A.K., Singh, J., Sharma, V.S.: Processing of materials at cryogenic temperature and its implications in manufacturing: a review. Mater. Manuf. Process. **33**(15), 1603–1640 (2018)
15. Kumar, T.V., Thirumurugan, R., Viswanath, B.: Influence of cryogenic treatment on the metallurgy of ferrous alloys—a review. Mater. Manuf. Process. **32**(11), 1789–1805 (2017)
16. Akincioğlu, S., Gökkaya, H., Uygur, İ.: A review of cryogenic treatment on cutting tools. Int. J. Adv. Manuf. Technol. **78**(9–12), 1609–1627 (2015)
17. Shokrani, A., Dhokia, V., Muñoz-Escalona, P., Newman, T.: State-of-the-art cryogenic machining and processing. Int. J. Comput. Integr. Manuf. **26**(7), 616–648 (2013)
18. Singla, A.K., Singh, J. and Sharma, V.S.: Microstructure and mechanical properties of lamellar Ti-6Al-4 V ELI alloy. In: Sharma V., Dixit U., Alba-Baena N. (eds.) Manufacturing Engineering. Lecture Notes on Multidisciplinary Industrial Engineering, pp. 109–116, Springer, Singapore (2019)
19. Bansal, A., Singh, J., Singh, H.: Slurry erosion behavior of HVOF-sprayed WC-10Co-4Cr coated SS 316 steel with and without PTFE modification. J Therm. Spray Tech. (2019). https://doi.org/10.1007/s11666-019-00903-y
20. Das, D., Ray, K.K., Dutta, A.K.: Influence of temperature of sub-zero treatments on the wear behavior of die steel. Wear **267**(9–10), 1361–1370 (2009)
21. Das, D., Dutta, A.K., Ray, K.K.: Correlation of microstructure with wear behaviour of deep cryogenically treated AISI D2 steel. Wear **267**(9–10), 1371–1380 (2009)
22. Patil, P. I.and Tated, R.G.: Comparison of effects of cryogenic treatment on different types of steels: a review. In: International Conference in Computational Intelligence (ICCIA) Proceedings published in International Journal of Computer Applications® (IJCA), 10–29 March 2012
23. Podgornik, B., Paulin, I., Zajec, B., Jacobson, S., Leskovsek, V.: Deep cryogenic treatment of toolsteels. J. Mater. Process. Tech. **229**, 398–406 (2016)
24. Molinari, A., Pellizzari, M., Gialanella, S., Straffelini, G., Stiasny, K.H.: Effect of deep cryogenic treatment on the mechanical properties of tool steels. J. Mater. Process. Technol. **118**(1–3), 350–355 (2001)

Chapter 18
Effect of Tool Rotation on Surface Roughness During Electro Discharge Machining of Hastelloy C-276

Nikhil Jain, Jinesh Kumar Jain, and Bhuvnesh Bhardwaj

Abstract In the research work, two-level full factorial design with Box-Cox transformation has been employed for the investigation of EDM conditions on surface roughness during the machining of Hastalloy C-276. The pulse on time, gap voltage, peak current and tool motion have been considered as EDM conditions. The pulse on time has been found most significant EDM condition that affects the surface roughness.

Keywords Hastelloy C-276 · EDM · Tool motion · Surface roughness

18.1 Introduction

The unconventional methods of machining have respective specific advantages over conventional methods of machining. These methods are not limited by brittleness, hardness and toughness of the material and can produce any intricate shape on any workpiece material by desirable control over the various physical parameters of the processes. In the present era, new alloys, super-alloys, ceramics and composites having high toughness, hardness and strength are employed in different industries. Li et al. [1] studied the surface characteristics of Ti–6Al-4 V by SiC abrasive mixed EDM with magnetic stirring. Rozenek et al. [2] studied the effect of EDM conditions with tool electrode feed rate on surface roughness (SR) during the machining of a metal matrix composite (MMC). Dwivedi and Choudhury [3] studied the effect of tool motion on SR, recast layers and micro-cracks during the EDM machining of AISI D3 steel. Saha and Choudhary [4] studied the dry EDM process with negative polarity and air as dielectric using central composite design (CCD). Khan et al. [5]

N. Jain (✉) · B. Bhardwaj
Department of Mechanical Engineering,
Jaipur Engineering College and Research Centre, Jaipur 302022, India
e-mail: 2019rme9056@mnit.ac.in

J. K. Jain
Department of Mechanical Engineering, Malaviya National Institute of Technology
Jaipur, Jaipur 302017, India

Table 18.1 EDM conditions and level of condition

Name	Units	Type	Minimum	Maximum	Mean
Pulse on time	Micro sec	Numeric	4	20	12
Gap voltage	V	Numeric	10	40	25
Peak current	A	Numeric	2	12	7
Tool motion	–	Categoric	Stationary	Rotating	–

used negative polarity and kerosene as a dielectric fluid while machining of workpiece Ti–6Al-4 V in EDM machining.

The Hastelly C-276 is widely used in the chemical processing industries. The literature reveals that very few researches work have been carried out to examine the effect of EDM conditions on surface roughness during the machining of this material. Accordingly, the main objective of the present research work is to investigate the effect of EDM conditions on surface roughness during the machining of Hastelly C-276. An attempt has also been made to develop surface roughness prediction model.

18.2 Machining Condition and Design Matrix

The pulse on time, peak current, gap voltage and tool motion (stationary and rotating) have been selected as EDM conditions. The pulse on time, peak current and gap voltage have been considered as numerical machining conditions while tool motion has been considered as category machining condition. The speed of rotating tool has been kept constant at 1000 RPM. Table 18.1 shows the selected EDM conditions and various levels of EDM machining conditions according to selected approach, *i.e.,* two-level full factorial design. Table 18.2 shows the design matrix for experimentation.

18.3 Materials and Methods

18.3.1 Experimentation

To achieve the objective of the present research work, all the experiments have been conducted on Hastalloy C-276 plate of dimension 80 mm × 50 mm × 10 mm using EDM die sinking machine (Model C-425), manufactured by Electronica Industries, India. The rotation of tool is given by rotating head through special arrangement. The copper tool having diameter 10 mm, thermal conductivity 412 W/mk and density 9.12 g/cc has been used for all experimentation. The kerosene has been taken as

Table 18.2 Design matrix and measured value of surface roughness

Std	A: Pulse on time (micro sec)	B: Gap voltage (V)	C: Peak current (A)	D: Tool motion	Surface roughness (microns)
1	4	10	2	Stationary	3.040
2	20	10	2	Stationary	5.055
3	4	40	2	Stationary	2.741
4	20	40	2	Stationary	4.445
5	4	10	12	Stationary	3.675
6	20	10	12	Stationary	6.818
7	4	40	12	Stationary	2.922
8	20	40	12	Stationary	5.540
9	4	10	2	Rotating	2.530
10	20	10	2	Rotating	4.207
11	4	40	2	Rotating	2.281
12	20	40	2	Rotating	3.769
13	4	10	12	Rotating	3.116
14	20	10	12	Rotating	5.780
15	4	40	12	Rotating	2.450
16	20	40	12	Rotating	4.645
17	12	25	7	Stationary	4.222
18	12	25	7	Rotating	3.138
19	12	25	7	Stationary	4.131
20	12	25	7	Rotating	3.257
21	12	25	7	Stationary	4.131
22	12	25	7	Rotating	3.365
23	12	25	7	Stationary	4.061
24	12	25	7	Rotating	3.410

dielectric fluid. The tool electrode is kept at negative polarity and workpiece is kept at positive polarity for the machining. Table 18.3 shows the chemical composition of Hastalloy C-276.

18.3.2 Measurement

In this work, CLA of the workpieces after the EDM machining was calculated using of a portable surface tester (Surf coder SE 1200). The measurements of surface roughness have been taken at three different places of machined part. Finally, the mean of SR measured at three places has been considered for that trial [6]. The measured values of SR have been presented in Table 18.2.

Table 18.3 Chemical composition of Hastalloy C-276

C	Co	Cr	Mo	V	W	Fe	Mn	Si	Ni
0.02	2.5	14.6	16.3	0.35	3.78	6.4	1	0.05	55

18.4   Results and Discussion

The measured values of SR along with the design matrix have been fed into the design expert 8.0.4.1 software for the formulation of surface roughness model and to examine the impact of EDM conditions on SR.

18.4.1   Development of Prediction Models

The first step for the formulation of models is ANOVA analysis. The ANOVA is based on two assumptions, (i) normal distribution of data and (ii) constant variance [7]. To diagnosis the first assumption of ANOVA, the normal probability plot of residuals for MRR and SR have been presented in Figs. 18.1 and 18.2, respectively. The plot indicates whether the residuals follow the normal distribution or not if the residuals follow normal distribution, most of the points should fall on the straight line. From the figures, it has been revealed that some of the residuals are lying outside the straight line, thus residuals are not completely normally distributed. Therefore, to make the data more normally distributed, some transformation is required.

The Box-Cox transformation is a family of transformations that is used to make data normally distributed by identify suitable exponent (λ). This transformation simultaneously increases the normality and homogeneity of the data. Figure 18.3
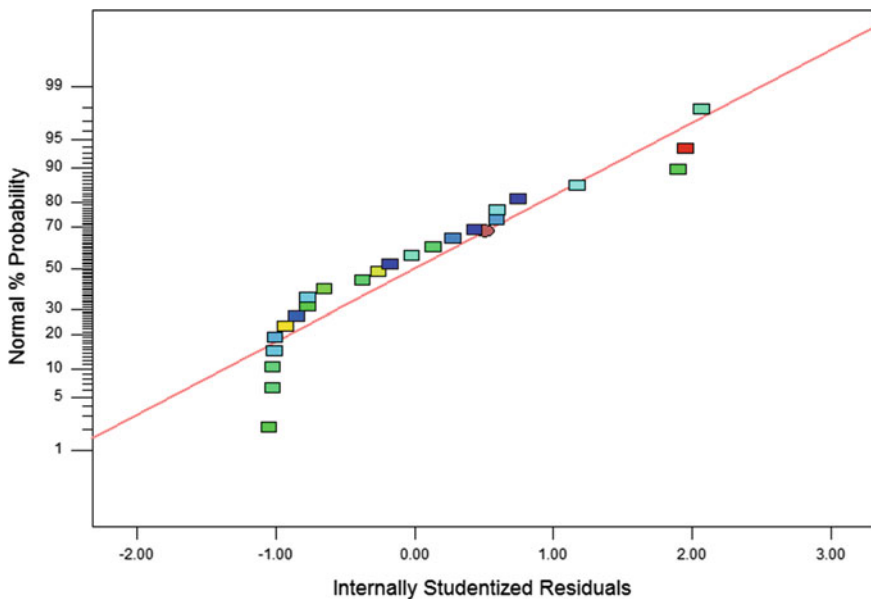
Fig. 18.1 Normal probability plot for surface roughness
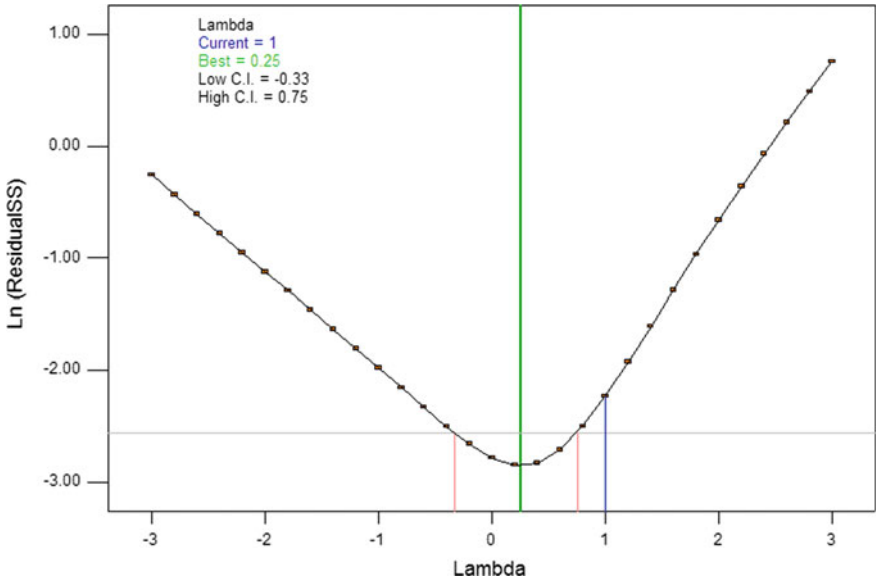
Fig. 18.2 Box-Cox plot for surface roughness
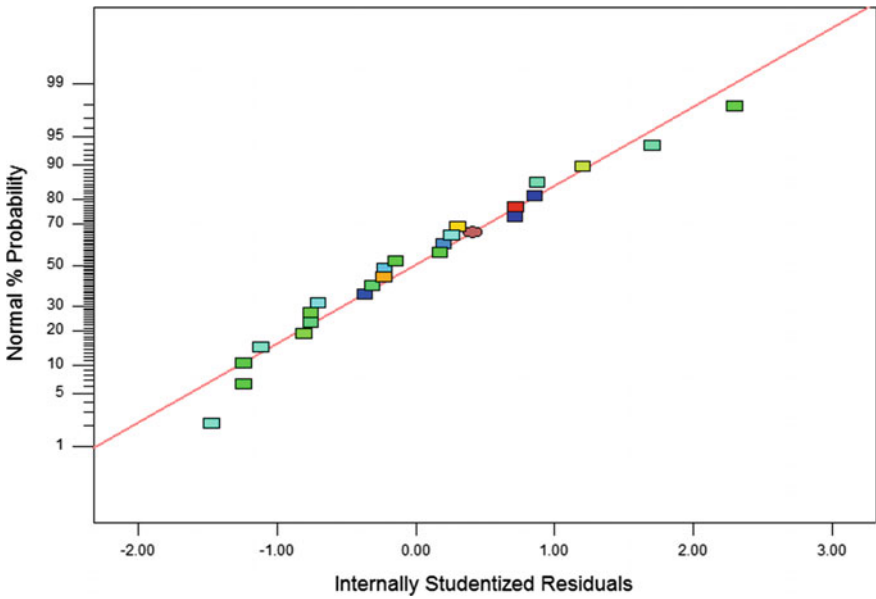
Fig. 18.3 Normal distribution plot after the transformation for the SR
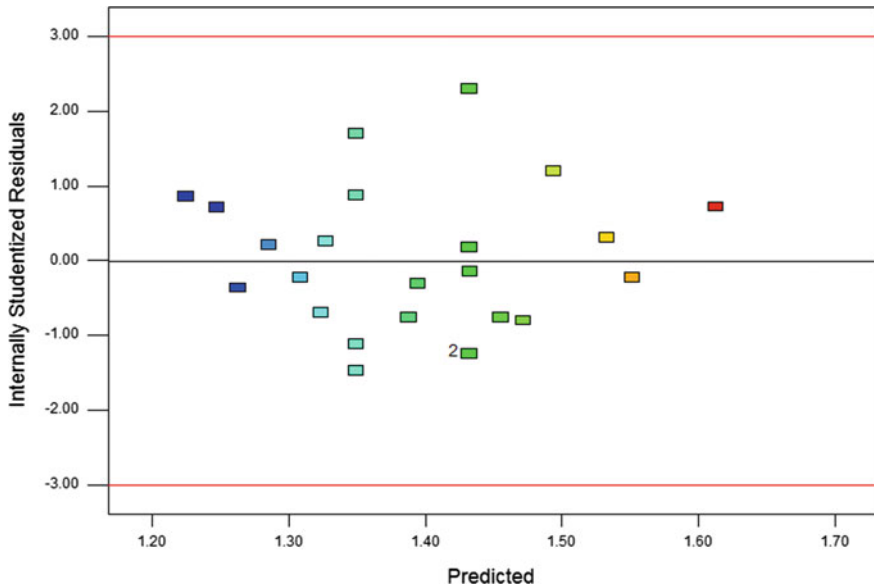
Fig. 18.4 Residuals versus the predicted response plot for SR

shows the Box-Cox plot for SR. The blue line shows the present value of "λ" while green line indicates the best recommended value of "λ" for transformation. In Fig. 18.3, the present value of "λ" is "1", but the recommended value of "λ" is 0.25. Thus, the power transformation is needed to make the data normally distributed.

Figure 18.3 shows the normal distribution plot after the transformation for the MRR and surface roughness. The figures display that the mostly residuals are falling on a straight line, therefore, now data is normally distributed. The residuals versus the predicted response plot for SR are presented in Fig. 18.4. For assumption of constant variance to be true, the plot should be a random scatter. Figure 18.4 reveals no specific pattern indicates that data is following assumption variance.

Table 18.4 shows that the surface roughness model is significant and the main effect of pulse on time, gap voltage, peak current, tool motion, two-level interaction of pulse on time and peak current, gap voltage and peak current are the significant model terms. The value of "Prob. $> F$" for lack-of-fit is 0.5263 indicates that the lack-of-fit is insignificant. The R^2 and adjusted R^2 values are equal to 0.994 and 0.992, respectively, which is very close to each other.

The final prediction models for SR in terms of actual machining conditions are given in Eqs. (18.1) and (18.2).

Table 18.4 ANOVA table after Box-Cox transformation for surface roughness

Source	Sum of squares	Degree of freedom	Mean square	F-value	p-value Prob $> F$
Model	0.222	6	0.037	472.672	< 0.0001
A-Pulse on time	0.155	1	0.155	1985.881	< 0.0001
B-Gap voltage	0.014	1	0.014	177.465	< 0.0001
C-Peak current	0.020	1	0.020	256.144	< 0.0001
D-Tool motion	0.028	1	0.028	356.652	< 0.0001
AC	0.003	1	0.003	37.707	< 0.0001
BC	0.002	1	0.002	22.182	0.0002
Residual	0.001	17	0.000	–	–
Lack-of-fit	0.001	11	0.000	1.004	0.5263
Pure error	0.000	6	0.000	–	–
Cor total	0.223	23	–	–	–
Std. Dev.	0.009		R-squared		0.994
Mean	1.393		Adj R-squared		0.992
C.V. %	0.63		Pred R-squared		0.990
Press	0.00		Adeq precision		82.684

Prediction models for surface roughness (in actual form)

(1) For stationary tool

$$
\begin{aligned}
(\text{surface roughness})^{0.25} ={}& +1.28349 + 9.94110\mathrm{E} - 003 * \\
& \text{Pulse on time} - 9.91785\mathrm{E} - 004 \\
& * \text{Gap voltage} + 6.47583\mathrm{E} - 003 \\
& * \text{Peak current} + 3.39450\mathrm{E} - 004 \\
& * \text{Pulse on time} * \text{Peak current} \\
& - 1.38856\mathrm{E} - 004 * \text{Gap voltage} * \text{Peak current}
\end{aligned}
$$

$$(18.1)$$

(2) For rotating tool

$$
\begin{aligned}
(\text{surface roughness})^{0.25} ={}& +1.21529 + 9.94110\mathrm{E} - 003 \\
& * \text{Pulse on time} - 9.91785\mathrm{E} - 004
\end{aligned}
$$

$$\ast \text{ Gap voltage} + 6.47583\text{E} - 003$$
$$\ast \text{ Peak current} + 3.39450\text{E} - 004$$
$$\ast \text{ Pulse on time} \ast \text{ Peak current}$$
$$- 1.38856\text{E} - 004 \ast \text{ Gap voltage} \ast \text{ Peak current}$$

$$(18.2)$$

18.4.2   Effect of EDM Conditions on SR

In order to examine the impact of EDM conditions on surface roughness, different plots between EDM conditions and surface roughness have been plotted using prediction models.

18.4.2.1   Impact of EDM Conditions on Surface Roughness

The 3D plots for SR in terms of EDM conditions have been shown in Figs. 18.5, 18.6, 18.7 and 18.8. Figures 18.5 and 18.6 show the impact of peak current and pulse on time on SR obtained using stationary and rotating tool, respectively. From the both figures, it has been revealed that SR increases with increase in pulse on time and peak current. It is due to increase in generation of pulsation energy or discharge
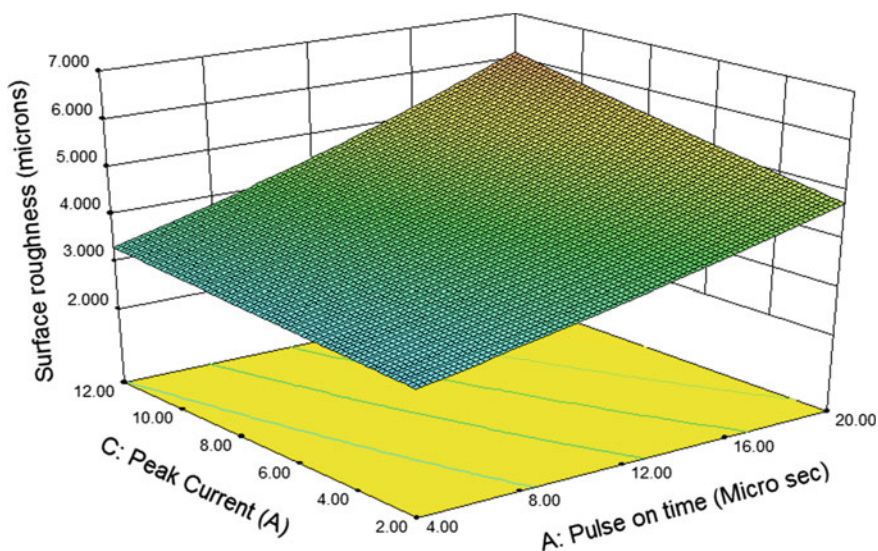
Fig. 18.5 Impact of peak current and pulse on time on SR without rotating tool
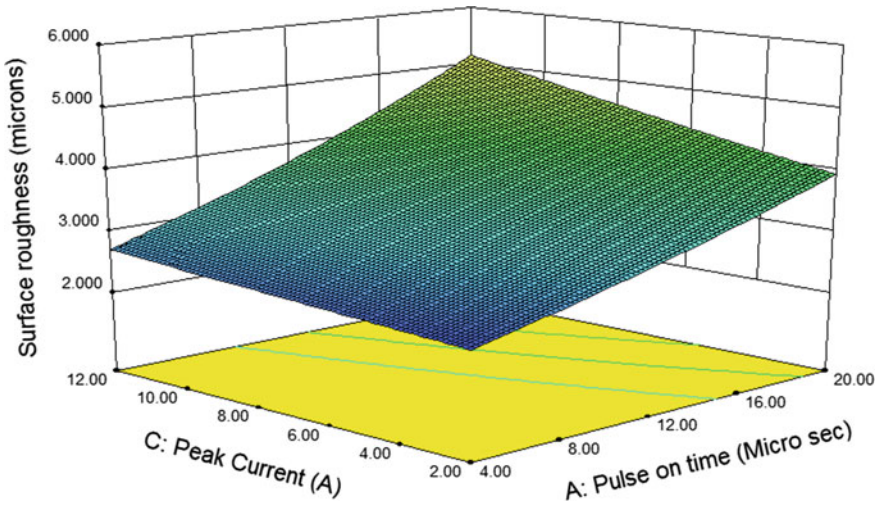
Fig. 18.6 Effect of peak current and pulse on time on SR with rotating tool
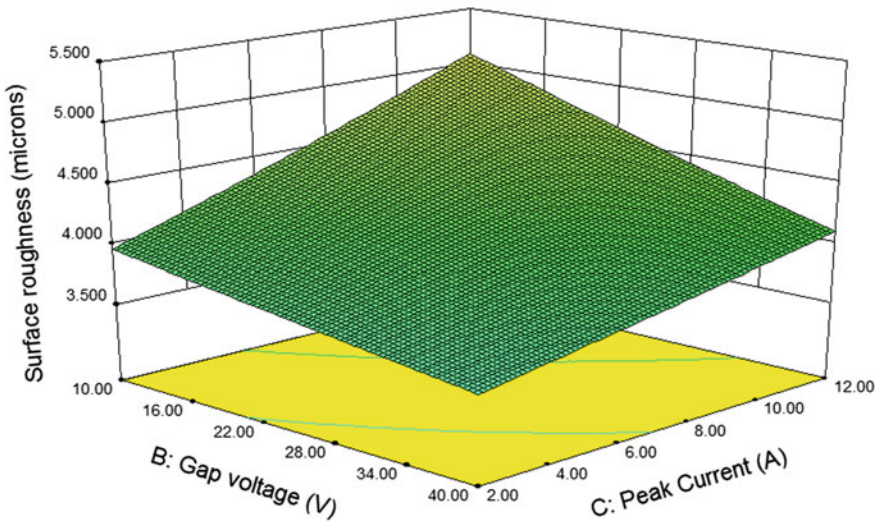
Fig. 18.7 Impact of peak current and gap voltage on SR without rotating tool

energy with increase in pulse on time. The increase in pulsation energy expands the plasma channel between the workpiece and tool electrode. This expanded plasma channel forms large size of craters at the surface of workpiece. This leads to higher SR at the surface of machined workpiece.

On the other hand, it is visible from the figures that SR increases with increase in peak current [8]. The upward trend attributed due to generation of intensely discharge
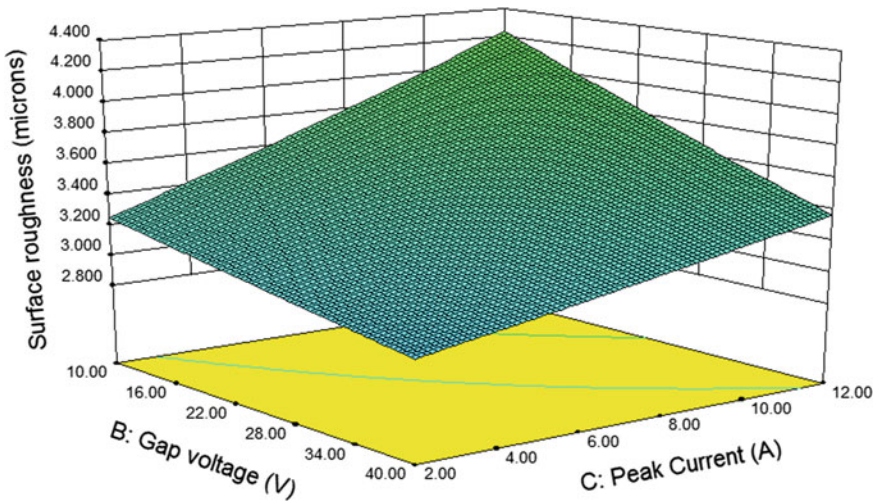
Fig. 18.8   Effect of peak current and gap voltage on SR with rotating tool

at high peak current. This intensely discharges strike the surface of the workpiece and produces large size of craters on the surface of workpiece, which deteriorates the surface of machined workpiece. Figures 18.7 and 18.8 show the effect of gap voltage and pulse on time on surface roughness obtained using stationary and rotating tool, respectively. It is visible from the both plots that SR continuously decreases with increase in gap voltage. It is due to the increase in discharge time with increase in voltage, which leads to decrease in number of discharge cycles within a given period. This decreases the discharge energy per unit time. The size of craters decreases with decrease in discharge energy per unit time, which leads to decrease in SR [5].

Figure 18.9 shows the effect of tool motion on surface roughness. It is visible from the plot that machining with stationary tool exhibited rougher surface as compare to rotating tool electrode. It is due to generation of centrifugal force with tool rotation, which efficiently flush out the debris from the melt pool and produce finer surface [9].

18.5   Conclusion

In this paper, two-level full factorial design with Box-Cox transformation has been employed to examine the effect of EDM conditions on SR during the machining of Hastalloy C-276. The result has led to the following conclusions.

- The pulse on time, gap voltage, peak current and tool motion have been found significant model terms for surface roughness.
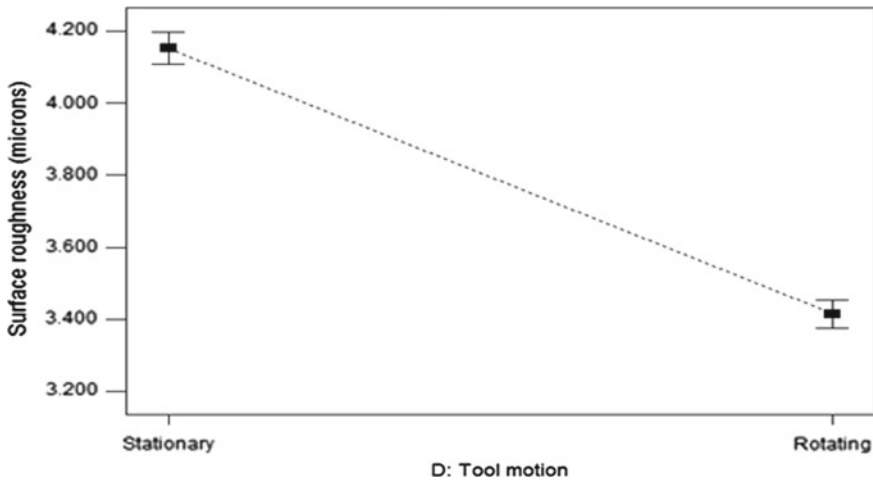
Fig. 18.9 Impact of tool rotation on SR

- The pulse on time has been found most significant EDM condition that affects the surface roughness followed by tool motion, peak current and gap voltage.
- The coefficient of determination (R^2) for SR has been found to be 0.994, which shows the excellent prediction ability of develop model.
- The results show that surface roughness decreases with decreasing the pulse on time, peak current and with tool rotation while decrease in the gap voltage increases the SR.

References

1. Teimouri, R., Baseri, H.: Study of tool wear and overcut in EDM process with rotary tool and magnetic field. Adv. Tribol. 1–8 (2012)
2. Rozenek, M., Kozak, J., Dabro, V.L., et al.: Electrical discharge machining characteristics of metal matrix composites. J. Mater. Process. Technol. **109**, 367–370 (2001)
3. Dwivedi, A.P., Choudhury, S.K.: Increasing the performance of EDM process using tool rotation methodology for machining AISI D3 steel. Procedia CIRP. **46**, 131–134 (2016)
4. Saha, S., Choudhary, S.K.: Experimental investigation and empirical modeling of the dry electric discharge machining process. Int. J. Mach. Tools Manuf. **49**, 297–308 (2009)
5. Ashikur Rahman Khan, Md., Rahman, M.M.: Surface characteristics of Ti-5Al-2.5Sn in electrical discharge machining using negative polarity of electrode. Int. J. Adv. Manuf. Technol. https://doi.org/10.1007/s00170-017-0028-4 (2017)
6. Bhardwaj, B., Kumar, R., Singh, P.: Effect of machining parameters on surface roughness in end milling of AISI 1019 steel. Proc. Inst. Mech. Eng., Part B **228**, 714 (2013)
7. Bhardwaj, B., Kumar, R., Singh, P.: Prediction of surface roughness in turning of EN 353 using response surface methodology. Trans. Indian Inst. Met. **67**(3), 313
8. Kanlayasiri, K., Boonmung, S.: Effects of wire-EDM machining variables on surface roughness of newly developed DC 53 die steel. J. Mater. Process. Technol. **192–193**, 459–464 (2007)

9. Chattopadhyay, K.D., Satsangi, P.S., Verma, S., et al.: Analysis of rotary electrical discharge machining characteristics in reversal magnetic field for copper-EN 8 steel system. Int. J. Adv. Manuf. Technol. **38**, 925–937 (2008)

Chapter 19
Advances in Electrical Discharge Machining: State-of-the-Art

Krishnakant Dhakar, Milind Dandekar, and Mohit Tyagi

Abstract Electrical discharge machining (EDM) is one of the widely used un-conventional machining processes. In EDM process, thermo-electric energy is utilized to remove undesired material from the parent material. The EDM is also referred as spark erosion machining. It has varied area of applications like die and amp; mold development, automotive and aerospace industries, medical implants, etc. With increase in demand of goods made by smart materials and alloys, more interest has gravitated toward the EDM process. The continuous improvement in the EDM process has drawn many researchers to carry out their study on this process. This article reviews the recent developments of EDM like powder EDM, near-dry and dry EDM, ultrasonic-assisted EDM, rotary EDM, magnetic-assisted EDM, etc.

Keywords Electrical discharge machining · Dry EDM · Ultrasonic · Near-dry · Powder etc.

19.1 Introduction

Electrical discharge machining (EDM) is a type of un-conventional machining process. Among all un-conventional machining methods, EDM is gaining widespread industrial attention. Unlike conventional machining methods, EDM is noncontact machining method which overlooks the hard and abrasive nature of reinforcement materials. In EDM process, hardness of the workpiece does not effect on the tool wear rate [1]. This technique has been developed in the late 1940s [2]. In this technique, thermo-electric energy is utilized to remove undesired material from the parent material by means of discrete electric discharges between tool (anode) and the work part (cathode) in the presence of a dielectric medium [3]. Tool is progressed

K. Dhakar (✉) · M. Dandekar
Department of Industrial and Production Engineering, S.G.S.I.T.S, Indore, M.P., India
e-mail: krishnakant.dhakar@gmail.com

M. Tyagi
Department of Industrial and Production Engineering, Dr B R Ambedkar National Institute of Technology, Jalandhar, Punjab 144011, India

toward the workpiece until the gap is minor enough, so that the impressed voltage is great enough to ionize the dielectric [4]. Discrete sparks are ignited in a liquid dielectric gap, which separates tool and workpiece. The work part is melted and evaporated due to the erosive effect of the electric discharges [5]. The requirement for high strength-to-weight ratio and high hardness materials in several industries like aerospace, automobile, etc., or defense applications had resulted in new class of advanced materials [6]. Machining of these materials by conventional method is generally a cumbersome and expensive task. EDM may be a feasible alternative instead of using conventional machining. EDM has drawn focus due to unique ability of eroding material from a conductive workpiece irrespective of its hardness [7]. The electrical discharge machining (EDM) has been a preferred choice for difficult-to-machine materials. Demand for optimization of its input parameters for efficiency improvement has been a matter of concern for research community. The focus area for researchers working in the field of EDM process variants includes near-dry EDM, powder-mixed EDM, dry EDM, rotary tool EDM, and ultrasonic vibration-assisted EDM, etc. [8]. A brief description is presented in this article to highlight the efforts of researchers and reflect the current trends in EDM research.

19.2 Powder-Mixed EDM (PMEDM)

PMEDM is one of the novel inventions to improve the capabilities of EDM process. In PMEDM, abrasive particles are mixed with the dielectric liquid. It becomes an electrically conductive medium, which causes reduction in dielectric insulating strength and increases the inter-electrode gap (IEG). This made process more stable and improved the MRR and surface finish.

19.2.1 Material Removal Rate (MRR)

Jeswani [9] reported that addition of powder in EDM, significantly increased the MRR. A slight increase in TWR was also reported. Tzeng and Lee [10] examined the influence of several powder characteristics on EDM performance. It was found that powder concentration, particle size, particle density, thermal conductivity, and electrical resistivity were important characteristics that affected the EDM performance. Chromium powder was found to produce greatest MRR and lowest TWR. However, the copper powder was found to have feeble influence on EDM performance. Kansal et al. [11] reported that peak current and concentration of the silicon powder were most significant parameters for surface roughness, MRR, and TWR in PMEDM. Izman et al. [12] mixed, multi-walled carbon nanotubes in kerosene dielectric medium for machining of Ti-6Al-4 V. It was observed that multi-walled carbon nanotubes improve MRR by 7% and surface roughness by 9% than conventional EDM.

19.2.2   Surface Roughness

Zhao et al. [13] performed experimental research on surface quality and machining efficiency in rough machining using PMEDM process. It was concluded that proper selection of process parameters improved machining efficiency with a good surface finish. Wong et al. [14] reported that dielectric fluid mixed with some abrasive powders distributed the electrical discharges at IEG to produce near-mirror-finish. It was also reported that mirror-finish can only be achieved with negative electrode polarity. Zhao et al. [13] performed experimental research on surface quality and machining efficiency in rough machining using PMEDM process. It was concluded that proper selection of process parameters improved machining efficiency with a good surface finish. Sidhu et al. [15] investigated surface alteration of three different types of metal matrix composites (MMCs) using PMEDM process. It was reported that PMEDM was an appropriate machining option for MMCs to enhance their surface properties.

19.3   Dry EDM

Dry EDM is a modification of conventional EDM in which the liquid dielectric is replaced by a gaseous dielectric medium. A high-velocity gas supplied between IEG assisted in debris removal dissipation of excessive heating. The National Aeronautics and Space Administration (NASA), USA, published a first research paper on dry EDM process in 1985 [16]. It reported that EDM can be used for drilling using different gases as dielectric mediums (argon, nitrogen, and helium). Figure 19.1 shows dry EDM process.

Fig. 19.1   Dry EDM process [Kuniedaet al.]
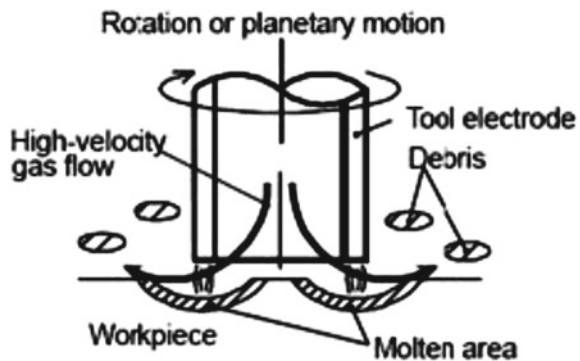
19.3.1 MRR

Kunieda and Furuoya [17] observed that the MRR was increased by using oxygen gas as dielectric fluid in EDM. A higher rate of discharge, enlarged crater, and increased MRR were reported. Kunieda and Yoshida [18] investigated that EDM can be achieved in gas. Flushing efficiency was improved by the high velocity of dielectric medium through hollow tool electrode. It resulted in better flushing of debris particles without getting reattached to the tool electrode. Kunieda et al. [19] performed high-speed EDM milling of 3D cavities. Experimental results revealed that MRR increased when current density exceeded a certain threshold value. It was also observed that the machining accuracy was better when gas was sucked rather than being ejected. Kao et al. [20] performed dry wire EDM on thin workpieces and found that MRR was low with dry EDM. Liqing and Yingjie [21] proposed two dry EDM techniques (oxygen-mixed dry EDM and dry EDM with cryogenically cooled workpieces). It was reported that 40% and more than 200% increase in MRR with cryogenically cooled workpieces and oxygen-mixed dry EDM processes, respectively.

19.3.2 Tool Wear Rate (TWR)

Kunieda and Yoshida [18] investigated the reasons for minimum tool electrode wear during dry EDM. It was observed that the molten material of workpiece adheres to the tool electrode and protects it against wear. The electrode wear ratio was nearly zero which was a major advantage of this process. Shue et al. [22] studied the effect of various machining parameters such as current and duty factor on MRR and relative electrode wear rate (REWR) of dry EDM. In this investigation, sputtering of molten metal from work surface was observed subsequently which stuck onto the tool surface. A shielding layer was formed which resulted in low REWR. Joshi and Govindan [23] presented dry electrical discharge drilling technique. It was found that tool wear rate was reduced due to the deposition of removed work material on the electrode surface.

19.3.3 Surface Roughness

Wanget al. [24] developed a thermal model of single spark in dry EDM. The simulation results exhibited that crater produced in the gas was larger in diameter and smaller in depth. This was the main reason for better surface roughness in dry finishing. Saha and Choudhury [25] performed parametric analysis of dry EDM process. Experimental results revealed that current, duty factor, and air pressure had a significant effect on surface roughness.

19.4   Near-Dry EDM

Near-dry electrical discharge machining is also a process variant of conventional EDM. It is an environment-friendly process. In this process, two-phase (liquid and gas) dielectric medium is used instead of a liquid dielectric medium. In this process, high-velocity two-phase dielectric flows into the gap. This assists in efficient debris flushing and also acts as a coolant to the tool. Figure 19.2 illustrates near-dry EDM. Tanimura et al. [26] explored the possibility of near-dry EDM in 1989. Further, the study was done by mixing different gases (argon, nitrogen, and helium) with water and used as a dielectric medium in EDM.

Kao et al. [28] conducted experiments on near-dry wire EDM and identified the advantage of near-dry as stable machining process and can produce finished components after machining. These results were reported at low discharge energies. The two-phase dielectric medium improved flushing efficiency of this process. Thus, good surface integrity was obtained for machined surface. Tao et al. [29] examined the influence of pulse energy, tool material, and dielectric fluid on response characteristics. It was found that kerosene mist and copper infiltrated graphite electrode can produce a mirror-like surface finish with 0.32 μmRa value. Tao et al. [30] reported that lower current and pulse time were important factors of near-dry
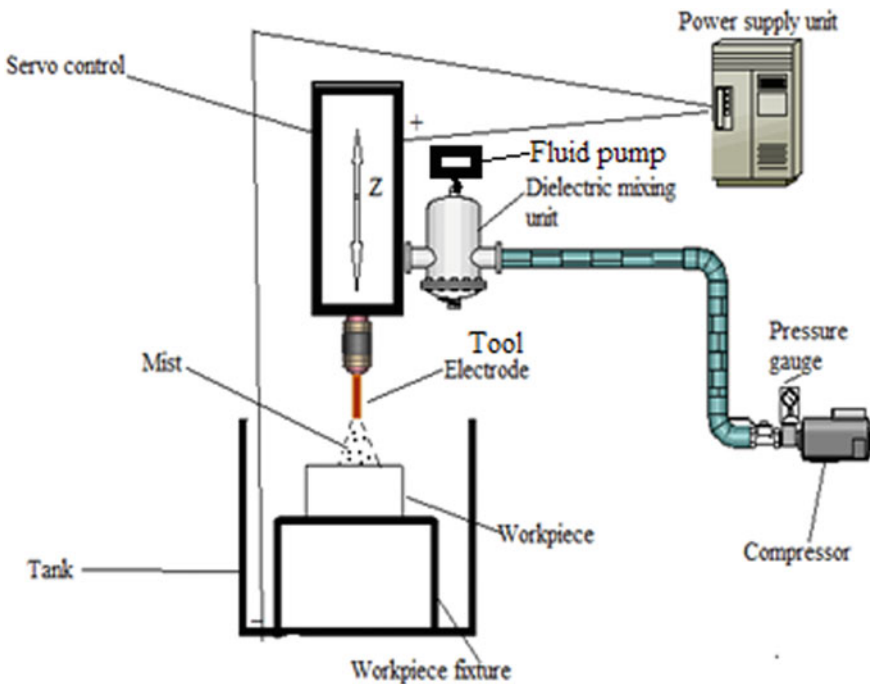
Fig. 19.2   Illustration of near-dry EDM [27]

EDM for improving the surface integrity. Further, it was also reported that process was advantageous for the finishing operation. Furthermore, near-dry EDM was compared with dry EDM. It was reported that dry EDM resulted in higher MRR but poor surface integrity. Fujiki et al. [31] studied the influence of dielectric flow rate on MRR and SR of the workpiece. The increase in the mass flow rate (air and kerosene mixture) increased MRR linearly and decreased tool electrode wear ratio. Further, the flow rate of dielectric medium did not have a significant effect on the surface roughness of the machined surface. Tao [32] investigated the effect of two key wire EDM process parameters, spark duration, and spark cycle on the SR and MRR. It was found that MRR of near-dry wire EDM of PCD-coated WC decreased with spark cycle and increased with increase in spark duration. The surface roughness values obtained by near-dry wire EDM were constantly better. Dhakar et al. [33] examined three different combinations of dielectric medium in near-dry EDM. It was reported that combination of glycerin and air provided very high material removal. Gholipoor et al. [34] compared near-dry EDM, conventional EDM, and dry EDM processes. It was found that at higher current, conventional EDM provided a higher value of R_a and MRR. However, better surface finish and higher MRR were found with near-dry EDM at low discharge current. Further, surface quality obtained by near-dry EDM process was better than conventional and dry EDM processes. Dhakar et al. [35] reported that near-dry EDM produced 97% less emission than conventional EDM, and it is green machining process.

19.5 Ultrasonic Vibration-Assisted Electrical Discharge Machining

Ultrasonic vibration aided to the electrode or workpiece is one of the methods to improve the machining performance of EDM on difficult-to-machine materials. The higher efficiency is gained by improvement in dielectric circulation through employment of ultrasonic vibration. This facilitated the debris removal and created a large pressure change between the electrode and the workpiece.

Tong et al. [36] investigated the effects of vibration assisted to the workpiece with gap and servo control on the EDM performance of micro-structures. It was suggested that higher frequency vibration helped to acquire higher machining efficiency. Good machining results can be obtained when vibration amplitude is set nearly equal to the discharge gap. Yan and Chen [37] presented a new method for improving the EDM performance of a Ti-6Al-4 V alloy. The experimental results indicated that MRR of the ultrasonic-assisted EDM was three times higher than the conventional EDM and the SR was also higher than EDM. Sundaram et al. [38] performed an experimental investigation on ultrasonic-assisted micro-electro-discharge machining by introducing ultrasonic vibration to the workpiece. Based on ANOVA, ultrasonic vibration at 60% of the peak power with the capacitance of 3300 PF was found to be significant for best MRR. Prihandana et al. [39] presented a new method that

consisted of suspending micro-MoS_2 powder in a dielectric fluid and using ultrasonic vibration during micro-EDM processes. Praneetpongrung et al. [40] combined EDM with an ultrasonic vibration system. The sintered Si_3N_4 insulating ceramic workpiece material was machined by using a cylindrical copper–tungsten bar as an electrode material. The results indicated that the MRR improved.

19.6   Rotary Tool Electrical Discharge Machining

Rotary EDM is tool-based EDM process variant. In EDM process, flushing of waste materials (debris) from the sparking gap is one of the major challenges. Accumulation of these materials in gap causes inactive pulses such as short-circuit and arc. Rotary tool electrical discharge machining has reduced these problems because high centrifugal force provided efficient flushing of debris from sparking gap.

Koshy et al. [41] used a rotating disk-type electrode instead of the conventional electrode to enhance the productivity and accuracy of EDM. By providing rotation to the electrode, better flushing of the sparking gap was achieved. It resulted in increased MRR and better surface finish. Soni and Chakravati [42] proposed an experimental design to study the performance of rotary electro-discharge machining (EDM). Copper–tungsten tool electrode was used to machine titanium alloy and die steel. The results indicated that MRR and surface integrity of the machined surface was improved. Fujun et al. [43] introduced shaping principle of machining of non-sphere with a rotary electrode. It was also analyzed the motion laws of machining of rotary workpieces. The authors established universal mathematical models for the said process. This laid a foundation of mathematics for computer simulation, virtual machining, and the establishment of the real machining system of machining non-sphere by rotary EDM. Aliakbari and Baseri [44] identified machining parameters for rotary EDM by using the Taguchi method. The machining parameters of current, pulse on time, electrode rotational speed, and electrode geometry were the most significant parameters on MRR, EWR, and SR.

19.7   Magnetic Field-Assisted Electrical Discharge Machining

In the magnetic field-assisted electrical discharge machining (MFEDM), a debris particle is subjected to two kinds of force, magnetic force, and centrifugal force. It is considered that application of magnetic force changes the path of the ion and causes better debris removal.

Shanker and Ghosh [45] investigated machining characteristics of few workpiece during EDM using electromagnet as spark gap controlling mechanism. Experimental result indicated that at a high capacitance, brass electrodes were more efficient

than copper electrodes. Therefore, it was advised to use brass electrode for rough machining. Chattopadhyay et al. [46] studied the enhancement of machining characteristics by introducing an induced magnetic field on work surface during EDM of steel with a rotary electrode. The work part was placed inside the induced magnetic field, wherein magnetic field's polarity gets reversed periodically. Hemant et al. [47] investigated the effect of magnetic field in EDM on machining characteristics. Experimental results revealed that the increase in the magnetic field increased the MRR and surface roughness. Furthermore, magnetic field-assisted EDM improved the process stability.

19.8 Conclusion

The review of the recent advancement of EDM is presented in this article. The ultrasonic-assisted method is appropriate for micro-machining, and dry EDM is economically effective. While near-dry EDM is economically as well as environment-friendly machining method. further it is provided safe and healthy atmosphere for working. Powder additives mixed with EDM is concerning more on increasing MRR and surface integrity. Literature revealed that PMEDM provides contrary results regarding MRR. Another process variant, the rotary tool EDM involved the rotation of tool electrode. In this process, rotation of tool improved flushing efficiency at IEG.

References

1. Benedict, G.F.: Non-traditional Manufacturing Processes, pp. 207–230, Marcel Dekker Inc. New York (1987)
2. Luo, Y.F., Chen, C.G.: Effect of a pulsed electromagnetic field on the surface roughness in super finishing EDM. Precis. Eng **12**, 97–100 (1990)
3. Abbas, N.M., Solomon, D.G., Bahari, M.F.: A review on current research trends in electrical discharge machining (EDM). Int. J. Mach. Tools Manuf **47**, 1214–1228 (2007)
4. Singh, A., Grover, N.K., Sharma, R.: Recent advancement In electric discharge machining. Rev. Int. J. Mod. Eng. Res. **2**, 3815–3821 (2012)
5. Chakraborty, S., Dey, V. Ghosh, S.K.: A review on the use of dielectric fluids and their effects in electrical discharge machining characteristics. Precis. Eng. **40**, 1–6 (2015)
6. Cheke, P.R., Khedekar, D.S., Pawar, R.S., Kadam, M.S.: Comparative performance of wet and near-dry EDM process for machining of oil hardened non-sinking steel material. Int. J. Mech. Eng Technol. **3**, 13–22 (2012)
7. Hung, N.P., Yang, L.J., Leong, K.W.: Electrical discharge machining of cast metal matrix composites. J. Mater. Process. Tech. **44**, 229–236 (1994)
8. Norliana, M.A., Noriah, Y., Rohidatun M.W.: Electrical discharge machining (EDM): practices in Malaysian industries and possible change towards green manufacturing. J. Miner. Mater. Charact. Eng. **9**(8), 709–739 (2012)
9. Jeswani, M.L.: Electrical discharge machining in distilled water. Wear, **72**, 81–88 (1981)
10. Tzeng, Y.F., Lee, C.Y.: Effects of powder characteristics on electro discharge machining efficiency. Int J Adv Manufact Technol **17**(8), 586–592 (2001)

11. Kansal H.K., Singh, S., Kumar P.: Parametric optimization of powder mixed electrical discharge machining by response surface methodology. J. Mater. Process. Technol. **169**(3), 427–436 (2005)
12. Izman, S., Hodsiyeh, D.G., Hamed, T., Rosliza, R., Rezazadeh, M.: Effects of adding multi walled carbon nanotube into dielectric when EDMing Titanium alloy. Adv. Mater. Res. **463–464**, 1445–1449 (2012)
13. Zhao, W.S., Meng, Q.G., Wang Z.L.: The application of research on powder mixed EDM in rough machining. J. Mater. Process. Technol. **129**, 30–33 (2002)
14. Wong, Y.S., Lim, L.C., Rahuman, I., Tee, W.M.: Near-mirror-finish phenomenon in EDM using powder-mixed dielectric. J. Mater. Process. Technol. **79**, 30–40 (1998)
15. Sidhu, S.S., Batish, A., Kumar S.: Study of surface properties in particulate-reinforced metal matrix composites (MMCs) using powder-mixed electrical discharge machining (EDM). Mater. Manufact. Process. **29**, 46–52 (2014)
16. NASA: Inert-Gas Electrical-Discharge Machining. NASA Technical Brief No. NPO-15660 (1985)
17. Kunieda, M., Furuoya, S.: Improvement of EDM Efficiency by supplying oxygen gas into gap. Anna. CIRP, **40**(1), 215–218 (1991)
18. Kunieda, M., Yoshida, M.: Electrical discharge machining in gas. Anna. CIRP **46**(1), 143–146 (1997)
19. Kunieda, M., Mlyoshl, Y., Tsutomu, T.: High speed 3D milling by Dry EDM. CIRP Anna. Manufact. Technol. **52**(1), 147–150 (2003)
20. Kao, C.C., Tao, J., Lee, S., Shih, A.J.: Dry wire electrical discharge machining of thin workpiece. Trans NAMRI/SME **34**, 253–260 (2006)
21. Liqing, L., Yingjie, S.: Study of dry EDM with oxygen-mixed and cryogenic cooling approaches. Procedia CIRP **6**, 344–350 (2013)
22. Shue K.Y., Tsai Y.Y., Chang Y.M.: An investigation of attachment on electrode surface in Dry EDM. Adv. Mater. Res. **126–128**, 407–412 (2010)
23. Govindan, P., Joshi S.S.: Experimental characterization of material removal in dry electrical discharge drilling. Inter. J. Mach. Tools Manufact. **50**(5), 431–443 (2010)
24. Wang, T., Zhe, J., Zhang, Y.Q., Li, Y.L., Wen, X.R.: Thermal and fluid field simulation of single pulse discharge in dry EDM. Procedia CIRP **6**, 427–431 (2013)
25. Saha, S.K., Choudhury, S.K.: Multi–objective optimization of the dry electric discharge machining process. hal-00396875, version 1–4 (2009)
26. Tanimura, T., Isuzugawa, K., Fujita, I., Iwamoto, A., Kamitani, T.: Development of EDM in the mist. In: Proceedings of Ninth International Symposium of Electro Machining (ISEM IX), pp. 313–316. Nagoya Japan (1989)
27. Dhakar, K., Dvivedi, A.: Parametric evaluation on near-dry electric discharge machining. Mater. Manufact. Process. **31**(4), 413–421 (2015)
28. Kao, C.C., Tao, J., Shih, A.J.: Near dry electrical discharge machining. Inter. J. Mach. Tools Manufact. **47**(15), 2273–2281 (2007)
29. Tao, J., Shih, A.J., Ni, J.: Near-dry EDM milling of mirror-like surface finish. Inter J. Electr. Mach. **13**, 29–33 (2008)
30. Tao, J., Shih, A.J., Ni, J.: Experimental study of the dry and near-dry electrical discharge milling processes. J. Manufact. Sci. Eng. **130**(1), 11002–11009 (2008)
31. Fujiki, M., Ni, J., Shih, A.J.: Investigation of the effects of electrode orientation and fluid flow rate in near-dry EDM milling. Inter. J. Mach. Tools Manufact. **49**(10), 749–758 (2009)
32. Tao, J.: Investigation of dry and near-dry electrical discharge milling processes. A dissertation, The University of Michigan (2008)
33. Dhakar, K., Dvivedi, A., Dhiman, A.: Experimental investigation on effects of dielectric mediums in near-dry electric discharge machining. J. Mech. Sci. Technol. **30**(5), 2179–2185 (2016)
34. Gholipoor, A., Baseri, H., Shabgard, M.R.: Investigation of near dry EDM compared with wet and dry EDM processes. J. Mech. Sci. Technol. **29**(5), 2213–2218 (2015)

35. Dhakar, K., Chaudhary, K., Dvivedi, A., Bembelge, O.: An environment friendly and sustainable machining method: near-dry EDM. Mater. Manufact. Process. (2019). https://doi.org/10.1080/10426914.2019.1643471

36. Tong, H., Li, Y., Wang. Y.: Experimental research on vibration assisted EDM of micro-structures with non-circular cross-section. J. Mater. Process. Technol. **208**, 289–298 (2008)

37. Yan, B.H., Chen, M.D.: Effect of ultrasonic vibration on electrical discharge machining characteristics of Ti-6Al-4 V Alloy. J. Jap. Inst. Light Met. **5**, 281–285 (1994)

38. Sundaram, M.M., Pavalarajan, G.B., Rajurkar, K.P.: A study on process parameters of ultrasonic assisted micro EDM based on Taguchi method. J. Mater. Eng. Perform. **17**, 210–215 (2008)

39. Prihandana, G.S., Mahardika, M., Mahardika, M.: Effect of low-frequency vibration on workpiece in EDM processes. Ind. J. Eng. Mater. Sci. **19**, 275–378 (2012)

40. Praneetpongrung, C., Fukuzawa, Y., Nagasawa, S., Yamashita, K.: Effects of the EDM combined ultrasonic vibration on the machining properties of Si3n4. Mater. Trans. **11**, 2113–2120 (2010)

41. Koshy, P., Jain, V.K., Lal, G.K.: Experimental Investigations into electrical discharge machining with a rotating disc electrode. Precis. Eng. **1**, 6–15 (1993)

42. Soni, J.S., Chakraverti, G.: Performance evaluation of rotary EDM by experimental design technique. Defense Sci. J. **1**, 65–73 (1997)

43. Fujun. R., Dechen. H., Dianjun. W.: Analysis of motion laws of machining non-sphere by EDM with rotary electrode. J. Mater. Process. Technol. **149**(1–3), 323–327 (2004)

44. Aliakbari, E., Baseri, H.: Optimization of machining parameters in rotary EDM process by using the Taguchi method. Internat. J. Adv. Manufact. Technol. **62**, 9–12, 1041–1053

45. Shanker, K., Ghosh, A.: A study of electro-spark machining characteristics with electro-magnetic spark- gap controlling mechanism. Inter. J. Mach. Tool Des. Res. **15**, 209–222 (1975)

46. Chattopadhyay, K.D., Satsangi, P.S., Verma, S., Sharma, P.C.: Analysis of rotary electrical discharge machining characteristics in reversal magnetic field for copper-en8 steel system. Inter. J. Adv. Manufact. Technol. **38**, 925–937 (2008)

47. Hemant, W., Vijaykumar, S.J., Singh, T.P.: Magnetic field assisted electrical discharge machining of AISI 4140. Appl. Mechan. Mater. **592–594**, 479–483 (2014)

Chapter 20
Effect of Re-normalizing and Re-tempering on Inter-critical Heat Affected Zone(S) of P91B Steel

Modassir Akhtar, Akhil Khajuria, and Raman Bedi

Abstract The novel perspective of this paper was to restore the grain boundary (GB) hardening effect in inter-critical heat affected zone (ICHAZ) of boron modified P91 steel (P91B). To achieve this, samples of the base metal (BM) of P91B steel were thermally simulated by Gleeble followed by post-weld heat treatment (PWHT) and were further re-normalized and re-tempered. With such heat treatment, four different ICHAZ(s) were reproduced. These ICHAZ(s) were subjected to impression creep testing. As impression creep testing brings local deformation, the suitable characterization technique was electron back scatter diffraction (EBSD) for in-depth investigations of microstructural deformation. High creep deformation was observed for simulated ICHAZ followed by PWHT-ICHAZ due to GB softening. Whereas, the least deformation was observed for re-normalized and re-tempered ICHAZ(s) restoring GB hardening. In this respect, type IV cracking was avoided by re-normalizing and re-tempering in P91B steel. This phenomenon was further correlated with the impression creep curves of each ICHAZ with BM.

Keywords Boron modified P91 steel · ICHAZ · Grain boundary hardening and softening effect · Impression creep

M. Akhtar (✉)
Department of Metallurgical and Materials Engineering, National Institute of Technology
Warangal, Warangal 506004, Telangana, India
e-mail: amodassir@student.nitw.ac.in

M. Akhtar · A. Khajuria
Department of Materials Engineering, CSIR—National Metallurgical Laboratory, Jamshedpur
831007, India

R. Bedi
Department of Mechanical Engineering, Dr B. R. Ambedkar National Institute of Technology
Jalandhar, Jalandhar, Punjab 144011, India

Nomenclature

EBSD   Electron back scatter diffraction
GB   Grain boundary
ICHAZ   Inter-critical heat affected zone
HAGB   High angle grain boundary
HAZ   Heat affected zone
LAGB   Low angle grain boundary
MCR   Minimum creep-damage rate
PWHT   Post-weld heat treatment

20.1   Introduction

P91 ferritic/martensitic steel has superior creep resistance and corrosion resistance that leads to its maximum usage in the form of high temperature and high pressure piping material in nuclear and thermal power plant industries [1, 2]. To obtain leak proof joints majorly that transfers steam, high heat input fusion welding processes such as submerged arc welding, manual metal arc welding, gas tungsten arc welding, etc., are used for fabrication of P91 steel components [3]. As these welding processes bring a narrow width of heat affected zone (HAZ) depending upon thermal gradient and phase transformation experienced, this practice has become a grievance issue due to the manifestation of type IV failure at outer HAZ [4, 5]. In a previous attempt, an effort was given to find type IV region by exclusively reproducing singular HAZs using Gleeble thermal simulation and the study confirmed ICHAZ as type IV region due to the formation of fine and soft grains, coarsening of $M_{23}C_6$ carbides, and recovery of martensitic substructure [6, 7]. Followed by welding, PWHT of P91 weldments is a recommended procedure to curtail both solidity and microstructural heterogeneity across HAZ [8, 9]. During PWHT, dynamic recovery and recrystallization occur at ICHAZ [8]. Subsequently, this microstructure receives an additional preferential recovery and recrystallization of ferritic lath structure during in-service exposure [9, 10].

These problems can be overcome by controlling alloying additions. The addition of carbon in P91B steel stabilizes austenite, which would ease in delaying the formation of delta ferrite. Its addition increases tensile strength, hardness, and hardenability. However, the carbon in P91B steel would promote $M_{23}C_6$ and MX precipitation. But, the high concentration of carbon coarsens these precipitates leading to a reduction in creep strength. The controlled addition of carbon in P91B steel maintains toughness and weldability [11–13]. The addition of chromium is beneficial in P91B steel in improving creep strength and to retain oxidation resistance at elevated temperature. It also forms carbides ($M_{23}C_6$ precipitation), decreases martensitic start temperature, and increases A_{c1} temperature (ferrite stabilizer). High diffusion coefficient of Cr than Mo results in the coarsening of $M_{23}C_6$ carbides [11, 12, 14–18]. While

the addition of Mo in P91B steel stabilizes ferrite (increases A_{c1} temperature) at high-temperature by raising the binding force and favors carbides formation. Similar to Cr, its addition also enhances creep strength and toughness by both preventing graphitization and inhibiting temper embrittlement. It decreases martensitic start temperature (Ms) but improves pitting corrosion resistance. Its concentration more than 1% accelerates $M_{23}C_6$ coarsening and laves phase precipitation by decreasing solid solution strengthening. Mo is also known for providing better hardenability and secondary hardening due to carbide formation during tempering. [11, 12, 14, 16, 17].

Similar to previous, vanadium and niobium are ferrite stabilizers, and carbide and nitride are formers. Formation of these vanadium and niobium phases helps in retaining fine subgrains. But, due to chromium diffusion, niobium carbo-nitrides transform into Z-phase, i.e., Cr[Nb(C,N)] [12, 14, 15]. In contrast to previous, nitrogen is an austenite former, which causes a delay in delta ferrite formation. Its addition promotes nitrides causing better hardenability. Nitrogen also provides solid solution hardening and segregates to dislocation to delay its motion at both high and room temperature. High nitrogen contents (>0.2%) cause both formations of unwanted Z-phase with Cr and porosities in the mould. It also lowers Ms temperature and gives resistance to pitting corrosion [12, 15, 17]. Mn does not provide enough solid solution strengthening and is the cheapest carbide former. It lowers A_{c1} temperature hence austenite stabilizer. Its addition delays carbides separation with M_6C precipitation but promotes $M_{23}C_6$ coarsening by partitioning. Mn is a deoxidant and behaves as sulfur segregation preventer by forming MnS, which promises sound weld deposits. This sulfur in addition to phosphorous promotes hot shortness in the free form at service and processing temperature hence must be kept under ppm. Increased Mn contents may cause temper embrittlement resulting in a loss in creep strength, but gain in hardenability [12, 14, 15, 17, 19].

Controlled addition of silicon stabilizes ferrite and delays lave phase formation resulting in better high-temperature mechanical properties. It improves oxidation resistance and graphitizes carbides by accelerated carbon diffusivity. This accelerated carbon diffusivity promotes $M_{23}C_6$ coarsening [12, 14, 15, 17, 18, 20]. Aluminium graphitizes carbides and in small quantities provides both improved mechanical strength and high-temperature oxidation and corrosion resistance. It is a deoxidant to clean steel, which results in enhanced toughness [14, 17, 19]. Ni graphitizes the carbides that cause a delay in the carbides separation and lowers A_{c1} temperature (austenite stabilizers). In small quantities, it provides better mechanical properties but lowers the ductile to brittle transition temperature. Its addition increases diffusion coefficient (i.e., $M_{23}C_6$ coarsening) but gives corrosion resistance in sulfuric acid [13, 15, 17].

In controlled concentrations, boron enhances creep strength, tensile and creep ductility, and quench hardenability by retaining fine subgrains. The fine grain and stable microstructure in P91B steel are due to its memory effect before and after welding. The decreased self-diffusion coefficient in P91B steel due to its addition delays coarsening of $M_{23}C_6$ carbides and refines MX type carbides/carbo-nitrides, which lead to the occupation of free boron in vacancies of GBs and in lattice site of $M_{23}C_6$ carbides. Such phenomenon promotes the formation of $M_{23}(C,B)_6$ carbides

at GBs and sub-GBs, which are responsible for a decrease in impact toughness and stabilization of ferrite/martensite matrix against both re-austenization during phase transformation and recovery during an early stage of tertiary creep. Boron is known for enhanced GB and sub-GB cohesion due to its segregating nature to these boundaries. These cohesions are mainly responsible for GB and sub-GB strengthening. But the addition of high amount of boron causes hot shortness, GB embrittlement, and intergranular embrittlement. Higher concentration of boron and nitrogen causes the formation of intermetallic phase, i.e., boron nitride, which depletes beneficial effect of boron [12, 14, 15, 17, 21–23].

Our previous studies also revealed a delay in type IV failure on modification of 100 ppm boron in P91 steel at ICHAZ [8, 24–27]. However, the role of all other elements is now clear, but the role of boron is still mysterious in coming to its true mechanism. It was reported that after PWHT, re-normalizing followed by re-tempering may alter type IV failure in P91 steel weldments [3]. However, continuous reports of weldment failure by type IV in boron-free P91 steel being treated by re-normalizing and re-tempering reduced research concentration on this side [28, 29]. Hence, no literature is available that describes phenomenological behaviour for 100 ppm boron added weldments being re-normalized and re-tempered after PWHT. Conventional uniaxial creep testing requires both longer testing time and bulk materials. However, the impression creep testing with flat indenter calls lower testing time and less material [6]. The main advantage of such testing is that it is highly sensitive to minor alloy modification and change in heat treatment [7]. But, the deformation produced by this technique is localized and require special microscopy technique to characterize. EBSD is one of those techniques, which locally characterizes the change in microstructure. However, the laboratory X-ray diffractometer scans bulk surfaces, while characterization through transmission electron microscopy is tedious and unreliable due to poor statistics and difficulty in identifying local substructure. Bearing all points, this paper deals to illuminate softening and hardening effects in ICHAZ during as-simulated, PWHT, and re-normalized and re-tempered conditions due to the presence of miraculous element boron in P91 steel.

20.2 Material and Methods

20.2.1 Material and Heat Treatment History

A 100 ppm boron modified P91 steel was received in normalized and tempered conditions. Its chemical composition and the history of heat treatments are shown in Table 20.1.

Table 20.1 Chemical composition and heat treatment history of as-received P91B steel

Elements	C	Cr	Mo	Mn	Si	V	Nb	Al	Ni	B	N	Fe	Normalizing	Tempering
wt.%	0.10	8.26	0.88	0.33	0.3	0.19	0.06	0.03	0.01	0.01	0.004	Bal.	1050 °C/0.5 h	760 °C/3 h

20.2.2 Physical Simulation of Inter-critical HAZ(s) and Their Re-Normalizing and Re-Tempering Treatments

The purpose of physical simulation of inter-critical HAZ(s) by Gleeble in vacuum was to optimize the process parameters of welding. The sample having a shape of rectangular prism with dimensions 78 mm × 11 mm × 11 mm was used for simulation purpose. The cycle of inter-critical HAZ(s) was consisted of linear heating it from room temperature to inter-critical temperature, i.e., between A_{c1} and A_{c3} temperature. In this temperature, both BCC and FCC phases were present. After reaching to inter-critical temperature range, it was soaked for 8 s and ultimately cooled according to Eq. 20.1. Equation 20.1 is used for exponential cooling. However, the definition and selection of inter-critical HAZ(s) were based on its conventional definition same as reported earlier [6–8, 10]. Four ICHAZ samples were physically simulated at heating and cooling rates of 40 °C and 20 °C, respectively, at the peak temperature and soaking time of 865 °C and 8 s, respectively. First condition, i.e., as-simulated ICHAZ is referred to as ICHAZ. Further, second ICHAZ sample in as-simulated condition was exposed to PWHT at 760 °C/3 h followed forced air cooling and is referred to as 760ICHAZ. Third sample after both simulation and PWHT was re-normalized at 1050 °C/0.5 h followed by re-tempering at 760 °C/2 h and is referred to as 6ICHAZ. Only one sample after re-normalizing and re-tempering was air cooled, i.e., 6ICHAZ. At last, fourth sample, which was not air cooled and was further exposed to 800 °C/2 h and is referred to as 7ICHAZ. Such heat treatments of ICHAZ(s) with heat treatment of BM are shown in Fig. 20.1.

$$T = T_{\mathrm{P}} \times \exp(-0.47t/\Delta t) \tag{20.1}$$

where T is instantaneous temperature in °C, T_{p} is peak temperature in °C, t is time in seconds, and Δt is time to cool from 800 to 500 °C in seconds. The heat input
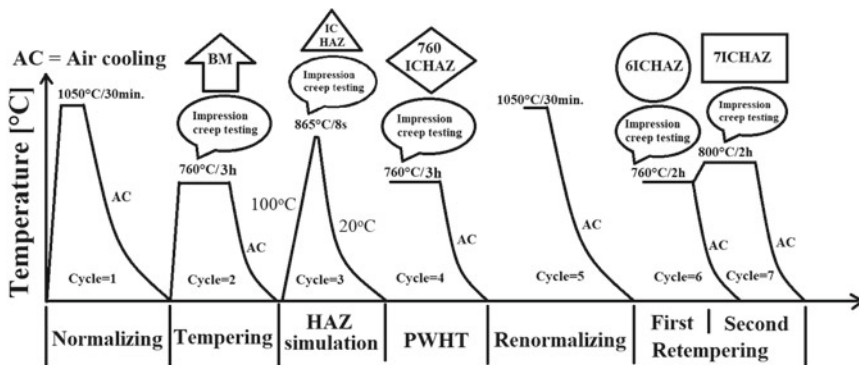
Fig. 20.1 Thermal history of P91B steel from as-received state to re-normalized and re-tempered state

experienced during the simulation was 1.6 kJ/mm, which was found using a real-time data acquisition system during submerged arc welding.

20.2.3 Impression Creep Testing

After completion of simulation of ICHAZ(s) and further heat treatments, samples from each condition were exposed to impression creep testing at an operating temperature of 625 °C and applied stress of 350 MPa. The impression creep testing was done for random time periods for all samples till minimum creep-damage rate (MCR) was obtained, just after the primary creep stage in each condition on the polished surface (polished up to 600 grit emery paper). Since high temperature causes the formations of Cr_7O_6 and $Cr_{23}O_6$ on sample surface, which may hinder to deform sample in compressive loading; therefore, the creation of vacuum in the order of 10^{-3} mbar was mandatory inside the chamber. The dimensions of the sample were $10 \times 10 \times 10$ mm^3 for impression creep testing. Impression creep testing considers compression type loading, which makes it mandatory to adopt a correlation factor to convert compressive stress of impression creep testing into tensile stress of uniaxial creep testing. This conversion factor was reported for many materials as 3.3 and can be compared with the ratio of hardness by its strength [30, 31]. In this respect, the compressive load (350 MPa) used in this paper would correspond to 106 MPa in tensile stress conditions. Linear variable differential transducer was used to obtain the values of depth of impression with respect to time during impression creep testing. For getting impression velocity to distinguish primary and secondary creep stage during impression creep testing, the values obtained from linear variable differential transducer, i.e., depth of impression were differentiated with respect to time. Subsequently, the impression velocity at the end of secondary stage creep was used to obtain MCR. The governing equations used to calculate stress, impression velocity, and MCR are given in Eqs. 20.2, 20.3, and 20.4 [7, 26, 31, 32].

$$\text{Stress} = \frac{4F}{\pi d^2} \tag{20.2}$$

$$\text{Impression velocity} = \frac{d(\text{depth of impression})}{d\tau} \tag{20.3}$$

$$\text{Minimum creep-damage rate} = \frac{\text{Impression velocity}}{\beta d} \tag{20.4}$$

where F is applied load in Newton, d is the diameter of indenter (1.5 mm) and the material was made up of tungsten carbide, τ is test time in seconds and β is the correlation factor (~1). Yu and Li reported this value of β to correlate the impression creep data and uniaxial tensile creep data by the finite element method [33]. After Yu and Li [33], this value has been used to relate both the creep testing for many materials [7, 26, 34–36].

20.2.4 Electron Back Scatter Diffraction

After impression creep testing, for EBSD characterization, samples were mechanical polished up to 1200 grit energy paper followed by electro-chemical polishing in the solution of 20% perchloric in methanol at 14–16 V for 5 s. EBSD measurements were done at deformed zone at a step size of 100 nm for $100 \times 100 \ \mu m^2$ surface area. The orientation data obtained from EBSD was processed in TSL–Orientation Imaging Microscopy 7 software.

20.3 Results and Discussion

20.3.1 Creep Deformation of ICHAZ(s) Under Different Heat Treatment Conditions

Impression creep testing results of ICHAZs are shown in Fig. 20.2 in terms of depth of impression as regards BM of P91B steel. Depth of impression of BM exhibited a sharp transition between primary and secondary creep deformation (as indicated by arrow) followed by 6ICHAZ and 7ICHAZ. While the relatively smooth transition was observed for ICHAZ and 760ICHAZ samples in Fig. 20.2a. Figure 20.2b shows primary and secondary impression velocity of all samples. It can be noted in Fig. 20.2a that longer primary impression velocity was obtained for 6ICHAZ followed by BM, 7ICHAZ, 760ICHAZ, and ICHAZ. This phenomenon signified the strain hardening capability of samples in the descending order, which was equilibrated with creep damage after primary impression velocity. Equilibrium strain hardening with creep deformation in terms of MCR was plotted (Fig. 20.3).

The term microstructural degradation comes when there are undesirable changes in microstructural features like coarsening of precipitates and subgrains, formation
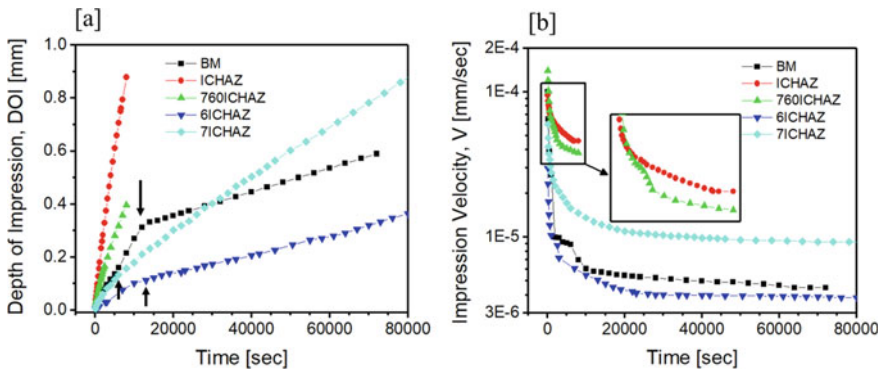
Fig. 20.2 Depth of impression and impression velocity of ICHAZs as regards BM of P91B steel

Fig. 20.3 Percent change in MCR of ICHAZ(s) as regards MCR of base metal
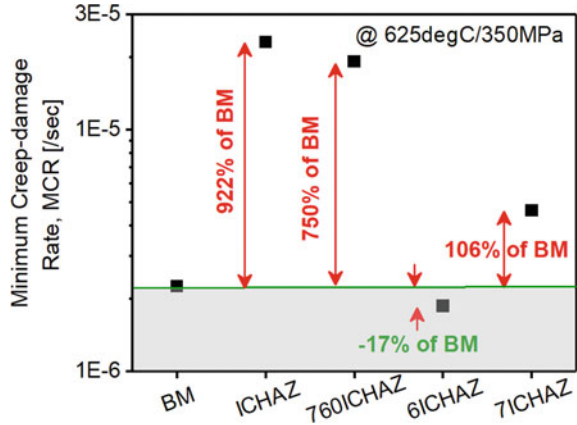
and growth of intermetallics by depleting solid solution from the matrix, etc. In impression creep testing, the degradation of microstructures may or may not occur depending upon chemical composition, heat treatment history, prior loading conditions, operating temperature, and applied load. In contrast to previous, creep damage comes due to the formation of creep cavities during the tertiary creep stage of tensile creep testing. In this testing, high accumulation of vacancies caused the formation of creep voids, which finally agglomerate to form creep cavities under tensile loading. But, during impression creep testing, an absence of tertiary creep stage caused a handicap in the formation of creep cavities. An application of compressive loading during impression creep testing, suppresses not only the tertiary creep stage but also reduces the availability of free vacancies to provide GB sliding, which is truly responsible for the failure of a component. Here, the key link between two-creep testing to use term creep damage is the manipulation of the number of available vacancies, which is essential to accommodate creep testing either in tensile loading and creep loading. Therefore, the term creep damage is also applicable for impression creep.

As observed from Fig. 20.3, MCR of BM was assumed as a reference value to understand the softening and hardening phenomena of GB onset from different heat treatment conditions. High GB hardening around more than 17% from BM was observed for 6ICHAZ followed by 7ICHAZ (106% weaker than BM). Whereas, high GB softening was observed in ICHAZ (around 922% of BM) followed by 760ICHAZ (around 750% of BM). Based on the Monkman–Grant relationship reported in [1], the ratio of creep life for BM: ICHAZ: 760ICHAZ: 6ICHAZ: 760ICHAZ was 1: 0.004: 0.01: 1.05: 0.4, respectively. Hence, it can be said that GB softening during impression creep testing in ICHAZ and 760ICHAZ caused 99.6% and 99% reduction in creep life as regards BM. Whereas, GB hardening during impression creep testing improved creep life for 6ICHAZ and 7ICHAZ as regards both simulated and PWHT treated ICHAZs. But, the creep life in 7ICHAZ decreased as regards creep life of BM by 60%, whereas the creep life of ICHAZ increased by 5% as regards creep life of BM.

20.3.2 EBSD Measurements of ICHAZ(s) Under Different Heat Treatment Conditions

20.3.2.1 Boundary Density

Ferritic/martensitic 9% Cr steels derive their creep strengths from various strengthening mechanisms that simultaneously occur to retard dislocation motion during creep exposure. Martensitic recovery in these grades becomes cumbersome on the application of thermal load since dislocations have to cross number of obstacles in their path like GBs/sub-GBs, precipitates, and solute atoms in solid solution or dislocations themselves. In this respect, GBs/sub-GBs act as barriers to the movement of dislocations across them, which contribute to this type of hardening mechanism in 9Cr steels. Therefore, an increase in the fraction of boundaries in microstructure creep strength can be improved, since small boundaries, i.e., sub-GBs would serve better to hinder the motions of dislocations in them. The sub-GBs are usually low angle grain boundaries (LAGB), whereas GBs are high angle grain boundaries (HAGB). With the application of EBSD technique, LAGB and HAGB can be distinguished based on specified misorientation angles.

Figure 20.4 shows the plot of boundary line per unit area versus misorientation angle, which is referred to as GB density. It can be observed that low angle grain boundary, i.e., 0°–15° (LAGB) does not exhibit much variation among ICHAZ, 760ICHAZ, and 6ICHAZ as the lath block structures were similar whereas it increased for 7ICHAZ. This was attributed to high tempering temperature for long time, which led to recrystallization of lath block structure. However, boundary density as regards high angle grain boundary, 15°–63° (HAGB) was higher in 7ICHAZ followed by ICHAZ while similar values of boundary density were observed for 760ICHAZ and 6ICHAZ.

Fig. 20.4 Boundary line per unit area versus misorientation angle
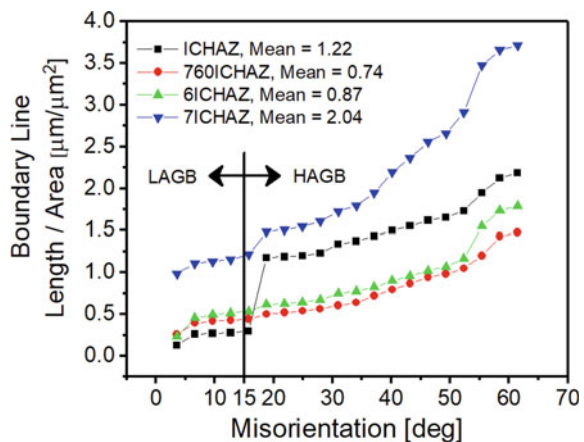
20.3.2.2   Grain Orientation Spread

The formation of dislocations in a material is indicated from the residual strain that occurs as local variations in the microstructure. To distinguish these strain variations, EBSD grain orientation spread parameter can be used. This method provides the same value to each scanned point within a single grain. Therefore, based on different strain values of different grains, variation in microstructural strain could be analyzed. Such an approach has been implemented to distinguish the recrystallized grain fraction, sub-structured grain fraction, and deformed grain fraction in P91 steel (Fig. 20.5, Table 20.2) [29, 37]. In this respect, Gleeble simulated and deformed ICHAZ showed higher recrystallization having no deformed grains. This recrystallization of ICHAZ
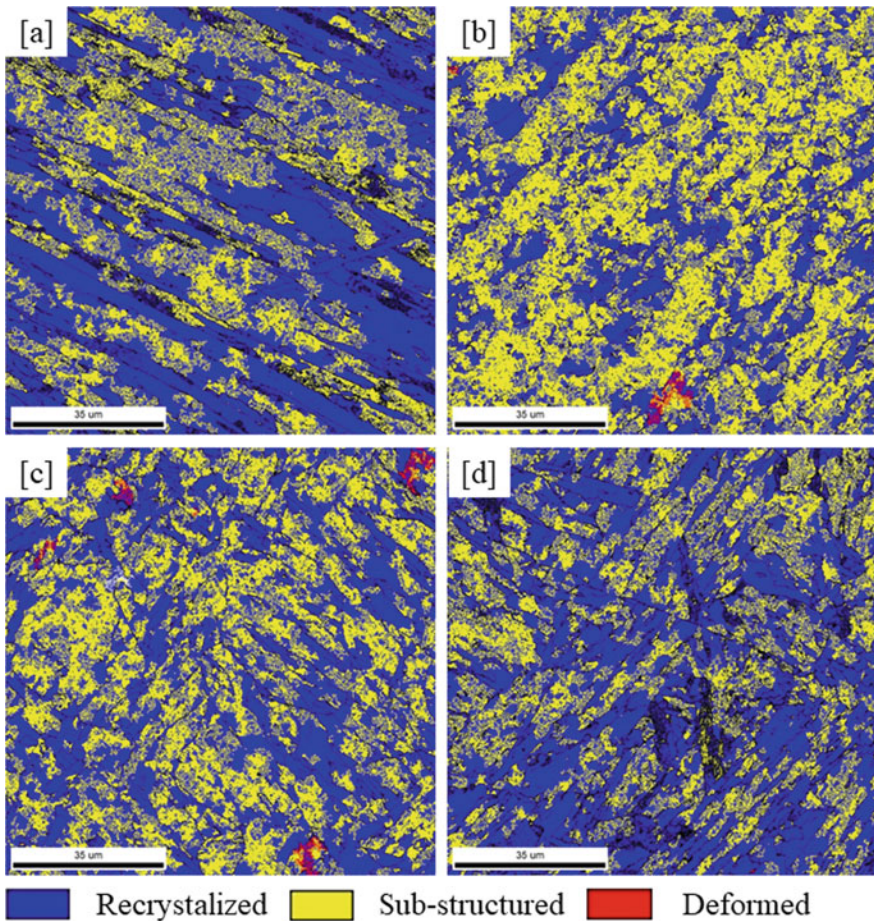
Fig. 20.5 Grain orientation spread showing recrystallized, sub-structured, and deformed grains of **a** ICHAZ, **b** 760ICHAZ, **c** 6ICHAZ, and **d** 7ICHAZ

Table 20.2 Grain orientation spread values and HAGB fraction for ICHAZ(s)

Grain orientation spread value (%)/sample	ICHAZ	760ICHAZ	6ICHAZ	7ICHAZ
Recrystallized [0–1.5]	69.3	48.3	59.0	69.8
Sub-structured [1.5–4]	30.7	51.4	40.3	30.2
Deformed [>4]	0.0	0.3	0.7	0.0
HABG [15–63°, %]	87.2	71.3	71.1	69.0

further decreased for deformed 760ICHAZ by increasing substructure. While re-normalizing and re-tempering with deformation further increased recrystallization by decreasing substructure of 760ICHAZ. It can be noted that this recrystallization value did not further decrease for 7ICHAZ rather than it increased by reducing substructure fraction. The presence of retained austenite in both ICHAZ and re-normalized 760ICHAZ transformed it into martensite in 760ICHAZ and 6ICHAZ, respectively. This transformation caused deformed grains in the latter samples. Table 20.2 also shows the values of HAGB, which confirmed that decreased HAGB in deformed 760ICHAZ was due to lath coarsening. This coarsening was constant in deformed 6ICHAZ. But, it slightly dropped for 7ICHAZ. During this characterization, it was observed that high deformed grains were present in ICHAZ followed by 760ICHAZ, 7ICHAZ, and 6ICHAZ.

20.3.2.3   Kernel Average Misorientation

Kernel average misorientation represents local strain distribution accumulated in microstructure [37] as shown in Fig. 20.6. Calculation of kernel average misorientation provides the average misorientation around the measured point with respect to the defined set of nearest neighbour points during EBSD. During kernel average misorientation calculation from EBSD data, the local misorientation was assigned to the centre point of any fixed grain with respect to all points in the perimeter of the kernel. Normally, the value of kernel average misorientation would be high in deformed grains due to a higher value of dislocation density. Also, the analysis of kernel average misorientation aids to understanding the localized deformation, local lattice distortions, and high dislocation density [38]. Furthermore, it qualitatively advises strain energy stored in a grain. The colour variation in kernel average misorientation maps depicts local strain distribution, i.e., blue colour represents no strain, whereas red represents highly strained region and green represents mild strain level. Therefore, the variation of colour in a kernel average misorientation map represents local strain distribution in the deformed microstructure of ICHAZ samples.

High values of kernel average misorientation were observed for 7ICHAZ followed 760ICHAZ and 6ICHAZ. Whereas, low values of kernel average misorientation existed in ICHAZ but they were more smoothly distributed in 6ICHAZ. High values of kernel average misorientation are attributed to the presence of carbide particles. In Fig. 20.6a, the heterogeneity was mainly observed around GBs. It means
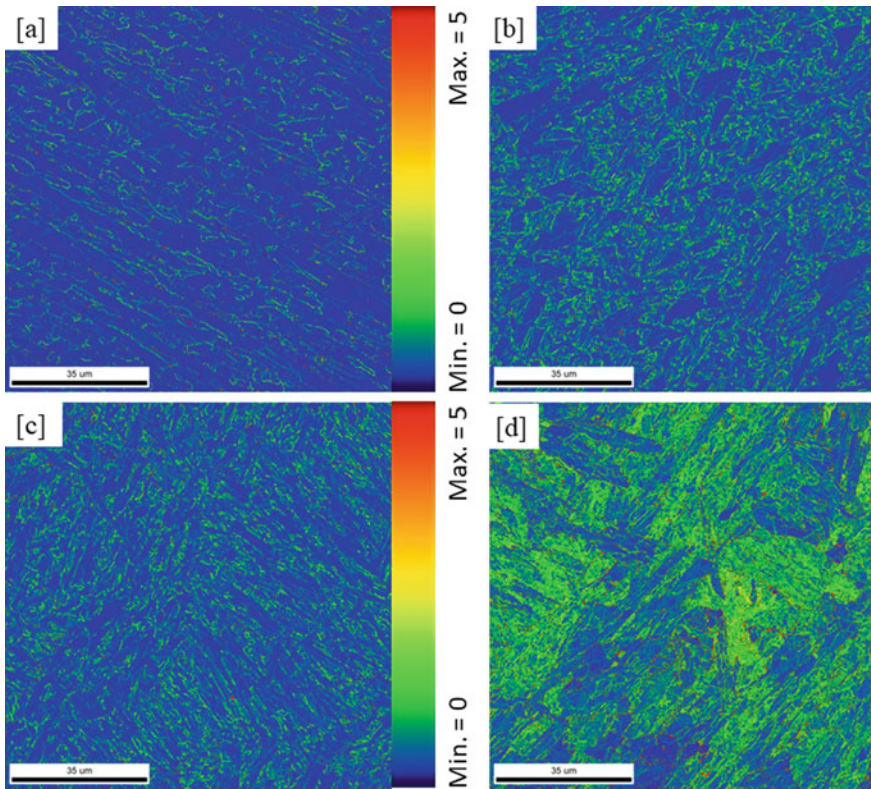
Fig. 20.6 Kernel average misorientation of **a** ICHAZ, **b** 760ICHAZ, **c** 6ICHAZ, and **d** 7ICHAZ

that carbides precipitated mainly at GBs, whereas in 760ICHAZ (Fig. 20.6b), heterogeneity was due to carbides formation both at GBs and inside the matrix. In both samples, owing to low values of kernel average misorientation after impression creep testing signified that de-alloying of matrix allowed higher creep deformation. The homogeneous kernel average misorientation distribution in 6ICHAZ confirmed that re-normalizing and re-tempering minimized heterogeneity in terms of refinement and softness by dissolving coarse carbides during re-normalizing that re-precipitated during re-tempering. This resulted in a delay in GB sliding during impression creep testing. However, the slight heterogeneity occurred during the second stage of tempering in 7ICHAZ. This was attributed to the high coarsening of carbides as notable in Fig. 20.6d.

20.4 Conclusions

Grain boundary hardening and softening effects of ICHAZ(s) were investigated by using impression creep testing and EBSD. Following conclusions were drawn from this study:

- Impression creep testing showed hardening in 6ICHAZ and 7ICHAZ while softening in ICHAZ and 760ICHAZ. In this respect, type IV cracking was absent for 6ICHAZ. The ratio of creep life for BM: ICHAZ: 760ICHAZ: 6ICHAZ: 760ICHAZ was 1: 0.004: 0.01: 1.05: 0.4, respectively.
- Less variation in boundary density as regards LAGB was found in ICHAZ, 760ICHAZ, and 6ICHAZ while slightly high values were observed 7ICHAZ. Whereas, boundary density as regards HAGB was higher in 7ICHAZ followed by ICHAZ and similar for the rest of ICHAZ(s).
- Higher recrystallization fraction was observed for ICHAZ and 7ICHAZ. This was less in 760ICHAZ and 6ICHAZ with an increasing sub-structured fraction. The presence of austenite caused high deformed fraction in 760ICHAZ and 6ICHAZ. HAGB was high in ICHAZ followed by 760ICHAZ, 6ICHAZ, and 7ICHAZ.
- High values of kernel average misorientation were present in 7ICHAZ followed by 760ICHAZ, 6ICHAZ, and ICHAZ. The homogeneity in kernel average misorientation among grains for 6ICHAZ caused hardening. While the degree of increased variation reduced hardening and invited softening.

References

1. Fujio, A., Kern, T.U., Viswanathan, R.: Creep-Resistant Steels. Elsevier (2008)
2. Khajuria, A., Kumar, R., Bedi, R.: Effect of boron addition on creep strain during impression creep of P91 steel. J. Mater. Eng. Perform. **28**(7), 4128–4142 (2019)
3. Laha, K., Chandravathi, K.S., Parameswaran, P., Rao, K.B.S., Mannan, S.L.: Characterization of microstructures across the heat-affected zone of the modified 9Cr-1Mo weld joint to understand its role in promoting type IV cracking. Metall. Mater. Trans. A **38**(1), 58–68 (2007)
4. Francis, J.A., Mazur, W., Bhadeshia, H.K.D.H.: Review type IV cracking in ferritic power plant steels. Mater. Sci. Technol. **22**(12), 1387–1395 (2006)
5. Abson, D.J., Rothwell, J.S.: Review of type IV cracking of weldments in 9–12% Cr creep strength enhanced ferritic steels. Int. Mater. Rev. **58**(8), 437–473 (2013)
6. Khajuria, A., Kumar, R., Bedi, R.: Characterizing creep behaviour of modified 9Cr1Mo steel by using small punch impression technique for thermal powerplants. J. mechan. Mechan. Engg. **4**(3), 47–61 (2018)
7. Akhtar, M., Khajuria, A., Kumar, V.S., Gupta, R.K., Albert, S.K.: Evolution of microstructure during welding simulation of boron modified P91 Steel. Phys. Met. Metallogr. **120**(7), 672–685 (2019)
8. Akhtar, M.: Metallurgical Characterisation of Simulated Heat Affected Zone in Boron Modified P91 Steel. National Institute of Technology, Warangal (2017)
9. Akhtar, M., Khajuria, A., Pandey, M.K., Ahmed, I.: Effects of boron modifications on phase nucleation and dissolution temperatures and mechanical properties in 9% Cr steels: sensitivity and stability. Mater. Res. Express **6**(12), 1265k1 (2019)

10. Akhtar, M., Khajuria, A., Kumar, R., Bedi, R.: Metallurgical investigations on dual heat cycled boron alloyed P91 ferritic/martensitic steel. In: Proceedings of Young Professionals Conference, International Institute of Welding, Chennai, India (2017). https://doi.org/10.13140/rg.2.2.18467.30241/2

11. Akhtar, M., Khajuria, A.: Probing true microstructure-hardening relationship in simulated heat affected zone of P91B steels. Metallogr. Microstruct. Anal. **8**(5), 656–677 (2019)

12. Akhtar, M., Khajuria, A.: Effects of prior austenite grain size on impression creep and microstructure in simulated heat affected zones of boron modified P91 steels. Mater. Chem. Phys. **249**, 122847 (2020)

13. Koisstinen, D.: A general equation prescribing the extent of the austenite-martensite transformation in pure iron-carbon alloys and plain carbon steels. Acta Metall. **7**, 59–60 (1959)

14. Akhtar, M., Khajuria, A., Pandey, M.K., Ahmed, I., Bedi, R.: Effects of boron modifications on phase nucleation and dissolution temperatures and mechanical properties in 9% Cr steels: alloy design. Mater. Res. Express **6**(12), 1265k3 (2019)

15. Maruyama, K., Kota, S., Jun-ichi, K.: Strengthening mechanisms of creep resistant tempered martensitic steel. ISIJ Int. **41**(6), 641–653 (2001)

16. Yan, W., Wang, W., Shan, Y., Yang, K., Sha, W.: 9–12Cr heat-resistant steels. Springer (2015)

17. Durand-Charre, M.: La microstructure des aciers et des fontes. SIRPE, Paris (2003)

18. Shi, P., Engström, A., Höglund, L., Sundman, B., Ågren, J.: Thermo-Calc and DICTRA enhance materials design and processing. Mater. Sci. Forum **475**, 3339–3346 (2005)

19. Goswami, P.: P(T) 91 steel—a review of current code and fabrication practices. In: Proceedings of the Sixth International Conference on Advances in Materials Technology for Fossil Power Plants, La Fonda, USA (2010)

20. Paul, V.T., Saroja, S., Vijayalakshmi, M.: Microstructural stability of modified 9Cr–1Mo steel during long term exposures at elevated temperatures. J. Nucl. Mater. **378**(3), 273–281 (2008)

21. Akhtar, M., Khajuria, A.: Probing true creep-hardening interaction in weld simulated heat affected zone of P91 steels. J. Manuf. Processes **46**, 345–356 (2019)

22. Abe, F., Tabuchi, M., Tsukamoto, S.: Alloy Design of Martensitic 9Cr-boron steel for A-USC boiler at 650°C-Beyond grades 91, 92 and 122. Energy Mater **2014**, 129–136 (2014)

23. Abe, F., Tabuchi, M., Kondo, M., Tsukamoto, S.: Suppression of Type IV fracture and improvement of creep strength of 9Cr steel welded joints by boron addition. Int. J. Press. Vessels Pip. **84**(1–2), 44–52 (2007)

24. Akhtar, M., Khajuria, A., Sahu, J.K., Swaminathan, J., Kumar, R., Bedi, R., Albert, S.K.: Phase transformations and numerical modelling in simulated HAZ of nanostructured P91B steel for high temperature applications. Appl. Nanosci. **8**(7), 1669–1685 (2018)

25. Khajuria, A., Bedi, R., Kumar, R.: Investigation of impression creep deformation behaviour of boron modified P91 steel by high end characterization techniques. In: Manufacturing Engineering, pp. 137–150. Springer, Singapore (2019)

26. Akhtar, M., Khajuria, A., Kumar, V.S., Gupta, R.K., Albert, S.K.: Evolution of microstructure during welding simulation of boron modified P91 steel. Phys. Met. Met. Sci **120**(7), 731–745 (2019). https://doi.org/10.1134/S0015323019070052

27. Vaibhav, A., Khajuria, A., Akhtar, M., Singh, M.P., Kumar, A.: Effects of heat treatments on grain size and hardness of P91 and boron added P91 steels, Behind The Teacher's Desk (BTTD-2017), CSIR-NML, Jamshedpur. India (2017). https://doi.org/10.13140/RG.2.2.20792.03841

28. Pal, S., Khajuria, A., Akhtar, M.: Influence of aging on hardness and tool wear of artificially aged aluminium alloy 6061. IAETSD J. Adv. Res. Appl. Sci. **5**(2), 477–481 (2018). http://iaetsdjaras.org/gallery/7-february-488.pdf

29. Huysmans, S., Vekeman, J., Hautfenne, C.: Dissimilar metal welds between 9Cr creep strength enhanced ferritic steel and advanced stainless steels—creep rupture test results and microstructural investigations. Weld. World. **61**(2), 341–350 (2017)

30. Hyde, T.H., Yehia, K.A., Becker, A.A.: Application of the reference stress method for interpreting impression creep test data. Mater. High Temp. **13**, 133–138 (1995). https://doi.org/10.1080/09603409.1995.11689511

31. Chu, S.N.G., Li, J.C.M.: Impression creep; a new creep test. J. Mater. Sci. **12**, 2200–2208 (1977). https://doi.org/10.1007/BF00552241

32. Khajuria, A., Akhtar, M., Kumar, R., Swaminanthan, J., Bedi, R., Shukla, D.K.: Effect of boron modified microstructure on impression creep behaviour of simulated multi-pass heat affected zone of P91 steel. In: Dutta, S., Chakraborty, S.S. (eds.) In: National Conference on Advanced Materials, Manufacturing and Metrology, pp. 150–157. CSIR-CMERI, Durgapur (2018). https://doi.org/10.13140/rg.2.2.34633.24164/2

33. Yu, H.-Y., Li, J.C.M.: Computer simulation of impression creep by the finite element method. J. Mater. Sci. **12**, 2214–2222 (1977). https://doi.org/10.1007/BF00552243

34. Chu, S.N.G., Li, J.C.M: Impression creep of β-tin single crystals. Mater. Sci. Eng. **39**, 1–10 (1979). https://doi.org/10.1016/0025-5416(79)90164-2

35. Talari, M.K., Kishore, B. N., Kallip, K., Leparoux, M., Koller, R.E., Alogab, K.A., Maedar, X.: Microstructure, mechanical, and impression creep properties of AlMg5–0.5 vol% Al2O3 nanocomposites. Adv. Eng. Mater. **18**, 1958–1966 (2016). https://doi.org/10.1002/adem.201600301

36. Dorner, D., Röller, K., Skrotzki, B., Stöckhert, B., Eggeler, G.: Creep of a TiAl alloy: a comparison of indentation and tensile testing. Mater. Sci. Eng., A **357**, 346–354 (2003). https://doi.org/10.1016/S0921-5093(03)00205-3

37. Wright, S.I., Nowell, M.M., Field, D.P.: A review of strain analysis using electron backscatter diffraction. Microsc. Microanal. **17**(3), 316–329 (2011)

38. Saraf, L.: Kernel average misorientation confidence index correlation from FIB sliced Ni-Fe-Cr alloy surface. Microsc. Microanal. **17**(S2), 424–425 (2011)

Chapter 21
Joining of Dissimilar Materials—Aluminium to Steel—Using CMT + P Weld-Brazing Process

Jaivindra Singh, Kanwer Singh Arora, and Dinesh Kumar Shukla

Abstract CMT + P weld-brazing technique was applied for dissimilar joining of aluminium alloy (AA5052) and DP780 steel. Results showed a reduction in wettability of joints on increasing the aluminium (Al) sheet thickness from 1 to 2 mm due to reduced spreading ability of molten filler over steel surface. To overcome the issue of wettability, two approaches were used: (i) increasing WFR and (ii) adding pulses in the weld cycle. A significant improvement in the wettability was observed using both methods. An increase of about 18% (4.8–5.7 kN) and 50% (4.8–7.2 kN) in the load to failure of joints during shear-tensile testing was observed on increasing WFR (5 m/min) and adding two pulses respectively. Spilling of hard and brittle intermetallic phases into fusion zone due to excessive turbulence in the molten pool and formation of geometrical necking resulted in a drop in failure load at WFR of 6 m/min and 4 pulses despite higher wettability at these two parameters. It is suggested to optimize the number of pulses and CMT cycles to improve the load bearing capacity of the joints because in addition to wettability, bead shape and distribution (formation and growth) of intermetallic phases at the interface also play a crucial role in determining the properties of weld-brazed joints. To overcome the issues arising from increased Al sheet thickness, CMT + P technique has the potential to improve the joint properties at a constant deposition rate owing to better control over heat input.

Keywords CMT + P weld-brazing · Dissimilar materials · Wettability · Shear-tensile strength

J. Singh (✉) · D. K. Shukla
Department of Mechanical Engineering, Dr B R Ambedkar National Institute of Technology, Jalandhar, Punjab 144011, India
e-mail: jaivindra321@gmail.com

D. K. Shukla
e-mail: shukladk@nitj.ac.in

K. S. Arora
Materials Welding & Joining Research Group, Research and Development, Tata Steel Limited, Jamshedpur 831007, India
e-mail: kanwer.arora@tatasteel.com

Nomenclature

CMT   Cold metal transfer
IMC   Intermetallic compound
WFR   Wire feed rate
MIG   Metal inert gas
TIG   Tungsten inert gas
EMF   Electromagnetic field
DP   Dual-phase steel
SEM   Scanning electron microscopy

21.1 Introduction

Hybrid/multi-material structure design in the automotive industry obtained via the interaction of dissimilar materials (i.e. chemically different constituents) is a promising approach to address the ecological and economic issues across the globe. Lightening of automobiles can be achieved by adopting high-strength steels of reduced thickness or by the use of materials with high specific strength (i.e. high strength-to-weight ratio) in the manufacturing of bodies. Aluminium alloys are being widely used in automobiles owing to its high specific strength and good corrosion resistance which brings the necessity to join aluminium with steel [1–3]. The key challenge of dissimilar joining of Al to steel includes differences in thermo-physical properties (e.g. melting point, thermal conductivity, and coefficient of thermal expansion) and the formation of hard and brittle intermetallic compound (IMC) layer at the joint interface [4]. Brazing is a promising technique to join materials with large difference in melting points as one of the materials remains solid and the other one melts with the filler metal. During the lap joining of Al to steel using Al-based filler metal, welding occurs between Al base metal and Al filler, whereas brazing takes place between the filler and the steel by means of inter-diffusion of atoms across the L/S interface [5]. Due to low solid solubility of Fe in Al (~0.03 at.%), formation of intermetallic phases is inevitable at the L/S interface and the thickness of IMC layer increases proportionally with the welding heat input. There are two contradictory phenomenons associated with the formation of intermetallic compounds: (i) It ensures strong atom-to-atom bonding between Al and steel by forming an interface reaction zone. (ii) Formation of thick IMC layer can degrade the mechanical properties of the joint due to high brittleness and low structure symmetry of the Al-rich intermetallic compounds (orthorhombic η-Fe_2Al_5 and monoclinic θ-Fe_4Al_{13}) [4, 6–8]. It has been reported that incorporation of silicon (Si) in the filler composition can suppress the rapid growth of intermetallic compounds by participating in the interfacial reaction zone. Reason claimed for this reduction is that Si blocked the easy diffusion path of Al atoms by occupying structural vacancies (~30%) along the long axis of η-Fe_2Al_5 and hence hindered the rapid growth of IMC layer. In the previous
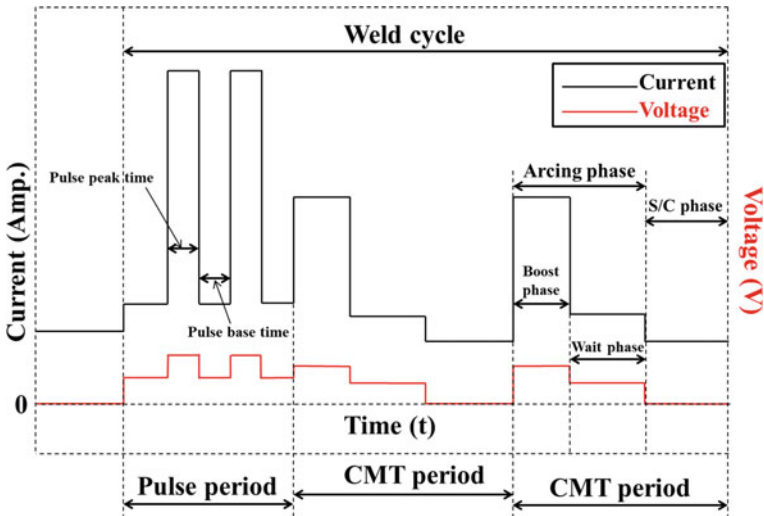
Fig. 21.1 Schematic of CMP + P weld cycle

studies, it has been suggested that the thickness of IMC layer should be less than 10 µm in order to achieve the desired properties [9–13].

A new cold metal transfer (CMT) method, CMT plus pulse (CMT + P) process, has been introduced by Fronius Company, Austria, which is a combination of conventional CMT process and pulsed welding process [14]. The schematic of variation of voltage and current variation during CMT + P weld-brazing cycle (for two CMT and two pulse cycles) is shown in Fig. 21.1. CMT brazing is an extension of MIG brazing process that combines the short-circuiting with wire retraction and enables the filler metal deposition at relatively low heat input than conventional MIG brazing. In CMT process, there are two phases, namely arcing phase and short-circuiting phase. In arcing phase, again there are two phases known as boost phase and wait phase, respectively. In boost phase, arc initiates and melting of filler wire takes place which leads to the formation of a droplet at the tip of filler wire. The current is very high in boost phase, while in wait phase current slightly drops down but remains constant and sufficient for the further melting of filler till the beginning of short-circuiting phase. In boost phase, the size of droplet increases with time which reduces the resistance for the flow of current between filler wire and base metal and hence voltage also drops down. Once the droplet makes contact with the base metal surface, the voltage becomes almost zero which facilitates the metal transfer at nearly zero heat input. Whereas in pulse brazing phase, high current pulses provide an opportunity to increase the welding heat input according to the joining requirement [15–18]. In pulsed brazing, there are phases known as peak current phase (droplet formation takes place at higher current level) and base current phase (deposition at comparatively low current).

Increase in welding heat input ensures improved wettability of filler metal over steel surface but also leads to the formation of comparatively thick IMC layer which may degrade the joint properties above a certain limit [16]. Wetting length determines the bonding area of the joint. The two primary reasons of joint failure from the interface are formation of thick IMC layer and low wetting length. CMT + P process combines the advantages of both joining processes (i) CMT brazing: deposition at comparatively low heat input in the absence of EMF which guarantees better weld stability along with formation of thin IMC layer at the interface and (ii) pulse brazing: increased melting of filler wire due to high current pulses ensures better wettability of filler metal. By varying the number of pulses and CMT cycles, the heat input during CMT + P weld-brazing process can be more easily adjusted and controlled compared with the conventional brazing processes (e.g. MIG brazing [7], TIG brazing [4] and laser brazing [19]). In a single CMT + P weld cycle, number of CMT and pulse cycles can be incorporated which ultimately governs the droplet transfer, i.e. pulse droplet transfer follows conventional CMT droplet transfer.

Available literature shows that wettability of CMT-brazed lap joints remains an issue. This becomes critical during the joining of thick (>1.5 mm) Al sheets with steel and results in poor joint strength. In this study, the effect of WFR and number of pulses is investigated on the bead shape, microstructure and load bearing capacity of CMT + P weld-brazed lap joints. The primary aim of this work is to improve the wetting ability of molten filler over steel surface for joining of 2-mm-thick Al alloy sheet with 1-mm-thick DP780 steel.

21.2 Materials and Methods

In this study, aluminium alloy (AA5052) of 1 mm and 2 mm thickness is joined with dual-phase steel (DP 780, 1 mm thickness) using CMT + P weld-brazing technique in lap configuration with an overlap distance of 25 mm at a joining speed of 400 mm/min as shown in Fig. 21.2. Chemical composition of steel, Al alloy and filler wire is given in Table 21.1. Al-based and Si-enriched filler wire (AlSi5) of 1.2 mm diameter was used for the joining. Surfaces of the sheets were degreased using acetone prior to joining. The travel angle of 20° was maintained opposite to the direction of brazing, i.e. push mode, and pure argon (99.9%) was used as shielding gas at a flow rate of 15 L/min. The process parameters are given in Table 21.2.

Samples for metallography and shear-tensile testing were cut from the as weld-brazed sheets in the transverse direction of deposited bead. Surface of metallography samples was polished progressively up to diamond slurry of 0.25µ size to achieve mirror finish. Etched surfaces were examined using LEICA DM6000M optical microscope and scanning electron microscope (SEM) equipped with energy-dispersive X-ray spectroscopy (EDS). Shear-tensile testing was done on a 100kN servo-electric Instron-8862 system following DIN EN 1002-1 standard under a displacement rate of 1 mm/min.
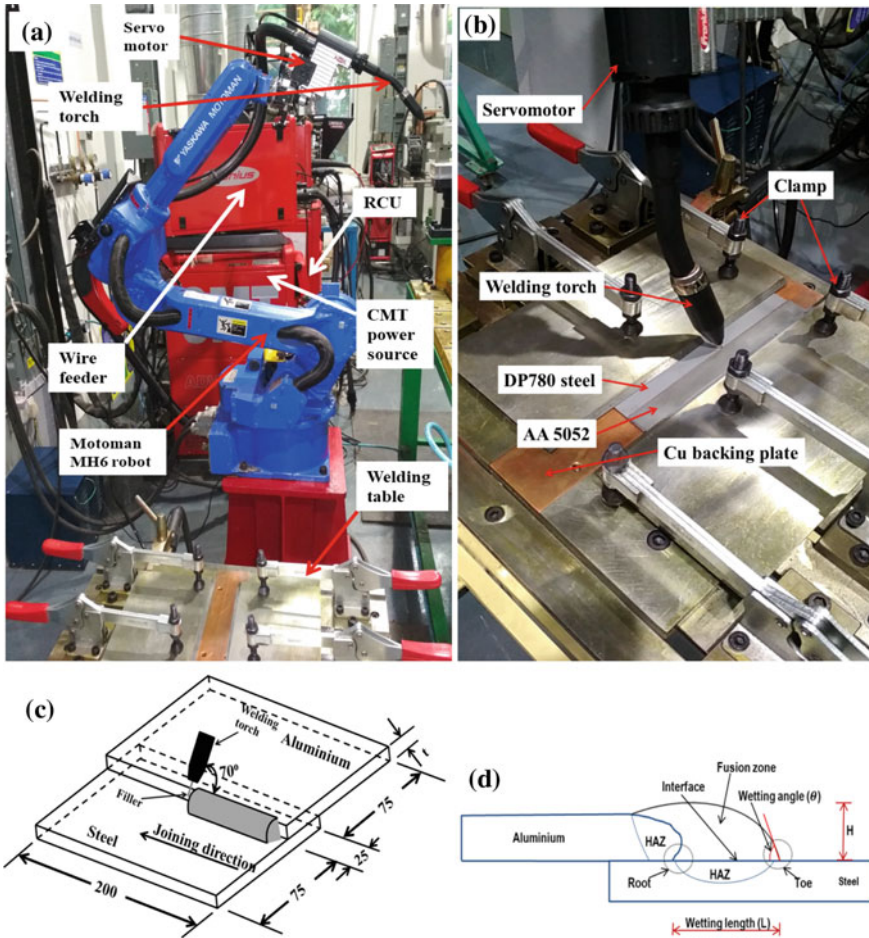
Fig. 21.2 a CMT brazing machine; **b** experimental set-up; **c** schematic of experimental set-up and **d** schematic of cross section of the weld-brazed lap joint

Table 21.1 Chemical composition of steel, Al alloy and filler wire

DP 780	C	Si	Mn	Cr	Al	Cu	Fe	Others
	0.16	0.25	1.8	0.4	0.04	0.04	Bal.	
AA5052	Si	Fe	Cu	Mn	Mg	Cr	Ti	Al
	0–0.25	0–0.4	0–0.1	0–0.1	2.2–2.8	0.1–0.35	0–0.05	Bal.
AlSi5 (ER4043)	Si	Fe	Cu	Mn	Mg	Zn	Ti	Al
	4.5–6	<0.8	<0.3	<0.05	<0.05	<0.1	<0.20	Bal.

Table 21.2 Joining parameters used in this study

Sample	CMT cycles	Number of pulses	WFR (mpm)	Al thickness (mm)
1	1	0	4	2
2	1	0	5	2
3	1	0	6	2
4	1	1	4	2
5	1	2	4	2
6	1	4	4	2

21.3 Results and Discussions

21.3.1 Effect of al Sheet Thickness

At first, AA5052 of 1 mm thickness was joined with DP780 steel of the same thickness in lap position at a WFR of 4mpm and welding speed of 0.4 mpm. Wettability of the joint decreased, i.e. wetting angle increased and wetting length decreased on increasing the Al sheet thickness to 2 mm. This reduction in wettability is attributed to the increase in effective cross-sectional area of the joint with 2-mm Al sheet for the same amount of material deposition. The cross section of the bead of 1- and 2-mm Al sheet is shown in Fig. 21.3. This increase in cross-sectional area led to increase in rate of dissipation of heat from molten filler in the direction of Al base metal which also reduced the spreading ability of molten filler over steel surface. Seffer et al. [20] also reported that sheet thickness (t) of the aluminium alloy affects the conditions of thermal conduction of the joint partners and also the energy per unit length. Hence, on increasing the sheet thickness, the effective interfacial area of

Fig. 21.3 Cross section of weld-brazed joints **a** for 1-mm Al sheet and **b** for 2-mm Al sheet
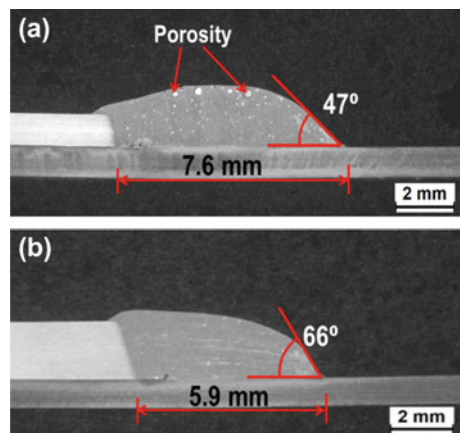
the joint decreased which resulted in the drop of shear-tensile from 5.21 to 4.8 kN and the failure location also changed from bead to interface.

To overcome this issue to wettability with increasing sheet thickness, there are two methods which are employed in the current work: (i) increasing WFR (increasing deposition rate) and (ii) adding pulses in weld cycle (increasing melting of Al base metal and filler). In the synergy mode, welding current and voltage increase with the WFR to maintain the stability of the CMT process, i.e. wire feed rate = burn-off rate. On increasing the WFR, volume of fusion zone can be increased by increasing the deposition rate according to the requirement of joint design, whereas in CMT + P method, the volume of fusion zone increases due to increased melting of Al base metal.

21.3.2 Effect of Pulsing

To enhance the spreading ability of the molten filler over steel surface, pulses are introduced into the weld cycle in addition to the CMT cycles using the remote control unit (RCU) of CMT machine. Addition of pulse increased the energy input per unit length per unit time which enhanced the melting of filler and Al base metal. On the other hand, short-circuit duration did not change on addition of pulses (Fig. 21.4).
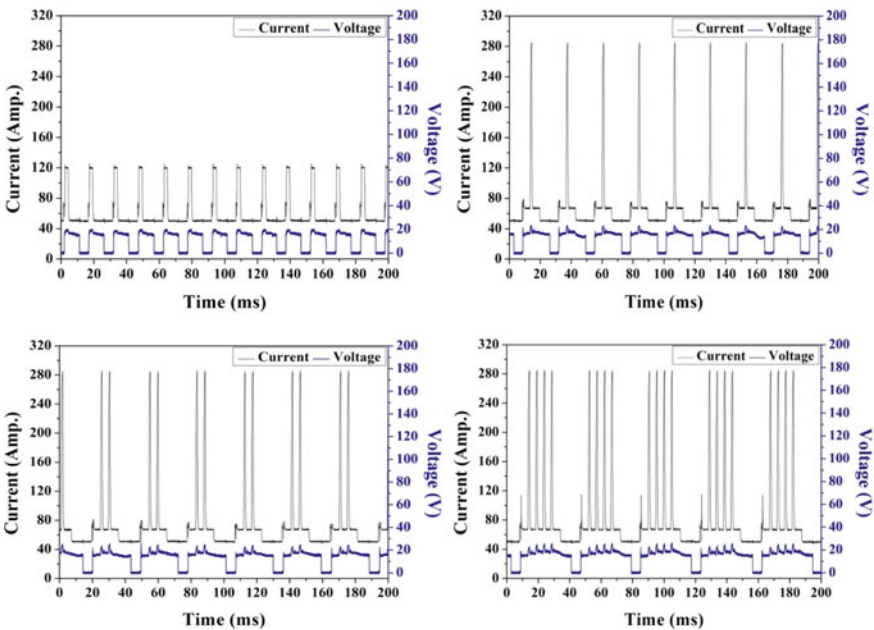
Fig. 21.4 Variation of welding current and voltage for **a** 1 CMT + 0P; **b** 1 CMT + 1P; **c** 1 CMT + 2P and **d** 1 CMT + 4P
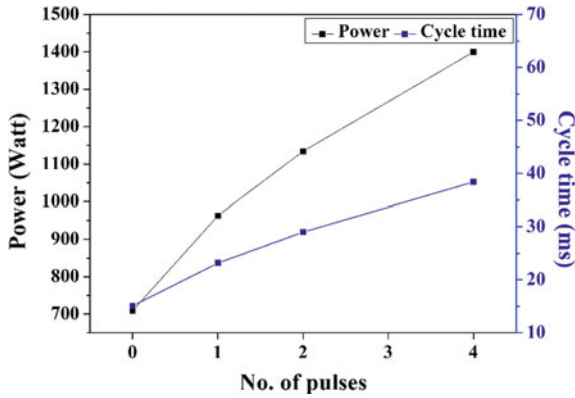
Fig. 21.5 Variation of arc power and weld cycle time with number of pulses

Insertion of pulse increased the power input per weld cycle successfully as shown in Fig. 21.5 which further increased the volume and fluidity of molten pool and hence spreading ability of molten pool increased over the base metal surface. Various combinations of pulse and CMT cycle per weld cycle were tested in order to maximize the load bearing capacity of the joint by increasing the wettability of the joint.

VI transients and bead cross section of four sets (CP 10 (1 CMT cycle + 0 pulse), CP 11, CP 12 and CP 14) of CMT + P process are shown in Figs. 21.4 and 21.6. It can be seen in Fig. 21.4 that the wetting length increased with pulsing while bead height and toe angle both decreased which affirms a significant increase in the wettability of molten pool over steel surface. In pulse brazing, metal transferred to the molten pool under globular mode that's why the base current during pulsing is almost twice of the s/c phase current of CMT cycle. At four pulses, due to the continuous impact
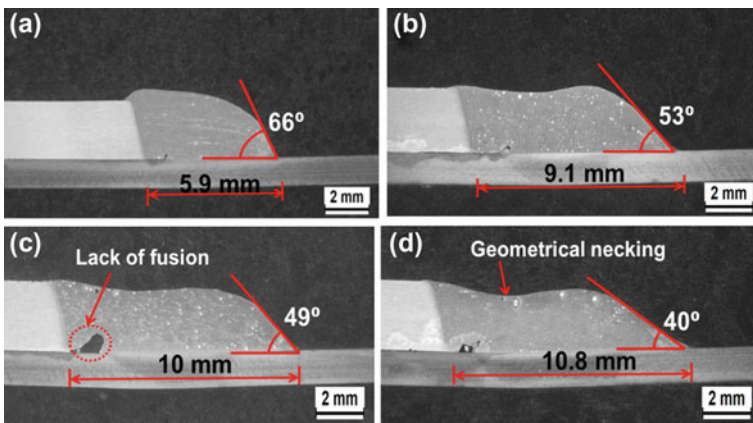
Fig. 21.6 Cross section of weld-brazed joints **a** 1 CMT + 0P; **b** 1 CMT + 1P; **c** 1 CMT + 2P and **d** 1 CMT + 4P
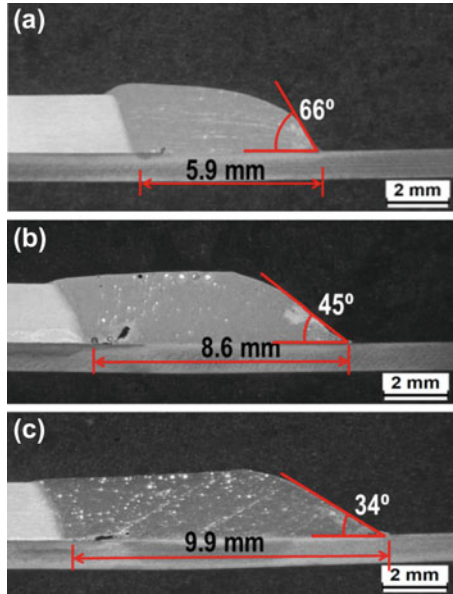
Fig. 21.7 Cross section of weld-brazed joints **a** 4 m/min; **b** 5 m/min and **c** 6 m/min

of molten droplets, geometrical necking was observed in the middle of deposited bead which reduced the effective contact area of the joint. Lack of fusion was also observed at the root of the joint which deteriorated the performance of the joint during tensile testing.

21.3.3 Effect of WFR

On increasing the WFR, the wettability of the joints increased successfully (Fig. 21.7) which can be attributes to increased filler metal deposition per unit length per unit time. The wetting length increased from 5.9 to 9.9 mm on increasing the WFR from 4 to 6 m/min, and the wetting angle decreased from 66° to 34°. Power input also increased from 710 → 850 → 1010 W on increasing the WFR from 4 to 5 to 6 m/min. This increase in power input enhanced the melting of filler wire, and hence, the fluidity of increased volume of molten filler also increased.

21.3.4 Microstructure of the Interface

At the interface of deposited filler metal and steel, a layer composed of Fe–Al–Si intermetallic compounds formed due to negligible mutual solubility of Fe and Al.

The microstructure and variation of IMC layer thickness with WFR and number of pulses is shown in Fig. 21.8a–f. An increase from 2.1 to 5.9 µm in the thickness of IMC layer was observed on increasing the WFR from 4 to 6 m/min. On increasing the WFR, heat input also increased which further enhanced the availability of Fe atoms at the interface, and hence, a thick IMC layer formed at WFR of 6 m/min via the inter-diffusion of Fe and Al across the interface. At WFR of 6 m/min, solidification cracks were observed in the middle of IMC layer due to increased brittleness of the intermetallics layer, and spilling of intermetallic phases into the fusion zone was also observed due to increased turbulence inside the molten pool. Both solidification cracking and spilling of intermetallic phases into fusion zone weakened the interfacial resistance against the failure during shear-tensile testing.

Similarly, an increase in the layer thickness was observed on adding pulses in weld cycle which can be attributed to the increased heat input to the molten pool
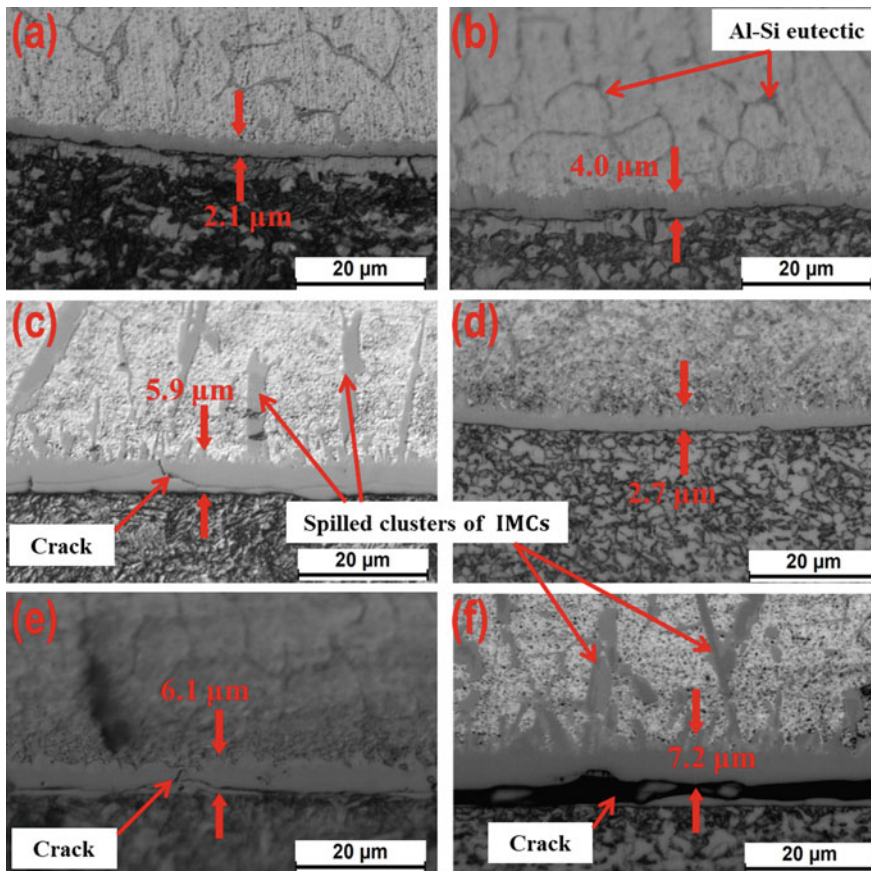
Fig. 21.8 Microstructure of the interface of weld-brazed joints **a** 4 m/min; **b** 5 m/min; **c** 6 m/min; **d** 1 CMT + 1P; **e** 1 CMT + 2P and **f** 1 CMT + 4P
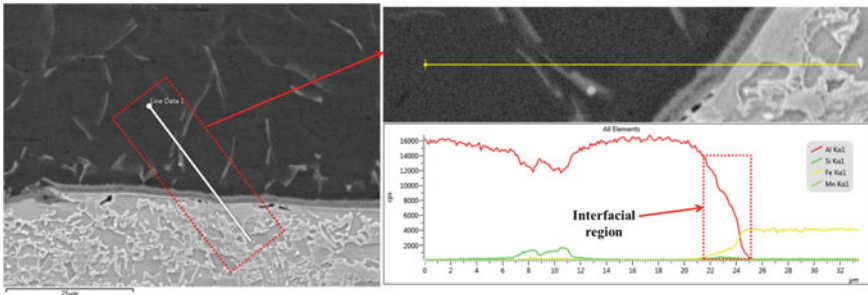
Fig. 21.9 EDS line scan of the interface (sample 1)

and the distribution of heat. The IMC layer thickness increased from 2.1 to 2.7 μm on adding one pulse and further increased to 7.2 μm for addition of four pulses. Murakami et al. [21] also observed that the average thickness of IM layer decreased on increasing the weld speed due to a decrease in the heat input, i.e. IMC layer thickness increased with heat input. Similar to the earlier case, solidification cracks were observed in the layer on adding two and four pulses. At four pulses, spilling of the intermetallic phases was observed due to increased turbulence in the molten pool caused by impact of filler material droplets onto the molten pool during pulsing. Whereas, in case of increasing WFR, increased deposition volume per unit time per unit length was the main source of increased turbulence in the molten pool. However, the final consequence of increased turbulence is same in both the cases which may degrade the joint performance during shear-tensile testing.

EDS analysis was carried to determine the elemental composition of IMC layer. Fe, Al and Si were identified as the main constituents of the layer, i.e. formation of ternary Fe–Al–Si intermetallic compounds took place at the interface (Fig. 21.9). It can be seen that wt% of Al decreased on moving towards steel and the spilled intermetallics were also composed of Fe, Al and Si.

21.3.5 Shear-Tensile Testing

The failure load experienced by the weld-brazed joints during shear-tensile for different parametric conditions is shown in Fig. 21.10. An increment of about 40% in the load to failure was observed on adding one pulse to the weld cycle which can be attributed to the increased wettability of the weld-brazed joint, and thickness of the IMC layer was also observed to be in the safe limit. On adding two pulses, the failure load again increased due to the same reason but dramatically dropped for four pulses due to increased brittleness of the joint. Additionally, the effective cross-sectional area of the joint was also reduced due to the formation of geometrical necking at four pulses which resulted in the failure of two samples from the bead and one from the interface, resulting in the observed high scatter for this combination of CMT and
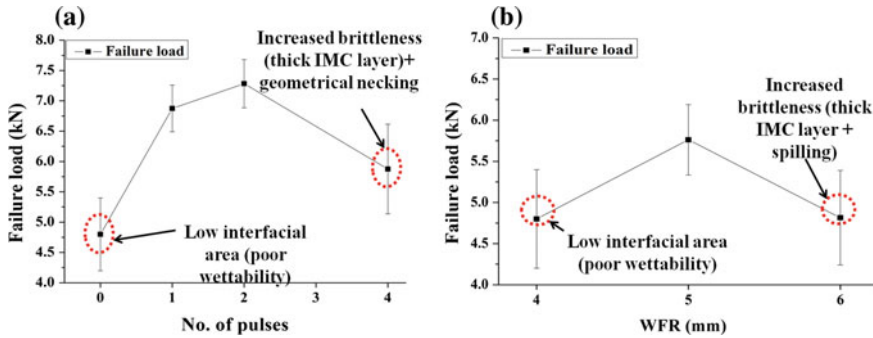
Fig. 21.10 Variation of failure load with **a** number of pulses and **b** WFR

pulses. Lack of fusion zone at the root of the joint acted as crack initiation site for all the joints due to stress accumulation and depending on the resistance to failure it propagated in the weaker direction.

On the other hand, the failure load increased from 4.8 to 5.7 kN on increasing the WFR from 4 to 5 m/min due to a corresponding increase in the wettability of the joint, whereas load dropped to 4.8 kN for a WFR of 6 m/min due to increased brittleness of the interface caused by the spilling of hard and brittle intermetallic phases into the fusion zone. Hence, the failure took place from the interface at smaller values of failure load.

21.4 Conclusions

In the current work, an attempt is made to enhance the wettability of dissimilar weld-brazed joints of Al to steel by using two approaches (i) increasing WFR and (ii) inserting pulses into the weld cycle. The concluding remarks of the work are as follows:

- An increase in the Al sheet thickness resulted in failure of joint from the interface at lower load due to low wettability of the joint. Increase in cross-sectional area enhanced the heat dissipation rate from molten filler in the direction of Al base metal which reduced the spreading ability of molten filler over steel surface.
- Increasing WFR improved the wettability of the molten filler due to enhanced fluidity and increased deposited volume per unit time per unit length. On the other hand, wettability increased due to increased melting of Al base metal on adding pulses in weld cycle which increased power input. Geometrical necking was observed in the deposited bead for two and four pulses addition due to the impact of droplets during pulses.
- Intermetallic layer composed of Fe–Al–Si ternary compounds formed at the interface due to negligible mutual solid solubility between Fe and Al. Thickness of

IMC layer increased with WFR and number of pulses due to increased heat input. Spilling of intermetallic phases into the fusion zone was observed at high WFR and pulses due to increased turbulence in the molten pool which increased the brittleness of the interface.

- An increment of about 18% (4.8–5.7 kN) in the failure load was observed on increasing the WFR to 5 m/min, and further increase in WFR led to reduction in load due to increased brittleness of the joint, whereas an increment of about 50% in the failure load (4.8–7.2 kN) was achieved at for two pulses. It is suggested to optimize the combination of pulses and CMT cycles systematically in order to maximize load bearing capacity of CMT + P weld-brazed joints.

References

1. Singh, J., Arora, K.S., Shukla, D.K.: Dissimilar MIG-CMT weld-brazing of aluminium to steel: a review. J. Alloy. Compd. **783**, 753–764 (2018)
2. Miller, W.S., Zhuang, L., Bottema, J., Wittebrood, A.J., De Smet, P., Haszler, A., Vieregge, A.: Recent development in aluminium alloys for the automotive industry. Mater. Sci. Eng., A **280**, 37–49 (2000)
3. Wang, P., Chen, X., Pan, Q., Madigan, B., Long, J.: Laser welding dissimilar materials of aluminum to steel: an overview. Int. J. Adv. Manuf. Technol. **87**(9–12), 3081–3090 (2016)
4. Pouranvari, M., Abbasi, M.: Dissimilar gas tungsten arc weld-brazing of Al/steel using Al-Si filler metal: microstructure and strengthening mechanisms. J. Alloy. Compd. **749**, 121–127 (2018)
5. Agudo, L., Eyidi, D., Schmaranzer, C.H., Arenholz, E., Jank, N., Bruckner, J., Pyzalla, A.R.: Intermetallic FexAly-phases in a steel/Al-alloy fusion weld. J. Mater. Sci. **42**(12), 4205–4214 (2007)
6. Yang, S., Zhang, J., Lian, J., Lei, Y.: Welding of aluminum alloy to zinc coated steel by cold metal transfer. Mater. Des. **49**, 602–612 (2013)
7. Basak, S., Das, H., Pal, T.K., Shome, M.: Characterization of intermetallics in aluminum to zinc coated interstitial free steel joining by pulsed MIG brazing for automotive application. Mater. Charact. **112**, 229–237 (2016)
8. Jácome, L.A., Weber, S., Leitner, A., Arenholz, E., Bruckner, J., Hackl, H., Pyzalla, A.R.: Influence of filler composition on the microstructure and mechanical properties of steel-aluminum joints produced by metal arc joining. Adv. Eng. Mater. **11**(5), 350–358 (2009)
9. Shi, Y., Shao, L., Huang, J., Gu, Y.: Effects of Si and Mg elements on the microstructure of aluminum–steel joints produced by pulsed DE-GMA welding–brazing. Mater. Sci. Technol. **29**(9), 1118–1124 (2013)
10. Song, J.L., Lin, S.B., Yang, C.L., Fan, C.L.: Effects of Si additions on intermetallic compound layer of aluminum-steel TIG welding-brazing joint. J. Alloy. Compd. **488**(1), 217–222 (2009)
11. Achar, D.R.G., Ruge, J., Sundaresan, S.: Joining aluminum to steel, with particular reference to welding-III. Aluminium **56**(4), 291–293 (1980)
12. Madhavan, S., Kamaraj, M., Vijayaraghavan, L., Rao, K.S.: Microstructure and mechanical properties of aluminium/steel dissimilar weldments: effect of heat input. Mater. Sci. Technol. **33**, 200–209 (2016)
13. Agudo, L., Weber, S., Pinto, H., Arenholz, E., Wagner, J., Hackl, H., Bruckner, J., Pyzalla, A.: Study of microstructure and residual stresses in dissimilar Al/Steels welds produced by cold metal transfer. Mater. Sci. Forum **571–572**, 347–353 (2008)
14. Pang, J., Hu, S., Shen, J., Wang, P., Liang, Y.: Arc characteristics and metal transfer behavior of CMT + P welding process. J. Mater. Process. Technol. **238**, 212–217 (2016)

15. Zhang, H.T., Feng, J.C., He, P., Zhang, B.B., Chen, J.M., Wang, L.: The arc characteristics and metal transfer behaviour of cold metal transfer and its use in joining aluminium to zinc-coated steel. Mater. Sci. Eng., A **499**(1–2), 111–113 (2009)
16. Zhang, H.T., Feng, J.C., He, P.: Interfacial phenomena of cold metal transfer (CMT) welding of zinc coated steel and wrought aluminium. Mater. Sci. Technol. **24**(11), 1346–1349 (2008)
17. Pickin, C.G., Young, K.: Evaluation of cold metal transfer (CMT) process for welding aluminium alloy. Sci. Technol. Weld. Joining **11**, 583–586 (2006)
18. Mou, G., Hua, X., Wu, D., Huang, Y., Lin, W., Xu, P.: Microstructure and mechanical properties of cold metal transfer welding-brazing of Titanium alloy (TC4) to stainless steel (304L) using V-shaped groove joints. J. Mater. Process. Technol. **266**, 696–706 (2018)
19. Mohammadpour, M., Yazdian, N., Yang, G., Wang, H.P., Carlson, B., Kovacevic, R.: Effect of dual laser beam on dissimilar welding-brazing of aluminum to galvanized steel. Opt. Laser Technol. **98**, 214–228 (2018)
20. Seffer, O., Springer, A., Kaierle, S.: Investigations on remote laser beam welding of dissimilar joints of aluminum alloys and steel with varying sheet thicknesses for car body construction. J. Laser Appl. **29** (2017)
21. Murakami, T., Nakata, K., Tong, H., Ushio, M.: Dissimilar metal joining of aluminum to steel by MIG Arc brazing using flux cored wire. ISIJ Int. **43**(10), 1596–1602 (2003)

Chapter 22
Performance Analysis of ECDM Process Using Surfactant Mixed Electrolyte

Check for updates

Viveksheel Rajput, Mudimallana Goud, and Narendra Mohan Suri

Abstract With rapid escalation in the utilization of glass materials in microelectromechanical systems (MEMS) applications, need is generated to develop more sophisticated process for machining these materials at a higher machining speed with excellent features. Electrochemical discharge machining (ECDM) is proven to be a successful method for machining glass materials with ease which utilizes the thermal heat of the sparks and chemical etching action of electrolyte for material removal simultaneously. However, low material removal rate and thermal cracks at the micro-hole entrance edges are some of the concerns which need to be enhanced. Several parameters influence the ECDM process but gas film formation and its thickness is the key determinant for obtaining higher quality machined surface. This present paper investigates the effect of surfactant addition, i.e., cationic surfactant cetyltrimethylammonium bromide (CTAB) in three different concentrations, into the 20 wt% alkaline solution of NaOH electrolyte for improving the material removal rate and thermal cracks during micro-drilling operation. Moreover, a transient thermal model based upon finite element modeling (FEM) is developed to analyze the material removal rate (MRR) with and without the presence of surfactants in the ECDM process. Simulation results are compared with the previously reported experimental results. Surfactant addition affects the electrochemical properties of the electrolyte and leads to the increase in tool electrode wettability which produces thin and stable gas film at the tool vicinity. As a result, more current densities are produced and hence faster material removal rate. Experimental results revealed that a significant increase in removal rate and reduction in thermal cracks were observed during micro-drilling process in the presence of surfactants. An increase of 39.31% was observed in material removal rate of soda–lime glass in the presence of CTAB surfactant at critical micelle concentration (CMC). Simulation results exhibit good similarity in

V. Rajput (✉) · M. Goud · N. M. Suri
Department of Production and Industrial Engineering, PEC, Chandigarh 160012, India
e-mail: sheelrajput03@gmail.com

M. Goud
e-mail: mudigoud@gmail.com

N. M. Suri
e-mail: nmsuri65@yahoo.com

the trend of the material removal rate with the experimental results. The developed thermal model can be effectively utilized to determine the removal rate of surfactant mixed ECDM process. Based on the observation of present investigation, a more reliable and effective surfactant mixed ECDM process with improved removal rate and surface quality is inferred.

Keywords Surfactant · Material removal rate · Electrolyte · Thermal cracks · Electrolyte viscosity · FEM · Modelingz

Nomenclature

MEMS	Microelectromechanical system
ECDM	Electrochemical discharge machining
CTAB	Cetyltrimethylammonium bromide
EDM	Electrodischarge machining
ECM	Electrochemical machining
MRR	Material removal rate
NaOH	Sodium hydroxide
KOH	Potassium hydroxide
CMC	Critical micelle concentration
DC	Direct current
A	Ampere
V	Voltage
G	Gram
Min	Minutes
μm	Microns
μs	Microseconds

22.1 Introduction

Electrochemical discharge machining is a proven technology for fabricating micro-features on non-conductive materials such as glass, quartz, and ceramics at a preferable machining rate [1, 2]. It combines the machining attributes of electro discharge phenomena (EDM) and electrochemical phenomena (ECM) together, and hence, material removal takes place through thermal melting due to electric discharge (or spark) followed by chemical etching action. Glass exhibits peculiar properties in terms of its transparency, resistance to chemical and toxic substances which make it more reliable components used in MEMS applications [3, 4]. ECDM process composed of non-reactive electrolytic cell in which tool electrode (cathode), auxiliary
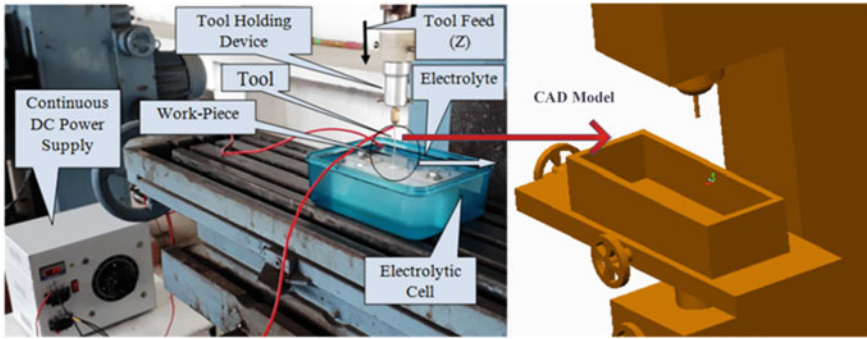
Fig. 22.1 Experimental setup of ECDM [25]

electrode (anode), and work material all immersed in an aqueous solution of electrolyte as shown in Fig. 22.1. A potential difference is generated across the electrodes which prompt the formation of tiny hydrogen gas bubbles and oxygen bubbles inside the electrolyte. These tiny hydrogen bubbles accumulate around tool electrode to from an insulating gas film which ceases the current flow. Thereafter, spark occurs through the gas film due to its electric breakdown. So far many experimental investigations have been done to study the machining characteristics of glass materials during micro-hole fabrication using ECDM process. Numerous ECDM hybrids and variants have also been developed over the past decades for enhancing its machining performance but low machining depth and thermal cracks at the hole's entrance edges are one of the utmost challenge to be taken care simultaneously [5, 6]. Hence, more investigations are still required to cope with the challenges faced during micro-drilling operations. This present study investigates the effect of surfactant mixed electrolyte on machining performance in terms of material removal rate and edge smoothness during micro-drilling operations in soda–lime glass with ECDM.

Kurafuji and Suda [7] were the first one to demonstrate the application of electric discharge during glass drilling process. The mechanism of sparks in ECDM process was first elaborated by Basak and Ghosh [2, 8] in which they emphasized that critical values of current and voltage are required to initiate the machining and further announced that the mechanism of spark is similar to a On/Off action of an electric switch. Jain et al. [9] observed that each gas bubble acts as a valve within the electrolyte which produces spark, once its breakdown occurs due to the formation of high electric field. Wuthrich et al. [10] emphasized that ECDM has a massive potential to machine non-conductive materials and electrolyte plays a significant role in material removal. They expressed that many electrolytes can be used in ECDM process such as NaOH, KOH, HCl, and NaCL but NaOH exhibits better results when compared to others. Harugade et al. [11] also studied the role of different electrolytes, viz. NaOH, $NaNO_3$, and H_2SO_4, during micro-machining with ECDM process and investigated its influence on material removal rate of glass material. They found that NaOH produces higher MMR followed by $NaNO_3$ and H_2SO_4 due to the presence of more OH radicals in NaOH electrolyte which enhances the etching action of the electrolyte.

Cheng et al. [12] investigated the gas film quality in ECDM and concluded that gas film thickness affects the machining characteristics in ECDM. El-Haddad et al. [13] have successfully built a mathematical model for computing critical current–voltage values for the formation of stabilized gas film at the tool electrode vicinity by incorporating gas film dynamics.

Further, Fascio et al. [14] investigated the gas film dynamics and comprehended five different regions in current–voltage characteristics in ECDM process. Five regions can be identified as: (i) thermodynamic region, (ii) Ohmic region, (iii) limiting current region, (iv) instability region, and (iv) arc region. Vogt [15, 16] made an immense contribution for studying gas film phenomena based upon bubble coalescence process and recommended that the tool electrode wettability is the crucial parameter in controlling the gas film thickness. It was observed that tool electrode material and electrolyte properties substantially affect the tool electrode wettability which further affects the gas film thickness and its stability. Jawalkar et al. [17] performed parametric studies on MRR during ECDM machining of glass and concluded that applied voltage is the most significant parameter affecting the removal rate followed by electrolyte concentration. Wuthrich et al. [18] stated that the mixing of surfactant to the electrolyte enhances the tool electrode wettability which further reduces the gas film thickness and ameliorate machining accuracy. Nasim et al. [19] evaluated the effect of surfactant on gas film thickness and surface quality of micro-channels. Results exhibited that surfactant alters the electrochemical properties which affects the gas film thickness and so the machining efficiency. As a result, micro-channels with enhanced material removal rate and surface quality were achieved. Christenson et al. [20] have successfully demonstrated that a surface tension gradient serves a pivotal role in bubble coalescence process in electrolytes which affect the gas film thickness and hence, removal rate of material and surface quality. Various researchers have demonstrated the application of FEM model for analyzing the single discharge and its behavior in ECDM process. Behroozfara et al. [21] built up a thermal model based on finite element method FEM to analyze the removal rate of the material in the ECDM process. They studied the plasma channel attributes to estimate the removal mechanism. Bhondwe et al. [22] built a transient thermal based on FEM to estimate the distribution of the temperature under a spark region. The temperature distributions were further post-processed to predict the material removal rate. Gaussian heat input was assumed within a spark region. Wei et al. [23] also developed a model based upon FEM to simulate single spark of ECDM process for micro-drilling process. The simulated results were analyzed to predict the removal rate. Goud et al. [24] successfully predicted the removal rate of alumina using FEM model with three-dimensional Gaussian distribution within the spark region for obtaining more accurate results. Experiments revealed good agreement with the FEM results which confirmed the validation of the developed model.

22.2 Experimentation

22.2.1 Material and Methodology

The soda–lime glass was chosen for micro-hole fabrication while stainless steel was used as a tool electrode. The 'in-house' experimental setup was designed and fabricated in laboratory for performing experiments as shown in Fig. 22.1. Electrolyte cell was made up of non-reactive polycarbonate material and filled with NaOH aqueous solution. Cetyltrimethylammonium bromide (CTAB) was used as a surfactant in three different concentrations including critical micelle concentration (CMC). Table 22.1 highlights the key properties of CTAB surfactant. The machining conditions used for micro-hole fabrication were selected on the basis of literature study and setup capabilities as given in Table 22.2. The material removal rate and thermal cracks at the hole's entrance edges were selected as response parameters. A full-wave and continuous DC voltage were applied between the tool electrode (cathode) and anode varying from 0 to 100 V, 10 A. Workpiece was fixed on non-reactive fixture inside the electrolytic cell and gravity assisted tool electrode feed was used. The experiments were performed according to one factor at a time (OFAT) in which one parameter was varied while other kept fixed. The study is further extended to develop the transient thermal model based upon FEM to simulate the results of MRR in the ECDM process for non-conductive work material. The simulation results were compared with the previously reported results on surfactant mixed electrolytes in the ECDM process. Two different surfactants, i.e., cetyltrimethylammonium bromide (CTAB) and

Table 22.1 CTAB surfactant properties [19]

Constant parameter	
Chemical formula	$(C_{16}H_{33})N(CH_3)_3Br$
Molar mass	364.45 g/mol
CMC	0.036 wt%
PH	6–7.5
Color	White solid

Table 22.2 Experimental conditions used for present investigation

Constant parameter			
Workpiece	Soda–lime glass	Applied voltage	45 V
Tool electrode	Stainless steel	Electrolyte	NaOH
Tool diameter	500 μm (Micron)	Electrolyte level	1 mm (Approx.)
Electrolyte Conc.	20% wt/v.	Inter-electrode gap	30 cm
Variable parameter			
Surfactant concentration	0.02 wt%	0.036 wt% (CMC)	0.04 wt%
Machining time = 1 min			

sodium dodecyl sulfate (SDS), were used for simulating the machining process for analyzing the material removal rate. The simulation results were compared with the results of study reported by Nasim and Mohammed [19] for validation. A parametric study of electrolyte concentration was also performed to investigate its influence on MRR.

CMC is critical micelle concentration and defined as the concentration above which the electrochemical properties of the electrolyte vary drastically [19]. This is a result of formation of micelles due to monomer aggregation. Three weight concentrations of surfactants were considered for this study.

22.2.2 Measurements

Material removal rate was computed as a weight difference of the work material before and after micro-hole fabrication divided by time of machining as shown in Eq. 22.1. A weighing machine having a least count of 0.0001 g was used for measurement, and an average of three readings was considered for material removal. In order to analyze the thermal cracks at the hole's entrance, the state of machined holes was analyzed through optical microscopy. Inverted metallurgical microscope was used for optical microscopy, and image analysis was done by utilizing IS capture software.

$$MRR = (wt_1 - wt_2/t) \tag{22.1}$$

where $wt_1 =$ Weight of soda–lime glass material before micro-hole fabrication (g), $wt_2 =$ weight of soda–lime glass material after micro-hole fabrication (g), and $t =$ time in minutes.

22.3 Thermal Modeling

A transient thermal model based on finite element model (FEM) was developed to analyze the material removal rate (MRR) due to single spark in the ECDM process. The dimensions of the work material for FEM analysis were taken as $0.6 \times 0.6 \times 0.4$ mm^3 as shown in Fig. 22.2. The work material chosen for FEM study was soda–lime glass. Table 22.3 highlights the thermal and physical properties of the soda–lime glass material. Kulkarni et al. [26] have successfully determined the spark radius by measuring the radius of the crater formed during micro-machining process. They have calculated the radius of the spark as $150\,\mu m$. Therefore, spark radius of $150\,\mu m$ was used in the simulation study which was also used by other authors [22, 23, 27]. Constant spark duration of $100\,\mu s$ was assumed for simulation study [24].

Fig. 22.2 Three-dimensional model of the work material with boundary condition
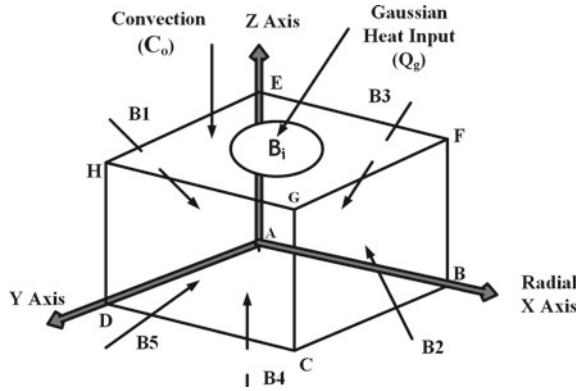
Table 22.3 Properties of soda–lime glass material used for simulation study

Property	Values	Units
Thermal conductivity *(k)*	1.6	W/m-K
Specific heat capacity (c)	670	J/kg-K
Melting temperature (T_m)	1673	K
Initial temperature (T_0)	298	K
Convective heat coefficient *(h)*	10,000	W/m^2 K
Density (ρ)	2170	kg/m^3

22.3.1 Assumptions

The following assumptions were used for the simulation study of the ECDM process and commonly preferred by the other authors also [22–24].

1. The properties of the work material were assumed to be isotropic and homogenous.
2. At one time, only single spark was generated under the tool tip and for single spark the shape of the crater was assumed dome shaped.
3. Gaussian heat distribution was assumed as a source of heat within the spark region, and it remains uniform and similar for all the sparks.
4. The energy transference to the work material was assumed to be a fraction of total spark energy.
5. Material removal due to the cavitation effect was neglected.
6. Effect of tool wear and drop of electrolyte level were also neglected.

22.3.2 Boundary Conditions

1. The temperature of the work material was assumed to be at room temperature (T_0), i.e., $T = T_0$ at $t = 0$ and completely dipped in aqueous solution of an electrolyte. The work material domain is designated 'ABCDEFGH' (Fig. 22.2).
2. Heat input to the work material was applied through the circular boundary 'B_i' during the machining process on the top of the work material surface, while boundary 'C_o' releases heat to the atmosphere through convection, $q_c = h(T - T_0)$. Other boundaries B1, B2, B3, B4, and B5 were assumed to be perfectly insulated for ant time $t \geq 0$.
3. The heat input was assumed to be Gaussian (Q_g) and calculated using Eq. 22.2.

$$Q_g = \frac{4.45 E_p V I}{\text{Volume of Spark}} \exp\left\{-4.5\left\{\left(\frac{r_x}{R}\right)^2 + \left(\frac{r_y}{R}\right)^2\right\}\right\} \tag{22.2}$$

where E_p is the energy transferred to the work material, V is the voltage; I is the current; r_x and r_y are the radial distances from the central axis of spark and R is the spark radius.

In this present study, the amount of energy transferred to the work material (E_p) was taken as 20% by referring the FEM study given by Bhondwe et al. [22]. It was assumed that the distribution of the energy was uniform within the spark region.

4. The value of V and I was determined through following Eqs. (22.3, 22.4) which is a function of electrolyte concentration [22].

$$V = 0.02381\, C^2 - 1.6095\, C + 43.536 \tag{22.3}$$

$$I = 3.2323 * 10^{-5} C^3 - 0.0027056\, C^2 + 0.091378\, C + 0.71429 (NaOH)$$
$$I = 3 * 10^{-6} C^3 - 0.0007\, C^2 + 0.0562\, C + 0.4424 (KOH) \tag{22.4}$$

22.3.3 Material Removal Estimation

The material removal in the ECDM process is caused by the thermal heating of the spark and chemical action over the top surface of the work material. It is difficult to anticipate the nucleation sites on the surface of the tool electrode, and thus, the formation of the bubble generation is a random process. Therefore, in order to simplify the model, the material removal was computed by estimating the total number of sparks per unit time [22, 24].

Further, the isothermal planes of temperature distributions are obtained from the FEM results which were used to estimate the volume of material removed as shown in

Fig. 22.3 Isothermal curve
for temperature distribution
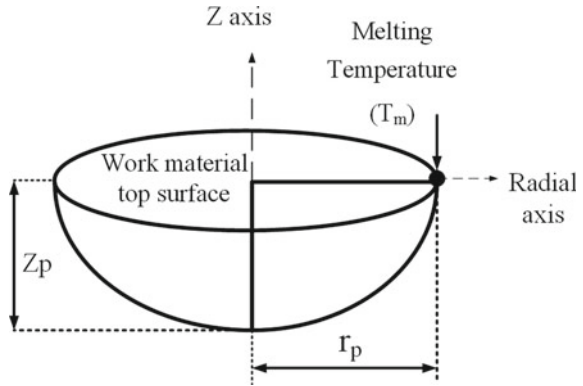
Fig. 22.3. The removal of the material takes place when the work material temperature (T) becomes higher than the work material melting temperature (T_m) which is given as:

$$T > T_m \tag{22.5}$$

These isothermal planes are further post processed to estimate the volume (V_m) of material removed which is given in Eq. 22.6. The geometry of the work material removed is assumed to be hemisphere.

$$V_m = \iiint r_p z_p \theta \mathrm{d}r \mathrm{d}z \mathrm{d}\theta = \frac{2}{3} \pi r_p^2 z_P \tag{22.6}$$

where r_p and z_p are the intercepts on the coordinate axis; V_m is the volume of material removed. The total volume (V_T) of material removed per unit time is calculated as

$$V_T = V_m \times \text{number of sparks per unit time} \tag{22.7}$$

Then, final material removal rate (MRR) is given as the product of volume removed with density (ρ).

$$\text{MRR} = V_T \times \rho(\text{density}) \tag{22.8}$$

22.4   Results and Discussions

22.4.1   Material Removal Rate

Effect of surfactant mixed electrolyte on material removal rate was investigated in four different conditions as shown in Table 22.3. It was seen that material removal rate was increased in the presence of surfactant and with the increase in surfactant concentration (Up to CMC) as illustrated in Fig. 22.4. It was explained on the fact that surfactant enhances the electrical conductivity of the electrolyte, and thus, material removal enhancement takes place due to increased number of current densities and OH radicals in the presence of cationic surfactant. As a result, more chemical reactions at the top of the glass work material occurred due to accumulation of OH radicals which further enhances the chemical etching action. Moreover, a reduction in critical voltage was also observed in the presence of surfactant which makes the process viable for machining at low voltages (Table 22.4). Thus, under same machining voltage, more hydrogen gas bubbles generated in the presence of surfactant which accelerates the gas film phenomena and thereby improving the material removal rate.

Fig. 22.4 Surfactant effect on MRR

Table 22.4 MRR and critical voltages at different CTAB concentrations

Experiments with different electrolyte	Critical voltage (V)	MRR (g/min)
Pure NaOH	29	0.0987
NaOH + 0.02 wt% CTAB	26	0.1282
NaOH + 0.036 wt% CTAB	24	0.1375
NaOH + 0.04 wt% CTAB	25	0.1231

22.4.2 Thermal Model Validations

The thermal model was developed to estimate the temperature fields over the work material surface which was further post-processed to predict the material removal rate (MRR) of the soda–lime glass. The simulation study was performed to estimate the material removal rate with and without the presence of surfactant. The geometrical model was discretized by using Hex-dominant method in ANSYS meshing tool to achieve better results. The boundary 'B_i' was refined further for enhancing the accuracies of the Gaussian heat input as shown in Fig. 22.5. The temperature higher than the melting temperature of the work material was observed, and any material above that melting temperature was assumed to be removed in the form of crater shown in Fig. 22.6.

In order to validate the model, the study of MRR was performed to compare the results of the simulation study with the previously reported studies. The current values for different surfactant concentrations were selected by referring to the study given by Nasim and Mohammed [19]. Figure 22.7 shows the comparison of the simulated results of MRR obtained at different concentrations of surfactant in the present study with the experimental results of the machining depth obtained at different concentrations of surfactant in the KOH electrolyte. It was observed that the trend of response parameter is similar in both the cases, and it increases with the
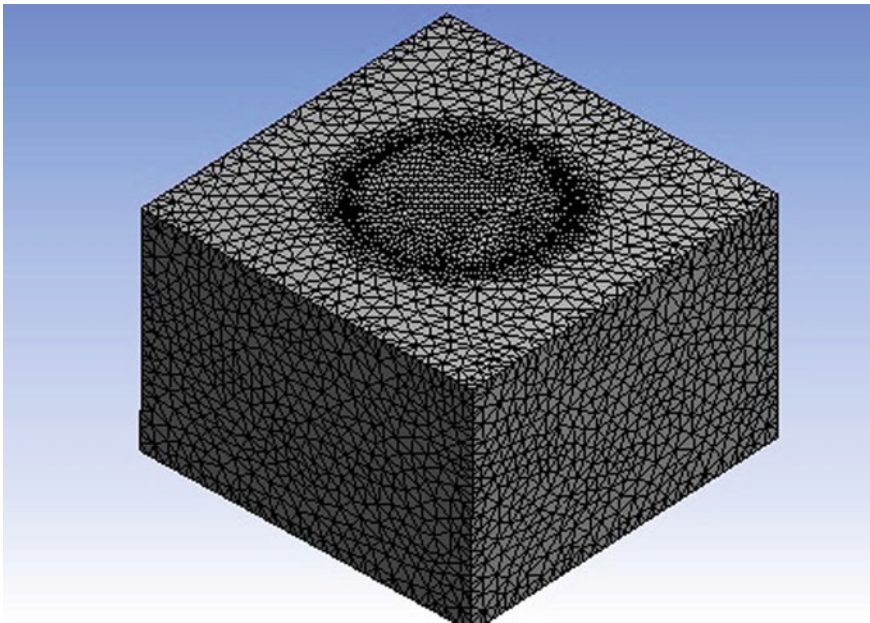
Fig. 22.5 Discretized model
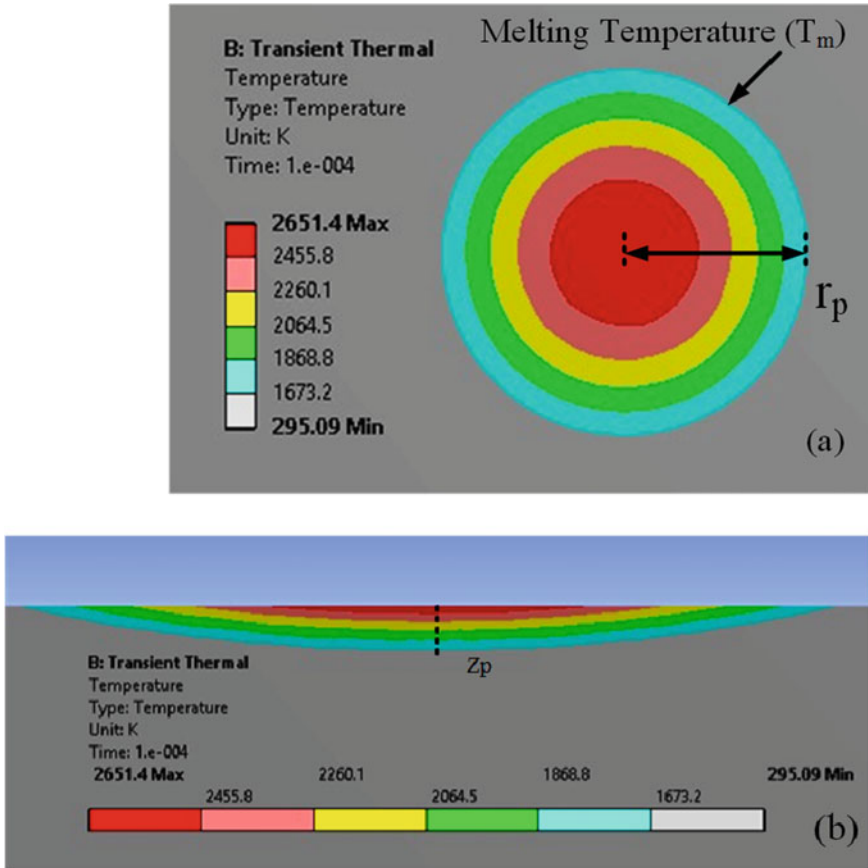
Fig. 22.6 Temperature distributions **a** top view; **b** sectional front view

increase in surfactant concentrations up to CMC. It was seen that any increase in the machining depth of micro-hole is the result of increase in the material removal rate.

Figure 22.8 illustrates the results of the parametric study for material removal rate (MRR) at different KOH electrolyte concentrations. It was seen that the material removal rate increases with the increase in electrolyte concentration from 25 to 50 wt%. It was explained on the fact that with increased electrolyte concentration, there is an increase in electrolyte conductivity which increases the current intensities within the circuit. Thus, higher MRR was obtained.
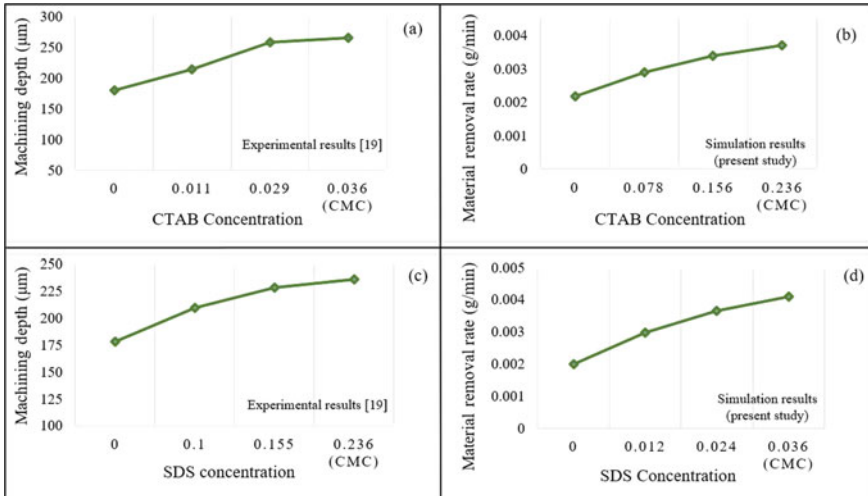
Fig. 22.7 Comparison of trend in response parameter **a** experimental with CTAB; **b** simulation with CTAB; **c** experimental with SDS; **d** simulation with SDS; at 25 wt% KOH and 30 V
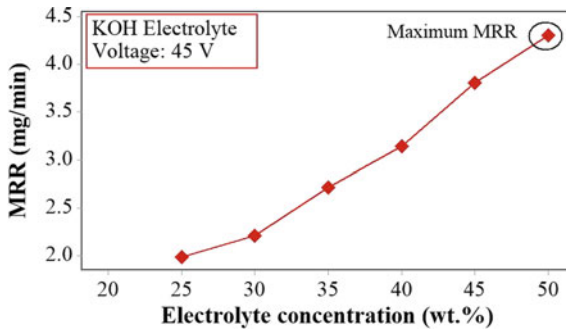
Fig. 22.8 Effect of electrolyte concentration on MRR (*Simulation Study*)

22.4.3   Cracks

Thermal cracks at the hole's entrance edges were reduced significantly in the presence of surfactant. It was seen that more smooth surface or least thermal cracks were obtained at critical micelle concentration when compared to other concentrations as shown in Fig. 22.9 (*Microscopic Images*). It was explained on the fact that surfactant addition increases the electrolyte viscosity which results into the smoothness of the machined surface. Surfactant produces a thinner gas film around the tool electrode which further results into the uniform release of sparks, thereby giving controlled thermal energy. Hence, reduced thermal cracks are at the hole's entrance edges.
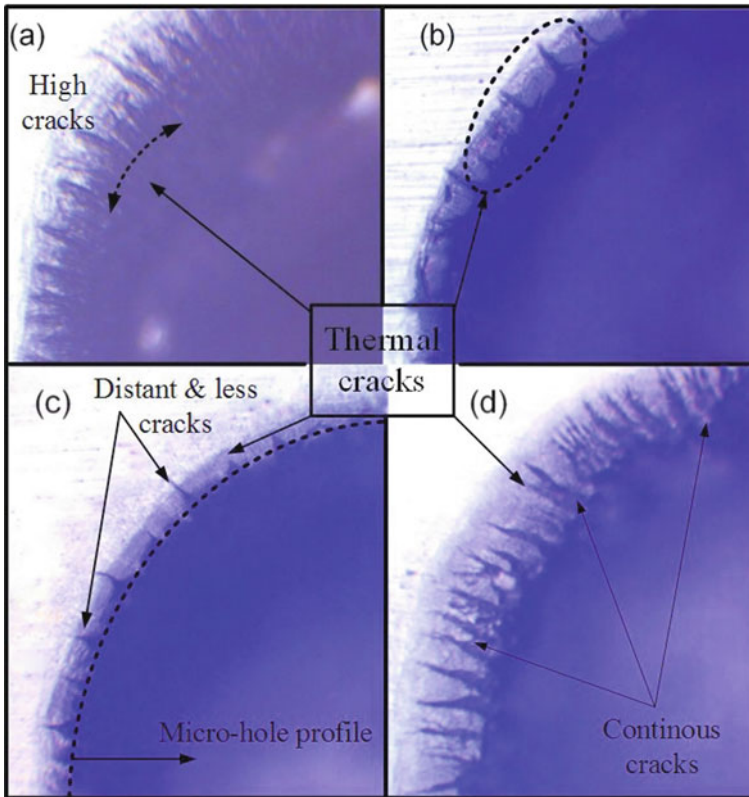
Fig. 22.9 Thermal cracks at hole's entrance edges with **a** Pure NaOH, **b** NaOH + CTAB (0.02 wt%), **c** NaOH + CTAB (CMC: 0.036 wt %), **d** NaOH + CTAB (0.04 wt %)

Moreover, increased number of OH radicals also enhances the etching action, thereby giving smooth surface.

22.5 Conclusions

Investigations on the effect of surfactant mixed electrolyte were done on material removal rate and thermal cracks at the hole's entrance edges. CTAB was used as a surfactant at various concentrations. Thermal model was also developed to simulate the single spark for analyzing the MRR and compared with the previous results. The major conclusions were withdrawn from the present study.

- The removal rate of material significantly affected by the presence of surfactants in the electrolyte due to increased electrical conductivity of the electrolyte and OH

radicals for etching action. An increase of 40% was observed in material removal rate in CTAB surfactant mixed electrolyte at CMC.

- Thermal damage and cracks at the hole's entrance edges were substantially reduced in the presence of CTAB surfactant due to the formation of thinner gas film which produced more channelized and uniform release of thermal energy.
- FEM results exhibit good similarity in the trend of response parameter with the previously reported results which confirmed the model validity.
- An increase in MRR was observed with the increase in the concentration of electrolyte.
- Surfactants have the potential to influence the response characteristics in ECDM process by altering the electrolyte electrochemical properties.
- Critical micelle concentration (CMC) exhibited the most significant result compared to other concentrations.

References

1. Zhiyuan, W., Yong, L., Minghong, M., et al.: Fabrication of glass micro-holes with high quality by electrochemical discharge machining with a rotary helix electrode. Recent Patents Mech. Eng. **11**(2), 168–173 (2018)
2. Basak, I., Ghosh, A.: Mechanism of material removal in electrochemical discharge machining a theoretical model and experimental verification. J. Mater. Process. Technol. **71**, 350–359 (1997)
3. Ziki, A.J.D., Didar, T.F., Wuthrich, R.: Micro-texturing channel surfaces on glass with spark assisted chemical engraving. Int. J. Mach. Tools Manuf. **57**, 66–72 (2012)
4. Daridon, A., Fascio, V., Lichtenberg, J., Wuthrich, R., Langen, H., Verpoorte, E., De Rooij, N.F.: Multi-layer microfluidic glass chips for microanalytical applications. Fresenius J. Anal. Chem. **371**, 261–269 (2001)
5. Maillard, P., Despont, B., Bleuler, H., Wuthrich, R.: Geometrical characterization of micro-holes drilled in glass by gravity-feed with spark assisted chemical engraving SACE. J. Micromech. Microeng. **17**, 1343–1349 (2007)
6. Wüthrich, R., Spaelter, U., Wu, Y., Bleuler, H.: A systematic characterization method for gravity-feed micro-hole drilling in glass with spark assisted chemical engraving SACE. J. Micromech. Microeng. **16**, 1891–1896 (2006)
7. Kurafuji, H., Suda, K.: Electrical discharge drilling of glass. Ann. CIRP. **16**, 415–419 (1968)
8. Basak, I., Ghosh, A.: Mechanism of spark generation during electrochemical discharge machining a theoretical model and experimental verification. J. Mater. Process. Technol. **62**, 46–53 (2003)
9. Jain, V.K., Dixit, P.M., Pandey, P.M.: On the analysis of the electrochemical spark machining process. Int. J. Mach. Tools Manuf. **39**, 165–186 (1999)
10. Wuthrich, R., Hof, L. A., Lal, A., Fujisaki, K., H., Bleuler., Mandin, Ph., Picard, G.: Physical principles and miniaturization of spark assisted chemical engraving SACE. J. Micromech. Microeng. **15**, 10 (2005)
11. Harugade, M.L., Waigaonkar, S.D.: Effect of different electrolytes on material removal rate diameter of hole and spark in electrochemical discharge machining. Adv. Manuf. Lect. Mech. Engine. (2018)
12. Cheng, C.P., Wu, K.L., Mai, C.C., Yang, C.K., Hsu, Y.S., Yan, B.H.: Study of gas film quality in electrochemical discharge machining. Int. J. Mach Tools Manuf. **50**, 689–697 (2010)

13. El-Haddad, R., Wuthrich, R.: A mechanistic model of the gas film dynamics during the electrochemical discharge phenomenon. J. Appl. Electrochem. **40**, 1853–1858 (2010)
14. Fascio, V., Langen, H., Bleuler, H., et al.: Investigations of the spark- assisted chemical engraving. Electrochem. Commun. **5**, 203–207 (2003)
15. Vogt, H.: Physical processes on gas-evolving electrodes. Chem. Ing. Tech. **52**, 418 (1980). https://doi.org/10.1007/BF01059293
16. Vogt, H.: On the supersaturation of gas in the concentration boundary layer of gas evolving electrodes. Electrochim. Acta **25**, 527–531 (1980)
17. Jawalkar, C.S., Sharma, A.K., Pradeep, K.: Micromachining with ECDM: research potentials and experimental investigations. World Acad. Sci. Eng. Technol. Sci. Direct. **61**, 90–95 (2012)
18. Wuthrich, R., Hof, L.A.: The gas film in spark assisted chemical engraving SACE—a key element for micro-machining applications. Int. J. Mach. Tools Manuf. **46**, 828–835 (2006)
19. Sabahi, N., Razfar, M.R., Hajian, M.: Experimental investigation of surfactant-mixed electrolyte into electrochemical discharge machining ECDM process. J. Mater. Process. Technol. 250 (2017)
20. Christenson, H.K., Yaminsky, V.V.: Solute effects on bubble coalescence. J. Phys. Chem. **99**, 10420 (1995)
21. Behroozfar, A., Razfar, M.R.: Experimental and numerical study of material removal in electrochemical discharge machining (ECDM). Mater. Manuf. Processes **31**(4), 495–503 (2015)
22. Bhondwe, K.L., Yadava, V., Kathiresan, G.: Finite element prediction of material removal rate due to electro-chemical spark machining. Int. J. Mach. Tool Manu. **46**, 1699–1706 (2006)
23. Wei, C., Xu, K., Ni, J., et al.: A finite element based model for electrochemical discharge machining in discharge regime. Int. J. Adv. Manuf. Tech. **54**, 987–995 (2011)
24. Goud, M.M., Sharma, A.K.: A three-dimensional finite element simulation approach to analyze material removal in electrochemical discharge machining. Proc IMechE Part C: J. Mech. Eng. Sci. (2016)
25. Rajput, V., Goud, M.M., Suri, N.M.: Experimental investigation to improve the removal rate of material in ECDM process by utilizing different tool electrode shapes. Int. J. Techn. Innov. Modern Eng. Sci. (IJTIMES) **5**(2), 333–341 (2019)
26. Kulkarni, A., Sharan, R., Lal, G.K.: An experimental study of discharge mechanism in electrochemical discharge machining. Int. J. Mach. Tool Manuf. **42**, 1121–1127 (2002)
27. Singh, D., Goud, M.M.: A 3D spark model to evaluate MRR in ECDM. J. Adv. Manufact. Syst. (2019)

Chapter 23
Effect of Welding Processes on the Mechanical Properties of Hardox 400 Steel Welded Joints

Ranbir Singh Multani, Varun Sharma, Ajay Gupta, and Jaswant Singh

Abstract The present paper investigates the effect of gas metal arc welding process and shielded metal arc welding process on the tensile, impact, and metallurgical properties of 20 mm quenched and tempered steel welded joints. To accomplish the established aim, double V groove joints with 60° groove angle were welded using gas metal arc welding process and shielded metal arc welding process using low hydrogen ferritic steel consumables. Microhardness studies carried out along and across the welded joints accompanied by the microstructural investigations revealed significant variation within the fusion and the heat affected zone of the weldments. Tensile and impact property studies of the shielded metal arc welding process welded joint shown better properties as compared to the gas metal arc welding process owing to the presence of fine acicular ferrite in the fusion zone due to low heat input. Extensive tempering due to weld thermal cycles has shown a more detrimental effect on the hardness of heat affected zone of all the welded joints with the reduction in hardness to around 50–60% for approximately 70 mm width around welded region.

Keywords Hardox 400 · Shielded metal arc welding process · Gas metal arc welding process · Microhardness · Microstructure · Mechanical properties

R. S. Multani (✉) · V. Sharma · A. Gupta
Department of Industrial & Production Engineering, Dr B R Ambedkar National
Institute of Technology, Jalandhar 144011, India
e-mail: ranbirking18@gmail.com

V. Sharma
e-mail: sharmav@nitj.ac.in

A. Gupta
e-mail: guptaa@nitj.ac.in

J. Singh
Department of Mechanical Engineering, Dr B R Ambedkar National Institute of Technology,
Jalandhar 144011, India
e-mail: jaswantsingh@nitj.ac.in

Nomenclature

GMAW	Gas metal arc welding
GTAW	Gas tungsten arc welding
UTS	Ultimate tensile strength
BHN	Brinell hardness number
VHN	Vicker's hardness number
ASTM	American Society for Testing and Materials
JG	Joint welded using GMAW process
JS	Joint welded using SMAW process
WCL	Weld center line
SCHAZ	Sub-critical heat affected zone
ACF	Acicular ferrite
PF	Polygonal ferrite

23.1 Introduction

Low-alloy steels having the total alloying content less than 5% and those in the quenched and tempered conditions possesses high yield strength of 560 N/mm^2 to 880 N/mm^2, greater notch toughness and nominal hardness. A sharp increase in wear resistance (by factors of 3–5) is seen only when tensile strength is increased to 1050–1400 MPa [1]. Currently, a new-generation modern steels are being used in the extreme engineering applications which possess very high tensile strength of UTS > 1200 MPa and high hardness around 400–600 BHN [2]. These steels find applications in the areas requiring high resistance to abrasion in chutes, hoppers, dump truck beds, cutter bars, scraper blades, liner plates, tipper bodies, containers, crushing mills, mills, excavator buckets and loading buckets, etc. [3–5].

Hardox 400 is one such standard type abrasion resistant steel developed which shows high hardness of around 400 BHN and high tensile strength of 1250 MPa, good weldability with certain precautions and good machinability. Currently, this steel is being used frequently in buckets and liner plates. GMAW, GTAW, SMAW, and FCAW are the commonly used processes used to weld this category of steels [6–8]. Generally, undermatched welds are used in joining these high strength steels with the aim of minimizing the hydrogen-induced cracking tendency [9, 10]. Apart from this, the commonly observed phenomenon that takes place in the welding of these steels is reduction in the hardness and strength of HAZ, improvement in the toughness of the weld zone but overall reduction in hardness and tensile strength of weld, etc., due to the weld heat thermal cycles, use of low heat input welding processes, and use of filler materials of low strength [11]. This paper reports the influence of GMAW and SMAW processes on the mechanical properties of welded joints fabricated by keeping minimum heat input. Ballistic performance of the armor grade steel welded joints, possessing unequal and equal double V joint configurations, and welded with

austenitic stainless steel using SMAW process, revealed that, the unequal double V joint configuration offered maximum resistance to the penetration of the bullet at the weld metal position and without any bulge at the rear position [12]. Similar investigations related to joint design variations of quenched and tempered steels using double V, double U, and mixed joint designs welded with ferritic filler materials using SMAW process have been studied in the literature [13].

23.2   Experimentation

The base metal used in this study was 20 mm thick quenched and tempered steel of grade name Hardox 400. Two welded joints were produced in the coupon plates of size $250 \times 125 \times 20$ mm using gas metal arc welding (GMAW) and shielded metal arc welding (SMAW) process. The chemical composition of the base metal and filler materials in the as received conditions is presented in Table 23.1. The mechanical properties of the base metal and the filler material in the as received condition are given in Table 23.2.

Double V groove joint with 60° groove angle and 2 mm root face was used in this study for preparing welded joints as shown in Fig. 23.1a. The test coupons were cleaned and clamped with C-clamps onto a fixture that was provided with a recess to lay down the other side weld. Before welding, the plates were preheated to a temperature of 100 °C as shown in Fig. 23.1b. One of the welded joints named JG was prepared using 2.15 mm diameter ER70s electrode using GMAW process with a mixture of argon and CO_2 as shielding gas. The joint named JS was prepared using 3.15 mm diameter electrode using SMAW process.

The welding parameters used during welding of both types of joints and the heat input used for laying each pass are given in Table 23.3. The heat calculating was done as per Eq. 23.1.

$$\text{Heat Input} = \eta \frac{VI}{S}$$
$$\eta = \text{arc efficiency}, \ V = \text{Voltage}\,(V), \text{I} = \text{Current}\,(A),$$
$$S = \text{Speed(mm/s)} \tag{23.1}$$

The arc efficiency for SMAW process and GMAW process was taken as 80% and 90%, respectively [14].

The specimens for mechanical and metallurgical testing were extracted as per the schematic shown in Fig. 23.2. Specimens used in the characterization of the microstructure, hardness, toughness, and tensile properties were extracted in a direction transverse to the welds. The macrostructures were analyzed through stereo zoom microscope. The microstructures of the joints were analyzed at various locations using optical microscope. The specimens were etched in 2% natal to reveal the

Table 23.1 Chemical composition of base metal and filler materials in wt%

Material	Chemical composition (wt%)								
	C	Si	Mn	P	S	Cr	Ni	Mo	B
Hardox 400	0.13	0.49	1.42	0.007	0.001	0.04	0.005	0.012	0.002
E7018	0.15	0.75	1.6	0.035	0.035	0.2	0.3	–	–
ER70S-6	0.07	0.67	1.22	0.009	0.013	–	–	–	–

Table 23.2   Mechanical properties of base metal and filler material

Mechanical properties of base material

Material	Tensile strength (MPa)	Yield strength (MPa)	Impact energy (J)	Hardness (HV)	Elongation (%)
Hardox 400	1250	800–1100	60	340–400	10

Mechanical properties of filler materials

AWS code	Process	Electrode diameter	Manufacturer	Yield strength (MPa)	Tensile strength (MPa)
E 7018	SMAW	3.15 mm	Ador	470	555
ER 70s-6	GMAW	2.15 mm	Ador	450	560
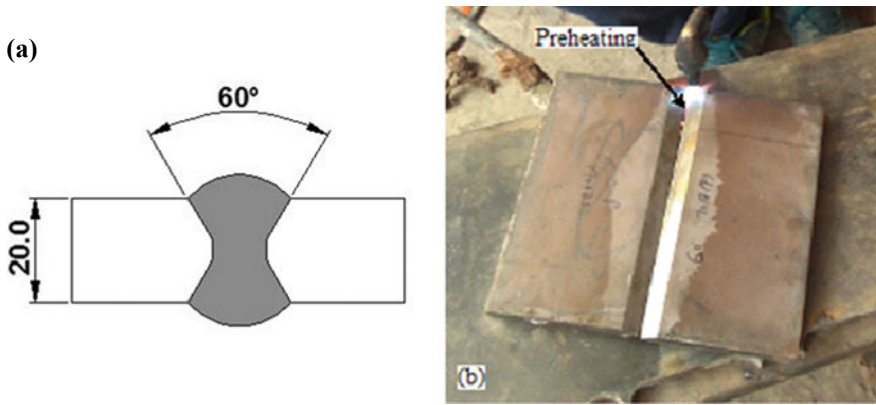
Fig. 23.1   a Double V groove design, **b** base metal plate after machining and illustrating preheating

microstructure of the weldments at the weld metal, fusion zone, and HAZ. The hardness measurements were carried out as per ASTM E-384-05 standard [15] using Vickers microhardness testing machine along weld center line (WCL) and across the WCL with 1000 gm load for a dwell time of 20 S.

The tensile test specimens as illustrated in Fig. 23.3a–c were extracted and prepared according to ASTM E-8 standard [16]. These tests were conducted at room temperature on a 60 ton static universal testing machine to obtain UTS, yield strength, percentage elongation, etc. Charpy impact toughness test specimens were extracted and prepared according to ASTM E-23 standard [17] and tested on a 300 J impact testing machine as shown in Fig. 23.3d.

Table 23.3 Welding process parameters and heat input of welded joints

Pass no.	Current (I)	Voltage (V)	Length (mm)	Time (s)	Speed (mm/min)	Efficiency	Heat input (KJ/mm)	Average (kJ/mm)
Joint JS E 7018 (SMAW)								
1	132	30	250	81	185.18	0.8	1.03	1.119
2	132	30	250	88	185.18	0.8	1.115	
3	132	30	250	84	185.18	0.8	1.06	
4	132	25.5	250	79	588.23	0.8	0.85	
5	133	25.5	250	89	588.23	0.8	0.965	
6	133	25.5	250	86	588.23	0.8	0.933	
7	133	25.5	250	110	588.23	0.8	1.19	
8	133	25.5	250	159	588.23	0.8	1.756	
Joint JG ER 70S-6 (GMAW)								
1	250	32	250	79	3.16	0.9	2.27	2.20
2	250	32	250	81	3.09	0.9	2.3	
3	250	32	250	78	3.27	0.9	2.20	
4	250	32	250	80	3.15	0.9	2.28	
5	250	32	250	77	3.4	0.9	2.1	
6	250	32	250	78	3.3	0.9	2.18	
7	250	32	250	76	3.5	0.9	2.05	
8	250	32	250	80	3.17	0.9	2.27	
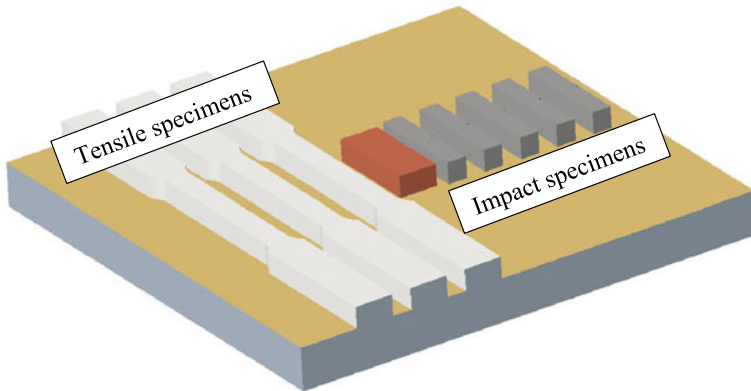
Fig. 23.2 Mechanical and metallurgical specimens extraction schematic
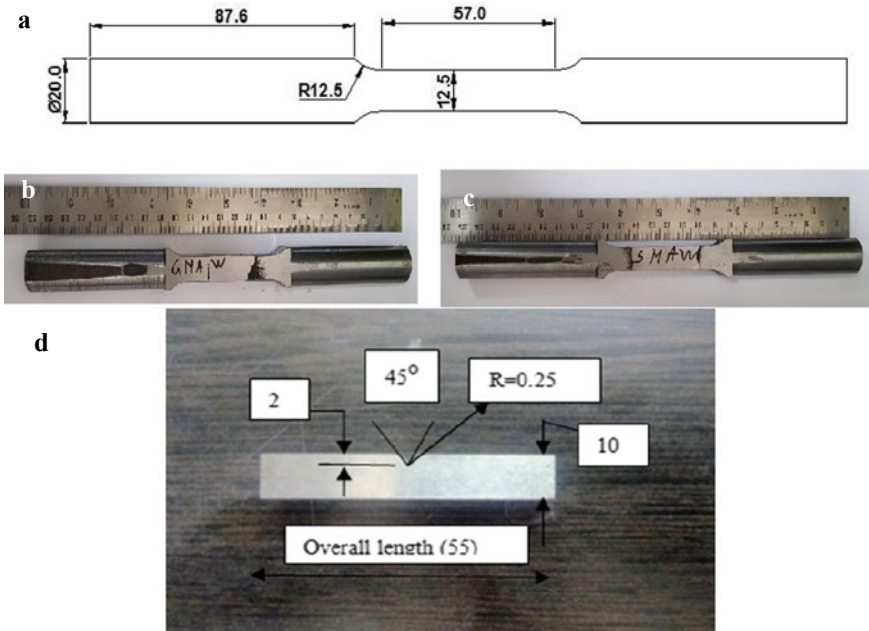
Fig. 23.3 **a** Schematic of tensile specimen, **b** tensile specimen of JG welded joint, **c** tensile specimen of JS welded joint, and **d** impact specimen with specifications

23.3 Results and Discussion

23.3.1 Microstructure

The microphotographs of the base metal and the welded joints were captured under different magnifications to carry out their microstructural investigations.

The micrograph of base metal shown in Fig. 23.4a clearly indicates the extra fine microstructure of acicular tempered martensite consisting of lath martensite which is separated by high angle boundaries. Similar microstructure of Hardox 400 had also been observed in the literature which is responsible for enhancing yield strength, hardness, and toughness of the steels [15]. The micrographs taken at the fusion zone of JG and JS welded joints indicate the presence of acicular ferrite (ACF) within the grain surrounded by polygonal ferrite (PF) content at the grain boundaries as shown in Fig. 23.4b. However, the presence of larger amount of PF (white region) in JG joint as shown in Fig. 23.4c indicates higher heat input in GMAW process as compared to JS joint with lower heat content by the SMAW process. Significant tempering of base metal in the sub-critical region of heat affected zone (HAZ) led to the coarsening of tempered martensite which is clearly evident from Fig. 23.4d.
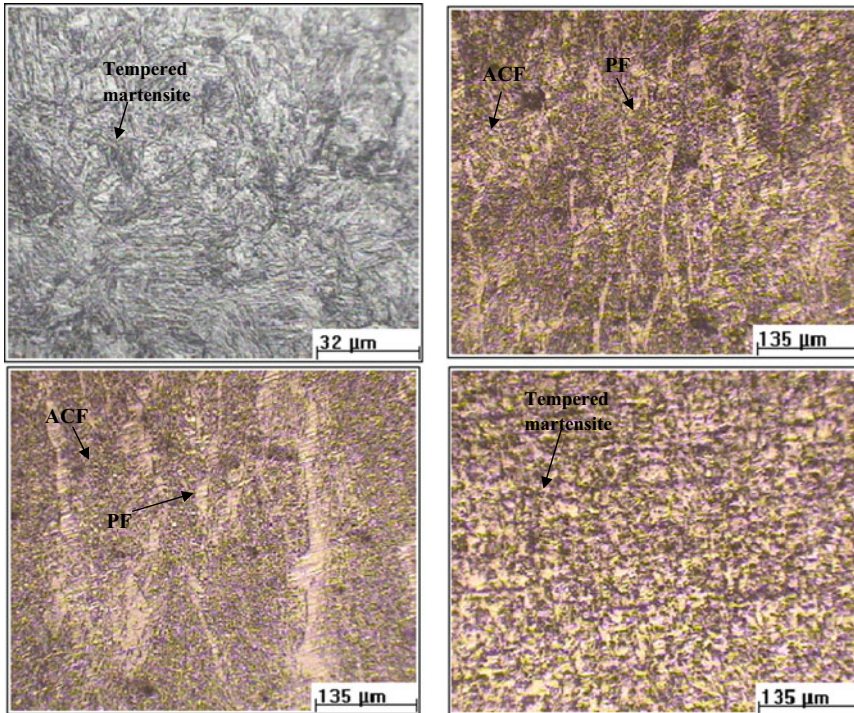
Fig. 23.4 Micrographs: **a** base metal, **b** welded joint JG, **c** welded joint JS and **d** sub-critical region of heat affected zone

23.3.2 Hardness

The hardness measurements were carried out in two different directions to evaluate the hardness variations both along and across the weld cross section. The microhardness values along weld center line are shown by *Y-Y* axis and across the weld cross section are represented by *X-X* axis. Microhardness plots along and across weld center line (WCL) are shown in Fig. 23.5 for JG and JS welded joints.

As observed from the plot for hardness variation along WCL, the average hardness of weld zone for JS joint was found to higher than the JG joint. It is further observed that for both the joints, the plot shows an increase in hardness at the root pass, which could be attributed to the higher dilution of base metal toward the root pass region. Microhardness plot across WCL for both the welded joints shows almost same hardness values at the weld zone. However, hardness dips to minimum value of 180.1 and 182.9 VHN for JS and JG joints, respectively, signifying the sub-critical heat affected zone (SCHAZ) which could have been developed due to excessive tempering effect. Further, traverse across WCL shows consistent increase in microhardness values owing to the decreasing tempering effect on the base metal. This could further be revealed from the microhardness plots that even after approaching 12 mm distance

Fig. 23.5 Graphical representation of microhardness along and across weld center line (WCL) for the welded joints welded using SMAW and GMAW process

Table 23.4 Tensile properties of base metal and welded joints

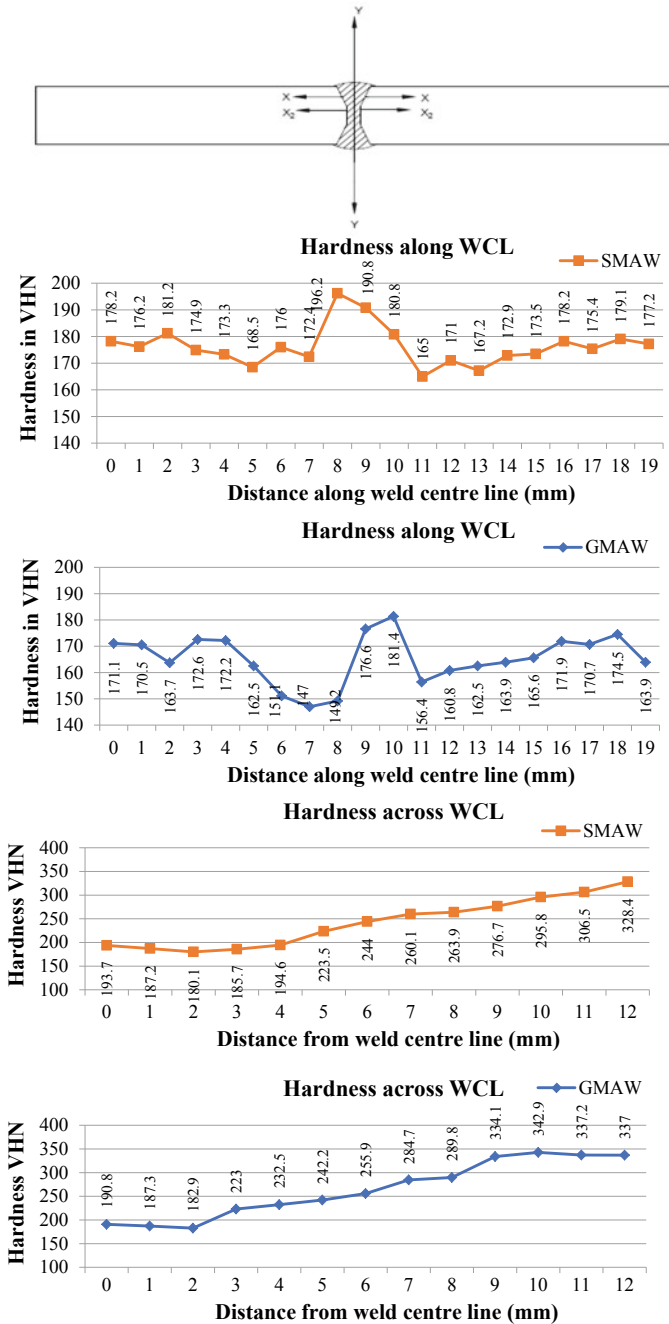| Joint type	Tensile properties					
	Yield strength (Mpa)	Ultimate tensile strength (Mpa)	(%)	Strength ratio (YS/UTS)	Joint efficiency (%)	Failure zone
Hardox 400	1000	1250	10.00	0.80	–	Base metal
JG	528	580	13.18	0.91	52.8	Weld metal
JS	560	600	20.51	0.93	56.0	Weld metal

from the weld center line for JS and JG welded joints, the microhardness reached up to 328 VHN and 337 VHN, respectively, indicating the large HAZ present in the quenched and tempered steels.

23.3.3 Tensile Properties

Transverse tensile properties of the base metal and the welded joints evaluated in accordance to ASTM E8 standard are given in Table 23.4.

During the tensile test, all the specimens (both types of joints) were found to fracture in the weld metal region indicating the weld zone to be the weakest link within the weldment. The JS joint shows higher UTS of 600 MPa, thus resulting in joint efficiency of 56% as compared to UTS of 580 MPa with joint efficiency of 52.8% for the JG joint. Further, it could be observed from the table that the JS joint shows higher ductility with 20.51 percentage elongation as compared to 13.18% for the JG joint which could be attributed to the higher heat input in the JG joint as compared to the JS welded joint. The higher ductility of the JS joint can further be visualized from the fractured ends of tensile sample shown in Fig. 23.6a, b which predicts an appreciable level of ductility possessed by the welded joint. The better ductility as possessed by the JS welded joint is also evident from Fig. 23.6b, d, where a higher degree of necking and protruded shear lips are observed as compared to the JG welded joint (Fig. 23.6a, c).

Its good ductile behavior can be further assessed from the shear lips and the extrusion at the center of fractured end as shown in Fig. 23.6c, d.

23.3.4 Toughness

Charpy V impact tests for the JG and JS welded specimens were carried out at room temperature to determine their impact toughness. The results show that the JS welded joint possessed impact toughness of 194 J as compared to JG joint (170 J).
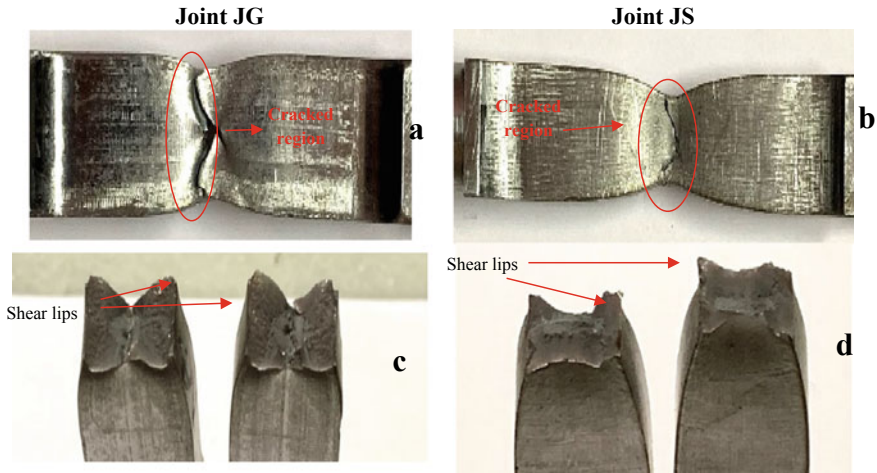
Fig. 23.6 Optical fractographs of fractured tensile specimens of the welded joints

The outcomes from the impact tests were further analyzed by carrying out fracture analysis of impact test specimens. It can be predicted from Fig. 23.7 that after impact test, the fractured ends remained un-separated indicating high toughness and ductility of the JG and JS joints. Further, the larger shear lips area and smaller uncontrolled fractured region indicate high ductility possessed by the JS joint as compared to JG welded joint. This could be attributed to the presence of softer microstructural phases present in the JS welded joint.

23.4 Conclusions

Based on the current investigation, the following major conclusions are drawn:

- Owing to higher heat input in JG joint, the average hardness within the fusion zone is lower as compared to JS welded joint.
- JS joint fabricated from SMAW process shows better tensile strength and ductility as compared to JG welded joint when fabricated using similar welding electrodes.
- JS welded joint showed better Charpy V notch impact toughness as compared to JG welded joint under similar testing conditions.

Joint JG   **Joint JS**
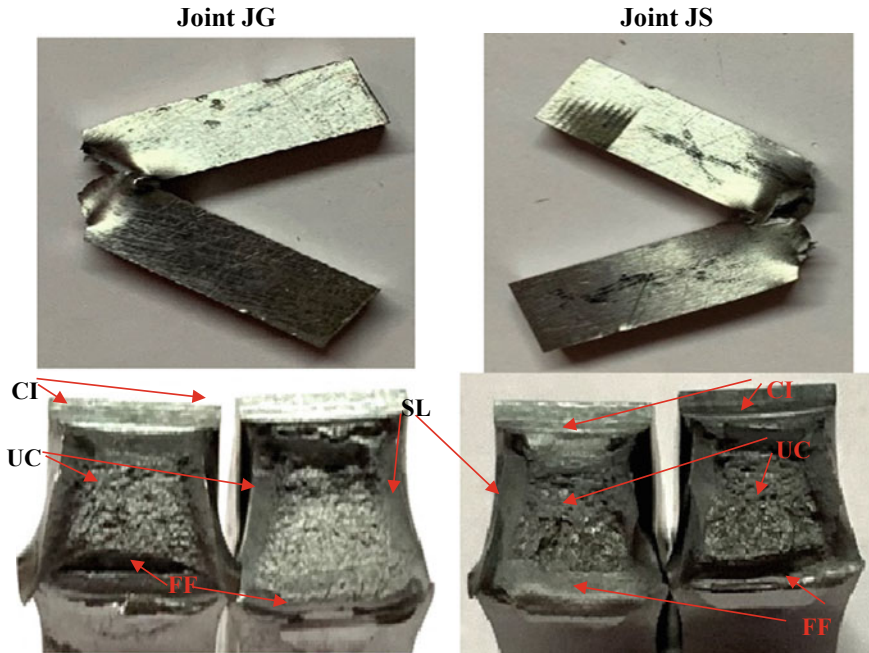
Fig. 23.7 Optical fractographs of fractured Charpy V notch impact specimens of the welded joints; CI—Crack initiation, SL—Shear lips, FF—Final fracture, and UC—Unstable crack region

References

1. Balakrishnan, M., Balasubramanian, V., Madhusuhan, G., Sivakumar, K.: Effect of buttering and hardfacing on ballistic performance of shielded metal arc welded armour steel joints. Mater. Des. **32**, 469–479 (2011)
2. Wang, J., Li, Y., L, P.: Effect of weld heat input on toughness and structure of HAZ of a new super high strength steel. Bull. Mater. Sci. **26**(3), 301–305 (2003)
3. Parmar, R. S.: Welding Engineering and Technology. Khanna Publishers (2003)
4. Manual JFE Everhard: JFE-EH series: abrasion-resistant steel plate (2004)
5. Sharma, V., Shahi, S.: Quenched and tempered steel welded with micro-alloyed based ferritic fillers. J. Mater. Process. Techn. **253**, 2–16 (2018)
6. Lakshminarayanan, A.K., Shanmugam, K., Balasubramanian, V.: Effect of welding processes on tensile and impact properties, hardness and microstructure of AISI 409 M ferritic stainless joints fabricated by duplex stainless steel filler metal. J. Iron. Steel Res. Int. **16**(5), 66–72 (2009)
7. Ragu Nathan, S., Balasubramanian, V., Malarvizhi, S., Rao, A.G.: Effect of welding processes on mechanical and microstructural characteristics of high strength low alloy naval grade steel joints. Defence Techn. **11**(3), 308–317 (2015)
8. Yayla, P., Kaluc, E., Ural, K.: Effects of welding processes on the mechanical properties of HY 80 steel weldments. Mater. Des. **28**(6), 1898–1906 (2007)
9. Loureiro Altino, J.R.: Effect of heat input on plastic deformation of undermatched welds. J. Mater. Process. Technol. **128**, 240–249 (2002)
10. Pekalski, G.: Structure and hardness changes in welded joints of Hardox steels. Arch Civil Mech. Eng. VIII **4**, 15–27 (2008)

11. Sharma, V., Shahi, A.S.: Quenched and tempered steel welded with mico-alloyed based ferritic filers. J. Mater. Process. Technol. **253**, 2–16 (2018)
12. Balakrishnan, M., Balasubramanian, V., Reddy, G.M.: Microstructural analysis of ballistic tests on welded armor steel joints. Metallography. Microstruct. Anal. **2**, 125–139 (2013)
13. Sharma, V., Shahi, A.S.: Effect of groove design on mechanical and metallurgical properties of quenched and tempered low alloy abrasion resistant steel welded joints. Mater. Des. **53**, 727–736 (2014)
14. Kou, S.: Welding Metallurgy. Wiley, Hoboken (2003)
15. ASTM E384: Standard Test Method for Micro Indentation Hardness of Materials
16. ASTM E8: Standard Test Methods for Tension Testing of Metallic Materials
17. ASTM E23: Standard Test Methods for Notched Bar Impact Testing of Metallic

Chapter 24
Effect of Lubrication on Energy Requirement and Joint Properties During FSSW of AA5052-H32 Aluminium Alloy

N. Bhardwaj, R. Ganesh Narayanan, and Uday S. Dixit

Abstract Heat produced due to friction and plastic deformation is considered to be the sources of energy for friction stir spot welding process. This paper propounds that plastic deformation plays a prominent role in heat generation and subsequent joining as compared to friction, contrary to what the name friction stir spot welding (FSSW) suggests. The effect of lubrication between the tool shoulder and the workpiece on the energy required for the welding process has been studied. It is found that due to lubrication the coefficient of friction decreased, resulting in a significantly lower torque and a decrease in plunge force. This resulted in successful welding using lower energy without reduction in joint strength as confirmed by peel and lap shear tests. Finite element (FE) simulation for the lubricated and unlubricated FSSW conditions using DEFORM-3D showed a good agreement with the experimental torque and plunge force after adjusting the friction factor. Temperature distribution from FE simulations, with and without lubricant, is compared which revealed the more important role of plastic deformation as compared to friction in governing peak temperature produced at the pin vicinity.

Keywords Finite element method · Friction · Friction stir welding · Lubrication · Plastic deformation · Solid state joining

24.1 Introduction

Friction stir spot welding (FSSW) is a solid-state welding process that utilizes heat generated by friction and plastic deformation to form the weld [1]. It is a variant of friction stir welding (FSW) process without the traverse of the tool. W. M. Thomas from The Welding Institute (TWI) in the UK first patented the process of FSW by modifying the existing friction welding process [2]. Initially, the process was mainly

N. Bhardwaj (✉) · R. Ganesh Narayanan · U. S. Dixit
Department of Mechanical Engineering, Indian Institute of Technology Guwahati, Guwahati, Assam 781039, India
e-mail: nitis176103008@gmail.com

used for butt welding of high-strength aluminium alloys, however, soon the application of the process extended to fabricate lap joints, T-joints, scarf, etc., for materials ranging from copper, magnesium and magnesium alloys to materials with high melting point like titanium and steel [3]. The heat during FSW is generated with the help of a non-consumable rotating tool that is inserted into the joint region of the workpiece. Localized plastic deformation and temperature generation are observed around the pin. Due to high temperature and large plastic strains, the material undergoes dynamic recrystallization which leads to equiaxed grains in the joint [4–7]. While FSW consists of plunging, dwelling, welding/traverse and retracting stages, its variant FSSW consists of three stages [8]. The process consists of (i) plunging, where a rotating tool with a shoulder and a pin, is inserted into the workpiece to produce heat due to friction and plastic deformation; (ii) dwelling, where the tool is allowed to rotate for a few seconds after the required plunge depth is given in order to enhance plasticization of the workpiece material and form the weld; (iii) retracting, where the tool is retracted from the workpiece leaving a pinhole. It operates at a lower temperature than the melting point of the workpiece, thereby avoiding problems of poor solidification, hot cracking and embrittlement [9]. FSSW process is also highly energy-efficient compared to conventional fusion welding process with energy savings up to 50% as reported in the literature. A weight reduction of 25–40% as compared to riveted and gas metal arc welded parts is claimed by various industries [10]. It is also reported that the process provides a safer working environment for the workers since it does not produce spatter, arc flash and harmful fumes. As such, FSSW is considered as a green alternative to conventional welding and riveting processes as it is more energy-efficient and environmentally friendly. During the last two decades, the application of FSW/FSSW and its variants has been increasing in many industries, viz. automobile, aerospace, railways and shipbuilding. A detailed review on the recent advances in FSW and its applications in various industries has been presented by Bhardwaj et al. [10].

Studies show that the material around the pin is extruded which implies severe plastic deformation and associated heat generation. Although material flow in FSW is very complex, there have been many studies to understand the material flow during welding. Tracer technique was used by Colligan [11] and Reynolds [12]; Liechty and Webb [13] used plasticine with dissimilar colours, while Gratecap et al. [14] used high-speed camera to understand material deposition. The process is explained as an in situ extrusion process by many researchers [12, 15]. The cold material outside the stir zone, where temperature and stress are insufficient to cause material flow, acts as an "extrusion chamber". It was observed that material is extruded around the pin and deposited at the back of the tool where it is forged by the plunging force of the tool shoulder. Along with horizontal circular motion of the material, the combination of stirring motion near the shoulder and extrusion around the pin also creates a secondary vortex of material which moves in vertically circular motion.

Investigations on heat generated and temperature distribution during FSW are important aspects to understand the underlying physics of the problem and to effectively control the process for improving weld quality. A 3D heat transfer model was developed by Chao and Qi [16] assuming only sliding friction and a constant heat

flux. However, the low accuracy of the model is evident from the fact that it only considered frictional heat generation as source of heat. Buffa et al. [17] improved the previous work by considering total heat to consist of heat produced due to plastic deformation in addition to frictional heat developed at the interface. Khandkar et al. [18] had proposed a torque-based heat input model which encompassed heat produced due to friction and plastic deformation. Shi et al. [19] on the other hand had developed a 3D finite element (FE) model which used experimental mechanical power as heat input, eliminating the need for separate considerations/calculations of heat due to plastic deformation and friction. At present, it is widely accepted that friction between the tool and the workpiece as well as plastic deformation are the sources of energy during FSW [20–22]. Su et al. [20] carried out a comprehensive study on the energy utilization during FSSW and observed that only a small percentage (4%) of the total heat generated is used for stir zone formation. Rest of the heat is dissipated into the clamping setup, tool assembly, sheet, anvil and the atmosphere. It was also found that about 70% of the energy was contributed by the pin during FSSW. Stationary shoulder FSW (SSFSW), a variant of the FSW process, utilizes a non-rotating shoulder and a rotating pin. The shoulder does not generate any frictional heat at the shoulder–workpiece interface and aids only in the application of forging force and confining of the stirred material in the weld zone [23, 24]. The major contributor for the formation of the weld in SSFSW is the rotating pin around which material undergoes severe plastic deformation. As such, friction between the tool shoulder and the workpiece is the primary factor in producing successful welds is debatable.

In this paper, a study on the effect of lubrication between the tool shoulder and the workpiece, thereby lowering friction, has been presented and the significant role of plastic deformation in heat generation during welding has been emphasized. The paper also suggests stir spot welding (SSW) as the name for the FSSW process that reduces the bias towards friction as the more important factor for heat generation during welding. The term "stir spot welding" acknowledges the more significant role of plastic deformation in producing heat for weld formation.

24.2 Experimental Details

FSSW was performed to study the effect of lubrication on plunge force and torque requirement during welding. Two AA5052-H32 sheets with 1 mm thickness were taken in overlap configuration and welded using a FSW machine as shown in Fig. 24.1a. The as-received material properties are given in Table 24.1. Four different lubrication conditions, namely (i) unlubricated, (ii) solid lubricant, (iii) liquid lubricant and (iv) coated lubricant (MoS_2), were used to check the effect of lowering friction between the tool and the workpiece (Table 24.2). The solid lubricant used was Chisel paste acquired from Cauldron Petrotech India Pvt. Ltd. The operating temperature of the lubricant was from room temperature up to 700 °C. The liquid lubricant used was ST Forge Star E (from ST Kool) which is a graphite-free water
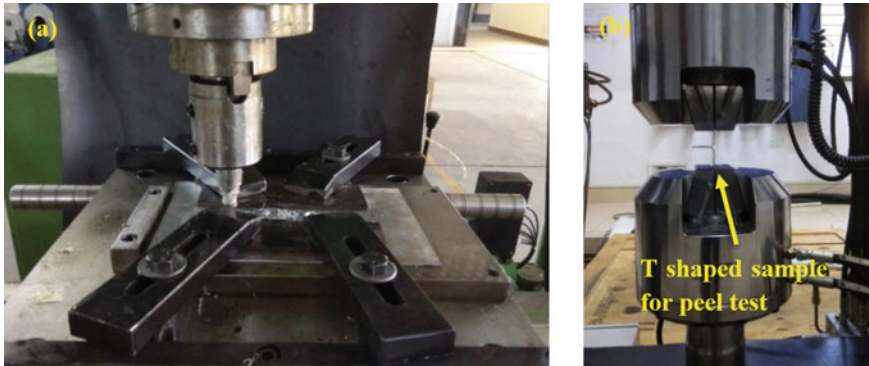
Fig. 24.1 Experimental details: **a** FSW machine with integrated force and torque sensors, **b** peel test samples tested in UTM at room temperature

Table 24.1 Tensile properties of AA5052-H32

Property	Value
Ultimate tensile stress	228 MPa
0.2% offset yield stress	193 MPa
Total elongation	12%
Strain hardening exponent	0.1
Strength coefficient	320 MPa
Plastic strain ratio	0.8

Table 24.2 Lubricants used for FSSW

Operating condition	Details of lubricant used
Unlubricated	No lubricant
Solid lubricant	Chisel paste (from Cauldron Petrotech India Pvt. Ltd.) Operating temperature up to 700 °C
Liquid lubricant	ST Forge Star E (from ST Kool): graphite-free water miscible hot forging die lubricant Working temperature range of 40–450 °C
Lubricant coating	MoS_2 bonded coating spray (from Release-On) 7–15 μm coating thickness for optimum performance. Operating temperature range of 100–450 °C

miscible hot forging die lubricant. The working temperature range of the lubricant was 40–450 °C. The lubricant was mixed with water in the ratio of 1:1 and continuously poured on the tool–workpiece interface during welding process. For the coated lubricant, MoS_2 bonded coating spray (from Release-on) was used. The optimum coating thickness of the lubricant given by the manufacturer was 7–15 μm for effective performance. The operating temperature range for the coated lubricant was

Fig. 24.2 Schematic diagrams: **a** FSW tool with dimensions, **b** peel test sample, **c** lap shear test sample (all dimensions are in mm; L is the gripping length; F is the force applied by UTM)

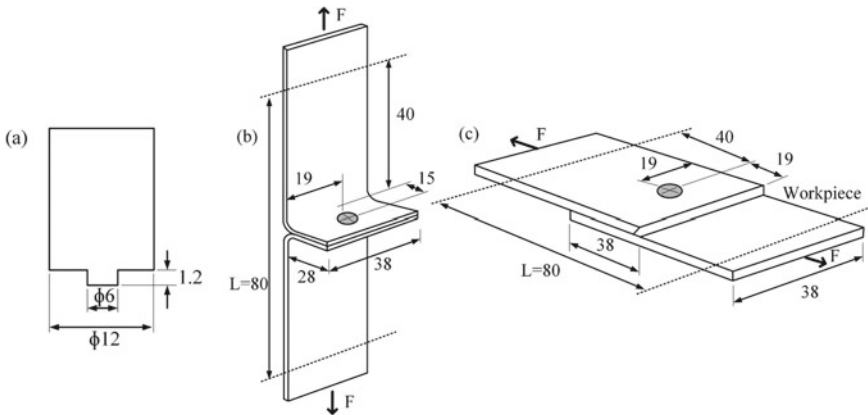100–450°C. An FSW tool with shoulder diameter of 12 mm with pin diameter of 6 mm, and pin length of 1.2 mm was used (Fig. 24.2a). For all the welds, a plunge depth of 0.2 mm, dwell time of 10 s and rotational speeds of 440 revolutions per minute (rpm) and 600 rpm were used. A constant plunge speed of 2 mm/min was used during plunging. In the unlubricated condition, welding was done as conventional FSSW process without lubricant. In case of solid lubricant, the tool and the workpiece were covered with a thick layer of Chisel paste during FSSW. In the third condition, the liquid lubricant was continuously poured on the interface of the tool and the workpiece during FSSW. The fourth condition involved spraying both the tool and the workpiece surfaces with MoS_2 coating of lubricant which was allowed to cure for 5 min after which welding was performed. Although the lubricant was intended to reduce friction between all contacting surfaces of the tool and the workpiece, it was observed that during plunging, the lubricant around the pin was scraped off as the pin went inside the workpiece. It can be effectively assumed that the lubricants reduced the friction between the shoulder surface and the workpiece. Integrated sensors were used to record the torque and plunge force during welding via a strain data logger MP31C09. The joint strength was checked by peel test and lap shear test as per AWS B4.0-2007 standards and was tested in a universal testing machine at room temperature with uniform cross-head speed of 1 mm/min (Fig. 24.1b). The schematic diagram of samples with dimensions for peel test and lap shear tests is shown in Fig. 24.2b, c, respectively. The maximum load-carrying capacity of the welds was recorded.

24.3   Numerical Modelling

A numerical analysis of the process was done using DEFORM-3D using Lagrangian implicit code and adaptive remeshing with sparse solver and direct iteration method. The model used was a fully coupled temperature-displacement analysis which calculated both temperature and displacement simultaneously at each node. Sheet and tool dimensions were kept as that of experiments. Tetrahedral meshing was done in both tool and sheet with minimum global element size of 2 mm and local minimum element size of 0.3 mm at the tool–workpiece interface for better accuracy. Figure 24.3 shows the DEFROM-3D model with global and local meshing.

   Mesh sensitivity analysis was carried out to arrive at the optimal mesh size. Initial mesh size of 2 mm was used globally which was reduced to 1.5, 1 and 0.5 mm locally at the tool–workpiece interface at the consequent steps. Further reduction in mesh size was carried out by reducing in steps of 0.1 mm. After a local element size of 0.3 mm, there was no significant change in the simulation results with further reduction in mesh size. Thus, 0.3 mm was chosen as the optimal mesh size for the simulation. The boundary conditions used were: (i) bottom surface of the sheet at zero velocity in Z-direction (vertical), (ii) tool free to rotate about Z-axis and translate in Z-direction, (iii) convective heat transfer coefficient between sheet and environment is 20 W/m^2 °C [25], (iv) heat transfer coefficient between bottom surface of sheet and backing plate is 200 W/m^2 °C [26]. Material was modelled as viscoplastic material with flow stress $\bar{\sigma}$ as a function of strain ε, strain rate $\dot{\bar{\varepsilon}}$ and temperature T. Heat generation $\dot{q}$ during welding comprises contributions from frictional heat $\dot{q}_f$ and plastic deformation $\dot{q}_p$:

$$\dot{q}_p = \eta \bar{\sigma} \dot{\bar{\varepsilon}}, \tag{24.1}$$

where η is the inelastic heat fraction (Taylor and Quinney coefficient) which is taken as 0.9. The temperature distribution is governed by Fourier heat conduction equation

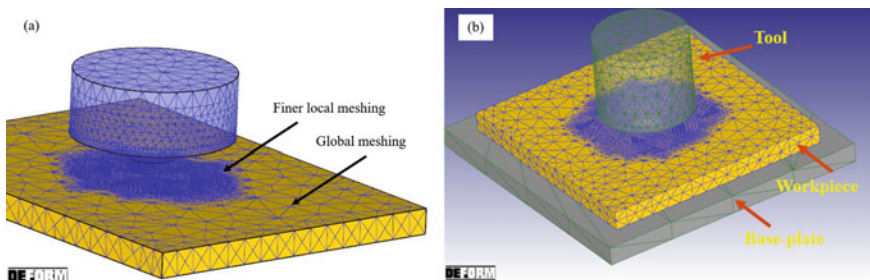$$k\nabla^2 T + \dot{q} = \rho c_p \frac{\partial T}{\partial t}, \tag{24.2}$$

Fig. 24.3 DEFORM-3D simulation: **a** local and global meshing, **b** tool, workpiece and baseplate

where ρ is the density, c_p heat capacity per unit mass and k the thermal conductivity. For the unlubricated condition, sticking friction has been assumed with $m = 1$ at the contacting surfaces as

$$\bar{\tau} = m\tau_{\max}, \tag{24.3}$$

where $\bar{\tau}$ is the frictional shear stress, m is the friction factor and $\tau_{\max}$ is the shear yield strength.

Finite element simulation was performed for $m = 1$ for the unlubricated condition, and the torque obtained from simulations was found to be close match with the experimentally obtained torque. Further, the plunge force obtained from the simulation was also compared with the experimental results to validate the assumption of friction factor as $m = 1$ for the unlubricated condition. For analysis of the lubricated condition, the pin surface was assigned local sticking friction with $m = 1$ since during experiment the lubricant was scrapped off the surface of the pin and it acted as an unlubricated surface. The value of m was varied locally for the shoulder surface in FE simulation, while keeping $m = 1$ for the pin surface constant, in order to match the experimentally found torque for the lubricated conditions. The value of m starting from 1 was decreased in steps of 0.1 for the shoulder–workpiece interface. With the decrease in m, there was a consequent decrease in torque obtained from the FE simulations. Close match with experimental torque values for coated lubricant and solid lubricant was found for $m = 0.5$ and $m = 0.4$, respectively. Further decrease in m resulted in increase of deviation from experimental results. Thus, m values were refined in the range of 0.4–0.5 by giving a deviation of ± 0.05. Close match was obtained with $m = 0.45$ for liquid lubrication condition. Thus, for the three lubrication conditions, i.e. liquid, solid and coated conditions, the value of m was found to be 0.45, 0.4 and 0.5, respectively, which gave close match between simulation and experimentally found torque values. Further, the plunge forces obtained from simulations for $m = 0.45$, $m = 0.4$ and $m = 0.5$ were compared with their corresponding experimental plunge forces which gave satisfactory agreement.

24.4   Results and Discussion

The experimental results revealed that the plunge force and torque during FSSW with lubricant (all three types) were lower than that of unlubricated condition. The plunge force and torque obtained during welding were used to calculate the energy applied during the welding using the following equation:

$$Q_{\text{applied}} = \sum_{n=1}^{n=N} F_n(x_n - x_{n-1}) + \sum_{n=1}^{n=N} M_n \omega_n \Delta t, \tag{24.4}$$

where x_n is plunge depth at step (n), ω the angular velocity, n step number, N the final step and Δt is the sampling time. F_n and M_n are plunge force and torque respectively [20].

Figure 24.4a shows that the plunge force for FSSW in lubricated cases is lower than that in unlubricated condition. Significant decrease in torque was also observed due to application of lubricant (Fig. 24.4b). Table 24.3 summarizes the average plunge
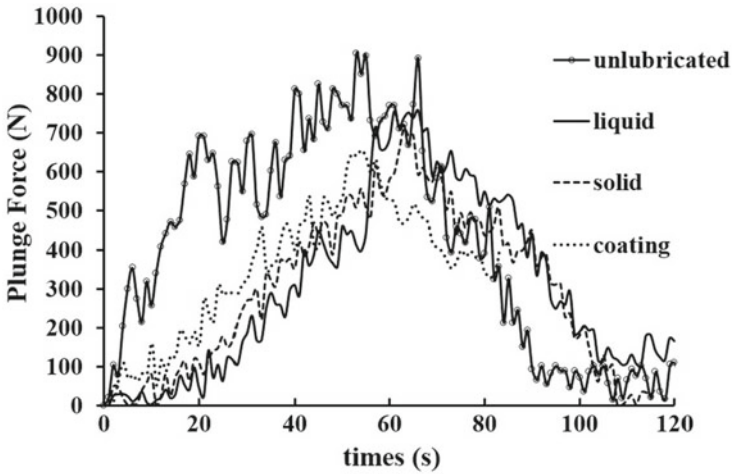
(a)
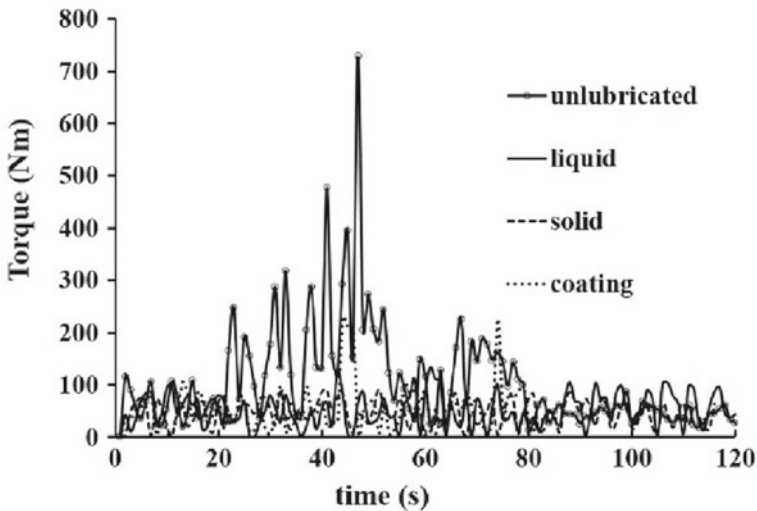
(b)

Fig. 24.4 Experimental plots for different lubrication conditions. **a** Plunge force versus time, **b** torque versus time

Table 24.3 Plunge force, torque and energy for different lubrication conditions during FSSW

Lubrication condition	Avg. torque (Nm)	Avg. plunge force (N)	% difference in torque from unlubricated condition	% difference in force from unlubricated condition	Energy (kJ)
Unlubricated	101.4	409.5	–	–	518.2
Liquid	52.8	309.1	48.7	24.4	193.4
Solid	45.7	304	54.9	25.7	182.7
Coating	56.1	359	44.7	12.2	219.3

force and torque (during $t = 0$ to $t = 94$ s) for the different lubrication conditions. It is seen that there is a reduction of 48.7%, 54.9% and 44.7% in torque due to use of liquid, solid and coated lubricants, respectively. A reduction of 24.44%, 25.67% and 12.22% is observed for the plunge force by use of liquid, solid and coated lubricants, respectively. By using Eq. 24.4, the energy required for the welding with different lubrication conditions was calculated. It was found that 518.2 kJ of energy was required to produce the weld in case of unlubricated condition. The calculated values of energy requirement for liquid, solid and unlubricated conditions were 193.4 kJ, 182.7 kJ and 219.3 kJ, respectively. There was a reduction of 63%, 65% and 57% in energy from unlubricated condition by use of liquid, solid and coated lubricants, respectively (Table 24.3). The use of lubricants reduced the friction at the contacting surfaces and resulted in the reduction in plunge force, torque and consequently the energy requirement for weld formation.

The decrease in torque and plunge force implies the reduction in friction between the contacting surfaces. However, there was no significant decrease in weld joint strength as observed from the peel test and lap shear test data for the joints as shown in Table 24.4. For the unlubricated case, maximum load-bearing capacity in peel test was achieved for 440 RPM which was 587 N. For the solid, coated and liquid lubrication conditions, the maximum load-bearing capacity was found to be 576 N, 593 N and 601 N, respectively, at 440 RPM. For all the cases, it was found that higher load-bearing capacity was observed for 440 RPM as compared to 600 RPM. A similar observation was made in case of lap shear tests as well where higher load-bearing capacity was observed for 440 RPM. Maximum load-bearing capacity in case of lap shear tests for unlubricated, solid, coated and liquid lubrication conditions was found to be 1056 N, 1065 N, 1074 N and 1077 N, respectively. It can be observed that there was no significant difference in the maximum load-bearing capacity for unlubricated and lubricated conditions for both peel test and lap shear tests. Although friction was higher in case of the unlubricated condition, it did not result in significant change in joint strength. It can be inferred from the above observation that plastic deformation plays a more vital role in joint formation in case of FSSW as compared to friction.

Table 24.4 Peel test and lap shear test results for various lubrication conditions

Lubrication condition	Rotational speed (RPM)	Maximum load-bearing capacity in peel test (N)		Maximum load-bearing capacity in lap shear test (N)	
		Trial 1	Trial 2	Trial 1	Trial 2
Unlubricated	440	587	581	1056	1049
	600	551	565	1047	1040
Solid	440	573	576	1065	1058
	600	568	563	1051	1055
Coating	440	593	582	1071	1074
	600	559	544	1065	1059
Liquid	440	588	601	1075	1077
	600	576	575	1061	1057

Figure 24.5 shows the temperature contour at the cross section of the weld obtained from FE simulations. It can be seen that even though there is a decrease in temperature adjacent to the shoulder in lubricated condition, the maximum temperature
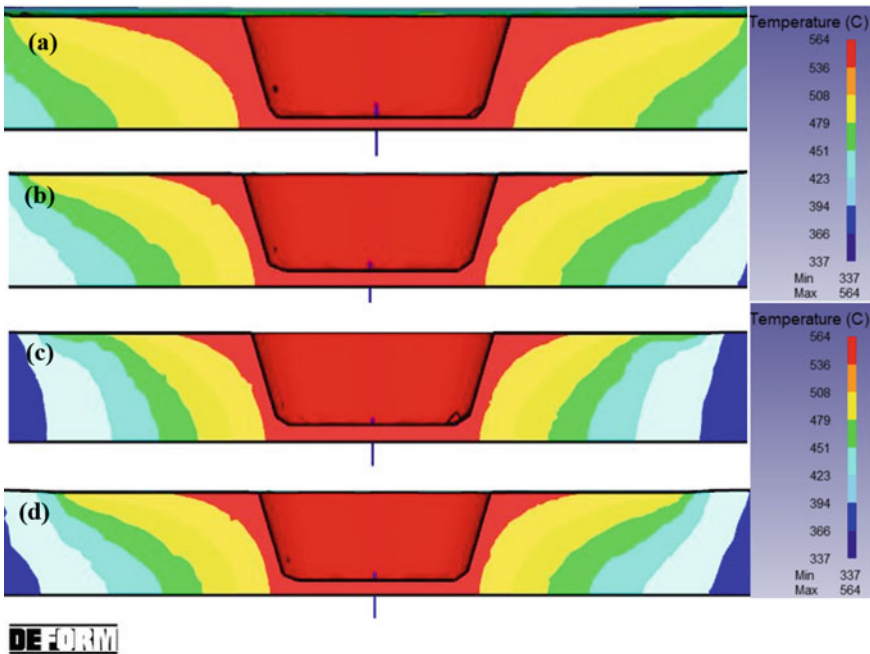

Fig. 24.5 Temperature contour simulation of cross section of the joint in **a** unlubricated condition, **b** solid lubricant, **c** liquid lubricant and **d** coated lubricant
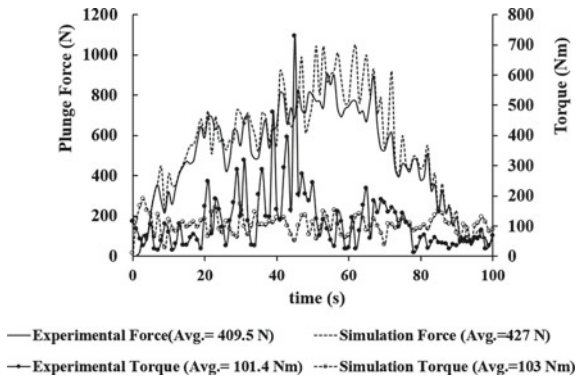
Fig. 24.6 Plunge force and torque versus time plots for simulation and experiment (unlubricated condition, $m = 1$)

generated around the pin (564 °C) remained the same for both lubricated and unlubricated conditions. It is known that material around the pin gets extruded around it and undergoes severe plastic deformation. This plastic deformation around the pin contributes significantly to heat generation at the vicinity of the pin. This phenomenon was captured well by the FE simulations which reveal that the reduction of friction between the shoulder and the workpiece had very little effect on the maximum temperature developed in the weld zone. The maximum temperature in the weld zone was governed by the plastic deformation of workpiece material. Although the maximum temperature generated was found to be same, the size of the heat-affected zone was less in case of lubricated conditions which may be beneficial for joint quality explaining a slight improvement in joint strength during peel test and lap shear test. The aforesaid observations suggest that plastic deformation plays a more important role in heat generation. The predicted force and torque evolutions agreed well with experimental data for unlubricated as well as lubricated conditions. Figure 24.6 shows comparison between experimental and simulation data for unlubricated condition. It can be observed that by matching the simulation torque values with experimental torque values and arriving at friction factor value as $m = 1$, the plunge force values for simulation and experiments showed good agreement. With an application of similar approach, it was found that for solid, liquid and coated lubrication conditions, at the shoulder–workpiece interface $m = 0.4$, 0.45 and 0.5, respectively, gave the closest match between experimental and simulation results. The comparison between experimental and simulation results for solid, liquid and coated lubrication conditions is shown in Figs. 24.7, 24.8 and 24.9, respectively. Also, the results have been compiled in Table 24.5.

Fig. 24.7 Plunge force and torque versus time plots for simulation and experiment (solid lubricant, $m = 0.4$)
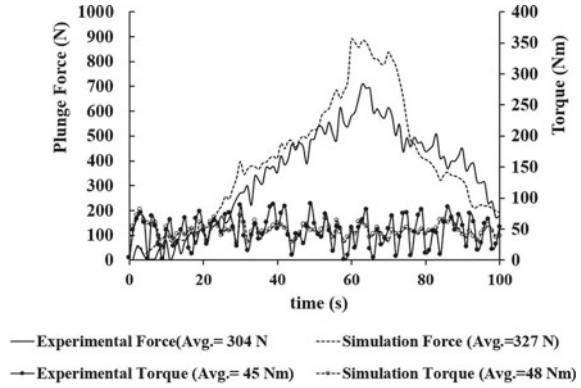

Fig. 24.8 Plunge force and torque versus time plots for simulation and experiment (liquid lubricant, $m = 0.45$)
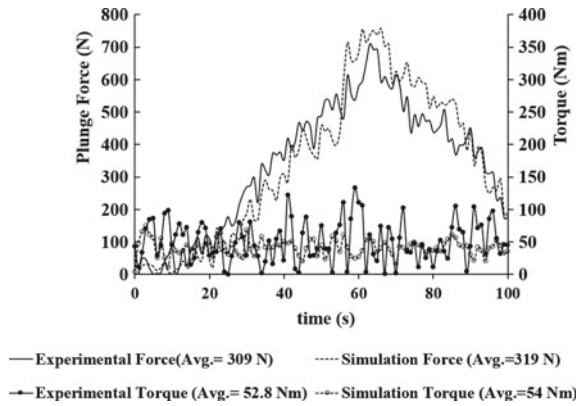

Fig. 24.9 Plunge force and torque versus time plots for simulation and experiment (coated lubricant, $m = 0.5$)
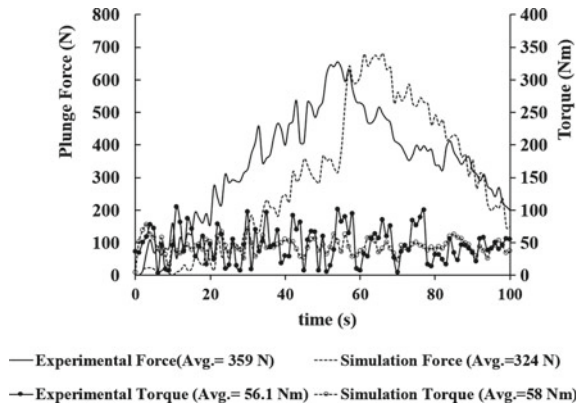
Table 24.5 Comparison between simulation and experimental torque and plunge force

Lubrication condition	Experimental torque (Nm)	Simulated torque (Nm)	% error in torque (%)	Experimental plunge force (N)	Simulated plunge force (N)	% error in force (%)
Unlubricated	101.4	103	1.5	409.5	427	4.2
Liquid	52.8	54	2.2	309.1	319	3.2
Solid	45.7	48	5	304	327	7.5
Coating	56.1	58	3.4	359	324	9.7

24.5 Conclusion

The present study reveals that the use of lubricant in FSSW process leads to decrease in torque and plunge force due to reduction in friction between tool shoulder and workpiece. This consequently results in lesser energy requirement for weld formation. More than 50% reduction in energy requirement was observed due to the use of lubricants with insignificant change in joint strength. It can be thus concluded that plastic deformation plays a more important role in joint formation in FSSW as compared to friction. Friction stir spot welding could be called as stir spot welding (SSW) to emphasize the predominant role of plastic deformation in welding. The finite element simulation results on plunge force and torque evaluation agree well with experimental data for the lubricated as well as unlubricated conditions by adjusting the friction factor, m. Finite element simulation also provided temperature distribution, which indicates that size of heat-affected zone can be reduced with proper lubrication.

References

1. Mishra, R.S., Ma, Z.Y.: Friction stir welding and processing. Mater. Sci. Eng. R Rep. **50**, 1–78 (2005). https://doi.org/10.1016/j.mser.2005.07.001
2. Thomas, W.: International Patent Application No. PCT/GB92. GB Patent Application No. 9125978 (1991)
3. Khan, N.Z., Siddiquee, A.N., Khan, Z.A.: Friction Stir Welding: Dissimilar Aluminium Alloys. CRC Press, London (2017)
4. Chang, W.S., Rajesh, S.R., Chun, C.K., Kim, H.J.: Microstructure and mechanical properties of hybrid laser–friction stir welding between AA6061–T6 Al alloy and AZ31 Mg alloy. J. Mater. Sci. Technol. **27**(3), 199–204 (2011)
5. Jata, K.V., Sankaran, K.K., Ruschau, J.J.: Friction–stir welding effects on microstructure and fatigue of aluminum alloy 7050–T7451. Metall. Mater. Trans. A **31**(9), 2181–2192 (2000)
6. Liu, G., Murr, L.E., Niou, C.S., McClure, J.C., Vega, F.R.: Microstructural aspects of the friction–stir welding of 6061–T6 aluminum. Scripta Mater. **37**(3), 355–361 (1997)
7. Rhodes, C.G., Mahoney, M.W., Bingel, W.H., Spurling, R.A., Bampton, C.C.: Effects of friction stir welding on microstructure of 7075 aluminum. Scripta Mater. **36**(1), 341–355 (1997)

8. Pan, T., Joaquin, A., Wilkosz, D.E., et al.: Spot friction welding for sheet aluminum joining. In: Proceedings of the Fifth International Conference on Friction Stir Welding, pp. 14–16 (2004)

9. Messler, R.W. (ed.): Principles of Welding. Wiley-VCH Verlag GmbH, Weinheim, Germany (1999)

10. Bhardwaj, N., Narayanan, R.G., Dixit, U.S., Hashmi, M.S.J.: Recent developments in friction stir welding and resulting industrial practices. Adv. Mater. Process. Technol. **5**(3), 461–496 (2019)

11. Colligan, K.: Material flow behavior during friction welding of aluminum. Weld. J. **75**(7), 229s–237s (1999)

12. Reynolds, A.P.: Visualisation of material flow in autogenous friction stir welds. Sci. Technol. Weld. Joining **5**(2), 120–124 (2000)

13. Liechty, B.C., Webb, B.W.: The use of plasticine as an analog to explore material flow in friction stir welding. J. Mater. Process. Technol. **184**(1–3), 240–250 (2007)

14. Gratecap, F., Girard, M., Marya, S., Racineux, G.: Exploring material flow in friction stir welding: tool eccentricity and formation of banded structures. Int. J.Mater. Form. **5**(2), 99–107 (2012)

15. Arbegast,W.J.: Hot Deformation of Aluminum Alloys III, p. 313. TMS,Warrendale, PA, USA (2003)

16. Chao, Y., Qi, X.: Thermal and thermo–mechanical modeling of friction stir welding of aluminum alloy 6061–T6. J. Mater. Process. Manuf. Sci. **7**, 215–233 (1998)

17. Buffa, G., Hua, J., Shivpuri, R., Fratini, L.: Design of the friction stir welding tool using the continuum based FEM model. Mater. Sci. Eng. **419**, 381–388 (2006)

18. Khandkar, M.Z.H., Khan, J.A., Reynolds, A.P.: Prediction of temperature distribution and thermal history during friction stir welding: input torque based model. Sci. Technol. Weld. Joining **8**(3), 165–174 (2003)

19. Shi, Q.Y., Dickerson, T.L., Shercliff, H.R.: Thermomechanical FE modelling of friction stir welding of Al-2024 including tool loads. In: Friction Stir Welding: Proceedings of the 4th International Symposium on Friction Stir Welding. TWI Limited, UK (2003)

20. Su, P., Gerlich, A., North, T.H., Bendzsak, G.J.: Energy utilisation and generation during friction stir spot welding. Sci. Technol. Weld. Joining **11**, 163–169 (2006). https://doi.org/10.1179/174329306X84373

21. Arora, A., Nandan, R., Reynolds, A.P., DebRoy, T.: Torque, power requirement and stir zone geometry in friction stir welding through modeling and experiments. Scripta Mater. **60**, 13–16 (2009). https://doi.org/10.1016/j.scriptamat.2008.08.015

22. Awang, M., Mucino, V.H.: Energy generation during friction stir spot welding (FSSW) of Al 6061-T6 plates. Mater. Manuf. Process. **25**, 167–174 (2010). https://doi.org/10.1080/10426910903206758

23. Maltin, C.A., Nolton, L.J., Scott, J.L., Toumpis, A.I., Galloway, A.M.: The potential adaptation of stationary shoulder friction stirwelding technology to steel. Mater. Des. **64**, 614–624 (2014). https://doi.org/10.1016/j.matdes.2014.08.017

24. Li, D., Yang, X., Cui, L., He, F., Zhang, X.: Investigation of stationary shoulder friction stir welding of aluminum alloy 7075-T651. J. Mater. Process. Technol. **222**, 391–398 (2015). https://doi.org/10.1016/j.jmatprotec.2015.03.036

25. Jain, R., Pal, S.K., Singh, S.B.: Finite element simulation of temperature and strain distribution during friction stir welding of AA2024 aluminum alloy. J. Inst. Eng. India Ser. C **98**, 37–43 (2017). https://doi.org/10.1007/s40032-016-0304-3

26. Asadi, P., Mahdavinejad, R.A., Tutunchilar, S.: Simulation and experimental investigation of FSP of AZ91 magnesium alloy. Mater. Sci. Eng. A **528**, 6469–6477 (2011). https://doi.org/10.1016/j.msea.2011.05.035

Chapter 25
Investigation of Weld Bead Shape Parameters in Relation to Heat Input During Submerged Arc Welding

Satish Kumar Sharma, Dinesh W. Rathod, Himanshu Payal, and Sachin Maheshwari

Abstract In this study, effects of heat input and cooling rate on the weld bead shape-related parameters such as weld penetration shape factor (WPSF) and weld reinforcement form factor (WRFF) are studied during submerged arc welding (SAW) of high strength pipeline steel. Experiments were planned and executed according to the approach of central composite rotatable design (CCRD) using five variables, each at five levels. Along with open circuit voltage, wire feed rate, trolley speed, and contact-tube to work distance, preheating temperature is also used as process variable which governs the cooling rate. For the purpose of prediction as well as better control of weld bead geometry, welding process is mathematically modeled for each weld bead shape-related parameter in relation to process variables. In addition to main and interaction effects, relationship of each weld bead shape-relationship parameter with heat input as well as weld cooling time is presented graphically and further analytically discussed.

Keywords Cooling time · Weld bead · Submerged arc welding · SAW · Heat input · Shape-relationship parameters

25.1 Introduction

For fabrication of oil and gas pipelines, steel grade of high strength such as API X80 is preferred because of its very-fine grain structure possessing high fracture toughness even at low temperatures and also its higher strength-to-weight ratio [1, 2].

S. K. Sharma (✉) · D. W. Rathod
Department of Mechanical Engineering, Thapar Institute of Engineering and Technology, Patiala 147004, India
e-mail: satishsharma847@gmail.com

H. Payal
Department of Mechanical Engineering, Sharda University, Greater Noida 201310, India

S. Maheshwari
Division of Manufacturing Processes and Automation Engineering, Netaji Subhas University of Technology, New Delhi 110078, India

For successful welding of this steel, submerged arc welding (SAW) is the commonly applied welding operation [3]. Geometry of weld bead decides the behavior of welded joint in different applications. However, shape of weld bead is governed by heat input and cooling rate during welding. Therefore, correlation between the welding process parameters and weld bead geometry is important to understand for the better quality of the welds. Due to the involvement of various factors, the relationship between weld bead geometry and welding process parameters is very complex [4–7]. However, control over operating variables in SAW is essential if good quality weld with high production rate is the target [8]. Therefore, in this study, values of weld bead shape-related parameters, weld penetration shape factor (WPSF), and weld reinforcement form factor (WRFF) were calculated. WPSF indicates the internal shape of the weld or centerline cracking possibility in the weld while WRFF indicates the external shape or smoothness of the weld. Table 25.1 summarizes the significance and effect of each weld bead characteristics on the mechanical and microstructure properties possessed by the welded joint.

25.2 Experimentation

25.2.1 Material and Method

High-strength low-alloy pipeline steel is used for bead on plate experiments. Consumables, i.e., electrode filler wire and flux of matching composition, are used according to the AWS specification. Experiments were planned as per CCRD approach of design of experiment, and regression analysis is carried out according to RSM.

25.2.2 Bead Geometry Measurement

Small pieces carrying the complete surface deposited weld bead cross-section and its heat affected zone were taken from 150 mm wide and 300 mm long plate. Figure 25.1 shows the weld deposited cross-sectioned surface after polishing and etching. Bead shape-related parameters were determined using the results of width, penetration, and reinforcement of weld bead measured through stereo-zoom microscope. Table 25.2 lists the process parameters and level values considered during the study. Submerged arc welding process with constant voltage power source is applied in this study.

Table 25.1 Weld bead geometry and its shape-related parameters with significance

Weld bead parameter	Measurement (direct/calculated)	Significance	When at low level	When at high level
Penetration (P)	Direct	Determines the stress-carrying capacity of welded joint	Weak weld joint	May cause centerline cracking
Reinforcement (R)	Direct	Improves the strength of the weld	Less material and lower strength	Excessive material consumption and stress concentration
Bead width (W)	Direct	Indicates the extent of parent material's involvement in welding	Improper fusion of parent material with the filler metal	Tendency for surface cracks. Large area is thermally affected with alterations in its microstructure
Dilution	Calculated as - $\frac{\text{Penetrated Area}}{\text{Total weld Area}}$	Determines the mechanical and chemical properties of a welded joint	A weak joint with lesser penetration	Increases the possibility for solidification cracking in the weld
Reinforcement form factor (WRFF)	Calculated as - $\frac{W}{R}$	Indicates the external shape or smoothness of the weld	Excess material in reinforcement area with non-smooth surface weld	Concave surface of the weld
Penetration shape factor (WPSF) or aspect ratio	Calculated as - $\frac{W}{P}$	Indicates the internal shape of the weld or centerline cracking possibility in the weld	Solidification cracking in the weld	Weld surface tends to crack

25.3 Results and Discussions

25.3.1 Regression Analysis and ANOVA Results

Experiments were carried out at random as given in Table 25.3. From the results of WPSF and WRFF, regression coefficients are determined for a second-order regression model for each weld bead shape-related parameter. ANOVA including tests for the significance of the regression model and coefficients was also performed to check the accuracy of the developed models. Along with goodness of fit test, lack of fit and

Fig. 25.1 For weld number
11, revealed bead geometry
after etching

Table 25.2 Process parameters with levels

Process parameters	Notation	Units	Levels				
			−2	−1	0	+1	+2
Open circuit voltage	A	Volt	30	32	34	36	38
Trolley speed	B	mm/min	250	300	350	400	450
Contact-tube to work distance (CTWD)	C	mm	24	28	32	36	40
Preheat temperature	D	°C	60	120	180	240	300
Wire feed rate	E	mm/s	20	25	30	35	40

model adequacy test were also conducted. ANOVA test results for quadratic model
are tabulated in Tables 25.4 and 25.5 for WPSF and WRFF, respectively. Quadratic
model for both, WPSF and WRFF is found non-aliased as well as significant. For
each model, p-value is found <0.0001. Regression model equation for actual values
of parameters is given in Eqs. 25.1 and 25.2 for WPSF and WRFF, respectively.

Regression model for actual values of process parameters:

$$\begin{aligned}
\text{WPSF} = &-85.702 + 4.246 * A + 0.564 * B + 0.701 * C - 0.0404 \\
&* D - 0.086 * E + 1.383\text{E}{-}003 * A * D - 7.08\text{E}{-}003 * B * C - 0.065 \\
&* A^2 - 5.22\text{E}{-}003 * B^2 - 6.66E{-}003 * C^2 - 2.593\text{E}{-}005 * D^2 \quad (25.1)
\end{aligned}$$

$$\text{WRFF} = -103.224 + 6.344 * A - 0.1545 * \text{E} - 0.091 * A^2 \quad (25.2)$$

Table 25.3 List of designed experiments with results of WPSF and WRFF

Run No.	A	B	C	D	E	Critical cooling time $\Delta t_{8/5}$(s)	Heat input (kJ/mm)	WPSF	WRFF
1	1	1	−1	1	−1	16.30	2.48	2.05	2.94
2	0	0	0	0	2	15.74	3.27	1.35	2.08
3	0	0	0	0	0	14.50	3.01	2.29	3.14
4	−1	1	−1	1	1	16.71	2.55	1.19	1.39
5	1	1	−1	1	1	18.15	2.77	1.40	2.24
6	−1	−1	−1	−1	1	12.90	3.49	1.52	2.04
7	0	0	0	0	0	14.35	2.98	2.15	2.79
8	−1	1	−1	−1	−1	8.36	2.26	2.16	3.43
9	0	0	0	0	0	14.37	2.98	2.56	3.92
10	1	−1	−1	1	1	24.37	3.71	1.35	2.18
11	1	−1	1	1	−1	20.86	3.18	2.96	4.56
12	−2	0	0	0	0	11.54	2.40	0.86	1.00
13	0	2	0	0	0	10.25	2.13	1.42	2.28
14	1	1	1	−1	−1	8.67	2.35	2.11	3.65
15	0	−2	0	0	0	18.09	3.76	2.00	2.78
16	0	0	0	0	0	14.35	2.98	2.42	3.60
17	0	0	0	2	0	26.19	2.74	1.41	2.31
18	0	0	0	0	0	14.35	2.98	2.34	3.42
19	−1	1	1	1	−1	14.06	2.14	1.58	2.54
20	1	−1	−1	−1	−1	12.12	3.28	2.42	3.77
21	0	0	0	−2	0	8.16	2.78	2.31	3.08

(continued)

Table 25.3 (continued)

Run No.	A	B	C	D	E	Critical cooling time $\Delta t_{8/5}$(s)	Heat input (kJ/mm)	WPSF	WRFF
22	1	−1	1	−1	1	10.71	2.90	1.68	2.18
23	−1	−1	1	1	1	20.11	3.06	1.17	1.39
24	0	0	2	0	0	13.10	2.72	2.06	2.24
25	−1	1	1	−1	1	8.82	2.38	1.27	1.36
26	−1	−1	−1	1	−1	19.38	2.95	1.37	1.88
27	0	0	0	0	0	14.35	2.98	2.23	3.30
28	−1	−1	1	−1	−1	10.47	2.83	2.76	3.93
29	0	0	0	0	−2	11.13	2.31	3.21	5.51
30	0	0	−2	0	0	13.36	2.77	1.56	2.74
31	2	0	0	0	0	15.02	3.12	1.53	2.41
32	1	1	−1	−1	1	10.44	2.82	1.30	2.23

Table 25.4 ANOVA results for WPSF

Source	Sum of squares	df	Mean square	F-value	p-value Prob > F	
Model	9.72	11	0.88	25.52	<0.0001	Significant
A-voltage	0.53	1	0.53	15.21	0.0009	
B-trolly speed	0.46	1	0.46	13.26	0.0016	
C-CTWD	0.28	1	0.28	8.04	0.0102	
D-Preheat temperature	0.66	1	0.66	18.93	0.0003	
E-wire feed rate	4.39	1	4.39	126.7	<0.0001	
AD	0.44	1	0.44	12.72	0.0019	
BC	0.32	1	0.32	9.26	0.0064	
A^2	2	1	2	57.68	<0.0001	
B^2	0.5	1	0.5	14.52	0.0011	
C^2	0.34	1	0.34	9.68	0.0055	
D^2	0.26	1	0.26	7.43	0.013	
Residual	0.69	20	0.035			
Lack of fit	0.59	15	0.039	1.87	0.2528	Not significant
Pure error	0.1	5	0.021			
Cor total	10.42	31				
Std. dev.	0.19		R-squared		0.9335	
Mean	1.88		Adj R-squared		0.8969	
C.V. %	9.92		Pred R-squared		0.8158	
PRESS	1.92		Adeq precision		21.561	

25.3.2 Main and Interaction Effects

Significance of each regression term is determined at 95% confidence level, and thereafter, using backward elimination, insignificant terms are eliminated. In this section, for each weld bead shape-related parameter, main effects of process parameters are given in terms of perturbation curve, and interaction effects are presented in the form of 3D surface plot.

WPSF: Main effects of SAW process variables on WPSF of the weld can be easily understood by knowing their effects on bead width and penetration, separately. Weld penetration shape factor is found to be affected significantly by all process parameters along with interaction effects of open circuit voltage with preheating temperature and of trolley speed with CTWD. As evident from Fig. 25.2a, WPSF is largely affected by wire feed rate. WPSF decreases almost linearly at very steep rate when wire feed rate is increased. Therefore, more metal deposition rate may be the contributing factor for

Table 25.5 ANOVA results for WRFF

Source	Sum of squares	df	Mean square	F-value	p-value Prob > F	
Model	21.35	3	7.12	22.66	<0.0001	Significant
A-voltage	*3.08*	*1*	*3.08*	*9.81*	*0.004*	
E-wire feed rate	*14.32*	*1*	*14.32*	*45.61*	*<0.0001*	
A^2	*3.95*	*1*	*3.95*	*12.57*	*0.0014*	
Residual	8.79	28	0.31			
Lack of fit	*8.04*	*23*	*0.35*	*2.33*	*0.1758*	*Not significant*
Pure error	*0.75*	*5*	*0.15*			
Cor total	30.14	31				
Std. dev.	0.56		R-squared		0.7083	
Mean	2.76		Adj R-squared		0.6771	
C.V. %	20.31		Pred R-squared		0.6271	
PRESS	11.24		Adeq precision		18.737	

this decrease. Trolley speed and preheating temperature also have a negative impact on WPSF value. Moreover, up to middle levels of open circuit voltage and CTWD, the value of WPSF increases. After that, it decreases with further increase of voltage while remains almost constant with the further increase of CTWD. 3D interaction plot as shown in Fig. 25.2b clearly depicts that higher value of WPSF is given when both preheating temperature and open circuit voltage are kept at their middle level. The interaction between trolley speed and CTWD shown in Fig. 25.2c reveals that higher value of CTWD and lower value of trolley speed are helpful in obtaining a weld with higher WPSF.

WRFF: It is found to be affected significantly by open circuit voltage as well as wire feed rate. As evident from Fig. 25.3, the value of WRFF decreases almost linearly with wire feed rate while it increases when open circuit voltage is increased up to its middle level. With wire feed rate, metal deposition rate also increases which causes higher reinforcement, and hence, a lower value of WRFF is obtained. When voltage is increased, it caused larger increase in bead width as compared to the increase in reinforcement. This change can be a contribution of the increasing arc length. For further increase of voltage, both bead width and reinforcement increase with the almost equal extent, and hence, no significant change in the value of WRFF is obtained.
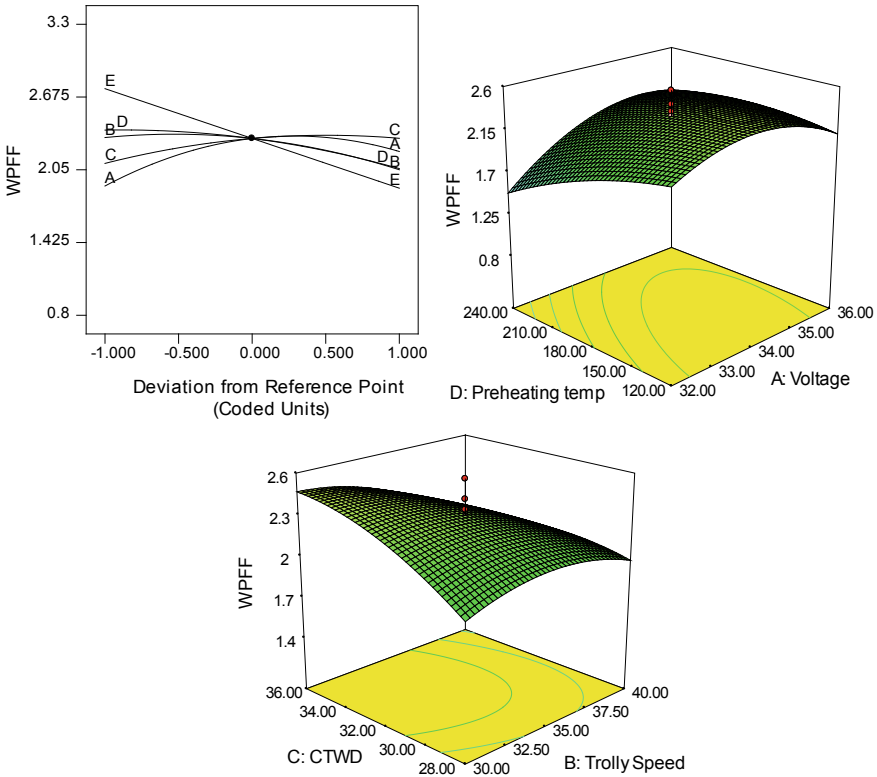
Fig. 25.2 Perturbation curve and interaction effects for WPSF

25.3.3 Relationship Between Bead Shape-Related Parameters and Critical Cooling Time

Critical cooling time ($\Delta t_{8/5}$) is the time period in seconds taken by the weldment to cool down from 800 to 500 °C. Normally, in case of steel, the transformation of its microstructure takes place in this range of temperature. More cooling time indicates the lower cooling rate of the weld with either higher heat input or higher preheating temperature or both. Time taken by the weld to cool down also affects the shape of its bead. In Fig. 25.4, the effect of critical cooling time on each bead geometry characteristic is depicted in the form of graphs. To achieve the desired weld bead shape-related parameters, it is important to understand their relationship with $\Delta t_{8/5}$.

Values of both shape-relationship parameters are decreasing with a slow rate as the $\Delta t_{8/5}$ is increasing as evident from Fig. 25.4. This occurs because bead width is independent of $\Delta t_{8/5}$ while P and R both having an increasing trend with it. This occurs as higher heat input and preheating temperature together yield to a higher cooling time.
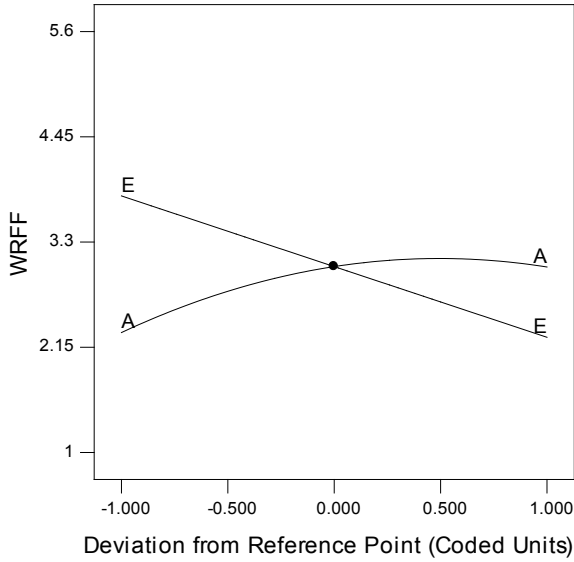
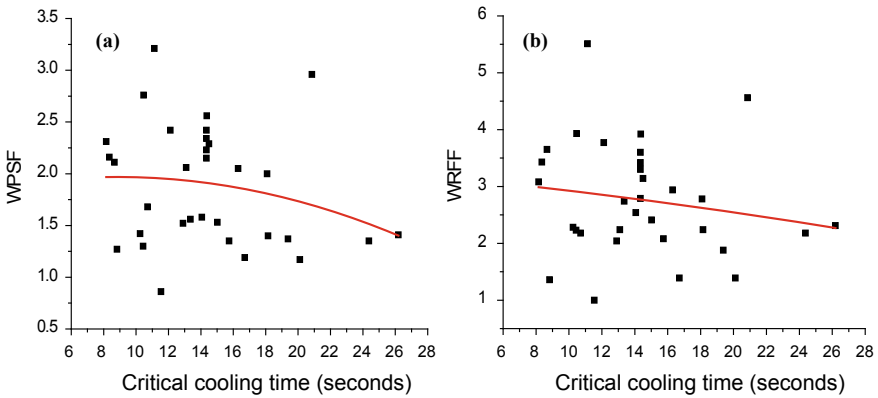**Fig. 25.3** Perturbation curve and interaction effects for WRFF

Fig. 25.4 Graph showing variation in **a** WPSF and **b** WRFF; with critical cooling time

25.3.4 Relationship Between Bead Shape-Related Parameters and Heat Input

Because of its higher metal deposition ability, SAW is also a high heat input welding process. Understanding the relation between weld bead shape-related parameters and heat input will help to limit and manage heat input of the process to have better control of the output. Figure 25.5a, b shows that values of bead shape-related parameters increase with heat input of welding. Increase in *W* and *R* is mainly because of
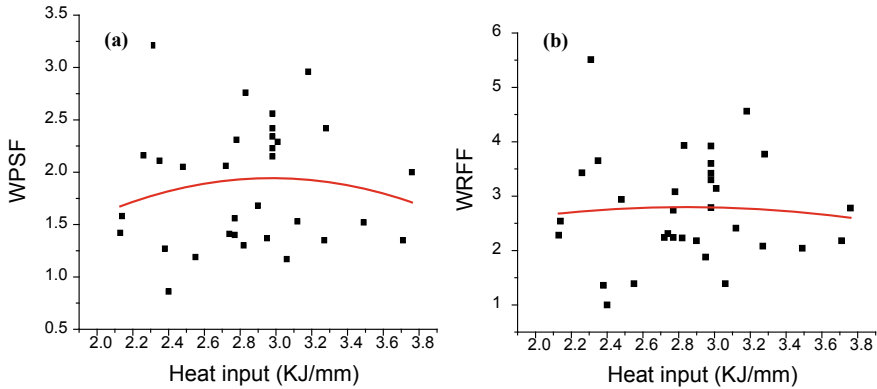
Fig. 25.5 Graph showing variation in **a** WPSF and **b** WRFF; with heat input

the lower trolley speed as well as a dependency of arc length over the voltage and electrode extension. Increased voltage yields to a higher heat input of the process and also increases the arc length as well as the probability for arc blow [9]. Also, voltage affects the dilution of the weld, not its penetration. Similarly, lower trolley speed and higher electrode extension which yields to a higher metal deposition rate as well as heat input in the process result in the increased W and R of the weld. The value of P increases with increase in heat input as with greater heat input, density of current is also high because of higher feed rate of welding electrode. Lower trolley speed with smaller electrode extension gives more concentrated heat to the weldment or plate with negligible arc wandering. This may occur due to increase in both reinforcement and penetration so their corresponding area.

25.4 Conclusions

In this experimental investigation, relationship of weld bead shape-related parameters with heat input of welding process and cooling time of weld is explored during SAW of high strength steel. From the results of the present experimental investigation, following conclusions are drawn:

1. RSM is the suitable approach for regression analysis to provide a quadratic model relating process parameters and process performance measures.
2. Relationship between critical cooling time and bead shape-related parameters provides a clear indication that with increase in critical cooling time, the value of both weld bead shape-related parameters decreases.
3. Up to a certain increase in welding heat input, there is an increase in WPSF due to increase in weld penetration.

4. Results of this study are beneficial for the pipeline industry where welding engineers and pipeline fabricators are more concerned about appropriate weld bead shape-related parameters for sufficient strength of weld and pipeline coating, respectively.

References

1. Felber, S.: Prediction of the mechanical properties and fracture mechanical value of welded joints out of pipeline-steels (X70 and X80). Weld. World. **51**, 14–22 (2007)
2. Sharma, S.K., Maheshwari, S.: A review on welding of high strength oil and gas pipeline steels. J. Nat. Gas Sci. Eng. **38** (2017). https://doi.org/10.1016/j.jngse.2016.12.039
3. Sharma, S.K., Maheshwari, S.: Arc characterization study for submerged arc welding of HSLA (API X80) steel. J. Mech. Sci. Technol. **31** (2017). https://doi.org/10.1007/s12206-017-0238-6
4. Sharma, S.K., Maheshwari, S., Singh, R.K.R.: Modeling and optimization of HAZ characteristics for submerged arc welded high strength pipeline steel. Trans. Indian Inst. Met. **72**, 439–454 (2019). https://doi.org/10.1007/s12666-018-1495-5
5. Sharma, S.K., Maheshwari, S., Rathee, S.: Multi-objective optimization of bead geometry for submerged arc welding of pipeline steel using RSM-fuzzy approach. J. Manuf. Sci. Prod. **16** (2016). https://doi.org/10.1515/jmsp-2016-0009
6. Sharma, S.K., Maheshwari, S., Singh, R.K.R.: Effect of heat-input and cooling-time on bead characteristics in SAW. Mater. Manuf. Process. **34**, 208–215 (2019). https://doi.org/10.1080/10426914.2018.1532578
7. Sharma, S.K., Maheshwari, S.: Multi-objective optimization of HAZ characteristics for submerged arc welding of micro-alloyed high strength pipeline steel using GRA-PCA approach. J. Manuf. Sci. Prod. **16**, 263–271 (2016). https://doi.org/10.1515/jmsp-2016-0027
8. Yin, L., Wang, J., Chen, X., Liu, C., Siddiquee, A.N., Wang, G., Yao, Z.: Microstructures and their distribution within HAZ of X80 pipeline steel welded using hybrid laser-MIG welding. Weld. World. **62**, 721–727 (2018). https://doi.org/10.1007/s40194-018-0582-x
9. Houldcroft, P.T.: Submerged Arc Welding, 2nd edn. Abington Publishing, Cambridge: England (1989)

Chapter 26
Investigating the Mechanical Properties and Pitting Potential of Heat-Treated AISI 4340 Steel in Various Corrosive Environments

Shailendra Singh Bhadauria, Varun Sharma, and Ajay Gupta

Abstract The corrosion and electrochemical behavior of high-strength steel AISI 4340 with or without nitrocarburizing heat-treated conditions was studied using salt spray test under 5% NaCl for 24 hours. Electrochemical experiments were also carried out under corrosive environment of a 1N H_2SO_4. Without heat-treated results obtained by electrochemical test between potential and *log* of ampere, it yields the value of corrosion potential to 269.2 mV, and in case of heat-treated sample, value obtained is to be -431.918 mV. For heat-treated samples, the rate of corrosion (I_{corr}) shows a continuous shifting of graph toward a positive direction, whereas in case of without heat-treated sample, the rate of corrosion (I_{corr}) for HT sample is higher. In salt spray test, the more corrosion product was found to be deposited on surface of heat-treated specimen. Surface morphology of the salt spray specimen is observed under SEM and optical microscope. It reveals large numbers of corrosion pits, with heavily corroded surface. It was caused due to the decrement of the chromium content in high-strength steel with an increase of nitrocarburizing heat treatment temperature. It was observed that with an increase in heat treatment time, Vickers hardness values of 4340 steel increases from 310.8 to 468.2 HV due to increase of nitrogen (N) content over the compound layer.

Keywords Ultra-high-strength steel · Corrosion rate · Electrochemical behavior

26.1 Introduction

The use of high-strength steel increases day by day in various engineering fields. High-strength steel components operating in various corrosive environments require an engineering approach grounded in the precise understanding of corrosion failure High-strength steels contribute 7–20% of commercial and military aircraft weight, and such components can be exposed to the various corrosive environments.

S. S. Bhadauria (✉) · V. Sharma · A. Gupta
Department of Industrial and Production Engineering, Dr B R Ambedkar National Institute of Technology Jalandhar, Jalandhar 144011, India
e-mail: bhadauriass@nitj.ac.in

341

In order to achieve high-strength-to-weight ratio, the manufacturers are adopting various heat treatment methods, which simultaneously increase the corrosion problems [1]. The high-strength steel AISI 4340 is a medium carbon steel, and nitrocarburizing heat treatment is the best-suited heat treatment to achieve high mechanical properties with corrosion and wear properties [2]. Liquid nitrocarburizing is a thermochemical diffusion process of nitrogen and carbon atoms into the specimen surface [1]. During liquid nitrocarburizing heat treatment, the surface of the high-strength steel gets enriched with a high amount of nitrogen atoms present at the compound layer after heat treatment which is also referred as white layer [3]. The small amount of carbon during heat treatment is also deposited over the compound layer, as reported earlier [4, 5]. After heat treatment, the steel surface consists of two different phase's compound layer present over the surface of the steel and diffusion zone underlying to compound layer. The main constituents of the compound layer are ε-Fe_{2-3}(C, N) and γ'-Fe_4(C, N), which is responsible for the improvement in wear and corrosion resistance properties. The depth and concentration of the ε-Fe_{2-3}(C, N) and γ'-Fe_4(C, N) phase present over the compound layer are dependent on the time and temperature of the heat treatment [6, 7], while the diffusion zone improves fatigue strength when compared to an untreated material. In this zone, N and C atoms are dissolved interstitially in the ferrite lattice and form nitride precipitates [11], and with the increase of heat treatment time, the concentration of N and C atoms increases which increase the fatigue strength of the heat-treated sample. However, it was found that in other heat treatment methods, which are similar to liquid nitrocarburizing such as plasma nitriding and ion nitriding decrease the chromium content with the increase of heat treatment temperature. C. X. Li and T. Bell reported earlier that the heat treatment temperature above 500 °C reduces the chromium content in the steel substrate [8]. The same effect was also reported earlier by Xi [9]. The chromium content is responsible for high corrosion resistance properties of the stainless steel, which contains more than 10% of chromium content which shows a high corrosion resistance properties compared to steel 300M and Aermet100 in salt spray test [10].

Various heat treatment processes are already in use for improvement of mechanical and corrosion resistance properties, the use of liquid nitrocarburizing heat treatment for high-strength steel at high temperature needs to be studied for further understanding of behavior of AISI 4340 in terms of mechanical and corrosion resistance properties with the increase of heat treatment time at 570 °C temperature. A liquid nitrocarburizing is a low-cost heat treatment technique, but instead of focusing toward lower-cost heat treatment techniques, it is desired to determine the effect of this heat treatment over high-strength steel AISI 4340, and that is why in this work, hardness samples heat-treated for 1, 2, 4 and 6 h were used to study the effect of compound layer on hardness value of the sample treated for different hours, and one sample for both salt spray test and electrochemical test were heated for 4 hours and then tested in NaCl and 1N H_2SO_4 for determination of corrosion properties of AISI 4340.

26.2   Experiment

26.2.1   Experimental Material and Heat Treatment

The steel used in this investigation was AISI 4340. The chemical composition is given in Table 26.1.

The material was received in the form of 30 mm diameter bars. A bar is cut into nine pieces to make two samples of size 10 mm diameter and 25.4 mm long round bar for electrochemical test, and 7 samples of size full ring with a 10 mm thickness out of which two samples were used for salt spray test and remaining 5 used for the micro-hardness test as shown in Table 26.2. All the specimens were grounded to a surface finish of 0.39 μm. For the comparative analysis of nitrocarburizing heat treatment on pitting corrosion potential and corrosion rate, one of the electrochemical test samples and salt spray specimen were heat treated for 4 hours at 570 °C, and four hardness samples were heat treated to determine the effective heat treatment hours 1, 2, 4, and 6 h on hardness value. In heat treatment processes, the specimens are dipped in a salt bath container which is continuously heated via electric furnace which maintains a temperature of 570 °C, and the specimens were removed after 1, 2, 4, and 6 h as shown in Table 26.3 and instantly quenched into water afterward kept in room for 1 hour; after heat treatment, both with and without heat-treated specimens were used for electrochemical test, salt spray test, and micro-hardness test.

26.2.2   Salt Spray Test

The corrosion rate of both with and without heat-treated ultra-high-strength steel specimens was evaluated by using the salt spray test; the test was conducted according to ASTM B-117 standard for 24 hours in the test environment of 5% NaCl having a pH value of 6.8. The test chamber maintains a temperature of 35 ± 2 °C, which was used to simulate the corrosive environment. All the materials were weighed before and after removing corrosion products. The mass increment and loss were calculated to determine the corrosion rate using Eq. 26.1.

$$\text{Corrosion Rate (mpy)} = \frac{\text{Sample Weight Loss (g)} \times 5.34 \times 105}{\text{Sample Density}\left(\frac{g}{cm^3}\right) \times \text{Sample Area}\left(in^2\right) \times \text{Time Exposure (h)}}$$

$$(26.1)$$

Table 26.1 Chemical composition of AISI 4340

Steel	C	Si	Mn	P	S	Cr	Mo	Ni	Al
AISI 4340	0.414	0.250	0.660	0.030	0.009	1.200	0.311	1.379	0.002

Table 26.2 Sample size

Experiment	Sample size	No. of sample
Electrochemical test	Dia. 10 mm, Hg. 20 mm	2
Salt spray test	Dia. 64 mm, Hg. 10 mm	2
Hardness test	Dia. 30 mm, Hg. 10 mm	5

Table 26.3 Nitrocarburizing heat treatment condition

No. of sample	Heat treatment temperature (°C)	Heat treatment hours
1	570	1
1	570	2
3	570	4
1	570	6

26.2.3 Potentiodynamic Polarization Test

The electrochemical corrosion of the high-strength steel AISI 4340 was evaluated through potentiodynamic polarization tests using Model: G750, Make Gamry Instruments; samples were taken from the billet of AISI 4340 to make specimens of 10 mm diameter × 25.4 mm long round bar. The corrosion behavior of the samples was examined in a 1N H_2SO_4 solution prepared using 0.5 mol of H_2SO_4 in 1 L of the solution, and then H_2SO_4 was added slowly in 900 ml water to make a solution of total 1 L. The tests were carried out using platinum as the counter electrode and the test specimens as the working electrode. A scan rate of 0.6 V per hour for both with or without heat-treated specimens was used.

The specimen was immersed in the solution to make its open-circuit potential (E_{ocp}) become stabilized, and then the potentiodynamic polarization was performed. Potentiodynamic polarization curves were obtained by changing the electrode potential as listed in Table 26.4 with a scan rate of 0.6 V per hour.

26.2.4 Hardness Test

A hardness test performed on total five specimens in which four of them were heat treated for 1, 2, 4 and 6 hours. To investigate the effect of compound layer deposited due to different heat treatment time, hardness test was performed at 10 kg load and 10 seconds dwell time. A diamond indenter was used as indenter, the impression of the intender was recorded by measuring the diagonals of the indent impression.

Table 26.4 Test conditions under which potentiodynamic polarization test was performed

S. No.	Parameters	With HT 4 hours	Without HT
1	Specimen area	1.76 cm^2	1.76 cm^2
2	Test solution	1N H_2SO_4	1N H_2SO_4
3	Electrode	Cathode: Platinum electrode	Cathode: Platinum electrode
4	Open-circuit potential	Min: −400 mV, Max: 334.7 mV	Min: 299.7 mV, Max: 1.585 V
5	Current	Min: 21.87 μA, Max: 228.4 mA	Min: 455.5 pA, Max: 2.070 μA
6	Scan rate	0.6 V/h	0.6 V/h

26.3 Result and Discussion

26.3.1 Salt Spray Test

In salt spray test, bolt HT and WHT sample were kept into the salt spray chamber for 24 hours. The corrosion rates of AISI 4340 in both HT and WHT conditions are given in Table 26.5. It can be seen from Fig. 26.1 that AISI 4340 with nitrocarburizing heat treatment has a large amount of red rust deposited over the surface of the specimen as the weight loss is 0.20 g and without heat-treated sample shows less amount of red rust and its weight loss is 0.15 g.

$$\text{Corrosion Rate (mpy)} = \frac{\text{Sample Weight Loss (g)} \times 5.34 \times 105}{\text{Sample Density}\left(\frac{g}{cm^3}\right) \times \text{Sample Area}\left(in^2\right) \times \text{Time Exposure (h)}}$$

where the density of high-strength alloy steel AISI 4340 is 7.85 g/cm^3.

Time exposure is 24 h.
Sample area is 5.30 in^2.

Table 26.5 Weight loss calculated from salt spray test for WHT and HT sample

Specimen condition	Weight loss (g) after 24 h time exposure	Corrosion rate (mpy)
AISI 4340 WHT	0.15	80.21
AISI 4340 HT	0.20	106.95

Fig. 26.1 Salt spray tested specimen in 5% NaCl after 24 h in spray chamber WHT specimen on left and HT specimen on the right

26.3.2 Open-Circuit Potential (OCP)

One simple way to study the film formation and passivation of implants/alloys in a solution is to monitor the open-circuit electrode potential as a function of time. A rise of potential in the positive direction indicates the formation of a passive film, and a steady potential indicates that the film remains intact and protective.

An open-circuit potential as a function of time for two materials tested in the present investigation is given in Figs. 26.2 and 26.3. It is clear that both the tested materials, i.e., AISI 4340 HT and WHT in 1N H_2SO_4 solution, are showing a continuous shifting toward more positive values with time which clearly indicates that the
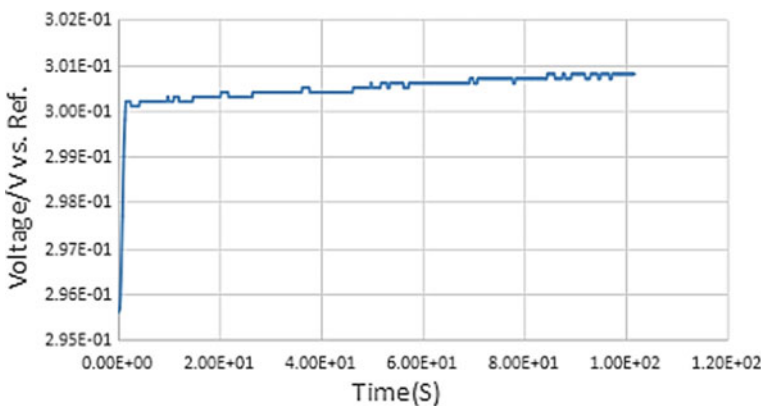
Fig. 26.2 Open-circuit potential as a function of time for WHT AISI 4340 in H_2SO_4 solution at 35 °C
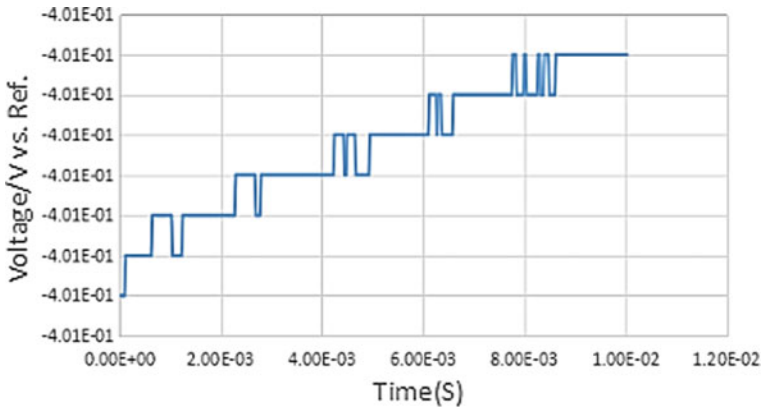
Fig. 26.3 Open-circuit potential as a function of time for HT AISI 4340 in 1N H_2SO_4 solution at 35 °C

formation of a passivation layer on their surfaces. Further, more shift in the positive direction for WHT AISI 4340 steel has observed. The continuous formation and breakage of film formation are observed in HT specimen which is a low amount of chromium content in the HT specimen.

26.3.3 Potentiodynamic Polarization Study

Figure 26.4 shows the typical polarization curves of AISI 4340 for HT and WHT steel specimen in 1N H_2SO_4 solution. It is obvious that the WHT AISI 4340 has the
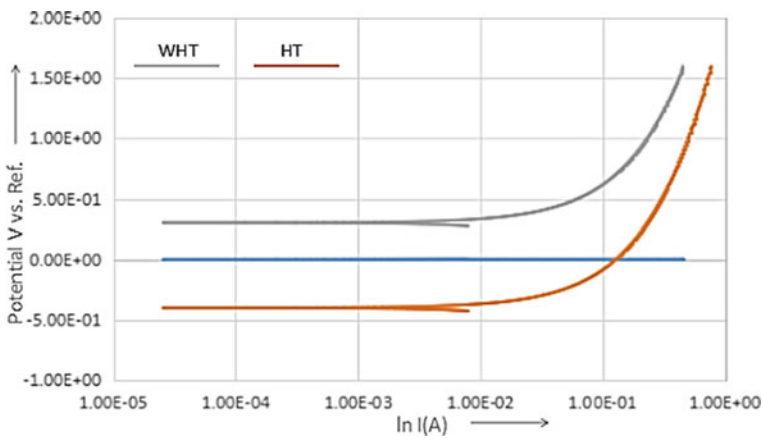
Fig. 26.4 Polarization curve for HT and WHT AISI 4340 specimen in 1N H_2SO_4 solution at 35 °C

most positive open-circuit potential value higher than HT AISI 4340. The potential is characterized by the transition from cathodic to anodic current at the corrosion potential (E_{corr}). The value of corrosion potential and corrosion rate is obtained by plotting a graph between potential (V vs. Ref) and log of ampere (Ln A) using Tafel fit curve in EC lab software, the E_{corr} value for WHT specimen obtained from the software is 269.202 mV which is higher than -431.918 mV value of HT specimen, and the value of I_{corr} is 11.48 mA, which is higher than WHT specimen value, i.e., 0.74×10^{-4} mA. The HT specimen shows the fastest corrosion as shown in Figs. 26.5 and 26.6, and the lower and higher values of corrosion potential and corrosion rate of HT sample are due to the difference in chromium content which occurs after the heat treatment processes. It can be seen that corrosion potentials for WHT specimen are nobler because of the presence of more number of chromium atoms in the steel substrate indicating that different amount of chromium atoms present in both the
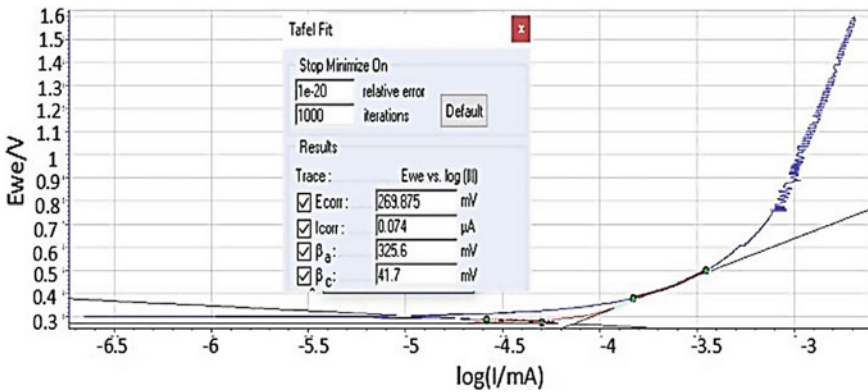

Fig. 26.5 Tafel fit curve plotted against the data obtained from electrochemical experiment for WHT sample
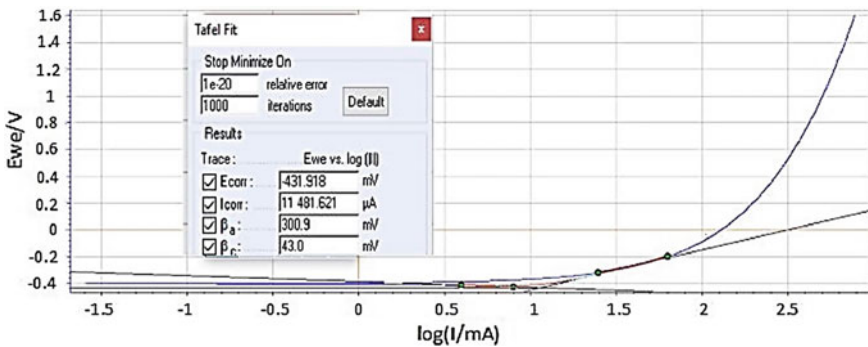

Fig. 26.6 Tafel fit curve plotted against the data obtained from electrochemical experiment for HT sample

specimens is responsible for a high amount of red rust deposition on HT sample. An SEM micrograph of nitrocarburizing heat treated for 4 h at 570 °C specimen shows a martensite microstructure with white layer deposited at the top of the specimen as reported by [10, 12–15] earlier shown in Figs. 26.7 and 26.8 (Table 26.6).

The corroded salt spray specimen was cleaned using a phosphoric acid solution to remove the corrosion product from the surface of both the specimens, the specimen was weighed before, and after removing corrosion products, the surface of both the specimens was polished using polishing cloth wheel and aged under Nital solution before performing SEM of the specimen.

The SEM image of WHT and HT specimen was shown in Figs. 26.9 and 26.10, respectively; it was clearly observed that the WHT specimen shows a less pitting effect, and the pits were uniformly distributed over the surface; on the other side HT

Fig. 26.7 SEM micrograph of nitrocarburizing heat-treated AISI 4340 specimen shows a compound white layer deposited at the surface
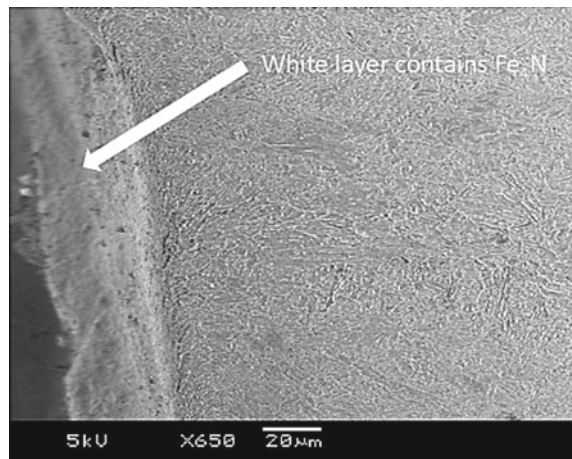
Fig. 26.8 SEM micrograph of the nitrocarburizing heat-treated sample at 570 °C for 4 h shows a martensite microstructure after heat treatment
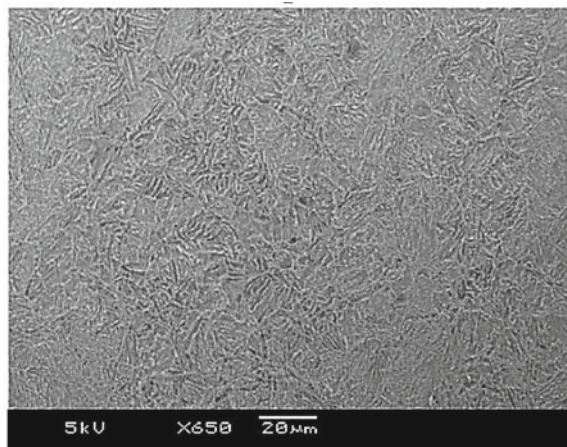
Table 26.6 Values of the parameters observed from polarization curves

Material	E_{corr}/mV versus Ref	I_{corr}/mA	bc/mV versus Ref	ba/mV versus Ref
WHT sample	269.202	0.74×10^{-4}	41.5	328.9
HT sample	−431.918	11.48	43	300.9

Note E_{corr} corrosion potential; I_{corr} corrosion current density; *ba* anodic Tafel slope; *bc* cathodic Tafel slope

Fig. 26.9 SEM image of WHT specimen at 570 °C for 4 hours shows a uniformly dispersed pitting over the surface of the specimen
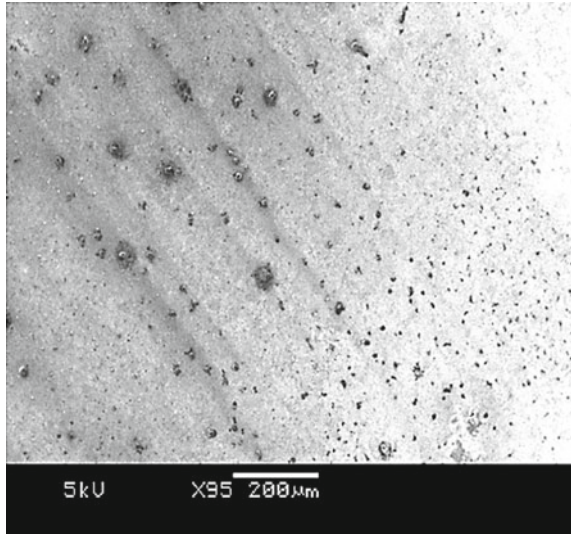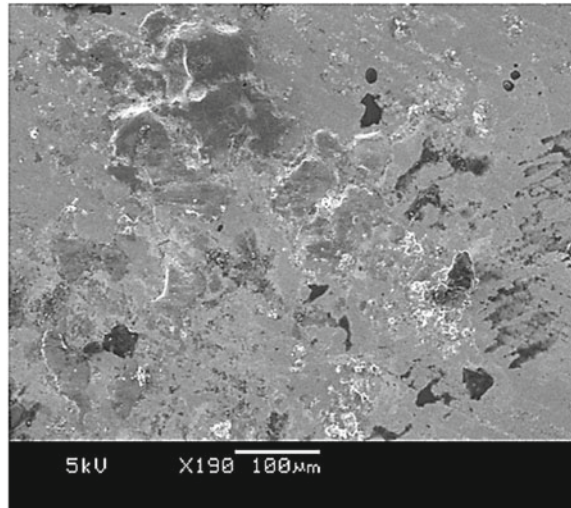

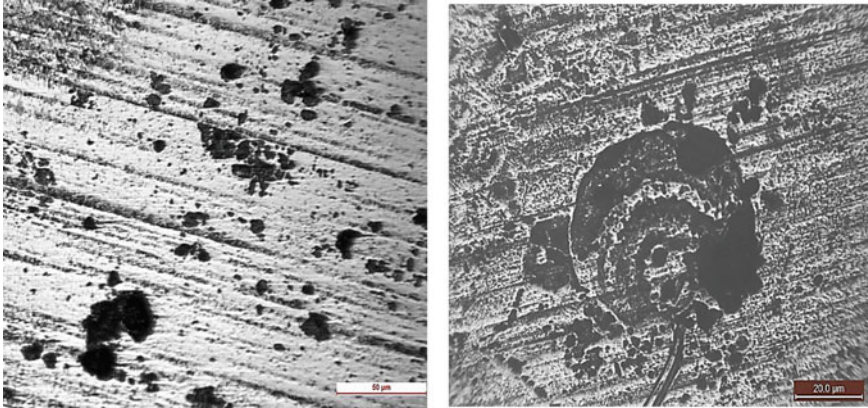**Fig. 26.10** SEM image of HT specimen shows that surface is heavily corroded after salt spray test

Fig. 26.11 Optical image of WHT (on left) and HT (on right) 4340 steel specimen

specimen, it has dense and large pits. Figure 26.9 shows that the WHT specimen is having less number of pits, which is due to the more chromium content in comparison with HT sample, which gets reduced after high-temperature heat treatment. The HT specimen contains martensite structure with very less or no chromium atoms which reduces corrosion resistance properties of the steel and with the addition of chromium content in steel substrate pitting corrosion resistance properties gets improved as reported earlier [10]. In support of SEM images, an optical was also performed on both HT and WHT specimens, which shows that an HT specimen is corroded heavily, and the size of pits was very large as shown in Fig. 26.11.

26.3.4 Hardness Test

Hardness values were measured on Vickers hardness tester model VM-50, at 10 kg load and 10 seconds dwell time; the observations are listed in Table 26.7 (Fig. 26.12).

With Vickers hardness test results, it was observed that with the increase of heat treatment time, the hardness value increases; for WHT specimen, the average value of five readings gives hardness value equal to 310.8 HV, and with an increase of time, the hardness value reaches to 468.2 HV for 6 hours heat treatment. The compound layer is very hard and brittle in nature, which is responsible for the increase of hardness value as moving from the inner core to the compound layer [16]. The diagonals of the diamond intender were automatically calculated by the hardness testing machine, and it was observed that the impression of the indenter is deeper in WHT specimen and impression getting shallow with the increase of heat treatment time. The N atoms are responsible for an increase of hardness of the specimen, which makes surface brittle and responsible for the shallow impression of the indenter. This shows that a gamma-phase compound layer is deposited on the heat-treated sample, and with

Table 26.7 Vickers hardness values for WHT and HT specimen

| Load and dwell time	Without HT	HT 1 hour	HT 2 hours	HT 4 hours	HT 6 hours
10 kg/10 s	304 HV a—0.2596 mm b—0.2474 mm	385 HV a—0.2192 mm b—0.2195 mm	440 HV a—0.2064 mm b—0.2044 mm	440 HV a—0.2050 mm b—0.2057 mm	477 HV a—0.1989 mm b—0.1955 m
10 kg/10 s	291 HV a—0.2527 mm b—0.2521 mm	413 HV a—0.2112 mm b—0.2126 mm	440 HV a—0.2071 mm b—0.2037 mm	470 HV a—0.1996 mm b—0.1976 mm	490 HV a—0.1928 mm b—0.1962 mm
10 kg/10 s	320 HV a—0.2425 mm b—0.2392 mm	402 HV a—0.2166 mm b—0.2132 mm	454 HV a—0.2051 mm b—0.1990 mm	472 HV a—0.2017 mm b—0.2044 mm	480 HV a—0.1976 mm b—0.1955 mm
10 kg/10 s	306 HV a—0.2473 mm b—0.2453 mm	424 HV a—0.2153 mm b—0.2030 mm	488 HV a—0.1962 mm b—0.1935 mm	442 HV a—0.2508 mm b—0.2037 mm	447 HV a—0.2051 mm b—0.2024 mm
10 kg/10 s	333 HV a—0.2344 mm b—0.2377 mm	419 HV a—0.2118 mm b—0.2091 mm	440 HV a—0.2057 mm b—0.2051 mm	453 HV a—0.2024 mm b—0.2023 mm	447 HV a—0.2043 mm b—0.2041 mm
Average value	310.8 HV a—0.2473 b—0.2443	408.6 HV a—0.2148 b—0.2114	452.4 HV a—0.2041 b—0.2011	455.4 HV a—0.2119 b—0.2027	468.2 HV a—0.1997 b—0.1987
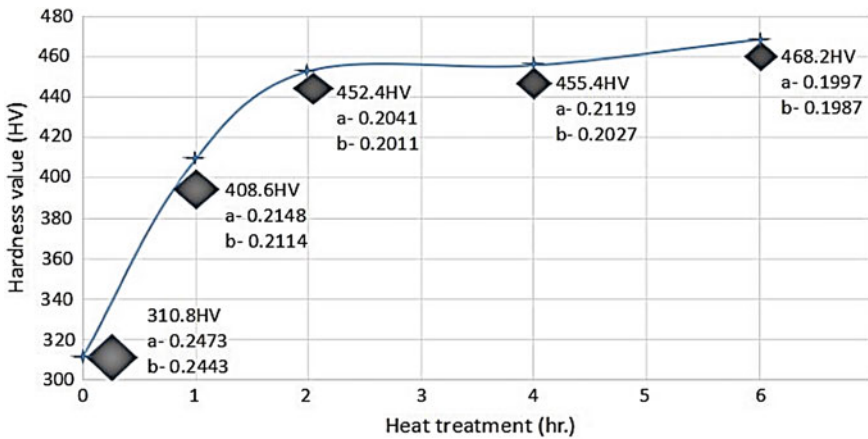
Fig. 26.12 Varitation of Vickers hardness values for different heat treatment time

the increase of heat treatment time, the concentration of N gets increased, but at the same time, chromium content gets decreased which is responsible for high corrosion rate on heat-treated sample.

26.4   Concluding Remarks

1. A liquid nitrocarburizing is a best-suited heat treatment for AISI 4340 in order to improve its wear and tear properties. It was found that with the increase of heat treatment time and temperature, nitrogen and carbon contents increase which makes the surface of the steel brittle in nature and is responsible for shallower indenter impression. This shows that hardness of the sample increases with heat treatment time.
2. Heat treatment time duration and temperature increase the Vickers hardness values, but on contrary, decrease in chromium content was observed, which reduced the corrosion resistance properties of the steel specimen.
3. A high-strength steel AISI 4340 is having a vast application in engineering fields, but it is desired to perform heat treatment, prior to its use in order to increase its application in other fields also. It was suggested for manufacture that chromium content is not getting reduced after heat treatment because it reduces the corrosion resistance properties of the steel, which may reduce the running life of the component.

References

1. Pound, B.G.: Hydrogen trapping in high-strength steels. Acta Mater. **46**(16), 5733 (1998)
2. Bhshan, B., Gupta, B.K.: Handbook of Tribology—Materials, Coatings and Surface Treatments. McGraw-Hill, New York (1991)
3. Celik, A., Karadeniz, S.: Investigation of compound layer formed during ion nitriding of AISI 4140 steel. Surf. Coat. Technol. **80**, 283–286 (1996)
4. Sun, Y., Bell, T.: Plasma surface engineering of low alloy steel. Mater. Sci. Eng. A **140**, 419–434 (1991)
5. Cho, K.S., Lee, C.O.: The effect of carbon on ion-nitriding. J. Eng. Mater. Technol. **102**, 229–233 (1980)
6. Robino, C.V., İnal, O.T.: Ion nitriding behaviour of several low alloy steels. Mater. Sci. Eng. **59**, 79–90 (1983)
7. Genel, K., Demirkol, M., Çapa, M.: Effect of ion nitriding on fatigue behaviour of AISI 4140 steel. Mater. Sci. Eng. A **279**, 207–216 (2000)
8. Li, C.X., Bell, T.: Corrosion properties of active screen plasma nitrided 316 austenitic stainless steel. Corros. Sci. **46**, 1527 (2004)
9. Xi, Y., et al.: Improvement of corrosion and wear resistances of AISI 420 martensitic stainless steel using plasma nitriding at low temperature. Surf. Coat. Technol. **202**, 2577–2583 (2008)
10. Zhong, J., Sun, M., Liu, D., Li, X., Liu, T.: Effects of chromium on the corrosion and electrochemical behaviors of ultra-high-strength steels. Int. J. Miner. Metall. Mater. **17**(3), 282 (2010)
11. Deng, X., Ju, D.: Prediction of phase composition and nitrogen concentration during the nitriding process in low-alloy steel. Mater. Res. http://doi.org/10.1590/1980-5373-MR-2015-0137
12. Sabelkin, V., Misak, H., Mall, S.: Fatigue behavior of Zn–Ni and Cd coated AISI 4340 steel with scribed damage in saltwater environment. Int. J. Fatigue 158–165 (2016)

13. Niazi, N., Nisar, S., Shah, A.: Austempering heat treatment of AISI 4340 steel and comparative analysis of various physical properties at different parameters. Int. J. Multi. Sci. Eng. **5**(10) (2014)
14. Sun, M., Zhong, P.: Stress corrosion cracking of ultra-high-strength martensite steel Cr9Ni5MoCo14 in 3.5% NaCl solution. Aerosp. Sci. Technol. 125–131 (2014)
15. Nanninga, N., Grochowsi, J., Heldt, L., Rundman, K.: Role of microstructure, composition and hardness in resisting hydrogen embrittlement of fastener grade steels. Corros. Sci. **52**, 1237–1246 (2010)
16. Figueroa, D., Robinson, M.J.: The effects of sacrificial coatings on hydrogen embrittlement and re-embrittlement of ultra-high-strength steels. Corros. Sci. **50**, 1066–1079 (2008)

Chapter 27
Analyzing the Properties of Medium Carbon Steel Alloys Prepared by Powder Metallurgy Technique

Sunil Kumar Katheria and Manvandra Kumar Singh

Abstract The main objective of this study is to investigate the physical and mechanical properties of the medium carbon steel alloys (MCSAs) prepared by the powder metallurgy technique. These alloys were designated as Fe-0.7 wt% Graphite (MCSA-1), Fe-0.7 wt% Graphite-5.0 wt% Mn (MCSA-2), Fe-0.7 wt% Graphite-5.0 wt% Cr (MCSA-3). Sintering was done at 1150 °C temperature for 2 h under the inert environment of helium gas to avoid any possibility of oxidation. The phase and microstructural examination of the MCSAs was done by using x-ray diffraction (XRD). The micro-hardness of the MCSAs studied with the help of Brinell hardness tester. MCSAs displayed higher hardness as compared to MCS; however, among the MCSAs, the hardness of the MCSA-2 and MCSA-3 revealed better results as compared to MCSA-1.

Nomenclature

PM	Powder metallurgy
XRD	X-ray diffraction
MCSA	Medium carbon steel alloys
Fe	Iron
Gr	Graphite
Cr	Chromium
Mn	Manganese
%	Percentage

S. K. Katheria (✉) · M. K. Singh
Department of Mechanical Engineering, Mewar University, Chittorgarh 321901, Rajasthan, India
e-mail: katheria.jenius@gmail.com

357

27.1   Introduction

Powder metallurgy (PM) has become an important processing method for creating metal components because of its high efficiency in moderate to high intensity output of net or near net shapes. Advantage of PM includes uniform properties, fine grain structures, and chemical homogeneity [1]. The disadvantage of PM is that the density levels obtained in sintering are always less than the theoretical values because of the difficulties involved in removing the small round pores [2]. The presence of such micropores always rendered the material weak because these pores acts as sites of originating of cracks during services [3]. Chromium (Cr) and manganese (Mn) metals are oxidation-sensitive alloying elements. These metals are effective alloying elements and low-cost metals, and they are used in conventional low-alloy steel. In PM steels, Cr and Mn are very limited. The reasons for this is that these elements have high affinity for oxygen and a strong tendency to form stable oxides. The tendency of the elements for oxidation and de-oxidation during PM processing is a challenging issue. Rather, the more processing friendly metals, copper, nickel, and molybdenum, are the most commonly used alloying elements in PM steels. Compaction and sintering is a process step in the route for manufacturing of PM steel components. During the compaction process, the powders were compacted together by cold welding and interlocking between the particles and also affect the green density and compressibility of green strength. In the sintering process, bonding between adjacent powder particles in the compacted green body occurs through the formation of sinter necks. The development of the necking between iron or steel particles starts due to diffusion rates [4] at high temperature from 800 to 1250 °C [5, 6], and mechanical strength is thereby provided to the PM component. Therefore, efficient sinter neck formation between the metal particles during sintering is essential for successful manufacturing of high-strength PM steel parts. Residual porosity is an unavoidable phenomenon in components produced by PM technique.

27.2   Experimentation

27.2.1   Material

The sample preparation for 30gm net weight amount is as follows: For graphite (Gr) 0.7 wt% = 30 × (0.7/100) = 0.21 gm. For iron (Fe) -99.3 wt% Fe = 30 × (99.3/100) = 29.79 gm and 94.2 wt% = 30 × (94.2/100) = 28.29 gm. For chromium (Cr) 5 wt% = 30 × (5/100) = 1.5 gm. For manganese (Mn) 5 wt% = 30 × (5/100) = 1.5 gm (Table 27.1).

Table 27.1 Chemical composition of MCSAs samples

Fe(gm.)	Gr(gm.)	Cr(gm.)	Mn(gm.)
29.79	0.210	–	–
28.29	0.210	–	1.5
28.29	0.210	1.5	–

27.2.2 Specimen Preparation

While preparing the medium carbon steel alloys, Fe–C, Fe–C–Mn, and Fe–C–Cr., powder metallurgy (PM) route is adopted (i). Preparation of powder (in this study, commercial iron powders are used whose particle size is less than 75 μm). (ii). Blending and mixing of powders to obtain a required proportion in the presence of 1.5 wt% of dextrin by using low energy ball mill for 2 h at 200 rpm. (iii). Compaction of the powder at a pressure of 618.935, 663.146, 707.355, and 751.565 MPa in a stainless steel closed die having a diameter of 12 mm without any hindrance as shown in Fig. 27.1. At this stage, due to cold welding between powder grains, the compacts maintained their shape. Since compacting is a major step in the PM technique, its final

Fig. 27.1 Hydraulic compaction machine (specification-maximum load = 250 KN, ram diameter = 75 mm, AMIL India, S. No. 86019, IITBHU

configuration and mechanical properties are highly depending on the uniformity of the compacts during this procedure. The satisfied densities depend to a great degree on press tool design [7]. During the compaction process, different stages have been identified (a). Fully elastic behavior, (b). Particle sliding, (c). Particle irreversible deformation. Initial stage of compaction leads to rearrangement of the powder from loose array to close packing. By applying pressure, the contact region between the grains increases and particle undergoes extensive plastic deformation [7–9]. Zinc stearate was used as die wall lubricant so as to avoid sticking of the powder to die surfaces. After the process is over, the sample is taken out for sintering process. (iv). Sintering the green compacted parts at high temperature is called sintering temperature. The ISO define the sintering as "the thermal treatment of a powder or compact at a temperature below the melting of the main constituent, for the purpose of increasing its strength by bonding together of the particles." Sintering is done (i). To achieve strength, hardness, and bonding, (ii). To produce a particular type of structure, and (iii). To produce a dense structure [10]. Sintering of compacts was carried out in high temperature muffle furnace as shown in Fig. 27.2 at temperature of 1150 °C for holding period of 2 h. The uniform heating was done at 2 h holding period of time in the furnace in nitrogen/hydrogen ($90N_2/10H_2$) atmosphere. As soon as sintering schedule was completed, the sintered pallets were cooled to room temperature inside the furnace itself after switching off the furnace. The MCSAs samples are shown

Fig. 27.2 High-temperature muffle furnace (maximum temperature of 1450 °C, 0–100 Amp, 0–150 V SISCO India, IITBHU)
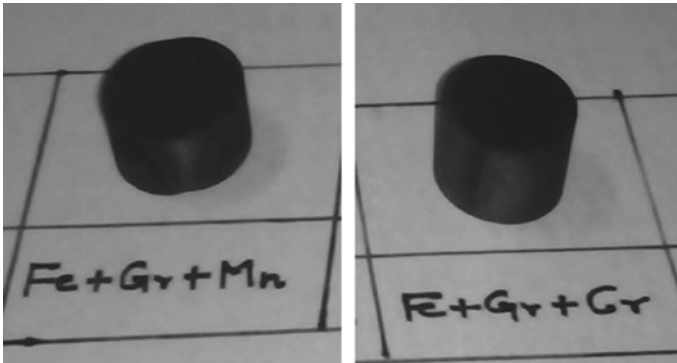
Fig. 27.3 MCSAs samples after sintering process

in Fig. 27.3 after sintering process. Protective gas atmosphere are used in sintering furnaces. The main function of the sintering atmosphere is to prevent oxidation of the compacts during sintering and participate in reduction of oxides remaining from the powder processing. However, steel containing oxidation sensitive elements (e.g., Cr and Mn) require protective atmosphere with lower oxygen content [11, 12]. The mechanism of sintering process is neck formation between adjacent particles and pore rounding and total volume shrinkage [4].

The Brinell hardness was evaluated from Rockwell hardness value. Therefore, Rockwell hardness test is used to measure hardness because they are hence simple to perform and free from human mistakes. For Rockwell, the minor load is 10 kg, and major loads are 60, 100, and 150 kg. There are two scales on a Rockwell testing machine—B scale and C scale. The B scale is used to record the hardness of soft metals, and its range is R_0 and R_{100}. For B scale, steel ball indentors are commonly used, C scale is used to test materials of hardness greater than R_B100, and a diamond–cone indentor is used for measuring hardness. Each scale is represented by a letter of the alphabet. The scale is designated by symbol HR followed by the appropriate scale identification [13]. In this study, B scale having 1.588 mm (1/16 in) steel ball indenter is used at the major load of 100 kg.

Since, both tensile strength and hardness are the indicators of metal's resistance to plastic deformation, they are roughly proportional. For most steels, the HB and tensile strength are related according to the following equation: Tensile strength (TS) = 3.45 x HB MPa. So, tensile strength can be calculated by the following relation [13].

$$\text{Tensile strength(TS)} = 3.45 \times \text{HB MPa}$$

(a) Tensile strength(TS) $= 3.45 \times$ HB MPa
$$= 3.45 \times 147$$

Table 27.2 Dimensions of MCSAs samples after sintering process

Steel alloys	Force applied (KN)	Applied pressure (MPa)	Dimensions before sintering			Dimensions after sintering		
			Wt. (gm)	Dia. (mm)	Height (mm)	Wt. (gm)	Dia. (mm)	Height (mm)
Fe–Gr	80	707.355	5.017	13.22	7.4	4.7952	13.15	6.95
Fe–Gr–Mn	80	707.355	4.181	13.13	6.09	4.0343	13.09	5.9
Fe–Gr–Cr	80	707.355	5.501	13.14	8.39	5.1825	13.11	7.69

$$\text{TS} = 507.15 \, \text{MPa for Fe–Gr MCSAs}$$

(b) Tensile strength (TS) $= 3.45 \times 209$
    $= 721.05 \, \text{MPa for Fe–Gr–Cr MCSAs}$

(c) Tensile strength(TS) $= 3.45 \times 129$
    $= 445.05 \text{MPa for Fe–Gr–Mn MCSAs}$

27.3 Results and Discussion

27.3.1 Dimensional Changes

See Table 27.2.

27.3.2 Sintered Density

The term sintered density means the density of the specimen after sintering. The density of the MCSAs specimen is increased due to decrease in dimensions after sintering. The graph is shown in Fig. 27.5. The sintered densities of the three specimens were increased due to decrease in volume and establish that the density of Fe–Gr–Mn pallet is high out Fe–Gr and Fe–Gr–Cr pallets. Sintered density can be calculated by the following relation.

Sintered density $= \left(\frac{\text{massof the specimen}}{\text{volume of the specimen}} \right)$ gm/cm^3 at at applied pressure $=$ 707.355 Mpa or at applied load $= 80$ KN

(i) **Fe–Gr**

$$\text{Green density} = \left(\frac{\text{mass of the specimen}}{\text{volume of the specimen}}\right) \text{gm/cm}^3$$

where

Volume of the specimen $\pi r^2 h$

r radius of the specimen $= \frac{13.15}{2} = 6.575$ mm $= 0.6575$ cm

h height of the specimen $= 6.95$ mm $= 0.695$ cm

ρ_{sintered} $\left(\frac{4.7952}{3.14 \times 0.6575 \times 0.6575 \times 0.695}\right) = 5.082$ gm/cm^3

(ii) **Fe–Gr–Cr**

$$\text{Sintered density} = \left(\frac{\text{mass of the specimen}}{\text{volume of the specimen}}\right) \text{gm/cm}^3$$

Volume of the specimen $\pi r^2 h$

r Radius of the specimen $= 13.11/2 = 6.555$ mm $= 0.6555$ cm

h Height of the specimen $= 7.69$ mm $= 0.769$ cm

ρ_{sintered} $\left(\frac{5.1825}{3.14 \times 06555 \times 0.6555 \times 0.769}\right) = 4.906$ gm/cm^3

(iii) **Fe–Gr–Mn**

$$\text{Sintereddensity} = \left(\frac{\text{mass of the specimen}}{\text{volume of the specimen}}\right) \text{gm/cm}^3$$

Volume of the specimen $\pi r^2 h$

r radius of the specimen $= 13.09/2 = 6.545$ mm $= 0.6545$ cm

h Height of the specimen $= 5.9$ mm $= 0.59$ cm

ρ_{sintered} $\left(\frac{4.181}{3.14 \times (.6545) \times 0.6545 \times 0.59}\right) = 5.269$ gm/cm^3

27.3.3 Fractional Porosity (γ) After Sintering

The porosity refers to the open volume in powder metallurgy components after sintering. It is very difficult to produce powder metallurgy component without porosity even after sintering. The presence of porosity which acts as a stress raiser [14] has much greater influence on the elongation, impact, and fatigue strength [7, 15]. The porosity of a powder metallurgy component greatly depends on the sintering temperature. The effect of porosity on MCSAs specimen at a particular temperature

Fig. 27.4 Fractional porosity of MCSAs
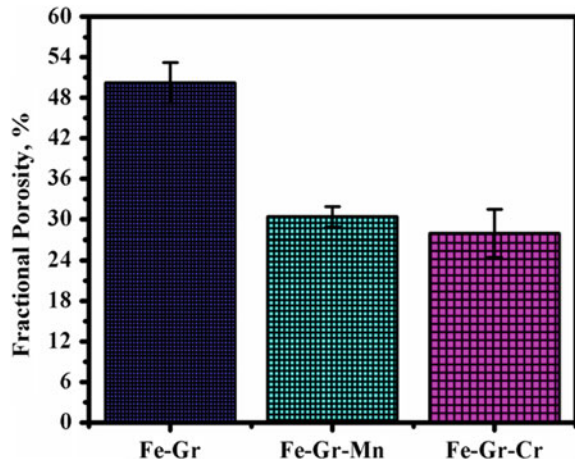
(1150 °C) is studied, and fractional porosity or total porosity of the PM component is derived from the sinter density. The total porosity (γ) present in the sintered component may be evaluated from the following relation [16].

$$\gamma = 1 - \left(\frac{\text{Sintered density of the pallets}}{\text{density of solid materials}} \right)$$

The pores can be considered as a defects, and decreased pore size is thus beneficial for mechanical performance of PM steel. The pore size also decreases with increasing PM parts density. Figure 27.4 clearly shows that the MCSAs specimen are 49.78% (50.22% porosity), 69.6% (30.4% porosity), and 72.04% dense (27.96% porosity) in the current study. Due to decrease in porosity (50.1, 29.6, and 27.3%), the sintered density of Fe–Gr and Fe–Gr–Mn increases and improves the mechanical properties, but sintered density of Fe–Gr–Cr decreases due to formation of oxides, no grain size reduction, and increase in density shows that an overall shrinkage occurs (Fig. 27.5).

27.3.4 Hardness and Tensile Strength

Hardness is a measure of a material's resistance to localized plastic deformation. The depth or size of the resulting indentation is measured, which in turn is connected to a hardness number. The material whose hardness index number is lower is softer, and hence larger and deeper is the indentation [13]. The Brinell hardness tester was used to evaluate the hardness of the MCSAs where a ball indenter of 10 mm diameter of hardened steel was used and 500 kg load was normally applied for 15 s on each and every specimen. A low powered microscopy was used to measure the indentation diameter left on the test materials (Figs. 27.6 and 27.7).

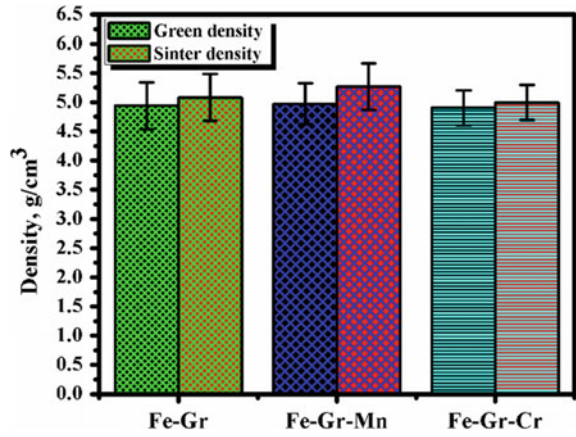**Fig. 27.5** Density of
MCSAs before and after
sintering process

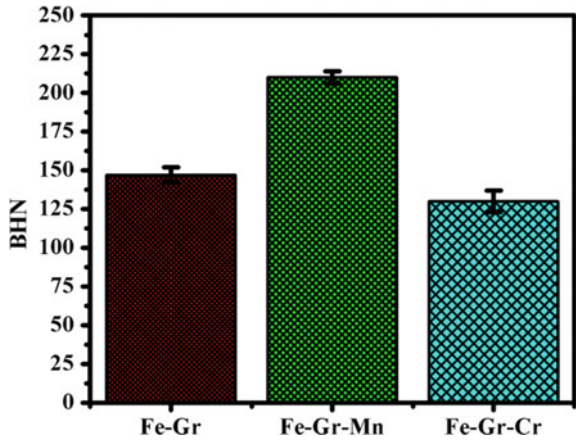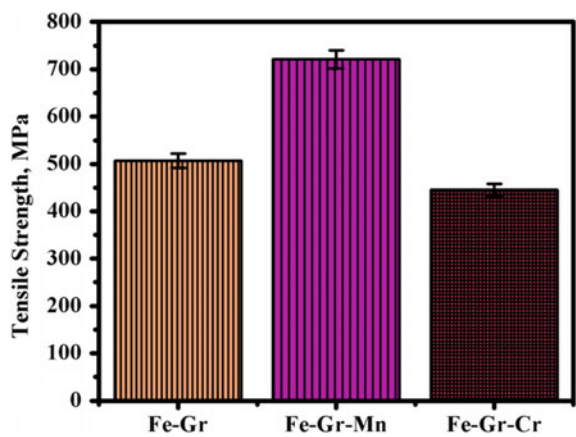**Fig. 27.6** Hardness Of
medium carbon steel alloys

Fig. 27.7 Variation of
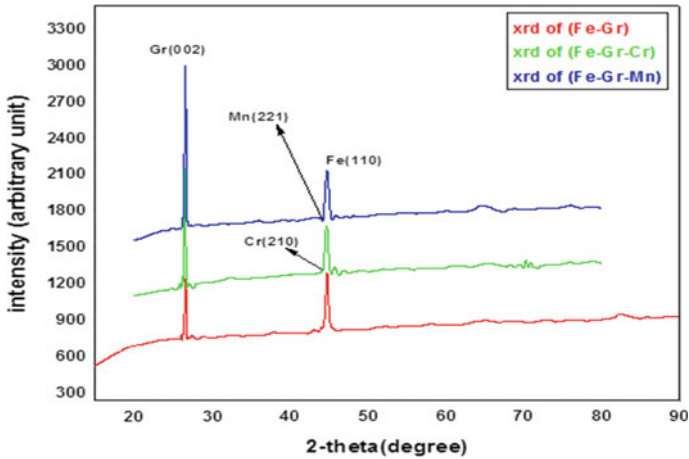tensile strength of medium
carbon steel alloys

Fig. 27.8 Combined XRD of MCSAs samples

27.3.5 Combined XRD of MCSAs

See Fig. 27.8.

27.4 Conclusions

From the current study, it is observed that the shape and size of powder particle of alloys are quit homogeneous and regular due to this the mechanical properties like strength and hardness of the sintered alloy product are enhanced. However, the sintered density of the alloys is observed lower with reference to iron. The sintered density of Fe–Gr, Fe–Gr–Mn and Fe–Gr–Cr alloy specimen is 5.082 gm/cm^3, 5.269 gm/cm^3, and 4.995 gm/cm^3 with the 50.1%, 30.4% and 27.96% porosity, respectively. The lowering in the sintered density of the alloys is attributed to the presence of this significant porosity. But by taking the advantages of this porosity, these materials may be used as self-lubricating materials for the applications of bearings, brakes, materials, etc. The Brinell hardness of Fe–Gr, Fe–Gr–Mn, and Fe–Gr–Cr alloy specimen is 147–148, 209–211, and 129–132 BHN, respectively. However, the tensile strength of Fe–Gr, Fe–Gr–Mn, and Fe–Gr–Cr alloy specimen is 507.15, 721.05 and 445.05 Mpa, respectively. After analyzing the physical and mechanical properties of MCSAs, Fe–Gr–Mn revealed high sintered density, high hardness, and tensile strength as compared to Fe–Gr and Fe–Gr–Cr.

References

1. Flumerfelt, J.F.: Aluminium powder metallurgy processing, Retrospective thesis, and Dessertation paper 11918. http://lib.dr.iastate.edu/rtd/11918
2. Arivudainambi, J., Ranganath, G., Mariappan, R.: Densification and mechanical properties of sintered PM AISI 4340 steel
3. Chandramouli, R., Kandavel, T.K. et al.: Deformation, densification, and corrosion studies of sintered powder metallurgy plain carbon steel performs. Mater Des. **28**, 2260–2264 (2007)
4. German, R.M.: Sintering Theory and Practice. Wiley (1996)
5. Hryha, E., Nyborg, L., et al.: Appl. Surf. Sci. **256**(12), 3946–3961 (2010)
6. Hryha, E., Nyborg, L.: Proceeding of PM2010 World Congress, vol. 2, pp. 268–275. Florence, Italy, October 2010, EPMA (2010)
7. Moon, I.M., Choi, J.S.: Dependence of green strength on contact area between powder particles for spherical copper powder compacts. Powder Metall. **28**(1), 21–28 (1985)
8. Poquillon, D., Lemaitre, J. et al.: Cold compaction of iron powders—relations between powder morphology and mechanical properties Part 1: Powder preparation and compaction. Powder Technol. **126**(2002), 65–74. Accepted 30 Jan 2002
9. Lund, J.A.: Origin of green strength in iron P/M compacts. Int. J. Powder Metall. Powder Technol. **18**(2), 117–127 (1982)
10. Backensto, A.B.: Effect of lubricants on the properties of copper- tin powders and compacts. Adv. Powder Metall. Part. Mater. **2**, 303–314 (1990) (Pittsburg, Pennsyvania)
11. Bergman, O., et al.: Influence of sintering parameters on the mechanical performance of PM steel pr- alloyed with chromium. PM2006, Busan, Korea, 26 Sept 2006
12. Bergman, O.: Studies of oxides reduction and nitrogen uptake in sintering of chromium alloyed steel powder. Licentiate thesis, Stockholm, Sweden (2008)
13. Callister WD.: Materials science and Engineering adapted by R. Balasubramaniam, John Wiley publication (2011) ISBN: 978-81-265-2143-2
14. Dutta, G., et.al.: Effect of sintering temperature on density, porosity and hardness of a powder metallurgy component. IJETAE **2**(8) (2012)
15. Sinha, A.K.: Powder Metallurgy, 2003 DhanpatRai Publications Pvt. Ltd, 67/4, Madras house, Daryaganj, New Delhi 110002
16. Angelo, P.C.: Powder Metallurgy Science Technology and Applications. Prentice- Hall of India pvt. Ltd. New Delhi 110001 (2008)

Chapter 28
Mechanical and Wear Properties of Aluminium Alloy Composites: A Review

Ravi Butola, Lakshay Tyagi, Luckshaya Kem, M. S. Ranganath, and Qasim Murtaza

Abstract Composite material comprises a mixture of two or more material having distinct properties in order to manufacture material that has different properties than that of its constituent material. Aluminium is one of the most abundant materials in the earth's crust and its alloys have a vast application like they are used to manufacture automobile and aircrafts parts, used in defence sectors, etc. Hardness, tensile strength and wear properties of aluminium composites are reviewed. This is done for enhancing the performance of the material in the desired way. Composites can be formed via various ways, i.e. stir casting, friction stir processing, etc. From the study, we found that hardness, tensile strength and wear performance of composites were better than that of their base alloys.

Keywords Aluminium · Hardness · Tensile properties · Wear

28.1 Introduction

Composite material is defined as the material which is formed by the combining two or more distinct materials and material formed shows different properties from its constituent materials. Composite material comprises of the matrix phase and reinforcement phase. There are three types of composite materials: (a) metal matrix composites. (b) Ceramic matrix composites. (c) Polymer matrix composites. And there are three types of reinforcement composites: (a) dispersion strengthened, (b) fibre reinforced, (c) particle reinforced. For producing Al composites, we can use various processes like casting, extrusion, spraying, forging and we can also use powder metallurgy technique [1, 2]. Aluminium is one of the most abundant metals in the world and found many applications in the aerospace, automobiles and marine due to its lightweight and high strength. It is used in defence sector and also in the nuclear industry as neutron absorber [3]. Due to low thermal expansion and conductivity, Al composites are used as connecting rods, automotive drives and

R. Butola (✉) · L. Tyagi · L. Kem · M. S. Ranganath · Q. Murtaza
Department of Mechanical Engineering, Delhi Technological University, New Delhi 110042, India
e-mail: ravibutola33855@gmail.com

cylinder liners [4, 5]. Properties concerned with the automobile industry are the ones found in Al-based MMC [6]. Aluminium matrix composites can be reinforced with SiC, B_4C, Al_2O_3, TiC, MgO, TiO_2, etc. There is an enhancement in the properties of hybrid composites so formed on addition of these reinforcing materials to aluminium composites [7]. Some recent studies also concluded that the tribological properties of aluminium can be enhanced by mixing it with ceramic reinforcements. Some processes like friction stir process can be used on aluminium [8]. Aluminium 7075 alloy is an alloy of aluminium and zinc, and it is a primary alloying element. Al-7075 has great properties like good strength-to-weight ratio, stiffness, hardness, ductility and wear resistance [9, 10]. It has better corrosion resistance when compared to 2000 other alloys. Its cost is high that is why it is used less. Al7075 consists of 5.6–6.1% Zn, 2.1–6.1% Mg, 1.2–2.5% Cu and less than 0.5% of Si, Fe, Mn, Ti, Cr and other metals. Secondary nanoparticle reinforcement is also used to increase the properties of surface composite [11].

28.2 Literature Review

28.2.1 Hardness

Physical property of the material is resistance to plastic deformation. Baradeswaran and Elaya Perumal [9] produced Al7075 particle reinforced composite with reinforcement B_4C through stir casting method and showed that on increasing reinforcement hardness increases (Fig. 28.1). Observations were made on hardness test of base alloy with B_4C as reinforcement and the hardness value of 5, 10, 15 and 20 vol% B_4C composite were higher than its base alloy. Alizadeh and Taheri-Nassaj [12] incorporated 2 and 4 wt% B_4C nanoparticles into the matrix of Al and concluded that hardness of nanostructural Al was more than that of coarse-grained Al, and the hardness was directly proportional to the content of B_4C present and it was higher than that of nanostructured Al (Fig. 28.2). Alihosseini et al. [13] prepared Al-$x$$B_4C$ composite with values of $x = 0, 1, 2, 3, 4$ and 5 in wt% and B_4C having an average

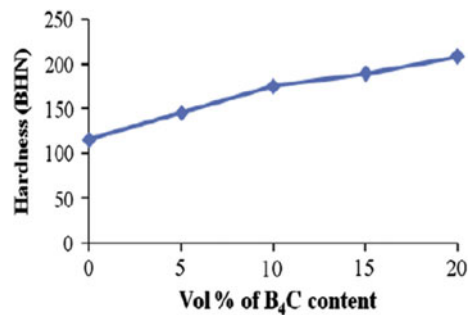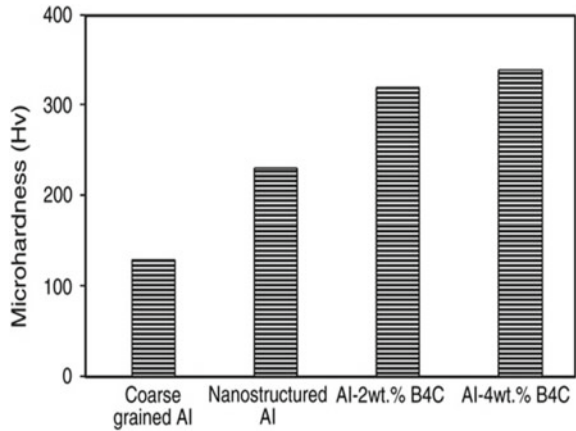**Fig. 28.1** Hardness value for various vol% of B_4C reinforcement [9]

Fig. 28.2 Microhardness of
various samples [12]

size of 50 nm using a high energy ball mill. Results were studied at different sintering
temperatures and with different B_4C compositions (Fig. 28.3). They found that the
hardness increases with an increase in both sintering temperature and the quantity
of B_4C nanoparticles. The author obtained the maximum value of hardness which is
165 HV for Al 5 wt% B_4C which was sintered at a temperature of 600 °C. Hardness
increment was assigned to grain refinement and uniform dispersion of reinforcement
within the matrix. Ravi et al. [14] fabricated aluminium matrix composites (AA6061)
reinforced with B_4C (average particle size 25 µm). They used stir casting method to
reinforce and produce specimens with a different weight percentage of B_4C. They
showed with the increase wt% of reinforcement the hardness value increased and
resisted plastic deformation (Fig. 28.4). This increased hardness can be the result
of the homogenous dispersion of B_4C particles which they revealed from optical
micrographs. Butola et al. [15] found that the hardness of metal matrix composites is

Fig. 28.3 Hardness versus
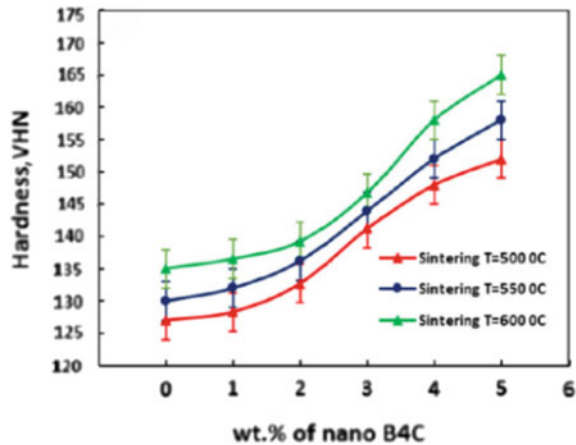wt% of nano-B_4C at different
sintering temperatures [13]

Fig. 28.4 Hardness value versus wt% B$_4$C reinforcement [14]
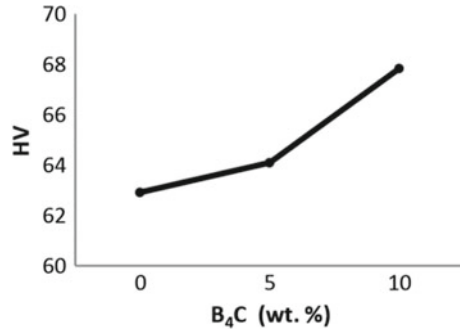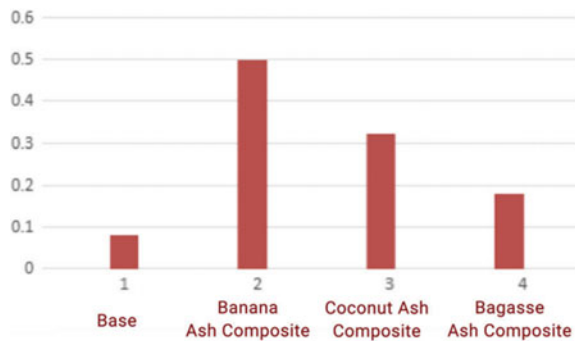

Fig. 28.5 Hardness of various composites [15]

much higher compared to aluminium sample which is not reinforced and they found Vickers hardness of base material, banana ash composite, coconut ash composite and bagasse ash composite and found maximum hardness in banana ash composite (Fig. 28.5). Subramaniam et al. [16] alloyed Al7075 with B$_4$C-CSFA hybrid composite and then hardness values were measured at three locations and from that, it was observed that the hardness of the composite material was improved on the adding of B$_4$C and CSFA and the values observed by the authors of hardness are increased from 127.5 to 169.5 BHN and the maximum value of hardness which was achieved by authors was 169.5 BHN due to both reinforcements of 15 wt% B$_4$C and CSFA and these same results were observed in the case of fly ash particle reinforced composites, which improves hardness (Fig. 28.6). Chandra et al. [17] investigated graph between hardness and albite particulate concentration (Fig. 28.7) and then analysed the result; they observed that on increasing the albite particulate in Al7075 matrix alloy, there was a significant increment in hardness which was up to 8 wt%, and after that, there was a decrease in hardness on increasing an albite particulate and this happened due to poor wettability between reinforcement and matrix; a similar type of results are founded by various researchers in the addition of hard ceramic particles. Yuvaraj et al. [18] observed the hardness variation along friction stir process zone. Hardness is observed for base metal, FSPed without particle, aluminium reinforced with TIC, base metal reinforced with B$_4$C and base material with a blend of B$_4$C and
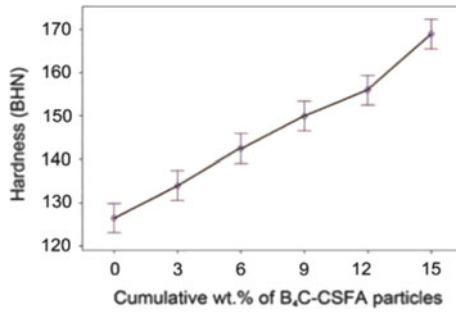
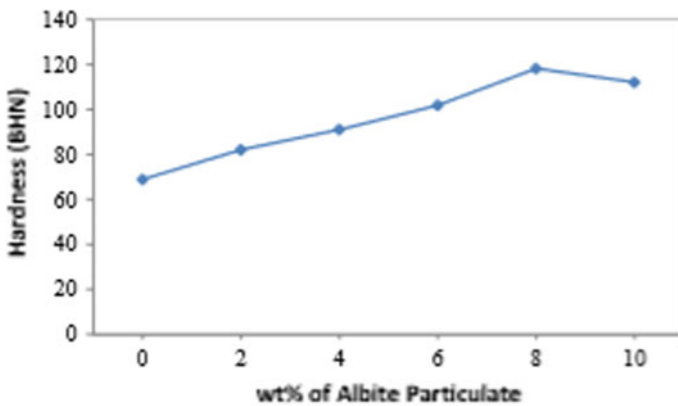**Fig. 28.6** BHN at different wt% of reinforcement [16]

Fig. 28.7 Hardness versus albite particulate [17]

TIC, and the graph found is shown in Fig. 28.8 and it can be observed clearly from the graph that hardness increases and the variation in hardness in-depth direction is approximately uniform and they confirmed that friction stir process provides consistency in the distribution of reinforcement. Kumar et al. [19] investigated the hardness values at different points from weld centre and from those values they concluded that the hardness was influenced due to the post-heat treatment. They found a graph of welded joints in different heat-treated conditions, and in Fig. 28.9, they took 150 HV as the hardness of the base metal. They calculated hardness values at 2 mm below the weld surface. They found that the hardness values were less than the hardness values of base metals and they observed high hardness in T6 condition than post-weld treatment. Imran et al. [20] observed the hardness by Brinell hardness number of composites. Firstly, by changing the composition of graphite and making bagasse ash percentage constant, and secondly, they did by changing the composition of bagasse ash and making graphite percentage constant. Firstly, they increase graphite percentage and kept bagasse ash constant at 2% by this they observed the gradual increment in Brinell hardness number; then, they did same by keeping bagasse ash
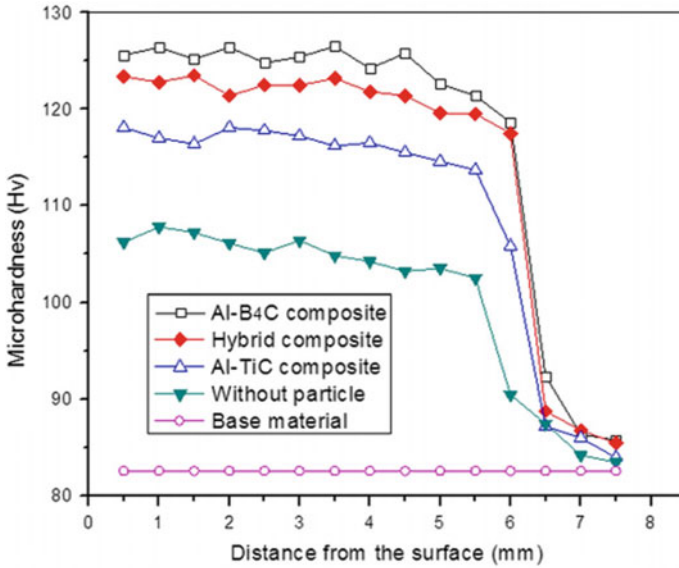
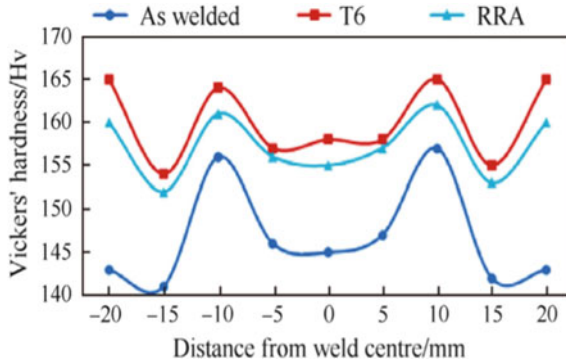**Fig. 28.8** Microhardness versus distance from the surface [18]

Fig. 28.9 Vickers hardness versus distance from weld centre in tempered conditions [19]

constant at 4% and they got more increase in Brinell hardness number, and then they did same again by keeping bagasse ash constant at 6% and more better results were there and now they did opposite where they now kept graphite percentage is constant to 1%, 3% and at last 5% and increases bagasse ash percentage and they observed the same gradual increase in BHN. Singh et al. [21] investigated that there was 15% increase in Brinell hardness which was maximum and got the process of quenching in brine solution and there is a decrease of 8% in Brinell hardness by quenching in OIL + CNT solution, and by the process of annealing, there is an extreme decrease in Brinell hardness and it is shown by Fig. 28.10. Muniamuthu et al. [22] investigated
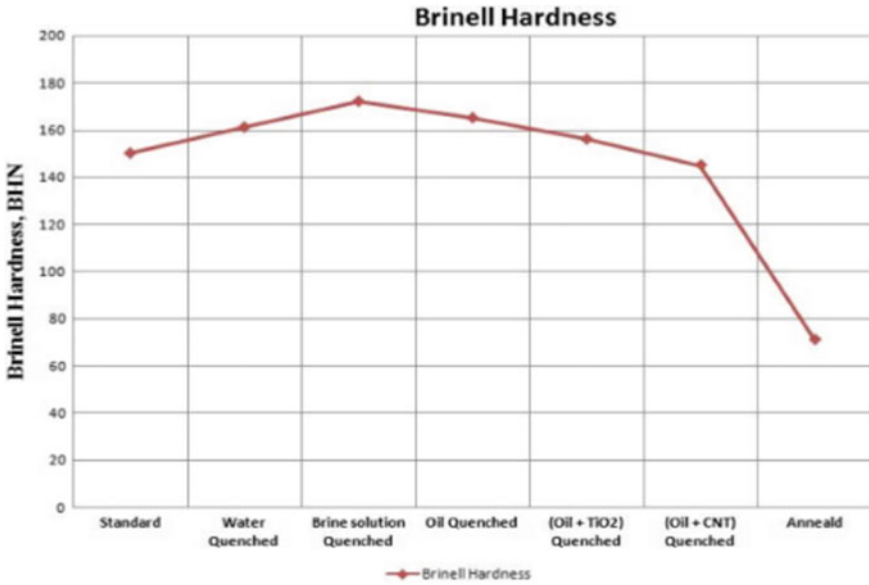
Fig. 28.10 Brinell hardness versus various heat treatments [21]

the Brinell hardness of metal matrix composite of Al7075 with reinforcement of Al_2O_3. Author took four samples of Al7075 with different percentage of reinforcement of Al_2O_3. Therefore, sample 1 consists of 2% Al_2O_3, sample 2 consists of 4% Al_2O_3, sample 3 consists of 6% Al_2O_3 and at last sample 4 consists of 8% Al_2O_3. They found a result of Brinell hardness in the form of a graph which is depicted in Fig. 28.11. Veeravalli et al. [23] investigated the sliding friction and wear behaviour
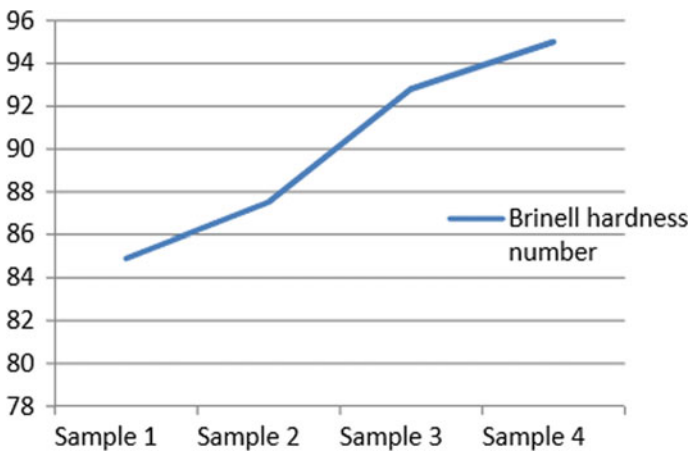

Fig. 28.11 Brinell hardness of MMC of Al7075 with wt% Al_2O_3 [22]

under dry sliding wear conditions of AA7075-TiC. TiC particles having an average size of 2 μm were used as reinforcement both as cast and heat-treated conditions and AA7075 as matrix. The composite were fabricated through stir casting method. Observed that the fabricated composite hardness was higher than that of matrix phase and increases till 8 wt% TiC. Hardness value varied from 98.4 to 118.6 VHN and 181 to 202.1 VHN for cast and heat-treated condition, respectively. It was observed that at 8 wt%, TiC particles were uniformly dispersed in the matrix and at 10 wt%, there was agglomeration and agglomeration leads to the formation of pores due to which there was no remarkable increase in hardness of 10 wt% of TiC. Yuvaraj et al. [24] observed the hardness of composite cross section 1 mm below from upper portion and also found the hardness of composite of FSP and TIG arc along depth direction and results found was the hardness of TIG arc specimen increases due to formation of intermetallic phases.

28.2.2 Tensile Property

Ravi et al. [14] observed that with the increasing percentage of B_4C, tensile strength also increased (Fig. 28.12) as there was better interfacial bonding between matrix and reinforcement and there was a distribution of load from matrix to reinforcement. As B_4C is strong reinforcement, it bears the entire load that acts upon matrix. Alizadeh et al. [12] found that the fine-grained (nanostructured) Al has higher yield strength and lower ductility than coarse-grained Al, and it was by confirmed Hall–Petch relationship (Fig. 28.13). They also found that on increasing the amount of B_4C, ultimate tensile strength (UTS) increases and composite became more brittle and it was observed that UTS of composite was more than that of nanostructured Al, and this shows the reinforcement effect of B_4C nanocomposites. Baradeswaran et al. [9] investigated that on increasing the amount of B_4C particles, the tensile strength also increased (Fig. 28.14) and was comparatively higher than the tensile strength

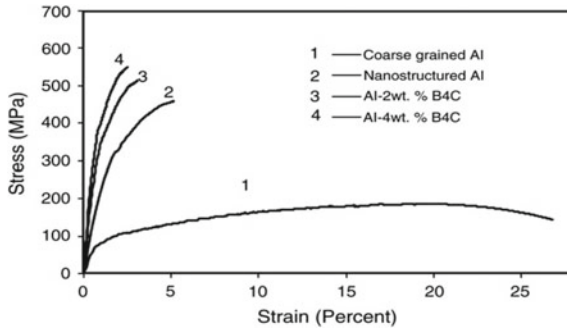**Fig. 28.12** UTS versus wt% B_4C [14]
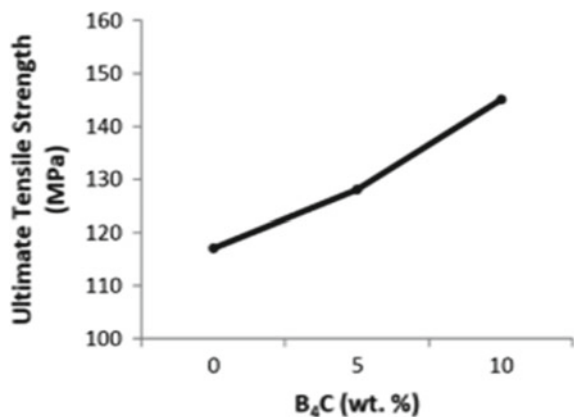
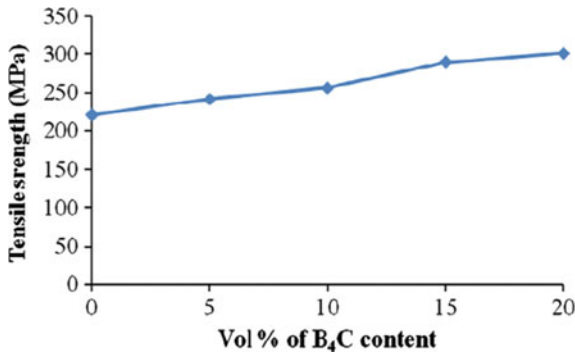**Fig. 28.13** Stress versus strain diagram of various samples [12]

Fig. 28.14 Tensile strength of different vol% of B_4C reinforcement [9]

of Al7075. This showed that reinforcement particle offered high resistance to tensile stresses and the load is transferred from the matrix to the hard reinforcement particles; this improves the tensile strength. Butola et al. [15] showed that the yield strength decreases in case of banana ash composite and it is maximum in case of bagasse ash composite and the same can be seen from Fig. 28.15a. In the case of tensile strength, it is maximum for banana ash composite as shown in Fig. 28.15b. Subramaniam et al. [16] have investigated that tensile strength was improved by increasing B_4C-CSFA wt% and the maximum tensile strength achieved was 189 MPa by taking the composition as 9 wt% B_4C and 3 wt% CSFA and this tensile strength was 66% higher than the reinforced Al7075 alloy. The graph is shown (Fig. 28.16) between tensile strength and cumulative weight percentage of B_4C-CSFA particles, and it can be observed that again adding of reinforcement reduces tensile strength. It was also observed that there was a constant decrease in ductility within a range of 9.6–13.8%. This happens because of the addition of reinforcements. In tensile specimen, fracture surfaces were found by using a field scanning electron microscope. Authors also did an SEM analysis and they observed component failure due to a combination of both ductile and brittle fracture. Chandra et al. [17] observed a graph between ultimate
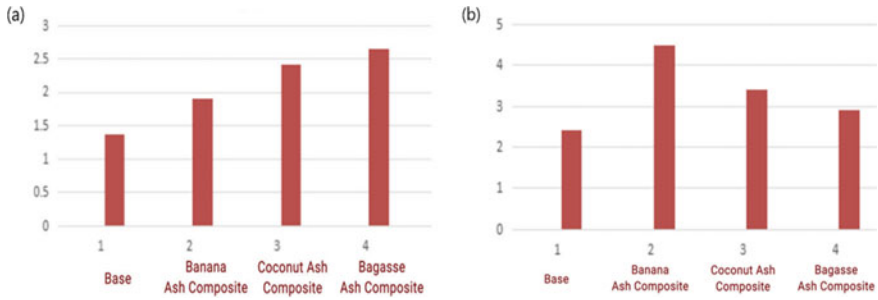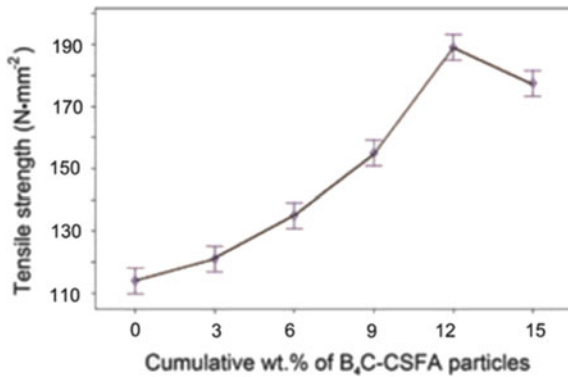
Fig. 28.15 a Yield strength of various composites. **b** Tensile strength of various composites [15]

Fig. 28.16 Tensile strength
at different wt% of
reinforcement [16]

tensile strength and the weight percentage of albite particulate (Fig. 28.17); there is an
increment in ultimate tensile strength on adding albite particulate at different weight
percentages and then ceramic particulate was added to a ductile matrix and due to
this, composite become brittle. This means that the strength is increased till 8 wt%
but after that strength decreases due to poor loading. Yuvaraj et al. [18] observed the
stress–strain curve of composites with nanoparticles which shows the hardness and

Fig. 28.17 UTS for different
wt% of albite particulate [17]
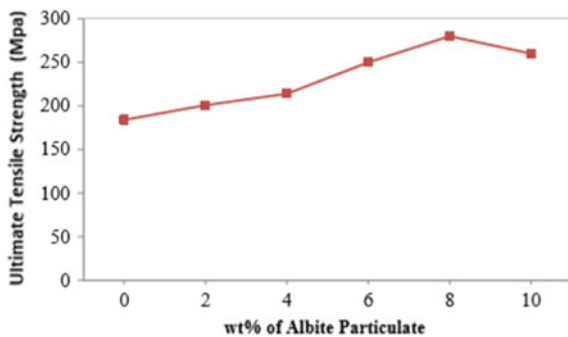
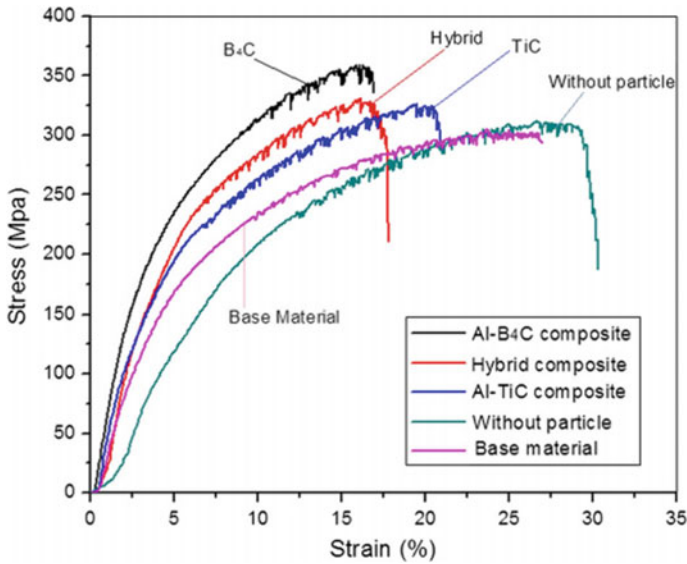**Fig. 28.18** Stress–strain curve of various composites [18]

tensile strength of FSPed composite observation are shown in Fig. 28.18, and tensile strength of FSPed Al composites is higher than the base alloy and this happens because matrix alloy softens due to frictional heat and it is found that frictional process with ceramic reinforcements increases the hardness and tensile strength. Kumar et al. [19] investigated the tensile properties of friction stir joint which depends on the microstructure of the material, and author analyses the stress–strain curve (Fig. 28.19) of base alloy and welded sample in different conditions of post-weld heat treatment. They also observed the improvement in tensile properties of the friction stir welding joint. All tensile properties like ultimate tensile strength, yield strength and percentage elongation increase and this increment is also shown in graph (Fig. 28.20). Imran et al. [20] observed the ultimate tensile strength of composites: firstly, by changing the composition of graphite and making bagasse ash percentage constant and secondly, they did by changing the composition of bagasse ash and making graphite percentage constant. Firstly, they increase graphite percentage and kept bagasse ash constant at 2% and by this they observed the increment in ultimate tensile strength and yield strength; then, they did same by keeping bagasse ash constant at 4% and they got more increment in ultimate tensile strength and yield strength; then they did same again by keeping bagasse ash constant at 6% and more better results were there and know they did opposite where they know kept graphite percentage constant to 1%, 3% and at last 5% and increasing bagasse ash percentage and they observed that properties are increasing by this also but there is major material loss. Singh et al. [21] investigated the increase in tensile strength of Al7075 and decrease in ductility by various processes. They observed that the increase in tensile strength was only by 1% after the process of water quenching which is minimum increment
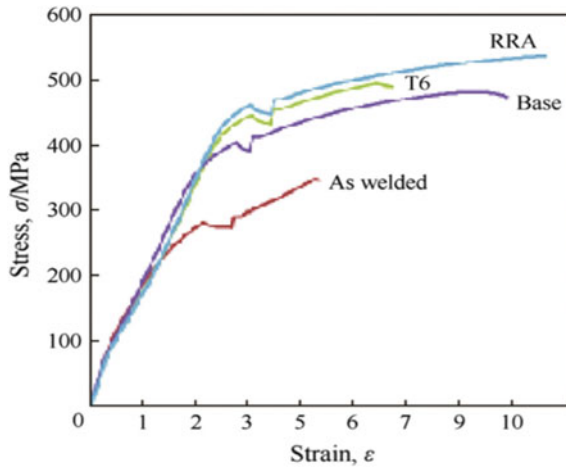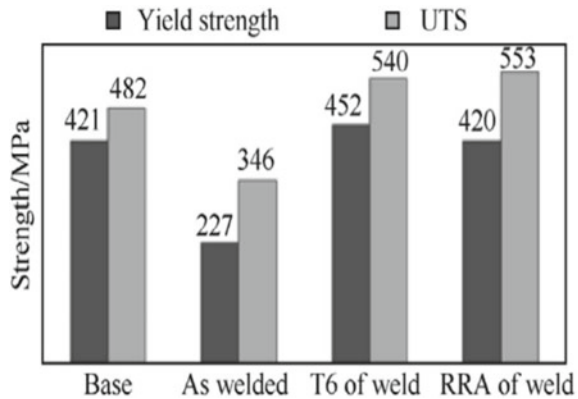
Fig. 28.19 Stress versus strain diagram of base alloy heat treatment [19]

Fig. 28.20 Tensile properties of FSW at various post-heat-treated conditions [19]

and there was maximum increment in tensile strength by oil quenching process and tensile strength decreases by annealing process and can be shown in Fig. 28.21. In the case of ductility, there was minimum percentage elongation by water quenching process and maximum percentage elongation by annealing process which can be shown in Fig. 28.22 investigated by them. Muniamuthu et al. [22] investigated the tensile strength of metal matrix composite of Al7075 with reinforcement of Al_2O_3. Author took four samples of Al7075 with different percentage of reinforcement of Al_2O_3. Therefore, sample 1 consists of 2% Al_2O_3, sample 2 consists of 4% Al_2O_3, sample 3 consists of 6% Al_2O_3 and at last sample 4 consists of 8% Al_2O_3. They found a result that there is a gradual increase in ultimate tensile strength as represented in Fig. 28.23. Veeravalli et al. [23] observed that with the introduction of TiC particles tensile strength increased and the increase was around 130 MPa for heat-treated 8 wt% TiC reinforcement. By increasing the TiC amount, percentage elongation decreased.
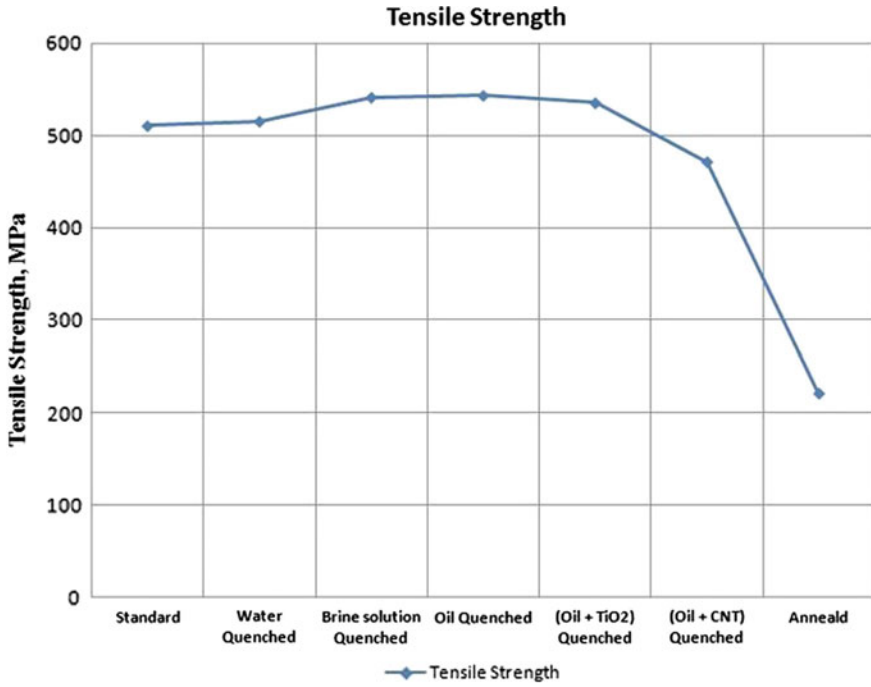
Fig. 28.21 Tensile strength versus various heat treatments [21]
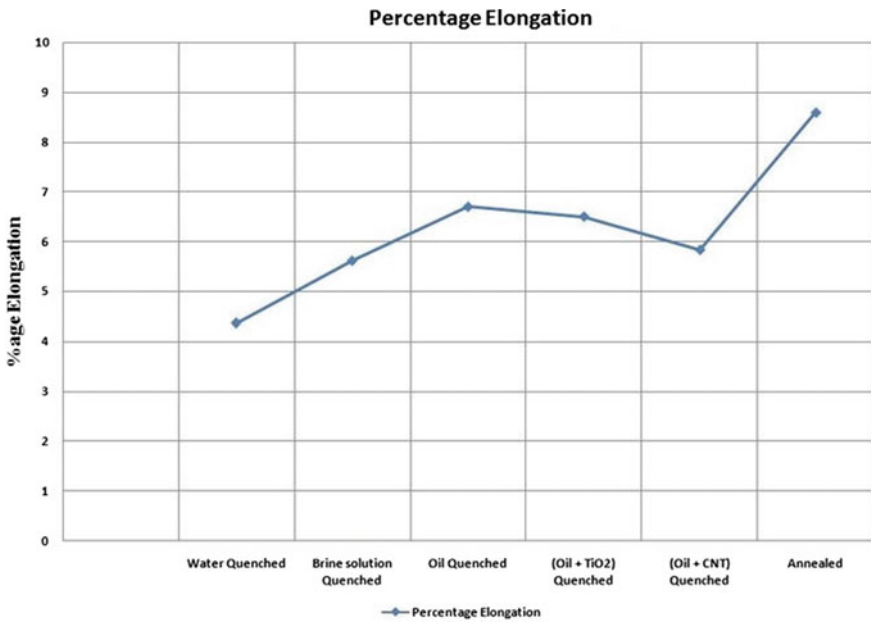
Fig. 28.22 Ductility versus various heat treatments [21]
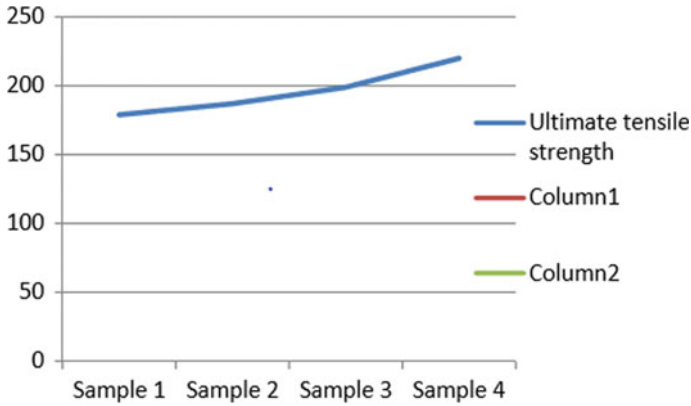
Fig. 28.23 Tensile strength of MMC of Al7075 with wt% Al_2O_3 [22]

The improvement in these mechanical properties is due to stress transfer from the matrix phase to hard TiC reinforcement. Cast condition showed lower tensile result than heat-treated conditions of same compositions.

28.2.3 Wear Properties

Alizadeh et al. [12] had the expected results, and wear rate of coarse-grained Al was more than that of nanostructured Al, whereas Al-B_4C nanocomposite and Al nanocomposite had nearly the same wear rate which increased gradually with the increased applied load (Fig. 28.24). Baradeswaran et al. [9] investigated that on the addition of B_4C as reinforcement, the wear rate decreases and shows the minimum value at 10 vol% B_4C (Fig. 28.25). This was due to the reduction in the contact
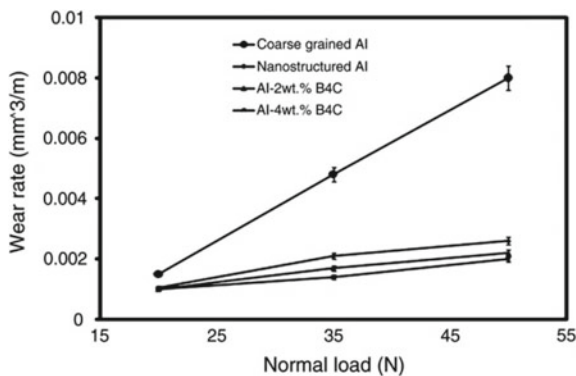
Fig. 28.24 Wear rate versus normal load [12]
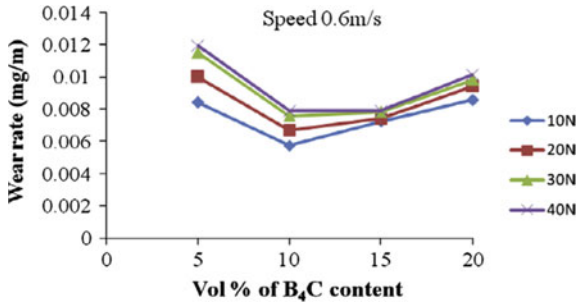
Fig. 28.25 Wear rate at different vol% B₄C at various loads [9]

of the matrix with the mating surface in the presence of hard B_4C reinforcement. On increasing applied load the wear also increases during abrasive wear, the softer matrix is protected by B_4C particles and these particles also strengthen the matrix. The sliding distance increases the wear mass loss, and it is minimum for the 10 vol% B_4C. Uvaraja et al. [25] observed that load which is applied is a necessary factor in deciding wear rate of composites and observations were made for wear rate at a constant speed, and they found that there was constant increment in wear with an increase in load (Fig. 28.26). They also investigated the wear resistance of composites influenced by the hard particle is better than the matrix materials. This happens because matrix material tends to be delaminated because of the absence of harder reinforcement. Base material showed higher wear as compared to composites with 15 wt% SiC and 3 wt% B_4C. Basithrahman and Abirami [26] conducted a wear test by using pin-on-disc wear testing machine with a load from 1.5 to 4.5 kgf. They observed that the wear resistance of AA7075 having a reinforcement of 3 wt% Al_2O_3, 5 wt% B_4C and 5 wt% TiO_2 is lower when compared to wear resistance of AA7075 having the reinforcement of 9 wt% Al_2O_3 and B_4C, TiO_2 remains constant. They got a graph between wear resistance and hybrid metal matrix composite (Fig. 28.27) they observed by the graph that the wear resistance of AA7075 with 9 wt% Al_2O_3 and others are constant was high at maximum load condition where the load equals to 4.5 kgf wear resistance of hybrid metal matrix composite increased by increasing alumina wt% and make B_4C and TiO_2 constant. Tee et al. [27] studied the dry sliding behaviour of Al-4.5%Cu-TiB_2 and Al-TiB composites made by the stir casting process. The authors also observed that the wear loss of both Al-4.5%Cu-TiB_2 and Al-TiB composite decreases with increase in the content of TiB_2. Observations were made by fig that by particle embedded in aluminium matrix that's why aluminium matrix is kept in debris formation during wear. From Fig. 28.28 as the sliding time increases the surface roughness decreases. The worn surface roughness was taken as a proof of wear mechanism and it is found by SEM analysis. Silicon carbide had more effect on wear resistance of aluminium alloy than B_4C because of good adhering property and also silicon carbide was more observed by Al-alloy than boron carbide. Lashgari et al. [28] investigated the graphical variation of weight loss with sliding behaviour at different loads of 20, 40 and 60 N. In Fig. 28.29 wear rate at different applied load is shown,
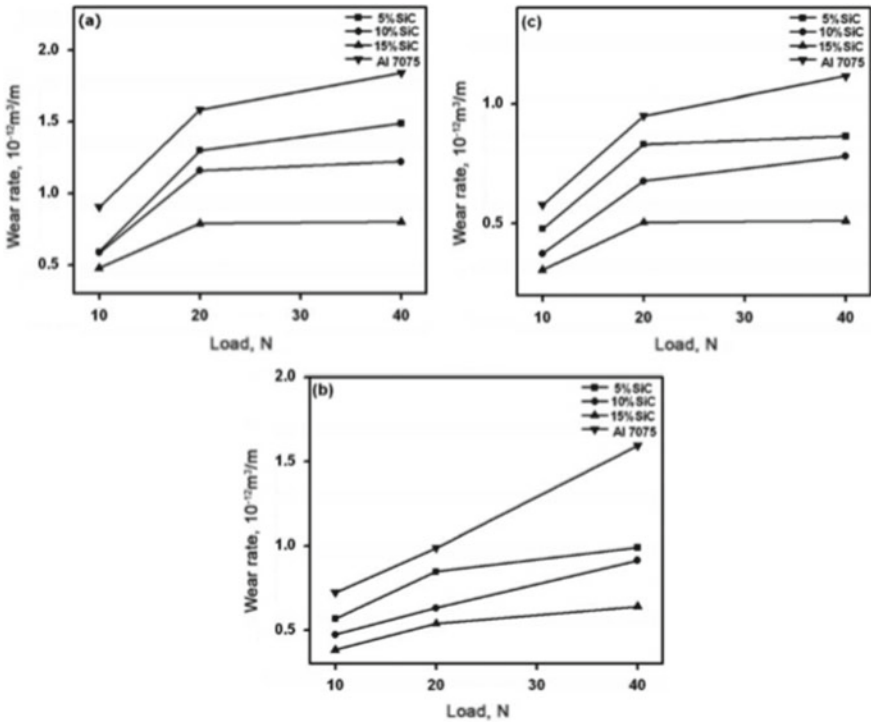
Fig. 28.26 Wear rate versus load at varying ageing duration [25]

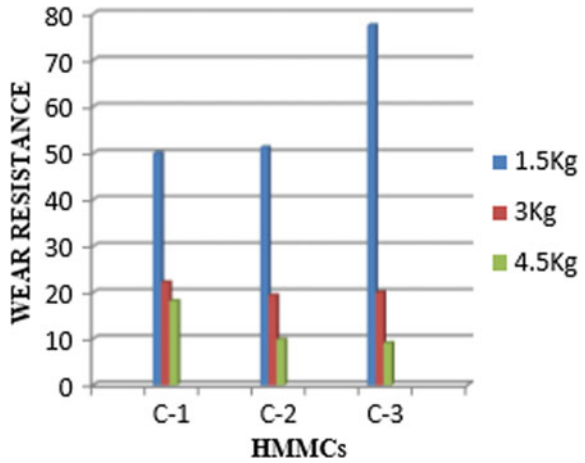**Fig. 28.27** Wear resistance for hybrid metal matrix composite (HMMC) at various loads [26]

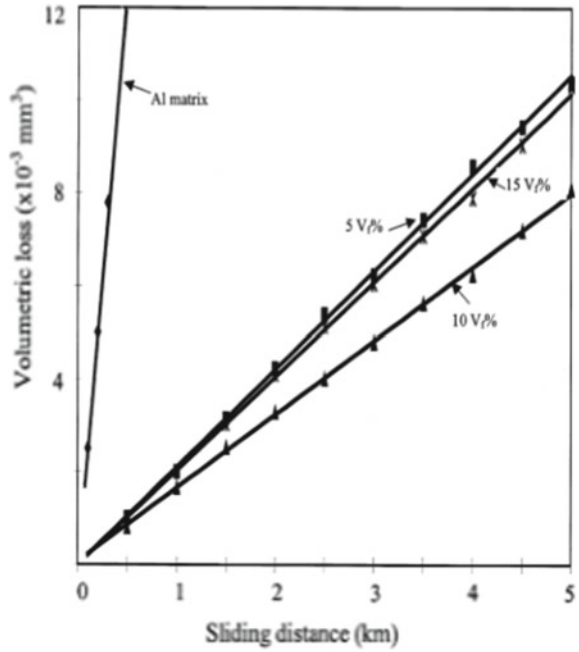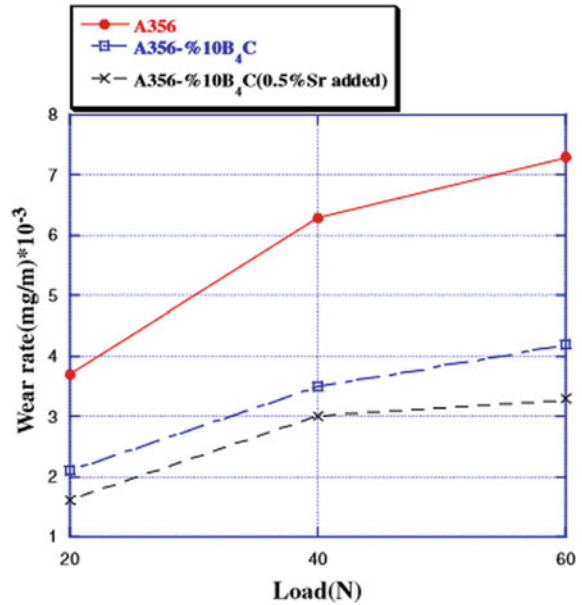**Fig. 28.28** Volume loss versus sliding distance of various samples [27]

Fig. 28.29 Variation of wear rate with load for various specimens [28]
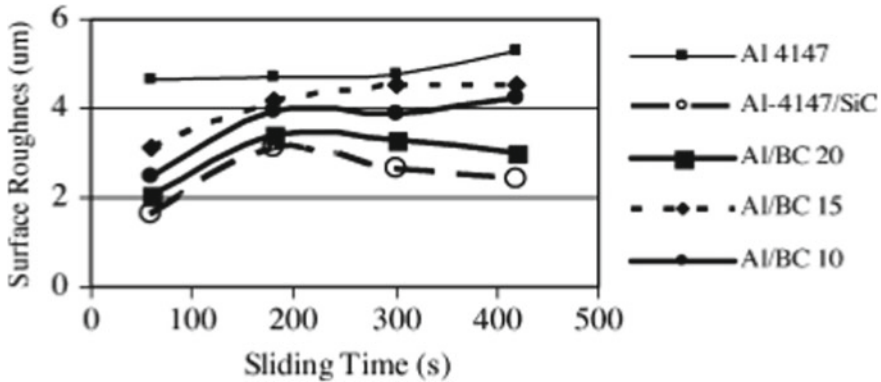
Fig. 28.30 Variation of surface roughness with sliding time [29]

For A356, and A356-10%B$_4$C, which was modified by adding 0.5% strontium which tends to higher wear resistance. Same results were shown by adding ceramic particles. It was concluded that wear resistance increases on adding strontium on all applied loads. The wear debris morphology was observed by EDS analysis for modified composites and unmodified composites on the applied load of 60 N. Wear debris can be formed by microcutting, plastic deformation and from the transfer of material from one surface to another. From EDS analysis, it is clear that adding strontium tends to an increase in the formation of oxides when compared to base composite. Increasing in the sliding distance, wear loss also increases but at low rate when compared to pure alloy. Ipek [29], the author, observed that the adhesive wear resistance of 4147Al/B$_4$C composite depends on the addition of B$_4$C particles. In beginning, the wear was adhesive type, and after increasing B$_4$C content, wear becomes abrasive in nature and this change in wear leads to fracture (Fig. 28.30). Sahin [30] investigated abrasive wear of Al matrix mixed with SiCp reinforcement and the result came out for two types of paper. First is SiC emery paper and other is Al$_2$O$_3$ paper. In SiC paper, wear rate depends on increment in applied load, sliding distance and abrasive wear, and for Al$_2$O$_3$ paper, decrement is found in the sliding distance. Suresha and Sridhara [31], the authors, investigated the dry sliding behaviour of hybrid-type aluminium matrix composite reinforced with a combination of silicon carbide and graphite particles. The result came out that for deciding the wear rate and friction rate load is a very necessary factor that is why on increasing load and sliding distance friction coefficient increases. Venkataraman and Sundararajan [32] studied the sliding friction and wear behaviour of Al, Al-7075 and Al-SiC matrix composite under dry sliding wear condition. Figure 28.31 shows the variation of wear rate of specimens with applied load and it was observed that wear rate increases with applied load though the rate of increase was different for different specimens. Al and Al-10 vol% SiC both showed high wear rates than Al-40%SiC, Al-Zn-Mg alloy (AA 7075) in solution treated (7075ST) and peak aged condition (7075A) and they also found the value of applied normal load (F_c) was responsible for transition, from mild wear to
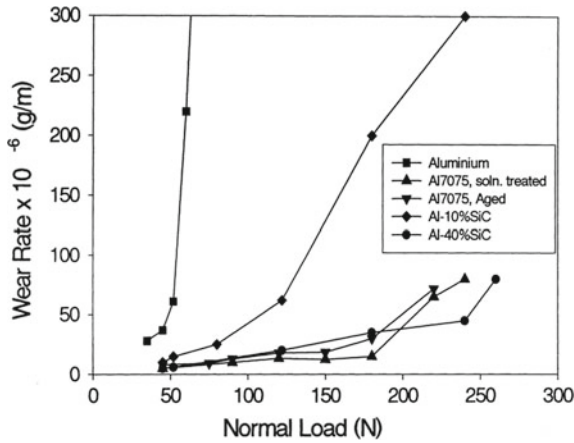
Fig. 28.31 Variation of wear rate with normal load [32]

severe wear. The values of F_c for Al, 7075ST, 7075A, Al-10SiC and Al-40SiC were 45, 180, 180, 120 and 240 N, respectively (Fig. 28.32). Veeravalli et al. [23] observed that with the increasing rate of TiC wear rate decreased and had minimum wear rate at 8% TiC. This was due to the decrease in an area of the real area of contact (ratio of the normal load to the hardness of the pin material) with the introduction of hard TiC particles. Increase in wear rate after 8 wt% can be due to the increase in porosity and cracks and degradation of mechanical properties. Yuvaraj et al. [18] found a graph of wear rates of base material and friction stir process surface composite shown in Fig. 28.33, and it is observed that wear resistance is improving significantly by adding reinforcement in all loads. He also observed that wear resistance is increased
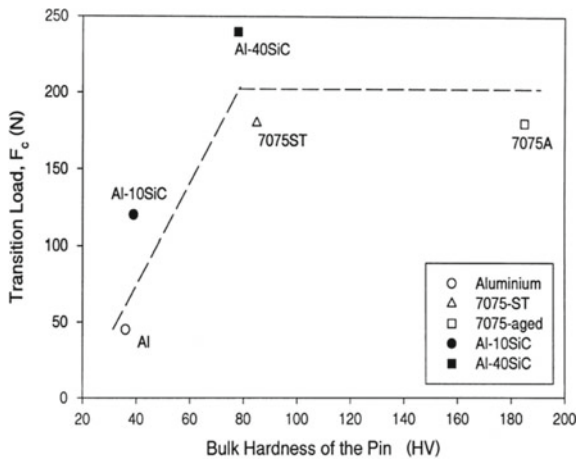
Fig. 28.32 Transition load versus bulk hardness of various specimens [32]
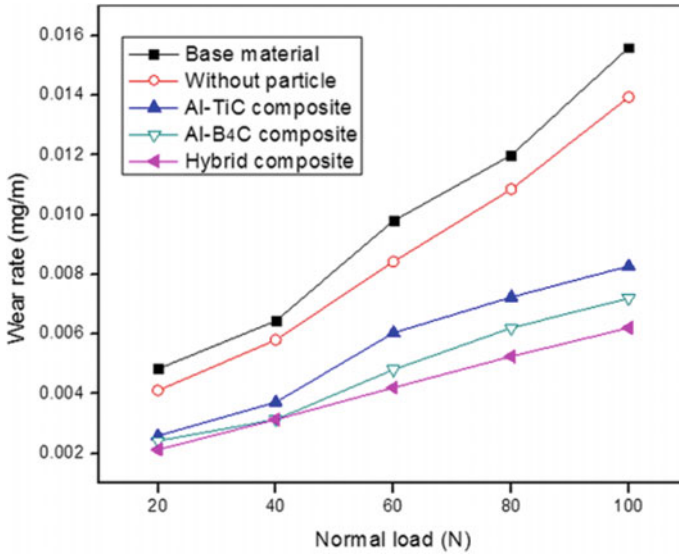
Fig. 28.33 Wear rate versus normal load [18]

at higher applied load for all samples. Yuvaraj et al. [24] tested a wear of TIG arc and FSPed composite at different loading condition and found weight loss of specimen whose wear is tested at normal load shown in Fig. 28.34a and also found change or variation in wear rate with respect to sliding distance of base material and specimen tested on 120 N observation are shown in Fig. 28.34b.
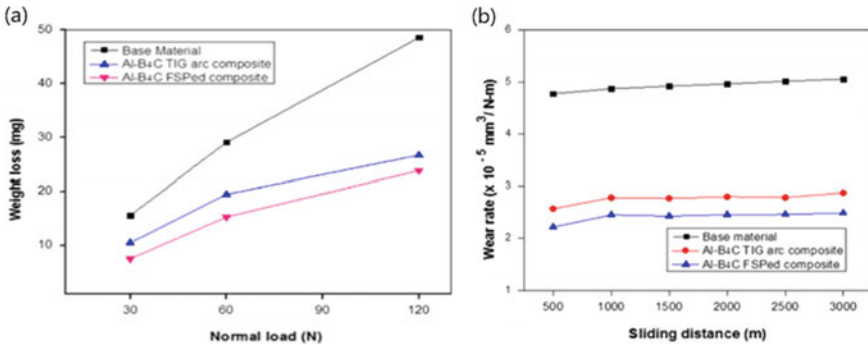
Fig. 28.34   a Weight loss versus normal load. **b** Wear rate versus sliding distance [24]

28.3 Conclusion

From the literature review, we can conclude that:

1. B_4C is expensive than other reinforcing elements but it very much improves the mechanical and tribological properties of Al7075 when compared to other reinforcing elements like SiC, TiB_2, etc.
2. After adding reinforcement to Al7075, the ductility of an Al7075 first increases and then decrease this happens due to the properties of Al7075 itself. So, the overall ductility of Al7075 decreases.
3. Using different composites, tensile strength, yield strength and hardness of Al7075 increase with additional reinforcement.
4. Wear resistance is a tribological property depends on many factors like: load applied, reinforcement element and reinforcement percentage. It also depends on many other properties if any heat treatment is done of a material. But the wear rate mainly depends on load in case of aluminium alloy composites.

28.4 Future Scope

B_4C gave better results compared to other reinforcements and not much study has been done on B_4C due to its high cost so more studies can be conducted on composites having nanoparticles of B_4C as reinforcement. Instead of stir casting process, friction stir process (FSP) can be used as it is easy to proceed and can be done directly on the surface and on the specific area as per the requirement. Addition of nanoparticles using FSP increases the hardness of composites.

References

1. Shin, C.S., Huang, J.C.: Effect of temper, specimen orientation and test temperature on the tensile and fatigue properties of SiC particles reinforced PM 6061 Al alloy. Int. J. Fatigue **32**(10), 1573–1581 (2010). https://doi.org/10.1016/j.ijfatigue.2010.02.015
2. Corrochano, J., Walker, J.C., Lieblich, M., Ibáñez, J., Rainforth, W.M.: Dry sliding wear behaviour of powder metallurgy Al–Mg–Si alloy-MoSi2 composites and the relationship with the microstructure. Wear **270**(9–10), 658–665 (2011). https://doi.org/10.1016/j.wear.2011.01.029
3. Abenojar, J., Velasco, F., Martínez, M.A.: Optimization of processing parameters for the Al + 10% B_4C system obtained by mechanical alloying. J. Mater. Process. Technol. **184**(1–3), 441–446 (2007). https://doi.org/10.1016/j.jmatprotec.2006.11.122
4. Khan, K.B., Kutty, T.R.G., Surappa, M.K.: Hot hardness and indentation creep study on Al–5% Mg alloy matrix–B_4C particle reinforced composites. Mater. Sci. Eng. A **427**(1–2), 76–82 (2006). https://doi.org/10.1016/j.msea.2006.04.015
5. Auradi, V., Rajesh, G.L., Kori, S.A.: Processing of B_4C particulate reinforced 6061aluminum matrix composites by melt stirring involving two-step addition. Procedia Mater. Sci. **6**, 1068–1076 (2014). https://doi.org/10.1016/j.mspro.2014.07.177

6. Chaudhary, A., Dev, A.K., Goel, A., Butola, R., Ranganath, M.S.: The mechanical properties of different alloys in friction stir processing: a review. Mater. Today Proc. **5**(2), 5553–5562 (2018). https://doi.org/10.1016/j.matpr.2017.12.146

7. Butola, R., Singari, R.M., Bandhu, A., Walia, R.S.: Characteristics and properties of different reinforcements in hybrid aluminium composites: a review. IJAPIE **10** (2017)

8. Butola, R., Malhotra, A., Yadav, M., Singari, R., Murtaza, Q., Chandra, P.: Experimental studies on mechanical properties of metal matrix composites reinforced with natural fibres ashes, 11 (2019). http://doi.org/10.4271/2019-01-1123

9. Baradeswaran, A., Elaya Perumal, A.: Influence of B_4C on the tribological and mechanical properties of Al7075–B_4C composites. Compos. B Eng. **54**, 146–152 (2013). https://doi.org/10.1016/j.compositesb.2013.05.012

10. Canakci, A., Arslan, F., Yasar, I.: Pre-treatment process of B_4C particles to improve incorporation into molten AA2014 alloy. J. Mater. Sci. **42**(23), 9536–9542 (2007). https://doi.org/10.1007/s10853-007-1896-z

11. Butola, R., Singari, R., Murtaza, Q.: A review on surface modification of aluminium alloy using friction stir processing. Int. J. Res. Appl. Sci. Eng. Technol. (IJRASET) **7**(4) (2019)

12. Alizadeh, A., Taheri-Nassaj, E.: Mechanical properties and wear behavior of Al–2wt.% Cu alloy composites reinforced by B_4C nanoparticles and fabricated by mechanical milling and hot extrusion. Mater. Charact. **67**, 119–128 (2012). https://doi.org/10.1016/j.matchar.2012.02.006

13. Alihosseini, H., Dehghani, K., Kamali, J.: Microstructure characterization, mechanical properties, compressibility and sintering behavior of Al-B_4C nanocomposite powders. Adv. Powder Technol. **28**(9), 2126–2134 (2017). https://doi.org/10.1016/j.apt.2017.05.019

14. Ravi, B., Balu Naik, B., Udaya Prakash, J.: Characterization of aluminium matrix composites (AA6061/B_4C) fabricated by stir casting technique. Mater. Today Proc. **2**(4–5), 2984–2990 (2015). https://doi.org/10.1016/j.matpr.2015.07.282

15. Butola, R., Pratap, C., Shukla, A., Walia, R.: Effect on the mechanical properties of aluminum-based hybrid metal matrix composite using stir casting method. Mater. Sci. Forum **969**, 253–259 (2019)

16. Subramaniam, B., Natarajan, B., Kaliyaperumal, B., Chelladurai, S.J.S.: Investigation on mechanical properties of aluminium 7075-boron carbide-coconut shell fly ash reinforced hybrid metal matrix composites. China Foundry **15**(6), 449–456 (2018). https://doi.org/10.1007/s41230-018-8105-3

17. Chandra, B.T., Sanjeevamurthy, Shiva Shankar, H.S.: Effect of cold quenching on mechanical properties of Al7075-albite particulate composite. Int. J. Sci. Res. Publ. **6**(8), 372–356 (2016)

18. Yuvaraj, N., Aravindan, S., Vipin: Wear characteristics of Al5083 surface hybrid nanocomposites by friction stir processing. Trans. Indian Inst. Met. **70**(4), 1111–1129 (2016)

19. Kumar, P.V., Madhusudhan Reddy, G., Srinivasa Rao, K.: Microstructure, mechanical and corrosion behavior of high strength AA7075 aluminium alloy friction stir welds—effect of post weld heat treatment. Defence Technol. **11**(4):362–369. https://doi.org/10.1016/j.dt.2015.04.003

20. Imran, M., Anwar Khan, A.R., Megeri, S., Sadik, S.: Study of hardness and tensile strength of aluminium-7075 percentage varying reinforced with graphite and bagasse-ash composites. Resour. Efficient Technol. **2**(2), 81–88 (2016). https://doi.org/10.1016/j.reffit.2016.06.007

21. Singh, G., Amandeep, B., Sarabjeet, S.: Study of mechanical properties of Al7075 alloy after heat treatment (2017). https://doi.org/10.13140/rg.2.2.14392.44801

22. Muniamuthu, S., Raju, N.L., Sathish Kumar, S., Sunil Kumar, K.: Investigation on mechanical properties of Al7075-Al_2O_3 metal matrix composites. Int. J. Mech. Eng. Technol. **7**(6), 474–482 (2016)

23. Veeravalli, R.R., Nallu, R., Mohiuddin, S.M.M.: Mechanical and tribological properties of AA7075–TiC metal matrix composites under heat treated (T6) and cast conditions. J. Mater. Res. Technol. **5**(4), 377–383 (2016). https://doi.org/10.1016/j.jmrt.2016.03.011

24. Yuvaraj, N., Aravindan, S., Vipin: Comparison studies on mechanical and wear behavior of fabricated aluminum surface nano composites by fusion and solid state processing. Surf. Coat. Technol. **309**, 309–319 (2017)

25. Uvaraja, V.C., Natarajan, N., Shivakumar, K., Jegadheeshwaran, S., Sudhakar, S.: Tribological behaviour of heat treated Al7075 aluminium metal matrix composites. Indian J. Eng. Mater. Sci. **22**, 51–61 (2015)
26. Basithrahman, A., Abirami, S.: Tribological behaviour of AA 7075 hybrid composite using stir casting method. Int. J. Eng. Res. **6**(01) (2017). https://doi.org/10.17577/ijertv6is010111
27. Tee, K.L., Lu, L., Lai, M.O.: Wear performance of in-situ Al–TiB$_2$ composite. Wear **240**(1–2), 59–64 (2000). https://doi.org/10.1016/s0043-1648(00)00337-9
28. Lashgari, H.R., Sufizadeh, A.R., Emamy, M.: The effect of strontium on the microstructure and wear properties of A356–10%B$_4$C cast composites. Mater. Des. **31**(4), 2187–2195 (2010). https://doi.org/10.1016/j.matdes.2009.10.049
29. Ipek, R.: Adhesive wear behaviour of B$_4$C and SiC reinforced 4147 Al matrix composites (Al/B$_4$C–Al/SiC). J. Mater. Process. Technol. **162–163**, 71–75 (2005). https://doi.org/10.1016/j.jmatprotec.2005.02.207
30. Sahin, Y.: Wear behaviour of aluminium alloy and its composites reinforced by SiC particles using statistical analysis. Mater. Des. **24**(2), 95–103 (2003). https://doi.org/10.1016/s0261-3069(02)00143-7
31. Suresha, S., Sridhara, B.K.: Friction characteristics of aluminium silicon carbide graphite hybrid composites. Mater. Des. **34**, 576–583 (2012). https://doi.org/10.1016/j.matdes.2011.05.010
32. Venkataraman, B., Sundararajan, G.: Correlation between the characteristics of the mechanically mixed layer and wear behaviour of aluminium, Al-7075 alloy and Al MMCs. Wear **245**(1–2), 22–38 (2000). https://doi.org/10.1016/s0043-1648(00)00463-4

Chapter 29
Investigation of Mechanical Properties in Silicon Carbide-Filled Carbon Fiber Composites

Monika Khurana, J. K. Purohit, R. Gupta, and Bhuvnesh Bhardwaj

Abstract The main aim of the present research is to investigate the mechanical properties (hardness, tensile strength, tensile modulus, flexural strength, flexural modulus, inter-laminar shear strength, and impact strength) of unfilled carbon reinforcement fiber composites and SiC-filled carbon reinforcement fiber composites and to identify the best combination in terms of wt% of filler, matrix, and reinforcement for best mechanical properties. The results revealed that SiC-filled carbon reinforcement fiber composite with 10 wt% of SiC particulates has been exhibited by the better mechanical properties among all fabricated unfilled carbon reinforcement fiber composites and SiC-filled carbon reinforcement fiber composites.

Keywords CFRP · SiC · Mechanical properties · Hand layup technique

29.1 Introduction

Recently, fiber-reinforced polymer (FRP) composites commonly used material in automobile and aerospace industries due to its excellent mechanical and tribological properties. In these composite, reinforcement and matrix largely maintain their properties which are the combination of the properties of constituents [7]. In the present scenario, carbon fiber-reinforced polymer (CFRP) composites are widely used in different manufacturing applications due to their better strength to weight and excellent

M. Khurana (✉)
Department of Mechanical Engineering, SKIT, Jaipur, India
e-mail: khurana.monika2009@gmail.com

J. K. Purohit · R. Gupta
Department of Mechanical Engineering, Poornima University, Jaipur, India
e-mail: jkp.mnit@gmail.com

R. Gupta
e-mail: rbngpta@gmail.com

B. Bhardwaj
Department of Mechanical Engineering, JECRC, Jaipur, India
e-mail: bhuvnesh.bhardwaj@gmail.com

corrosion resistance. Suresha and Chandramohan [12] examined the abrasive wear behavior of glass vinyl–ester (G-V) composites filled with SiC and graphite filler. Raju et al. [10] examined the influence of SiO_2 as a filler material on abrasive wear behavior of silicon dioxide-filled glass fabric reinforced epoxy composite. Sujesh and Ganesan [11] developed bidirectional woven glass fiber-reinforced epoxy polymer (GFRP) composite filled with nanosilica to study the tensile behavior. Irina et al. [6] fabricated hybrid composites using plain-woven glass fiber, stitched bi-axial $\pm 45°$ glass fiber, and plain-woven carbon fiber to examine the mechanical properties of developing composites. Gao et al. [5] propagated poly-amido amine dendrimers on the surface of carbon fiber using in situ polymerization for the fabrication of carbon fiber composites to investigate the mechanical properties. Dong et al. [4] introduced carbon black on to the surface of carbon fibers using chemical vapour deposition to enhance the mechanical properties of fibers/epoxy composites. The addition of carbon black increases the wettability and surface energy of treated carbon fibers as compared to untreated carbon fibers.

Based on literature review, it is cleared that various investigators used different filler materials for improving the mechanical and wear properties of composites. Furthermore, carbon-reinforced polymer composites with SiC as filler material have not been much explored. Therefore, current research work deals with the investigations about mechanical properties of CFRP based composited with SiC as filler material.

29.2 Experimentation and Measurement

In this research work, woven carbon fibers have been used as a reinforcement material, epoxy resin used as a matrix material, while Si-C particulates are used as a filler material for the fabrication of carbon-reinforced polymer hybrid composites. The bisphenol-A-diglycidyl-ether is used as matrix materials with Hinpoxy C hardener in the required proportion by weight, i.e., 30:100 ratio. The carbon-reinforced polymer hybrid composites have been fabricated using hand layup technique. Total six carbon-reinforced polymer hybrid composites have been fabricated in the current research work.

The Rockwell hardness of all samples has been measured according to ASTM: E-18 standard using Rockwell cum Brinell hardness tester machine, manufactured by Engineering Models and Equipment, Roorkee, India. The uniaxial tensile tests and flexural tests on all specimens have been carried out on universal testing machine Instron 1195. The inter-laminar shear strength (SS) and flexural strength (F.S) are calculated using Eqs. 29.1 and 29.2. The load and cross-head displacements have been recorded using software and a data acquisition computer.

$$ILSS = \frac{3P}{4bt} \tag{29.1}$$

$$\text{F.S} = \frac{3PL}{2bt^2} \tag{29.2}$$

where

P Maximum load,
b Width of specimen,
t Thickness of the specimen, and
L Span length of the sample (60 mm).

The Izod impact test for all specimen to calculate impact strength has been carried out using impact tester manufacturer by Engineering Models and Equipment, Roorkee. The specimens for impact testing have been prepared according to ASTM D256 standard, i.e., 60 mm × 13 mm with different thickness according to composites. The impact strength of the specimen is calculated using Eq. 29.3.

$$I = \frac{K}{A} \tag{29.3}$$

where

I Impact strength,
K Impact energy, and
A ross-sectional area.

29.3   Result and Discussion

The present work is divided into two stages. In the first stage, unfilled carbon fiber reinforcement composites have been fabricated in different percentage of fiber and matrix (CE 30, CE 35, and CE 40) and mechanical testing have been carried out for the selection of best combination of fiber and matrix ratio for the fabrication of composite among the fabricated composites. In the second stage, SiC particulates have been added in different percentage in the composition of carbon fiber and matrix which is selected in the first stage and mechanical testing have been carried out for the selection of best SiC-filled carbon fiber reinforcement composites among the SiC-filled fabricated composites.

29.3.1   *Mechanical Testing of Unfilled Carbon Reinforcement Composites*

Initially, three unfilled carbon reinforcement composites (CE30, CE 35, and CE40) have been fabricated in the different percentage of weight of fiber and reinforcement

Table 29.1 Chemical composition for different wt% of fiber, matrix, and filler material

Composites fabricated for the present research work composite designation	Fiber (wt%)	Matrix (wt%)	Filler (wt%)
Carbon epoxy (CE30)	30	70	0
Carbon epoxy (CE35)	35	65	0
Carbon epoxy (CE40)	40	60	0
5% SiC-filled carbon epoxy (5SCE40)	40	55	5
10% SiC-filled carbon epoxy (10SCE40)	40	50	10
15% SiC-filled carbon epoxy (15SCE40)	40	45	15

as shown in Table 29.1. After that, mechanical tastings have been carried out on these specimens.

Figure 29.1 shows that hardness of the composites (CE30, CE35, and CE40). The hardness of the composites increases with increase in carbon fiber loading from 30 to 40 wt%. This is because of the increase in better stress transfer and indentation resistance of the matrix with an increase in carbon fiber loading. Also, an increase in the hardness of composites indicates better bonding of matrix with the reinforcement materials [2].

Figure 29.2 shows that tensile strength of the composites (CE30, CE35, and CE40). The tensile strength of the composites increases with increase in carbon fiber loading from 30 to 40 wt%. This is because of the increase in carbon fiber loading which reduces the brittleness and increases the ductility of the composite [9]. Figure 29.3 shows the tensile modulus of the unfilled carbon fiber reinforcement composites (CE30, CE35, and CE40).
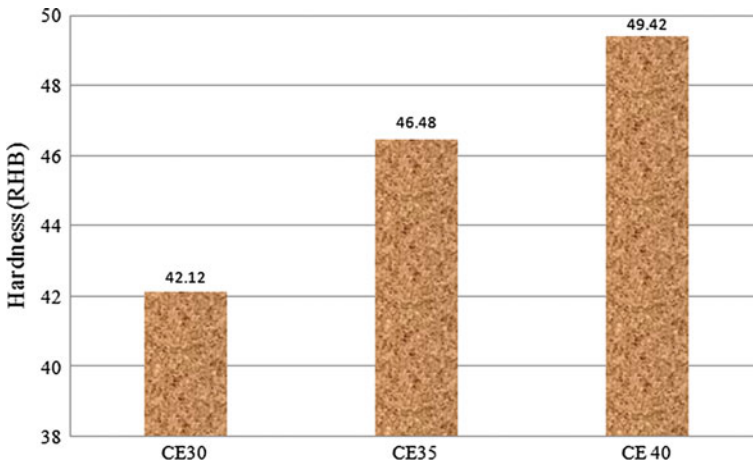
Fig. 29.1 Hardness of unfilled composites
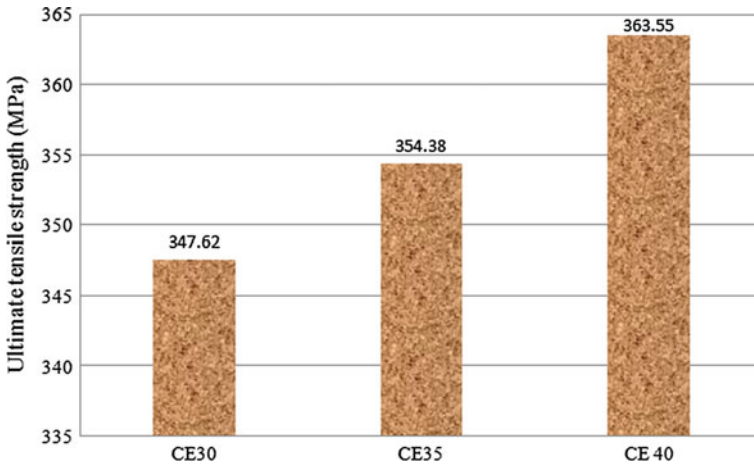
Fig. 29.2 Tensile strength of unfilled composites
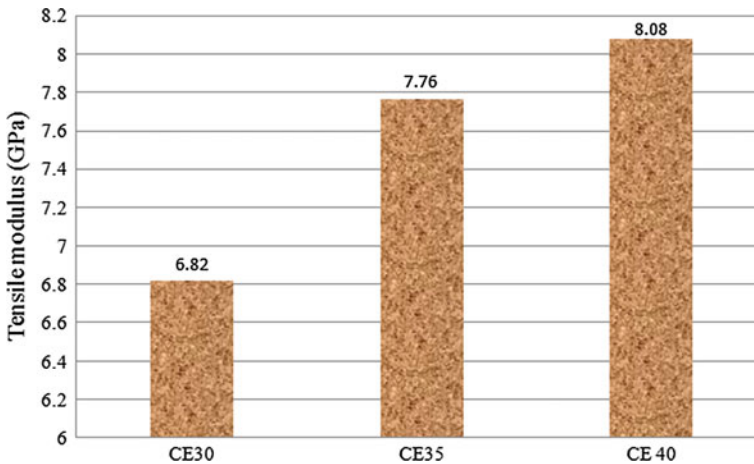
Fig. 29.3 Tensile modulus unfilled composites

From the figure, it is clear that as the percentage of fiber loading in the composite increases, the tensile modulus also increases because of the increase in load-bearing strength of composite with an increase in percentage fiber loading in the composite which results in the improvement in tensile strength and tensile modulus of CFRP composite.

Figure 29.4 shows the flexural strength; Fig. 29.5 shows the flexural modulus and Fig. 29.6 shows the inter-laminar shear strength of unfilled carbon fiber reinforcement composites (CE30, CE35, and CE40). The figures show the positive reinforcement effect of carbon fiber on flexural strength, flexural modulus, and inter-laminar shear
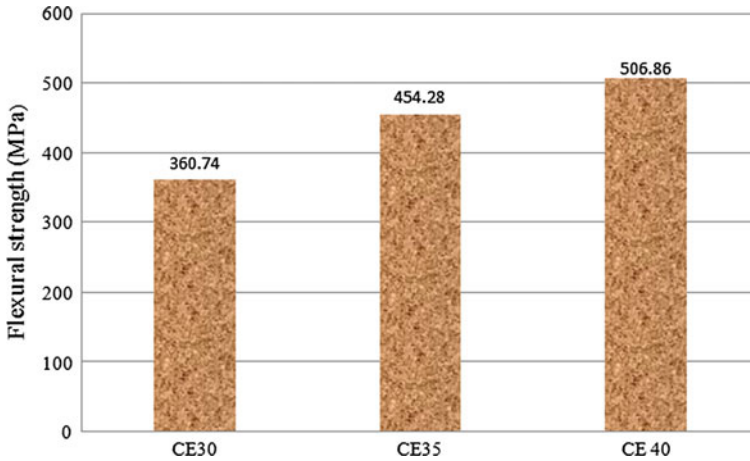
Fig. 29.4 Flexural strength of unfilled composites
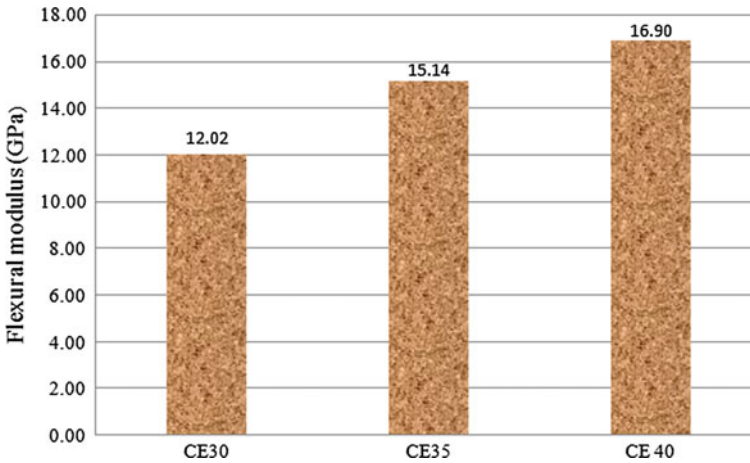
Fig. 29.5 Flexural modulus of unfilled composites

strength. As the fiber percentage increases, homogeneous distribution of fibers in the composites is also increases which prevent the early sliding of the polymer phase. This is due to the higher modulus of carbon fibers as compared to matrix and stress transfer occur near the fibers. Therefore, the crack initiation and propagation take place in different directions in place of crack propagation in mainly one direction, and fibers effectively participated in stress transfer in different directions [13].

Figure 29.7 shows the impact strength of unfilled carbon epoxy composites (CE30, CE35, and CE40). It is clear from the figure that impact strength increases with increase in percentage of carbon fiber reinforcement in the composite. From the analysis of mechanical properties, i.e., hardness, tensile strength, tensile modulus,
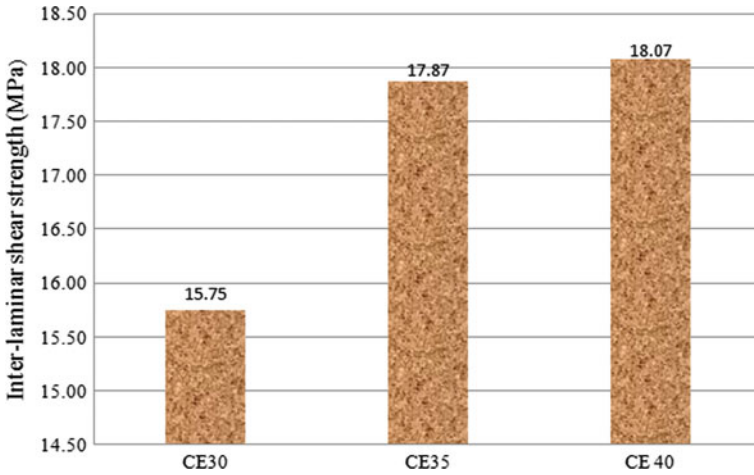
Fig. 29.6 Inter-laminar shear strength of unfilled composites
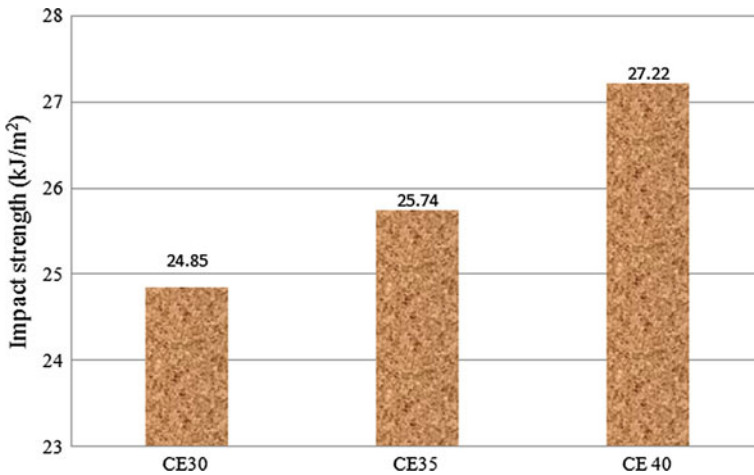
Fig. 29.7 Impact strength of unfilled composites

flexural strength, flexural modulus, inter-laminar shear strength, and impact strength of unfilled carbon reinforcement fiber composites, i.e., CE30, CE 35, and CE40, it is clear that CE40 has been exhibited excellent mechanical properties.

Therefore, the combination of carbon fiber and matrix of CE 40 unfilled carbon reinforcement fiber composite has been selected for the fabrication and analysis of SiC-filled carbon reinforcement fiber composites, i.e., 5% SiC-filled carbon epoxy (5SCE40), 10% SiC-filled carbon epoxy (10SCE40), and 15% SiC-filled carbon epoxy (15SCE40).

29.3.2 Mechanical Testing of SiC-Filled Carbon Reinforcement Composites

As mention above, among the CE30, CE 35, and CE40, the CE40 has been exhibited excellent mechanical properties. Therefore, this combination is selected for the fabrication of SiC-filled carbon reinforcement composites in different percentage of SiC as shown in Table 29.1.

The hardness of CE40, 5SCE40, 10SCE40, and 15SCE40 is shown in Fig. 29.8. From the figure, it is clear that SiC-filled carbon reinforcement composites exhibited more hardness as compared to unfilled carbon reinforcement composites. It is due to the uniform distribution of SiC particulates in the composites, which further increase the density of composite [1]. It has also been revealed that as the SiC content increases the hardness also increases. The 15SCE40 exhibited the highest hardness among the CE40, 5SCE40, 10SCE40, and 15SCE40. It is because of the increase in density of composite due to the addition of filler particles, which further increases the hardness of composite. [1].

Figures 29.9 and 29.10 show the tensile strength and tensile modulus of CE40, 5SCE40, 10SCE40, and 15SCE40. From both figures, it has been revealed that the tensile strength and tensile modulus both increase with increase in SiC filler particles from 0 to 10 wt% after that further increase in SiC particles decreases the tensile strength and tensile modulus. This is due to the filler particles. The filler particles behave as an obstacle for the stress transfer from one place to another. Further increase in SiC percentage beyond 10 wt% in the composite increases the transfer of stresses from one place to another.

This is due to the increase in bonding surface area with an increase in fiber/filler content. Hence, due to inadequate bonding between three different elements of
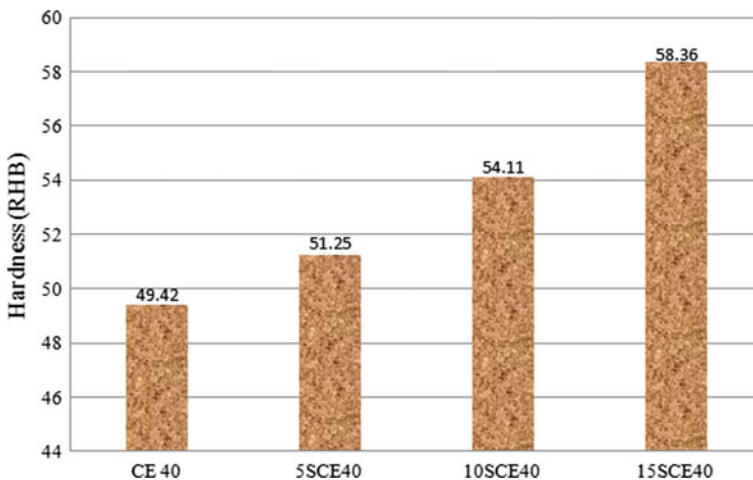
Fig. 29.8 Hardness of SiC-filled carbon reinforcement composites
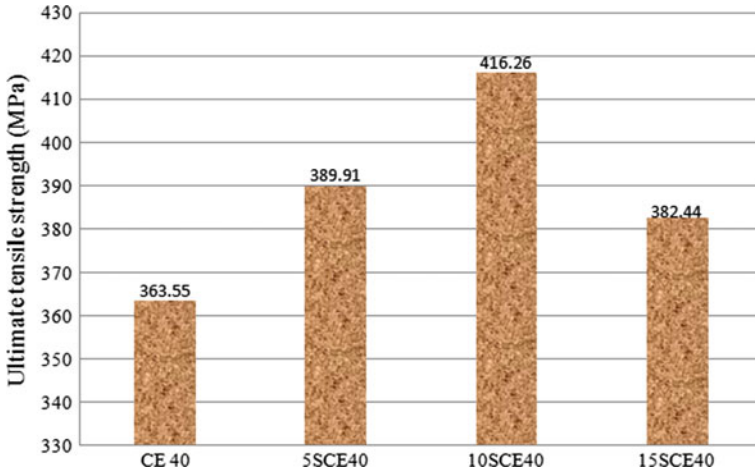
Fig. 29.9 Tensile strength of SiC-filled carbon reinforcement composites
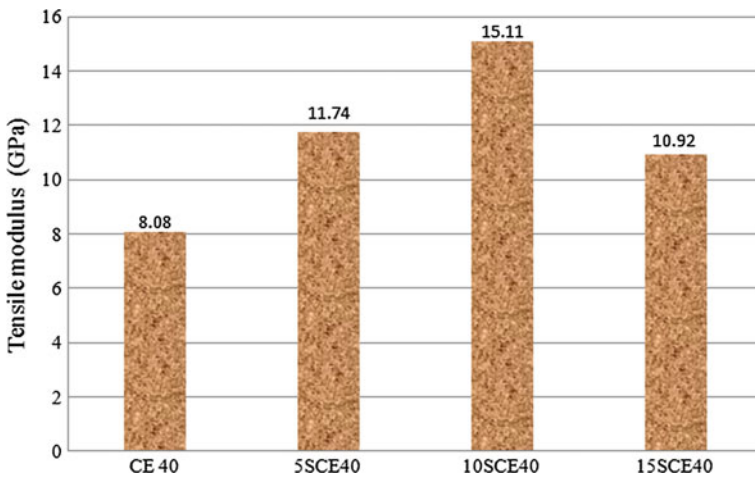
Fig. 29.10 Tensile modulus of SiC-filled carbon reinforcement composites

composite, the loads transfer capacity of the composite from one place to another decreases, which results in the decrease in tensile strength [1, 3].

Figures 29.11, 29.12, and 29.13 show the flexural strength, flexural modulus, and inter-laminar shear strength of unfilled carbon fiber reinforcement composite (CE40) and SiC-filled carbon fiber reinforcement composites (5SCE40, 10SCE40, and 15SCE40).

From all figures, it has been revealed that SiC carbon fiber reinforcement composites exhibit better flexural strength, flexural modulus, and inter-laminar shear strength as compared to unfilled carbon fiber reinforcement composite. It is due to
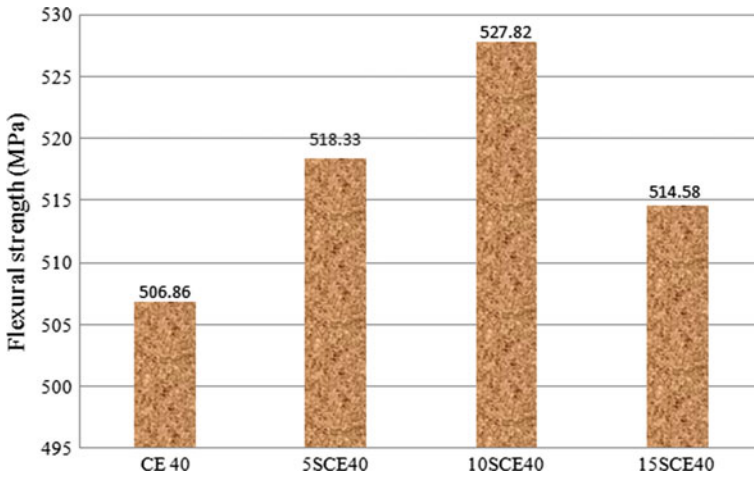
Fig. 29.11 Flexural strength of SiC-filled carbon reinforcement composites
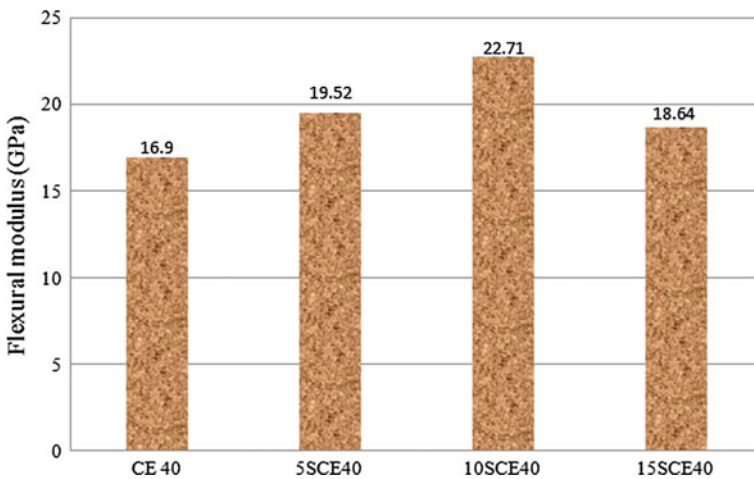
Fig. 29.12 Flexural modulus of SiC-filled carbon reinforcement composites

the presence of SiC particles with the carbon fiber reinforcement composites, which increase the interfacial bonding between the carbon fabric and epoxy matrix. Strong interfacial bonding between the fiber and matrix also contributes to higher flexural strength, flexural modulus, and inter-laminar shear strength.

From Figs. 29.11, 29.12, and 29.13, it has also been appeared that as the SiC filler particles increase from 0 to 10 wt%, the flexural strength, flexural modulus, and inter-laminar shear strength also increase, whereas the further increase in SiC particles from 10 to 15 wt% results in the decrease in the values of flexural strength, flexural modulus, and inter-laminar shear strength. The addition of 0 to 10 wt% of
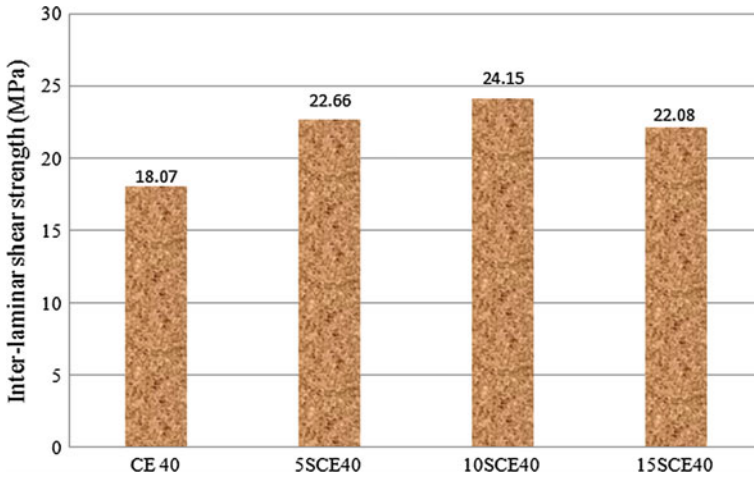
Fig. 29.13 Inter-laminar shear strength of SiC-filled carbon reinforcement composites
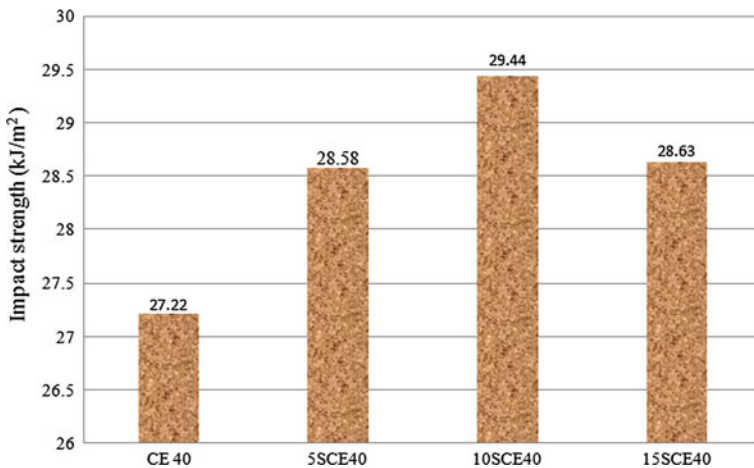
Fig. 29.14 Impact strength of SiC-filled carbon reinforcement composites

SiC particles increased the bonding between the three elements of composite, and hence, this strong bonding transfers load from one end to another, which further increase the flexural strength, flexural modulus, and inter-laminar shear strength of the composites [1]. Further, the wt% of fiber/SiC exceeds from 10 to 15 wt%, decreases the bonding strength due to decrease in weight percentage of the matrix, which further decreases the tendency of load transfer one part to another resulting in the decrease in the flexural strength, flexural modulus, and inter-laminar shear strength of the composite [8].

Figure 29.14 shows the impact strength of unfilled carbon fiber reinforcement composite (CE40) and SiC-filled carbon fiber reinforcement composites (5SCE40, 10SCE40, and 15SCE40).

From the figure, it has been revealed that SiC-filled carbon fiber reinforcement composites exhibit better impact strength as compared to unfilled carbon fiber reinforcement composite. It is due to the fact that addition of SiC particles increases the bonding between fiber and matrix which further increases the capacity of absorbing the energy before fracture, i.e., impact strength. From the figure, it has also been revealed that impact energy increases with increase in SiC particles from 0 to 10 wt%. Further increase in SiC particles from 10 to 15 wt% decreases the impact strength of composites due to the decrease in the bonding strength [1, 8].

29.4 Conclusion

The following conclusions are drawn from the analysis of the results of this current study:

1. Among the all fabricated unfilled carbon reinforcement fiber composites, i.e., CE30, CE 35, and CE40, unfilled carbon reinforcement fiber composite with 40 wt% carbon fiber, i.e., CE40 has been exhibited excellent mechanical properties (hardness, tensile strength, tensile modulus, flexural strength, flexural modulus, inter-laminar shear strength, and impact strength).
2. The tensile strength, tensile modulus, flexural strength, flexural modulus, inter-laminar shear strength, and impact strength of SiC-filled carbon reinforcement fiber composite with 10 wt%
3. SiC particulates, i.e., 10SCE40 have been found much better as compared to all fabricated composites. On the other hand, hardness of 15SCE40 has been found much better as compared to all fabricated composites.

References

1. Agarwal, G., Patnaik, A., Sharma, R.K.: Thermo-mechanical properties of silicon carbide-filled chopped glass fiber-reinforced epoxy composites. Int. J. Adv. Struct. Eng. **5**(21), 1–8 (2013)
2. Aquaro, D., Fontani, E.: Erosion of ductile and brittle materials. Meccanica **36**, 651–661 (2001)
3. Devendra, K., Rangaswamy, T.: Determination of mechanical properties of Al_2O_3, Mg $(OH)_2$ and SiC filled E-glass/epoxy composites. Int. J. Eng. Res. Appl. **2**(5), 2028–2033 (2012)
4. Dong, J., Jia, C., Wang, M., Fang, X., Wei, H., Xie, H., Zhang, T., He, I., Jiang, Z., Huang, Y.: Improved mechanical properties of carbon fiber-reinforced epoxy composites by growing carbon black on carbon fiber surface. Compos. Sci. Technol. **149**, 75–80 (2017)
5. Gao, B., Du, W., Zhang, R., Lu, F., Zhang, J.: Propagation of generation1-3 dendritic poly (amidoamine) on carbon fiber surface and its effect on the mechanical properties of fiber composites. Mater. Lett. **179**, 16–19 (2016)

6. Irina, M.M.W., Azmi, A.I., Tan, C.L., Lee, C.C., Khalil, A.N.M.: Evaluation of mechanical properties of hybrid fiber reinforced polymer composites and their architecture. Procedia Manuf. **2**, 236–240 (2015)
7. Jha, A.K., Mantry, S., Satapathy, A., Patnaik, A.: Erosive wear performance analysis of jute epoxy SiC hybrid composites. J. Compos. Mater. **44**(13), 1623–1641 (2010)
8. Kaundal, R., Patnaik, A., Satapathy, A.: Comparison of the mechanical and thermo-mechanical properties of unfilled and SiC filled short glass polyester composites. Silicon **4**, 175–188 (2012)
9. Patnaik, A., Satapathy, A., Biswas, S.: Investigations on three body abrasive wear and mechanical properties of particulate filled glass-epoxy composites. Malays. Polym. J. **5**, 37–48 (2008)
10. Raju, B.R., Suresha, B., Swamy, R.P.: Triboperformance of silicon dioxide filled glass fabric reinforced epoxy composites. ARPN J. Eng. Appl. Sci. **7**(4), 485–491 (2012)
11. Sujesh, G., Ganesan, C.: Tensile behaviour of nano filled GFRP at different strain rates. In: Proceeding ICMMAE, Pattaya (2012)
12. Suresha, B., Chandramohan, G.: Three body abrasive wear behavior of particulate filled vinylester composites. J. Mater. Process. Technol. **200**, 306–311 (2008)
13. Zhang, G., Karger-Kocsis, J., Zou, J.: Synergetic effect of carbon nanofibers and short carbon fibers on the mechanical and fracture properties of epoxy resin. Carbon **48**, 4289–4300 (2010)

Chapter 30
Air Erosion Behavior of SiC-Filled Carbon Fiber–Epoxy Composites

Monika Khurana and Bhuvnesh Bhardwaj

Abstract The carbon fiber-reinforced composites have all the ideal properties and have been widely used in many applications over the last decade. The objective of the present research is to optimize the erosion conditions for minimum erosion rate of SiC particulate-filled carbon-reinforced polymer composites. An attempt has also been to investigate the effect of erosion conditions on erosion rate. It has been found that erosion rate increases with increase in erodent size and impact velocity, while it decreases with increase in impingement angle and SiC loading. The minimum erosion rate is achieved at highest level of SiC loading, lowest level of erodent size, lowest level of impact velocity, and highest level of impingement angle.

Keywords SiC · Carbon fiber · Erosion · Optimization

30.1 Introduction

In the present era, carbon fiber polymer composites are replacing metals in many applications such as aircraft, space, satellites, automobiles, ships, and civil infrastructure because of its excellent mechanical, physical, and thermal properties [1]. The failure in machine parts takes place because of the wear. The wear is the main influencing factor for the failure of the machine parts. In the past, a number of researchers investigated the effect of different wear conditions on tribological properties of fabricated fiber reinforcement composites.

Vina et al. [2] examined the wear behavior of glass fiber fabric-reinforced polyetherimide composites. The study concludes that wear rate of composite

M. Khurana (✉)
Department of Mechanical Engineering, SKIT, Jaipur, India
e-mail: khurana.monika2009@gmail.com

B. Bhardwaj
Department of Mechanical Engineering, JECRC, Jaipur, India
e-mail: bhuvnesh.bhardwaj@gmail.com

decreases with increase in ambient temperature. Zhang et al. [3] used ring-on-block apparatus to examine the friction and wear characteristics of carbon fiber-reinforced phenolic composites. El-Tayeb [4] examined the two-body abrasive wear behavior of sugarcane fiber-reinforced polyester and synthetic R-glass fiber (GRP)-reinforced polyester composites. Suresha and Sivakumar [5] examined the mechanical and two-body abrasive wear behavior of glass vinyl ester and carbon vinyl ester composites.

Biswas and Satapathy [6] made comparison between the alumina-filled glass–epoxy composites and unfilled glass–epoxy composite on the basis of wear and mechanical properties.

Patnaik et al. [7] examined the three-body abrasive wear behavior of silicon carbide (SiC), alumina (Al_2O_3), and pine bark dust (PBD)-filled random glass fiber–epoxy resin composites. Chairman et al. [8] examined the two-body abrasive wear behavior of titanium carbide-filled glass fabric–epoxy (G-E) composites. It has been found that TiC particles improve the wear resistance of glass fabric–epoxy composite. Raju et al. [9] studied the two-body abrasive wear behavior and mechanical properties of silicon dioxide-filled glass fabric–epoxy composite. Irina et al. [10] examined the mechanical properties of plain-woven glass fiber, stitched bi-axial glass fiber, and plain-woven carbon fiber. Dong et al. [11] enhanced the mechanical properties of carbon fibers–epoxy composites by the application of carbon black coating on the surface of carbon fibers. The coating has been carried out using chemical vapor deposition. Wu et al. [12] improved interface bonding and impact toughness of carbon fiber-reinforced unsaturated polyester composites using amino-functionalized carbon nanotubes containing sizing agent. Zhao et al. [13] improved bonding between the surfaces of carbon nanotubes and carbon fibers using layer-by-layer grafting method.

The carbon fiber-reinforced composites have been widely used in aerospace and automotive industries for making different parts due to their superior properties. The literature reveals that very few efforts have been made to investigate the effect of air erosion conditions of SiC particulate-filled carbon-reinforced polymer composites on erosion rate. Accordingly, the main objective of the present work is to optimize the erosion conditions for minimum erosion rate of SiC particulate-filled carbon-reinforced polymer composites. An attempt has also been to investigate the effect of erosion conditions on erosion rate.

30.2   Fabrication, Experimentation, and Measurement

To achieve the objective of the present research, woven carbon fiber supplied by Hindoostan Composite Solutions Pvt. Ltd., Mumbai, has been used for the fabrication of composites. The bisphenol A diglycidyl ether supplied by Hindoostan Composite Solutions Pvt. Ltd., Mumbai, has been used as a matrix material, while Hinpoxy C Hardener supplied by Hindoostan Composite Solutions Pvt. Ltd., Mumbai, has been used with bisphenol A diglycidyl ether in the required proportion by

Table 30.1 Composites fabricated for the present research work

Composite designation	Fiber (wt%)	Matrix (wt%)	Filler (wt%)
Carbon–epoxy (CE40)	40	60	0
5% SiC-filled carbon–epoxy (10SCE40)	40	55	5
10% SiC-filled carbon–epoxy (10SCE40)	40	50	10
15% SiC-filled carbon–epoxy (15SCE40)	40	45	15

weight, i.e., 30:100 ratio. Silicon carbide is a hard synthetic material. Due to its high-temperature strength, high thermal conductivity, low thermal expansion, and chemical reaction resistance properties, silicon carbide is valuable as a filler material for the fabrication of composites. In the present work, silicon carbide particulates have been used as a filler material. The carbon-reinforced polymer hybrid composites have been fabricated using hand lay-up method. Table 30.1 represents the fabricated carbon-reinforced polymer composites in four different weight proportions.

The erosion test has been conducted using erosion test rig as per ASTM G76 Test standard. As per standards, the dimensions of all the specimens were kept as 40 mm × 40 mm. Depending on the direction of erodent flow, different impingement angles are set up for creating an impact with the erodent particle. In the present study, dry silica sand of 180 μm is used as erodent particle. During the erosion testing, erosion rate is calculated by the help of weight loss.

The weight loss of specimen per kg of erodent is calculated as follows:

$$\text{Weight loss} = (\text{Initial weight of specimen} - \text{final weight of specimen}) \big/ \text{weight of erodent}$$

30.3 Taguchi Methodology for the Optimization of Air Erosion Condition for Minimum Wear

The complete results along with respective treatments of the 16 experiments performed as per the L_{16} orthogonal array-based experimental plan were inputted into the MINITAB 15 software for further analysis.

30.3.1 Air Erosion Conditions and Development of Design Matrix for Experimentation

In the present research, L_{16} orthogonal array-based Taguchi methodology has been adopted for the optimization of erodent conditions. The SiC loading, erodent sizes, velocity of impact, and impingement angle have been considered as air erosion conditions. Table 30.2 shows the erosion conditions and level of erosion conditions

Table 30.2 Air erosion conditions and levels

Erosion conditions	Levels			
SiC loading (%wt)	0	5	10	15
Erodent size (μm)	300	400	500	600
Velocity of impact (m/s)	30	40	50	60
Impingement angle (degree)	30	50	70	90

Table 30.3 Design matrix for experimentation and measurement results

S. No.	SiC loading (% wt.)	Erodent size (μ)	Impact velocity (m/s)	Impingement angle (°)	Erosion (mg/kg)
1	0	300	30	30	0.368
2	0	400	40	50	0.457
3	0	500	50	70	0.490
4	0	600	60	90	0.604
5	5	300	40	70	0.231
6	5	400	30	90	0.207
7	5	500	60	30	0.523
8	5	600	50	50	0.680
9	10	300	50	90	0.109
10	10	400	60	70	0.348
11	10	500	30	50	0.429
12	10	600	40	30	0.697
13	15	300	60	50	0.244
14	15	400	50	30	0.381
15	15	500	40	90	0.211
16	15	600	30	70	0.567

according to Taguchi methodology. Table 30.3 shows the design matrix for the experimentation. The measurement results after the experimentation are also presented in Table 30.3.

30.3.2 Effect of Erosion Conditions on Erosion Rate

The first step to investigate the effect of erosion conditions on erosion is analysis of variance (ANOVA). The ANOVA indicates that erosion condition is significant or not. In the present work, the ANOVA has been carried out at 95% confidence level. Table 30.4 shows the ANOVA table.

Table 30.4 ANOVA table for erosion rate

Source	Degree of freedom	Sum of squares	Mean square	F-value	p-value (Prob $> F$)
SiC loading	3	0.03419	0.0114	100.864	0.002
Erodent size	3	0.33927	0.1131	1000.78	0.001
Impact velocity	3	0.00332	0.0011	9.796	0.047
Impingement angle	3	0.09926	0.0331	292.81	0.001
Residual	3	0.00034	0.00011		
Total	15				
R-square		99.90%	Adj. R-square		99.60%

From the table, it is clear that "Prob. $> F$" values for SiC loading, erodent size, impact velocity, and impingement angle are less than 0.05, which indicates that these are significant parameters that affect the erosion. The R^2 value and adjusted R^2 value are equal to 0.999 and 0.996, respectively. The result shows that the adjusted R^2 values are very close to 1, which indicates that the erosion parameters have significant impact on erosion.

To investigate the effect of erosion conditions on erosion, different plots between the erosion conditions and erosion have been plotted as shown in Fig. 30.1a–d. Figure 30.1a shows the effect of SiC loading on erosion rate. From the figure, it is clear that erosion rate continuously decreases with increase in % weight of SiC
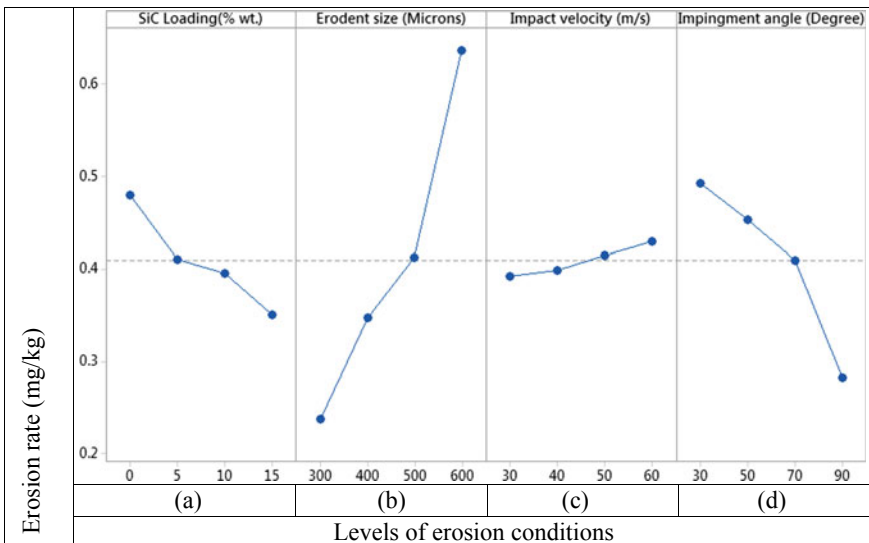
Fig. 30.1 Effect of erosion conditions on erosion

particles. It is due to increase in density of composites with increase in % weight of SiC particles, which further increases the hardness of the composites.

The erosion strength of the composites depends on the hardness of the material and increases with increase in hardness. Figure 30.1b, c shows the effect of erodent size and impact velocity on erosion rate, respectively.

It is clear from the figures that erosion rate increases with increase in erodent size and impact velocity. It is due to increase in momentum of the erodent particles. The momentum of the erodent particles increases with increase in erodent size and impact velocity. At the time of collision, the erodent particles transfer their momentum and kinetic energy on to the surface of test specimen, and this causes high material removal from the surface.

Figure 30.1d shows the effect of impingement angle on the erosion rate. The erosion rate continuously decreases with increase in impingement angle. It is because of the decrease in contact area between the erodent particles and test specimen with increase in impingement angle [7].

30.3.3 Ranking of Erosion Conditions for Erosion Rate

Table 30.5 shows the rank of the erosion conditions. The rank of erosion conditions indicates the ranking of erosion condition that affects the erosion rate. The ranking of erosion conditions has been obtained by making comparison between the maximum and the minimum values of erosion rate at all levels. From the table, it has been revealed that the most significant erosion condition that affects the erosion rate is erodent size, followed by impingement angle, SiC loading, and impact velocity.

From the table, it has also been revealed that minimum erosion rate is achieved at 4th level of SiC loading, 1st level of erodent size, 1st level of impact velocity, and 4th level of impingement angle.

Table 30.5 Response table for erosion rate

Erosion conditions	Levels				Max.–Min.(Δ)	Rank
	1	2	3	4		
SiC loading	0.4796	0.4103	0.3957	**0.3509**	0.1287	3
Erodent size	**0.2383**	0.3481	0.4132	0.6369	0.3986	1
Impact velocity	**0.3928**	0.399	0.4149	0.4298	0.037	4
Impingement angle	0.4923	0.4527	0.409	**0.2826**	0.2097	2

30.4 Conclusion

The main objective of the present work is to optimize the erosion conditions on erosion rate. An attempt has also been to investigate the effect of erosion conditions on erosion rate. The following conclusions have been drawn from the analysis of the results:

1. Among all the erosion conditions, the erodent size has been found as the most significant erosion condition that affects the erosion rate, followed by impingement angle, SiC loading, and impact velocity.
2. The erosion rate increases with increase in erodent size and impact velocity, while it decreases with increase in impingement angle and SiC loading.
3. The minimum erosion rate is achieved at 4th level of SiC loading, 1st level of erodent size, 1st level of impact velocity, and 4th level of impingement angle.

References

1. Pathak, A.K., Borah, M., Gupta, A., Yokozeki, T., Dhakate, S.R.: Improved mechanical properties of carbon fiber/graphene oxide-epoxy hybrid composites. Compos. Sci. Technol. **135**, 28–38 (2016)
2. Vina, J., Garcia, M.A., Castrillo, M.A., Vina, I., Arguelles, A.: Wear behavior of a glass fiber-reinforced PEI composite. J. Thermoplast. Compos. Mater. **21**, 279–286 (2008)
3. Zhang, X., Pei, X., Wang, Q.: Friction and wear properties of combined surface modified carbon fabric reinforced phenolic composites. Eur. Polym. J. **44**, 2551–2557 (2008)
4. El-Tayeb, N.S.M.: Two-body abrasive behaviour of untreated SC and R-G fibres polyester composites. Wear **266**, 220–232 (2009)
5. Suresha, B., Shiva Kumar, K.N.: Investigations on mechanical and two-body abrasive wear behavior of glass/carbon fabric reinforced vinyl ester composites. Mater. Des. **30**, 2056–2060 (2009)
6. Biswas, S., Satapathy, A.: A study on tribological behavior of alumina filled glass-epoxy composites using Taguchi experimental design. Tribol. Trans. **53**(4), 520–532 (2010)
7. Patnaik, A., Satapathy, A., Biswas, S.: Investigations on three body abrasive wear and mechanical properties of particulate filled glass-epoxy composites. Malays. Polym. J. **5**, 37–48 (2010)
8. Chairman, C.A., Babu, S.P.K., Selvam, M.D., Balasubramanian, K.R.: Investigation on two-body abrasive wear behavior of titanium carbide filled glass fabric-epoxy composites-a Box-Behnken approach. Int. J. Eng. Sci. Technol. **3**(4), 119–129 (2011)
9. Raju, B.R., Suresha, B., Swamy, R.P.: Triboperformance of silicon dioxide filled glass fabric reinforced epoxy composites. ARPN J. Eng. Appl. Sci. **7**(4), 485–491 (2012)
10. Irina, M.M.W., Azmi, A.I., Tan, C.L., Lee, C.C., Khalil, A.N.M.: Evaluation of mechanical properties of hybrid fiber reinforced polymer composites and their architecture. Procedia Manuf. **2**, 236–240 (2015)
11. Dong, J., Jia, C., Wang, M., Fang, X., Wei, H., Xie, H., Zhang, T., He, I., Jiang, Z., Huang, Y.: Improved mechanical properties of carbon fiber-reinforced epoxy composites by growing carbon black on carbon fiber surface. Compos. Sci. Technol. **149**, 75–80 (2017)
12. Wu, Z., Cui, H., Chen, L., Jiang, D., Weng, L., Ma, Y., Li, X., Zhang, X., Liu, H., Wang, N., Zhang, J., Ma, Y., Zhang, M., Huang, Y., Guo, Z.: Interfacially reinforced unsaturated polyester carbon fiber composites with a vinyl ester-carbon nanotubes sizing agent. Compos. Sci. Technol. **164**, 195–203 (2018)

13. Zhao, M., Meng, L., Ma, L., Ma, L., Yang, X., Huang, Y., Ryu, J.E., Shankar, A., Li, T., Guo, C., Guo, Z.: Layer-by-layer grafting CNTs onto carbon fibers surface for enhancing the interfacial properties of epoxy resin composites. Compos. Sci. Technol. **154**, 28–36 (2018)

Chapter 31
On Performance Evaluation of Triplex Hybrid Process of UA-ECDTrepanning: An Experimental Investigation, Modeling and Optimization

Tarlochan Singh and Akshay Dvivedi

Abstract Electrochemical discharge trepanning (ECDT) is a variant of the electrochemical discharge machining (ECDM) process. In the present research endeavor, an ultrasonic system was incorporated with the ECDT system, and the developed process is termed as a triplex hybrid of ultrasonic-assisted ECDT process. The incorporation of ultrasonic vibrations in ECDT system exerts additional drag forces over the gas film and results in the formation of thin and stable gas films. In comparison with the ECDT process, the developed UA-ECDT process improves the material removal rate by 5 times. Central composite design of the response surface methodology was used to design the experimental plan. The process parameters selected were applied voltage, pulse on time, tool rotation rate and power rating. The material removal rate was considered as the response characteristic. Analysis of variance was also performed. In order to establish the relation between MRR and above-mentioned process parameters, a regression modeling was developed. Genetic algorithm was used to optimize the process parameters for higher MRR.

Keywords ECDM · Trepanning · Ultrasonic assistance · ECDTrepanning · Modelling · Optimization

31.1 Introduction

Electrochemical discharge machining (ECDM) is an emerging hybrid non-conventional machining process. It can be utilized to machine any kind of material regardless of their chemical, mechanical and electrical properties [1]. In ECDM, the thermal energy liberated by the tool electrode after the breakdown of the gas film

T. Singh (✉) · A. Dvivedi
Mechanical and Industrial Engineering Department, Indian Institute of Technology Roorkee, Roorkee 247667, India
e-mail: tsingh.iitr@yahoo.com

A. Dvivedi
e-mail: akshaydvivedi@gmail.com

removes the material from the work surface [2, 3]. Whereas, in this process, the electrochemical action generates the hydrogen gas film over the tool electrode owing to the electrolysis of alkaline electrolyte present in between the two electrodes (i.e., tool electrode and auxiliary electrode). The auxiliary electrode is generally used 100 times larger than the tool electrode. And for effective machining, the position of the auxiliary electrode is suggested beneath the tool electrode at a fixed distance. DC power supply is used to connect both the electrodes. The entire arrangement including both the electrodes, DC power supply and electrolyte chamber forms the electrolytic cell circuit (ECC) [4, 5]. The modified forms of thermal energy generated through this ECC can be employed to perform the drilling, milling, trepanning and die-sinking operations [1]. Among these operations, the electrochemical discharge trepanning is an important process variant of the ECDM process that is generally used to machine the big diametric holes [6]. The schematic view to illustrate the working principle of the ECDT process is shown in Fig. 31.1. In this process, an offset tool electrode is used to rotate about the spindle axis. The circular path traced by the thermal energy liberated tool electrode generates the circular groove on the work material. The cross-sectional view of the machined groove is depicted in Fig. 31.1. Literature provides a few articles that have been published related to the ECDT process. Gautam et al. pioneered this process, and they recommended the use of offset distance equal to the diameter of the tool electrode [7]. However, the increase in offset distance beyond a certain limit (particularly beyond the diameter of tool electrode) deteriorates the machining performance.

Jain et al. first time used this process to improve the depth of machined features. They used a copper wire electrode having a diameter of 1.24 mm to machine the quartz and alumina materials. In this study, they reported the machining of irregular features due to the ineffective channelization of electrochemical discharge energy
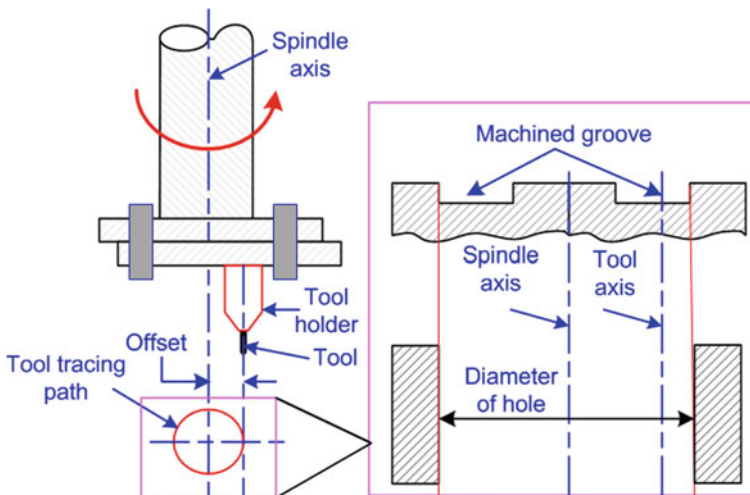

Fig. 31.1 Working principle of UA-ECDT process

[8]. In order to improve the profile of machined features and material removal rate through effective energy channelization, Chak et al. used abrasive coated tools to machine the glass materials. The micro-cavities generated by the abrasive coated tool produce thin and stable gas films. The breakdown of these gas films resulted in high-frequency spark discharges. The energy liberated by these spark discharges consequences improved process performance in terms of higher material removal rate and low over cut. Apart from it, the abrasion action imparted by the tool electrode removes the passivation layer from work material. In such a way, the use of abrasive coated tools in ECDT process assists to channelize the ECD energy in effective manners and finally improved the process performance [9]. However, the fabrication of abrasive coated tools required additional facility, and thereby, it increases the overall manufacturing cost. In order to improve the energy channelization index, Kapil et al. employed ultrasonic vibrations to tool electrode. The use of ultrasonic vibrations produced thin and stable gas film over the tool electrode, and the upward and downward strokes of the tool electrode effectively replenish the electrolyte from the machining zone. They reported the improvement in energy channelization index, depth and overcut of machined features due to the incorporation of ultrasonic vibrations in ECDT process [6]. Material removal rate is an important characteristic in machining that implies the productivity of any machining operation [10]. In case of UA-ECDT process, the effect of ultrasonic vibrations on process productivity is still not investigated. Thus, in order to analyze the effect of ultrasonic vibrations with ECDT process on process productivity, the material removal rate (MRR) is investigated in the present study. The selection of process parameters and their optimized combination to achieve the maximum MRR is reported in the subsequent sections. The experimental facility and the measurement techniques that have been employed to perform the present investigation are reported in the next section of this manuscript.

31.2 Materials and Methods

In the present study, an in-house developed ECDT facility was used to perform the experiments. The schematic view of the same is shown in Fig. 31.2. The experimental facility mainly comprises three units that are ECDM unit, ultrasonic unit and rotary unit. In ECDT system, a tool electrode of 600 μm diameter was accommodated in the tool holder at an offset distance of 3 mm from the spindle axis. The photographic view of the tool holder to accommodate the tool electrode is depicted in Fig. 31.2. Further, this tool holder was connected to the horn. Ultrasonic generator was used to supply the power to the transducer and further transducer converts the electrical signals into mechanical vibrations and ultimately delivers up and down movements to the tool electrode. The knobs provided on the ultrasonic generator controls the power rating. And the power rating decides the amplitude of vibrations at the tip of the tool electrode. Figure 31.3 describes the relation between power rating and amplitude of ultrasonic vibrations. As can be seen from Fig. 31.3, with an increase in power rating the amplitude of vibrations increases. A rotary unit was used to rotate
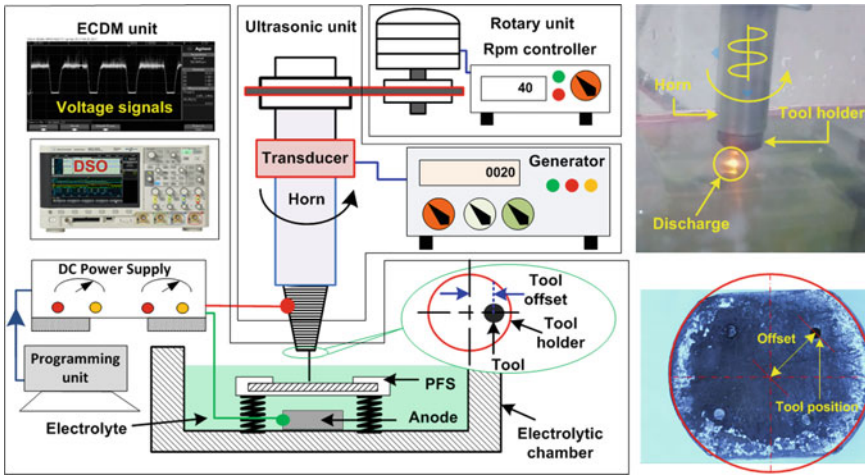
Fig. 31.2 Schematic view of UA-ECDT setup

Fig. 31.3 Effect of power rating on amplitude of vibrations
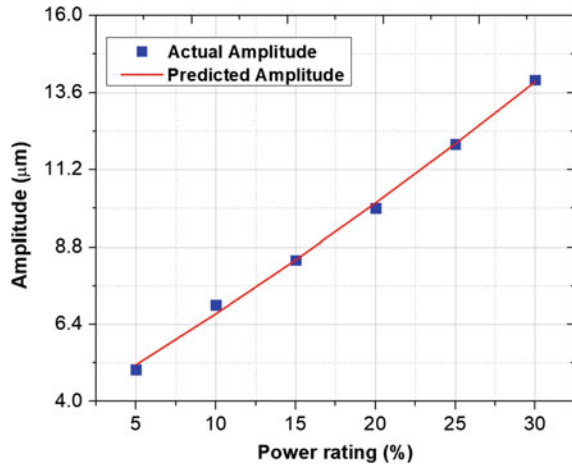
the tool electrode. And an rpm controller was installed to control the speed of the tool electrode.

During experimentation, the tool electrode was placed above the work material at zero working gap. Further, this gap was maintained through the pressurized feeding system afterward the removal of material from the work surface. The schematic view of the pressurized feeding system is shown in Fig. 31.2. A block of graphite was used as an auxiliary electrode and it was placed beneath the tool electrode at a fixed distance of 20 mm. A work material of glass and auxiliary electrode was fully immersed in the electrolytic chamber, while the tool electrode was dipped in the electrolyte up to 3 mm. Auxiliary electrode and tool electrode both were connected
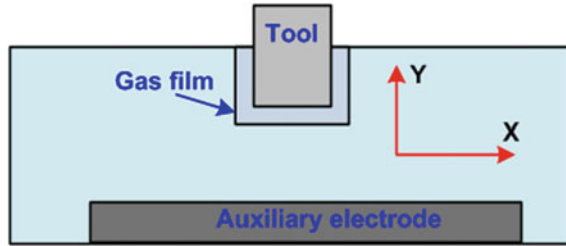
to the DC pulsed power supply. Whereas the tool electrode was connected with the negative terminal, auxiliary electrode was connected with the positive terminal of the power supply. In ECDM, the discharge characteristics play an important role to describe the physics behind the particular parametric values [11]. In general, voltage and current signals are used to describe the discharge characteristics. Thus, in the present investigation DSO was used to access the voltage signals. The photographic view of the DSO and recorded image of voltage signals are depicted in Fig. 31.2. As mentioned in Introduction section, the thermal energy (via spark discharges) released by the tool electrode removes the material from work surface. A glimpse of spark discharging is depicted in Fig. 31.2. In ECDM process, the electric field intensity plays an important role as it decides the discharge characteristics and subsequent process performance. Here, in this investigation a rotary motion of tool electrode and the ultrasonic vibrations will definitely affect the thickness of the gas film. Thereby, in order to investigate the effect of gas film thickness on electric field intensity a simulation was performed. A 2D model was developed and further used to perform the simulation. The schematic view of the above-mentioned model is depicted in Fig. 31.4. A tool electrode of SS-304 was considered as the cathode. The electrical characteristics of the UA-ECDT system were assumed constant. The governing condition for the processing system is given in Eq. 31.1.

$$\frac{\partial^2 \emptyset}{\partial x^2} + \frac{\partial^2 \emptyset}{\partial y^2} \tag{31.1}$$

The boundary conditions for both electrode surfaces are given in Eqs. 31.2 and 31.3.

$$\emptyset_c = 0 \tag{31.2}$$

$$\emptyset_a = U \tag{31.3}$$

where $\emptyset_c$ and $\emptyset_a$ are the electric potentials at the surface of the tool electrode and auxiliary electrode, respectively. U is the applied voltage.

In the present work, the material removal rate (MRR) was calculated by using the formula given in Eq. 31.4.
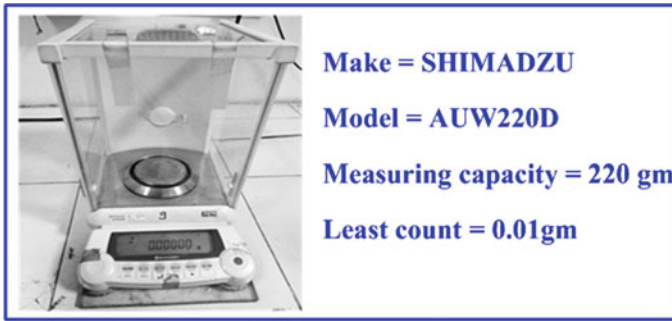
Fig. 31.5 Measurement instrument

$$\text{MRR} = \left(W_i - W_f\right)\big/ t_m \tag{31.4}$$

where W_i and W_f are the weights of work material prior to the machining and after the machining, respectively. An electronic balance was used to measure the weight of the work material. The photographic view of electronic balance and their measurement specifications are given in Fig. 31.5. Ultrasonic cleaner was used to wash the work material before and after the machining. Dryer was used to remove the moisture from work material. Then, finally, dry work material was used to measure their weights. t_m is a machining time, and in this study, it was taken 4 min for all the experiments.

31.3 Preliminary Experimentation

In order to assess the feasibility of the UA-ECDT process and to select the range of process parameters, preliminary experiments were performed. In these experiments, the power rating was varied from 0 to 30%, while the rest of parametric values were maintained at constant levels (applied voltage = 60 V, pulse-on time = 3 ms, electrolyte concentration = 20%, machining time = 4 min, tool rotation rate = 35 rpm, pulse-off time = 1 ms and exerted pressure = 3 N/mm^2). The results obtained from the experimentation are shown in Fig. 31.6. It was observed that with an increase in power rating the MRR increases. The MRR exhibited by UA-ECDT process is more than the ECDT process.

In ECDT process, as the tool electrode rotates about the spindle axis, a centrifugal force originates over the gas bubbles evolved from the surface of the tool electrode. The schematic view to describe the forces acted over the gas bubble during UA-ECDT action is illustrated in Fig. 31.7 [6]. This centrifugal force (FC) assists to eject the gas bubbles in an outward direction. Surface tension (FS) helps to adhere to the gas bubbles over the surface of tool electrode, while the drag force (FD) and buoyancy force (FB) both act in an upward direction to eject the gas bubbles. The collective action of centrifugal force (FC), drag force (FD) and buoyancy force (FB) against
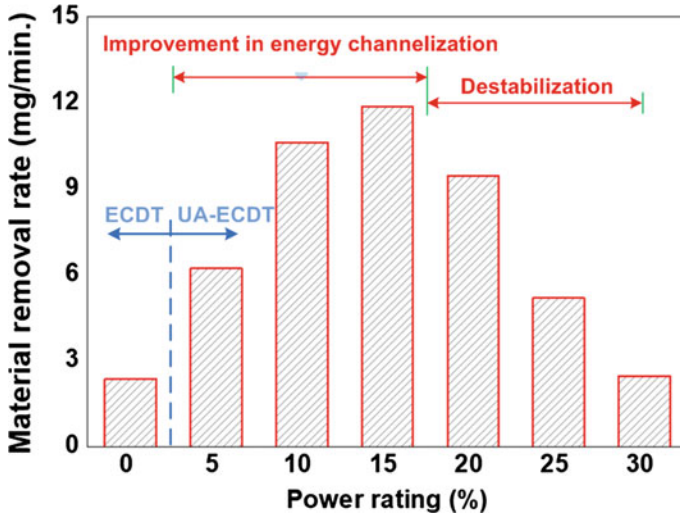
Fig. 31.6 Effect of power rating on material removal rate
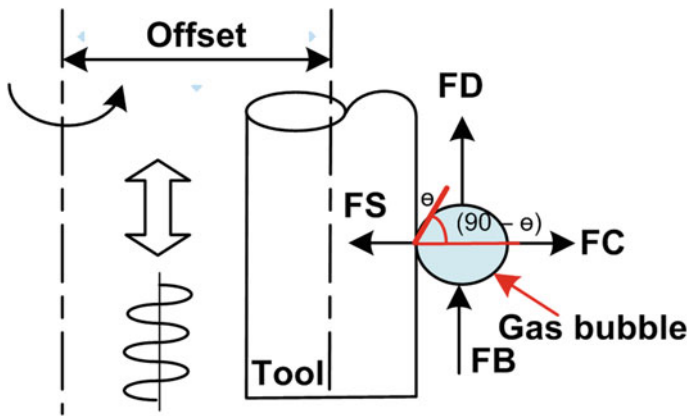
Fig. 31.7 Gas film formation mechanism during UA-ECDT process

the surface tension develops the thin and stable gas film over the tool electrode. The effect of gas film thickness on electric field intensity is shown in Fig. 31.8.

It was observed that with an increase in power rating, the MRR increases as can be seen from Fig. 31.6. The reason for higher MRR is the generation of thin and stable gas film over the tool electrode due to acting of high magnitude drag forces on it. Because the magnitude of drag forces is directly proportional to the power rating. As can be seen from Fig. 31.8, the decrease in gas film thickness increases the electric field intensity. Thereby, the breakdown of thin and stable gas film produces high frequency, high-intensity spark discharges and the energy liberated by these
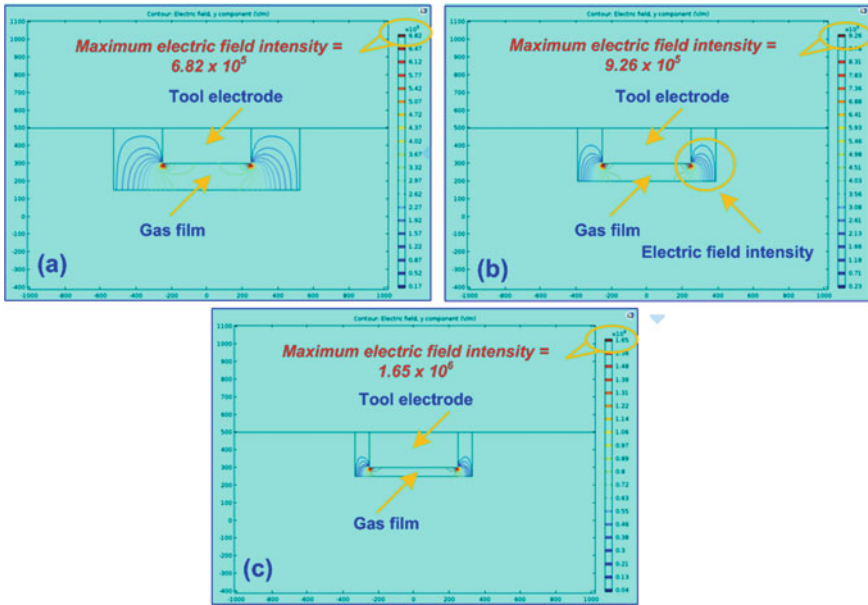
Fig. 31.8 Effect of gas film thickness on electric field intensity

spark discharges improves the MRR. Figure 31.8 depicts the effect of power rating on discharge characteristics. At zero power rating, the thickness of the gas film was high in value, thereby, the breakdown of thick gas film produces high-intensity low-frequency spark discharges as given in Fig. 31.9a. The intensity of discharges is 116 V. Whereas, at 15% power rating, the frequency of discharges improves as evident in Fig. 31.9b. The improved frequency of discharges implies the generation of stable gas film over the tool electrode. The features machined at zero power rating and 15% power rating depicts a big difference in terms of energy penetrated by the stable discharges with high frequency at 15% power rating.

However, beyond 15% power rating, with an increase in power rating the MRR decreases. The reason that attributes for the decrease in MRR is the generation of thin and unstable gas film over the tool electrode due to the high amplitude of ultrasonic vibrations. The intensity and frequency of discharges received from signals at 30%
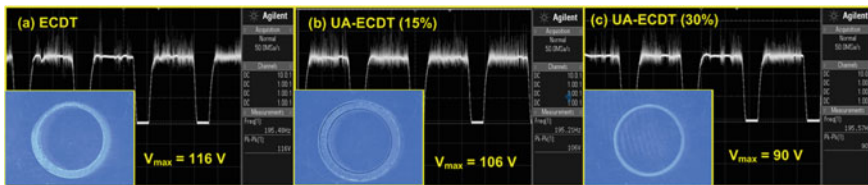
Fig. 31.9 Effect of power rating on discharge signals and profile of machined holes

Table 31.1 Process parameters and their levels

Process parameters		Levels and units				
Variable process parameters		−2	−1	0	1	2
1	Voltage (*A*) (V)	50	55	60	65	70
2	Pulse-on time (T$_{on}$) (*B*) (ms)	1	2	3	4	5
3	Tool rotation speed (*C*) (rpm)	20	30	40	50	60
4	Power rating (*D*) (%)	5	10	15	20	25
Constant process parameters						
5	Pulse-off time	1 ms				
6	Electrolyte concentration	20 (% wt/vol)				
7	Electrolyte	NaOH				
8	Tool diameter	600 μm				
9	Tool material	SS-304				
10	Offset distance	3 mm				
11	Machining time	4 min				

power rating evidence the generation of thin and unstable gas film from the tool electrode. From preliminary experiments, it can be concluded that the higher power rating is not suitable to assist the ECD action. Thus, for subsequent experiments the value of power rating is selected from 5 to 25%. Whereas, the other process parameters were selected on the basis of the literature review, and the selected values of process parameters are given in Table 31.1.

31.4   Statistical Analysis

Design of experiments is a primary and essential part to understand the process behavior in respect of the process parameters as well as to establish the appropriate relationship between responses and process controlling parameters. As in previous investigations related to the manufacturing processes, researchers extensively used central composite design (CCD) of response surface methodology to execute the experiments [12, 13]. Thus, in the present investigation, CCD was used to plan the experiments. The design of experiments along with quality characteristic is given in Table 31.2.

Further, analysis of variance was performed to access the variations along with the parametric values (Table 31.3). It was found that all the process parameters are significant. The model is also significant, while the lack of fit is non-significant as it is required. The values of R-square are also above 90%. The second-order regression model to establish the relation between response characteristic and process parameters is presented in Eq. 31.4. In order to depict the difference between actual MRR and the predicted MRR results obtained from the regression model, the bar

Table 31.2 Design of experiments with performance characteristics

Runs	A (V)	B (ms)	C (rpm)	D (%)	Avg. Y_1 (mg/min.)
1	60	5	40	15	15.23
2	55	4	50	20	5.86
3	60	3	40	15	11.58
4	65	2	30	20	9.76
5	55	2	50	20	2.6
6	65	2	30	10	10.7
7	60	3	20	15	10.98
8	60	3	60	15	4.92
9	60	3	40	15	11.02
10	70	3	40	15	16.51
11	60	3	40	5	4.6
12	65	4	30	10	17.24
13	55	2	30	10	5.18
14	65	2	50	10	8.16
15	55	2	30	20	4.44
16	65	4	50	10	13.4
17	60	1	40	15	5.18
18	55	4	50	10	6.48
19	60	3	40	15	12.22
20	50	3	40	15	4.08
21	60	3	40	25	3.92
22	65	2	50	20	6.78
23	55	4	30	20	8.82
24	65	4	30	20	15.92
25	60	3	40	15	12.46
26	60	3	40	15	12.02
27	60	3	40	15	13.54
28	55	4	30	10	9.6
29	65	4	50	20	12.8
30	55	2	50	10	3.4

A is applied voltage, B is pulse-on time, C is tool rotation rate, D is amplitude, Y_1 = material removal rate

graph is plotted in Fig. 31.10. It can be observed that the values of actual and predicted results are very close to each other. Thus, it can be inferred that the regression model developed from experimental results shows a very close affinity to read the basic phenomenon in UA-ECDT process, and further, this model can be used to analyze the effect of process parameters on MRR.

Table 31.3 Analysis of variance for second-order quadratic model of MRR

Source	SS	DOF	MS	F-value	Prob > F	
Model	535.9301	14	38.28072	86.05804	<0.0001	Significant
Residual	6.672367	15	0.444824	–	–	–
Lack of fit	3.021167	10	0.302117	0.413722	0.8899	Not significant
Pure error	3.6512	5	0.73024	–	–	–
Cor total	542.6025	29	–	–	–	–

Standard deviation $= 0.67$, mean $= 9.31$, coefficient of variation (%) $= 7.16$, predicted residual error of sum of squares $= 22.65$, $R^2 = 0.98$, adjusted $R^2 = 0.97$, predicted $R^2 = 0.95$, adequate precision $= 30.97$
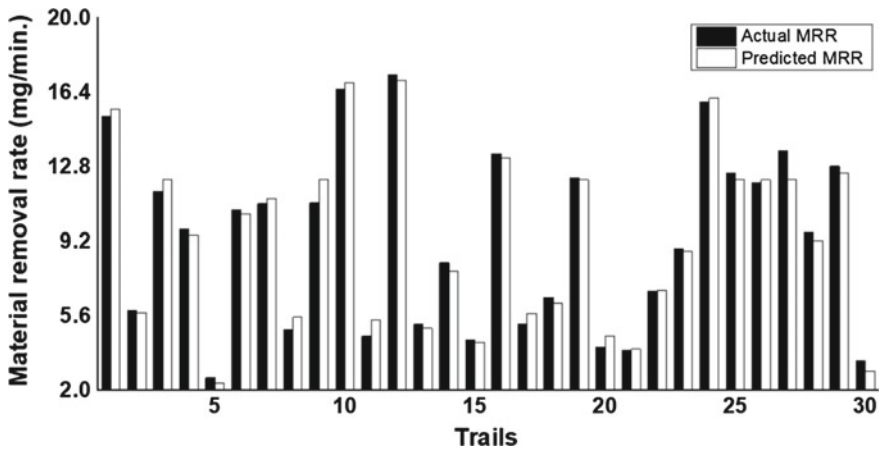
Fig. 31.10 Actual versus predicted results during UA-ECDT process

$$Y_1(\text{mg/min}) = -105.01792 + 2.16633 \times A - 1.01583 \times B + 0.88375$$
$$\times C + 2.31983 \times +0.11025 \times A \times B - 0.003475 \times A \times C$$
$$- 0.00325 \times A \times D - 0.024375 \times B \times C + 0.00675 \times B$$
$$\times D + 0.000475 \times C \times D - 0.014158 \times A^2 - 0.37646 \times B^2$$
$$- 0.00940208 \times C^2 - 0.074508 \times D^2 \pm \varepsilon \qquad (31.4)$$

A is applied voltage, B is pulse-on time, C is tool rotation rate, D is amplitude of vibrations, $Y_1 = $ material removal rate.

31.5   Parametric Evaluation

In this section, the effect of individual process parameters on MRR is analyzed. The
effect of process parameters (applied voltage, pulse-on time, tool rotation rate and
power rating) on MRR is depicted in Fig. 31.11. The graphs illustrated in Fig. 31.11
were plotted by varying the process parameters from their lower level to higher level
as defined in Table 31.1, while the rest of the process parameters were kept at their
central level.

The effect of applied voltage on MRR is depicted in Fig. 31.11a. It can be observed
that with an increase in applied voltage, the MRR increases. Because the increased
applied voltage increases, the electrochemical reactions in the electrolytic bath and
produces a large number of hydrogen gas bubbles over the tool electrode. The coa-
lescence of hydrogen gas bubbles forms a thick gas film over the tool electrode.
The breakdown of thick gas film produces high-intensity discharges. The energy
liberated by these high-intensity discharges removes the excessive material from the
work surface and consequently results in increased MRR with an increase in applied
voltage.

Fig. 31.11 Effect of individual process parameters on material removal rate **a** applied voltage,
b pulse-on time, **c** tool rotation rate and **d** power rating

In ECDM process, the use of pulse power supply is suggested by the previous investigators [14]. Where pulse-on time implies the heat input durations. The effect of pulse-on time on MRR is given i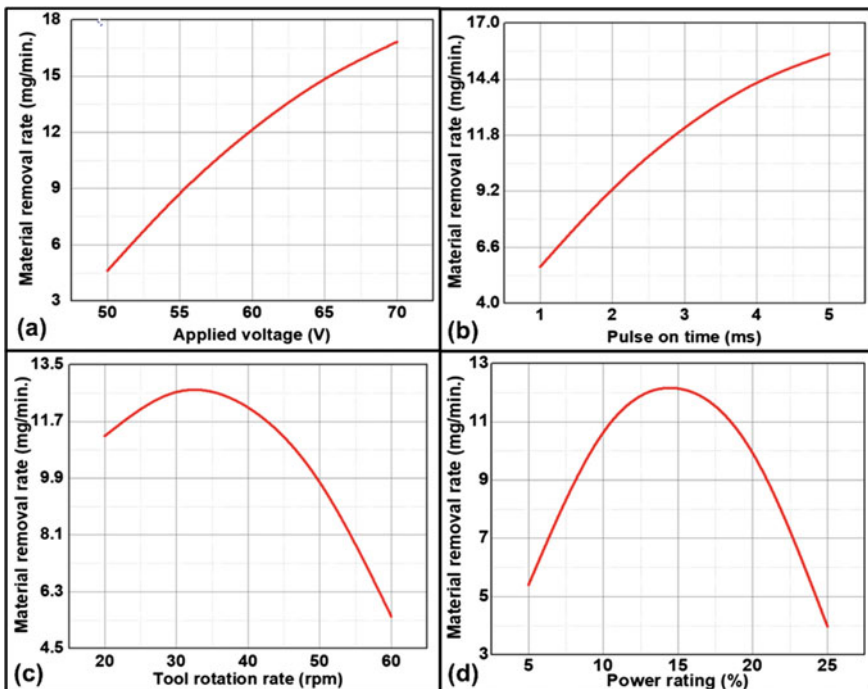n Fig. 31.11b. It was observed that with an increase in pulse-on time, the MRR increases linearly. The increased pulse-on time provides increased time duration to accumulate the gas bubbles over the tool electrode. Thus, it develops a thick gas film over the tool electrode. The breakdown of thick gas film produces high-intensity discharges. The energy liberated by these high-intensity spark discharges removes excessive material from the work surface and thereby results in higher MRR.

In ECDT process, the tool rotation rate is an important process parameter that decides the tracing rate of the tool electrode over the work material. In this investigation, the effect of the tool rotation rate is analyzed, and the respective plot is given in Fig. 31.11c. It was observed that with an increase in tool rotation rate, the MRR increases initially. However, beyond 30 rpm, the increase in the tool rotation rate decreases the MRR. Because higher tool rotation rate destabilizes the gas film formation due to the dominance of high centrifugal forces acted on gas film. The breakdown of thin and unstable gas film produces low-intensity low-frequency spark discharges and the energy liberated by these spark discharges resulted in low MRR.

The effect of power rating on MRR is depicted in Fig. 31.11d. It was observed that with an increase in power rating, the MRR increases up to 15%. This increase in MRR indicates the generation of thin and stable gas film over the tool electrode and the evacuation of debris and sludge from the machining zone. Thus, the replenished electrolyte at the machining zone generates stable gas film over the tool electrode, and the energy generated from this gas film removes the material in effective manners and exhibits higher MRR. However, beyond 15% power rating, the increase in power rating decreases the MRR. Because higher power rating possesses higher amplitude of vibrations and exerts high drag forces on gas bubbles. The acting of high drag forces on gas bubbles develops thin and unstable gas films over the tool electrode, whereas the electrolyte replenishment process works continuously with an increase in power rating. The energy generated by unstable gas film results in low MRR as shown in Fig. 31.11d.

31.6 Optimization

In manufacturing processes, the parametric optimization is an essential activity which has been motivated to save the energy resources through the selection of an appropriate combination of process parameters [15]. In the present investigation, a genetic algorithm was used to optimize the process parameters for higher MRR. The process parameters and functional settings that were used to iterate the genetic objective function in respect of the parametric combinations are tabulated in Table 31.4. The variation in MRR with a number of generations is provided in Fig. 31.12a. The value of individual process parameters to optimized the response characteristic is given in Fig. 31.12b.

Table 31.4 Parameters and functional settings for genetic algorithm

Operations/parameters	Function/values
Population type	Double vector
Size	90
Creation function	Feasible population
Selection (Size)	Tournament (2)
Reproduction	Crossover fraction (0.7)
Mutation	Adaptive feasible
Crossover function/ratio	Intermediate/1
Generation	75
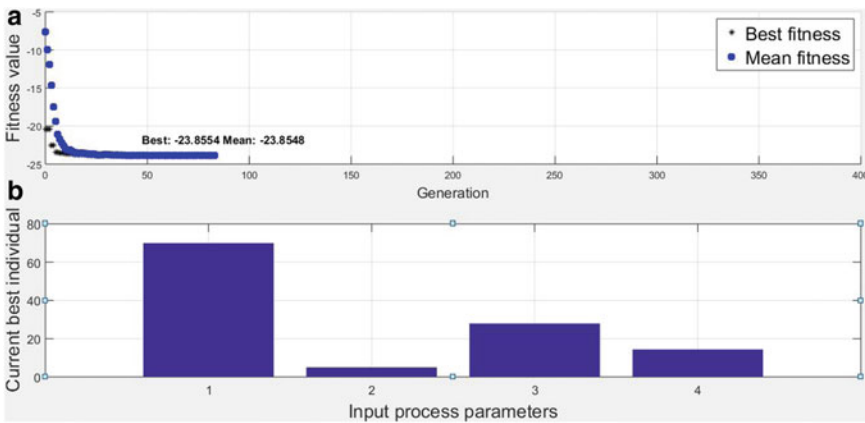
Fig. 31.12 **a** Variation of MRR with number of generations and **b** value of individual process parameters

The limits of process parameters are given in Table 31.5. The optimized parametric combination obtained from the genetic algorithm optimized technique is given in Table 31.5. Further, to validate the optimized parametric combination, the confirmation experiments were conducted. Figure 31.13 shows the optical profile of machined work material obtained at optimized conditions. The confirmation results exhibit an average error below 2%. This indicated a good combination of parameters predicted through the optimized technique for higher MRR.

31.7 Conclusions

The conclusions drawn from the present investigation are as follows:

1. The incorporation of ultrasonic vibrations in ECDT system improves the material removal rate (MRR) by 5 times than the ECDT process.

Table 31.5 Predicted and confirmation results to optimized the process parameters for higher MRR

Predicted results					
Predicted optimum parameter levels					Predicted responses
	A	B	C	D	Y_1
Limits	$50 \leq A \leq 70$	$1 \leq B \leq 5$	$20 \leq C \leq 60$	$5 \leq D \leq 25$	
Units	(V)	(ms)	(rpm)	(%)	(mg/min.)
	70	5	28	15	23.92
Conformation results					
	Optimum parameter level				Responses
	A	B	C	D	Y_1
Trails	(V)	(ms)	(rpm)	(%)	(mg/min)
1	70	5	28	15	22.40
2	70	5	28	15	23.85
3	70	5	28	15	25.04
4	70	5	28	15	25.82
Avg. (Y_1)					24.27
Error (%) = 1.49%					

Fig. 31.13 Machined work material at optimized conditions
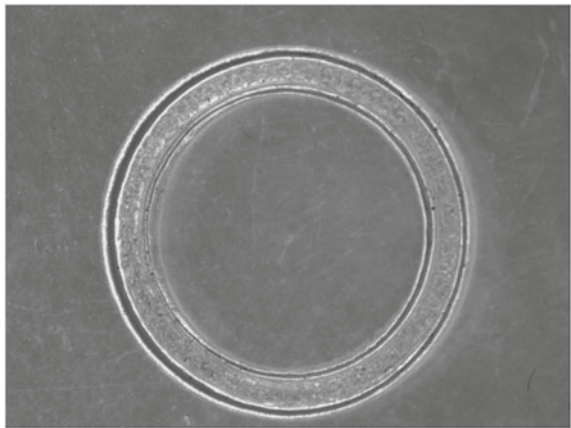
2. The use of ultrasonic vibrations in ECDT process develops thin and stable gas film over the tool electrode, and the breakdown of this gas film produces high-frequency, high-intensity spark discharges.
3. The use of higher ECD energy in terms of higher applied voltage and pulse-on time results in higher MRR during UA-ECDT process.
4. The regression model exhibited a close agreement with experimental observations.

5. The use of tool rotation rate improves the MRR. But beyond a certain limit, it deteriorates the gas film characteristics and consequences low MRR.
6. The power rating of 15% was found appropriate value to produce stable gas film and higher MRR.
7. The parametric combination of applied voltage of 70 V, pulse-on time of 5 ms, tool rotation rate of 28 rpm and power rating of 15% is found more suitable to obtain the higher MRR during UA-ECDT process.

References

1. Singh, T., Dvivedi, A.: Developments in electrochemical discharge machining: a review on electrochemical discharge machining, process variants and their hybrid methods. Int. J. Mach. Tools Manuf. **1**(105), 1–3 (2016)
2. Singh, T., Dvivedi, A.: An ECDM approach for the development of 3D microchannels on glass substrates. Int. J. Res. Eng. Techn. **5**, 125–127 (2016)
3. Jha, N.K., Singh, T., Dvivedi, A., Rajesha, S.: Experimental investigations into triplex hybrid process of GA-RDECDM during subtractive processing of MMC's. Mater. Manuf. Processes **34**(3), 243–255 (2019)
4. Singh, T., Dvivedi, A.: On performance evaluation of textured tools during micro-channeling with ECDM. J. Manuf. Processes **30**(32), 699–713 (2018)
5. Singh, T., Arya, R.K., Dvivedi, A.: Experimental investigations into rotary mode electro-chemical discharge drilling (RM-ECDD) of metal matrix composites. Mach. Sci. Technol. (2019)
6. Pawariya, K., Dvivedi, A., Singh, T.: On performance enhancement of electrochemical discharge trepanning (ECDT) process by sonication of tool electrode. Precis. Eng. **1**(56), 8–19 (2019)
7. Gautam, N., Jain, V.K.: Experimental investigations into ECSD process using various tool kinematics. Int. J. Mach. Tools Manuf. **38**(1–2), 15–27 (1998)
8. Jain, V.K., Chak, S.K.: Electrochemical spark trepanning of alumina and quartz. Mach. Sci. Technol. **4**(2), 277–290 (2000)
9. Chak, S.K., Rao, P.V.: Trepanning of Al2O3 by electro-chemical discharge machining (ECDM) process using abrasive electrode with pulsed DC supply. Int. J. Mach. Tools Manuf. **47**(14), 2061–2070 (2007)
10. Sarkar, B.R., Doloi, B., Bhattacharyya, B.: Investigation into the influences of the power circuit on the micro-electrochemical discharge machining process. Proc. Inst. Mech. Eng., Part B J. Eng. Manuf. **223**(2), 133–144 (2009)
11. Singh, T., Sharma, A.K., Dvivedi, A.: Experimental investigations on the effect of energy inter-action durations during micro-channeling with ECDM. In: AIMTDR 2018, Anna University, Chennai
12. Venkatesh, G., Singh, T., Sharma, A.K., Dvivedi, A.: Finishing of micro-channels using abrasive flow machining. In: Proceedings of the International Conference on Research and Innovations in Mechanical Engineering 2014, pp. 243–252. Springer, New Delhi
13. Singh, T., Sharma, A.K., Dvivedi, A.: Influence of process parameters during Fabrication Of SI Microchannels Using Microultrasonic Machining. i-Manager's J. Mech. Eng. **3**(3), 1 (2013)
14. Gupta, P.K., Dvivedi, A., Kumar, P.: Effect of pulse duration on quality characteristics of blind hole drilled in glass by ECDM. Mater. Manuf. Processes **31**(13), 1740–1748 (2016)
15. Singh, T., Dvivedi, A.: On pressurized feeding approach for effective control on working gap in ECDM. Mater. Manuf. Processes **33**(4), 462–473 (2018)

Chapter 32
Acoustical Properties of Secondary Fibre-Based Natural Materials and Their Composites—A Brief Study

K. M. Rakesh, N. S. Sujith, and Srinidhi Ramachandracharya

Abstract Natural fibre-based materials and their composites in recent times are gaining much relevance for acoustical applications. This is primarily because their sound absorption properties are very much closer to existing commercial synthetic materials available in the market. And secondarily, due to an added advantage like lower cost, better availability, faster decomposition, lesser carbon emission during manufacturing and unique thermal properties on burning when compared to synthetic- or polymer-based absorption materials. Further, the mechanical properties of these materials are also found to be good and can be considered for design and development of structures for practical interior acoustical applications. Thus, researchers are considering natural fibre-based materials as the potential materials for replacing existing commercial acoustical materials for ensuring greener and safer environmental conditions for future generations.

Keywords Natural fibres · Sound absorption · Mechanical properties · Acoustical applications

32.1 Introduction

Natural fibres were known to people as a type of fabric material since 8000 BC. Flax could be the oldest fibre used by mankind [1]. Silk is a natural protein fibre; according to oldest Chinese literature, silk culture began when a Chinese empress observed and studied life of silkworms and their features [2]. During 5000–3300 BC, Ramie was known to be used in mummy cloths in Egypt. Around 4000 BC, linen and hemp fabrics existed in Europe and the use of hemp fibre dates back into Stone Age [3]. Cotton fibres were found in caves in Mexico over 7000 years back. Grass and straw were used as reinforcing fibre in mud bricks for many generations. Until first artificial fibres were made commercially available in 1885, textile industry was completely dependent on plant- and animal-based natural fibres [4]. Animal fibres include silk

K. M. Rakesh (✉) · N. S. Sujith · S. Ramachandracharya
Department of Mechanical Engineering, JSS Science and Technology University, Mysuru, Karnataka, India

fibre and hairs of animals like horse, bovine, rabbit, goat and camel family. These animal fibres are used to make luxury and high-valued products mainly because of their unique features of comfort and softness. The market share represented by these luxury animal fibre is less than 0.1% in global fibre production as reported by Hunter [5]. All these literatures suggest us that, the awareness and application of plant fibres increased from raw fibres to fabric material, cloths to reinforcing fibres to composite materials along with animal fibres for making apparel to luxury and high-valued products with passage of time. UN and its Food and Agriculture Organization (FAO) proclaimed year 2009 as International Year of Natural Fibres (IYNF) to encourage governments to form friendly policies to address problems faced by natural fibre industries and to promote international partnership [6].

Natural fibre is defined as fibrous plant material produced as a result of photosynthesis [7]. Plants producing natural fibres are generally classified into two types in terms of utilization as primary plants (grown mainly for their fibre content) and secondary plants (where fibres come as a by-product from some primary utilization). Cotton, hemp, jute, sisal and kenaf are some examples of primary plant fibres, while coir, sugarcane bagasse, paddy straw, pineapple, cereal stalks, oil palm, etc., are some example for secondary plant fibres. Natural fibres can also include hair, feather, wool and silk fibres and mineral fibres such as asbestos and glass. These natural fibres can be extracted from plants by three methods, namely mechanical, biological and chemical methods. Based on its botanical type, natural fibres are classified into bast fibre, leaf fibre, grass or reeds fibres, etc. Natural fibres can also be classified into different types like organic or inorganic, hard or soft fibres, long or short fibres, cellulose content, strength, colour and source (primary or secondary). Further, classification can also be made based on its applications like use in paper making, textiles, composites, etc.

Natural fibres find numerous applications in textile, agriculture, paper, automobile and construction industries to name a few. In greenhouse culture, agrotextiles made out of natural fibres, namely hemp or flax fibre bundle can be used as a substitute for plastic mulch for protecting young plantings [8]. Sivakumar Babu et al. [9] report that swelling behaviour of expansive soils is reduced by use of coir and use of coir further improved their engineering properties. Good sorption capacity of natural fibres finds application in geotextiles and insulating material manufacturing [10]. Piotrowski and Carus [11] reports that pulp of natural fibres are particularly used for making special papers for bank notes, technical filters, cigarettes, etc., as they are desired to be thinner with good strength and durability. He further mentions that flax and hemp pulps dominate in production of cigarette paper production. Hemp fibre reinforced plastics were used by Henry Ford to form car panels as early as 1930s. Karus et al. [12] reports that use of natural fibre in automotive composites increased from 10,000 tons in 1999 to 19,000 tons in 2005. Of this 19,000 tons, flax contributed for more than 60%. Interesting fact is that, the flax used was in most cases as a by-product of textile long flax production from Europe. Construction industry being a major consumer of composite material earlier dominated by glass reinforced plastics (GRPs) is now exploring natural fibre composites (NFCs) because of their potential to be used as constructional and structural material and a suitable material

Table 32.1 Mechanical properties of selected natural fibres

Fibre	Density (g/m^3)	Length (mm)	Diameter (mm)	Elongation at break	Tensile strength (MPa)	Equilibrium moisture content EMC (%)
Pineapple (PALF)	1.5	3–8	8–41	1–3	170–1627	13
Bagasse	1.2	0.8–2.8	10–34	0.9	20–290	10
Jute	1.23	0.8–6	5–25	1.5–3.1	187–773	12
Coir	1.2	0.3–3	7–30	15–25	176–234	10
Cotton	1.21	15–56	12–35	2–10	287–597	8
Flax	1.38	10–65	5–38	1.2–3	343–1035	7

Courtesy Pickering [7]

for replacing GRPs [13]. In recent years, natural fibres are heading their way towards acoustical applications.

32.2   Natural Fibre Properties

Unlike synthetic fibres, the properties of natural fibres vary significantly from one region to another region. The reason is that, these plants from which fibres are extracted depend upon climatic conditions, type and fertility of soil, water and sunlight availability, etc. And animal hair fibres and silk fibres depend upon the health and climatic conditions where animals live in. Thus, it can be noticed that same fibre may have different properties for different regions.

32.2.1   Mechanical Properties

The mechanical properties of some of the natural fibres represented in Table 32.1 was obtained from literature studies [7]. The equilibrium moisture content (EMC) of different natural fibres at 65% relative humidity (RH) and 21 °C is shown in Table 32.1.

32.2.2   Fibre Composition

The chemical composition of natural fibres is essential features to be known in order to study the material behaviour. The literature has shown that, this composition of

Table 32.2 Fibre composition of selected natural materials

Fibre	Cellulose	Lignin	Pentosan	Ash	Silica
Paddy straw	28–48	12–16	23–28	15–20	9–14
Sugar cane	32–48	19–24	27–32	1.5–5	0.7–3.5
Wheat	29–51	16–21	26–32	4.5–9	3–7
Jute bast	45–63	21–26	18–21	0.5–2	–
Kenaf bast	44–57	15–19	22–23	2–5	–

Courtesy Pickering [7]

plant fibres varies depending upon the growth or age of plant, the region where it is grown, availability of water, etc. The results found in the literature are represented here in Table 32.2.

32.3 Secondary Fibres

As discussed earlier, secondary fibres refer to those fibres which are not grown primarily for their fibre content. In other words, these are the fibres obtained mainly as a by-product or waste in the process of cultivation or processing of the parent plant parts or its fruit. Pineapple leaf fibre (PALF), coconut coir fibre (CCF), sugarcane bagasse and paddy fibre are some examples of these secondary fibres discussed in this chapter.

32.3.1 Pineapple Leaf Fibre (PALF)

Pineapple also called as Ananas Comosus belongs to the family of Bromeliaceous which is a short tropical plant that grows 1–3 m in height and width [14]. Originated in Brazil, this fruit has spread to other parts of the world. Asia, South Central America and Africa are the main producers. As per the reports of FAOSTAT of United Nations, 27.4 million tons of pineapple was produced in the 2017 worldwide, out of which India's share is 1.8 million tones. In India, it is abundantly grown in entire north eastern parts, West Bengal, Karnataka, Kerala, Goa, Maharashtra and Bihar. Pineapple plants usually consist of a rosette of 60–80 leaves that are generally 1–2-centimetre wide and 1 m in length. About 100 tones of fresh leaves are produced from a hectare. These leaves yield about 2.5–3.5% which are white, creamy and soft in texture [14]. PALF extraction from plant to fibre is shown in Fig. 32.1.

After harvesting pineapple fruit, generally, the leaves are disposed due to ignorance from farmers and local communities about the commercial use of these leaves.
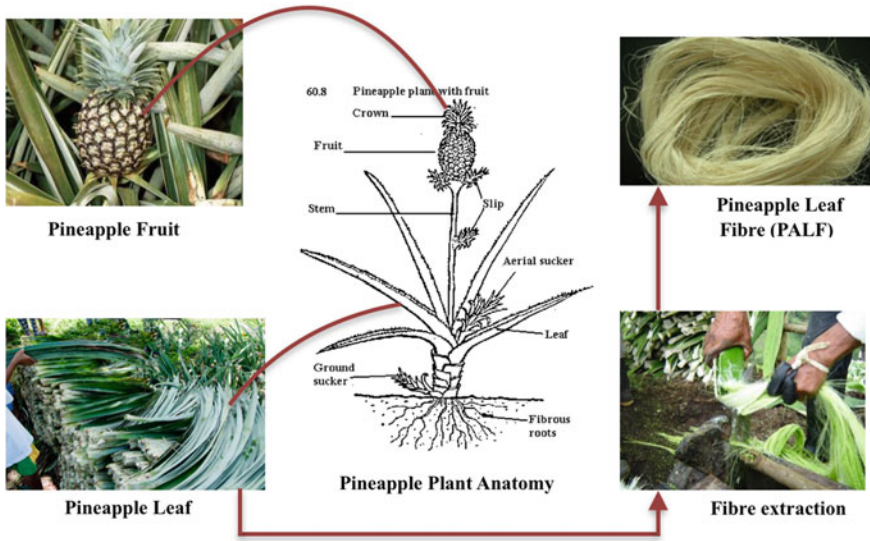
Fig. 32.1 PALF extraction from plant to fibre

Several studies are done in order to find out the potential of these leaves. There are numerous studies done by researchers on various aspects of pineapple leaf fibres (PALF). Several authors analysed its physical, mechanical, chemical and even acoustical properties of various pineapple species [2].

PALF extraction methods: Following methods can be employed to extract PALF fibres.

32.3.1.1 Retting

It is a process employing the action of microorganisms and moisture on plants to dissolve or rot away much of the cellular tissues surrounding bast-fibre bundles, and so facilitating separation of the fibre from the stem [14] as shown in Fig. 32.2. It is used in the production of fibre from plant materials.

32.3.1.2 Scraping

In this method, the fibre is separated from the surrounding leaf tissue by decortication, a hand or machine scraping or peeling process, then cleaned and dried as shown in Fig. 32.3.

Fig. 32.2 Retting

Fig. 32.3 Scraping

32.3.1.3 PALF Machine Extraction

In this work, PALF is produced by novel technology invented as illustrated in Fig. 32.4. PALF is extracted by a decortication machine named pineapple leaf fibre machine 1 (PALF M1) shown in Fig. 32.4. This machine uses blades to remove the waxy layer on the pineapple leaf rather than forcing it out by crushing. Furthermore, the blades are designed in uniquely, where the number of blades used, its size along with the angle of the two blades ensure that the leaf does not snap during the extraction process. Upon entering the blades, the leaf is subjected to a sort of "grinding" and the outer waxy layer will be removed during this first step. During second step, when the leaf is being pulled off, yet again, the leaf will be subjected to grinding for the second time, which removes the entire waxy layer left out during the first step. The extracted PALF is then being scoured and dried by using pineapple leaf fibre machine 2 (PALF M2) as shown in Fig. 32.5. At this stage, the green debris accumulated at PALF surface will be further cleaned and removed. Apart from green debris removal, this machine also will dry the fibre at the same time [15].

Fig. 32.4 Pineapple leaf fibre machine 1

Fig. 32.5 Pineapple leaf fibre machine 2

Putra et al. [16] experimentally investigated the effect of density, thickness and application of air gap behind PALF sample to analyse its sound absorption characteristics using ISO 10534-2 Impedance tube testing. Based on their test results, they claimed that with increase in density of PALF, there is increase in the flow resistivity and tortuosity. Keeping bulk density constant, they studied sound absorption characteristics by varying the thickness of sample. They found that, increasing the thickness of the sample has increased sound absorption coefficient level ($\alpha > 0.5$) towards lower frequencies.

Sound absorption coefficient further improved in the lower frequency range with the inclusion of air gap layer behind thinner samples. For thicker samples of PALF, application of air gap layer behind the sample had minor improvement of sound absorption coefficient but the values still remained over 0.5. So, the researchers found introducing air gap behind sample as a good alternative technique instead of

increasing the thickness of the sample. Researchers also compared performance of PALF with PU-foam absorber and mineral rock wool. PALF had comparable results as that of mineral rock wool and superior value for rock wool at frequency range of 500–1 kHz, but above 2.5 kHz PALF had superior sound absorption coefficient with an average of 0.9. These test results encouraged the researchers to propose PALF as potential sound absorbing material above 2.5 kHz. PALF is found to have good mechanical properties too; so, there exists a need to explore sound absorption properties of PALF in combination with other natural and synthetic fibres.

Uma Devi et al. [17] have investigated extensively on the tensile, flexural and impact behaviour of PALF-reinforced polyester composites as a function of fibre loading, fibre length and fibre surface modification. The tensile strength and Young's modulus of the composites were found to increase with fibre content in accordance with the rule of mixtures. They found that, mechanical properties of PALF fibres were optimum at a fibre length of 30 mm. The specific flexural stiffness of the composite is about 2.3 times greater than that of neat polyester resin. They noticed a significant improvement in tensile strength for the composite when fibres were treated with silane A172. They claim, PALF polyester composites possess superior mechanical properties compared to other cellulose-based natural fibre composite.

Arib et al. [18] studied tensile, flexural and impact behaviour of PALF—Polypropylene composite as a function of volume fraction. They found that, increase in fibre content in accordance with rule of mixtures had increased tensile modulus and tensile strength of the composite material. The flexural strength of the composites containing 5.4% volume fraction was found to be higher than that of pure polypropylene resin. The flexural modulus and flexural stress of the composites increased with the increase of volume fraction. They suggested that, the cellular structures of the plant fibres provide excellent insulation against heat and noise. They claim, superior mechanical properties of PALF are associated with their high cellulose content. The results of this study conclude that a useful composite with good strength could be successfully developed using pineapple fibres as a reinforcing agent for the polyester matrix.

32.3.2   *Coconut Coir Fibre (CCF)*

Coir is a fruit fibre obtained from coconut palm (Cocos Nucifera Linn) grown in tropical regions. It is a hard, versatile and natural fibre available in large quantities [19]. As per the reports of FAOSTAT of United Nations, 60.7 million tons of coconut was produced in the year 2017 worldwide, out of which India's share is 11.4 million tones. It is abundantly grown in Kerala, Karnataka, Tamil Nadu and several other states in India. Coir fibre is obtained by dehusking coconut and separating it from the hard-internal shell.

Coconut coir fibres (CCF) are extracted by a process of retting. Retting may be carried out at any time during the year either in freshwater or saline water, flowing water or stagnant water, deep waters or backwaters. The husks may be placed for
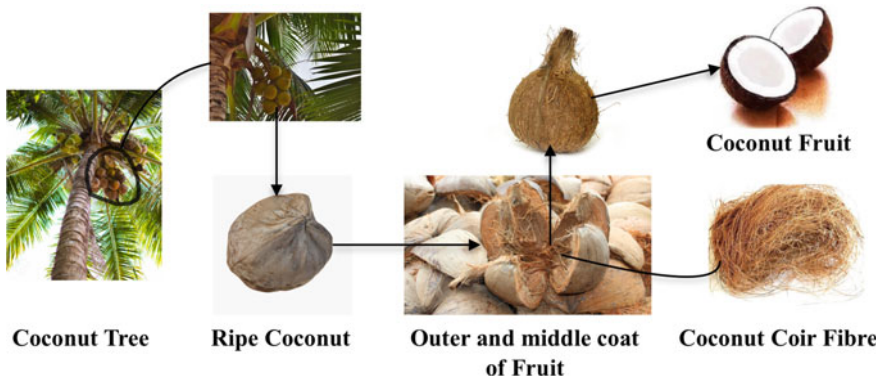
Fig. 32.6 Coconut fibre extraction from fruit to coir fibre

retting either in nets or in pits. It has been reported that the retting is quicker in the summer months but the colour of the fibre is brown. The fibres obtained from the husks retted in saline water are stronger and have a better colour (golden yellow); if fibres obtained from husks placed in fresh water, the retting is incomplete resulting in same amount of pith adhering to the fibre. Fibres obtained from retting in stagnant water were found to be weak. Husks soaked in the backwaters and placed upright in coir nets yielded better quality fibres, both in terms of strength and colour for grading purposes [19]. Coconut fibre extraction from fruit to coir fibre is shown in Fig. 32.6.

Zulkifi et al. [20] investigated the noise control using coconut coir fibre (CCF) with porous layer backing and perforated panel for sound absorption. From experimental data, they noticed that, noise absorption coefficient (NAC) of samples with 20 mm thickness without porous layer backing had maximum value in the frequency range of 3680–3860 Hz and the peak noise absorption value of 0.83 at frequency 3784 Hz. For samples with 10 mm thickness, the noise absorption coefficient (NAC) had a maximum value of 0.39 at frequency 5000 Hz. When samples were backed with woven cotton cloth (WCC), researchers noticed an overall increase in NAC values. With 10 mm thickness sample, there were maximum NAC values at 3753–3834 Hz with peak value of 0.96 at 3800 Hz. At lower frequency, NAC values increased significantly. Thus, with porous layer backing, there was overall increase in NAC values at all frequency range when compared to CCF without porous layer backing. The experimental results showed that CCF with perforated plate had higher value in lower frequency range from 600 to 2400 Hz and an optimum value was around 0.94–0.95 for frequency range of 2600–2700 Hz. Also, researchers noticed shift in the absorption coefficient peak to lower frequency range and decrease in NAC value at higher frequencies when perforated panels were used.

Lee et al. [21], in their research work suggests that, use of porous material promotes acoustic absorption and shifts the acoustic resonance frequencies to lower frequency bands. Thus, the researcher concludes with remarks that use of perforated panels and/or porous layer backing enhances NAC values of CCF, so that CCF can be used

as an alternative or replacement material for glass fibre-and mineral-based synthetic materials in future.

Nor et al. [22], in their research work studied the sound absorption using multi-layer coconut fibre as absorbing material component. The main parameter considered in this study is the acoustic absorption coefficient. Multi-layer acoustic absorbers consisting perforated plates, airspaces or porous materials are commonly applied in order to absorb broadband noise. The results indicated that the porosity of the perforated plate and the density of the porous material would considerably change the acoustic impedance and absorption coefficient of the acoustic absorber. The effect of airspace layer will increase the sound absorption in the low-frequency range. In the case of microperforated facing, the structure promotes the sound absorption coefficients in the low-frequency region, but it has the reverse effect in the high-frequency region. This study concludes that multi-layer coconut coir fibres and airspaces could increase the acoustic absorption coefficient.

Thus, we can conclude that coconut coir fibre (CCF) with porous layer backing and perforated panel increases that NAC significantly. Multi-layer coconut fibre consisting perforated plates, airspaces or porous materials increases the acoustic absorption coefficient. Since CCF possess good mechanical properties along with acoustical properties, it could be used as a potential sound absorbing material.

32.3.3 Sugarcane Bagasse

Sugarcane is a perennial grass and cultivated in tropical and sub-tropical regions in the world as a commercial crop. Sugarcane is mainly cultivated for its juice/sugar content, and it accounts to over 79% of sugar produced in the world. Beside this, it is also used as raw material for various food preparations like jaggery, falsernum, panela and beverages like fresh sugarcane juice, syrup, basi, rum, cachaca, etc., in different countries. A mature sugarcane stalk is typically composed of 11–16% fibre, 12–16% soluble sugars, 2–3% nonsugars and 63–73% water [23]. On harvesting the crop, its juice is extracted for its sugar content and only waste fibres are left behind which is called sugarcane bagasse. And it is processed further to serve it as a fodder for animals. Figure 32.7 describes the sequence involved in the same.

Sugarcane crop → Sugarcane waste straws → Sugarcane bagasse → Processed sugarcane bagasse material

Fig. 32.7 Sequence of stages involved in getting processed sugarcane bagasse material from raw sugarcane crop

Sugarcane bagasse is known for its applications as a potential fuel for energy production, as pulp for making papers, raw material to make plates and other one-time use food containers. However, only recently, researcher thought of utilizing this bagasse as a raw material for developing acoustical material, when they were exploring a suitable substitution for synthetic materials to address its environmental impact. Azam Putra et al. [24] studied utilization of sugarcane-wasted fibre as a sustainable acoustic material. They prepared two test samples with both having thickness of 1/2 inch with density of 1 and 3 grams, respectively, in two stages, pre-treatment stage and fabrication stage. Through impedance tube test results and comparative study of sugarcane sample with three layers of woven cloth absorber used in automotive applications, they found that acoustical performance of the sugarcane absorber with 1/2 inch thickness had comparable results as that of commercial sound insulator with average absorption coefficient of 0.65 at frequency 1.2–4.5 kHz.

Othmani et al. [25] studied acoustic properties of sugarcane waste-based material both experimentally using impedance tube and theoretically using Delany–Bazley model, Miki model and Komatsu model. They measured flow resistivity and sound absorption coefficient and used these two parameters for evaluation of material behaviour in absorbing noise. From their experimental test results, they claim that sound absorption coefficient was very close to 1 for some frequencies and was above 0.8 for frequencies above 500 Hz up to 4000 Hz. They also observed that the increase in flow resistivity decreased acoustic absorption coefficient. Loh et al. [26] claim that sugarcane bagasse can be easily modified chemically to improve its mechanical properties like tensile strength, flexural strength, impact strength and hardness. They also state that during manufacturing of polymeric composites, sugarcane bagasse can act as an effective reinforcement fibre. Further, they can also be used in various forms like cellulose fibre, comrind, pith, sugarcane bagasse ash, sugarcane straw ash, etc., during manufacturing of composites.

Thus, from literature, sugarcane bagasse is found to exhibit good mechanical and acoustical properties when used in suitable form. They are found to be compatible with adhesives and chemical modifications. Further, studying their chemical behaviour when used to form a composite with other natural and synthetic fibres will help researcher to develop a good sound absorber from bagasse.

32.3.4 Paddy Fibre

Paddy is derived from the Malay word *padi*, meaning "rice plant" [27]. Paddy is a well-known crop grown in tropical and sub-tropical regions. Processed rice is obtained from paddy after removal of rice-husk. Rice is a major staple food for most of the people in the world and is used as an essential ingredient of their diet. India and China together contribute to about 2/3rd of the total rice produced in the world. Notably, Asia is the world's largest producer as well as consumer of rice (Fig. 32.8).
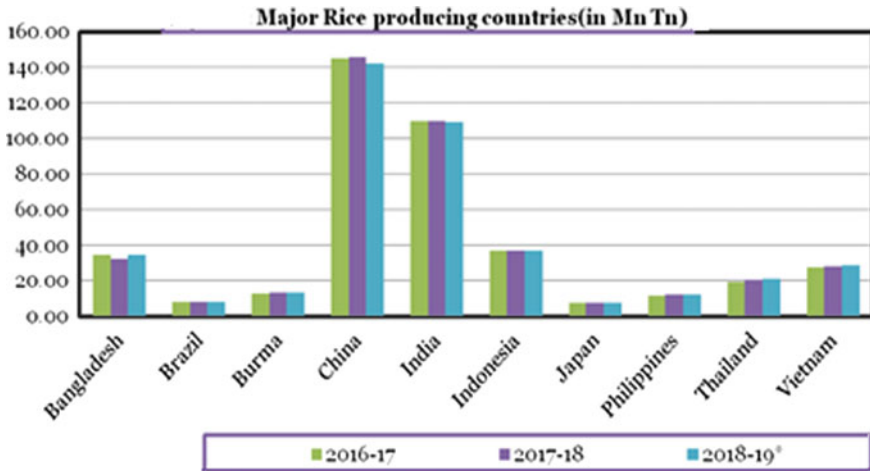
Fig. 32.8 Major rice producing countries in the world [28]. *Source* United states Department of Agriculture

Putra et al. [29] studied utilization of biomass from paddy waste fibres as sustainable acoustic material. Impedance test results for 2 g sample with 10 and 20 mm thickness showed that, 10 mm thick sample had good acoustic performance (α > 0.5) for frequencies above 3 kHz. For 20 mm thick sample, acoustic performance was good for frequencies below 3.5 kHz. The researcher noticed that with less density, there was reduction in flow resistivity. So, they prepared a new sample with fibre weight of 4 grams and noticed an overall increase in absorption coefficient to around 0.9 above 3.5 kHz. Samples with fibre weight of 6 grams showed a nonlinear relation between density and sound absorption coefficient. Researcher observed that, more fibres created more tortuous path with increase in resistivity. Introducing air layer behind the absorber improved sound absorption at low frequencies. They found that synthetic glass wool with thickness of 20 mm and paddy waste fibre with same thickness and 3 grams of fibre weight had the absorption coefficient of more than 0.5 above 1 kHz and can reach 0.8 on average above 1.5 kHz. Further, introduction of single layer of polyester fabric or air gap behind the sample had improved sound absorption coefficient. They proposed additional environmental tests like fire retardancy, fungal growth and humidity tests as the scope for future work and paddy fibre extraction from panicle and rice-husk of paddy is as shown in Fig. 32.9.

Mahzan et al. [30] studied sound absorbing properties of rice-husk-reinforced composite. Samples were prepared by mixing cleaned rice-husk with PU mixture in varying proportions like 5, 10, 15, 20, 25 and 30% for different samples. All samples showed good sound absorption properties at 250 Hz, while sample with 25% rice-husk had highest value. At lower frequencies 25% rice-husk sample had better absorption coefficient when compared to virgin PU, but at higher frequencies, virgin PU had better values of sound absorption. Thus, researchers claim that at a frequency range of 0–500 Hz, rice-husk samples showed good absorption values.
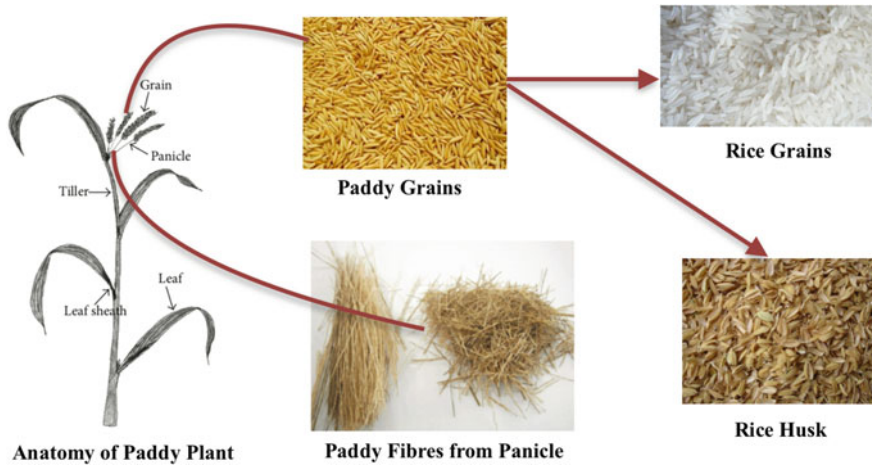
Fig. 32.9 Paddy fibre extracted from panicle and rice-husk of paddy

Basuchaudhuri in his book [31] referenced at the end, mentions that rice producers face competition among themselves and with other crop producers due to shortage of fertile land for paddy cultivation with increase in demand for rice production because of growing population. He has discussed about scientific and advanced way of increasing the yield of the paddy crop with available land. Thus, as acousticians, one can help them to increase their source of income by purchasing their cultivation waste, i.e. paddy fibres for development of acoustic properties, which otherwise would be used as either fodder for castles or as a means of firehood.

32.4 Acoustical Testing Methods

Gokulkumar et al. [32] have discussed various methods to measure acoustical properties as described in Fig. 32.10. The acoustical properties of materials in general can be found by experimental methods or can be predicted by using any of the theoretical models, empirical models and microstructure models.

32.4.1 Experimental Methods

Impedance tube test based on ISO 10534-2 or ASTM e1050 can be used to determine sound absorption coefficient for normal incidence.
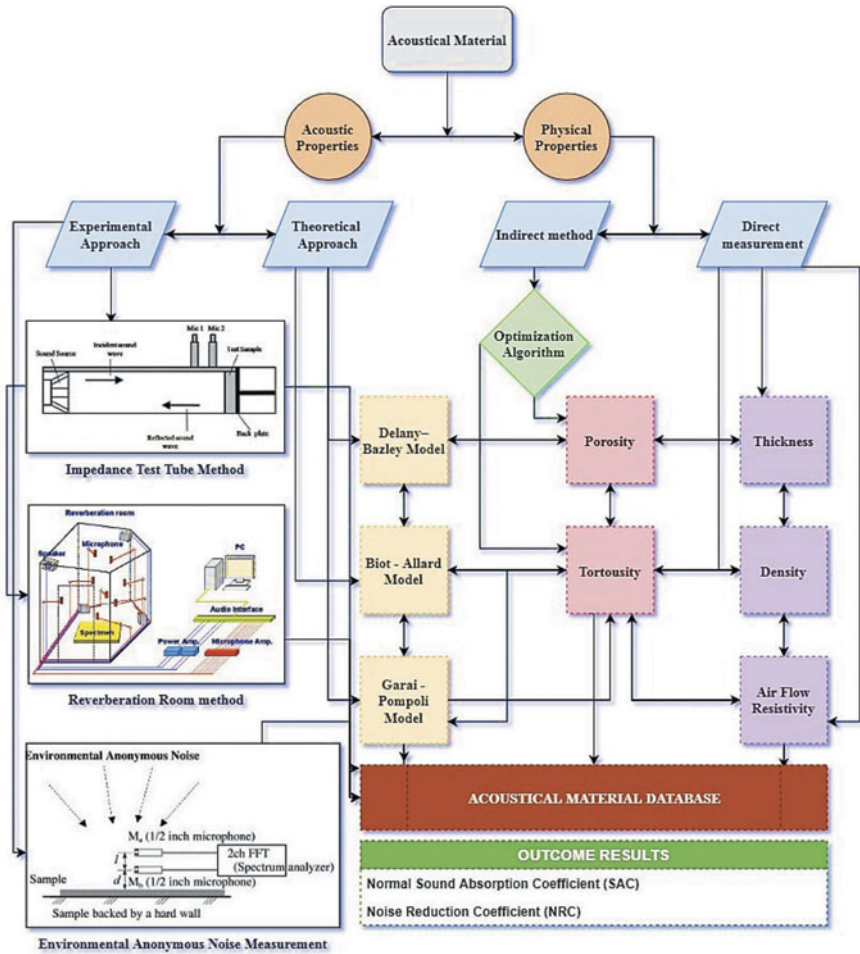
Fig. 32.10 Acoustic properties measuring methods. *Courtesy* Gokulkumar [32]

32.4.2 Empirical Methods

These models were created by applying regression equations to various parameters concerning the impedance and specific flow resistivity. And each empirical method is valid for restricted types of fibrous materials with certain intrinsic characteristics [33]. Some of these methods are Delany–Bazley model, Biot–Allard model, Miki model, Takeshi Komatsu model, Garai–Pompoli model, Ramis mode, Yoon model, etc.

32.4.3 Micro-structural Models

Microstructural approaches are based on the microscopic physical characteristics of acoustic wave propagation during fibrous materials. The complex independent variables including porosity, tortuosity, fibre density, viscoelasticity, thermal loss and air movement are emphatically considered during the modelling process [34]. Johnson–Allard method and Kino–Ueno methods are some of the microstructural models used.

32.5 Environmental Impact Assessment

The study and understanding about environmental impact of any developed material assume the significance due to increased concern for use of green and clean materials and technology. In this regard, natural fibres are found be environmentally friendly by many researchers due to their biodegradability. As most of the natural fibres are plant based, they are renewable in nature and easily available as they are either grown by farmers or themselves in forest and other areas. When compared to any synthetic fibres developed by man, which results in emission of greenhouse gases either during their manufacturing or during their burning, natural fibres stand out of this. By the way, plant-based natural fibres before their extraction from plants, actually consumes carbon monoxide, carbon dioxide etc., during photosynthesis and releases oxygen to environment. Even after they are used, they are harmless to environment.

In most of the under developed or developing countries, many of these secondary fibres, namely paddy fibre, wheat fibre, etc., are used as fodder, while fibres like coconut coir as a means of firehood and for making mats/carpets, etc. But, in this chapter, we have discussed briefly, how these secondary fibres can be used for technical applications like noise control other than already known applications. The development of commercial technical materials and products out of these natural fibres will enhance the income level for its manufactures as they are cheaply available in market or freely in nature. Further, the replacement cost is minimal as their manufacturing cost itself is minimum due to their easy and better availability. Their disposal at the end of their use is friendly to environment.

32.6 Challenges for the Use of Natural Fibres

Use of natural fibres for any commercial applications has following challenges, may be due to their chemical composition or cultivation and harvesting methods.

- Moisture absorption
- Poor flame retardancy
- Fungal or microbial growth

- Variation in fibre composition

Researchers are trying to fix these issues, may be individually addressing each such issue. But the fact is that, each of these issues is interdependent. For example, moisture absorption may appear to be good in terms of increasing the fire retardancy of these fibres. However, moisture absorption can degrade the functionality of developed material and may attract microbial growth on the material. Moreover, the percentage of constituents of fibres, namely cellulose, hemicellulose, lignin and pectin has a direct impact on their resistance to moisture absorption, flame propagation or fungal growth. Thus, addressing these challenges in a mutually inclusive way is the need of the hour.

32.7 Conclusion

Literature reveals that, secondary natural fibre-based materials and their composites have a high potential for replacing commercial synthetic sound absorption materials. Further, as secondary fibre-based materials are developed from agrarian waste, materials used with the appropriate standard formats for specific applications could serve as a source of revenue for growers/farmers too. These natural fibres have an added advantage of environmental friendliness, low cost, etc. However, fibre sensitivity issues are present in natural fibres and these fibres in applications may suffer with problems relating to humidity, fungal growth and fire hazard to name a few apart from degradation with time and other natural conditions under which the same are used. Hence, there is a huge potential for exploring combination of these secondary natural fibres with other natural fibres and polymer/synthetic fibres. Materials used as composites, their combined properties, methods to humidify fibres and maintaining their property profiles are few of the challenges which could foresee the increase in applications with relative dependence. Short-term applications with few of the changes may be the immediate answer to seeking solutions as alternatives. Exploring the long-term perspectives fulfilling the acoustical properties apart from others are to be focused into futuristic studies in applications. Further, investigation may be made towards generating various models to suggest optimization in fibre properties to enable the use of appropriate combinations to get the best desired results for acoustical applications of different fibres in these secondary fibre-based composites.

References

1. Taylor, J.H.: Unwrapping a Mummy: The Life, Death and Embalming of Horemkenesi. British Museum Press, London (1995)
2. Franck, R.R. (ed.): Silk, mohair and other luxury fibres. Woodhead Publishing, Cambridge (2001)

3. Czerniak, L., Kirkowski, R., Kozlowski, R., Zimniewska, M.: Proceedings: Symposium of Hemp, Flax and Other Bast Fibrous Plants: Production, Technology and Ecology. Institute of Natural Fibers, Poznan, Poland, p. 18 (1998)
4. Kozlowski, R.M. (ed.): Handbook of Natural Fibres: Types, Properties and Factors Affecting Breeding and Cultivation. Elsevier (2012)
5. Hunter, L.: Mohair, cashmere and other animal hair fibres. In: Handbook of Natural Fibres, pp. 196–290. Woodhead Publishing (2012)
6. Moir, B., Plastina, A.: International year of natural fibers. Cotton Promotion Bull. (2009)
7. Pickering, K.L.: Properties and Performance of Natural—Fibre Composites. Woodhead Publishing limited, Cambridge, England (2008)
8. Carus, M., Gahle, C., Pendarovski, C., Vogt, D., Ortmann, S., Grothenhermen, F., Breuer, T., Schmidt, C.: Studie zur Markt- und Konkurrenzsituation bei Naturfasern und Naturfaser-Werkstoffen (Deutschland und EU), Gu¨lzower Fachgespra¨che 26, FNR, Gu¨lzow, Germany (2008)
9. Sivakumar Babu, G.L., Vasudevan, A.K., Sayida, M.K.: Use of coir fibers for improving the engineering properties of expansive soils. J. Nat. Fibre **5**(1), 61–75 (2008)
10. Graupner, N., Müssig, J.: Technical applications of natural fibres: An overview. In: Industrial Applications of Natural Fibres: Structure, Properties and Technical Applications 1 (2010)
11. Piotrowski, S., Carus, M.: Natural fibres in technical applications: market and trends. In: Industrial Applications of Natural Fibers: Structure, Properties and Technical Applications, pp. 73–86. Wiley, Chichester (2010)
12. Karus, M., Ortmann, S., Gahle, C. Pendarovski, C.: Use of Natural Fibres in Composites for the German Automotive Production from 1999 till 2005. nova-Institut, Huerth, Germany (2006)
13. Fan, M., Fu, F. Introduction: A perspective–natural fibre composites in construction. In: Advanced High Strength Natural Fibre Composites in Construction, pp. 1–20. Woodhead Publishing (2017)
14. Reddy, N., Yang, Y.: Innovative Biofibers from Renewable Resources. Springer, Berlin Heidelberg (2015). https://doi.org/10.1007/978-3-662-45136-6_10
15. Yusofa, Y., Yahyaa, S.A., Adama, A.: Novel technology for sustainable pineapple leaf fibers productions. Procedia CIRP **26**, 756–760 (2015)
16. Putra, A., Or, K.H., Selamat, M.Z., Nor, M.J.M., Hassan, M.H., Prasetiyo, I.: Sound absorption of extracted pineapple-leaf fibres. Appl. Acoust. **136**, 9–15 (2018)
17. Uma Devi, L., Bhagawan. S.S., Thomas, S.: Mechanical Properties of Pineapple Leaf Fiber-Reinforced Polyester Composites. Wiley (1997). CCC 0021-8995/97/091739-10
18. Arib, R.M.N., Sapuan, S.M., Ahmad, M.M.H.M., Paridah, M.T., Khairul Zaman, H.M.D.: Mechanical properties of pineapple leaf fibre reinforced polypropylene composites. Mater. Des. **27**, 391–396 (2006)
19. Satyanarayana, K.G., Kulkarni, A.G., Rohatgi, P.K.: Regional Research Laboratory, Trivandrum 695019. Proc. Indian Acad. Sci. (Eng. Sci.) **4**(4), 419–436 (1981), Printed in India
20. Zulkifi, R., Zulkarnain, Z., Nor, M.J.M.: Noise control using coconut coir fiber sound absorber with Porous layer backing and perforated panel. Am. J. Appl. Sci. **7**(2), 260–264 (2010). ISSN 1546-9239
21. Lee, F.C., Chen, W.H.: Acoustic transmission analysis of multi-layer absorbers. J. Sound Vibr. **248**, 621–634 (2001)
22. Nor, M.J.M<=., Jamaludin, N., Tamiri, F.M.: A preliminary study of sound absorption using multi-layer coconut coir fibers. Electron. J. Tech. Acoust. (2004). http://webcenter.ru/~eeaa/ejta/
23. Sugarcane, In Wikipedia, The Free Encyclopedia (2019, August 22). Retrieved 15:42 from https://en.wikipedia.org/wiki/Sugarcane
24. Putra, A., Abdullah, Y., Efendy, H., Md Razali, W.M.F., Py, M.S.: Utilizing sugarcane wasted fibres as a sustainable acoustic absorber. Procedia Eng. **53**, 632–638 (2013)
25. Othmani, C., et al.: Experimental and theoretical investigation of the acoustic performance of sugarcane wastes-based material. Appl. Acoust. **109**, 90–96 (2016)

26. LohY, R., et al.: Sugarcane bagasse—the future composite material: a literature review. Resour. Conserv. Recycl. **75**, 14–22 (2013)
27. "Paddy", Merriam Webster. Retrieved 15 July 2007
28. Commodity profile for Rice—March 2019. http://agricoop.nic.in/sites/default/files/
29. Putra, A., Adbullah, Y., Efendy, H., Mohamad, W.M.F.W., Salleh, N.L.: Biomass from paddy waste fibres as sustainable acoustic material. Adv. Acoust. Vibr. (2013)
30. Mahzan, S., et al.: Investigation on sound absorption of rice-husk reinforced composite. In: Proceedings of MUCEET 2009 Malaysian Technical Universities Conference on Engineering and Technology (2009)
31. Basuchaudhuri, P.: Cold Tolerance in Rice Cultivation. CRC Press (2014)
32. Gokulkumar, S., et al.: Measuring methods of acoustic properties and influence of physical parameters on natural fibers: a review. J. Nat. Fibers, 1–20 (2019)
33. Oliva, D., Hongisto, V.: Sound absorption of porous materials—accuracy of prediction methods. Appl. Acoust. **74**(12), 1473–1479 (2013)
34. Tang, X., Yan, X.: Acoustic energy absorption properties of fibrous materials: a review. Compos. A Appl. Sci. Manuf. **101**, 360–380 (2017)

Chapter 33
Design and Development of Retrofittable Fixture to Enhance the Effectiveness of LN$_2$ Delivery During Drilling Operation

Harsh Radadiya and Navneet Khanna

Abstract High temperatures generated during machining, that tend to damage the tool needs to be mitigated in order to achieve better tool life. Cryogenic machining addresses the issue of reducing high temperatures at cutting zone by using liquid nitrogen (LN$_2$). However, during supply, liquid nitrogen gets converted into gaseous form easily due to substantial temperature difference between surrounding and coolant. Another challenge lies in proper channelling of LN$_2$ to ensure efficient delivery of coolant at the cutting zone during machining process. Conventional nozzle used to spray coolant being not highly efficient to subjugate such an issue at high cutting speeds; an effective fixture for channelling and supply of liquid nitrogen is introduced. The ability of the fixture to fit into Vertical Milling Centre (VMC) and to perform its function without deterring any functions of VMC is its peculiarity. The fixture has the flexibility to facilitate numerous sizes of drill bits up to 16 mm diameter. Moreover, the fixture is designed to effectively work with varying work-piece thickness from 1 to 18 mm. This development work will enable higher cutting speeds for increased material removal and longer tool life by effectively transmitting liquid nitrogen directly to the cutting edge.

Keywords Design · Development · Retrofittable fixture · LN2 delivery · Drilling

Nomenclature

LN$_2$	Liquid nitrogen
VMC	Vertical milling centre
SS	Stainless steel

H. Radadiya (✉) · N. Khanna
Institute of Infrastructure Technology Research and Management, Ahmedabad, Gujarat 380026, India
e-mail: harshradadiya24@gmail.com

N. Khanna
e-mail: navneetkhanna@iitram.ac.in

33.1 Introduction

Dry machining often leads to excessive temperature at cutting zone that tends to damage the tool by reducing the hardness of cutting tool [1]. Coolant supplied at high pressures has substantially better impact on tool performance [2] than dry machining. However, high-pressure supply of coolant during wet machining demands for larger floor space, capacity to recycle and cool down the coolant for better performance [3]. Mineral oil-based cutting fluids are hard to recycle and insignificant in environment friendliness as compared to cryogenic coolant [4]. Improved tool life by using cryogenic machining for various hard-to-cut materials is well documented [5–7]. Proper heat dissipation and alleviation of chemical affinity between workpiece and tool lead to better surface integrity of workpiece in cryogenic machining [8]. Cryogenic machining also aids in higher material removal rates [9] which make cryogenic machining best for high-value end-use product.

Because cryogenic coolants operate at extremely low temperature, it becomes necessary to insulate it well while storing and supplying it to the cutting zones. However, storing the coolants is not as challenging as the supply of coolant effectively to weld zones. Not only a highly insulated path is required for supply of coolant with minimal heat loss but also a channel to spray cryogenic coolant to cutting zones. The work presented in this paper reflects about developing a fixture that effectively focalize the liquid nitrogen to the cutting edge of the drill bit. The work done includes the behaviour study of various materials in the sub-zero temperatures and designing a fixture attached with VMC machine for acute convergence of liquid nitrogen at the cutting zones to alleviate machining temperatures.

Before finalizing the design aspects for the cryogenic path, it becomes of utmost significance to understand the characteristics of liquid nitrogen which is used in cryogenic machining. Liquid nitrogen has an expedient property of achieving extremely low temperatures in its liquid form. Liquid nitrogen at 1 atmospheric pressure in equilibrium state has −196 °C temperature which allows instantaneous cooling of cutting zone during machining process. However, 1 atmosphere pressure does not allow for pressurized spraying of liquid nitrogen into cutting zone. As the pressure increases, temperature of liquid nitrogen increases at equilibrium phase [10] as shown in Fig. 32.1.

It is evident from Table 32.1 that there is a huge density difference for liquid and gaseous forms of nitrogen. But as the pressure increases, the difference in densities largely decreases. The table also shows how the difference in density does not change much in 10.8–13.8 bar as compared to initial difference in 1–10 bar. For such a high difference in the densities at lower pressure when the liquid is converted to gaseous form while transportation from its storage to the machining element, a huge density difference is likely to damage the supply line as well as other components associated with it. Liquefaction of nitrogen at very high pressure is again an expensive process due to which extremely high pressures cannot be used where difference in densities is substantially lower; this justifies the reason of using close to 10–15 bar pressure in application for cryogenic machining.
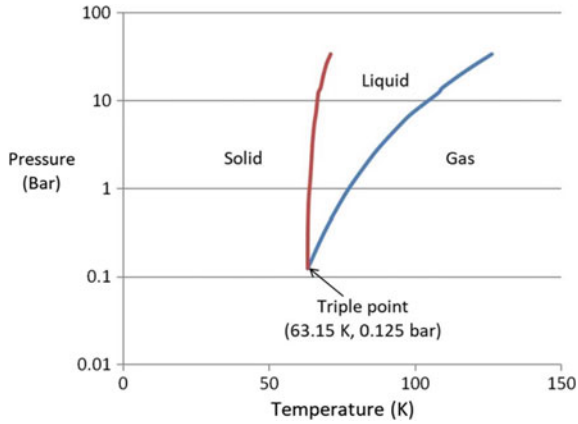
Fig. 32.1 Nitrogen phase diagram

Table 32.1 Density and specific weight of nitrogen at given temperatures and pressures [11]

State	Pressure (bar)	Temperature (K)	Density (kg/m^3)	Specific weight (N/m^3)	Difference in densities
Liquid at equilibrium	1.22	79	798.6	7831	145.35
Gas at equilibrium	1.22	79	5.494	53.9	
Liquid at equilibrium	5.41	95	718.3	7044	32.25
Gas at equilibrium	5.41	95	22.27	218	
Liquid at equilibrium	10.8	105	657.5	6448	14.62
Gas at equilibrium	10.8	105	44.96	441	
Liquid at equilibrium	13.8	109	629.1	6169	10.72
Gas at equilibrium	13.8	109	58.59	575	

33.2 Standard Set-up for Spraying Cryogenic

Conventionally, a nozzle performs the function of guiding LN$_2$ flow to appropriate location in workplace. Figure 32.2 demonstrates use of nozzle set-up to concentrate liquid nitrogen on drill bit. In this case, the tool gets cooled before machining takes place, but while machining the workpiece, liquid nitrogen does not reach the cutting
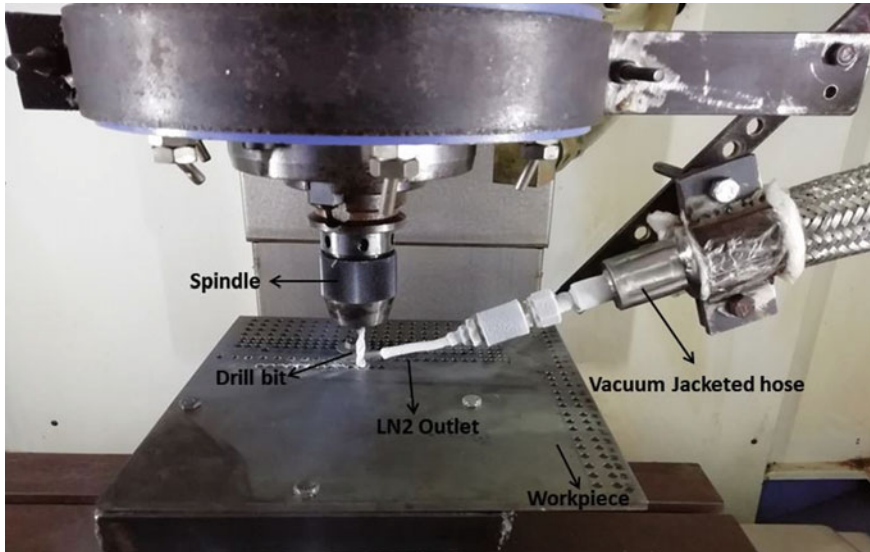
Fig. 32.2 Set-up used at manufacturing workshop of IITRAM for drilling of Ti6Al4V in VMC machine

zone. Here, the liquid nitrogen is supplied through a vacuum jacketed hose which takes liquid nitrogen from cryogen phase separator as presented in Indian Patents 201721031291A [12]. Hence, supplying liquid nitrogen through nozzle in similar way does not predominantly produce best result. For higher depth of cut in drilling operation, LN_2 does not reach the cutting zone but rather is sprayed on the part of tool that do not effectively take part in drilling. Hence, this issue needs to be addressed in an optimal way such that liquid nitrogen reaches the cutting zone even when the machining is taking place.

It is evident from Figs. 32.2 and 32.3 that although liquid nitrogen helps in increasing the tool life, but during the time of machining, due to the use of single-jet apparatus to spray LN_2, it is found that the liquid nitrogen is not used to its maximum potential. To further improve the tool life, a development of a new assembly to transfer the cryogenic fluid (LN_2) to the desired locations is designed and successfully developed in this work.

33.3 Explicit Concept for Spraying Liquid Nitrogen

As depicted in Fig. 32.4, a channel is designed which is placed concentric to the drill bit and sprayed LN_2 at the tip of the drill bit with four inclined holes present on the bottom surface of the channel. LN_2 enters into the channel through the threaded inlet and passages out through four inclined holes which concentrate the LN_2 to the
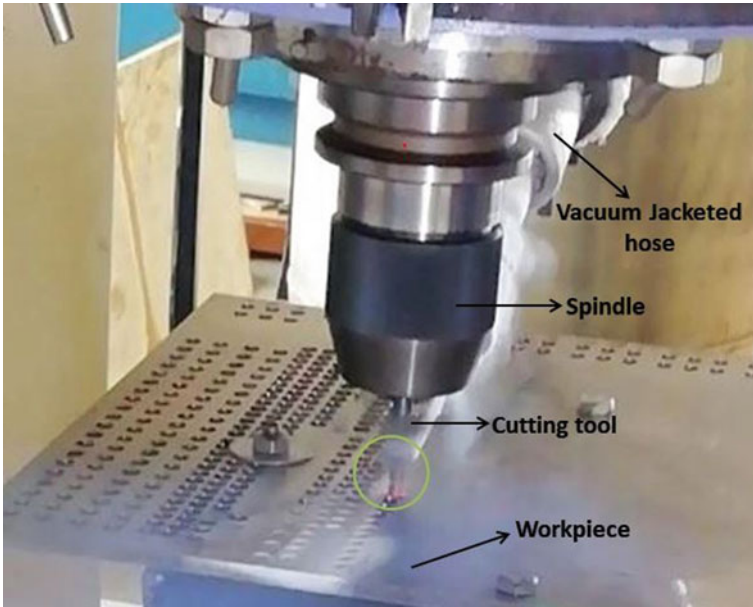
Fig. 32.3 Effect of liquid nitrogen not reaching the cutting zone while drilling is done at depth
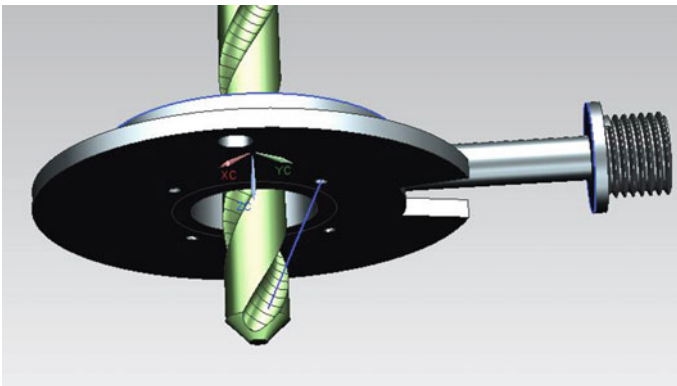

Fig. 32.4 Proposed design of channel for spraying LN$_2$ at tip of drill bit

tip of drill bit. This configuration allows the cryogenic coolant to reach the cutting zone even when drilling the workpiece at higher depth (Fig. 32.4). The exploded view of the component depicts the passage present in the channel subassembly for circulation of liquid nitrogen inside the channel (Fig. 32.5).

Fig. 32.5 a Complete
assembly of components.
b Exploded view of the
channel
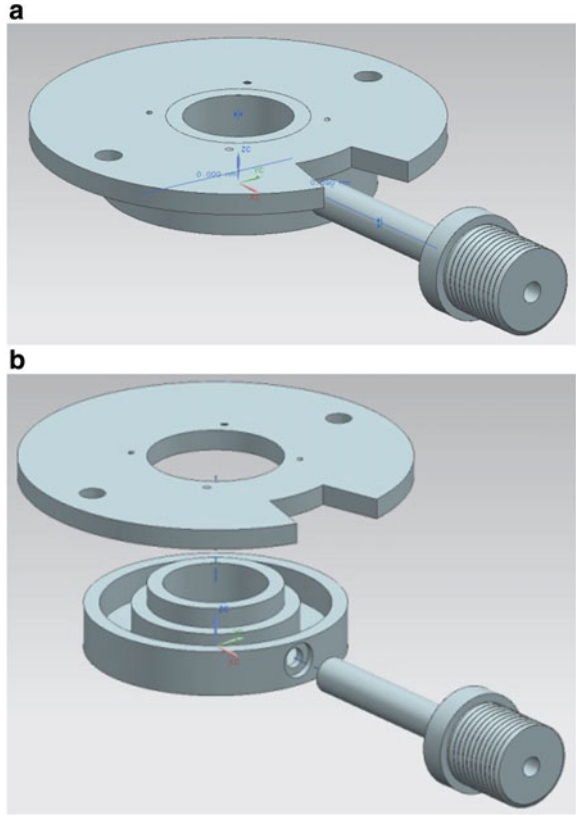
33.3.1 Design Specification

The drill bit is kept concentric to the assembly as the four inclined holes converge to a tip of the drill bit. As shown in Fig. 32.6, the internal hole diameter of grooved chamber is selected as 20 mm so that any drill bit diameter up to 16 mm, concentric with the inner hole, could be accommodated in the hole provided. Hence, a wide array of drill bits of numerous sizes up to 16 mm is suitable for this set-up.

It is evident from Fig. 32.6 that the grooved chamber forms the shape of hollow cylinder. Volume of this slot is given by $\pi h\left(R^2 - r^2\right)$ and surface area by $2\pi(R + r)(R - r + h)$ [13]. Hence, surface area (SA) to volume (V) ratio is $2(R - r + h)/h(R - r)$. If a torus shape is selected for the LN$_2$ flow, then its volume would be $2\pi^2 R r^2$ and surface area would be $4\pi^2 R r$ [14]. Surface area to volume ratio is $2/r$. The values of R, r and h are 22 mm, 16 mm and 6 mm, respectively, as provided by Fig. 32.6. SA/V ratio for hollow cylinder slot is 2/3. Considering the dimension of hollow torus similar to that of hollow cylinder as shown in Figs. 32.7a, b and considering value of r to be 3 mm for torus, the SA/V ratio for torus is 2/3. Torus being of cross-section of circle exhibits lowest SA/V ratio among all the cross
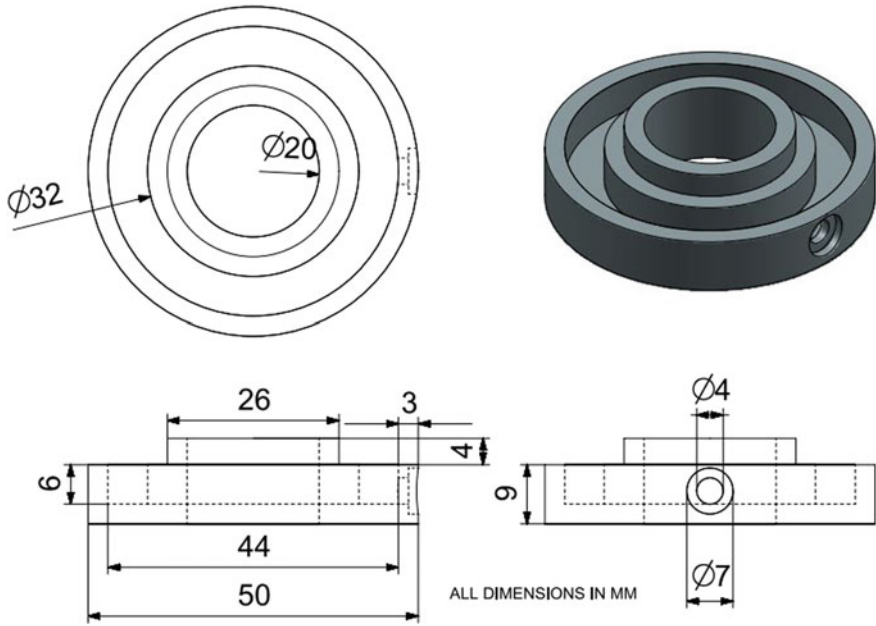
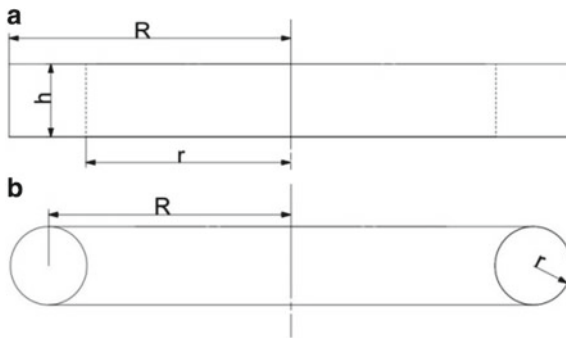**Fig. 32.6** Dimensional specification of grooved chamber

Fig. 32.7 a Hollow cylinder nomenclature. **b** Torus nomenclature

sections that are swept 360° [15]. But for the hollow rectangular slot as per the dimensions provided in Fig. 32.6, the SA/V ratio equals to that of a torus. As sphere shows least heat transfer among solids due to its low SA/V ratio [16], it implies the proposed design to be best in terms of achieving minimum heat transfer owing to similar SA/V ratio as that of circular cross-section.

Hence, along with the possibility of drill bits of numerous sizes to get advantage of getting supply of liquid nitrogen at its tip, it is dimensionally designed to yield minimum heat transfer which leads to lesser conversion of liquid nitrogen to gaseous form while delivery.
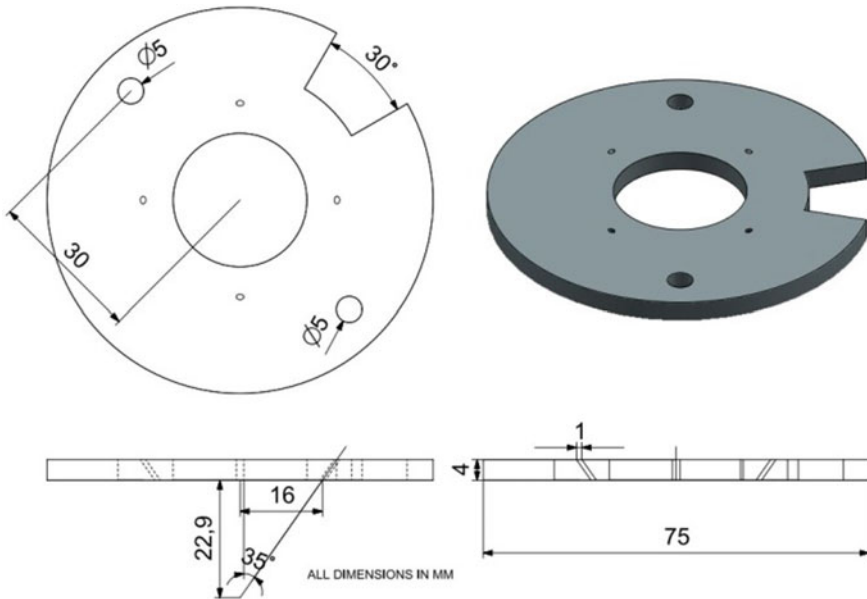
Fig. 32.8 Specification of top plate

As shown in Fig. 32.8, there are four inclined holes for outlet of LN_2 that allows the cryogenic coolant to converge at a specific point. Considering PCD of four holes 16 mm and an angle of 35° with the vertical, liquid nitrogen will converge at 22.9 mm below the bottom layer of the plate. This allows the assembly to spray liquid nitrogen at the tip effectively in varying work-piece depth from as small as 1 mm to as high as 20 mm.

As illustrated by Fig. 32.9, LN_2 converges at point B, outlet is point A and origin of the component is represented by point O. The distance between the origin and outlet is fixed at 16 mm. The distance of converging point from top surface plate is given by OB (OA/tan alpha) while total distance travelled by LN_2 is provided by AB (OA/sin alpha), where alpha is angle of inclination of holes with vertical.

The designed channel is connected in such a way that it moves up and down along with the drill bit. When drilling operation takes place, the channel also moves down equivalent to the depth of cut. Hence, it becomes necessary to set position of channel in a way that LN_2 reaches to tip of tool as well as the channel does not collide with the workpiece for at least a specific depth of cut. Alpha was selected as 35 so that the distance between tip of drill bit and bottom face of the component could be approximately 22.85 mm as indicated from Table 32.2. This allows for depth of cut up to 18 mm even with clearance for interference of nearly 5 mm. For alpha values higher than 35°, the depth of cut is highly compromised and also the length of drill bit outside spindle could only be less than 30 mm making higher values of alpha
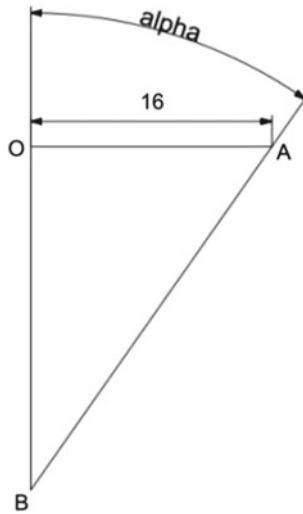
Fig. 32.9 Nitrogen phase diagram direction of flow of LN$_2$ forming triangular pattern

Table 32.2 Different distance values with varying alpha

Alpha (○)	OB (mm)	AB (mm)
25	34.31	37.86
30	27.71	32
35	22.85	27.89
40	19.07	24.88
45	16	22.62
50	13.42	20.88

ineffective. For values lower than 35°, the length of path from outlet of the channel to the tip of drill bit increases which would lessen the effective focus on the tool.

The inlet of the pipe has internal diameter of 4 mm as shown in Fig. 32.10. Area provided for the flow of liquid nitrogen is 4π mm^2. While the outlet of the channel is through four holes of 1 mm diameter each which has outlet area of π mm^2 combined.
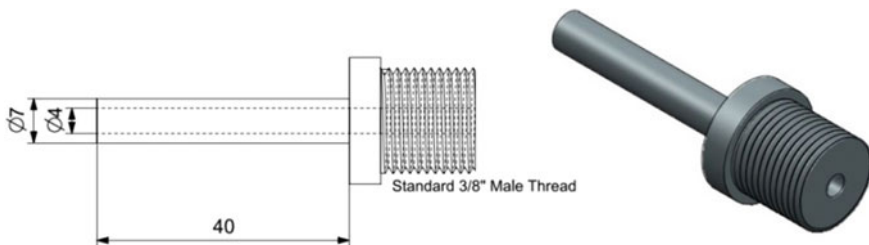

Fig. 32.10 Specification of inlet pipe

Assuming the density of the liquid nitrogen to remain constant, the continuity equation is given by $A_{in} \times v_{in} = A_{out} \times v_{out}$ [17]. This continuity equation implies that the velocity of LN2 at the outlet is 4 times than velocity at inlet. Higher outlet velocity allows for more precise trajectory of liquid nitrogen due to lesser divergence from its intended path and allowing more coolant to reach the cutting zone. However, smaller holes may not allow the adequate flow at such high pressures. So, outlet diameter of 1 mm is well suited for concentration of liquid nitrogen at cutting zones.

33.4   Fixing the Component into VMC

The proposed component cannot always be in motion with respect to drill bit, i.e. it should also move along with the drill bit to ensure that the liquid nitrogen reaches to the exact location unlike previous set-ups which do not move while drilling operation takes place, thereby not able to supply cryogen at heating zone. Hence, the component must be held within VMC machine only such that it is stationary w.r.t. drill bit.

As shown in Fig. 32.11, the stationary head in VMC has two threaded holes of 8 mm each and are 125 mm apart which could be used for holding the component.

Figure 32.12 shows the entire fixture wherein channel is supported by a structure that could move up and down through threaded connection. The long studs have diameter and pitch matching the holes present in VMC to fix them into the holes making the fixture stable. The ability to move the fixture up and down along the studs subjugate the issue of varying drill bit length. In this way, it is possible to adjust the channel exactly specific amount of distance above the tip of the drill bit irrespective of different sizes and lengths of drill bits.
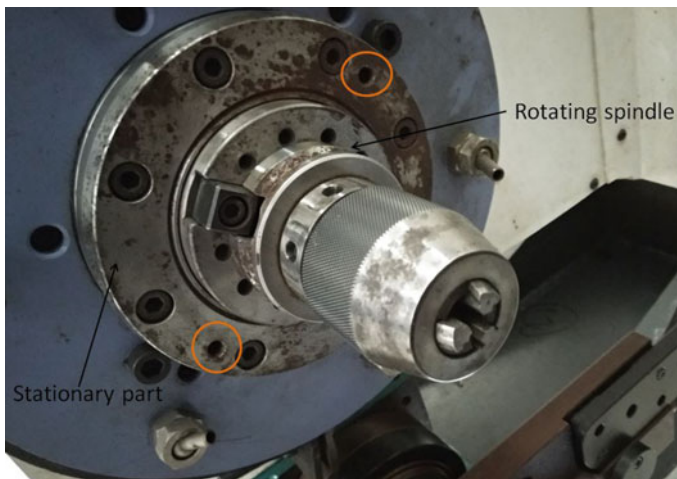

Fig. 32.11 Spindle and head of VMC (macpower V-544) facility present at IITRAM
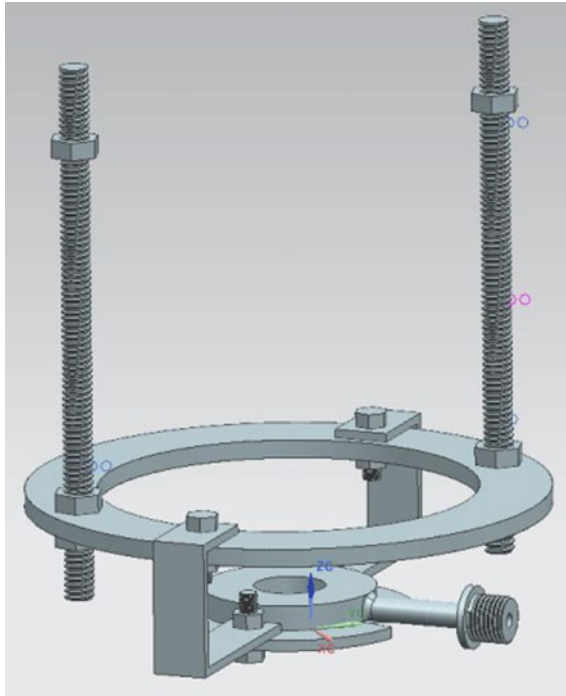
Fig. 32.12 Complete fixture to be fitted in VMC (macpower V-544)

It is evident from Figs. 32.13 and 32.14 that the tip of the drill bit is being effectively cooled and not only its flutes. Hence, during machining, the channel will follow the drill bit and cool down the heating zone that tend to damage the tool, thereby further increasing its tool life.

The cryogen supply channel has a fixed dimension but the support structure could be varied in accordance with the VMC machine to fulfil the same function as considered here.

As shown in Fig. 32.15, four holes present on the top surface supporting spindle of VMC (macpower ECO-500 model) are of 6 mm diameter with 0.75 mm pitch fine threads. Long studs fastened into the holes could be used in fabricating a frame supported by the studs similar to the case of prototype (Fig. 32.16). Proposed design for the same is shown in Fig. 32.17 wherein a rectangular frame is fastened through four studs. This rectangular frame supports the circular path for liquid nitrogen through two support structures fastened by nut and bolt. Here, the rectangular frame could move up or down if the nuts associated with studs are moved up or down, thereby varying the height of the structure (Fig. 32.16).
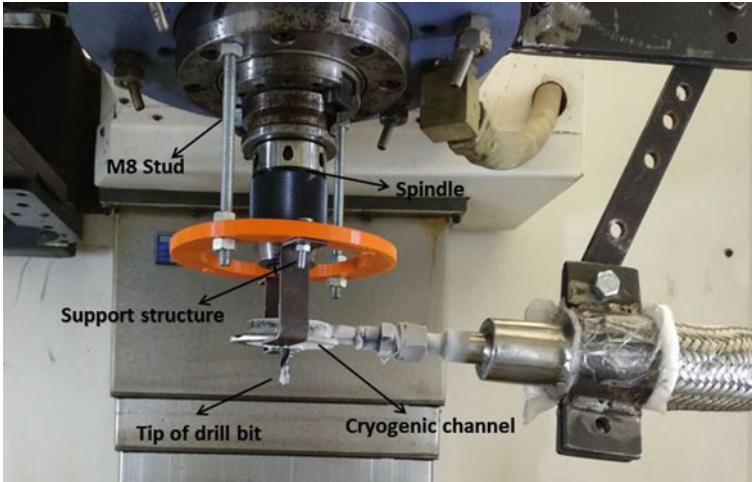
Fig. 32.13 Tip of drill bit getting cooled just after initiating LN_2 flow
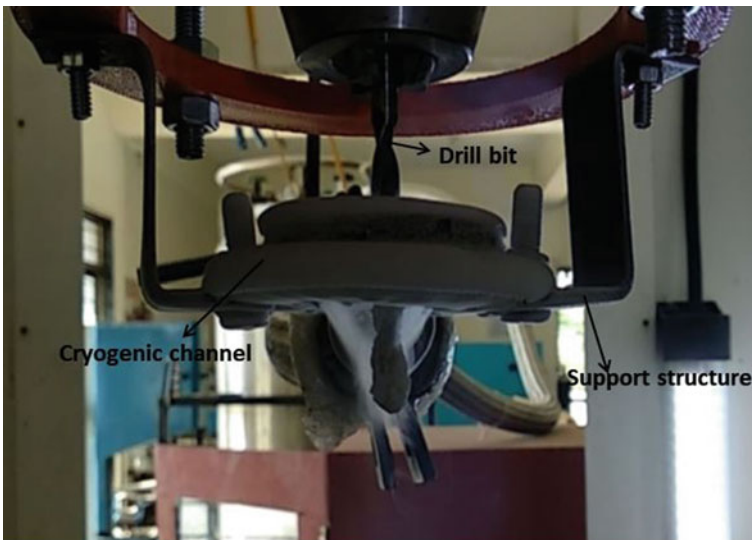
Fig. 32.14 Liquid nitrogen concentrating on drill bit

33.5 Conclusion

The fixture fitted in macpower V-544 and ECO-500 VMC machines could very well be used for varying drill bit diameters from 1 to 16 mm effectively. Variable height of the fixture is facilitated by long studs to account for varying length of drill bits. The design is made to address the issue of varying work-piece length with

Fig. 32.15 Holes in stationary base in VMC machine (macpower ECO-500 model)
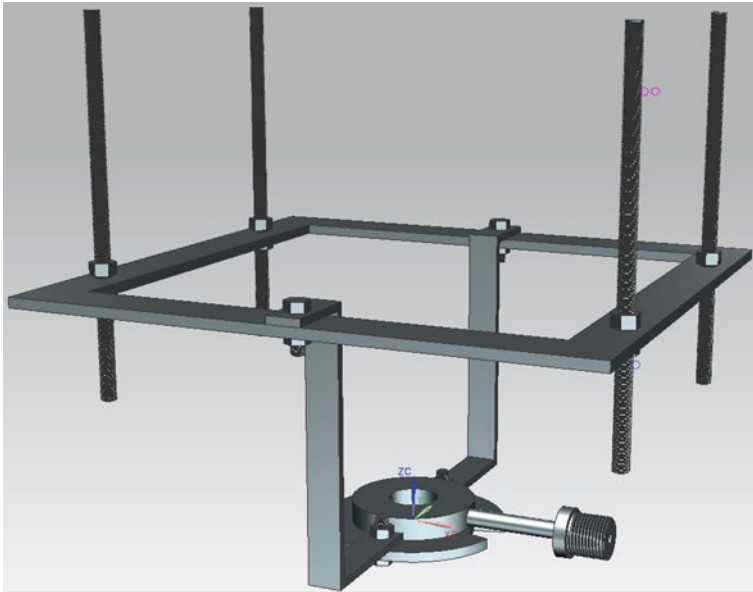
Fig. 32.16 Complete structure of model to be fitted in VMC (macpower ECO-500)
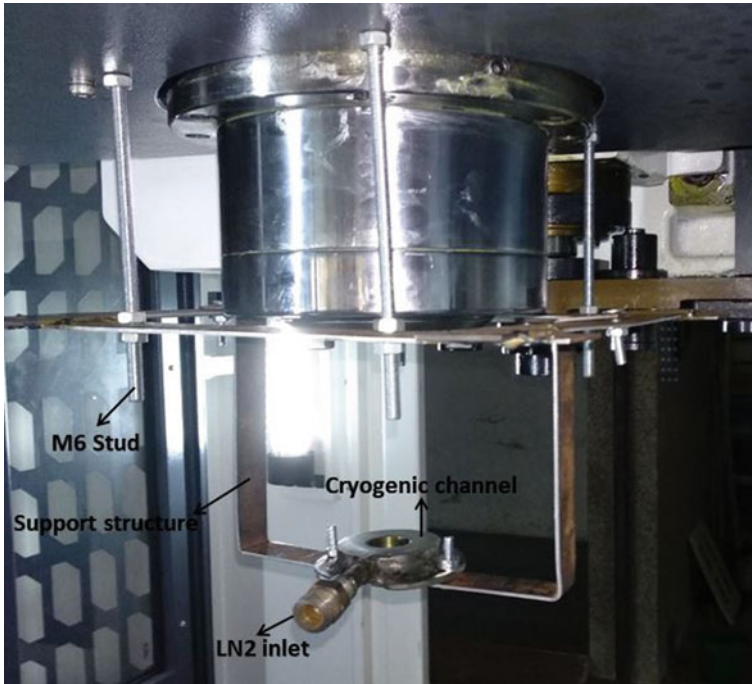
Fig. 32.17 Fabricated design attached with VMC for conducting its intended function

this fixture having the ability to easily perform its intended function for work-piece thickness up to 18 mm. This fixture could be used in other VMC machines with only a slight modification as per the dimension of VMC. This development work will enable higher cutting speeds f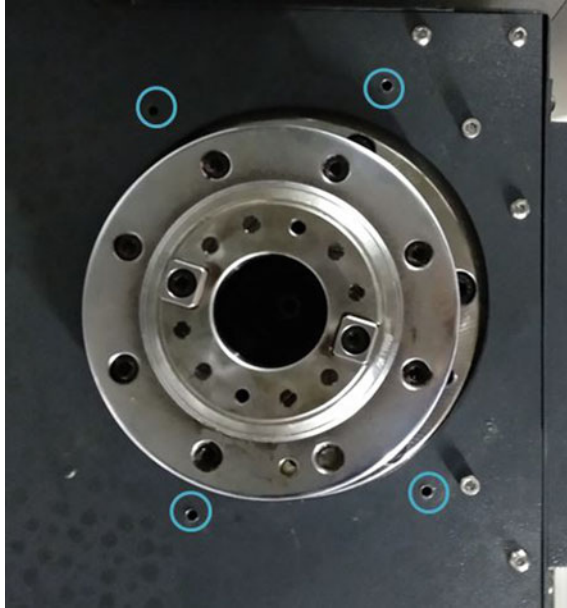or increase material removal and longer tool life by effectively transmitting liquid nitrogen directly to the cutting edge.

References

1. Sreejith, P.S., Ngoi, B.K.: Dry machining: machining of the future. J. Mater. Process. Technol. **101**(1–3), 287–291 (2000)
2. Ezugwu, E.O., Bonney, J.: Effect of high-pressure coolant supply when machining nickel-base, Inconel 718, alloy with coated carbide tools. J. Mater. Process. Technol. **10**(153), 1045–1050 (2004)
3. Khan, A.A., Ahmed, M.I.: Improving tool life using cryogenic cooling. J. Mater. Process. Technol. **196**(1–3), 149–154 (2008)

4. Debnath, S., Reddy, M.M., Yi, Q.S.: Environmental friendly cutting fluids and cooling techniques in machining: a review. J. Clean. Prod. **15**(83), 33–47 (2014)
5. Bermingham, M.J., Kirsch, J., Sun, S., Palanisamy, S., Dargusch, M.S.: New observations on tool life, cutting forces and chip morphology in cryogenic machining Ti-6Al-4V. Int. J. Mach. Tools Manuf **51**(6), 500–511 (2011)
6. Paul, S., Dhar, N.R., Chattopadhyay, A.B.: Beneficial effects of cryogenic cooling over dry and wet machining on tool wear and surface finish in turning AISI 1060 steel. J. Mater. Process. Technol. **116**(1), 44–48 (2001)
7. Wang, Z.Y., Rajurkar, K.P.: Cryogenic machining of hard-to-cut materials. Wear **239**(2), 168–175 (2000)
8. Nalbant, M., Yildiz, Y.: Effect of cryogenic cooling in milling process of AISI 304 stainless steel. Trans. Nonferrous Met. Soc. China **21**(1), 72–79 (2011)
9. Dandekar, C.R., Shin, Y.C., Barnes, J.: Machinability improvement of titanium alloy (Ti–6Al–4V) via LAM and hybrid machining. Int. J. Mach. Tools Manuf. **50**(2), 174–182 (2010)
10. Pušavec, F., Stoić, A., Kopač, J.: The role of cryogenics in machining processes. Tehničkivjesnik **16**(4), 3 (2009)
11. Engineering ToolBox, Nitrogen—density and specific weight (2018). https://www.engineeringtoolbox.com/nitrogen-N2-density-specific-weight-temperature-pressure-d_2039.html. Accessed 19 March 2019
12. Khanna, N., Agrawal, C., Joshi, V.: Zero vapor loss integrated cryogen phase separator. Indian Patents 201721031291 A (2017)
13. Kumosa, L., Armentrout, D., Benedikt, B., Kumosa, M.: An investigation of moisture and leakage currents in GRP composite hollow cylinders. IEEE Trans. Dielectr. Electr. Insul. **12**(5), 1043–1059 (2005)
14. Essén, H., Sten, J.C., Nordmark, A.B.: Magnetic energy of surface currents on a torus. Progr. Electromagnet. Res. **46**, 357–378 (2013)
15. Böhringer, B., Guerra Gonzalez, O., Eckle, I., Müller, M., Giebelhausen, J.M., Schrage, C., Fichtner, S.: Polymer-based spherical activated carbons-from adsorptive properties to filter performance. ChemieIngenieurTechnik **83**(1–2), 53–60 (2011)
16. Bergman, T.L., Incropera, F.P., Lavine, A.S., DeWitt, D.P.: Introduction to Heat Transfer. Wiley (2011)
17. Munson, B.R., Okiishi, T.H., Huebsch, W.W., Rothmayer, A.P.: Fluid Mechanics. Wiley, Singapore (2013)

Chapter 34
Effect of Temperature on Creep Stresses in Thick Spherical Vessels Made of Composite Material

Sukhjinder Singh Sandhu, Tejeet Singh, and V. K. Gupta

Abstract The steady-state creep in Al–SiCp composite sphere subjected to internal pressure was investigated. The effect of parameter like operating temperature on the stresses and strain rates in the composite sphere was investigated, and it was found that the stresses in the sphere did not have significant variation with varying temperature. But, the tangential strain rates, radial strain rates as well as effective strain rates in the sphere could be reduced to a significant extent by decreasing the operating temperature. The secondary stage creep deformations and creep stress in thick-walled spherical vessels made of functionally graded composites have been obtained in the present study. The spherical pressure vessel chosen for the investigation is subjected to internal and external pressure under the constant temperature field. The material of the vessel is incompressible. The creep behavior of material is governed by threshold stress-based creep law. The study reveals that for linear variation of reinforcement and assumed pressure ratio, the compressive value of radial stress reduces with an increase in pressure ratio from 2 to 5 over the entire radial distance. However, the longitudinal stress remains compressive at the inner radius, and the value becomes tensile for pressure ratio 3, 4 and 5.

Keywords Sphere · Creep · Composite · Internal pressure and external pressure

34.1 Introduction

The spherical vessels made up of monolithic materials may fail under severe environmental conditions such as high temperature/or thermal gradient and high pressures. The beginning of modern civilization and advancements in technical knowledge has led to the development of newer materials for applications involving stringent operating conditions such as high service temperature and pressure, highly corrosive

S. S. Sandhu (✉) · T. Singh
Department of Mechanical Engineering, S.B.S.S.T.C, Ferozepur 152004, India
e-mail: 33sukhjinder@gmail.com

V. K. Gupta
Mechanical Engineering, UCoE, Punjabi University, Patiala 147002, India

environments, which the monolithic materials failed to survive. Therefore, over the last few decades, the composite materials, plastics and ceramics have been the dominant emerging materials. In addition, these materials become more popular because of increased global competition for lightweight components of greater strength and stiffness. Hence due to lightweight, composites are extensively used to manufacture various components of automobile, sports, aerospace, marine and oil industries. Composites provide significant weight reduction (25–45%) over conventional monolithic materials due to their low density [1]. In recent years, the problem of creep in composite spheres operating at high pressure and temperature has attracted the interest of many researchers. Fukui et al. [2] extended the work to investigate the effect of graded components of residual stresses in a thick-walled FG tube under uniform thermal loading. The effect of variation in material parameters on the stresses induced in the sphere was investigated. The study indicated that stresses in FGM sphere could be load by tailoring the material properties along the radial direction of the sphere [2–5]. Sim [6] analyzed the creep behavior of thick-walled spheres subjected to internal pressure and a negative thermal gradient. The study indicates that at a steady state, the displacement rate in the radial direction of the vessel is proportional to the creep rate for single stress and temperature. Durban and Baruch [7] analyzed the behavior of thick-walled spheres subjected to both internal and external pressures. The material of the sphere was assumed to follow an incrementally elastic constitutive law. Hulsurkar (1978) used Seth's transition theory to obtain the creep stresses in a spherical vessel made of compressible composite material and subjected to internal pressure. Miller [8] presented mathematical solution to obtain elastic as well as creep stresses and displacements in a thick spherical shell subjected to both internal and external pressures. Nayebi and Abdi [9] analyzed plastic and creep behavior of a thick-walled sphere subjected to cyclic pressure and/or temperature. In this study, the steady-state behavior of the pressure vessels using linear kinematic hardening in the plastic condition and Norton's power law in the creep condition has been investigated. Aleayoub and Loghman [10] performed the time-dependent creep stress redistribution analysis of functionally graded thick-walled spheres subjected to internal pressure and constant temperature. The material's properties were assumed to change through the thickness according to the power law. Nie et al. [11] proposed a technique to tailor materials for functionally graded linear elastic hollow spheres. The volume fractions of a functionally graded material were assumed to vary only with the radius and the material properties were obtained from either the rule of mixtures or the Mori–Tanaka scheme. Nejad et al. [12] presented an exact solution for creep stresses in isotropic and homogeneous thick spherical pressure vessels. The creep behavior of the material of the spherical vessel was described by Norton's law. Sadeghian and Toussi [13] obtained the distributions of elastic and plastic thermal stress in spherical pressure vessels made of functionally graded material. The properties of the material were considered to be a power function of radial distance. Pankaj [14] used Seth's transition theory to analyze the creep stresses in an isotropic thick-walled spherical shell by finitesimal deformation. The sphere was subjected to internal pressure and steady-state temperature. Bhatnagar and Arya [15] applied finite strain theory for analyzing the creep behavior of an isotropic thick-walled spherical

vessel subjected to internal pressure. A mathematical model has been developed to describe the study creep behavior of composite material. Bayat et al. [16] carried out thermo-mechanical analysis of functionally graded hollow sphere subjected to mechanical loads and uniaxial steady-state thermal stresses. The study revealed that the stresses in the spherical vessel are affected by a dimensionless parameter like operating temperature on the steady-state creep response of the composite sphere.

34.2 Creep Law and Creep Parameters

In aluminum-based composites, undergoing steady-state creep, the effective creep rate, $\dot{\varepsilon}_e$, is related to the effective stress, σ_e, through well-documented threshold stress, σ_0, based creep law:

$$\dot{\varepsilon}_e = A'\left(\frac{\sigma_e - \sigma_0}{E}\right)^n \exp\left(\frac{-Q}{RT}\right) \tag{34.1}$$

symbols A', n, Q, E, R and T denote, respectively, structure-dependent parameter, true stress exponent, true activation energy, temp-dependent Young's modulus, gas constant and operating temperature.

The creep law given by Eq. (34.1) may alternatively be written as:

$$\dot{\varepsilon}_e = [M(\sigma_e - \sigma_0)]^n \tag{34.2}$$

$$\text{Particle content } V(r) = V_{\max} - \frac{(r-a)}{(b-a)}(V_{\max} - V_{\min}) \tag{34.3}$$

$V_{\max}$ and $V_{\min}$ are respectively the maximum and minimum SiCp, at the inner and outer radii.

(V_{avg}) in spherical vessel can be expressed as,

$$V_{\text{avg}} = \frac{\int_a^b r^2 \cdot V(r)\mathrm{d}r}{b^3 - a^3} \tag{34.4}$$

Substituting the value of particle content, $V(r)$, from Eq. (34.1) into Eq. (34.2) and integrating

$$V_{\min} = \frac{4V_{\text{avg}}\left(1 - \alpha^3\right)(1 - \alpha) - V_{\max}\left(1 - 4\alpha^3 + 3\alpha^4\right)}{\left(3 - 4\alpha + \alpha^4\right)} \tag{34.5}$$

where α is the ratio of inner to outer radius (i.e. a/b) of spherical vessel.

During the regression analysis, P, V and T are taken as independent variables and M and σ_0 are selected as dependent variables. The developed regression equations

are given below,

$$M(r) = 0.0287611 - \frac{0.00879}{P} - \frac{14.02666}{T} - \frac{0.032236}{V(r)} \qquad (34.6)$$

$$\sigma_o(r) = -0.084P - 0.0232T + 1.1853(V(r)) + 22.207 \qquad (34.7)$$

where P, $V(r)$, T, $M(r)$ and $\sigma_0(r)$ are, respectively, the particle size, particle content, temperature, creep parameter and threshold stress at any radius (r) of the FGM spherical pressure vessels.

34.3 Mathematical Solution

Let us consider a thick-walled, spherical vessel made of functionally graded Al–SiCp composite. The vessel is assumed to have inner and outer radii as a and b, respectively, and is subjected to internal pressure p and external pressure q. The geometric relationships between radial and circumferential strain rates and radial displacement rate are

$$\dot{\varepsilon}_r = \frac{d\dot{x}_r}{dr} \qquad (34.8)$$

$$\dot{\varepsilon}_\theta = \frac{\dot{x}_r}{r} \qquad (34.9)$$

where, $\dot{\varepsilon}_r$ and $\dot{\varepsilon}_\theta$ are, respectively, radial and circumferential strain rates, $\dot{x}_r \left(= \frac{dx}{dt} \right)$ is the radial displacement rate and x is the radial displacement.

Eliminating $\dot{x}_r$, from Eqs. (34.8) and (34.9) the deformation compatibility condition is obtained as,

$$r \frac{d\dot{\varepsilon}_\theta}{dr} = (\dot{\varepsilon}_r - \dot{\varepsilon}_\theta) \qquad (34.10)$$

Considering the equilibrium of forces on an element of the spherical vessel along the radial direction, we get the equilibrium equation as below

$$\frac{r}{2} \frac{d\sigma_r}{dr} = (\sigma_\theta - \sigma_r) \qquad (34.11)$$

where σ_θ and σ_r are, respectively, the circumferential and radial stresses. Since the material of the sphere is assumed to be incompressible, therefore,

$$\dot{\varepsilon}_r + \dot{\varepsilon}_\theta + \dot{\varepsilon}_z = 0. \qquad (34.12)$$

where, $\dot{\varepsilon}_z$ is the axial strain rate.

The constitutive equations for creep along with the principal direction r, θ and z can be written as below,

$$\dot{\varepsilon}_r = \frac{\dot{\varepsilon}_e}{2\sigma_e}\left[2\sigma_r - (\sigma_\theta + \sigma_z)\right] \tag{34.13}$$

$$\dot{\varepsilon}_\theta = \frac{\dot{\varepsilon}_e}{2\sigma_e}\left[2\sigma_\theta - (\sigma_r - \sigma_z)\right] \tag{34.14}$$

$$\dot{\varepsilon}_z = \frac{\dot{\varepsilon}_e}{2\sigma_e}\left[2\sigma_z - (\sigma_r - \sigma_\theta)\right] \tag{34.15}$$

where is the equivalent strain rate, σ_e is the equivalent stress and σ_r, σ_θ and σ_z are the stresses along with r, θ and z directions, respectively.

Due to the spherical symmetry, $\sigma_\theta = \sigma_z$, thus Eqs. (34.13), (34.14) and (34.15) become,

$$\dot{\varepsilon}_r = \frac{\dot{\varepsilon}_e}{\sigma_e}(\sigma_r - \sigma_\theta) \tag{34.16}$$

$$\dot{\varepsilon}_\theta = \frac{\dot{\varepsilon}_e}{2\sigma_e}(\sigma_\theta - \sigma_r) \tag{34.17}$$

$$\dot{\varepsilon}_z = \frac{\dot{\varepsilon}_e}{2\sigma_e}(\sigma_z - \sigma_r) \tag{34.18}$$

From Eqs. (34.16) and (34.17), the relationship between the radial and circumferential strain rates can be obtained as,

$$\dot{\varepsilon}_r = -2\dot{\varepsilon}_\theta \tag{34.19}$$

It should be pointed out that Eq. (34.19) can also be obtained from the incompressibility condition Eq. (34.12) and the condition of spherical symmetry ($\dot{\varepsilon}_z = \dot{\varepsilon}_\theta$), as given

$$\dot{\varepsilon}_r + \dot{\varepsilon}_\theta + \dot{\varepsilon}_z = \dot{\varepsilon}_r + 2\dot{\varepsilon}_\theta = 0$$
$$\text{Or,}$$
$$\dot{\varepsilon}_r = -2\dot{\varepsilon}_\theta$$

Substituting Eq. (34.19) into Eq. (34.10), the deformation compatibility becomes,

$$\frac{d\dot{\varepsilon}_\theta}{\dot{\varepsilon}_\theta} = -3\frac{dr}{r} \tag{34.20}$$

The integration of Eq. (34.20), gives the circumferential strain rate as,

$$\dot{\varepsilon}_\theta = \frac{A_1}{r^3} \tag{34.21}$$

where A_1 is constant of Integration.

The effective stress in thick-walled spherical vessels subjected to internal pressure is assumed to be expressed by a well-known von Mises equation [17],

$$\sigma_e = \frac{1}{\sqrt{2}} \left[(\sigma_\theta - \sigma_r)^2 + (\sigma_r - \sigma_z)^2 + (\sigma_z - \sigma_\theta)^2 \right]^{\frac{1}{2}} \tag{34.22}$$

Due to spherical symmetry, the von Mises equation becomes,

$$\sigma_e = (\sigma_\theta - \sigma_r) \tag{34.23}$$

Using Eq. (34.23) into Eq. (34.17), we get,

$$\dot{\varepsilon}_e = 2\dot{\varepsilon}_\theta = \frac{2A_1}{r^3} \tag{34.24}$$

Using Eq. (34.5) into above Eq. (34.24), we get,

$$[M(r)(\sigma_e - \sigma_0(r))]^n = \frac{2A_1}{r^3} \tag{34.25}$$

Equation (34.25) can be simplified to get,

$$\sigma_e = \frac{(2A_1)^{\frac{1}{n}}}{r^{3/n} M(r)} + \sigma_o(r) \tag{34.26}$$

Using Eq. (34.23) into above Eq. (34.26), we get,

$$\sigma_\theta - \sigma_r = \frac{A_2(r)}{r^{\frac{3}{n}}} + \sigma_o(r) \quad \text{where} \quad A_2(r) = \left[\frac{(2A_1)^{\frac{1}{n}}}{M(r)} \right] \tag{34.27}$$

Substituting equilibrium Eq. (34.11) into the above equation and integrating the resulting equation between limits a to r, we get,

$$\sigma_r = 2 \int_a^r \frac{A_2(r)}{r^{\frac{(n+3)}{n}}} dr + 2 \int_a^r \frac{\sigma_o(r)}{r} dr + A_3 \tag{34.28}$$

where A_3 is constant of integration.

The following boundary conditions are assumed for the spherical vessel,

$$\text{(i)} \quad at \, r = a, \sigma_r = -p \tag{34.29}$$

$$\text{(ii)} \quad at \, r = b, \sigma_r = -q \tag{34.30}$$

Equation (34.28) may be solved between limits a and b and under the enforced boundary conditions given in Eqs. (34.29) and (34.30) to get the value of 'A_1' as

$$A_1 = \frac{1}{2} \left[\frac{p - q - 2A_4}{2A_5} \right]^n \tag{34.31}$$

where $A_4 = \int_a^b \frac{\sigma_0(r)}{r} dr$ and $A_5 = \int_a^b \frac{1}{r^{(n+3)/n} M(r)} dr$

Applying boundary conditions in Eq. (34.28), the radial stress is obtained as,

$$\sigma_r = 2 \int_a^r \frac{A_2(r)}{r^{\frac{(n+3)}{n}}} dr + 2 \int_a^r \frac{\sigma_o(r)}{r} dr - p \tag{34.32}$$

Substituting Eqs. (34.31) and (34.32) into Eq. (34.27), we get circumferential stress as,

$$\sigma_\theta = \frac{A_2(r)}{r^{3/n}} + \sigma_o(r) + 2 \int_a^r \frac{A_2(r)}{r^{\frac{(n+3)}{n}}} dr + 2 \int_a^r \frac{\sigma_o(r)}{r} dr - p \tag{34.33}$$

Substituting values of σ_r and σ_o in Eqs. (34.16) and (34.17), strain rates in the sphere can be obtained (Tables 34.1, 34.2 and 34.3; Fig. 34.1).

A computer program has been developed to calculate the steady-state creep response of the FG spherical vessel for various combinations of size and content of the reinforcement and operating temperature. For the purpose of numerical computation, the inner and outer radii of the spherical vessel are taken 500 mm and 800 mm, respectively, and the internal pressure is assumed to be 100 MPa and external pressure varies as 50, 33.33, 25 and 20 MPa so that ratio of $p/q = 2, 3, 4$ and 5. T radial stress at different radial locations of the sphere is calculated respectively from Eq. (34.32). The creep parameters $M(r)$ and $\sigma_o(r)$, required during the computation process, are estimated, respectively, from Eqs. (34.6) and (34.7).

Table 34.1 When $T = 623$ K

Radius	Radial stress	Tangential stress	Effective stress	Eff. strain rate	Tang. strain rate	Rad. strain rate
500	−100	36.63	136.63	0.00181	0.000906	−0.00181
530	−84.49	44.91	129.4	0.00152	0.000761	−0.00152
560	−70.66	51.79	122.45	0.00129	0.000645	−0.00129
590	−58.22	57.56	115.78	0.0011	0.000552	−0.0011
620	−47.05	62.34	109.39	0.000951	0.000476	−0.000951
650	−37	66.52	103.52	0.000825	0.000413	−0.000825
680	−27.92	69.73	97.65	0.000721	0.00036	−0.000721
710	−19.75	72.11	91.86	0.000633	0.000317	−0.000633
740	−12.39	73.81	86.2	0.00056	0.00028	−0.00056
770	−5.75	75.11	80.86	0.000496	0.000248	−0.000496
800	0	75.43	75.43	0.000443	0.000221	−0.000443

Table 34.2 When $T = 673$ K

Radius	Radial stress	Tangential stress	Effective stress	Eff. strain rate	Tang. strain rate	Rad. strain rate
500	−100	31.98	131.98	0.0169	0.00847	−0.0169
530	−84.99	40.68	125.67	0.0142	0.00711	−0.0142
560	−71.48	48.38	119.86	0.0121	0.00603	−0.0121
590	−59.26	55	114.26	0.0103	0.00515	−0.0103
620	−48.18	60.88	109.06	0.00888	0.00444	−0.00888
650	−38.13	65.74	103.87	0.00771	0.00385	−0.00771
680	−28.98	69.89	98.87	0.00673	0.00337	−0.00673
710	−20.66	73.25	93.91	0.00591	0.00296	−0.00591
740	−13.09	76.07	89.16	0.00523	0.00261	−0.00523
770	−6.2	78.16	84.36	0.00464	0.00232	−0.00464
800	0	79.68	79.68	0.00414	0.00207	−0.00414

34.4 Results and Discussions

On the basis of mathematical analysis, numerical calculations have been carried out to obtain the secondary stage creep behavior of functionally graded spherical pressure vessels. The results have been obtained for different pressure ratios in FG spheres. The internal pressure is taken as 100 MPa, and however, external pressure is varied to obtain pressure ratio as 2, 3, 4 and 5.

Table 34.3 When $T = 723$ K

Radius	Radial stress	Tangential stress	Effective stress	Eff. strain rate	Tang. strain rate	Rad. strain rate
500	−100	29.89	129.89	0.0681	0.034	−0.0681
530	−85.19	39.04	124.23	0.0572	0.0286	−0.0572
560	−71.84	46.98	118.82	0.0485	0.0242	−0.0485
590	−59.71	53.93	113.64	0.0415	0.0207	−0.0415
620	−48.68	59.97	108.65	0.0357	0.0179	−0.0357
650	−38.57	65.42	103.99	0.031	0.0155	−0.031
680	−29.41	69.95	99.36	0.0271	0.0135	−0.0271
710	−21.03	73.73	94.77	0.0238	0.0119	−0.0238
740	−13.38	76.97	90.35	0.021	0.0105	−0.021
770	−6.39	79.51	85.9	0.0187	0.00933	−0.0187
800	0	81.53	81.53	0.0166	0.00831	−0.0166

34.5 Variation of Particle Content and Creep Parameters

The distribution of SiC particles in the spherical vessel is linear with maximum particle content is 30 vol% at the inner radius. The content of reinforcement is assumed to decrease linearly along with the radial distance. The average particle content is kept as 20 vol%.

The threshold stress will reduce linearly (Fig. 34.2) with maximum value at a radius and minimum value at the outer radius of the spherical vessel. The threshold stress is higher at locations which have a greater density of silicon carbide particles. The variation of σ_o becomes stepper with an increase in particle gradient in functionally graded spherical vessel.

On the other hand, the value of creep parameter 'M' will increase with an increase in radial distance (Fig. 34.3). The increase observed in the value of 'M' may be due to the decrease in particle content at outer regions.

34.6 Variation of Radial and Axial Stresses

To observe the effect of pressure ratio on radial and axial stresses in a thick-walled spherical vessel, the pressure ratio is kept at 2, 3, 4 and 5. The compressive value of radial stress decreases parabolically from inner radius to outer radius due to imposed boundary conditions (Fig. 34.4). The compressive value of σ_r will reduce as the pressure ratio increases from 2 to 5.

The tangential stress σ_θ and axial stress σ_z remain equal due to spherical symmetry and observed to increase with radius. Further, the value of axial stress remains compressive at the inner and outer radius for pressure ratio 2. On the other hand, the
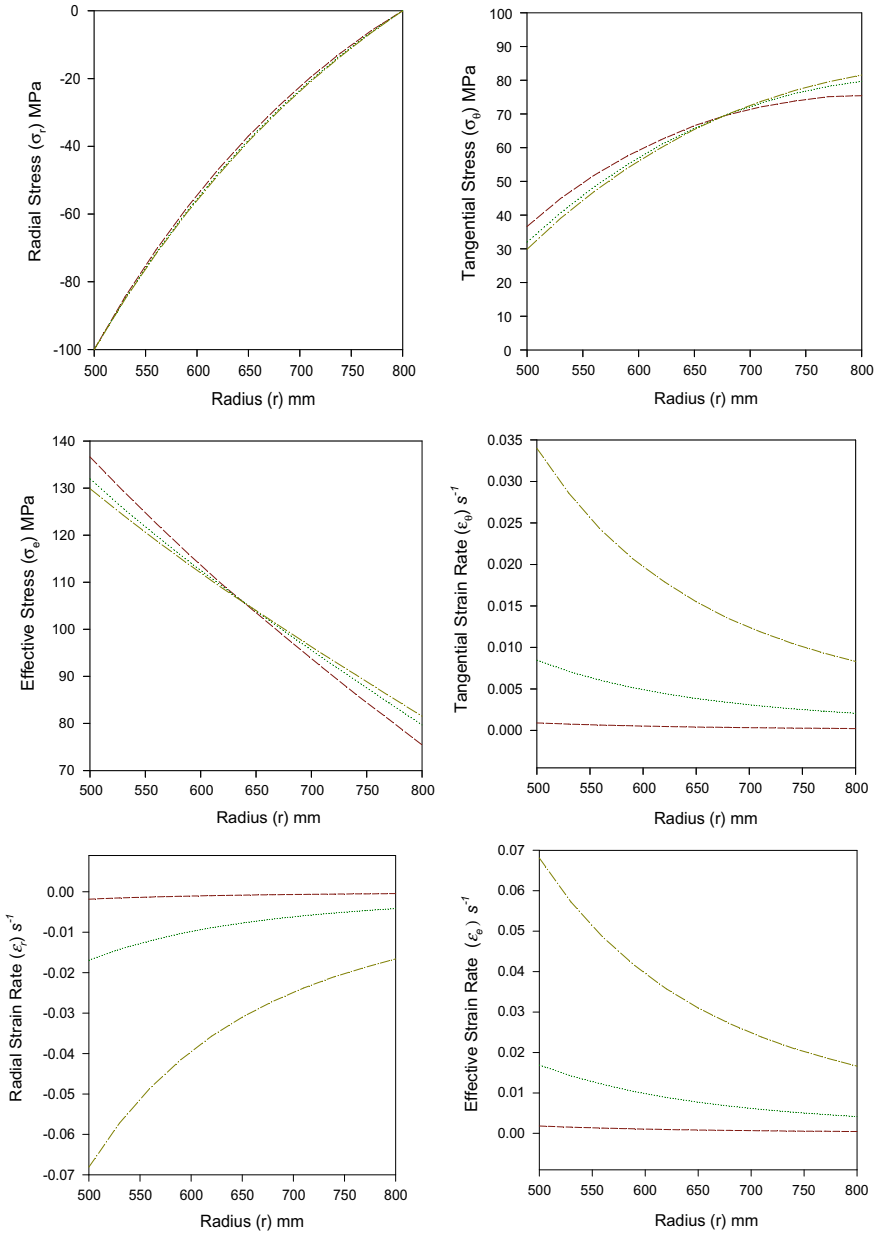
Fig. 34.1 Effect of temperature on radial stress, tangential stress, effective stress, tangential strain rate, radial strain rate and effective strain rate with respect to radius

Fig. 34.2 Variation of
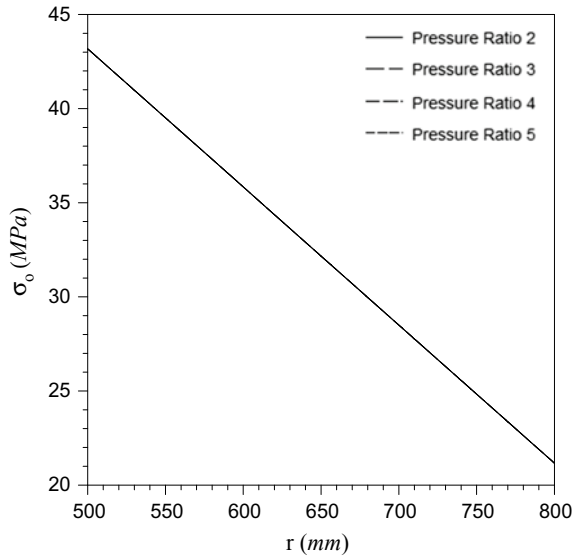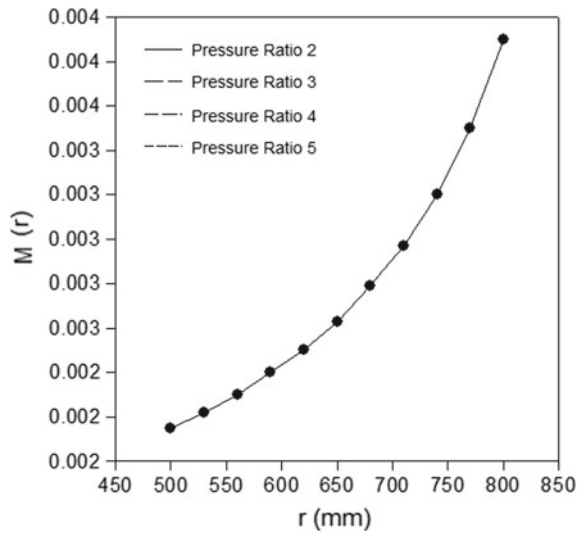threshold stress

Fig. 34.3 Variation of creep
parameter '*M*'

stress becomes tensile at the middle portion as the pressure ratio is increased from
2 to 3. Further increase in pressure ratio from 4 to 5) leads to a shift in tensile axial
stress near the inner region of the sphere. Further, the distribution of axial stress
remains parabolic in nature (Fig. 34.5).
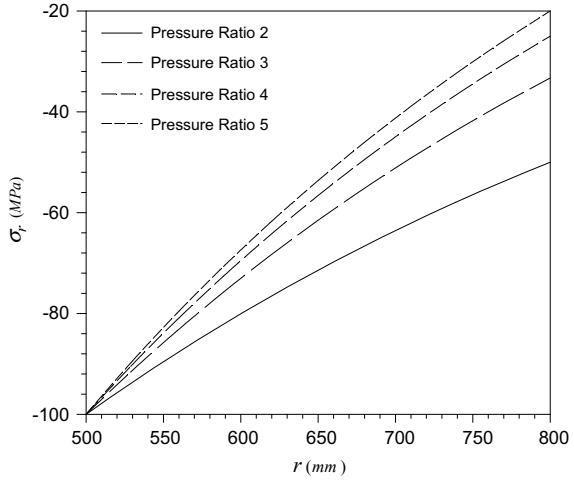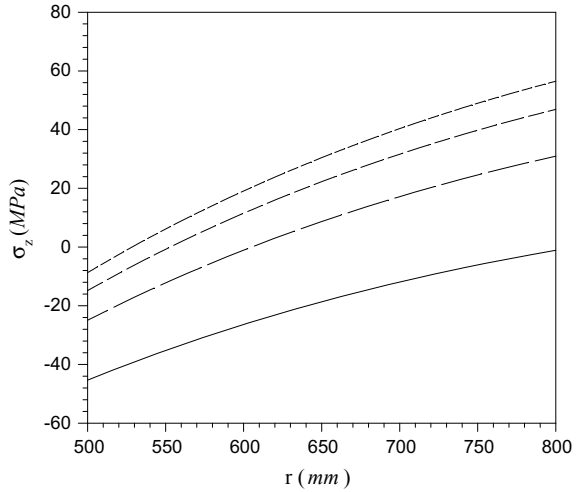
Fig. 34.4 Variation of radial stress

Fig. 34.5 Variation of axial stress

34.7 Conclusions

The present study has led to the following conclusions:

(1) The steady-state radial and tangential stresses increase on moving from the inner to the outer radius of a thick-walled composite sphere. The stress distributions in composite sphere do not vary significantly for various combinations of operating temperature. The tangential as well as radial strain rates in an isotropic thick wall internally pressurized Al–SiC$_P$ sphere decreases on moving from the inner to the outer radius. The strain rates induced in the composite sphere could be reduced significantly by decreasing the operating temperature.

(2) The radial stress in spherical pressure vessel decreases throughout with the increase in pressure ratio. The radial stress remains zero at the inner radius due to imposed boundary condition.

(3) The axial stress is compressive near the inner and outer radius of spherical pressure vessel for pressure ratio 2.

(4) The axial stress becomes tensile with an increase in pressure ratio 3, 4 and 5.

References

1. Kaw, K.: Mechanics of composite materials. Publishers of Taylor and Francis Group, second edition, ISBN (10): 0-8493-1343-0 (2006)
2. Fukui, Y., Yamanaka, N., Wakashima, K.: The stresses and strains in a thick-walled tube for functionally graded material under uniform thermal loading. JSME **36A**(2), 156–162 (1993)
3. Nieh, T.G.: Creep rupture of a silicon carbide reinforced aluminium composite. Metall. Trans. **15A**(1), 139–145 (1984)
4. Roy, A.K., Tsai, S.W.: Design of thick composite cylinders. ASME J. Press. Vessel Technol. **110**(3), 255–261 (1988)
5. Salzar, R.S., Pindera, M.J., Barton, F.W.: Elastoplastic analysis of layered metal matrix composite cylinders. Part 1: Theory. ASME J. Press. Vessel Technol. **118**(1), 13–20
6. Sim, R.G.: Reference stresses and temperatures for cylinders and spheres under internal pressure with a steady heat flow in the radial direction. Int. J. Mech. Sci. **15**, 211–220 (1973)
7. Durban, D., Baruch, P.: Behavior of an incrementally elastic thick walled sphere under internal and external pressure. Int. J. Non-Linear Mech. **9**, 105–119 (1974)
8. Miller, G.K.: Stresses in a spherical pressure vessel undergoing creep and dimensional changes. Int. J. Solids Struct. **32**(14), 2077–2093 (1995)
9. Nayebi, A., El, A.R.: Cyclic plastic and creep behavior of pressure vessels under thermo mechanical loading. J. Comput. Mater. Sci. **25**, 285–296 (2002)
10. Aleayoub, S.M.A., Loghman, A.: Creep stress redistribution analysis of thick-walled FGM spheres. J. Solid Mech. **2**(2), 115–128 (2010)
11. Nie, G.J., Zhong, Z., Batra, R.C.: Material tailoring for functionally graded hollow cylinders and spheres. J. Compos. Sci. Technol. **71**, 666–673 (2011)
12. Nejad, M.Z., Hoseini, Z., Niknejad, A., Ghannad, M.: A new analytical solution for creep stresses in thick-walled spherical pressure vessels. J. Basic Appl. Sci. Res. **1**(11), 2162–2166 (2011)
13. Sadeghian, M., Toussi, H.E.: Axisymmetric yielding of functionally graded spherical vessel under thermo-mechanical loading. J. Comput. Mater. Sci. **50**, 975–981 (2011)
14. Pankaj, T.: Creep transition stresses of a thick isotropic spherical shell by finitesimal deformation under steady-state of temperature and internal pressure. J. Therm. Sci. **15**(2), 157–165 (2011)
15. Bhatnagar, N.S., Arya, V.K.: Creep of thick-walled spherical vessels under internal pressure considering large strain. Indian J. Pure Appl. Math. **6**(10), 1080–1089 (1975)
16. Bayat, Y., Ghannad, M., Torabi, H.: Analytical and numerical analysis for the FGM thick sphere under combined pressure and temperature loading. J. Arch. Appl. Mech. **82**, 229–242 (2012)
17. Singh, T., Gupta, V.K.: Effect of anisotropy on steady state creep in functionally graded cylinder. Compos. Struct. **93**(2), 747–758 (2011)

Chapter 35
Adiabatic Analysis of Spherical and Cylindrical Textured Hydrodynamic Journal Bearing

Mohammad Arif, Saurabh Kango, Dinesh Kumar Shukla, and Nitin Sharma

Abstract The present article highlights on the dual role of viscous heating and surface texturing on the performance of hydrodynamically lubricated finite journal bearing. The Reynolds and energy equations are coupled together, and the solution of these governing equations has been accomplished using finite difference technique. To find more realistic results, JFO boundary conditions are used to solve the Reynolds equation. Based on the investigations reported herein, it is observed that out of two surface textures, the cylindrical texture is the best for improving the load and friction coefficient at high speeds as compared to spherical texture, whereas the improvement in average temperature is highest at low speeds.

Keywords Thermal analysis · JFO boundary condition · Spherical and cylindrical dimpling · Average temperature · Coefficient of friction

List of Symbols

c_r	Radial clearance (μm)
$\bar{F}_\mathrm{Smooth/Texture}$	Dimensionless friction force
$f_\mathrm{Smooth/Texture}$	Coefficient of friction
g	Switch function
i	Number of nodes in X-direction
j	Number of nodes in Y-direction
k	Number of nodes in Z-direction
I	Number of iterations
N	Shaft speed (rpm)
N_θ	Number of nodes in circumferential direction
N_Z	Number of nodes in axial direction

M. Arif (✉) · S. Kango · D. K. Shukla · N. Sharma
Department of Mechanical Engineering, Dr. B R Ambedkar National Institute of Technology, Jalandhar 144011, India
e-mail: mohammada.me.18@nitj.ac.in

$N_{t\theta}$	Number of textures in circumferential direction
N_{tZ}	Number of textures in axial direction
p	Bearing pressure (Pa)
P	Dimensionless pressure: $P = \frac{pc_r^2}{\eta RU}$
p_c	Cavitation pressure
R	Shaft radius (m)
r_y	Dimple depth (μm)
r	Dimple radius (m)
T_0	Inlet temperature (°C)
T	Lubricant temperature (°C)
$\bar{T}$	Dimensionless temperature: $\bar{T} = \gamma(T - T_0)$
U	Shaft speed (m/s)
u	Lubricant velocity in X-direction (m/s)
w	Lubricant velocity in Z-direction (m/s)
$\bar{W}_{\text{Smooth/Texture}}$	Dimensionless load for smooth and texture bearing $= (W * c_r^2)/(\eta * U*L*R^2)$
θ	Circumferential angle (degree)
γ	Viscosity-temperature index
ϕ	Film content of the lubricant
β	Bulk modulus of the lubricant
ε	Eccentricity ratio
τ	Shear stress (Pa)
ρ	Lubricant density (Kg/m^3)
α	Dissipation number $= \frac{R\gamma\eta_0 U}{\rho c_r^2}$

35.1 Introduction

It is being widely reported in the literature that micro-texturing/dimpling on the surfaces of the tribological elements is proving to be beneficial in terms of reduction in friction and wear at the lubricated interface [1]. Dimples at the mating interface of tribo-elements act as micro-hydrodynamic bearings, which generate the pressure in the lubricating film for supporting the external load efficiently. Moreover, the micro-dimples of texture pattern fabricated on the surfaces of tribo-elements serve as innumerable micro-fluid film bearings. However, these shallow micro-dimples work as lubricant reservoirs, which provide lubricant to spread at the interface of tribo-elements in case of mixed/boundary lubrications. Moreover, these dimples also may act as wear debris/foreign particles [2]. Research on the influences of surface roughness, corrugations, and textures on the bearing performance has been attempted in different forms in the past. Huynh [3–5] carried out numerical analysis for slider bearing with sinusoidal corrugations and concluded that the location of sinusoidal roughness affects the performance of slider bearing strongly. The influence of surface

roughness on journal bearing was studied by Maharshi et al. [6], where authors concluded that the roughness has pronounced influence on the performance of bearing. The effect of positive micro-grooving at different locations on the journal bearing surface has been investigated by Kango and Sharma [7], wherein the authors concluded that the load-carrying capacity is very high in the minimum film thickness region for optimum eccentricity ratio. The authors also performed a comparative study of sinusoidal, full- and half-wave positive micro-grooving and observed that longitudinal sinusoidal roughness is best suited for decreasing the friction force. Kango et al. [8] reported that the half-wave negative roughness texture enhances the bearing performance more in comparison with full-wave texture on the journal bearing surface. In other works, Sharma et al. [9] studied the combined effect for a finite journal bearing with JFO boundary conditions of spherical textures with couple stress fluids and reported that load-carrying capacity gets increased with couple stresses at different eccentricity ratios. However, with textures, the increase in load-carrying capacity was noted significant only at low eccentricity ratios. Yamada et al. [10, 11] studied the effect of square dimples on static and dynamic characteristics of journal bearing and concluded that static and dynamic characteristics of journal bearing get improved by square dimples. Wang et al. [12] carried out thermo-hydrodynamic analysis of journal bearing with surface texturing and concluded that the textured bearing gave a higher load-carrying capacity, a lower maximum oil pressure, and a lower oil temperature rise than the un-textured bearing based on an optimal design of texture. Tala-Ighil et al. [13, 14], Cupillard et al. [15], Brizmer and Kligerman [16] have studied the roles of different surface dimpling (spherical and cylindrical) in their respective studies under certain assumptions and considerations for hydrodynamic journal bearings. The authors concluded that the partial surface texturing has a great influence on the performance characteristics of the journal bearings. However, these researchers have presented their respective investigations for isothermal operating conditions. Moreover, the authors of the present paper could not notice any research paper dealing with the analysis of surface dimpled/textured journal bearings using the JFO boundary condition by incorporating viscous heat dissipation in the lubricating film. Thus, the objective of this paper is to present a numerical model for the thermal analysis of hydrodynamically lubricated journal bearing having spherical and cylindrical surface dimpling on the bearing surface by incorporating realistic JFO boundary condition in order to satisfy the mass conservation in cavitation zone.

35.2 Theoretical Analysis

35.2.1 Mathematical Model

Schematic diagram of journal bearing adopted in the present investigation with coordinate system is shown in Fig. 35.1. The circumferential length in the X-direction, length in Z-direction, and film thickness in Y-direction are represented by $R\theta$, L, and
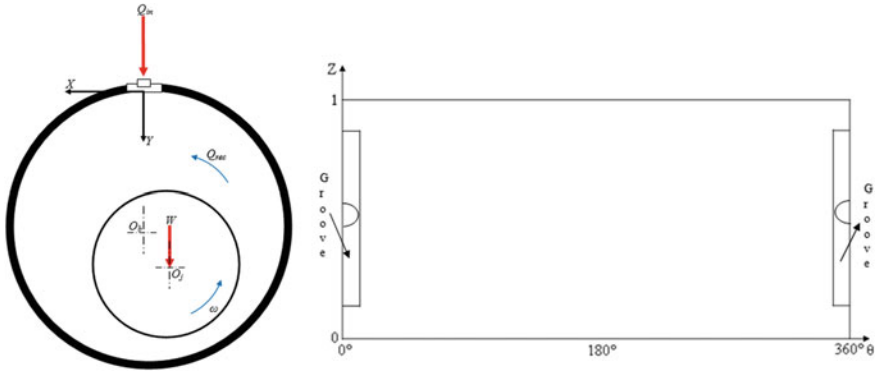
Fig. 35.1 Schematic diagram of journal bearing

H, respectively. It is essential to mention here that the proposed investigation has been carried out for incompressible and steady-state laminar flow of lubricating oil. Moreover, body and inertia forces have been ignored. The expression for lubricating film thickness is defined as follows:

$$H = (1 + \varepsilon \cos \theta) + \Delta h(\theta, Z) \tag{35.1}$$

where $\Delta h(\theta, Z)$, the dimensionless film thickness component due to different surface dimples, has been adopted from Tala-Ighil et al. [13, 14] and is computed as follows:

$$\Delta h(\theta, Z)_{\text{cylindrical}} = r_y$$
$$\Delta h(\theta, Z)_{\text{spherical}} = \frac{r_y}{r}\sqrt{r^2 - (R\theta - x_c)^2 - (z - z_c)^2}$$

where 'ε' is the eccentricity ratio.

Reynolds equation suggested by Elrod [17] for incorporating the cavitation/mass conservation feature is used in computation as follows:

$$\frac{\partial}{\partial \theta}\left(\frac{H^3 g}{\bar{\eta}}\frac{\partial \phi}{\partial \theta}\right) + \left(\frac{R}{L}\right)^2 \frac{\partial}{\partial Z}\left(\frac{H^3 g}{\bar{\eta}}\frac{\partial \phi}{\partial Z}\right) = \frac{6}{\bar{\beta}}\frac{\partial(\phi H)}{\partial \theta} \tag{35.2}$$

The switch function (g) is taken from the works of Elrod [17] as follows:

$$g = 0 \quad \phi < 1 \quad \text{and} \quad g = 1 \quad \phi < 1 \tag{35.3}$$

The pressure in the full film region is determined from the following relation:

$$p = p_c + \beta(\phi - 1) \tag{35.4}$$

For accounting the temperature rise in the lubricating film due to viscous heat dissipation, the following energy equation is used [18]:

$$\bar{u}\frac{\partial \bar{T}}{\partial \theta} + \bar{w}\frac{\partial \bar{T}}{\partial Z}\left(\frac{R}{L}\right) = \frac{\alpha \bar{\eta}}{H^2}\left[\left(\frac{\partial \bar{u}}{\partial Y}\right)^2 + \left(\frac{\partial \bar{w}}{\partial Y}\right)^2\right] \tag{35.5}$$

In this investigation, it is assumed that the heat generated within the lubricating film is completely carried away by the lubricant through convection mode of heat removal. Moreover, herein, temperature variation across the lubricating film has been neglected.

Lubricating oil viscosity variation with temperature is taken by the following expression:

$$\bar{\eta} = \exp(-\bar{T}) \tag{35.6}$$

Load-carrying capacity ($\bar{W}$), friction force ($\bar{F}$), and coefficient of friction (f) are computed using the following relations:

$$\bar{W}_{\text{texture}} = \int_0^1 \int_0^{2\pi} P\,\mathrm{d}\theta\,\mathrm{d}Z \tag{35.7}$$

$$\bar{F}_{\text{texture}} = \int_0^1 \int_0^{2\pi} \bar{\tau}\,\mathrm{d}\theta\,\mathrm{d}Z \tag{35.8}$$

$$f_{\text{texture}} = \frac{\bar{F}_{\text{texture}}}{\bar{W}_{\text{texture}}} \tag{35.9}$$

$$\bar{T}_{\text{average}_{\text{texture}}} = \frac{\sum \bar{T}(i,k)}{N_\theta \times N_Z} \tag{35.10}$$

$$\text{Percentage variation in } \bar{W} = \frac{\bar{W}_{\text{texture}} - \bar{W}_{\text{smooth}}}{\bar{W}_{\text{smooth}}} \times 100 \tag{35.11}$$

$$\text{Percentage variation in } f = \frac{f_{\text{texture}} - f_{\text{smooth}}}{f_{\text{smooth}}} \times 100 \tag{35.12}$$

$$\text{Percentage variation in } \bar{T}_{\text{average}} = \frac{\bar{T}_{\text{average}_{\text{texture}}} - \bar{T}_{\text{average}_{\text{smooth}}}}{\bar{T}_{\text{average}_{\text{smooth}}}} \times 100 \tag{35.13}$$

Discretization of Reynolds and energy equations has been done using finite difference method. In the present work, coupled solution of the governing equation is achieved for evaluation of pressure and temperature in the domain. Gauss–Seidel iterative method with modified switch function algorithm purposed by Fesanghary and Khonsari [19] is adopted for speedy convergence. Following convergence criteria

are used in acquiring the numerical results of the domain variables:

$$\sum\sum \left| \frac{(P_{ik})_N - (P_{ik})_{N-1}}{(P_{ik})_N} \right| < 10^{-06} \tag{35.14}$$

$$\sum\sum \left| \frac{(\bar{T}_{i,k})_N - (\bar{T}_{ik})_{N-1}}{(\bar{T}_{ik})_N} \right| < 10^{-08} \tag{35.15}$$

where i, k, and N represent the number of nodes in X-direction, Z-direction, and number of iterations, respectively. The numerical results presented in this paper are tested for grid independence and have been generated using the grid size (217, 70). Corresponding to this grid size (217, 70), a dimple has about 100 nodes. Results negligibly varied if nodes were kept more than 100 in a dimple.

35.3 Results and Discussion

35.3.1 Validation of the Smooth Bearing Model

Numerical results have been presented for different input parameters of journal bearing and lubricating oil mentioned in the captions of various figures reported herein. Moreover, the input parameters used in this work are also presented in Table 35.1. Figure 35.2a, b presents comparisons of numerical results for pressure and temperature variations achieved from the proposed mathematical model with the works of Elrod [17] and Jang and Chang [18], respectively. Good correlations between both the results can be seen in these figures. This develops a fairly reasonable confidence in the proposed numerical model.

35.3.2 Influence of Number of Dimples in Circumferential Direction

Brizmer and Kligerman [16] have investigated the influence of spherical texture on the performance of short and infinite bearing at low and high eccentricity ratios. The authors concluded that the more improvement in load-carrying capacity is achieved only at a low eccentricity ratio with partial surface texturing. Therefore, the present work is based on low eccentricity ratio ($\varepsilon = 0.3$).

The schematic representation for textures is shown in Fig. 35.3 for one and ten number of dimples in circumferential direction. It is essential to mention here that in the surface texturing, 3D shape of the micro-dimple is spherical and cylindrical as shown in Fig. 35.4a–e. Figures 35.5a–e and 35.6a–e depict the 3D representation of the dimensionless thermal pressure and temperature for both the cases (smooth

**Table 35.1** Input parameters for the present work

Sr. No.	Initial parameters	Values	Unit
1	Eccentricity ratio (ε)	0.3	
2	Dynamic viscosity (η)	0.08	(Pa.s)
3	Shaft speed (N)	1000, 3000, 5000	(rpm)
4	Radial clearance (Cr)	50	(μm)
5	Shaft radius (R)	0.02	(m)
6	Bearing length (L)	0.04	(m)
7	Specific heat (cp)	1840	(J/kg °C)
8	Lubricant density (ρ)	881.6	(Kg/m^3)
9	Nodes (N_θ and N_z)	217 and 70	—
10	dθ and dz	0.00058 and 0.00058	(m)
11	Dimple radius (r)	0.0028	(m)
12	Area density of dimple (S_p)	0.68	
13	a	0.00058	(m)
14	b	0.00058	(m)
15	L_x	0.006	(m)
16	L_z	0.006	(m)
17	Inlet temperature	40	(°C)
18	Viscosity-temperature index	0.0315	(°C^{-1})

and dimpled). In the present study, the influence of location of surface texture in the circumferential direction, and dimple depth on performance parameters of journal bearing (load, friction coefficient, and average temperature) is investigated. In this study, the number of dimples in axial direction has been kept constant ($N_{tZ} = 6.0$) throughout, whereas, the numbers of dimples in the circumferential direction vary from 1 to 10 as shown in Fig. 35.3b–e, and this has been considered in the convergent zone from 0 to 210 degrees. Moreover, in this investigation, the textured surface area fraction is 0.68.

Figures 35.7, 35.8 and 35.9 show the influence of number of dimples ($N_{t\theta}$) for both textured bearings (spherical and cylindrical) with and without constant viscosity (isothermal and thermal). It has been observed that the percentage load increases up to 4.0, and after this value, it starts to decrease as shown in Fig. 35.7 for both the cases. More reduction in % load is achieved for cylindrical texture at higher number of dimples. The improvement in % load for spherical and cylindrical textures is 3.901% and 3.828%, respectively, at $N_{t\theta} = 4.0$. Figure 35.8 elucidates similar behaviour in terms of improvement in friction coefficient for both the cases. This may be due to the fact that friction coefficient is the ratio of load and friction force, as and when the load increases, the friction force gets increased. Therefore, the friction coefficient shows more reduction at $N_{t\theta} = 4.0$, i.e. up to 4.809 and 5.075% for
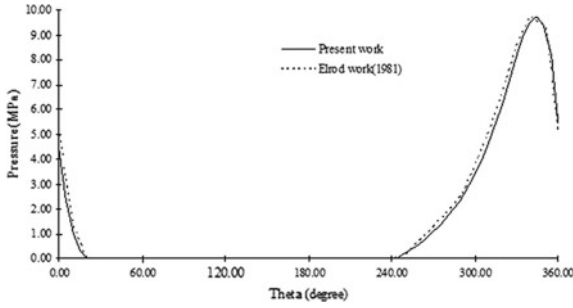
(a) Comparison of pressure results for smooth journal bearing
[D=62.8mm, h₀=55μm, L/D=10, Location of grooves= 60° and 240°,
Number of grooves=2, U=19.7m/s, ε =0.8, η=0.0035 Pa.
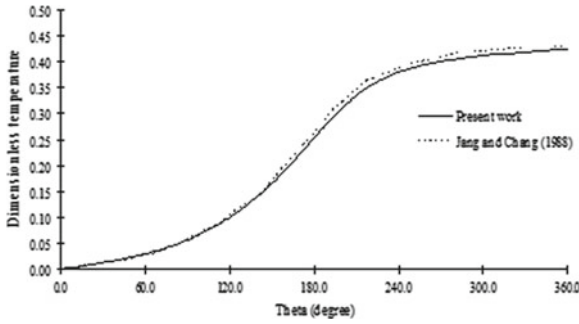
(b) Comparison of the dimensionless temperature for smooth bearing
[Cp=1840 J/Kg/°C, cr =100 μm, D=100 mm, L/D=1.0, N=1000 rpm,
ε =0.6, η=0.0416 Pa.s, γ=0.0315/°C]

Fig. 35.2 Validation of the proposed model with the published results of researchers
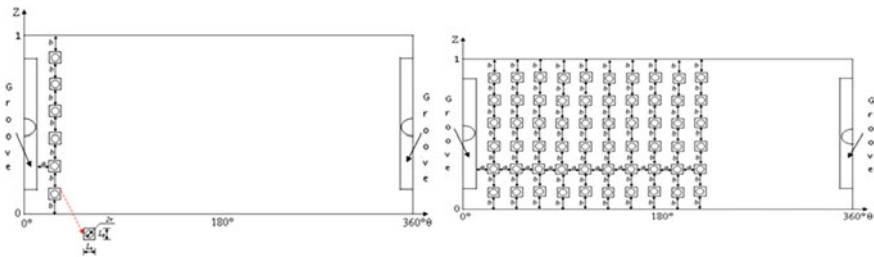
Fig. 35.3 Schematic diagram for textured hydrodynamic journal bearing
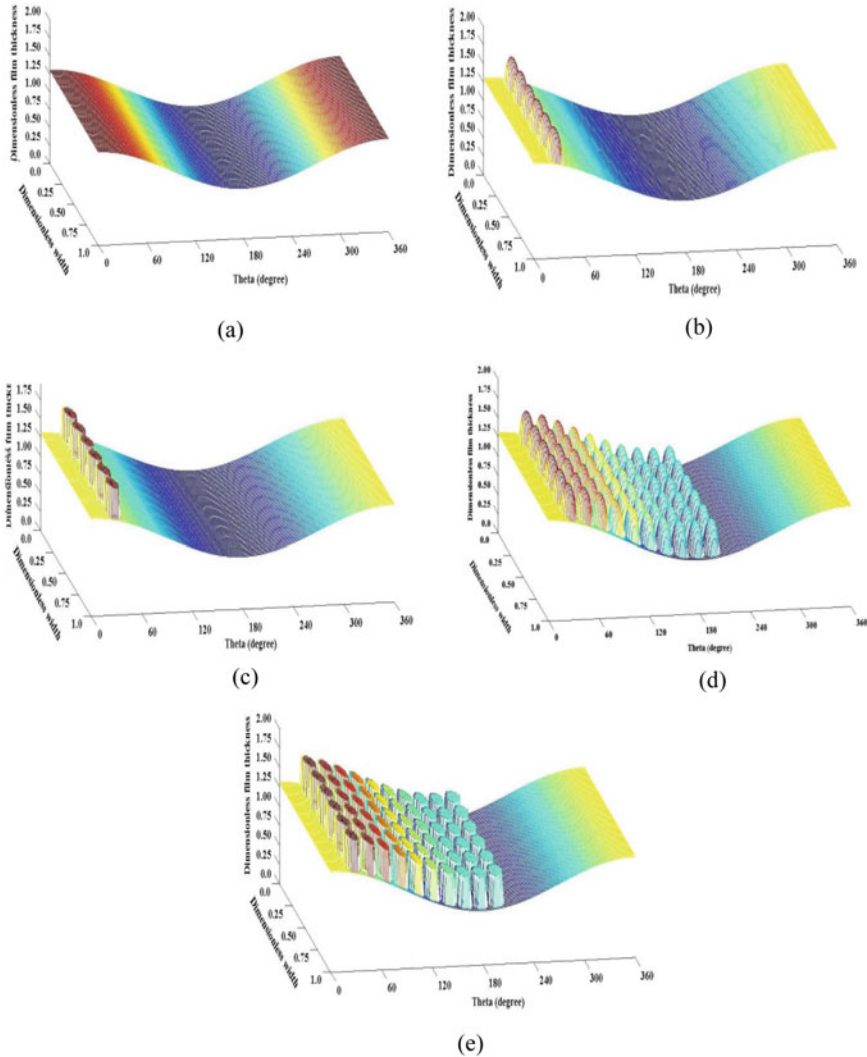
Fig. 35.4 Lubricant film thickness for configurations of smooth, spherical, and cylindrical textured bearing surface [$N = 1000$ rpm, $r_y = 20\ \mu$m, $N_{t\theta} = 1.0$ to 10.0, $N_{tZ} = 6.0$]

spherical and cylindrical textures, respectively. Considerably higher reduction in average temperature is achieved for cylindrical texture (4.218%) as compared to spherical texture (3.258%). Thus, it is observed that the cylindrical texture improves the bearing performance more in terms of friction, and average temperature reduction as compared to spherical texture for constant geometry and similar input parameters.

There is less variation in values of load and friction coefficient for isothermal and thermal cases as shown in Figs. 35.7a, b, and 35.8a, b. The main reason behind this
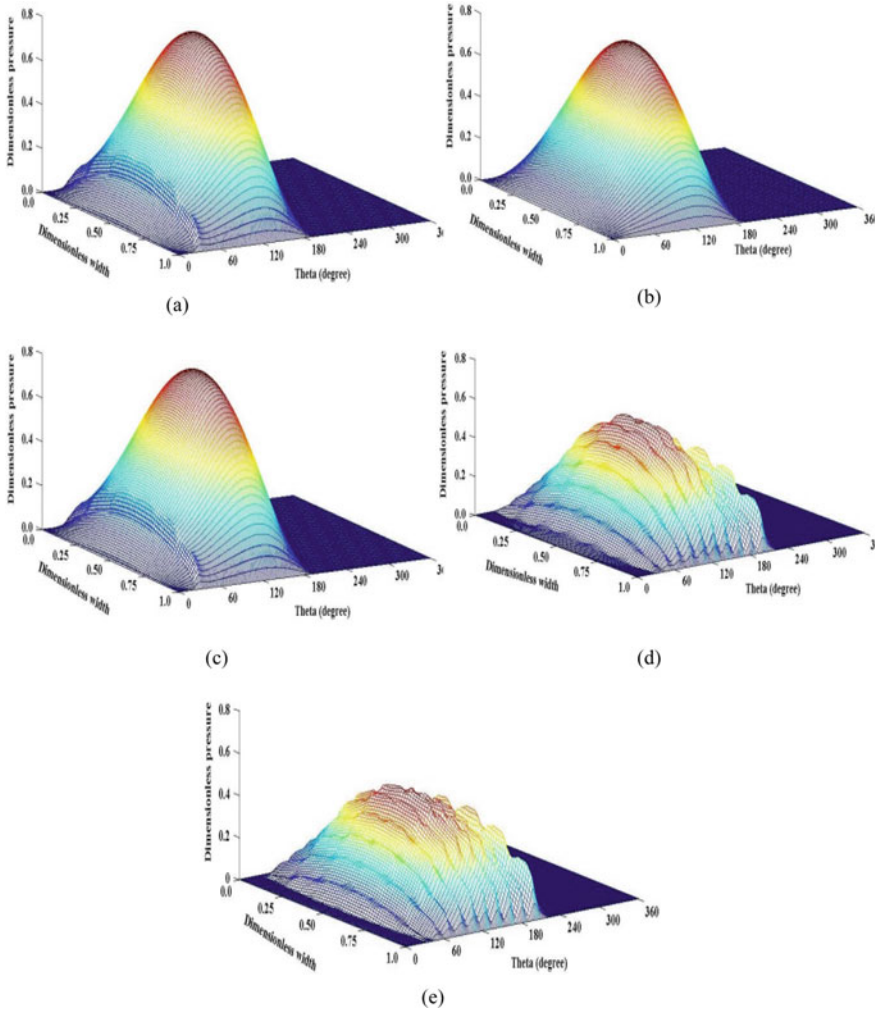
Fig. 35.5 Lubricant pressure (with thermal effect) for configurations of smooth, spherical, and cylindrical textured bearing surface [$N = 1000$ rpm, $r_y = 20\,\mu$m, $N_{t\theta} = 1.0$ to 10.0, $N_{tZ} = 6.0$]

is lower journal speed (1000 rpm) as at low speeds, the heating effect due to sliding of intermediate lubricant layers on viscosity is less and leads to less degradation of the lubricant. Therefore, the percentage variation in performance parameters of the bearing is almost the same for isothermal and thermal cases (3.828 and 3.351% reduction in friction coefficient for isothermal and thermal cases, respectively). As the best performance has been observed to be corresponding to four numbers of dimples in circumferential direction, i.e. $N_{t\theta}$ value, hence, for further analysis, four numbers of dimples in the circumferential direction have been taken.
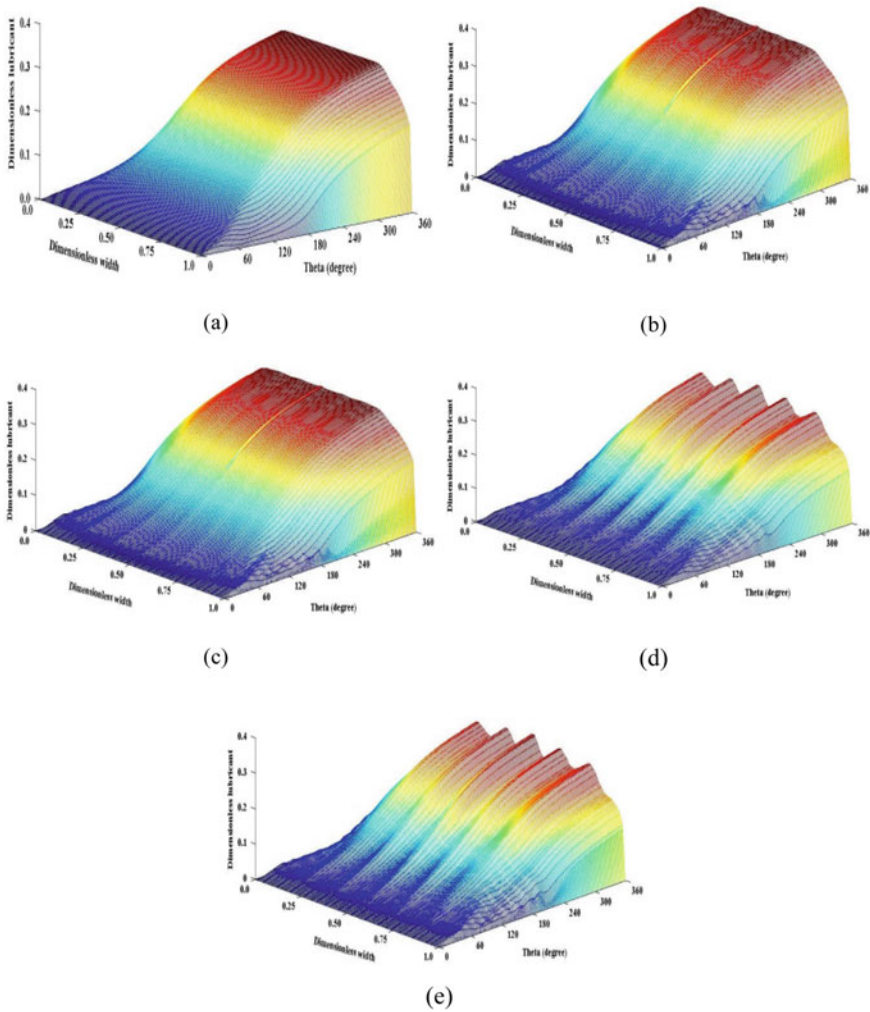
Fig. 35.6 Lubricant temperature for configurations of smooth, spherical, and cylindrical textured bearing surface [$N = 1000$ rpm, $r_y = 20\,\mu$m, $N_{t\theta} = 1.0$ to 10.0, $N_{tZ} = 6.0$]

35.3.3 Influence of Journal Speed

The values in terms of percentage variation for thermal case at low speeds are almost the same due to less heat dissipation and corresponding lower temperature generation as discussed earlier. However, at higher speeds, the influence of journal speed with both textured bearings is visible as presented in Table 35.2. The percentage improvement in performance parameters is approximately same for all journal speeds in isothermal case. This is happening due to constant lubricant viscosity in this case.
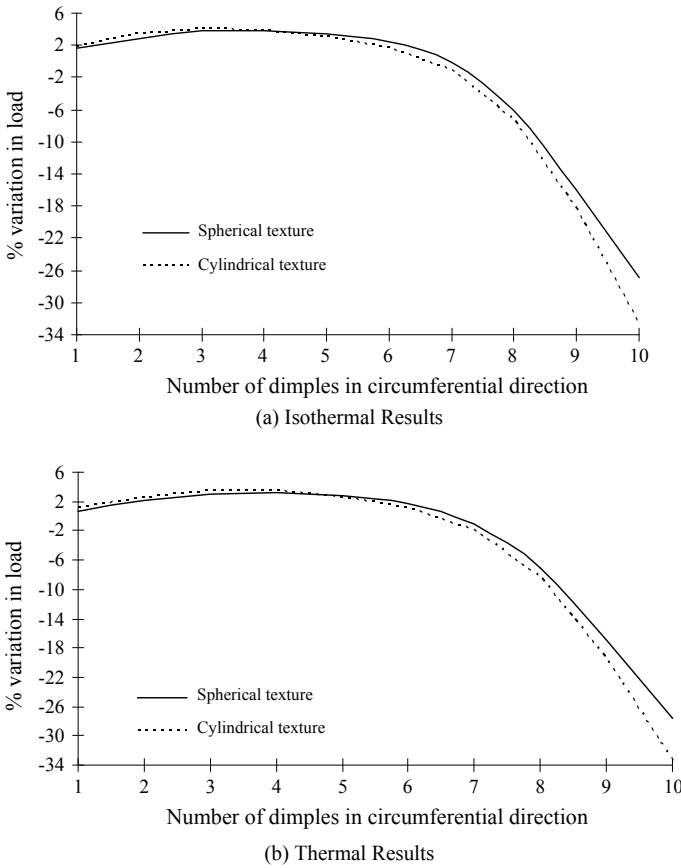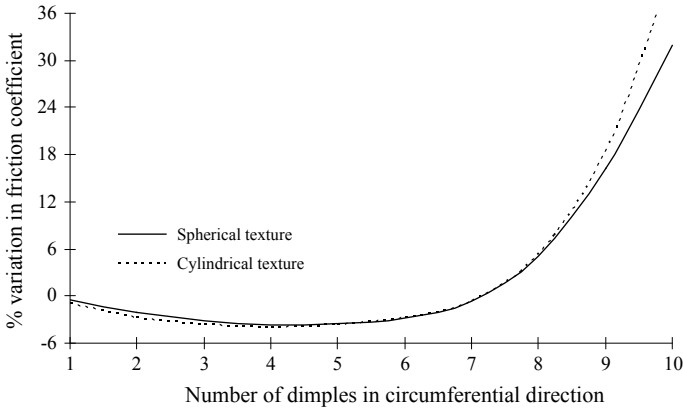
Fig. 35.7 Comparison of different textures on the basis of % variation in load with change in $N_{t\theta}$ [$N = 1000$ rpm, $r_y = 20\,\mu\text{m}$, $N_{t\theta} = 1.0$ to 10.0, $N_{tZ} = 6.0$]

However, there more difference is achieved in terms of percentage improvement with change of journal speed for thermal case. Two main observations from Table 35.2 are given below:

1. Higher percentage reduction up to 5.73% in friction coefficient is seen for cylindrical texture at high speed (5000 rpm).
2. Higher percentage reduction up to 4.22% in average temperature has been observed for cylindrical texture at low speed (1000 rpm).

It is therefore indicative that the journal speed influences the performance of textured bearings.

(a) Isothermal Results
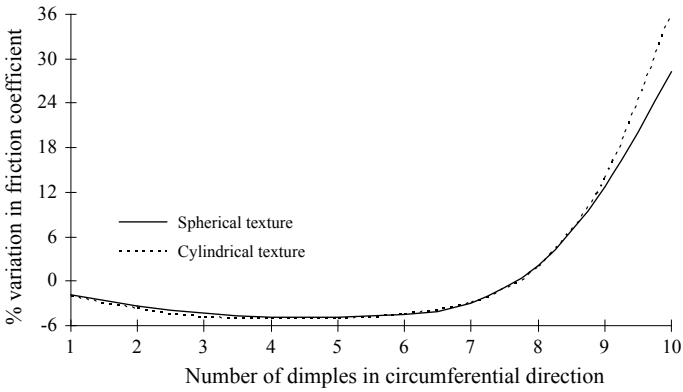
(b) Thermal results

Fig. 35.8 Comparison of different textures on the basis of % variation in friction coefficient with change in $N_{t\theta}$ [$N = 1000$ rpm, $r_y = 20$ μm, $N_{t\theta} = 1.0$ to 10.0, $N_{tZ} = 6.0$]

35.3.4 Influence of Dimple Depth

The percentage variation due to thermal conditions in load, friction coefficient, and average temperature with different dimple depths for textured bearings is shown in Figs. 35.10, 35.11, and 35.12, respectively. The load-carrying capacity increases with increasing the dimple depth up to 15 μm for cylindrical texture (3.794%, 5.879%, and 6.537% at 1000, 3000, and 5000 rpm, respectively, at 15 μm) and up to 20 μm for spherical texture (3.211%, 5.229%, and 5.807% at 1000, 3000, and 5000 rpm, respectively, at 20 μm) as depicted in Fig. 35.10. The corresponding reduction in friction coefficient is 4.265, 5.764, and 6.008% for cylindrical texture at 15 μm and 3.620, 5.128, and 5.342% for spherical texture at 20 μm with three different speeds,
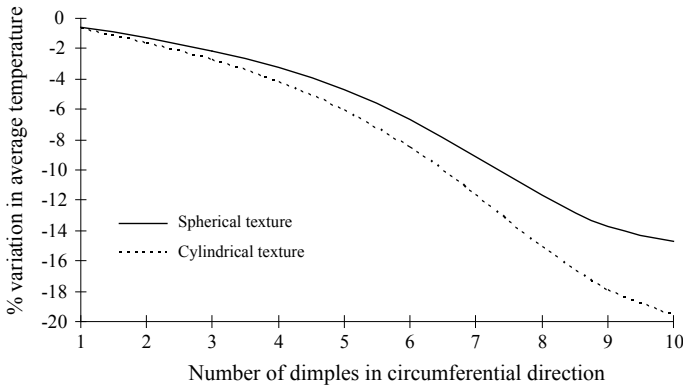
Fig. 35.9 Comparison of different textures on the basis of % variation in average temperature with change in $N_{t\theta}$ [N = 1000 rpm, r_y = 20 μm, $N_{t\theta}$ = 1.0 to 10, N_{tZ} = 6.0]

Table 35.2 Comparison of % variation in load, friction coefficient, and average temperature for spherical and cylindrical textures with change in journal speed [r_y = 20 μm, $N_{t\theta}$ = 4.0, N_{tZ} = 6.0]

| Journal speed (rpm)	Texture	% variation in load	% variation in friction coefficient	% variation in average temperature
Isothermal results				
1000	Spherical	+3.901	−4.809	—
	Cylindrical	+3.828	−5.075	—
3000	Spherical	+3.895	−4.734	—
	Cylindrical	+3.821	−4.998	—
5000	Spherical	+3.895	−4.729	—
	Cylindrical	+3.821	−4.991	—
Thermal results				
1000	Spherical	+3.211	−3.620	−3.258
	Cylindrical	+3.351	−3.985	−4.218
3000	Spherical	+5.229	−5.128	−3.068
	Cylindrical	+5.460	−5.447	−3.954
5000	Spherical	+5.807	−5.342	−2.913
	Cylindrical	+6.218	−5.733	−3.762
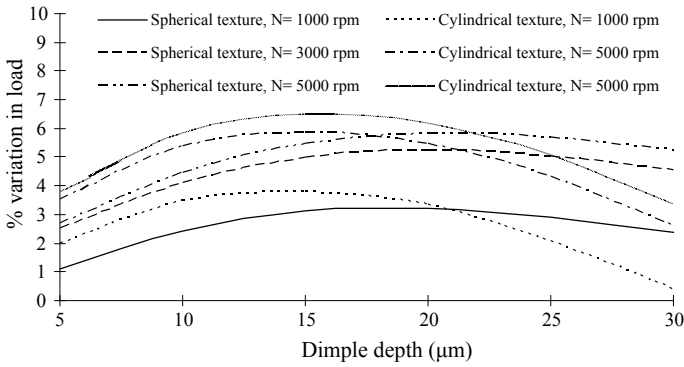
Fig. 35.10 Comparison of different textures on the basis of % variation in load with change in dimple depth [$N = 1000$ rpm, $r_y = 20$ μm, $N_{t\theta} = 4.0$, $N_{tZ} = 6.0$]
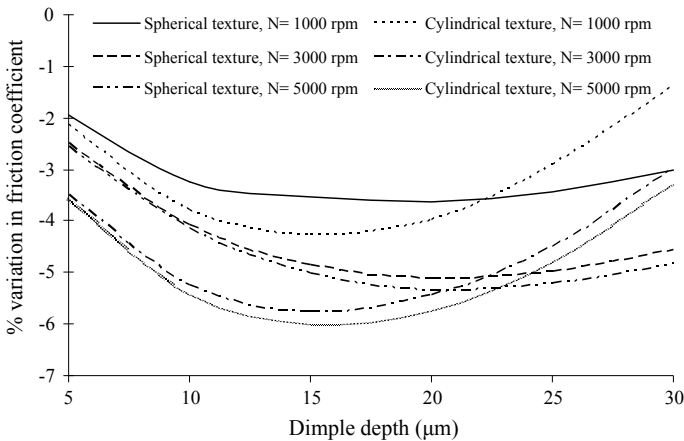

Fig. 35.11 Comparison of different textures on the basis of % variation in friction coefficient with change in dimple depth [$N = 1000$ rpm, $r_y = 20$ μm, $N_{t\theta} = 4.0$, $N_{tZ} = 6.0$]

respectively, as observed from Fig. 35.11. The percentage reduction in average temperature is 3.658, 3.438, and 3.268% for cylindrical texture and 3.258, 3.068, and 2.913% for spherical textures for different speeds as shown in Fig. 35.12.

It can therefore be concluded from above discussion that the optimal value of dimple depth for cylindrical and spherical textures is 15 and 20 μm, respectively, at all three journal speeds. It is also observed that the percentage improvement is less for cylindrical texture when compared with spherical texture at high dimple depths.
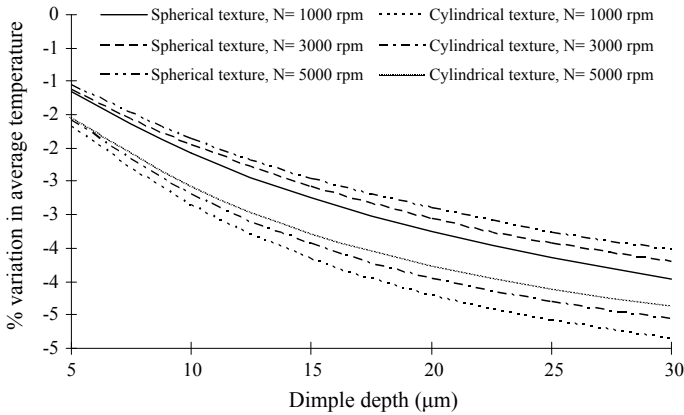
Fig. 35.12 Comparison of different textures on the basis of % variation in average temperature with change in dimple depth [$N = 1000$ rpm, $r_y = 20$ μm, $N_{t\theta} = 4.0$, $N_{tZ} = 6.0$]

35.4 Conclusions

In the present work, a comparative study has been reported between two different surface textures (spherical and cylindrical) for isothermal and thermal cases with different journal speeds and dimple depths.

Following are the broad outcomes of this study:

1. The number of dimples in circumferential direction has a great influence on the bearing performance characteristics. From the present study, four numbers of dimples in circumferential direction at inlet zone have been found to be best for improving the load, friction coefficient, and average temperature.
2. The percentage variation of thermal results is more at higher speeds as compared to isothermal results.
3. Higher reduction in friction coefficient is achieved at high speeds. However, the reduction in average temperature is high at low speed.
4. The optimum value of dimple depth is different for both the textured bearings.

It has been observed that out of two surface textures, the cylindrical texture is the best for improving the load and friction coefficient at high speeds as compared to spherical texture, whereas the improvement in average temperature is highest at low speeds.

References

1. Etsion, I.: Laser surface texturing and applications In: Nikas, G.K. (ed) Recent developments in wear prevention, friction and lubrication. 137–157 (2010)
2. Etsion, I.: State of the art in laser surface texturing. ASME J. Tribol. **127**, 248–253 (2005)

3. Huynh, B.P.: Numerical study of slider bearings with limited corrugation. ASME J. Tribol. **127**, 582–595 (2005)
4. Huynh, B.P.: Numerical investigation of slider bearings with limited corrugation and power-law Lubricant. In: Proceedings of the ASME 2011 International Mechanical Engineering Congress & Exposition IMECE2011, Denver, Colorado, USA
5. Huynh, B.P: Thermal effects in slider bearings with limited corrugation and power-law lubricant. In: Proceedings of the ASME 2012 International Mechanical Engineering Congress & Exposition IMECE2012, Houston, Texas, USA
6. Maharshi, K., Mukhopadhyay, T., Roy, B., Roy, L., Dey, S.: Stochastic dynamic behaviour of hydrodynamic journal bearings including the effect of surface roughness. Int. J. Mech. Sci. **142**, 370–383 (2018)
7. Kango, S., Sharma, R.K.: Studies on the influence of surface texture on the performance of hydrodynamic journal bearing using power law model. Int. J. Surf. Sci. Eng. **4**(4/5/6): 505–524 (2010)
8. Kango, S., Singh, D., Sharma, R.K.: Numerical investigation on the influence of surface texture on the performance of hydrodynamic journal bearing. Meccanica **47**, 469–482 (2012)
9. Sharma, N., Kango, S., Tayal, A., Sharma, R.K., Sunil: Investigation on the influence of surface texturing on a couple stress fluid based journal bearing by using JFO boundary conditions. Tribol. Trans. **59**, 579–584 (2016)
10. Yamada, H., Taura, H., Kaneko, S.: Numerical and experimental analyses of the dynamic characteristics of journal bearings with square dimples. J. Tribol. **140**(1), 011703 (2018)
11. Yamada, H., Taura, H., Kaneko, S.: Static characteristics of journal bearings with square dimples. J. Tribol. **139**(5), 051703 (2017)
12. Wang, L., Han, Z., Chen, G., Su, H.: Thermo-hydrodynamic analysis of large-eccentricity hydrodynamic bearings with texture on journal surface. Proc. Inst. Mech. Eng. Part C: J. Mech. Eng. Sci. **232**(19), 3564–3569 (2018)
13. Tala-Ighil, N., Maspeyrot, P., Fillon, M., Bounif, A.: Effects of surface texture on journal bearing characteristics under steady state operating conditions. Proc. Inst. Mech. Eng. Part C: J. Eng. Tribol. **221**, 623–633 (2007)
14. Tala-Ighil, N., Fillon, M., Maspeyrot, P.: Effect of textured area on the performances of a hydrodynamic journal bearing. Tribol. Int. **44**, 211–219 (2011)
15. Cupillard, S., Glavatskih, S., Cervantes, M.J.: CFD analysis of journal bearing with surface texturing. Proc. Inst. Mech. Eng. Part J: J. Eng. Tribol. **222**, 97–107 (2008)
16. Brizmer, V., Kligerman, Y.: A laser surface textured journal bearing. ASME J. Tribol. **134**, 031702-1-9 (2012)
17. Elrod, H.G.: A cavitation algorithm. ASME J. Tribol. **103**, 350–354 (1981)
18. Jang, J.Y., Chang, C.C.: Adiabatic analysis of finite width journal bearings with non-newtonian lubricants. Wear **122**, 63–75 (1988)
19. Fesanghary, M., Khonsari, M.M.: A modification of the switch function in the elrod cavitation algorithm. ASME J. Tribol. **133**, 024501-1-024501-4 (2011)

Chapter 36
Analysis of Aluminum AA6061 in Electromagnetic Forming

Nilesh Tiwari and Megha Nagrale

Abstract Weight reduction in the automotive and aerospace industries is of special importance. This leads to lower fuel consumption and high efficiency. Discharge circuit parameters and mechanical properties vary during the electromagnetic forming process. The mechanical properties change along with time and tube length during the electromagnetic expansion. A coupled analytical model is developed to predict the parametric variation of the discharge circuit, corresponding radial pressure and stress acting on the tube. The electromagnetic forming simulation was performed on 2.5 mm thick aluminum tube with a length of 100 mm using 7 turns helical copper coil. A 2D coupled simulation model is developed using COMSOL MULTIPHYSICS software and simulation results are used to compare with analytical results. Based on which maximum deformation is predicted during the electromagnetic forming process and work-piece hardness is obtained.

Keywords Electromagnetic forming · High strain rate · Plastic deformation · Lorentz' force

Nomenclature

EMF Electromagnetic forming
$I(t)$ Current at that instant (A)
$U_{(t)}$ Charging voltage (V)
$E_c(t)$ Stored energy in the capacitor (KJ)
ω Frequency of the current (Hz)
β Damping coefficient
v Velocity of the tube at a point (m/sec)
d Displacement of the tube (mm)

N. Tiwari (✉) · M. Nagrale
Department of Mechanical Engineering, Sardar Patel College of Engineering,
Mumbai 400 058, India
e-mail: ntiwari252@gmail.com

36.1   Introduction

Due to low density, high strength to weight ratio aluminum alloy is increasingly focused on and widely applied fields such as automotive, aerospace industry which craves the lightweight designs to enhance fuel utilization and reduce the cost of production [1]. Electromagnetic forming is an impulse or high-speed forming technology which uses a pulse magnetic field to apply Lorentz' force on the work-piece made up of highly electrically conductive material without mechanical contact or working medium. In the electromagnetic forming process, it can shape and weld similar or dissimilar metal along with other benefits (e.g., high precision, short cycle time, uniform strain distribution). The main components of the electromagnetic forming process are high voltage power supply, capacitor bank, switch (trigger), and forming coil. In the electromagnetic forming process, a capacitor bank charges with a significant amount of electrical energy at constant current and then discharges the coil quickly. The energy is dissipated in a coil is in damped form because of the presence of resistance and inductance in coil and tube. A high-intensity magnetic field is generated which induces an eddy current in nearby conductive materials tube [2]. This eddy current produces a repulsive field called Lorentz forces which deform the work-piece plastically when magnetic pressure exceeds the flow stress of work-piece.

   When the work-piece starts deforming due to magnetic pressure, the gap between the coil and work-piece increases which causes two opposite effects, First, the flux density between the coil and the work-piece gets reduced and the magnetic force decreases because magnetic pressure is proportional to magnetic flux density. Secondly, due to the plastic deformation of work-piece strain hardening takes place due to which more force is required to deform further [3].

   In a loose coupling simulation approach, magnetic pressure and solid mechanics physics are solved separately. This approach doesn't consider the work-piece deformation on the magnetic force or discharge circuit parameters. In the sequentially coupled simulation approach, both the magnetic and solid mechanics are used to solve sequentially and the feedback of work-piece displacement is taken into account to calculate the magnetic pressure at every step. When high energy is applied, more deformation occurs due to which gap increases between the tube and coil. This effect is not considered in the loose coupling due to which more errors occur in the loosely coupled approach compared to sequential coupling approach [4].

36.2   Analytical Approach

Figure 36.1 represents the systematic arrangement of tube and coil and the system specification is shown in Table 36.1. To accelerate the tube, internally the gap of 0.5–2 mm is provided between work-piece and coil.

   As tube deforms the gap between the coil and tube increases due to which the resistance and inductance of system increase which is calculated by the author Dond
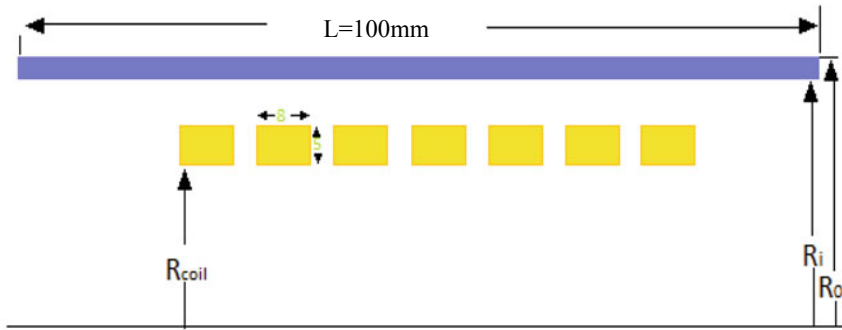
Fig. 36.1 Cross-section of coil and tube (work-piece) in the EMF process

Table 36.1 System specification

R_{system}	L_{system}	C_{system}	Coil c/s	Rcoil	R_i	Thickness
14.83 mΩ	1.3 μH	112 μF	8 × 5 mm	16.5 mm	25 mm	2.5 mm

[3]. In the case of COMSOL software both physics (solid mechanics and magnetics) are used to solve the simulations simultaneously such that after resistance iteration the inductance changes. Therefore, only the initial numerical value is used for software analysis.

36.2.1 Analytical Approach to Find Flow Stress of the Material

When the strain rates increase, the mechanical property of materials changes. The variation in material strength with applied strain rate is an important consideration in the design of classes of materials used in structures subjected to suddenly applied loads. It has been observed that for many materials the stress is found to increase rapidly with strain rate for a given suddenly applied load (Fig. 36.2).

To evaluate the constitutive response of the materials the flow stress is determined as a function of plastic strain, strain rate and the temperature induced during the model, to evaluate the flow stress using Johnson–cook model[J-C] [5].

$$\sigma = \left(A + B\left(\varepsilon^n\right)\right)\left(1 + c\ln\left(\frac{\overset{\circ}{\epsilon}}{\overset{\circ}{\epsilon_0}}\right)\right)\left(1 - \left(\frac{T - T_{room}}{T_{melt} - T_{room}}\right)\right) \tag{36.1}$$

In the electromagnetic forming process only work-piece is deformed and hence the temperature induced is very less which can be neglected. In the case of magnetic pulse welding, impact between tube and block causes temperature rise that is calculated
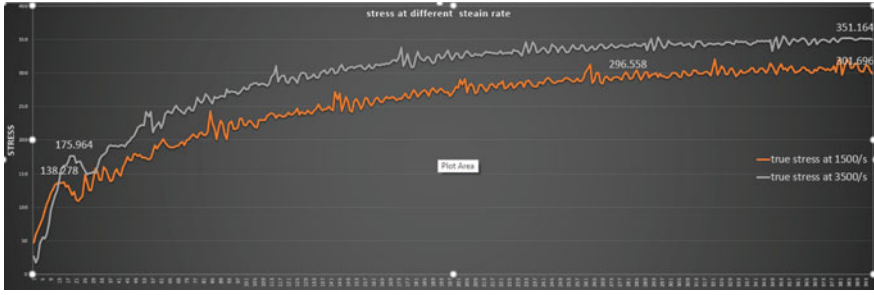
Fig. 36.2 Stress versus strain at different strain rate

by using a joule effect.

$$Q = J^2 \rho_r \tag{36.2}$$

Q Heat generated per unit volume (W/m^3)
J Current density in (A/m^2)
ε Equivalent plastic strain
$\in^\circ$ Equivalent plastic strain rate
$\in_0^\circ$ Reference plastic strain

In Eq. (36.1), parameter A represents the initial yield strength of the material at room temperature where B, C, N and M are constant which is determined by stress and strain curve.

In the present work, work-piece of aluminum alloy (AA6061) has been used as a tube for calculation. The constitutive parameter required by the Johnson–cook constitutive model is shown in Table 36.2 for aluminum alloy [6].

Table 36.2 Johnson–cook model for aluminum alloy (AA6061)

Density (ρ)	2700 kg/m^3	A	110 MPA
Modulus of rigidity (G)	26 GPA	B	114 MPA
Modulus of elasticity (E)	68.9 GPA	C	0.002
Poisson's ratio (γ)	0.31	N	0.42
Heat capacity (C)	896 J/Kg-K	T_m	925 K
Thermal conductivity (k)	167 W/m-k	M	1.34
Electrical conductivity (σ)	25 MS/m	T_{room}	298 K

36.3 Experimental Setup

36.3.1 Materials

In Table 36.3 for material compositions and their constituents are shown. Work-piece is made of aluminum and coil made of copper.

Figure 36.3 shows the setup of an electromagnetic forming configuration that corresponds to a resonant circuit.

A constant current source used to charge the capacitor through switch 1 at a certain level of energy which energy discharge into a coil in the form of a pulse. A pulse generator achieves the high magnetic field that is necessary for forming of work-piece having high electrical conductivity. The coil and work-piece units are characterized as transformer [7].

The forming machine is represented by a series circuit consisting of a capacitor C, an inductance Li as well as resistor R_i. Resistance Rcoil and inductance Lcoil both are connected in series to the pulse power generator represent the tool coil as shown in Fig. 36.4. To analysis the process EMF circuit to equivalent circuit.

In the electromagnetic forming process, the capacitor charges up to the desired energy level $E_c(t)$.

Through the constant current, according to Eq. (36.3), energy can be calculated by multiplication of the capacity C and the charging voltage $U(t)$ and rapidly discharged

Table 36.3 Material composition

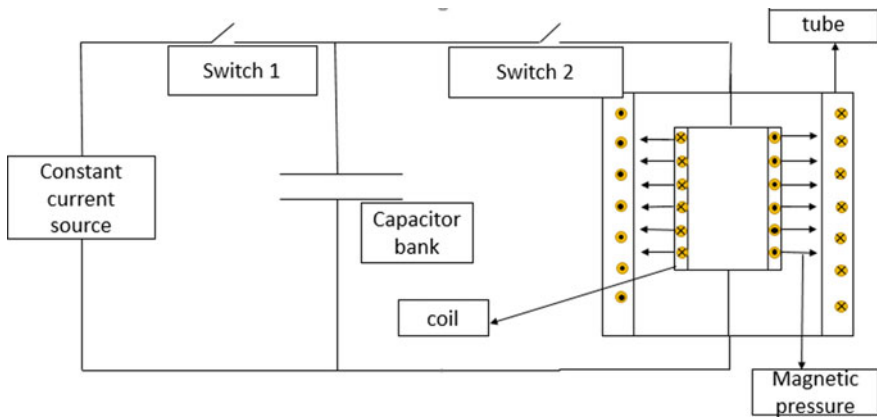| Material (%wt)	Si	Fe	Cu	Mn	Mg	Cr	Ti	Al
AA6061	0.6	0.58	0.202	0.042	0.741	0.207	0.052	Bal.
Coil materials	00	00	99	0.06	0.56	0.07	0.31	00

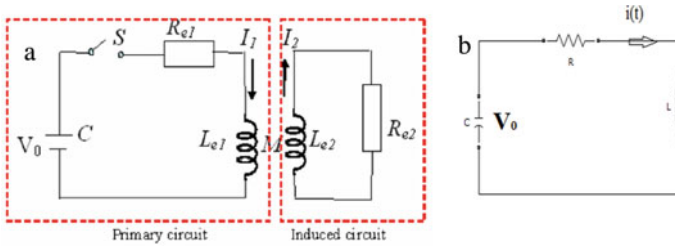
Fig. 36.3 Schematic of the EMF system

Fig. 36.4 Equivalent circuit diagram **a** Detailed version **b** Reduced version [7]

into the coil by closing switch (trigger).

$$E_c(t) = \frac{1}{2}CU(t)^2 \tag{36.3}$$

The resulting current $I(t)$ is a damped sinusoidal oscillation which is determined by the electrical property of the resonant circuit. For the calculation purpose, all parameters of EMF are converted into a single parameter that is the inductance of the system, inductance of coil and inductance of tube into equivalent inductance.

From the Fig. 36.4b,

$$I(t) = \frac{U(t)}{S\left(R + LS + \frac{1}{CS}\right)} \tag{36.4}$$

After solving the equation, we get the damped sinusoidal current waveform, i.e.,

$$I(t) = \frac{U(t)}{\omega L}e^{-\beta t}\sin(\omega t) \tag{35.5}$$

where

Damping coefficient (β) $\frac{R}{2L}$

The Frequency of current (ω) $\sqrt{\frac{1}{LC} - \beta^2}$

The current is related to the corresponding magnetic field which is concentrated between the work-piece and the tool coil. This magnetic field creates an eddy current that flows in the opposite direction in the work-piece. These are located close to the surface of the work-piece due to skin depth effect. The depth of penetration of the current into the work-piece is called skin depth (δ), where

μ_0 Magnetic permeability in vacuum
f Represents the frequency of discharge current.

$$\delta = \sqrt{\frac{1}{\pi f k \mu_0}} \qquad (36.6)$$

The volume force $\vec{F}$ acting on work-piece can be determined based on the current density $\vec{J}$ and the magnetic flux density $\vec{B}$:

$$\vec{F} = \vec{J} \times \vec{B}$$
$$\vec{J} = -\frac{\partial H}{\partial r} \qquad (36.7)$$

$$\vec{B} = \mu \times H$$
$$F_r = \frac{1}{2}\mu \frac{\partial H^2}{\partial r} \qquad (36.8)$$

The volume force acting on the work-piece can be transformed mathematically to the virtual surface that called magnetic pressure (p) for that apply surface integral to convert volumetric force into surface pressure [8].

$$P(r,t) = \int_{ro}^{ri} F(r,t)\mathrm{d}r = \frac{1}{2}\mu H_{\mathrm{gap}}^2(t) \qquad (36.9)$$

$$H(t) = \frac{N * I(t)}{l}$$
$$P = \mu \left(\frac{NU(t)}{l\omega L}\right)^2 e^{-2\beta t}(1 - \cos(2wt)) \qquad (36.10)$$

Figure 36.5 show that the actual pressure acting on the tube that decreases with time, when tube deforms, its stress increases but for simplicity take as constant.

The Lorentz force is used as an input to the mechanical model. In the solid mechanics to solve 3-D stress problem used compatibility equation. Due to axis-symmetric, the problem reduced to a 1-D problem as shown in Eq. (36.11).

$$\rho \frac{\partial^2 u}{\partial t^2} - \nabla . \sigma_s = \vec{F} \qquad (36.11)$$

$$a = \frac{p}{\rho * s} - \frac{\sigma * S * ri(t)}{ri * \rho * ri} \qquad (36.12)$$
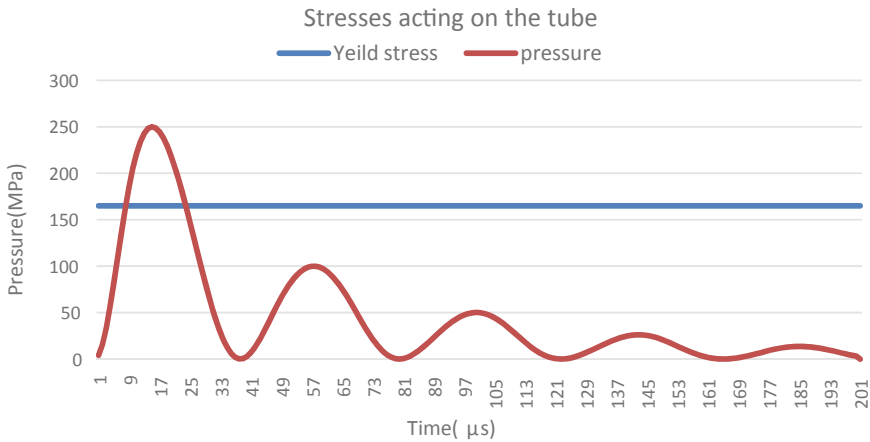
$$v = \int_0^t a * \mathrm{d}t \qquad (36.13)$$

Fig. 36.5 Stress acting on the tube during the EMF process

$$\text{dis} = \int_0^t v * \mathrm{d}t \tag{36.14}$$

The forming process is completed within 200 μs. In this process up to 500 MPa pressure is applied in an extremely short time. When the stress exceeds the flow stress work-piece due to magnetic pressure it deforms plastically. In 200 μs only up to 50 μs force is effective after which pressure decreases below the yield stress. The yield stress depends on the strain rate, which is calculated by Johnson–cook model.

As shown in Fig. 36.6 displacement of tube during when the pressure acting on the with respect to time. First 50 μs deformation takes place by magnetic pressure
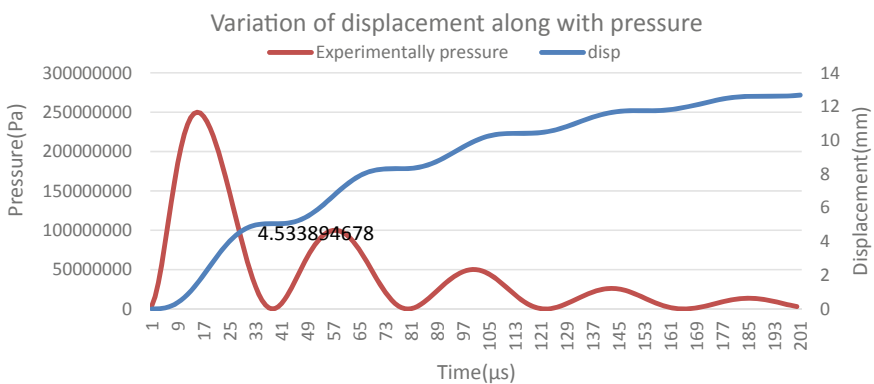

Fig. 36.6 Displacement variation with respect to pressure

after which deformation takes place because of inertia of tube. In the first 50 μs inertia oppose the deformation after which it helps in the deformation of work-piece.

36.3.2   Simulation Approach

As shown in Fig. 36.7. It consists of seven turns helical copper coil having dimensions of 8 × 5 mm and its length 47 mm and place an aluminum tube having length 100 mm in front of copper coil. For the experiment, the tube of outer diameter 55 mm is used. After completing drawing as per specification next is to add material like copper to coil and aluminum to tube and also air for surrounding tube and coil. After adding materials add physics which is used to analyze in EMF process for this add magnetic field and solid mechanics. After adding physics apply the boundary conditions after which apply type of study, i.e., time-dependent. After adding the type of study, mesh the model. Meshing is important because if meshing is coarse then results are approximate, if mesh is fine then it gives accurate results but time-consuming hence optimize the mesh. In EMF, mesh size is from 0.1 to 1 mm after which results are not accurate because the gap between tube and coil varies from 1 to 2.5 mm.
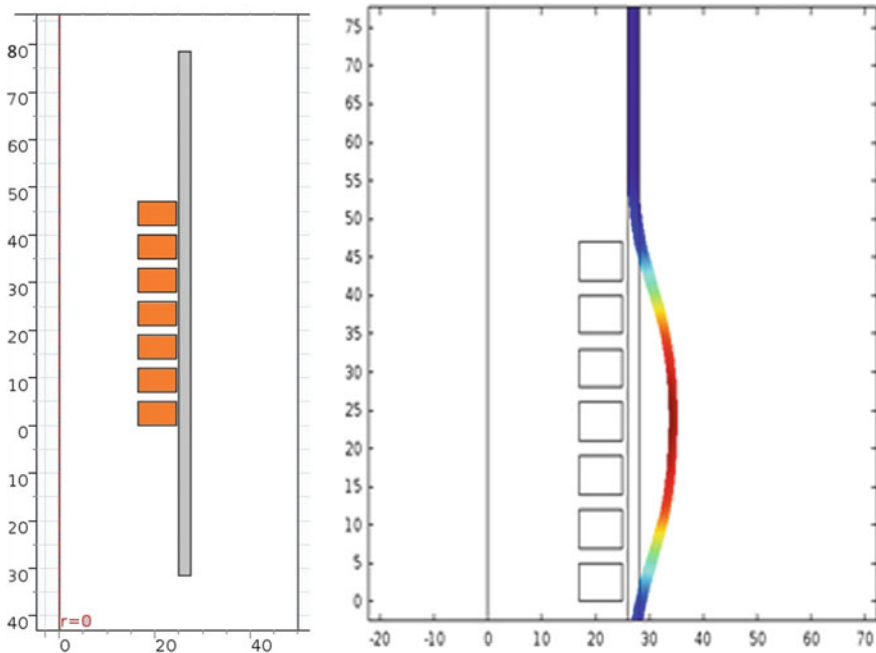

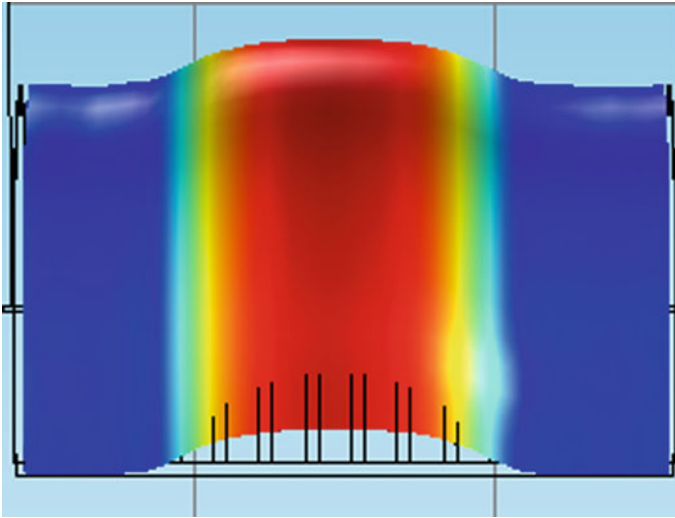**Fig. 36.7**   2-D view of work-piece before and after deformation

Fig. 36.8 Deformation of tube along the length of tube

The magnetic field is more concentrated at centre of the coil, as we move from the centre of coil magnetic field reduces so magnetic pressure reduces which in turn reduces deformation in longitudinal direction as shown in Fig. 36.8.

36.4 Results and Discussions

Based on the above formula, the required minimum pressure is calculated with the work-piece deformation after which the developed 2D coupled simulation model is used to evaluate displacement curve. As energy increases so the strain rate increases due to which mechanical property improves. As shown in Fig. 36.9 when charging energy increases more deformation takes place during the EMF process.

As shown in Fig. 36.9. Displacement increases with the increase in charging energy but it has not shown after work-piece so that experiment is performed. From the experiment, the result concludes that a maximum 36.2% lateral direction.

Figure 36.10 shows that pressure acts on the tube are calculated by only the analytical approach but in the sequential coupling, consider the variation of inductance and resistance and also variation in displacement. Inductance and resistance depend upon the gap between the tube and the coil. The first pick of pressure approximates the same for both analytical and sequential because during this time deformation of the tube is very small so that the inductance and resistance are the same for both the process. During the second pick of pressure deformation of the tube is considerable so that the inductance and resistance change due to which sequential pressure more drops then the analytical pressure.
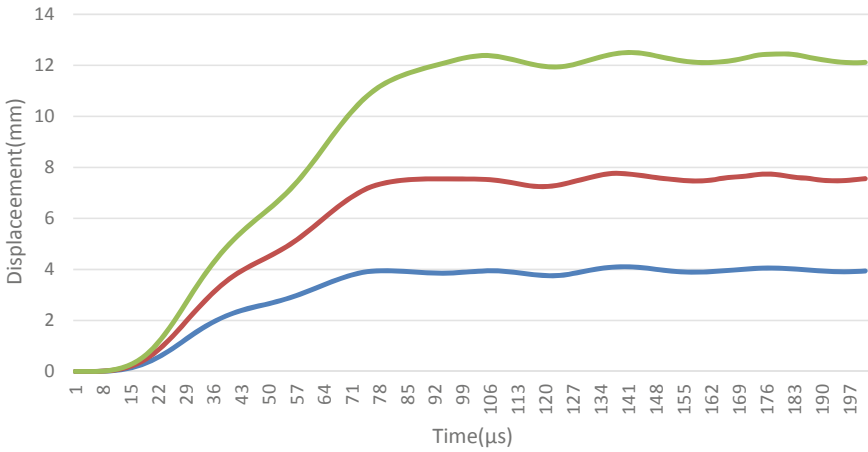
Fig. 36.9 Displacement at different charge energy (Strain rate)
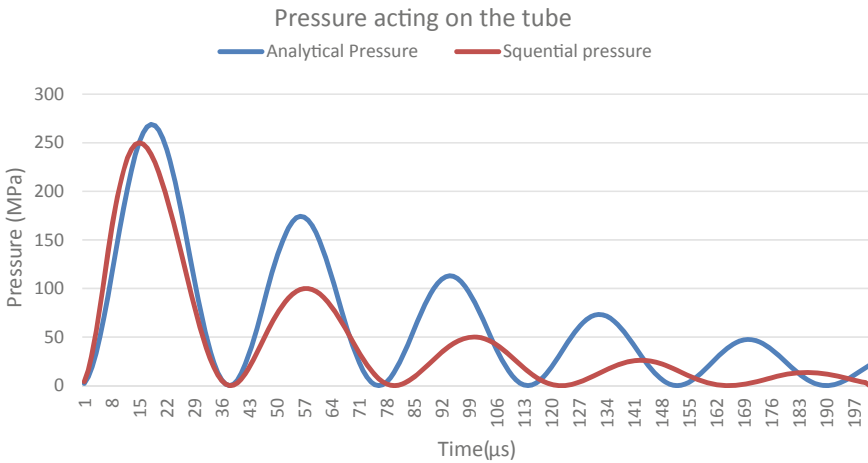

Fig. 36.10 Stress acting on the tube during the EMF process

As shown in Fig. 36.11b, stress increases with the increase in charging energy. It signifies that deformation increases with the strain rate so it shows high formability and high hardness value at a higher strain rate. Figure 36.11a shows the variation in analytical and simulation value of displacement.
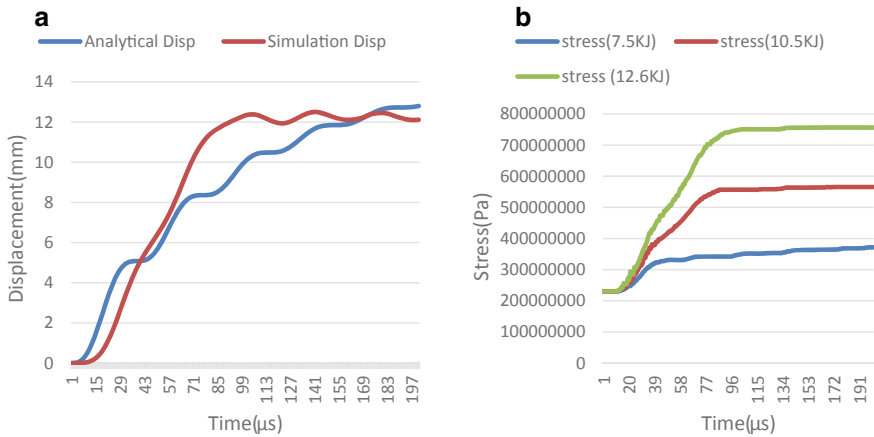
Fig. 36.11 **a** Comparison between analytical and simulation results **b** Stress versus time

36.5 Conclusions

Forming process for aluminum AA6061 is achieved at high strain rate. The following conclusions were drawn from the study:

- During the constant standard process (Low strain rate), maximum deformation in a lateral direction is 12%, and in the case of electromagnetic forming process, it increases to 36.2%.
- In the electromagnetic forming process, high strain causes huge plastic deformation which in turn increases hardness up to 58.6%.
- The percentage error in the estimated tube displacement is reduced from 19 to 5.81% in the sequential coupling.

References

1. Tian, Y., Huang, L., Ma, H., Li, J.: Establishment and comparison of four constitutive models of 5A02 aluminium alloy in high-velocity forming process. Mater. Des. 1980-2015 **54**, 587–597 (2014)
2. Nassiri, A., Campbell, C., Chini, G., Kinsey, B.: Analytical model and experimental validation of single turn, axi-symmetric coil for electromagnetic forming and welding. Procedia Manuf. **1**, 814–827 (2015)
3. Dond, S., Choudhary, H., Kolge, T., Sharma, A.: Analysis of the variation of the discharge circuit parameters during electromagnetic forming processes. Int. J. Precis. Eng. Manuf. **20**(3), 375–382 (2019)
4. Dond, S., Choudhary, H., Kolge, T., Sharma, A., Dey, G.K.: Robust electromagnet design for pulse forming application. COMPEL - Int. J. Comput. Math. Electr. Electron. Eng. COMPEL-05-2018-0229 (2019)

5. Kore, S.D., Date, P.P., Kulkarni, S.V.: Effect of process parameters on electromagnetic impact welding of aluminum sheets. Int. J. Impact Eng **34**(8), 1327–1341 (2007)
6. Doley, J.K., Kore, S.D.: Electromagnetic formability of an aluminium ice tray. Key Eng. Mater. **611–612**, 1124–1131 (2014)
7. Psyk, V., Risch, D., Kinsey, B.L., Tekkaya, A.E., Kleiner, M.: Electromagnetic forming—a review. J. Mater. Process. Technol. **211**(5), 787–829 (2011)
8. Kleiner, M., Beerwald, C., Homberg, W.: Analysis of process parameters and forming mechanisms within the electromagnetic forming process. CIRP Ann. **54**(1), 225–228 (2005)

Chapter 37
Finite Element Modeling of Autoclave Aerated Concrete (AAC) Masonry for Estimation of Strength

Amit Raj, Arun Chandra Borsaikia, and Uday S. Dixit

Abstract Nowadays, the autoclaved aerated concrete (AAC) has become a very common building material used in the construction of buildings/structures. For a load-bearing structure as well as framed structure, in-plane compression is an important mode of failure in the masonry walls. In this work, the finite element micro-modeling, governed by plastic-damage constitutive relation in tension and compression, has been used to model the AAC block and mortar, while cohesive zone modeling strategy is adopted to model the block–mortar interface. The developed model has been used for the estimation of AAC masonry strength. The nature of lateral stress developed due to the application of axial stress is discussed. The comparative study on stress distribution in AAC block and clay brick masonries is also presented. The results obtained from modeling have good agreement with the experimental results. It is envisaged that AAC masonry can be a sustainable option for constructing buildings.

Keywords Finite element modeling · Cohesive zone model · Concrete damage plasticity · Compressive strength · Lateral stresses

37.1 Introduction

The autoclaved aerated concrete (AAC) has emerged as one of the potential sustainable alternatives to burnt clay bricks and fly ash bricks. AAC block is lighter than conventional clay brick, which provides opportunities to improve the quality of the building wall at a lower cost [1]. Since AAC block is a new product in India, it is

A. Raj (✉) · U. S. Dixit
Department of Mechanical Engineering, Indian Institute of Technology Guwahati, Assam 781039, India
e-mail: amit.raj@iitg.ac.in

U. S. Dixit
e-mail: uday@iitg.ac.in

A. C. Borsaikia
Department of Civil Engineering, Indian Institute of Technology Guwahati, Assam 781039, India
e-mail: arubors@iitg.ac.in

essential to know its behavior under the frame of building structure. Experimental studies on the behavior of AAC masonry structure when subjected to dynamic or in-plane load have been carried by a number of investigators for many years [2–4]. Researchers [2] investigated the microstructure and compositional analysis of AAC and non-autoclaved aerated concrete (NAAC). AAC is steam cured and is practically stable, whereas NAAC is moisture cured and undergoes changes in structure with time. Raj et al. [3] investigated the compressive and tensile bond strengths of AAC masonry prepared with various combinations of sand–cement mortar. The effect of mortar strength on the masonry strength was studied.

Mallikarjuna [5] carried out a two-dimensional linear elastic finite element analysis of a masonry shear wall under a pre-compression load of 0.1 MPa. The aim was to study the normal stress and shear stress distribution in masonry units and AAC unit–mortar bond interface assuming a plane-stress condition. The potential failure mechanism and collapse load were estimated from the analysis. It was concluded that the simplified micro-modeling is a convenient method for finite element modeling of the masonry shear wall. The stiffness of the wall depends mainly on brick–mortar interface bond strength rather than the strength of the mortar.

Ferretti et al. [6] investigated the tensile and compressive strength of AAC beams both experimentally and numerically. They studied the fracture mechanics of AAC by performing three-point bending tests on beams. Małyszko et al. [7] numerically modeled the Brazilian (tensile) test on the cylindrical and cubic AAC specimen. The failure mechanisms were discussed based on finite element simulations and experiments with the digital image correlation. Researchers [8] used the experimental results to calibrate a well-known macroscopic anisotropic constitutive model already developed for ordinary masonry. For both tension and compression, the behavior of AAC masonry as well as full-scale AAC masonry wall in uniaxial directions was simulated. It was concluded that the numerical anisotropic models proposed for traditional masonry can also be used for AAC masonry, if calibrated properly.

Although several researchers have studied the numerical modeling of AAC masonry strength such as compressive strength and bond strength, none has modeled the development of lateral stresses corresponding to the applied axial compression load. However, it is difficult to obtain it experimentally. The aim of this research work is to present finite element modeling of AAC masonry under compressive load. The nature of lateral stresses developed due to the application of an axial compressive stress is discussed and compared with that of clay brick masonry. A standard masonry prism using AAC unit and mortar (mix of cement and sand) has been modeled for estimating the compressive behavior. The detailed strategies for finite element (FE) modeling are discussed.

37.2 A Brief Survey on Modeling of a Masonry

Understanding theoretical behavior of any engineering materials and system has very important prospects. This can be achieved through numerical or computational studies. In the last few decades, there has been a lot of effort in developing a new method of modeling and analysis of masonry structures. The aim was to provide efficient tools for better understanding of the complex behavior of masonry structures. A masonry is formed by joining two or more bricks with the help of a bonding agent called mortar. The basic mechanical properties of the masonry are strongly influenced by its constituents, viz. mortar and brick. Using the mechanical properties of brick, mortar and joint, the behavior of masonry structure can be analyzed by finite element (FE) modeling.

There are two approaches to FE modeling of masonry structures—macro-modeling (homogenous) and micro-modeling (heterogeneous) [9]. In a macro-modeling approach, the mortar joints and brick units are combined into a uniform composite material with average properties of brick and mortar as illustrated in Fig. 37.1a. Although the regular masonry usually shows an orthotropic behavior because of typical stacking of blocks and mortar, the isotropic approach is followed in the case of macro-modeling. The purpose of this assumption is to achieve the homogenization, which limits the number of mechanical parameters required to define the material model. The assumed material properties can be obtained through simple testing aimed at deriving the basic masonry information [10]. Hence, this method is efficient due to less computational time and is suitable for the large-scale modeling of structure. The influence of mortar joint acting as a plane of weakness in the masonry structure cannot be addressed by macro-modeling; it is not able to predict the local behavior of masonry wall properly. To model more accurately, different types of masonry constituents need to be considered [9].

The micro-modeling is found to be more appropriate method to evaluate the actual behavior of masonry. The mortar and units are simulated explicitly. The micro-modeling considers the masonry constituents as different materials. The brick–mortar bond is considered to be formed by a continuum brick–mortar interface layer as shown
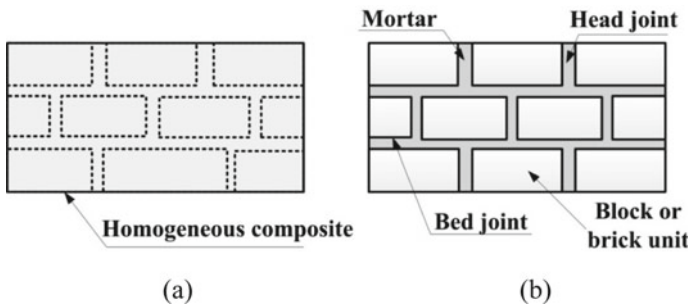

Fig. 37.1 Modeling strategy of brick masonry: **a** macro-modeling and **b** micro-modeling

in Fig. 37.1b. The micro-modeling regards the masonry as a heterogeneous material and requires the determination of considerably higher number of parameters leading to an expensive test [9]. Although the micro-modeling approach is more precise and can predict the local behavior of masonry, modeling becomes complicated by considering all the individual properties of masonry constituents. However, it needs more computational time.

Lourenco [11] used both micro-modeling and macro-modeling to study the behavior of masonry wall. The elastic model was used to represent the behavior of brick while the gradual softening model was used to represent the interface element. A three-dimensional FEM model using concrete damage plasticity (CDP) model for a partially grouted wall was developed by Minaie [12]. Alberto et al. [13] characterized the mechanical behavior of interface and predicted the de-bonding phenomena between brick and mortar through a cohesive crack model. Zhang et al. [14] developed a detailed micro-modeling method for modeling of diagonal compression test for historical stone masonry structure using extrinsic cohesive elements.

37.2.1   Concrete Damage Plasticity (CDP) for Material Modeling

The behavior of the masonry can be simulated in a commercial available FEM package such as ABAQUS using the CDP model, which can be used for concrete and other brittle materials [15]. The failure is caused by cracks in tension and crushing in compression. The concrete damage plasticity provides a general capability for modeling concrete and other quasi-brittle materials in all types of structures (beams, trusses, shells, and solids). In CDP model, the evolution of the yield (or failure) surface is governed by two hardening variables, viz. compressive equivalent plastic strain ($\tilde{\varepsilon}_c^{pl}$) and tensile equivalent plastic strain ($\tilde{\varepsilon}_t^{pl}$) which are linked to failure mechanisms under compression and tension loading, respectively.

The stress–strain behavior under uniaxial tension follows a linear elastic relationship until it reaches the failure stress (σ_{t0}). The stress corresponding to the onset of micro-cracking in the concrete material is the failure stress [15]. The formation of micro-cracks with a softening stress–strain response induces strain localization in the structure of concrete. However, under the uniaxial compression loading, the response is linear until it reaches the initial yield stress (σ_{c0}). The response is typically characterized by stress hardening followed by strain softening beyond the ultimate stress (σ_{cu}) in the plastic region. The uniaxial stress–strain curve can be converted into stress versus plastic strain curves by ABAQUS from stress versus plastic strain data. Thus,

$$\sigma_t = \sigma_t(\tilde{\varepsilon}_t^{pl}, \dot{\tilde{\varepsilon}}_t^{pl}, f_i, \theta) \tag{37.1}$$

$$\sigma_c = \sigma_c(\tilde{\varepsilon}_c^{pl}, \dot{\tilde{\varepsilon}}_c^{pl}, f_i, \theta), \tag{37.2}$$

where the subscripts t and c indicate tension and compression, respectively. $\tilde{\varepsilon}_c^{pl}$ and $\tilde{\varepsilon}_t^{pl}$ are the equivalent plastic strains, $\dot{\tilde{\varepsilon}}_c^{pl}$ and $\dot{\tilde{\varepsilon}}_t^{pl}$ are the equivalent plastic strain rates, f_i (for $i = 1, 2, 3,…$) are the other predefined field variables and θ is the temperature.

When the concrete specimen is unloaded from any point on the strain-softening branch, the stiffness decreases. The elastic stiffness of the material seems to be degraded or damaged. The elastic stiffness damage is characterized by two damage variables, d_t (for tension) and d_c (for compression), which are the functions of the plastic strains, temperature, and field variables. The damage variables can be varied from 0 to 1. Thus,

$$d_t = d_t(\tilde{\varepsilon}_t^{pl}, \theta, f_i); \quad 0 \le d_t \le 1, \tag{37.3}$$

$$d_c = d_c(\tilde{\varepsilon}_t^{pl}, \theta, f_i); \quad 0 \le d_c \le 1. \tag{37.4}$$

For undamaged materials, the damage variable is 0, whereas 1 indicates the total loss of strength [15]. Letting E_0 as the initial or undamaged elastic stiffness of the material, the stress–strain relations under uniaxial tension and compression become

$$\sigma_t = (1 - d_t)E_0(\varepsilon_t - \tilde{\varepsilon}_t^{pl}), \tag{37.5}$$

$$\sigma_c = (1 - d_c)E_0(\varepsilon_c - \tilde{\varepsilon}_c^{pl}). \tag{37.6}$$

A non-associative flow rule is considered to define the plastic strain rate in CDP model. The multiple hardening Drucker–Prager type surface is adopted as a yield surface. The yield surface is governed by the parameters such as dilation angle (φ), ratio of biaxial compressive strength to the uniaxial compressive strength (f_{b0}/f_{c0}), and a constant k [16–18]. The dilation angle or dilatancy is basically the measure of change in the volumetric strain with respect to the changes in shear strain. The dilation angle defines the amount of plastic volumetric strain induced in the body during the plastic shear. The constant k is the ratio of second stress invariant on tensile meridian to that on the compressive meridian at the failure point. The tensile and compressive meridians are the intersection curves between the plane (meridian plane) containing the hydrostatic axis and the failure surface [19].

37.2.2 Cohesive Zone Modeling

Cohesive zone (CZ) models are widely used to investigate the behavior of interfaces between any two materials. This model, introduced by Dugdale and Barenblatt [20], has attracted a growing interest to describe the failure and delamination process for composite materials in details. The cohesive interaction is the function of displacement or separation between the edges of cracks. The CZ model is generally applied to concrete and cementitious composites but can also be used for other materials.

The application of CZ model may widen the knowledge of material properties and more powerful computer programs.

Previous researches have studied the parameters that affect the cohesive interaction performance for brittle materials. They have concluded that the mechanical behavior of cohesive elements can be defined by three methods: (1) uniaxial stress-based, (2) continuum-based, and (3) traction–separation constitutive model. In this work, the third method is used. The traction–separation model represents the corresponding initial separation caused by pure normal stresses, in-plane and out-of-plane shear stresses. The Coulomb frictional contact behavior is applied to the traction–separation model by introducing a coefficient of friction (μ), which prevents components penetration, especially for the normal contact behavior. For this study, surface-to-surface contact is chosen and the contacting properties for the tangential and normal behavior are specified. This type of contact is generally used to describe the behavior of two deformable surfaces connecting together. This focuses all the damage mechanisms in and around a crack tip on the interface, leading to a constitutive relation between the traction and opening displacement (separation). The crack initiation is related to the cohesive strength, also called the maximum traction on the traction separation law. The variation in traction in relation to separation or displacement is plotted as a curve and is called the traction–separation curve, as illustrated in Fig. 37.2.

When the area under the traction–separation reaches the fracture toughness, the traction declines to zero and new crack surfaces are generated. The crack initiation is related to the cohesive strength, also called the maximum traction on the traction separation law. From Fig. 37.2, it can be observed that the material is initially bonded and the failure occurs after the maximum traction is reached, beyond which the traction starts decreasing.
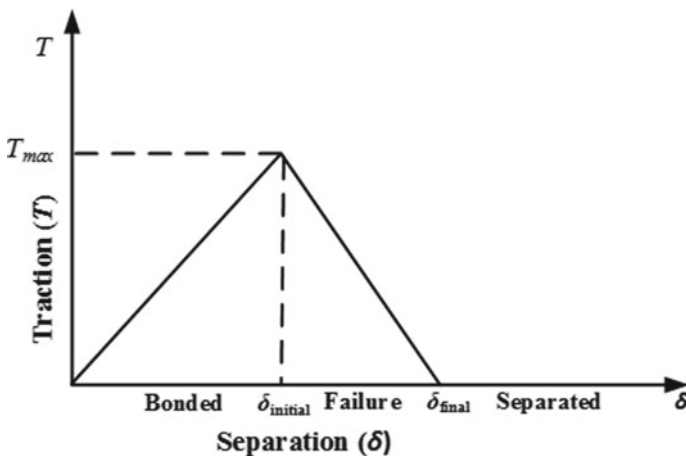

Fig. 37.2 The effective linear traction–separation relationship

Cohesive zone modeling relates the relative displacement ("opening" δ) of two associated points of the interface to the force per unit of area ("Traction" T) needed for separation. A difference is made between normal (n) and tangential (t) direction. Hence, the cohesive zone law comprises two relations, i.e., T_n (δ_n) and T_t (δ_t). The cohesive zone laws can be uncoupled or coupled [9]. In an uncoupled cohesive zone law, the normal/tangential traction is independent of the tangential/normal opening, while both normal and tangential tractions depend on both the normal and tangential opening displacement in case of coupled cohesive zone law. Uncoupled laws are intended to be used when the debonding process occurs under normal (mode-I) or tangential (mode-II) loading. The majority of cohesive zone laws have a partial coupling between normal and tangential directions, which is achieved by introducing coupling parameters in the model. A large variety of cohesive zone laws are available in literature such as (a) polynomial model, (b) piece-wise linear model, (c) exponential model, and (d) rigid linear model.

The shear strength or bond strength of the masonry depends mainly on the interface between unit and mortar. The masonry interface modeling can be done using cohesive zone modeling [14]. Cohesive zone model (CZM) can be used to predict the local fracture initiation and continued propagation in a material. It offers an alternative way to analyze failure along material interfaces. The CZM can be employed in FE analysis by relating the traction to displacement at interfaces.

Ramamurthy et al. [21] studied the delamination between polyethylene terephthalate (PET) and polyvinyl chloride layers in polymer-coated steel using two approaches to model cohesive zone for delamination, viz. elemental cohesive zone model (ECZM) and surface cohesive zone model (SCZM). The surface cohesive zone modeling was found to be more desirable because of the advantages of reduced computational time, fewer input parameters, and easy modeling. In this study, unit–mortar interface is modeled by adopting the surface-based cohesive zone model. Turon et al. [22] determined the various constitutive parameters such as interface stiffness coefficient and length of cohesive zone for the simulation of delamination. The equation for the selection of the interface stiffness parameter was derived. The expression to adjust the maximum interfacial strength used in the computations with a coarse mesh was presented.

Moslemi and Khoshravan [23] proposed a new test methodology to determine the cohesive strength of the composite laminates. The various cohesive parameters such as cohesive strength and separation energy for mode-I interlaminar fracture of E-glass/epoxy woven fabrication was computed from the experimental tests. The results from the simulation were compared with experimental tests and confirmed the adequacy of normal cohesive strength. Kowalewski and Gajewski [24] determined the failure modes in the brick walls using cohesive element approach. The micro-modeling approach with the application of cohesive elements to describe the mortar joint has been used in the analysis. Ferretti et al. [8] performed an inverse extended finite element (XFEM) analysis to calibrate a proper cohesive law suitable for the AAC material. The XFEM is basically an extension of conventional FE method.

37.3 Modeling of AAC Masonry Compressive Strength

A masonry prism is an assemblage of brick units and mortar, which is constructed to serve as a test specimen to determine the compressive strength of masonry. The micro-modeling of compression test of AAC masonry has been carried out with the help of a FEM package, ABAQUS 6.14. The individual properties of both AAC bricks and mortars used in this study are depicted in Table 37.1. The properties were experimentally evaluated based on the compressive strength test results of AAC blocks and mortar. The material properties for mortar corresponding to mortar grade 1:4 (cement: sand) was considered in this work. The block and mortar were modeled separately using concrete damage plasticity. The softening behavior of AAC block and mortar using the plastic stress–strain data were used as input parameter in the concrete damage plasticity modeling of block and mortar. The plastic stress–strain data of AAC block in compression and tension is depicted in Table 37.2. The plastic stress-strain data of mortar in compression is shown in Table 37.3. Tensile strength for mortar was taken as 3.51 MPa [5]. For quasi-brittle material, such as masonry, the value of dilation angle (φ), f_{b0}/f_{c0}, and k is generally taken as 10°, 1.16 and 2/3, respectively [16–18]. Hence, for material modeling, the same values of the respective parameters have been considered in this work.

Table 37.1 Material and interface properties of AAC block and mortar

Material properties for FE modeling			Interface properties [25]	
Properties	AAC block	Mortar (1:4 grade)	Stiffness coefficient (N/mm^3)	
Elastic modulus (MPa)	272.5	1046		
Poisson's ratio	0.14	0.22	K_{nn}	143
Yield strength in compression (MPa)	2.90	21.08	K_{ss}	85
Yield strength in tension (MPa)	0.50	3.51	K_{tt}	85

Table 37.2 Plastic stress–strain data for AAC block

Compression		Tension	
Plastic strain	Stress (MPa)	Plastic strain	Stress (MPa)
0	2.90	0	0.50
0.0008	2.89	0.0023	0.49
0.0012	2.86	0.0040	0.48
0.0014	2.82	0.0058	0.47
0.0016	2.77	0.0075	0.42
0.0019	2.71	0.0092	0.40

Table 37.3 Plastic compression stress–strain data for mortar

Plastic strain	Compressive stress (MPa)
0	21.08
0.0022	21.07
0.0050	20.10
0.0067	17.54
0.0084	16.39
0.0096	14.97

Surface-based cohesive zone model has been used to model the block–mortar interface. Surface-to-surface interaction module with contact pairs available in finite element package ABAQUS/Standard was used. The following uncoupled stiffness coefficient was used: (a) stiffness coefficient in normal or opening direction (K_{nn}), (b) stiffness coefficient in in-plane shear direction (K_{ss}), and (c) stiffness coefficient in out-of-plane shear direction (K_{tt}) [25]. The values are provided in Table 37.1.

The masonry prism of size $210 \times 110 \times 398$ mm^3 was modeled with five AAC blocks ($210 \times 110 \times 70$ mm^3) and four mortar layers of 12 mm thickness (see Fig. 37.3). The 8-node continuum element having three degrees of freedom at each node (C3D8R) element was used to model the masonry unit and mortar joint. The uniform mess element of sizes 8 mm and 2 mm was considered for block and mortar, respectively, shown in Fig. 37.3b. The bottom surface of the masonry was encastered. A vertical axial concentrated load of 65 kN was applied at the top block. The
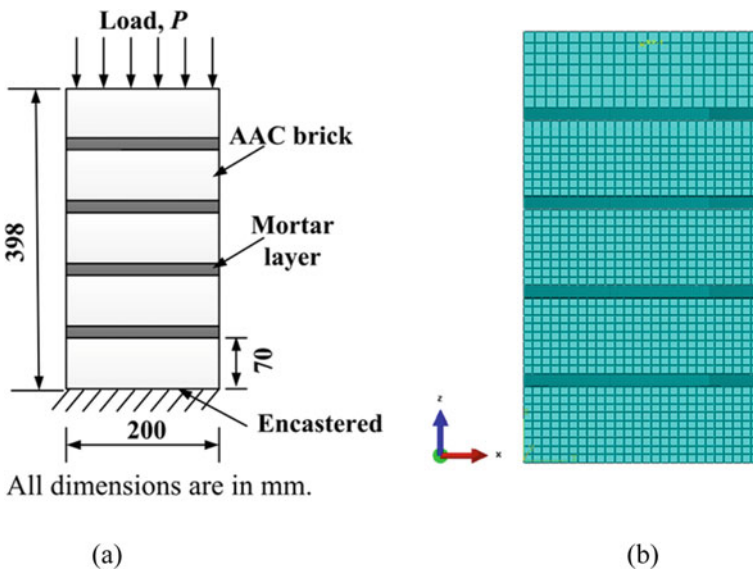

Fig. 37.3 The masonry prism subjected to compressive load: **a** loading and boundary condition and **b** meshing of masonry prism adopted in FEM modeling

schematic representation of loading and the boundary conditions is presented in Fig. 37.3.

37.4 Results and Discussion

Rankine theory also called maximum principal stress theory has been used to estimate the masonry prism strength. This theory is basically applied for the brittle material. The principal stress distribution for the axial vertical load of 65 kN (z-direction) is shown in Fig. 37.4a. The minimum and maximum principal stress developed in the block are 2.62 MPa and 2.96 MPa, respectively. Since the maximum principal stress developed in the prism model exceeds the AAC block yield strength, i.e., 2.90 MPa, the failure takes in block region. Due to the stress concentration, the maximum principal stress of 3.63 MPa is observed at the corner of the top and bottom block. This is also based on the elastic analysis and just indicates failure. Considering that the maximum stress with 65 kN load is 3.63 MPa, while the yield strength of the block is 2.90 MPa, a proportionate reduction in loading is needed to avoid failure. From that logic, the maximum load comes out to be 52 kN (without applying a factor of safety).

The obtained result has a good agreement when compared with the experimental results of Raj et al. [3]. The researchers [3] evaluated the compressive strength of AAC masonry using the same 1:4 (cement: sand) grade mortar, as considered in this study. The geometrical properties of AAC block used to prepare the masonry prism specimens were also same. The specimens were prepared using one block in length and five blocks in height with four mortar layers of 12 mm thickness. The
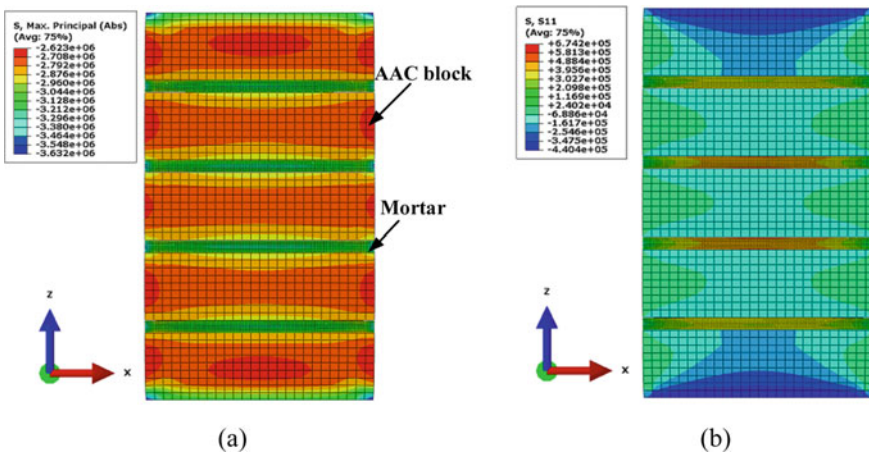

Fig. 37.4 Results of FE modeling of AAC masonry prism for a load of 65 kN: **a** maximum principal stress distribution and **b** lateral stress distribution (x-direction)

compressive strength test was performed on a total of three AAC prism specimens using the hydraulic universal testing machine of capacity 1000 kN. The test was performed after curing the specimens in a moist condition for 28 days. The individual compressive strength of individual AAC block and mortar was found to be 2.93 MPa and 24.22 MPa, respectively. However, in this modeling, the input value of individual compressive strength of AAC block and mortar has been considered to be 2.90 MPa and 21.08 MPa, with a relative error of 1% and 13%, respectively. The overall average masonry compressive strength of 2.53 MPa, corresponding to the peak load of 55.67 kN, was obtained in the experimental study. Hence, in this work, the observed maximum load of 52 kN has a relative error of 7.5% with respect to the experimental result of Raj et al. [3].

It is worthwhile to discuss the difference in stress distributions between clay brick and AAC masonries. In both types of masonries, the bricks and mortar expand laterally when the masonry is subjected to the compressive forces. However, both the constituent materials exhibit different mechanical properties. In the case of clay brick masonry, the brick unit has higher modulus of elasticity and lower Poisson's ratio as compared to the mortar [26–28]. As a result, when the masonry is subjected to an axial compressive force, higher lateral strain is developed in mortar as compared to the clay brick. Since the lateral deformation is constrained to be equal due to bond strength and friction at the brick–mortar interface, the lateral compressive stress and lateral tensile stress are induced in mortar and clay brick, respectively [26]. Therefore, the brick is subjected to a combination of vertical compression and biaxial lateral tensions. Similarly, the mortar is subjected to the triaxial lateral compression. However, in the case of AAC masonry, the nature of lateral stress developed is different for axial compression load. Since the modulus of elasticity of AAC block is less than that of mortar, although the Poisson's ratio is also less but its effect is less significant, the stresses induced are of opposite nature.

The AAC block is subjected to triaxial lateral compressive stress, while the combination of vertical compressive and biaxial lateral tensile stress is developed in the mortar layer, as illustrated in Fig. 37.5. In Fig. 37.5b, σ_z is the vertical compressive stress applied to the AAC masonry in z-direction, σ_{xb} (compressive) and σ_{xm} (tensile) are lateral stresses developed in the block and mortar in x-direction. Similarly, σ_{yb} (compressive) and σ_{ym} (tensile) are the lateral stresses developed in block and mortar in y-direction.

Similar stress behaviors were observed during the FEM modeling of AAC masonry. As can be seen from Fig. 37.4b, showing the lateral stress developed in x-direction for an axial vertical load of 65 kN (z-direction), the lateral compressive stress is developed in the block portion, while the lateral tensile stress is developed in mortar layer. Similar nature of lateral stress distribution for block and mortar was found in the y-direction as observed for x-direction.
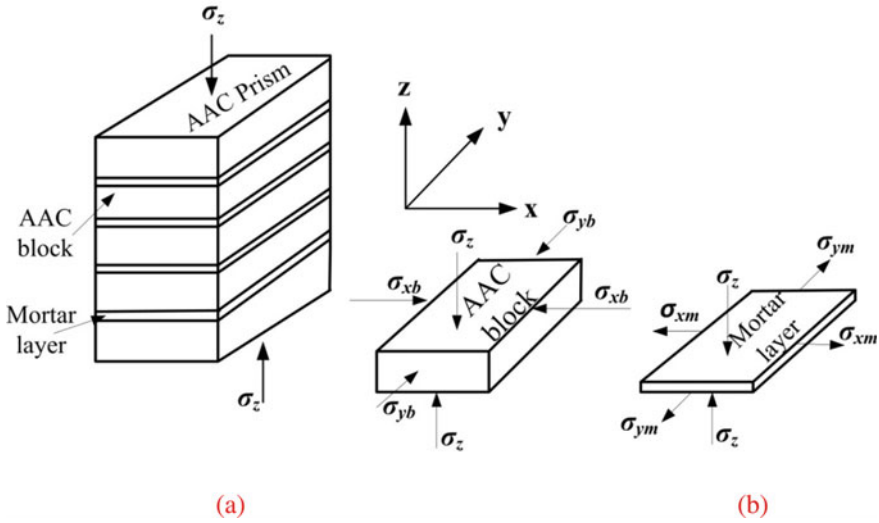
Fig. 37.5 Stress distribution in AAC masonry for axial vertical compression load **a** AAC masonry prism and **b** lateral stress distribution in block and mortar

37.5 Conclusions

FE modeling methodology to model the masonry strength has been discussed in detail. The concrete damage plasticity and cohesive zone model can be used to simulate the masonry behavior. The behavior of AAC masonry in axial compression loading has been discussed. The nature of developed lateral stress due to the applied axial compressive stress has been studied and found different from that of clay brick masonry. For AAC masonry, the lateral compressive stress and lateral tensile stress was developed in AAC block and mortar, respectively. This is contrast to clay brick masonry, where lateral compressive stress and lateral tensile stress are developed in mortar and brick, respectively.

References

1. Raj, A., Borsaikia, A.C., Dixit, U. S.: Manufacturing of autoclaved aerated concrete: present status and future trends. In: Proceedings of 6th International and 27th All India Manufacturing Technology, Design and Research Conference (AIMTDR-2018). Anna University, Chennai, India (2018)

2. Narayanan, N., Ramamurthy, K.: Microstructural investigations on aerated concrete. Cem. Concr. Res. **30**(3), 457–464 (2000)
3. Raj, A., Barman, S., Borsaikia, A.C., Dixit U.S.: Stress-strain behavior of materials used in a building wall system made of AAC blocks. In: Proceeding of the National Conference on Sustainable Mechanical Engineering Today and Beyond, Tezpur University, India (2017)
4. Alexanderson, J.: Relations between structure and mechanical properties of autoclaved aerated concrete. Cem. Concr. Res. **9**, 507–514 (1979)
5. Mallikarjuna, S.: Experimental determination of parameters for a micro-modeling based failure criterion for AAC block masonry shear wall. Mtech. thesis, Indian Institute of Technology, Guwahati, India (2017)
6. Ferretti, D., Michelini, E., Rosati, G.: Cracking in autoclaved aerated concrete: experimental investigation and XFEM modeling. Cem. Concr. Res. **67**, 156–167 (2014)
7. Małyszko, L., Kowalska, E., Bilko, P.: Splitting tensile behavior of autoclaved aerated concrete: comparison of different specimens' results. Cons. Build. Mat. **157**, 1190–1198 (2017)
8. Ferretti, D., Michelini, E., Rosati, G.: Mechanical characterization of autoclaved aerated concrete masonry subjected to in-plane loading: Experimental investigation and FE modelling. Cons. Build. Mat. **98**, 353–365 (2015)
9. Bolhassani, M., Hamid, A.A., Lau, A.C., Moon, F.: Simplified micro modeling of partially grouted masonry assemblages. Const. Build. Mat. **83**, 159–173 (2015)
10. Miccoli, L., Garofano, A., Fontana, P., Müller, U.: Experimental testing and finite element modeling of earth block masonry. Eng. Struc. **104**, 80–94 (2015)
11. Lourenco, P.B.: Analysis of masonry structures with interface elements. Rep. No. 03-21-22-0. (1994)
12. Minaie, E., Mota, M., Moon, F.L., Hamid, A.A.: In-plane behavior of partially grouted reinforced concrete masonry shear walls. J. Struct. Eng. **136**(9), 1089–1097 (2010)
13. Alberto, A., Antonaci, P., Valente, S.: Damage analysis of brick-to-mortar interfaces. Procedia Eng. **10**, 1151–1156 (2011)
14. Zhang, S., Mousavi, S.M.T., Richart, N., Molinari, J.F., Beyer, K.: Micro-mechanical finite element modeling of diagonal compression test for historical stone masonry structure. Int. J. Solids Struc. **112**, 122–132 (2017)
15. Dassault Systems.: Abaqus analysis user's manual 6.13-3. RI2013; Dassault Systems Providence, Waltham, MA, USA (2013)
16. van Zijl, G.P.: Modeling masonry shear-compression: role of dilatancy highlighted. J. Eng. Mech. **130**(11), 1289–1296 (2004)
17. D'Altri, A.M., Messali, F., Rots, J., Castellazzi, G., de Miranda, S.: A damaging block-based model for the analysis of the cyclic behavior of full-scale masonry structures. Eng. Fract. Mech. **209**, 423–448 (2019)
18. Lubliner, J., Oliver, J., Oller, S., Oñate, E.: A plastic-damage model for concrete. Int. J. solids struc. **25**(3), 299–326 (1989)
19. Chen, W.F.: Plasticity in Reinforced Concrete. J. Ross Publishing, Cengage learning (2007)
20. Dugdale, D.S.: Yielding of steel sheets containing slits. J. Mech. Phys. Solids **8**(2), 100–104 (1960)
21. Ramamurthi, M., Lee, J.S., Yang, S.H., Kim, Y.S.: Delamination characterization of bonded interface in polymer coated steel using surface based cohesive model. Int. J. Precis. Eng. Manuf. **14**(10), 1755–1765 (2013)
22. Turon, A., Davila, C.G., Camanho, P.P., Costa, J.: An engineering solution for mesh size effects in the simulation of delamination using cohesive zone models. Eng. Fract. Mech. **74**(10), 1665–1682 (2007)
23. Moslemi, M., Khoshravan, M.: Cohesive zone parameters selection for mode-I prediction of interfacial delamination. Strojniškivestnik-J. Mech. Eng. **61**(9), 507–516 (2015)
24. Kowalewski, Ł., Gajewski, M.: Determination of failure modes in brick walls using cohesive elements approach. Proc. Eng. **111**, 454–461 (2015)
25. Lizárraga, J.F., Pérez-Gavilán, J.J.: Parameter estimation for nonlinear analysis of multi-perforated concrete masonry walls. Cons. Build. Mater. **141**, 353–365 (2017)

26. Francis, A.J., Horman, C.B., Jerrems, L.E.: The effect of joint thickness and other factors on the compressive strength of brickwork. In: Proceedings 2nd Int. Brick Masonry Conference H. W. H. West, ed. British Ceramic Association, Stoke-on-Trent. U.K. 31–37 (1971)
27. Sarangapani, G., Venkatarama Reddy, B.V., Jagadish, K.S.: Brick-mortar bond and masonry compressive strength. J. mater. Civil Eng. **17**(2), 229–237 (2005)
28. Totaro, N.: A hybrid elastic theory for evaluation of compressive strength of brick masonry. In: Proceedings 10th Int. Brick and Block Masonry Conference. pp. 1443–1451 (1994)

Chapter 38
FE Analysis of Cup Plugin HHP (NH/NT) Cylinder Head

Durgaprasad Pitcha, Jagjit Singh Randhawa, Jawed Ali, and Ashfak Ali

Abstract In an internal combustion engine, the cylinder head is a casting bolted to the top of the cylinder block. One of the parts of head assembly is the cup plug (Expansion plug/Welch plug). The fundamental motivation behind the cup attachments is to fill the gaps that were made during the throwing procedure, so the foundry could expel the center sand from the coolant entries. Obviously Saving the cylinder head from splitting if there should be an occurrence of a stop was never the maker's purpose for these cup plugs. The study aims to find the contact pressure developed due to interference fit in Standard Cup Plug and Standard cylinder head of water-cooled diesel engine in FEA. This is done using, 3D simulation model for Standard Head and FEA and Leak Test setup for Standard Head. The investigation aims to provide the design intent to resolve cup plug loosing issue in operating conditions.

Keywords FEA analysis · Cylinder head

Nomenclature

D_o Outer diameter of cylinder head (mm)
D Inner diameter of cylinder head or outer diameter of cup plug (mm)
D_i Inner diameter of cup plug (mm)
P Contact pressure (MPa)
E_H Modulus of elasticity of cylinder head (MPa)
E_s Modulus of elasticity cup plug (MPa)
L Length of cup plug (mm)
C Coefficient

D. Pitcha · J. S. Randhawa (✉)
Centre of Excellence (Industrial and Product Design), Punjab Engineering College, Vidya Path, Sector-12, Chandigarh 160012, India
e-mail: jagjitsingh@pec.ac.in

J. Ali · A. Ali
Cummins Technologies India Pvt. Ltd., Pithampur, Madhya Pradesh 454775, India

D_3 Outer diameter of cylinder head (mm)
f Coefficient of friction
d_o Original diameter (mm)
d_f Final diameter (mm)
μ_H Poisson's ratio of cylinder head
μ_s Poisson's ratio of cup plug
σ_H Hoop stress in the cylinder (MPa)
σ_r Radial stress in the cylinder (MPa)
σ_z Axial stress in the cylinder (MPa)
σ_{eq} Equivalent stress, i.e., von-Mises stress (MPa)
δ Interference (mm)
D_1 Inner diameter of cup plug (mm)
δ_s Change in diameter (mm)

38.1   Introduction

Threaded plugs are not 100% airtight and may cause spillage and are costly. Accompanies parcel of issues like interruption/Protrusion. While in activity they may come free with activity. At Cummins ReCon, these are the sorts of heads more often than not. As a most ideal arrangement strung plugs ought to be evacuated and will be supplanted with Cup plugs. The interface between cup fitting and cylinder head must be airtight. The obstruction ought not to cause any harm either to cup fitting or chamber head.

The following steps describe the measures Cummins takes to remanufacture its engines and parts, creating a product that is comparable to a new Cummins product.

Core Acceptance: A great benefit of Cummins remanufacturing is that you can get money back for exchanging your worn-out engine or part. Any Cummins authorized repair facility worldwide will accept your old part, perform a simple external visual inspection and give you an immediate credit towards its replacement.

Disassembly: Cummins engines and parts are completely disassembled with great care to prepare key components for processing—right down to the last screw, nut, bolt and spring. Our factory technicians follow standard quality processes to ensure that we only remanufacture the highest quality components.

Cleaning: Hardworking Cummins engines have a habit of getting dirty. That's why once disassembled into individual components, each part is carefully cleaned using

the latest technology to remove debris without removing any metal. These methods include the use of dry ice, enzymes and even lasers for specialized cleaning needs.

Inspection: We will only restore parts that meet stringent quality standards. Using the latest inspection technology including ultrasonic, X-ray, magnetic particle inspection and coordinate measuring machine (CMM), we verify that every part is ready for the restoration process. You won't find this level of detailed inspection on traditional in-shop rebuilds.

Restoration: We use a variety of techniques to ensure that our ReCon parts meet original specifications and improved standards of performance.

Worn surfaces are restored with thermal spray and laser deposition. Computer-controlled lathes, machining centers, and honing and grinding equipment renew worn surfaces. Upgrades or super sessions in components are included as part of the Cummins remanufacturing process. Our state-of-the-art techniques and highly trained workforce provide measurable quality results.

Testing: Cummins validation testing employs fail-safe processes to verify that the performance and reliability of the finished remanufactured engine or part meet Cummins original factory standards. This produces a remanufactured product that's as good as new at a fraction of the cost.

Re-introduction: Once the remanufacturing process is complete, ReCon engines and parts are ready to be reintroduced into the field, where the true test of quality is performed. That's why Cummins conducts extensive testing of our products (as well as the competition's), verifying superior performance and value for your repair dollar.

38.2   Literature Review

Zhang et al. [1] have studied interference fit via FEM. In their studies of interference fits in-ring gear-wheel connections show that the traditional design method based on thick-wall cylinder theory had some limitations. Lame's equations did not give good results for the interference stresses and deformations. This is because of the complex geometry of the problem, which involves a thin ring on a hollow, stepped shaft that protrudes unspecified, large distances beyond the He has introduced two safety factors λs and λp which provides a new method for evaluating the quality of interference fits.

Katait [2] has studied the effect of stress distribution at the interface between valve guide cylinder head of diesel engine, by changing the thickness of the valve guide and stiffness of the material. He observed that when the stiffness of cylinder head increases and thickness of valve guide decreases, the contact pressure on valve

guide and cylinder head increases by 17% for loose interference fit and 31% for tight interference fit. According to him, because of the complex geometry of the problem the analytical results are not perfectly matched with FEA and experimental results. Contact pressure results match within 11 and 6% error.

You [3] proposed all-inclusive research on the non-contact areas since the non-contact locales produce safe power in the press-fit procedure, the non-contact districts impacted press-mounting power and assumed a significant job in press-fit procedure.

Huyuk [4] proposed another systematic technique that was set up dependent on the TCT and safe power figuring strategy. The press-mounting power is essentially brought about by safe power when the contact area has a little length. Toward the start of the get-together process, section A and part B travel from non-contact to contact locale and the contact length begins to increment. So when the contact length is equivalent to 0.04 mm, the press-mounting power is viewed as safe power.

Zhang [5] is committed to shape the enhancement of the obliged contact power issue. A straight unwinding model of contact power leeway connection is created. It is demonstrated that such unwinding is basic to maintain a strategic distance from zero affectability estimations of zero contact power regarding structure factors and to drive the fulfillment of contact power imperative at the particular contact locale. In this work, both frictionless and frictional contact advancement issues are researched by methods for an angle based streamlining calculation.

Study of stress distribution on interference fits by focusing on the following objectives:

1. Calculate the contact pressure between cup plug and cylinder head for Standard Head.
2. Compare the analytical results with FEA and experimentally results of contact pressure.

38.3 Methodology

In CUMMINS ReCon Plant, Remanufacturing process works:

- Complete disassembly, cleaning and inspection of every part.
- Remanufacturing and testing to verify that every engine meets Cummins factory specifications.
- Replacing worn parts and components that are obsolete (in materials, design or manufacture) with Genuine Cummins parts.

The connection in the cylinder head and cup plug occurs between inner surface of cylinder head and outer surfaces of the cup plug. Stresses in the contact surface of selected machine elements were investigated in FEA. Also experimentally we have done leak test for Grey Cast Iron cylinder head and AISI Type 304 Stainless Steel Cup plug for Standard Head.

38.4 Engine Details

For CUMMINS NH220 (N-series water-cooled 6 cylinder) NH/NT Diesel engine specifications are given in Table 38.1 (Fig. 38.1).

Table 38.1 Specification of NH220 diesel engine

S. No.	Parameter	Specification
1	Engine name	CUMMINS NH220
2	Compression ratio	15.5:1
3	Displacement volume	12.2 L
4	Engine type	Diesel engine
5	Max. power of engine	142–208 kW @ 2100 rpm
6	Cup plug material	Stainless steel type 304
7	Cylinder head material	Grey cast iron (Ferrous)
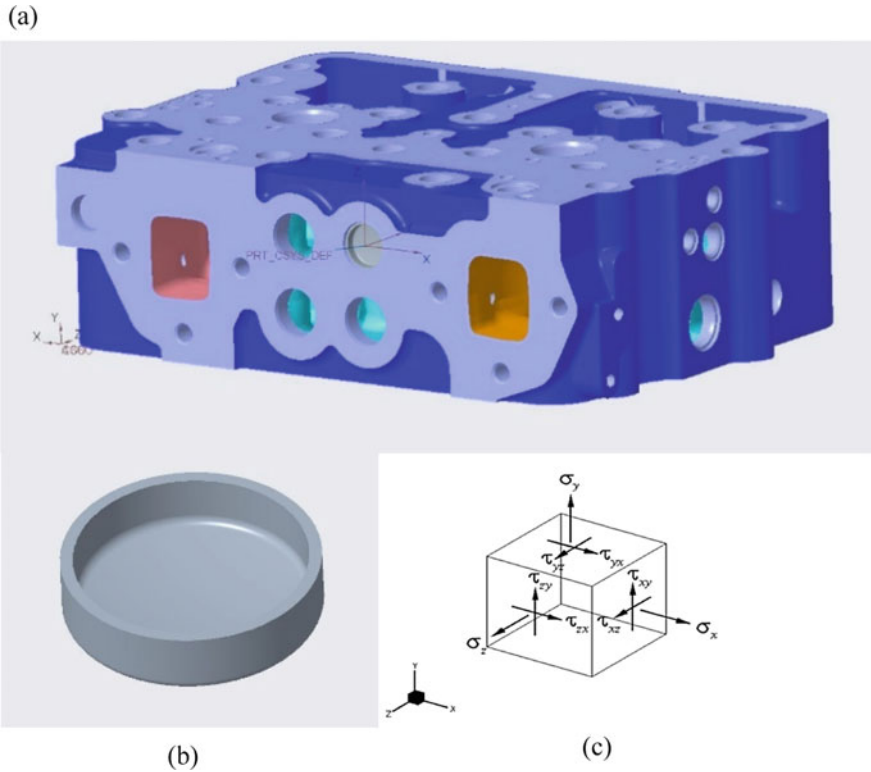
Fig. 38.1 a Actual cylinder head and cup plug assembly. **b** Simple cup plug. **c** Stresses acting on an element of the mating surface

38.5 Material Properties

Material properties of grey cast-iron

S. No.	Parameters	Values
1	Tensile strength	289 MPa
2	Yield strength	188 MPa
3	Thermal conductivity	0.496 kW/m K
4	Young's modulus	113 GPa
5	Poisson's ratio	0.25

Material properties of AISI type 304 stainless steel

S. No.	Parameters	Values
1	Tensile strength	725 MPa
2	Yield strength	415 MPa
3	Thermal conductivity	0.01629 kW/m K
4	Young's modulus	193 GPa
5	Poisson's ratio	0.29

38.6 Computation of Stresses Based on FEM

The focus of this paper is to find out the results of the contact pressure with the finite element method for Standard Cup Plug assembly. This work is the foundation of analytical results for different interference values in order to obtain contact pressure Values between for Standard Cup Plug.

Due to the existence of plastic region around the cup plug a plastic model is developed with bilinear isotropic hardening material and assigned for both cylinder head and cup plug.

The developed analytical approach was validated using the finite element model shown in figure that runs under ANSYS 2019 R1 Version (Figs. 38.2, 38.3, 38.4 and 38.5).

The FEA model is built-up in which contact is defined between cup plug and cylinder head as shown in Fig. 38.6. The interference is relatively small compared with the sizes of cup plugs; the interference can vary numerically by an offset value.

Under Contact region, the contact and Target surfaces are highlighted. The surfaces of contact are displayed in red and Target surfaces are displayed in Blue.
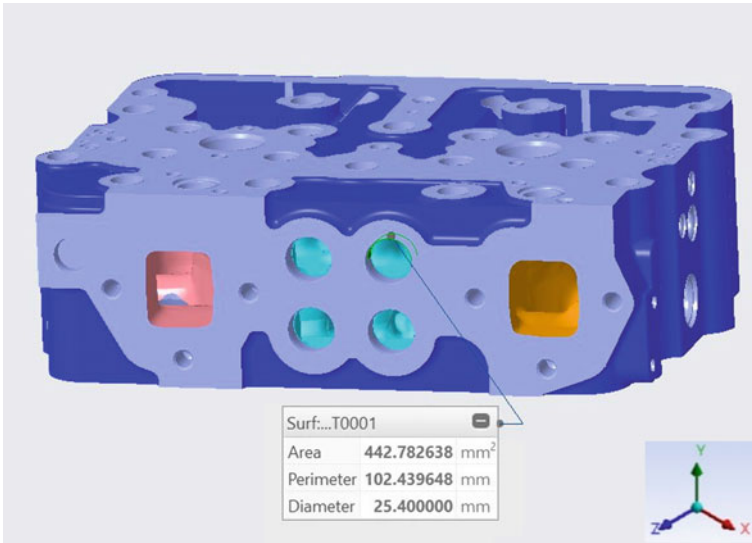
Surf:...T0001	⊖
Area	442.782638 mm²
Perimeter	102.439648 mm
Diameter	25.400000 mm

Fig. 38.2 Standard cylinder head CAD model

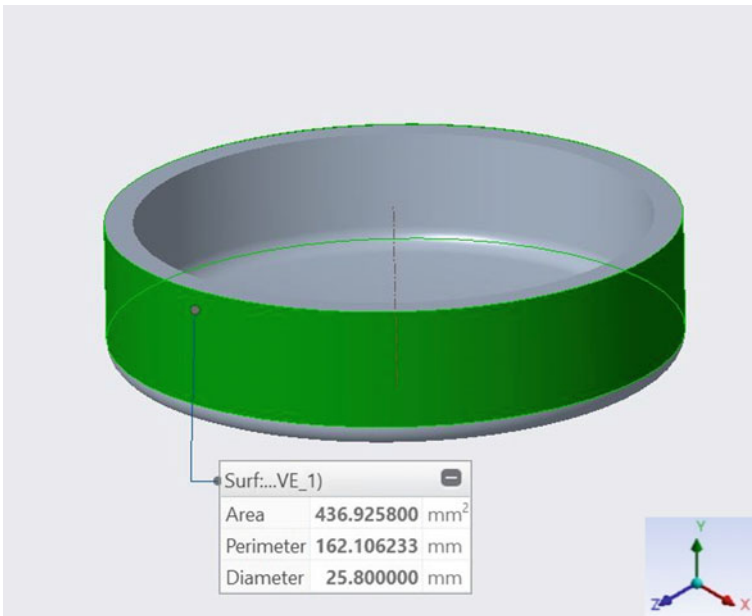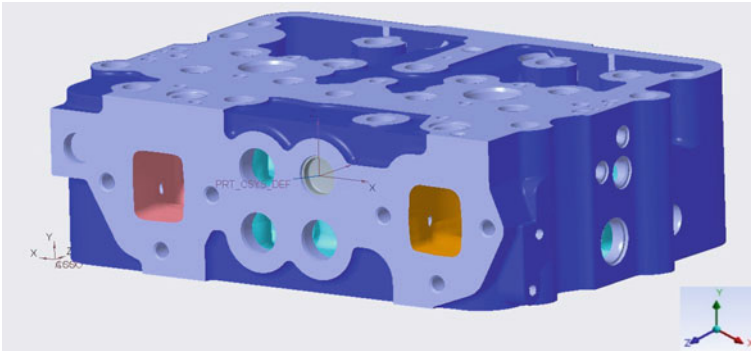| Surf:...VE_1)	⊖
Area	436.925800 mm²
Perimeter	162.106233 mm
Diameter	25.800000 mm

Fig. 38.3 Standard cup plug CAD model

Fig. 38.4 Standard cup plug and cylinder head assembly
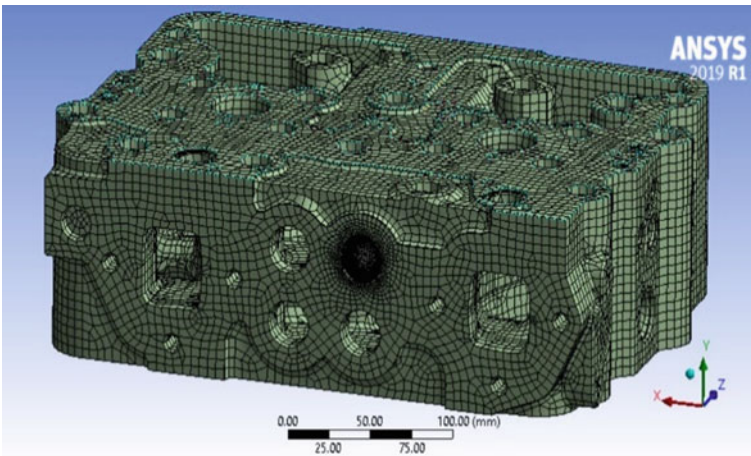
Fig. 38.5 Contact finite element mesh

Convergence is always difficult to FEA since FEA results are acceptable when they approximate to accurate value. The solution should not be influenced by a parameter is a clear indication of Convergence (Fig. 38.7).

Special contact and target elements were employed to model the contact surfaces of the assembly.

CONTA174 and TARGE170 are used for contact and target elements respectively.

The node to node connectivity (Fig. 38.5) is achieved through the combination of Sweep and Face Sizing of mating faces with same element size. So that no penetration occurs.
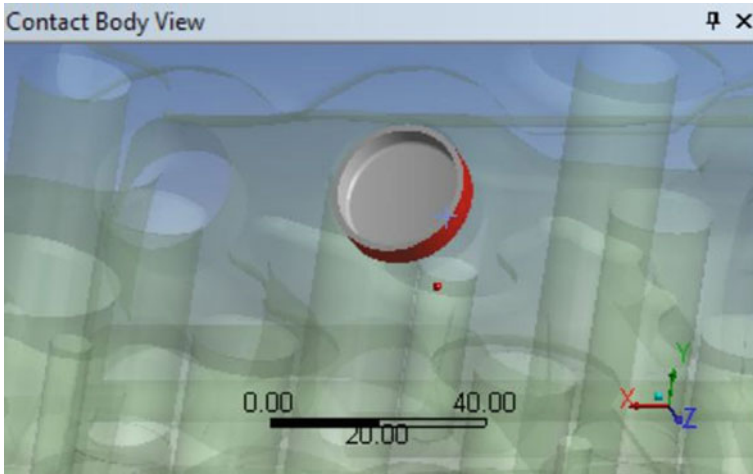
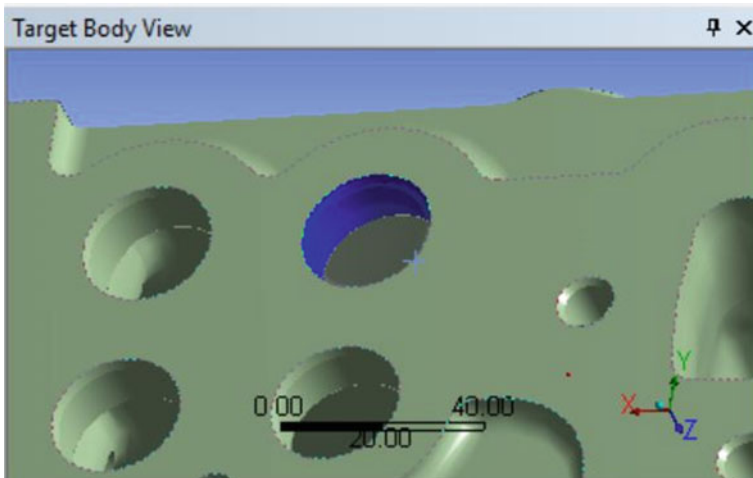**Fig. 38.6** Contact body view (cup plug outer surface)

Fig. 38.7 Target body view (cylinder head plug bore inner surface)

38.7   Boundary Condition

Displacement DX = 0 at left and right face
Displacement DY = 0 at upper and bottom face
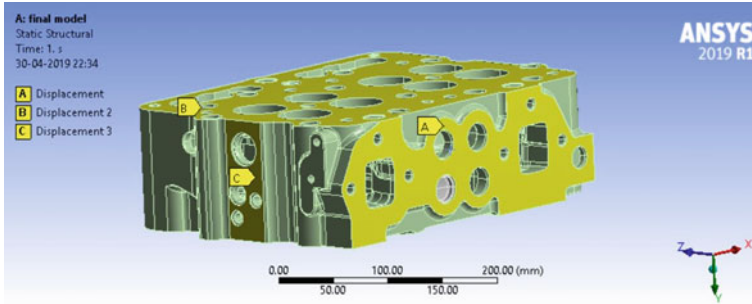Displacement DZ = 0 at front and back face

Fig. 38.8 Boundary condition

The friction between the contact and target surfaces was considered as friction and may have a significant impact on the final results; the friction coefficient considered is 0.125 (Fig. 38.8).

Convergence is always difficult to FEA since FEA results are acceptable when they approximate to an accurate value. The solution should not be influenced by a parameter is a clear indication of Convergence.

The Augmented Lagrangian method was chosen for the simulation since it is a penalty based approach with the addition of λ lower penetration can be obtained, with this Augmented Lagrangian algorithm is better than any other approach when lower penetration is primary requirement in the simulation.

$$F_{\text{contact}} = K_{\text{contact}} * X_{\text{penetration}} + \lambda.$$

where K is Contact Stiffness, X is the contact penetration and F is the contact force.

The temperature considered for the analysis is around 110 °C since the cylinder head temperature varies in operating condition. The residual contact pressure analysis, as well as the radial, tangential and equivalent stresses were captured for standard interference value for standard cylinder head.

38.8   Contact Pressure

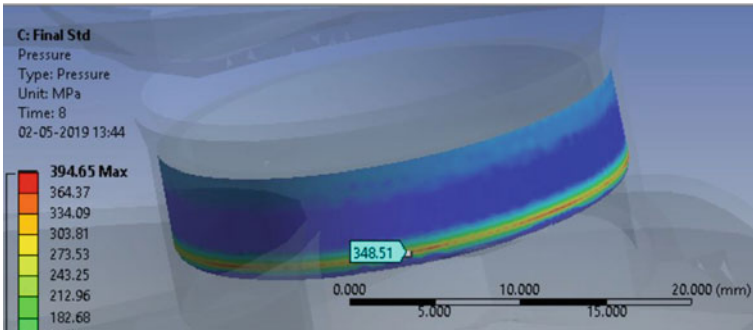The Radial Stress at the interface is almost the same as the contact pressure (Figs. 38.9 and 38.10).

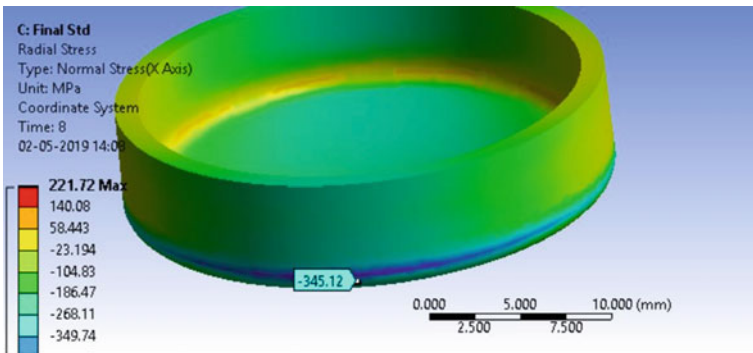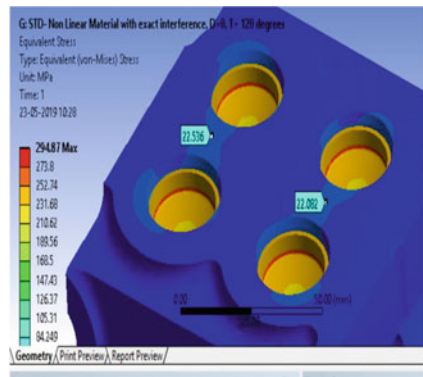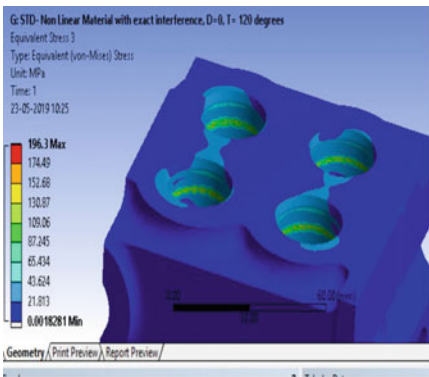**Fig. 38.9** Contact pressure at interface for standard cup plug in standard head

Fig. 38.10 Radial compressive stress at interface for standard cup plug

Equivalent stress on cylinder head and cup plug

Fig. 38.11 Experimental setup-test pressure

38.9 Experimental Setup

1. Section the cylinder head and take the associated section part for the experiment.
2. Make a Through hole on backside of Exhaust face cup plug bore area.
3. To make through hole first find the hole axis by drilling from cup plug bore area with small drill bit.
4. Once axis is found from bottom side, then using 26 mm dia drill and a chamfer tool the ID of cylinder head is Oversized.
5. Assemble the oversized Cup Plugin Standard Procedure.
6. Clamp the cylinder head in such a way that the plunger will force the cup plug from bottom side so that it will push out and measure the force using Load cell.

A Leak Test was carried out for standard test samples with which the working medium 'air' at test pressure of 20.1 PSI. Few more trials were carried out at different test pressure values up to 40.2 PSI for better knowing of critical results. If air is failed to leak the cup plug assembly no any other medium can cause its effect. The test samples are successfully passed and no issue was found during testing (Figs. 38.11 and 38.12).

38.10 Observation and Conclusion

The simulation results are within plastic range. Based on the contact pressure P which tends to contract the cup plug and expand the cylinder head, the cup plug is in plastic range based on the contact pressure value P and yielding to hold the cylinder
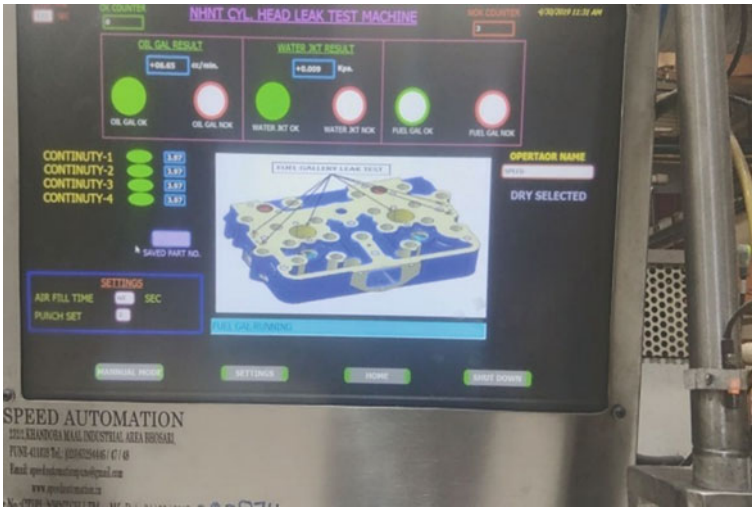
Fig. 38.12 Leak test monitor

head tightly. The standard interference limits are not causing any leakage and they are valid (Fig. 38.13).

Because of the complex geometry of the problem, the analytical results are not perfectly matched with experimental results. Push out force results are match within 10 and 6.2% error.

The error is due to static friction between cup plug and cylinder head when cup plug is about to move from its original position. Since the error is not exceeding 20% the experimental results are valid. The maximum interference condition was taken

	Result	Push out force (kg)
Base line	Analytical	699
	Experimental	774.7
	Error	10%
Oversized	Analytical	695
	Experimental	741
	Error	6.2%

Fig. 38.13 Comparison of analytical and experimental data

for experimental validation and found a push out force of 6.8 kN was absorbed by cup plug to disturb from its original position (Figs. 38.14 and 38.15).

The data that was collected from the standard method was plotted against the push out force at that interference. The minimum pushout force in the standard cylinder

Standard Head Data		
Interference (microns)	Pressure (Mpa)	Push out force (KN)
177	96	2.941
287	159.34	4.844
300	166.86	5.073
350	194.49	5.96
400	225.55	6.857
450	257.32	7.766
500	285.71	8.686
550	318.51	9.617

Fig. 38.14 Push out force with interference for standard head
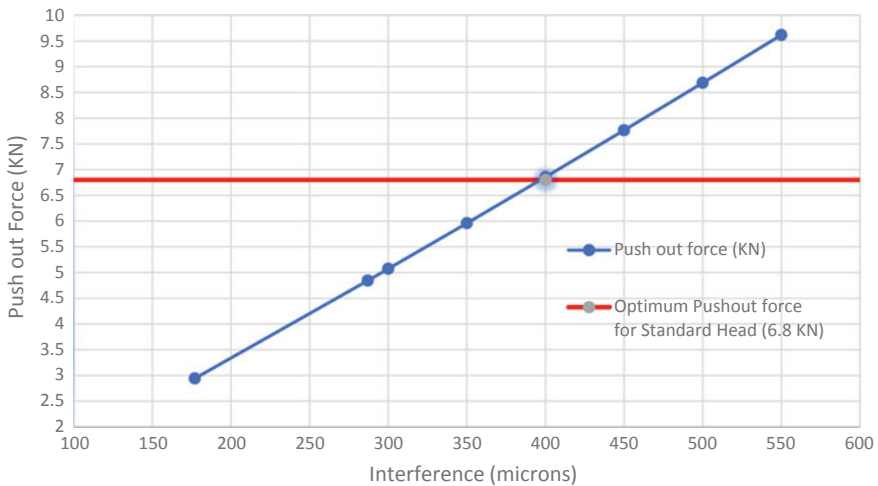

Fig. 38.15 Interference versus pushout force for standard head

head case is drawn at 6.8 kN while on the *X*-axis: interference values and on the *Y*-axis: pushout force.

The upward trend of interference shows that pushout force is gradually increasing with interference. The interference limits that are used here are valid only for standard cylinder heads. The independent variable is interference while dependent variables are pressure and pushout force. The units of interference are microns whereas MPa for contact pressure and kN for pushout force. The interference value is limited since the pressing of the cup plug becomes difficult if the interference value is more.

38.11   Future Scope

The following work can be added to the present study.

1. The study can be conducted on complex geometry of the cup plug as variation in thickness and shape of the cup plug affects the pushout force significantly.
2. Future work can also be done to study the effect of variation of temperature of the cylinder head which may affect the tightness of the cup plug when the engine is in running condition.
3. Study can be conducted on calculating optimum wall thickness in cylinder head.
4. Another study can be conducted on calculating the diameter of the cup plug which maintains the stiffness between cup plug and cylinder head.

References

1. Zhang, Y., McClain, B., Fang, X.D.: Design of interference fits via finite element method. Int. J. Mech. Sci. **42**, 1835–1850 (2000)
2. Katait, N.A., Hujare, D.P.: Stress analysis of shrink-fitted cylinder head and valve guide connections via finite element analysis. IJARIIE **1**(4) (2015). ISSN(O)-2395-4396
3. You, B., Luo, Y., Wang, X.: Contact algorithm of finite element analysis for prediction of press-fit curve. J. Inf. Comput. Sci. **10**(9), 2591–2600 (2013)
4. Huyuk, H., Music, O., Koc, A., Karadogan, C., Bayram, C.: Analysis of elastic-plastic interference-fit joints. In: 11th International Conference on Technology of Plasticity, ICTP 2014, 19–24 Oct 2014, Nagoya Congress Center, Nagoya, Japan
5. Zhang, W., Niu, C.: A linear relaxation model for shape optimization of constrained contact force problem. Comput. Struct. **200**, 53–67 (2018)

Chapter 39
Design and Analysis of I_{ON} and Ambipolar Current for Vertical TFET

Shailendra Singh and Balwinder Raj

Abstract This draft investigates about the vertical tunnel FET (VTFET) with heterostructure at channel/source interface of SiGe layer using Sentaurus Technology computer-aided design simulation. As MOSFET is scaled down to the nanoscale dimensions, the problems arise such as short channel effects, the I-OFF leakage current grow drastically because to the non-versatility of edge voltage as the subthreshold slope or swing (SS) is restricted to 60 mV/decade. Tunnel FET (TFET) smothered the point of confinement of 60mV/decade by utilizing quantum-mechanical band-2-band tunneling (B2BT) due to which the performance of this circuit for low power applications improved. The vertical tunnel FET (VTFET) has dispersal of source channel drain in the vertical direction which will enhance the scalability of the simulated device. Further introduction of 10 nm silicon germanium layer to the channel makes aggressive improvement in the numerical simulations of VT, subthreshold swing (SS) found to be 31.05 mV/decade, high on/off current ratio of the order of 1010 in 40 nm channel length. Further, it is observed form the device simulation that optimizing the gate oxide material, workfunction (WF), and SiGe molefraction will increase the drive current exponentially along with the reduced ambipolarity by gate underlap region to the drain terminal. Additionally, high Ion/Ioff current ratio (~1010), VT threshold voltage (~ 0.352 V), and maximum ion current with 1.126 x10^{-05} (A/μm) are reported to the paper.

Keywords TFET: Tunnel-FET · VTFET: Vertical-Tunnel FET · MOSFETs: Metal Oxide Semiconductor Field Effect Transistor · B2BT: Band-2-Band Tunneling · SS: Subthreshold Swing or Subthreshold Slope · LP: Low Power · WF: Work Function

S. Singh (✉) · B. Raj
Nanoelectronics Research Lab, Department of Electronics and Communication Engineering, NIT Jalandhar, Jalandhar, India
e-mail: shailendras.ec.18@nitj.ac.in

B. Raj
e-mail: rajb@nitj.ac.in

39.1 Introduction

With the advancing time, metal-oxide-semiconductor field-effect transistors (MOS-FETs) dimensions have been continuously scaled down with the big challenge of reduction in power dissipation and leakage current. In order to follow up with the latest trend, low-power (LP) devices for future digital application are the major requirement. The continuous reduction in the channel length, oxide thickness, and channel width of the MOSFETs lead to increase in short channel effect such as drain-induced barrier lowering (DIBL), hot carrier effect (HCE), and mobility degradation [1–5] as well as limits the physical capability of the thermally transmitted carriers with restricted the subthreshold slope to the 60 mV/decade at room temperature [6, 7]. To address these issues, alternative transistor has been evaluated to achieve lower subthreshold slope (SS < 60 mV/decade) at room temperature with respect to the MOSFET by using Band-to-band tunneling mechanism technique. One such device is tunnel field-effect transistor (TFET) is being found to a replacement of the conventional MOSFET to overcome the limitations of short channel effects and improved input characteristics of the device like steeper subthreshold slope (SS) and low threshold voltage (V_T) with high I_{ON}/I_{OFF} current ratio [8–10]. TFET works on the principle of band-to-band tunneling (BTBT) of charge carriers for current generation irrespective to the MOSFET, which works on Drift-Diffusion mechanism [9]. With the above listed benefits of TFETs, it comes with the own sets of issues that include the poor I_{ON} current and the unwanted device's ambipolar conductivity for positive and negative voltage biasing. Certain strategies are connected to bring improvement over these issues. For case, heterostructure utilizing small bandgap materials like Ge, InAs, and SiGe are presented on source side for improving drive current [11–14]. Oxide material of high k-dielectric will also improve the on-drive current. On a comparative relationship, ambipolar flow control procedures incorporate heterostructure utilizing large bandgap materials like silicon in the drain–channel region.

39.1.1 Physics Behind the Band-to-Band Tunneling (BTBT)

The band-to-band tunneling phantasm is based on the WKB approximation that provides an analytical model expression which gives the tunneling probability of charge carriers (electrons) from source to channel. In TFET generally, vertical tunneling FET and lateral tunneling FET models are employed. The tunneling probability is given by Eq. (39.1.1) [15]. Where m^*, E_g, $\Delta\varphi$, t_{si}, t_{ox}, ε_{ox}, and ε_{si} are effective carrier mass, energy bandgap, energy range which provides tunneling, thickness of silicon, oxide thickness, silicon dielectric constant, and oxide dielectric constant, respectively.

$$T(E) \approx \exp\left(\frac{4^{\wedge}\sqrt{2m*}\, E_g^{\frac{3}{2}}}{3|e|h\left(\Delta\Phi + E_g\right)} \right) \qquad (39.1.1)$$

Thus, tunneling probability of carriers can be improved by understanding the four important conditions. The first state condition is to tunneling from i.e. source, second state condition is tunneling to i.e. channel, third state condition is efficient steeper tunneling for potential barrier and fourth one is the momentum of charge carrier [16].

39.1.2 Advantage of TFET

Subthreshold slope: The definition of the subthreshold slope is different for the TFET as compared to MOSFET. In case of tunnel FETs, the average subthreshold slope (AV-SS) is calculate by given Eq. (39.1.2) [17].

$$\text{AVSS} = \frac{(V_{th} - V_{OFF})}{\log\left(I_{V_{th}}\right) - \log\left(I_{V_{OFF}}\right)} \qquad (39.1.2)$$

where V_{th} is the threshold voltage, which is determined by constant current method and it is gate-to-source voltage where drain current becomes 1×10^{-7} A/µm, V_{OFF} is the gate-to-source voltage at OFF state, I_{VT} is the current at threshold voltage, and $I_{V_{OFF}}$ is the drain current at OFF state. The AVSS is calculated by Eq. (39.1.2) and is 37.38 mV/dec, as shown in Fig. (39.1).

Drain current: The DG-TFETs have significantly large ON-to-OFF current ratio and ON-current also improved as compared to conventional single gate TFET without having much effect on the OFF current as shown in Fig. (39.2). The DG-TFET immunes the short channel effects, and speed is also increased. The subthreshold
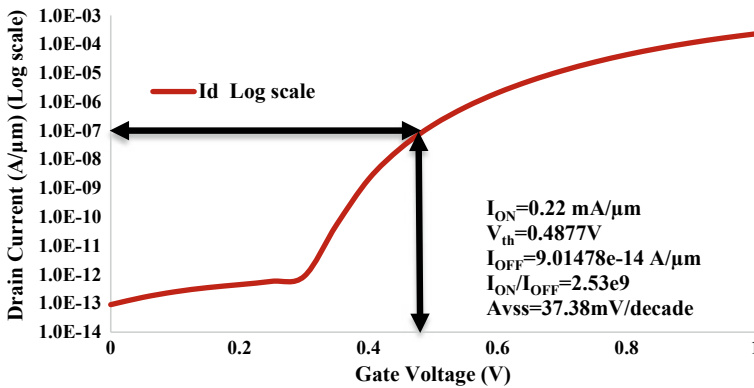

Fig. 39.1 Transfer characteristic of conventional DG-TFET at $V_d = 1.0$ V and $V_g = 1.0$ V by Sentaurus TCAD simulation tool
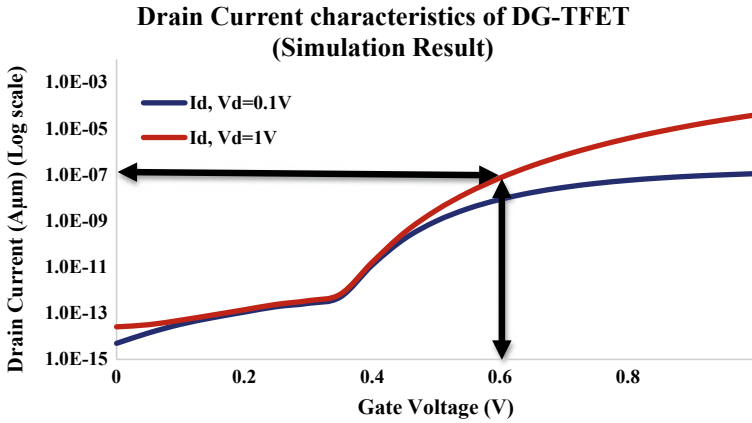
Fig. 39.2 Transfer characteristics of the DG-TFET at $V_{ds} = 0.1$ V and $V_{ds} = 1$ V by Sentaurus TCAD simulation tool

slope also improved which was the limiting factor in conventional MOSFET [18, 19].

DIBL: In case of TFET, DIBL is explained as the ratio of threshold voltage difference at two different drain bias voltages to the difference of drain voltage which is applied in the transfer curve and calculate by the given Eq. (39.1.3).

$$\text{DIBL} = \frac{V_{\text{th}(V_D=1V)} - V_{\text{th}(V_D=0.1V)}}{V_{\text{DS}(V_D=1V)} - V_{\text{DS}(V_D=0.1V)}} \tag{39.1.3}$$

39.1.3 Limitations of TFET

Even though a conventional TFET has very low OFF-state current and considerably high $I_{\text{ON}}/I_{\text{OFF}}$ current ratio, low subthreshold swing [20, 21] and low leakage current in OFF state, still it suffers from many problems as given below:

i. In conventional devices manufacturing, whether it is MOSFET or TFET, source and drain are molded in intrinsic silicon semiconductor with the help of diffusion or ion implantation process. Hence, we cannot achieve the same doping concentration in a different device. This results in random dopant fluctuation problem in doped devices. The RDFs are undesirable in the TFETs because they enhance the OFF-state current. Hence, the ON-current-to-OFF-current ratio decreases, which degrades the performance of the TFET.

ii. In conventional TFET, abrupt junctions are required for efficient tunneling of the carriers from VB to CB. But abrupt junction formation is high-temperature process, and it is unsuitable for conventional TFET at working temperatures.

iii. The conventional TFETs require high manufacturing budgets. Because the drift and ion implantation techniques are used in the manufacturing of the TFET, which are costly.

iv. A conventional TFET also requires expensive thermal annealing techniques in the manufacturing.

39.1.4 Vertical TFET

Vertical TFET erases the limitation of 60 mV/dec of MOSFET and having very small range of subthreshold slope. Due to this, the situation of design flow and the doping profile also changes. So, in the upcoming days, the subthreshold slope is important parameters to decide the device characteristics. Along with this, the vertical TFET is also useful in finding the maximum I_{ON}/I_{OFF} current ratio. As per the down scaling of ITRS roadmap for semiconductors, the scalability is the main advantage of vertical TFET as comparison to the Lateral TFET [22, 23].

39.1.5 Vertical Over Lateral Structures

One might say that lateral TFET designs do not suffer from parasitic tunneling, but the issue is tunneling current density of a lateral structure is so much smaller than a vertical structure. Tunneling only happens at an edge of the gate for a lateral TFET, whereas it is all below gate for a vertical TFET. Even with vertical designs, it is hard to achieve desirable current density which is previously mentioned in the introduction. One other disadvantage of a lateral design is when the gate is scaled down, direct tunneling between source and drain starts happening resulting an increased leakage current. Study of the dimensionality of TFETs was done by Sapan Agrawal, James Teherani, and their colleagues in 2011, to show vertical how vertical TFET structures have step response like $I–V$ curve, that is, of course, neglecting parasitic tunneling, lattice vibration, and lack in doping uniformity (Fig. 39.3).
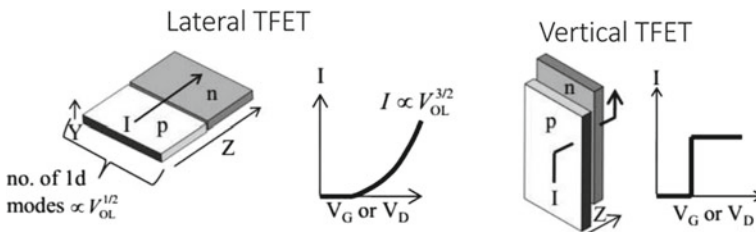

Fig. 39.3 $I–V$ characteristics of ideal lateral and vertical TFET [24]
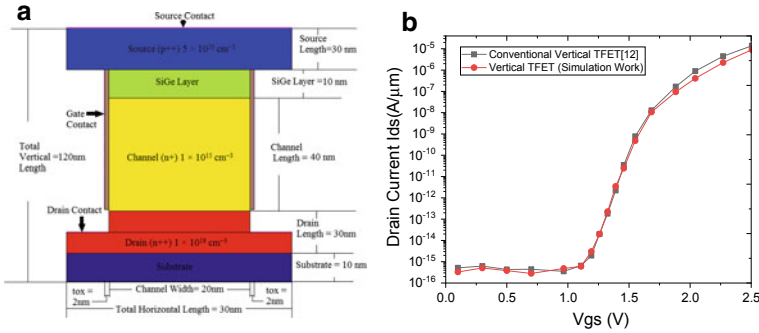
Fig. 39.4 **a** Schematic diagram of tunnel FET (VTFET) with embedded $Si_{1-x}Ge_x$ layer between source and channel. **b** Calibrated drain current characteristics of vertical TFET compared with that of the corresponding conventional vertical TFET [16]

39.1.6 Proposed Device Parameters and Simulation Models

Figure 39.4a shows the schematic representation of proposed vertical tunnel FET (VTFET) consists of source, channel, and drain of silicon material with the introduced silicon–germanium layer of 10 nm in the channel for enhancement of input characteristics. The device channel length (L) is 40 nm with source and drain length of 30 nm. The schematic representation of the TCAD simulated VTFET with metal gate work function (ϕ_m) of 4.15 eV and HfO_2 [25, 26] as the oxide layer of 2 nm thickness. Figure 39.4b represents the conventional vertical tunnel FET structure of silicon material calibrated with the drain characteristics curve. Silicon material-based structure consists (p++ type) of source doping concentration of 5×10^{20} cm^{-3}, (n+ type) channel doping concentration of 1×10^{15} cm^{-3} and (n++ type) drain doping concentration of 1×10^{18} cm^{-3}, respectively. The device simulation is performed using a 2-D and 3-D simulator via using non-local path band-to-band tunneling model without including quantum effect because of simplicity in the Sentaurus device TCAD simulator package [10, 27]. The entire tunneling potential path is traced by non-local path band-to-band tunneling model. Furthermore, for simulation work, Lombardi's mobility model and the Standard Shockley–Read–Hall recombination are also used [28–30].

39.2 Methodology

For designing electronics devices, such as transistors, nowadays, there are a lot of 2D and 3D simulation tools are available, which provides all facilities that are required for simulation and fabrication a device and they become very popular. One such tool is Sentaurus TCAD which is generally based on the finite element methods (FEMs), where device fabrication and its parameters (electrical characteristics) are assessing

by physical mechanism rather than electrical processing in the device. It provides a virtual fabrication and characterization facility without using actual fabrication process for the actual behavior of the device. Thus, both static and dynamic solutions are provided by these TCAD simulators for the electrical characterization. Technology computer-aided design (TCAD) is basically used for computer simulations to develop and enhance technologies used in semiconductor handling. TCAD simulation tools are used for unraveling physical, fundamental, and partial differential equations, for example, transport and diffusion equation for discretized geometries, which represents the silicon wafer layer in a device of semiconductor. So, it is possible with the help of TCAD tool to make and simulate the device virtually instead of the time-consuming and costly physically wafer preparation for the new design and characterization of the semiconductor devices.

39.2.1   Sentaurus TCAD Tool

A Sentaurus TCAD Tool is a manufacturing and business standard simulator tool which has many factory components and simulated models that are calibrated to experimental data. Sentaurus TCAD tool is capable to offer an accurate projection on the proposed forthcoming device and also provide proposed device characteristics [22, 31]. There is three type framework used in the Sentaurus TCAD Tool, i.e., Sentaurus Workbench for datasheet like excel, Sentaurus Structure Editor for design, and Sentaurus Visual to plot and visualize.

39.2.1.1   Sentaurus Workbench

In TCAD Sentaurus, Sentaurus Workbench provides a single platform for the user interface for designing, developing, organizing, and to run simulation for the new parameter's devices of semiconductor research and engineering. It is the graphical user front which integrates all the Sentaurus simulation tool in the sole environment. Many tools like Sentaurus process, Sentaurus Device, Sentaurus Mesh (meshing tool), and the inspect tool which is used for analysis and plotting are help user to work simultaneously (Fig. 39.5).

39.2.1.2   Sentaurus Structure Editor

Sentaurus Structure Editor is basically the device editor in 2-dimensional and 3-dimensional. All kinds of 3D device structure can be made using different geometrically primitives such as polygons, cuboids, rectangles, cylinders, and spheres. Various predefined materials are saved in the list to fill directly in the structure of user built. A different doping distribution option along with the Gaussian distribution is available for the structure built. In Sentaurus Structure Editor, meshing can
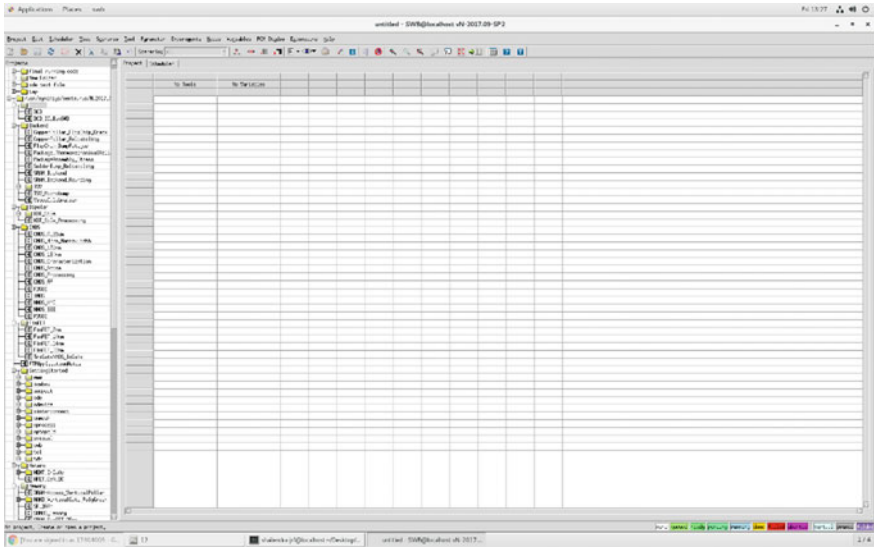
Fig. 39.5 Simulation TCAD window representation of Sentaurus Workbench

also be done which can be course and fine depending on the requirement of device specification (Fig. 39.6).
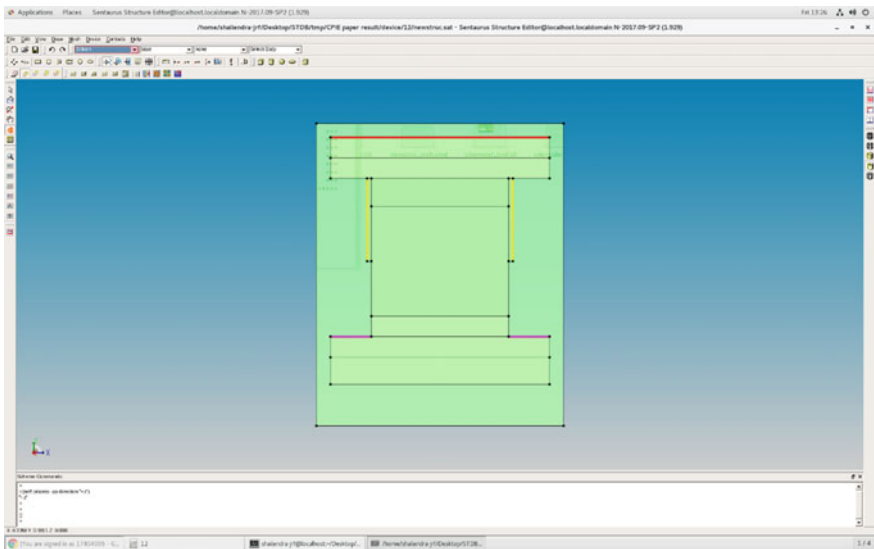

Fig. 39.6 Simulation TCAD window representation of Sentaurus Structure Editor

39.2.1.3 Sentaurus Visual

Sentaurus Visual is used to produce enlightening information in 2D and 3D sights in terms of data picturing and post-processing. It is an interactive tool for exploring and analyzing data to generate presentation-quality designs and computer graphics and to segment outcomes on the Web (Fig. 39.7).

39.2.2 Framework for Device Design Steps

Sentaurus TCAD is a 2-D and 3-D design simulator tool for designing a proposed device. Figure 39.11 shows all steps which are intricate from the development of device assembling to calibrate its electrical characteristics as given in flowchart Fig. 39.8.

The device simulator always takes the device specifications as the input and processes it with different specified models with given boundary conditions with plot file as represent with the block diagram Fig. 39.9.

On successful designing of the proposed device structure, successive steps are used in a correct manner like defining the physical models, boundary conditions and numerical methods which is used to determine the performance of analysis done. Sentaurus device is provided many models for design and simulation of a device. Thus, efficient model selection is required for correct analysis of a device. Now, there are two types' electrodes contacts in the device, former one is Ohmic contacts and
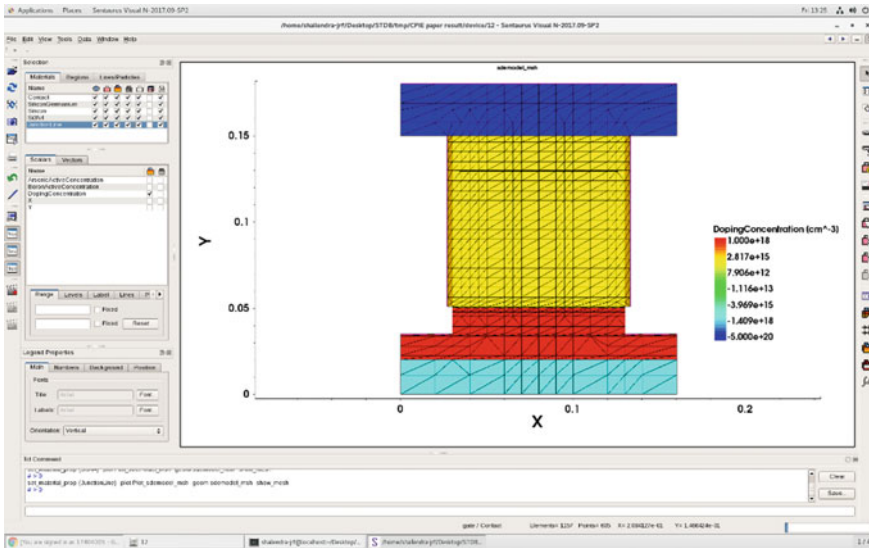

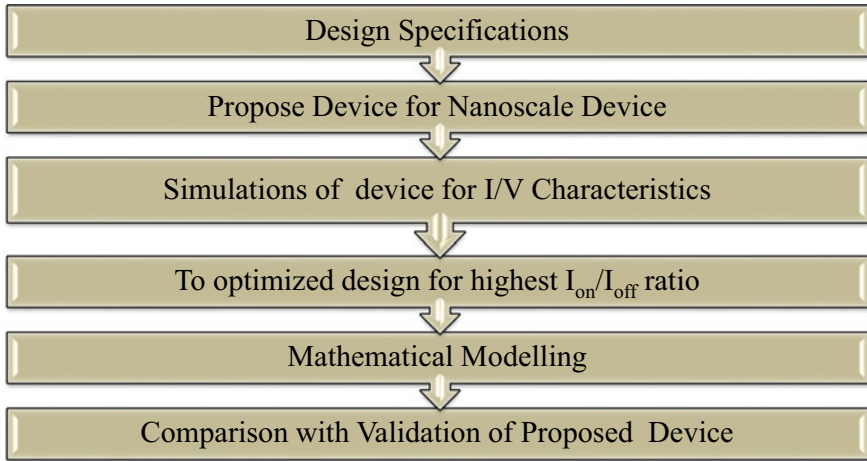**Fig. 39.7** Simulation TCAD window representation of Sentaurus Visual

Design Specifications

Propose Device for Nanoscale Device

Simulations of device for I/V Characteristics

To optimized design for highest I_{on}/I_{off} ratio

Mathematical Modelling

Comparison with Validation of Proposed Device

Fig. 39.8 Flowchart of device design steps

Models
Band to band Tunneling Models,
Generation recombination Model,
Lombardi Mobility Model, Shockley-
Read-Hall.

Boundary Conditions
Ohmic and Schottky
Insulators
Interface Charges

Analysis
AC/DC
Transient

Input Statements
Meshing
Material selection
Region selection
Electrode formation
Doping

Output Statements
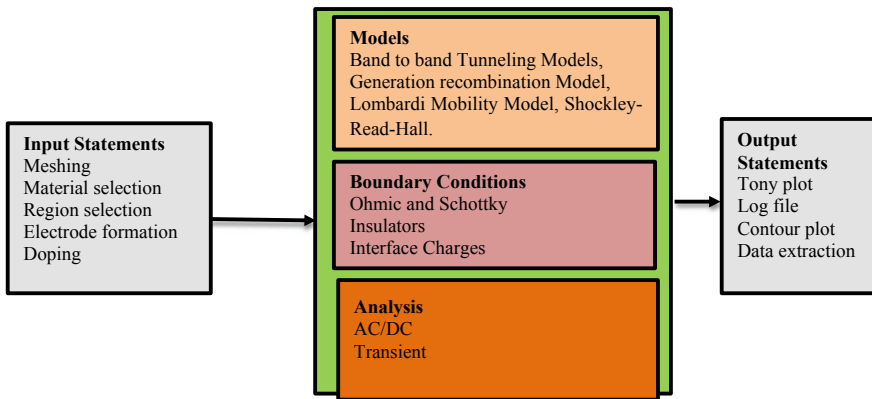Tony plot
Log file
Contour plot
Data extraction

Fig. 39.9 Block diagram of device design steps and its characterization

later one is Schottky contact that is decided by boundary conditions. A wide range of numerical methods are existing in the simulator for determining the solutions of the semiconductor devices. Thus, device meshing is important characteristics of finding the equation solutions because solutions are present only meshing points. So, meshing should be fine at all junctions.

Models are also able to solve the linear or nonlinear partial differential equations. Normally, required solutions are getting by applying a biasing voltage at each electrode and setting the analysis such as AC, DC, or transient. At last, the output is displayed in the simulator in the log files.

39.2.2.1   Electrostatics and Carrier Density

Mathematical models are defined in semiconductor device operations. Hence, they provide link electrostatics with carrier density. Sentaurus simulator is used for solving the basic model equations which comprise of well-known Poisson equation, continuity equation, and Boltzmann's statics [32–35]. We obtain a relation between charge carrier density and electrostatic potential by solving the Poisson equation. Under thermal equilibrium conditions, charge carriers, such as semiconductor electrons, behave according to Fermi-Dirac statics and also Fermi-Dirac distribution function defines the probability of occupancy of the electrons in the permissible energy state of the carriers which is given by Eq. (39.2.1).

$$f(E) = \frac{1}{1 + e^{\frac{E - E_{\mathrm{F}}}{k \cdot T}}} \qquad (39.2.1)$$

where $f(E)$ is Fermi-Dirac distribution function, E is energy state occupied by an electron, E_{F} is Fermi level, T and k are temperature and Boltzmann's constant, respectively.

39.2.2.2   Poisson's Equation

The Poisson equation delivers a relation between charge distribution and electrostatics surface potential in the semiconductor which is given by Eq. (39.2.2).

$$\nabla^2 \Psi = \frac{q}{\varepsilon}(p - n + N_{\mathrm{D}} - N_{\mathrm{A}}) \qquad (39.2.2)$$

where q, ε, p, n, $N_{\mathrm{D,}}$ and N_{A} are electronic charge, permittivity, holes concentration, electrons concentration, ionized donor, and ionized acceptor atoms. Thus, solution of Eq. (39.2.2) provides electrostatic surface potential in the device.

39.2.2.3   Band-to-Band Tunneling (BTBT) Models

In TFET, charge carriers are flowing by band-to-band tunneling mechanism. In a semiconductor, electrons get tunnel from VB of source to CB of channel across the bandgap that acts like potential barrier via BTBT. Tunneling process is generally classified into two type, former one is direct tunneling and later one is indirect tunneling. In direct tunneling, when an electron is tunneling from VB to CB, there is no absorption or emission of a photon. Similarly, in indirect tunneling, when electrons are tunneling from VB to CB, it used an intermediate state or it absorbs or emits a phonon, hence there is a change in momentum of an electron in tunneling process. In TCAD tool, BTBT models are divided into two types, former one is local BTBT model and later one is non-local BTBT model [35–38].

Non-local BTBT Model

The non-local BTBT model is developed by WKB. So, it is known as WKB approximation model which is compute tunneling probability of charge carriers. The statement of this model is "non-local" [22, 39].

39.2.2.4 Physical Models

Mobility Model

When an electric field is applied across the device, there electrons and holes are accelerated from VB to CB and momentum of these carriers are losses. This is happened due to several scattering effects such as impurity scattering, lattice variations, roughness characteristics of surface, and other inadequacies inside the material. The mobility of a semiconductor is a function of electric field, lattice temperature, doping concentration, etc. And these all effects are considered for better performance when choosing mobility mode. Broadly, mobility mode is divided into four subsection such as (a) high-field mobility, (b) low-field mobility, (c) mobility in a bulk semiconductor region, and (d) mobility in an inversion layer [17, 40].

Generation and Recombination Models

When electrons travel from VB to CB in a semiconductor device, where free charge carriers density is maintained constant via generation and recombination mechanism. Both momentum and energy are conserved during this process. The product of hole and electron concentration is constant at thermal equilibrium condition. The recombination and generation mechanism are described by the following process.

Shockley–Read–Hall (SRH) model is very much helpful and useful for the indirect bandgap material such as silicon material. The leakage current is also considered by this model which is generated due to minority carriers. According to the need, lifetime of carriers is adjusted. We know, the charge carriers are trapped at the silicon–oxide interface and consideration of these types of carriers are necessary for model accuracy. SRH model is also known as trap-assisted recombination process [22, 41].

39.3 Design and Analysis of Vertical Tunnel FET

39.3.1 Vertical Tunnel FET (n-Type) with Gate Oxide Dielectric Material k

Figure 39.10a shows the transfer characteristics for different dielectric constant material at gate oxide with the value of $\varepsilon = 22$ (HfO$_2$), $\varepsilon = 7.0$ (Si$_3$N$_4$), and $\varepsilon = 3.9$ (SiO$_2$) at $V_{ds} = 1$ V. It is depicted from the figure that higher the value of the dielectric constant more the ON-state current will enhance. This will also improve the subthreshold slope (SS) with subthreshold voltage (V_T). Form the above analysis, it can be concluded that higher value of the dielectric constant will be used for further parameter analysis. HfO$_2$ is approx. 5.6 times higher than the SiO$_2$ as shown in Fig. 39.10b different color representation for different oxide.

39.3.2 Vertical Tunnel FET (n-Type) with SiGe Mole Fraction x and Work Function

In vertical TFET device, we have used the concept of hetero-material to get better performance of device. SiGe is used as source–channel inter-junction which has lower bandgap of 0.7 eV as that of silicon material (1.1 eV) because of low bandgap of germanium (Ge) [42–45]. SiGe as source material increases the tunneling area at source–channel junction which leads to increase in ON-current as shown in Fig. 39.11a. As we increase the mole fraction ($x = 0.4$–0.8) of germanium, the current increases because of the decrease in bandgap of SiGe material. Improved
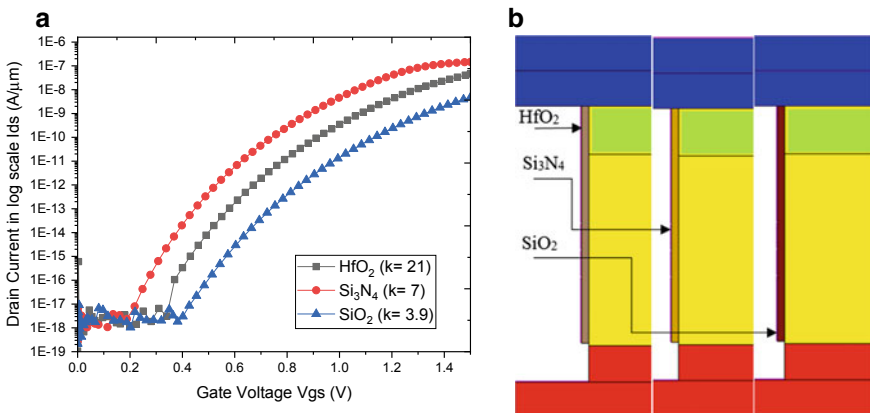

Fig. 39.10 a Transfer characteristics of Id versus V_{gs} as a function of different dielectric constant for gate oxide. **b** Schematic diagram showing different color representation for different oxide
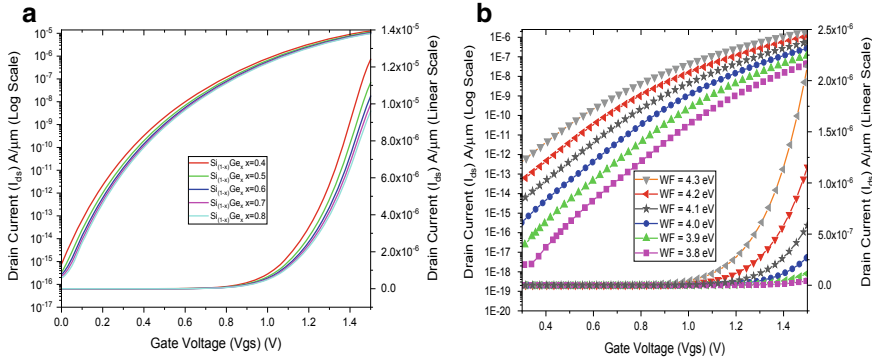
Fig. 39.11 **a** Transfer characteristics of Id versus V_{gs} as a function of different mole fraction of $Si_{(1-x)}Ge_x$ form $x = 0.4$ to $x = 0.8$. **b** Id versus V_{gs} as a function of work function variation from 3.8 to 4.3 eV

I_{ON} current and I_{OFF} current recorded as 1.126×10^{-05} (A/μm) and 2.684×10^{-16} (A/μm) at $x = 0.8$. Figure 39.11b shows the transfer Id-V_{gs} characteristics of with the variation of work function. The variation of the work function is taken from the value to 4.3–3.8 eV. As the work function increases, the ON-current will also increase proportionally but the graph will shift toward the left side and makes this OFF current increases. Further, this will decrease the ratio of I_{ON}/I_{OFF} ratio as well.

39.3.3 Vertical Tunnel FET (n-Type) with Variation of V_{gs} in Ids Versus V_{ds} Transfer Characteristics

Figure 39.12 shows the simulated output characteristics of Ids versus V_{ds} with the variation of the V_{gs} voltage form (0.2–1.0 V) of n-type vertical TFET device for high dielectric gate oxide. Equivalent to MOSFETs, the vertical TFET also displays the saturation behavior, since the higher value of V_{ds} is independent of the tunneling barrier width. However, up to $V_{ds} < 0.4$ V, the drain–source current will vary linearly to the drain–source voltage. The tunneling probability is more for the higher value of the V_{gs} which contributes to increase in the drain current.

39.3.4 Vertical Tunnel FET (n-Type) with the Variation of V_{ds} in Ids Versus V_{gs} Transfer Characteristics

Figure 39.13a shows the Id-V_{gs} characteristics of vertical TFET as a function of V_{ds} (drain-to-source voltage). It is depicted from the figure that the drain voltage will
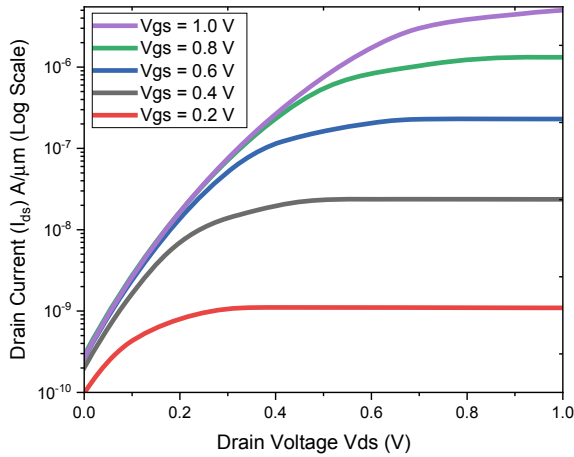
Fig. 39.12 Transfer characteristics of Id versus V_{ds} as a function of different V_{gs} varied from 0.2 to 1.0 V
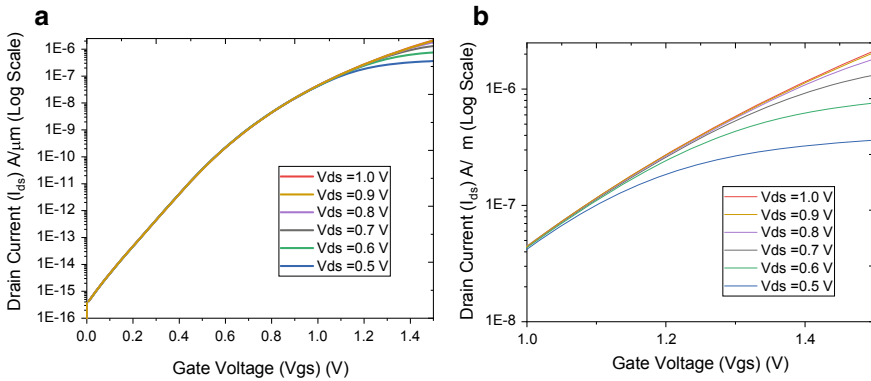

Fig. 39.13 **a** Transfer characteristics of Id versus V_{ds} as a function of different V_{gs} varied from 0.2 to 1.0 V. **b** Magnification of the same graph

have very little influence on the drive current as shown in Fig. 39.13b indicating well control of the gate across the tunneling path of the device.

39.3.5   Vertical Tunnel FET (n-Type) for Reduction of Ambipolar Conduction

Figure 39.14 (a) shows schematic diagram and (b) shows the transfer Id-V_{gs} characteristics of vertical TFET as a function of gate underlap region to reduce ambipolar
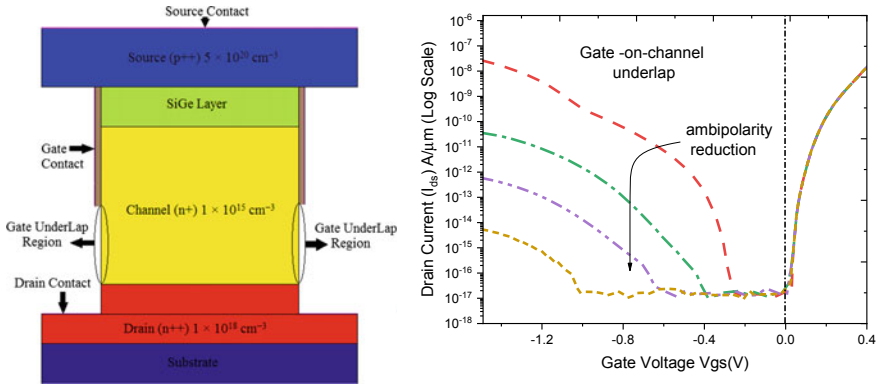
Fig. 39.14 **a** Schematic diagram of gate underlap technique for the reduction of ambipolarity. **b** *I–V* characteristics showing suppression of the ambipolarity

conduction. As this reduction of gate contact with drain region makes the tunneling barrier which leads to reduction of ambipolarity even if the V_{gs} is negatively biased [46].

39.4 Summary

In this paper, vertical tunnel FET has been examined with some scaling issue. TCAD Sentaurus simulation and measurements have been used to enumerate the physics of the embedded $Si_{1-x}Ge_x$/Si gated diodes operating in the vertical TFET. The device characteristics are found to be improving and promising with the increase in germanium content in terms of mole fraction, work function, and dielectric constant k via simulation using non-local tunneling model. The vertical tunnel FET can achieve a relatively high I_{ON}/I_{OFF} current ratio (~10^{10}), V_T threshold voltage (~0.352 V), and maximum Ion current with 1.126×10^{-5} (A/μm). Furthermore, the ambipolar reduction is also done with the technique of gate underlap region. However, still, there is a scope left for enhancing the device characteristics with a suitable choice of the heterojunction material. Thus, vertical tunnel FET is found to be a promising candidate for the low power digital applications and suitable for future technology.

39.4.1 Future Work

Following are the ideas which could be explored in future

i.   The conventional MOSFETs and conventional TFETs further could be replaced by vertical TFET in the future for analog as well as digital applications.

ii. Development of different types of sensors such as image sensor and pressure sensor using vertical tunnel FET.
iii. Designing inverter circuits using vertical tunnel FET.
iv. Designing and development of low power for smart safety system.

References

1. Dawon, K.: Electric field-controlled semiconductor device. US Patent 3,102,230 (1963)
2. K, Dawon: A historical perspective on the development of MOS transistors and related devices. IEEE Trans. Electron Devices **23**(7), 655–657 (1976)
3. Moore, G.E.: Cramming more components onto integrated circuits. Proc. IEEE **86**(1), 82–85 (1998)
4. Borkar, S.: Getting gigascale chips: challenges and opportunities in continuing moore's law. Queue 1(7), 26 (2003)
5. Veeraraghavan, S., Fossum, J.G.: Short-channel effects in SOI MOSFETs. IEEE Trans. Electron Devices **36**(3), 522–528 (1989)
6. Bulucea, C., Wang, F.-C., Chaparala, P.: Field-effect transistor for alleviating short-channel effects. US Patent 6,548,842 (2003)
7. Young, K.K.: Short-channel effect in fully depleted SOI MOSFETs. IEEE Trans. Electron Devices **36**(2), 399–402 (1989)
8. Semenov, O., Vassighi, A., Sachdev, M.: Leakage current in sub-quarter micron MOSFET: a perspective on stressed delta IDDQ testing. J. Electron. Test. **19**(3), 341–352 (2003)
9. Boucart, K., Ionescu, A.M.: Double-gate tunnel FET with high-κ gate dielectric. IEEE Trans. Electron Devices **54**(7), 1725–1733 (2007)
10. Dubey, P.K., Kaushik, B.K.: T-shaped III–V heterojunction tunneling field-effect transistor. IEEE Trans. Electron Devices **64**(8), 3120–3125 (2017)
11. Wadhwa, G., Raj, B.: Parametric variation analysis of charge-plasma-based dielectric modulated JLTFET for biosensor application. IEEE Sens. J. **18**(15) (2018)
12. Kumar S., Raj, B.: Compact channel potential analytical Modeling of DG-TFET based on evanescent–mode approach. J. Comput. Electron. **14**(2), 820–827 (2015)
13. Kumar S., Raj, B.: Analysis of ION and ambipolar current for dual-material gate-drain overlapped DG-TFET. J. Nanoelectron. Optoelectron. **11**, 323–333 (2016)
14. Sun, M.-C., et al.: Scalable embedded Ge-junction vertical-channel tunneling field-effect transistor for low-voltage operation. In: Nanotechnology Materials and Devices Conference (NMDC), IEEE, (2010)
15. Singh, S., Raj, B.: Vertical tunnel-FET analysis for excessive low power digital applications. In: 2018 First International Conference on Secure Cyber Computing and Communication (ICSCCC). IEEE, 2018
16. Bhuwalka, KK, et al.: Vertical tunnel field-effect transistor. IEEE Trans. Electron Devices **51**(2), 279–282 (2004)
17. Saurabh, S., Kumar, M.J.: Novel attributes of a dual material gate nanoscale tunnel field-effect transistor. IEEE Trans. Electron Devices **58**(2), 404–410 (2011)

18. Khatami, Y., Banerjee, K.: Steep subthreshold slope n-and p-type tunnel-FET devices for low-power and energy-efficient digital circuits. IEEE Trans. Electron Devices **56**(11), 2752–2761 (2009)
19. Zhi, J., et al.: Vertical-dual-source tunnel FETs with steeper subthreshold swing. J. Semicond. **37**(9), 094003 (2016)
20. Wang, P.-Y., Tsui, B.-Y.: Band engineering to improve average subthreshold swing by suppressing low electric field band-to-band tunneling with epitaxial tunnel layer tunnel FET structure. IEEE Trans. Nanotechnol. **15**(1), 74–79 (2016)
21. Nigam, K., Kondekar, P., Sharma, D.: High frequency performance of dual metal gate vertical tunnel field effect transistor based on work function engineering. Micro Nano Lett. **11**(6), 319–322 (2016)
22. Sentaurus User's Manual, Synopsys, Inc., Mountain View, CA, USA,2017.09 (2009)
23. Semiconductor Industry Association (SIA): International Technology Roadmap for Semiconductors (ITRS) (2015)
24. Samuel, T.S., et al.: Analytical modeling and simulation of dual material gate tunnel field effect transistors. J. Electr. Eng. Technol. **8**(6), 1481–1486 (2013)
25. Krishnamohan, Tejas, et al.: Double-gate strained-Ge heterostructure tunneling FET (TFET) with record high drive currents and ≪60 mV/dec subthreshold slope. In: 2008 IEEE International Electron Devices Meeting. IEEE, 2008
26. Zhou, G., et al.: Vertical InGaAs/InP tunnel FETs with tunneling normal to the gate. IEEE Electron Device Lett. 32(11), 1516–1518 (2011)
27. Singh, S., Vishvakarma, S.K., Raj, B.: Analytical modeling of split-gate junction-less transistor for a biosensor application. Sens. Bio-Sens. **18**, 31–36 (2018)
28. Choi, W.Y., et al.: Tunneling field-effect transistors (TFETs) with subthreshold swing (SS) less than 60 mV/dec. IEEE Electron Device Lett. **28**(8), 743–745 (2007)
29. Baba, J.T.: Proposal for surface tunnel transistors. Jpn. J. Appl. Phys. **31**(4B), L455–L457 (1992)
30. Gopalakrishnan, K., Griffin, P.B., Plummer, J.D.: I-MOS: a novel semiconductor device with a subthreshold slope lower than kT/q. In: Digest. International Electron Devices Meeting, IEEE (2002)
31. Kao, Kuo-Hsing, et al.: Direct and indirect band-to-band tunneling in germanium-based TFETs. IEEE Trans. Electron Devices **59**(2), 292–301 (2012)
32. Hoefflinger, B.: ITRS 2028—international roadmap of semiconductors. CHIPS 2020 **2**, 143–148 (2016)
33. Neisser, M., Wurm, S.: ITRS lithography roadmap 2015 challenges. Adv. Opt. Technol. **4**(4), 235–240 (2015)
34. Bhuwalka, K.K., Schulze, J., Eisele, I.: Scaling the vertical tunnel FET with tunnel bandgap modulation and gate workfunction engineering. IEEE Trans. Electron Devices **52**(5), 909–917 (2005)
35. Singh, S., Raj, B.: Design and analysis of a heterojunction vertical t-shaped tunnel field effect transistor. J. Electron. Mater. 1–8 (2019)
36. Lang, N.D., Kohn. W.: Theory of metal surfaces: work function. Phys. Rev. B **3**(4), 1215 (1971)
37. Knoll, L., Richter, S.: Strained silicon based complementary tunnel-FETs: steep slope switches for energy efficient electronics. Solid-State Electron **98**(3), 32 (2014)
38. Ford, A.C., Yeung, C.W., Chuang, S.: Ultrathin body InAs tunnelling field-effect transistors on Si substrates. Appl. Phys. Lett. **98**(11), 113105 (2011)
39. Kazazis, D., Jannaty, P., Zaslavsky, A.: Tunneling field-effect transistor with epitaxial junction in thin germanium-on-insulator. Appl. Phys. Lett. **94**(26), 263508 (2009)
40. Sze, S.M., Ng. K.K.: Physics of Semiconductor Devices. wiley (2006)
41. Zhao, Y., White, M.H.: Modeling of direct tunneling current through interfacial oxide and high-*k* gate stacks. Solid-State Electron. **48**(10), 1801–1807 (2004)
42. Stuetzer, O.M.: Junction fieldistors. Proc. IRE **40**(11), 1377–1381 (1952)
43. Sharma, S., Raj, B., Khosla, M.: Comparative analysis of MOSFET, CNTFET and NWFET for high performance VLSI circuit design: a review. J. VLSI Des. Tools Technol. (JoVDTT), STM J. **6**(2), 19–32 (2016)

44. Jain, A., Sharma, S., Raj, B.: Design and analysis of high sensitivity photosensor using cylindrical surrounding gate MOSFET for low power sensor applications. Eng. Sci. Technol., Int. J. **19**(4), 1864–1870 (2016)
45. Schenk, A.: Rigorous theory and simplified model of the band-to-band tunneling in silicon. Solid-State Electron. **36**(1), 19–34 (1993)
46. Abdi, D.B., Kumar. M.J.: 2-D threshold voltage model for the double-gate pnpn TFET with localized charges. IEEE Trans. Electron Devices **63**(9), 3663–3668 (2016)

Chapter 40
Finite Element Based Simulation Model for Micro Turning of Nanoparticle-Reinforced Aluminum Alloy (7075-T6) Composite

Sant Ram Chauhan, U. Gokul Krishna, and Sunil Setia

Abstract MMCs reinforced with nanoparticles exhibit better mechanical properties including higher yield strength and creep resistance with the retention of ductility when compared with its micro counterpart. The difficulty in machining these materials leads to modeling the machining process to get a better understanding of the process and to predict the fundamental output variables such as cutting force and temperature. Since the surface roughness of the machined part is known to be affected mainly by the feed, a higher surface finish is achieved by turning with micron-level feed rates. A finite element based coupled temperature displacement model for turning aluminum 7075 alloy reinforced with nanosilicon carbide particles at micron-level feed rates are developed. The model is validated experimentally.

Keywords MMC · Microturning · FEA

Nomenclature

MMC   Metal matrix composite
PCD   Poly crystalline diamond
SiC   Silicon carbide
Al_2O_3 Alumina
FEM   Finite element method

S. R. Chauhan (✉) · U. Gokul Krishna (✉) · S. Setia (✉)
Department of Mechanical Engineering, National Institute of Technology,
Hamirpur 177005, India
e-mail: srchauhan@nith.ac.in

U. Gokul Krishna
e-mail: gokulkr161@gmail.com

S. Setia
e-mail: sunilsetia@nith.ac.in

40.1 Introduction

Metal matrix composites are used in many industrial applications including transportation, electronics, thermal management, filamentary superconducting magnets, recreational products, aerospace and wear-resistant materials. These applications of MMCs are enabled by their excellent functional properties such as high strength to weight ratio, high structural efficiency, high modulus to weight ratio, fatigue resistance and corrosion resistance, excellent wear resistance and attractive thermal characteristics. These properties also make them highly competitive against unreinforced metals and conventional materials. Another advantage of these materials is, by selecting the right combination of matrix and reinforcement, one can get the desired property suitable for a particular application [1, 2]. Difficulty in shaping composite materials into accurate parts with good surface finish prevents them from being used in different applications [2]. MMCs reinforced with nano-sized reinforced particles show better properties such as higher yield strength and creep resistance compared to microparticle reinforced composite counterparts [3]. With the addition of nanoparticles, mechanical properties are improved without compromising the ductility of material [4].

Experimental methods, modeling using conventional cutting mechanics and numerical simulation are used to study the machining of MMCS [5–7]. Different researchers depicted from experimentation that with the increase in feed rate, surface roughness increases. So, for higher surface finish, the feed rate should be less [8]. Among different tools used for machining of MMC, PCD tool was found to be best suited. PCD exhibited high wear resistance and good surface finish compared to carbide, polycrystalline cubic boron nitride (PCBN) and coated carbide tools. This is due to PCDs high hardness and thermal conductivity [5, 9–11].

Many finite element based models have been developed for the machining of microparticle reinforced metal matrix composite. Zhu et al. [12] developed a model for machining aluminum 6061 composites reinforced with 10% alumina reinforced particles. The particle size used in this model was 15 μm. A model was developed by Pramanic et al. [13] for simulating the orthogonal machining aluminum composites reinforced with SiC particles of the size 18 μm. Tool particle interaction during machining was analyzed. More recently another FEM based model that simulated the different phases including matrix, particles, and the interface was developed by Ghandehariun et al. [14]. The model was used to investigate the effect of cutting speed on MMC behaviors such as tool particle interaction, stress, and temperature generated. Aluminum Al6061 was used as a matrix in this model with 20% Al_2O_3 particles of size 23 μm. Cutting tool used was of tungsten carbide. Teng et al. [15] conducted a study on machining magnesium-based nanocomposites that have 1.5% of SiC nanoparticle of the size 100 nm. Finite element model is used to simulate the micro-milling operation with the consideration of cutting-edge radius.

In the present work, attempt was made to develop the FEM model for machining of aluminum 7075 alloy reinforced with nano Silicon Carbide particles with micron-level feeds by using ABAQUS/Explicit.
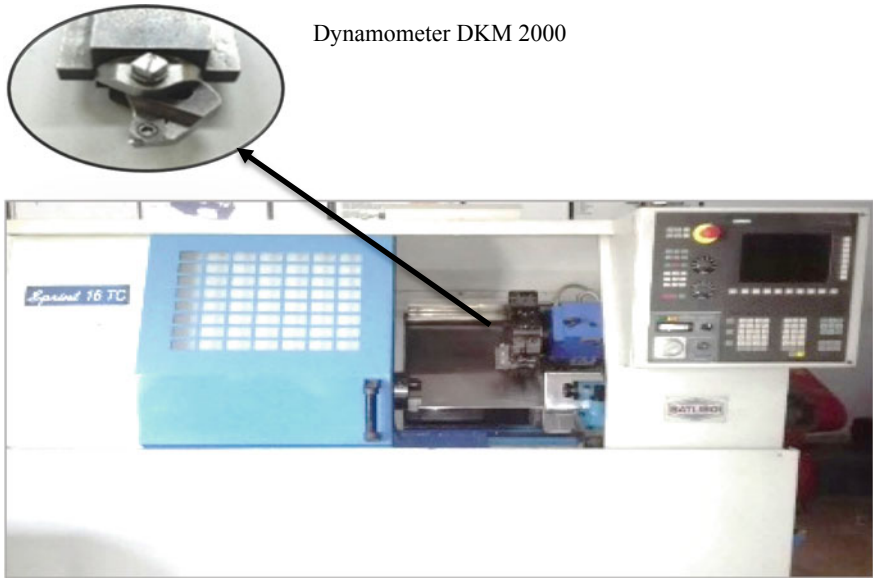
Dynamometer DKM 2000

Fig. 40.1   Machine tool setup

40.2   Experimental Procedures

The MMC was fabricated using stir casting process. The machining was carried out in CNC turning center. Polycrystalline diamond (PCD) tool with tool specification of CCGW09T304 was used for machining. Cutting forces are measured using the lathe tool dynamometer (DKM 2000 by Telc Germany). Machine setup is shown in Fig. 40.1.

40.3   Finite Element Modeling Procedures

From modeling point of view, the factor that decides how a system behaves during a process is geometry, the property of the materials in that system, boundary conditions, and initial conditions. Solving problems using an analytical method with considering all factors can be very difficult for engineering problems. Steps involved in computational modeling are discussed below.

40.3.1   Modeling of the Geometry

In this step, the geometry of the system is identified and created in the software. Many times, representing the geometry in the exact form is also difficult, so the geometry is converted into a simplified form so that it can be easily analyzed. The actual turning process is simplified into orthogonal machining and created a 2D orthogonal model. The model for machining of nano-Al/SiC MMC was developed using Abaqus/Explicit, a commercial FEM package. The model has a workpiece and a tool (Fig. 40.2a, b). The workpiece has a matrix in which particles are distributed as shown in Fig. 40.3. Particles are assumed to be circular in shape and are assumed to be distributed in an ordered manner as in Fig. 40.2a. Size of the particle is taken as 300 nm with a distance between each nearby particle as 0.002 mm this gives a volume percentage of 5.5%. The particles are modeled only in the areas, where the tool comes to contact with the workpiece. This is done to reduce computational cost. The tool has a rake angle of 10°, clearance angle of 7° and a cutting-edge radius of 0.01 mm. Cutting tool geometry is shown in Fig. 40.2b. The tool and workpiece are modeled as 2D parts, assuming plane strain condition.

According to Eq. 40.1, when the approach angle is 90°, the feed will be equal to uncut chip thickness a_1. In this study, the approach angle is taken as 90° which allows taking feed and uncut chip thickness interchangeably.

$$F \sin(\emptyset) = a_1 \tag{40.1}$$

40.3.2   Material Modeling

The properties of the material involved in the domain are applied to the corresponding elements. For example, Young's modulus has to be uploaded for stress analysis whereas properties such as thermal conductivity have to be given for thermal analysis. The properties are usually found out experimentally and used in the model. The Al 7075-T6 matrix is modeled as deformable. Elastic properties are defined using poison's ratio and young's modulus. Johnson–Cook constitutive model (Eq. 40.2) is used to predict the flow stress in the metal matrix that subjected to high strain, strain rate, and temperature. Thermal properties such as specific heat and thermal conductivity are also defined for aluminum alloy.

$$\bar{\sigma} = \left[A + B(\bar{\varepsilon}^{\mathrm{pl}})^n \right] \left[1 + C \ln \left(\frac{\dot{\bar{\varepsilon}}^{\mathrm{pl}}}{\dot{\bar{\varepsilon}}_0} \right) \right] \left[1 - \left(\frac{T - T_{\mathrm{room}}}{T_{\mathrm{melt}} - T_{\mathrm{room}}} \right)^m \right] \tag{40.2}$$

In this equation, $\bar{\sigma}$ is the flow stress, $\bar{\varepsilon}^{\mathrm{pl}}$ the plastic strain, $\dot{\bar{\varepsilon}}^{\mathrm{pl}}$ is the plastic strain rate, $\dot{\bar{\varepsilon}}_0$ is the reference strain rate and T is the temperature, T_{melt} and T_{room} are the melting and ambient temperature of materials. A is the yield strength, B is the strain
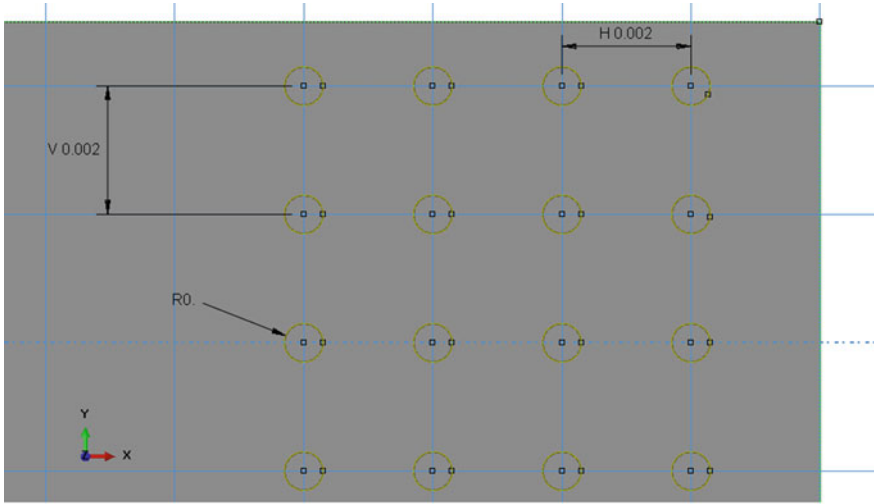
(a) Workpiece geometry
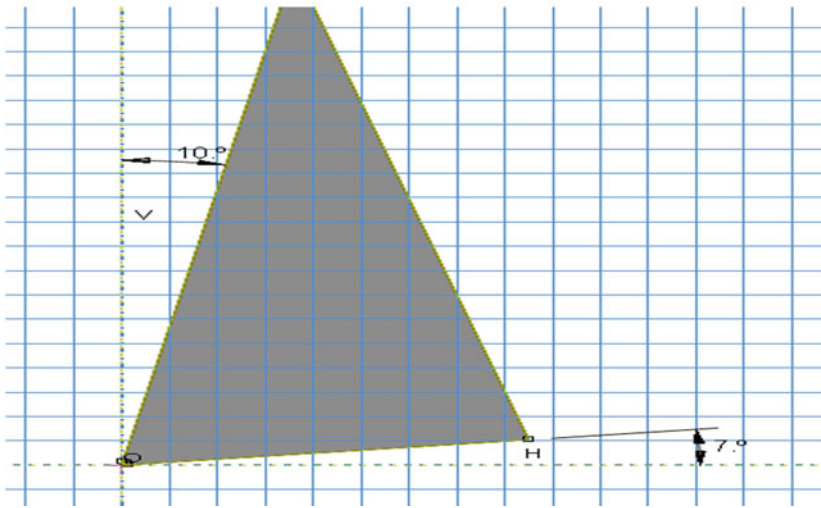
(b) Tool Geometry

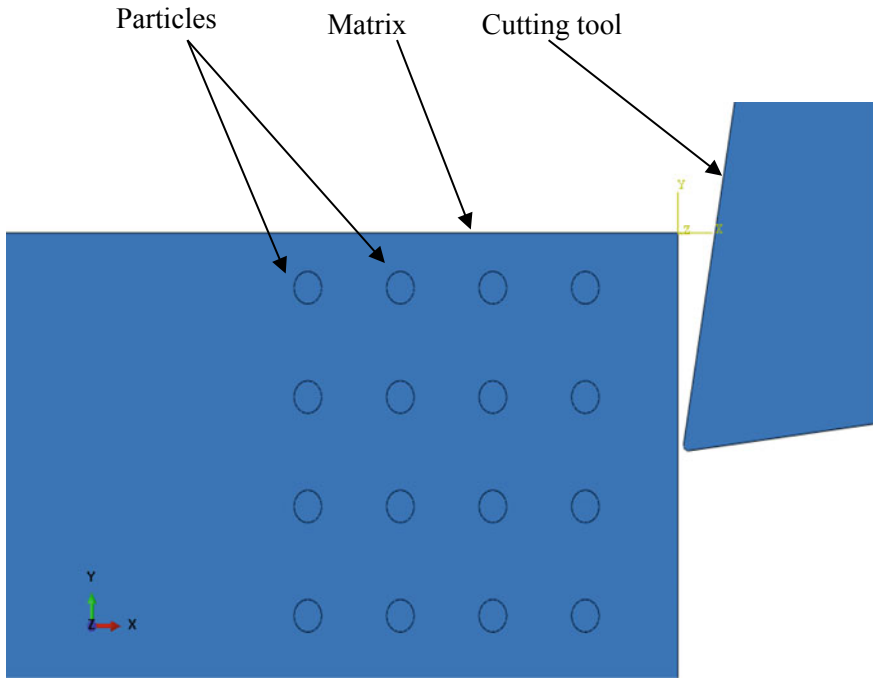Fig. 40.2 Geometries of workpiece and tool. **a** Workpiece geometry, **b** tool geometry

Fig. 40.3 Assembly showing tool and workpiece

hardening constant, C is strain rate sensitivity coefficient, n is the strain hardening exponent and m is the thermal softening coefficient.

The materials failure criterion for an aluminum matrix was defined by Johnson–Cook fracture equation (Eq. 40.3). Strain and strain rate hardening and temperature softening effects are considered in this equation. It has been widely used to define the fracture criterion in metal machining. Equivalent plastic strain at fracture, $\overline{\varepsilon_f^{Pl}}$ defined as:

$$\overline{\varepsilon_f^{Pl}} = (d_1 + d_2)e^{d_3\eta}\left[1 + d_4 \ln\left(\frac{\dot{\overline{\varepsilon}}^{Pl}}{\dot{\varepsilon}_0}\right)\right]\left[1 + d_5\left(\frac{T - T_{room}}{T_{melt} - T_{room}}\right)\right] \qquad (40.3)$$

Here η is the stress triaxiality and $\dot{\varepsilon}_0$ is the reference strain rate. Silicon carbide particles are modeled as elastic and plastic region is not defined for them. Material constants used are shown in Tables 40.1, 40.2 and 40.3.

Table 40.1 Mechanical properties of materials

Properties	Material	Reinforcement	Tool
	Al 7075	SiC	PCD
Density (tonne/mm^3)	2810×10^{12}	3200×10^{12}	3500×10^{12}
Elastic modulus E (GPa)	71.7	408	800
Poisson ratio	0.33	0.35	0.07
Specific heat (J/kgK)	960	755	525
Thermal conductivity (W/mK)	130	120	2100

Table 40.2 Johnson–Cook material parameters for Al 7075

A	546
B	678
N	0.71
C	0.024
M	1.56

Table 40.3 Johnson–Cook failure parameters for Al 7075

d_1	−0.068
d_2	0.451
d_3	−0.952
d_4	0.036
d_5	0.697

40.3.3 Interaction and Boundary Conditions

Further boundary conditions and loading conditions are applied to the model. This includes the initial displacements, velocity, loading and other boundary conditions in different steps. Surface to surface contact interaction is defined between the workpiece and tool. Kinematic contact method is used for mechanical constraint formulation. Mechanical tangential contact with a coefficient of friction 0.5 is used. The workpiece is fixed and the tool is allowed to move with a constant velocity of 1000 mm/s. The workpiece is fixed using encastre conditions.

40.3.4 Meshing

In this step, the geometry is divided into a finite number of elements. The precision of the solution will be subject to the number of elements. It increases with enlargement in the number of elements. With the increase in the number of elements, the computation time and cost increase. Explicitly coupled temperature displacement,
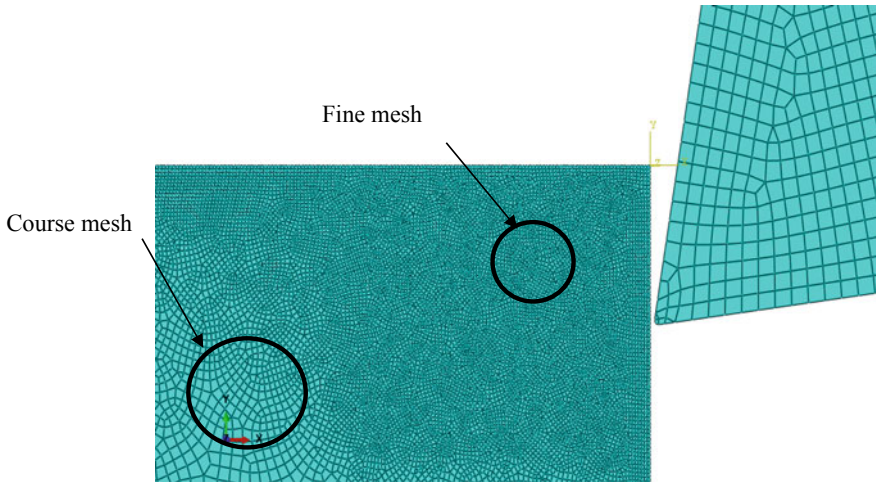
Fig. 40.4 Meshed tool and workpiece

plain strain, linear elements are used and the element deletion is allowed. There are 24045 elements in the model. Element size on the right side is 0.0001 mm on the left side it is 0.0005 mm. Since the area of interest is around the tool and workpiece interaction, fine mesh is given in that area and relatively coarse mesh is given in other regions, as shown in Fig. 40.4.

40.3.5 Equation Solvers and Visualization

The developed computational model is fed into a solver to solve and get the field variables at different node positions. This step requires computer hardware including CPU and memory. Further visualization function has been performed to depict the results. The result may include big data. Representing that into an easily understandable format is done in the visualization module of the software package.

40.4 Results and Discussion

The simulation was performed for single-chip formation for a fixed cutting speed of 1000 m/s at different feed rates of 4 and 6 μm. Chip formation process, von Mises stress distribution, equivalent plastic strain, the temperature generated and cutting force are obtained as simulation results. Cutting force accounts, force due to contact pressure and frictional stress. Figure 40.5 shows chip formation process. The results show that cutting mechanism has been greatly influenced by the presence
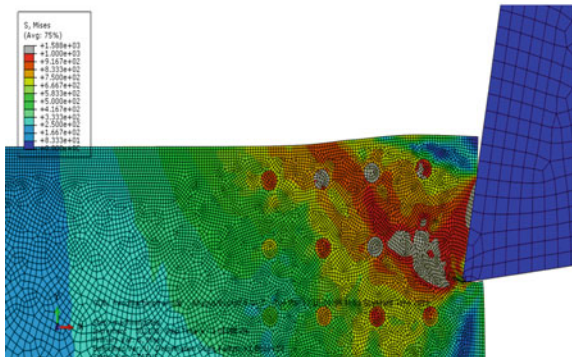
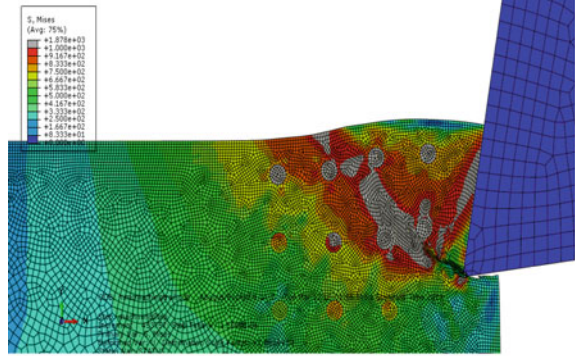**Fig. 40.5** Chip formation process in the sequence of a, b, c, d, e and f
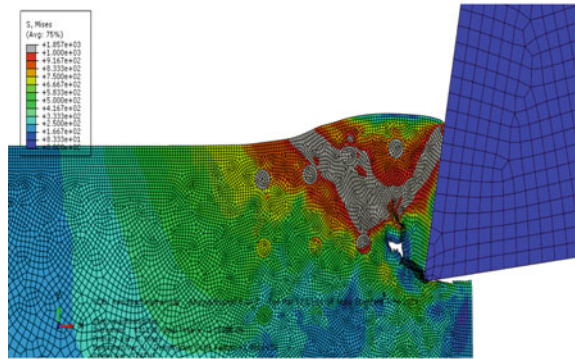

(a)

(b)
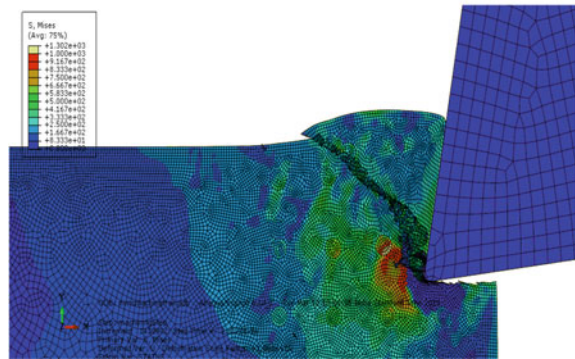

(c)
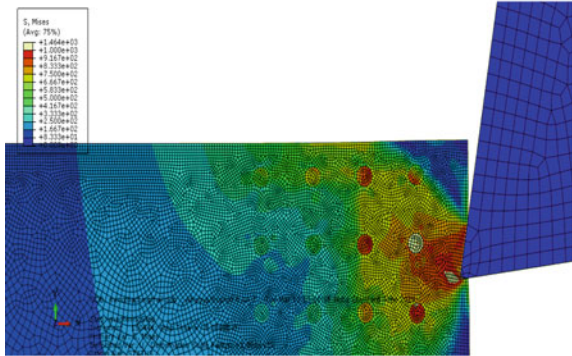
(d)
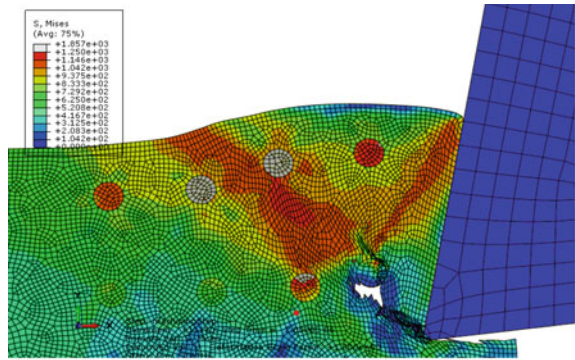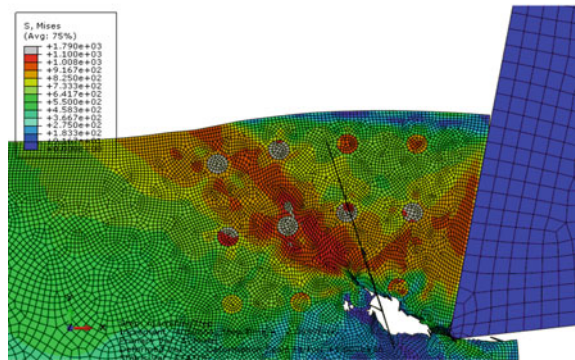

(e)

(f)

Fig. 40.6 Von Mises stress distribution during chip formation. **a** When feed is 4 μm, **b** feed is 6 μm


(a) When **feed is 4μm**

(b) **feed is 6μm**

of reinforced particles. It can be observed from Fig. 40.6 that von Mises stress distribution is different from that of an unreinforced homogenous metal during chip formation.

The shear zone is found to be irregular due to the presence of particles in the shear zone. The cracks generated in the shear zones are found to be propagated around the particle when the particles are present in the path of crack.

It was found that cutting force first increases and then decreases during the chip formations. Since the second chip formation will be an exact repetition of first chip formation process, it is not carried out. To compare with the experimental value, the average of this cyclic value is taken.

Cutting force is also influenced by the presence of particles in the primary shear zone. In the starting of cutting operation cutting force for 4 μm feed is higher than 6 μm feed. This may be due to the absence of particles in the shear zone in first case, and crack propagates in between two particles. It was observed that equivalent plastic strain also concentrated in between particles and particles act as barriers to prevent plastic stress flow (Fig. 40.7). It also can be seen that the zone of high equivalent

Fig. 40.7 Equivalent plastic
strain. **a** Feed is 4 μm, **b** feed
is 6 μm
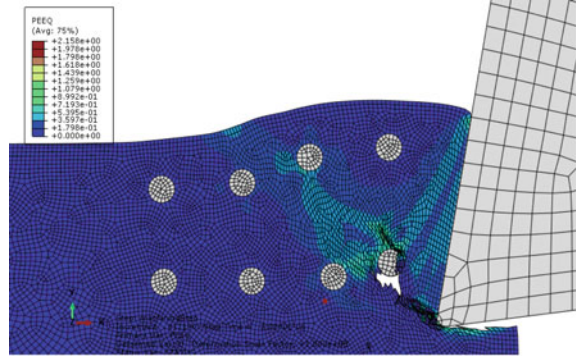
(a) feed is 4μm
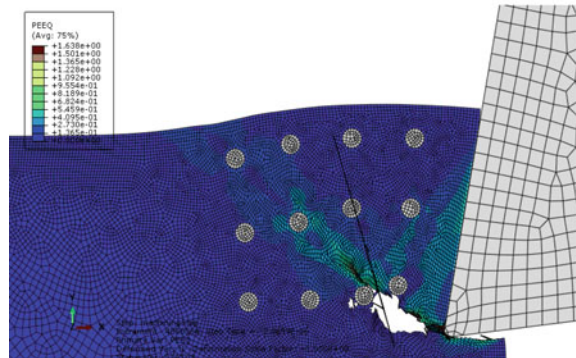
(b) feed is 6μm

plastic strain making more angle with horizontal in (Fig. 40.7a) than in (Fig. 40.7b).
Temperature is measured at cutting-edge of the tool. Temperature rise is more in the
case of small feed which indicates the presence of a particle in the shear zone which
is not there in the case of higher feed. The model was validated by comparing cutting
forces to experimental results. Experimentally cutting force was found to be 7 N
during machining with a feed of 6 μm. In the simulation, the average cutting force
during chip formation is 6 N which is in good agreement with the experimental data.

40.5   Conclusion

In this paper, finite element based coupled temperature displacement model was
developed for simulating the micro turning of the aluminum 7075 based metal matrix
composite reinforced with nano Silicon Carbide particles. Chip formation process is
presented. The cutting force and temperature rise in the tool during chip formation are
found out at two different feed rates (Figs. 40.8 and 40.9). Further, model validation
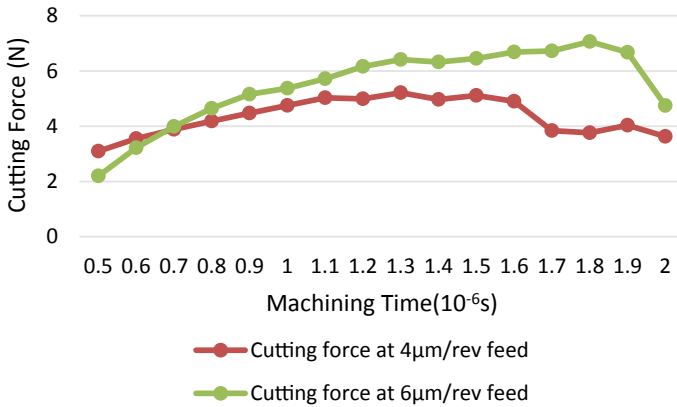
Fig. 40.8   Cutting force during machining
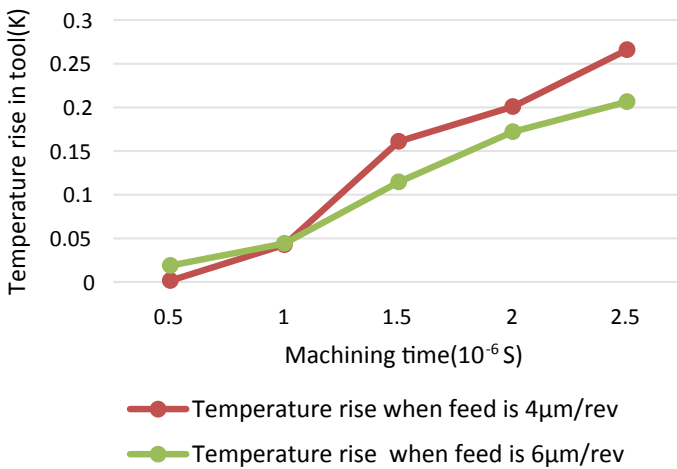
Fig. 40.9   Temperature rise in tool

is done by comparing experiment force data with FEM model data value. It was found that model accuracy is around 85%.

References

1. Chawla, N., Chawla, K.K.: Metal Matrix Composites. Springer, New York, NY (2013)
2. Dandekar, C.R., Shin, Y.C.: Modeling of machining of composite materials: a review. Int. J. Mach. Tools Manuf **57**, 102–121 (2012). https://doi.org/10.1016/j.ijmachtools.2012.01.006
3. Liu, J., Li, J., Xu, C.: Interaction of the cutting tools and the ceramic-reinforced metal matrix composites during micro-machining: a review. CIRP J. Manuf. Sci. Technol. **7**, 55–70 (2014).

https://doi.org/10.1016/j.cirpj.2014.01.003

4. Cao, G., Konishi, H., Li, X.: Mechanical properties and microstructure of Mg/SiC nanocomposites fabricated by ultrasonic cavitation based nanomanufacturing. J. Manuf. Sci. Eng. **130**, 031105 (2008). https://doi.org/10.1115/1.2823086

5. Ding, X., Liew, W.Y.H., Liu, X.D.: Evaluation of machining performance of MMC with PCBN and PCD tools. Wear **259**, 1225–1234 (2005). https://doi.org/10.1016/j.wear.2005.02.094

6. Muthukrishnan, N., Murugan, M., Rao, K.P.: An investigation on the machinability of Al-SiC metal matrix composites using pcd inserts. Int. J. Adv. Manuf. Technol. **38**, 447–454 (2008). https://doi.org/10.1007/s00170-007-1111-z

7. Manna, A., Bhattacharayya, B.: A study on machinability of Al/SiC-MMC. J. Mater. Process. Technol. **140**, 711–716 (2003). https://doi.org/10.1016/S0924-0136(03)00905-1

8. Liu, K., Melkote, S.N.: Effect of plastic side flow on surface roughness in micro-turning process. Int. J. Mach. Tools Manuf **46**, 1778–1785 (2006). https://doi.org/10.1016/j.ijmachtools.2005.11.014

9. Tomac, N., Tannessen, K., Rasch, F.O.: Machinability of particulate aluminium matrix composites. CIRP Ann.—Manuf. Technol. **41**, 55–58 (1992). https://doi.org/10.1016/S0007-8506(07)61151-2

10. El-Gallab, M., Sklad, M.: Machining of Al/SiC particulate metal-matrix composites: part I: tool performance. J. Mater. Process. Technol. **83**, 151–158 (1998)

11. Andrewes, C.J.E., Feng, H.Y., Lau, W.M.: Machining of an aluminum/SiC composite using diamond inserts. J. Mater. Process. Technol. **102**, 25–29 (2000). https://doi.org/10.1016/S0924-0136(00)00425-8

12. Zhou, L., Huang, S.T., Wang, D., Yu, X.L.: Finite element and experimental studies of the cutting process of SiCp/Al composites with PCD tools. Int. J. Adv. Manuf. Technol. **52**, 619–626 (2011). https://doi.org/10.1007/s00170-010-2776-2

13. Pramanik, A., Zhang, L.C., Arsecularatne, J.A.: An FEM investigation into the behavior of metal matrix composites: tool-particle interaction during orthogonal cutting. Int. J. Mach. Tools Manuf **47**, 1497–1506 (2007). https://doi.org/10.1016/j.ijmachtools.2006.12.004

14. Ghandehariun, A., Kishawy, H.A., Umer, U., Hussein, H.M.: On tool–workpiece interactions during machining metal matrix composites: investigation of the effect of cutting speed. Int. J. Adv. Manuf. Technol. **84**, 2423–2435 (2016). https://doi.org/10.1007/s00170-015-7869-5

15. Teng, X., Huo, D., Chen, W., Wong, E., Zheng, L., Shyha, I.: Finite element modelling on cutting mechanism of nano Mg/SiC metal matrix composites considering cutting edge radius. J. Manuf. Process. **32**, 116–126 (2018). https://doi.org/10.1016/j.jmapro.2018.02.006

Chapter 41
Implementation of Yield Criteria in ABAQUS for Simulations of Deep Drawing: A Review and Preliminary Results

Check for updates

Arpit Tripathi, R. Ganesh Narayanan, and Uday S. Dixit

Abstract In the present work, two yield functions, von Mises and Hill's 1948, are implemented in ABAQUS via UMAT/VUMAT subroutine for deep drawing simulations. The thickness strain distribution during cup deep drawing is predicted and validated with results from ABAQUS simulation with existing yield functions, and existing experiments. The influence of rolling direction and material properties is also studied. It is observed that predictions from von Mises and Hill's 1948 yield functions agree reasonably well. However, in a direction perpendicular to rolling direction, the error is large indicating the requirement for a better yield criterion for the anisotropic case. The sensitivity of thickness strain distribution with rolling direction, initial sheet thickness, die corner radius, and material properties highlight the importance of anisotropic yield function.

Keywords Sheet forming · Plasticity · Deep drawing · Modelling · Yield function

41.1 Introduction

A yield function is used to define a constitutive model of the material to simulate any forming process. Different yield criteria are used for different engineering applications. Hence, choosing the most appropriate yield criterion is an important task in the modeling of any forming process [1]. The constitutive material model should have the ability to explain relevant phenomenon, e.g., Bauschinger effect, anisotropic yielding and strain hardening [2]. Deep drawing is a sheet metal forming process,

---

A. Tripathi—Deceased on April 26, 2019.

Dedication. This article is dedicated to the sweet memory of first author Mr. Arpit Tripathi who left us for his heavenly abode on April 26, 2019.

A. Tripathi · R. Ganesh Narayanan (✉) · U. S. Dixit
Department of Mechanical Engineering, Indian Institute of Technology Guwahati, Guwahati, Assam 781039, India
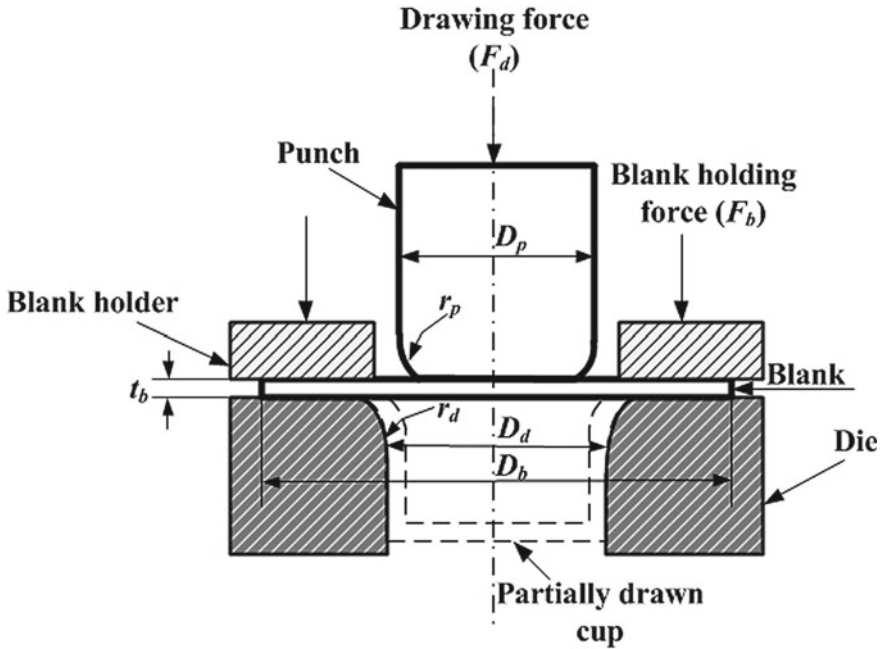e-mail: ganu@iitg.ac.in

Fig. 41.1 Deep drawing process and parameters

in which a blank placed on a die with a cavity is drawn into the required shape with
the help of a punch. The process is used to manufacture products like beverage cans,
pressure vessels, automobile panels, etc. The punch has corner radius r_p and diameter D_p exerting a drawing force F_d on a circular blank having initial diameter D_b
and thickness t_b (Fig. 41.1). The die has a corner radius r_d. The blank holder exerts
a blank holding force F_b on the flange region. To avoid sheet shearing, a clearance
of 10% more than the initial sheet thickness is generally used [3]. The blank material properties, its thickness, clearance between die cavity and punch wall, blank
holding force, die and punch corner radius, blank diameter to punch diameter ratio
and blank/tool interface friction conditions affect the deep drawing behavior in a
synergistic manner.

This article mainly presents a tutorial on the implementation of various yield criteria in the simulation of deep drawing process using ABAQUS, a commercially available finite element method (FEM) package. An extensive review is provided in the
area of modeling and simulation of the deep drawing process. After that, some preliminary results of deep drawing simulation using ABAQUS are presented. Only two criteria—von Mises and Hill's 1948 are implemented. However, the described methodology is quite general and similar procedure may be followed for the implementation
of other yield criteria.

41.2 Literature Review

In the past, different yield criteria were implemented to describe the forming behavior of the selected material. Tresca and von Mises yield functions are the oldest yield functions used for the isotropic materials [4]. In 1948, Hill proposed a quadratic anisotropic yield function, which is basically a generalization of von Mises yield function [5]. However, it shows anomalous behavior in the case of some aluminum alloys and steel sheets as pointed out by Woodthorpe and Pearce [6]. There are several anisotropic yield functions proposed since 1948 as described elsewhere [7, 8]. The experimental studies in the last several decades show that the previously defined material models are unable to predict forming behavior accurately. Rigorous experiments are required to determine the material coefficients to describe the anisotropic behavior of the material.

A detailed review of such yield functions and research aspects are described here. Vrh et al. implemented BBC2008 yield criterion, which is considered as a plane stress orthotropic yield criterion for prediction of earing phenomenon in deep drawing process using VUMAT subroutine in ABAQUS/Explicit [9, 10]. VUMAT is a user subroutine in ABAQUS/Explicit which allows users to input user-defined material by implementing the constitutive equations governing the material behavior. Materials used were AA2090 and AA5042 for testing the constitutive model. NICE scheme was used to integrate the implemented constitutive model. It is an explicit numerical scheme for efficient integration, primarily developed for solving boundary value problems using direct solution methods. It is helpful for solving non-linear constitutive equations and combines the simplicity of Forward–Euler scheme with accuracy of backward Euler scheme. Uniaxial and biaxial tensile tests were conducted to determine all the parameters of the yield function. They were determined with the help of R-values and yield stress values found from experiments. R-values, also known as Lankford values or plastic strain ratio, give a measure of plastic anisotropy in sheet metal. One of the major defects that arise due to anisotropy during deep drawing is earing, which results in the edges of the cup formed to be wavy in nature. Earing phenomena in deep drawing of AA5042-H2 were compared with the experimental results and predicted using YLD2000-2D and CPB06ex2 yield criteria [11]. Simulations using CPB06ex2 yield function predicted eight ears as observed in experiments. In another attempt, the earing profiles were compared with predictions from YLD2004-13p and Yld2004-18p yield functions [12]. The results indicate the efficacy of Yld2004-18p as it can predict at least six ears during cup deep drawing and needs 18 parameters to be evaluated as compared to YLD2004-13p.

Moreira et al. implemented Ferron's plane stress orthotropic yield criterion in ABAQUS software with the help of VUMAT subroutine [13]. Cylindrical deep drawing experiments were conducted on interstitial free steel and on tinplate steel. Thickness strain distribution and earing phenomena from simulation results were compared with experimental findings. The results were compared between Hill's 1948 model and Ferron's model. The results show the efficacy of Ferron's model in describing the anisotropic characteristics.

Guner et al. [14], in their work, implemented Yld2000-2d yield criterion [15] in ABAQUS Explicit with the help of VUMAT subroutine and performed FE simulation of deep drawing of AA6016-T4. Equibiaxial tests and tensile tests were performed for determining the material model parameters. Hill's 1948 yield function predicted a lower (about 12%) thickness in the cup corners as compared to experiments. Thickness strain distributions obtained by implementing Yld2000-2d yield criterion were in good agreement with experimental data.

Laurent et al. [16] compared the effects of Hill's 1948, von Mises and Barlat'91 [17] yield criteria combined with isotropic and kinematic hardening models implemented in ABAQUS during spring back evaluation by split-ring test. These models were implemented as user-defined UMAT subroutine. Measurement of released residual stresses and spring back was done by measuring the change in the ring's diameter during the experiment. Thickness strain distributions obtained from Hill's model with isotropic hardening were slightly more than those of experimental findings. In addition, they were higher than those predicted by the other two yield criteria. It was concluded that Barlat'91 yield criterion combined with kinematic hardening was in good agreement with experimental findings. Eggertsen et al. [18] implemented Hill'48 yield criterion and Banabaic/Aretz eight parameter model (BBC2005), which is an extension of Barlat-Lian Yld89 yield function, combined with isotropic and mixed hardening law. A variety of steel grades is used for testing. BBC2005 yield function delivered accurate results in all the rolling direction, while other yield functions show accurate results only when the loading direction coincides with rolling direction.

Soare et al. [19] implemented plane stress orthotropic yield criterion in ABAQUS FE code. They have considered this criterion as homogenous polynomials of fourth, sixth and eighth orders called Poly4, Poly6, and Poly8, respectively. AA2090-T3 and AA2008-T4 were used as materials in their study. FE simulations of the deep drawing were performed. Poly4 is recommended only during the description of mild anisotropic properties. For strong anisotropic properties in yielding, like in the case of AA2090-T3, Poly6 and Poly8 are recommended. Hong and Yoon [20] implemented Yld2004-18p and Yld2000-2d yield criteria in LS-DYNA FE code. They predicted earing during cup drawing and spring back of an automotive component made of AA5182-O. FE simulations showed good agreement with experimental spring back data and Yld2000-2d showed excellent computational efficiency. Aretz et al. [21] implemented a new plane stress yield function exhibiting anisotropy and having eight parameters meant for orthotropic materials. In their study, the materials used were AA6111-T4, AA2090-T3, and low carbon steel. Yld2003-8p was as flexible as Yld2000-2d criterion and has simplified mathematical form providing good computational efficiency.

Xu et al. [22] implemented Yld2004-18p [23], Yld2000-2d, Hill's 48, and Karafillis and Boyce 1993 yield criteria [24] in ABAQUS software. AISI430 and AISI409L stainless steels were used as test materials. It was concluded that Yld2000-2d and Yld2004-18p models were in good agreement with experimental findings of flow stresses and R-values, while it is not so when Karafillis and Boyce (1993) yield criterion and Hill's 48 models were used.

Banabic et al. [25] proposed a new plane stress orthotropic yield criterion, which combines the merits of Barlat and Lian, and Karafillis and Boyce criteria. A method called "error function minimization" was used to determine the seven material coefficients of the proposed yield criteria. In their study, R-values and uniaxial yield stresses along the rolling direction were obtained. Yield loci obtained from finite element simulations for AA6xxx-T4 and SPCE sheets were in good agreement with the available experimental results [26, 27].

Mattiaasson et al. [28] proposed a MS-6p yield criterion with six parameters. It was developed as a special case of BBC2000 and Yld2000 criteria for improving computational efficiency. Also, BBC2000 [29], Yld2000 [30], and Yld89 [31] were used to predict the anisotropic behavior of metal sheets of AA2090-T3 and DC06 mild steel sheets. "Error minimization method" and Newton–Raphson method were used to find out the material coefficients. Main results and conclusions drawn from their work are as follows:

(1) Yld89 criterion fits poorly in equibiaxial region of the yield locus.
(2) MS-6p criterion fits well for the materials having moderate in-plane anisotropy.

Moreover, it was recommended that it is good to use Yld2000 and BBC2000 with eight parameters for materials having strong anisotropy.

Wu et al. [32] proposed a hardening rule, which extends the concept of isotropic and kinematic hardening to Hill's 1948 criterion. The proposed model was in good agreement with the experimental findings of AA7108-T1 and AA6061-O aluminum alloys. Dasappa et al. [33] had done a comparison between Hill's (1948, 1990, 1993) [5, 34, 35], Barlat-Lian (1989) [31] and CPB06 [36] criteria to predict the Forming Limit Diagram (FLD) for AA5754 aluminum alloy sheet. FLD was predicted by Marciniak–Kuczinsky method [37]. The yield criteria implemented correctly predicted the variation of R-values and yield stress except for CPB06. Barlat-Lian criterion under predicted the limit strains in biaxial stretching zone, whereas Hill's 48 yield criterion accurately predicted the limit strains. CPB06 yield criterion has shown resemblance with Hill'93 criterion in predicting the desired forming behavior.

Hu et al. [1] proposed a three-yield-system hypothesis and applied it on AA2090-T3, AA3104-H19, and AA5182-O sheets. An anisotropic yield function was proposed using such a hypothesis and implemented in finite element program. The proposed model showed good agreement in predicting yield stress and plastic strain ratio as compared to experimental data. It is worth noting that in the theory proposed by Choi et al. [38], the hardening model includes yield surface growth (isotropic hardening), translation in stress space (kinematic hardening) and yield surface rotation (rotation of anisotropic axes). Such a model would be useful in evaluating material behavior under the multi-path loading conditions.

The present work aims to implement the chosen yield functions in ABAQUS/CAE for the prediction of deep drawing behavior. As per current status, von Mises and Hill's 1948 yield functions are implemented via UMAT/VUMAT subroutine in ABAQUS. The results from finite element simulation after implementation are compared with already existing yield models in ABAQUS and with literature.

41.3   FE Simulation of Circular Deep Drawing

In the present study, the FE simulation of deep drawing of AA2090-T3 sheet was carried out in ABAQUS/CAE 6.13. The results obtained from ABAQUS/CAE simulations were compared with those obtained by implementing UMAT or VUMAT subroutine. Thickness strain distribution in the deformed cup was taken for comparison. Because of symmetry and less computational time for simulation, a quarter section of cup deep drawing was modeled and analyzed. Blank was taken as a deformable body, whereas blank holder, punch and die were modeled as rigid surfaces. The blank was meshed with C3D8R elements, which are linear brick elements (8 nodes) with reduced integration ability. The modeling set up had $D_b = 158.76$ mm; $t_b = 1.60$ mm; $D_p = 97.46$ mm; $r_p = 12.70$ mm; $D_d = 101.48$ mm; $r_d = 12.70$ mm. The material properties of AA2090-T3 were: density $(\rho) = 2.59$ g/cc; Young's modulus $(E) = 69$ GPa; Poisson's ratio $(\nu) = 0.33$; Yield stress $(\sigma_Y) = 279.16$ MPa; strain hardening law: $\sigma_{eq} = 646(0.025 + \varepsilon_{eq}^p)^{0.227}$. In addition, AA6022-T4 was used for analyzing the effect of different material properties. The material properties of AA6022-T4 were: density $(\rho) = 2.69$ g/cc; Young's modulus $(E) = 70$ GPa; Poisson's ratio $(\nu) = 0.33$; Yield stress $(\sigma_Y) = 162$ MPa. The strain hardening law was given by

$$\sigma_{eq} = 396 - 234 \exp\left(-6.745\varepsilon_{eq}^p\right). \tag{41.1}$$

Coulomb's coefficient of friction of 0.1 was used for all the interfaces. The friction at the sheet–die interface was modeled by Coulomb's law, while at sheet–punch interface, sticking friction was assumed. $F_b = 5.5$ kN was incorporated for maintaining the contact at sheet–die interface. The nodes at the sheet–punch interface may lose contact. It depends on the tensile or compressive nature of the punch reaction vector in z-direction at the node. Sticking friction conditions was assumed at the nodes at sheet–punch interface when they are in contact. This means incremental displacement vector's $(_t\Delta u)$ component in x and y-direction at the nodes becomes zero. Since the punch is moving in z-direction only, its component in z-direction will be equal to the incremental displacement of the punch (Δu^*). Now, if a node is not in contact, then all the components of the incremental stress vector $(_t\Delta s)$ will be zero at that node. In the x–y plane of symmetry, both incremental shear stress component vector $(_t\Delta t)$ were zero. Also, normal (z) component of displacement vector was zero. In the y–z plane of symmetry, both incremental shear stress component vector $(_t\Delta t)$ were zero. The normal (x) component of the displacement vector was also zero. The essential boundary conditions $(U1 = U2 = U3 = UR1 = UR2 = UR3 = 0)$ were applied to die and blank holder. The punch was allowed to translate in negative y-direction only.

41.4 Implementation of Yield Criteria in ABAQUS/CAE

The implementation of yield criteria was carried out with the help of a user material subroutine UMAT written in FORTRAN. The steps adopted in the implementation of von Mises model in ABAQUS/CAE are as follows:

- Initially, the material deformation was assumed to be in elastic state only.
- In the next step, the strain tensor was decomposed into its hydrostatic and deviatoric part.
- The elastic predictor was used to check yielding.
- The plastic corrector was used to obtain equivalent plastic strain using Newton–Raphson method. The plastic corrector was used to check for convergence of the solution.

Similarly, Hill's 48 yield criterion was implemented using semi-implicit backward Euler method. The important feature of this method is that it is implicit in plasticity parameter and explicit in plastic moduli and the plastic flow directions. This simply means that plasticity parameter increments were calculated at the end of the on-going step, whereas plastic moduli and the plastic flow direction were calculated at the beginning of the step.

41.5 Results and Discussions

Cylindrical deep drawing process was analyzed incorporating von Mises and Hill's 1948 yield functions with isotropic hardening. When using von Mises yield function, no ear formation is observed in the final drawn component, while ear formation is seen when Hill's 1948 yield function was used (Fig. 41.2).

The thickness strain distribution along the radial direction in the deformed cup from centre to radially outermost point has been predicted. The material is made of
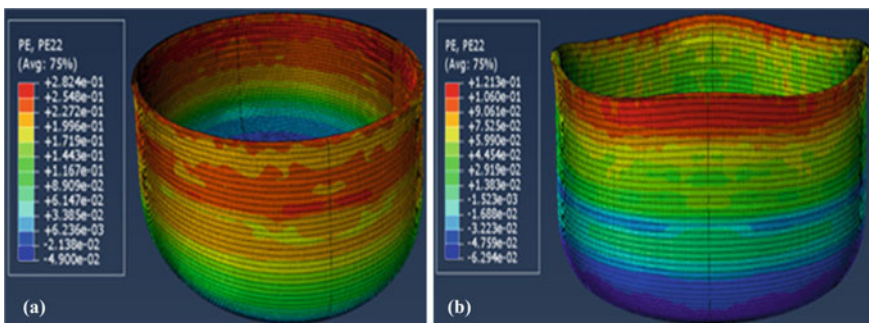

Fig. 41.2 Final deep drawn cup from FE simulation using: **a** von Mises yield function and **b** Hill's 1948 yield function

AA2090-T3. Figure 41.3 shows that there is no difference in thickness strain distribution along 0°, 45° and 90° to rolling direction when isotropic material is considered. Considering the material isotropy, the thickness strain distributions obtained from standard ABAQUS simulation, UMAT subroutine implementation, and experiments are compared in Fig. 41.4. The experiment results are taken from Yoon et al. [39]. The thickness strain distributions from ABAQUS simulation and UMAT subroutine implementation are found to match well with the experimental results. The thickness strain distribution of AA2090-T3 using Hill's 1948 yield criterion was also predicted along 0°, 45° and 90° to rolling direction (Fig. 41.5). The predicted behavior agrees well with experimental results available in [39], and larger thinning is found in the case of 45° to the rolling direction.
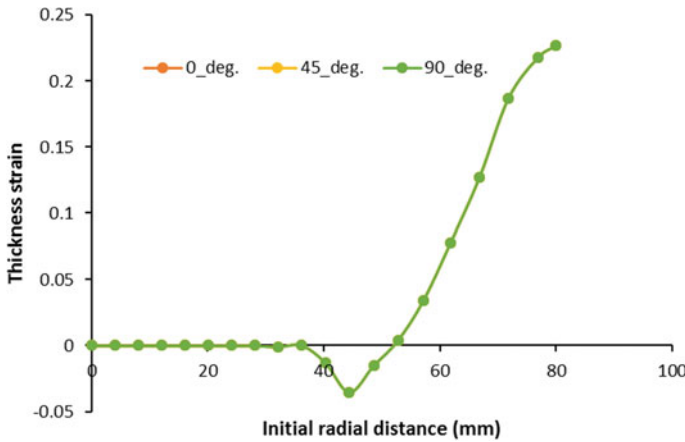

Fig. 41.3 Thickness strain distributions along 0°, 45°, and 90° to rolling directions (considering isotropic material)
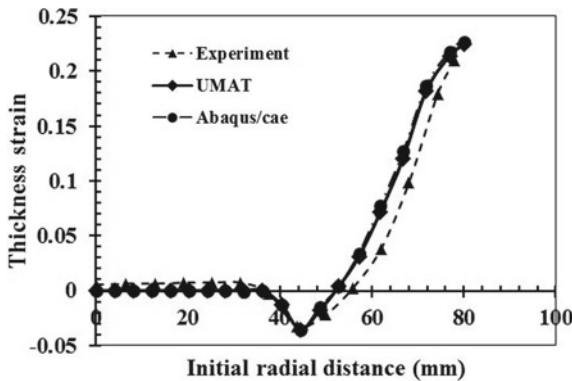

Fig. 41.4 Thickness strain distributions from ABAQUS/CAE, UMAT, and experiments, considering isotropic material (experimental data from [39])
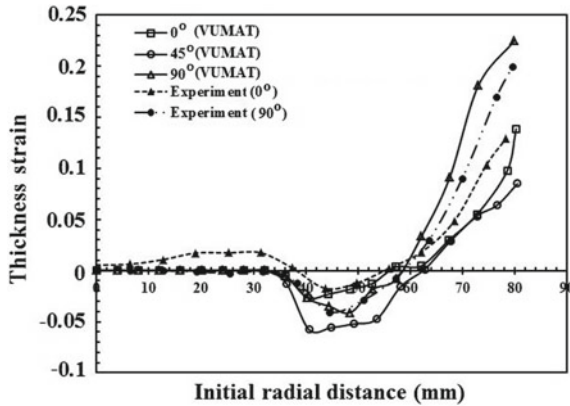
Fig. 41.5 Thickness strain distributions along 0°, 45°, and 90° to rolling directions, considering anisotropic material (experimental data from [39])

The effect of die corner radius r_d was predicted by varying it at three intervals, 10, 12.7, and 16 mm. Figure 41.6 shows the thickness strain variation along 45° direction for three different die profile radii obtained from ABAQUS simulations. It is observed that the maximum thickness strain decreases with the increase in die profile radius, which agrees well with the general understanding. Now, for the case of $r_d = 12.7$, the comparison is done between the results obtained from ABAQUS/CAE simulation and simulation using VUMAT subroutine (Fig. 41.7). Thickness distribution from both the methods agrees well with minor difference in the cup corner location. Figure 41.8 depicts the effect of change in initial sheet thickness on the thickness strain distribution during cup deep drawing. The curves match well throughout the radial distance, except at the cup corner, with larger thickness sheet showing larger thinning. For 1.6 mm initial sheet thickness, thickness strain distribution from ABAQUS/CAE
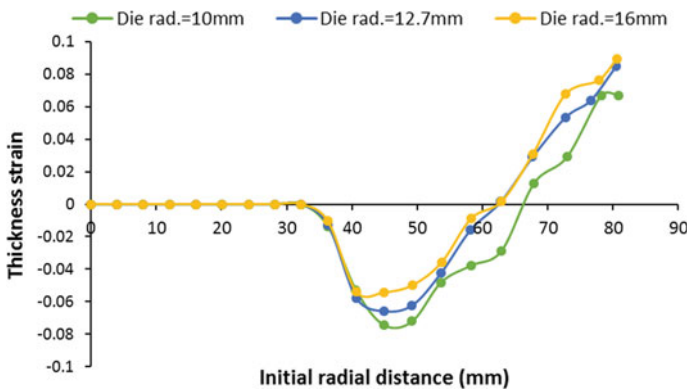
Fig. 41.6 Thickness strain distribution along 45° rolling direction at different die corner radii
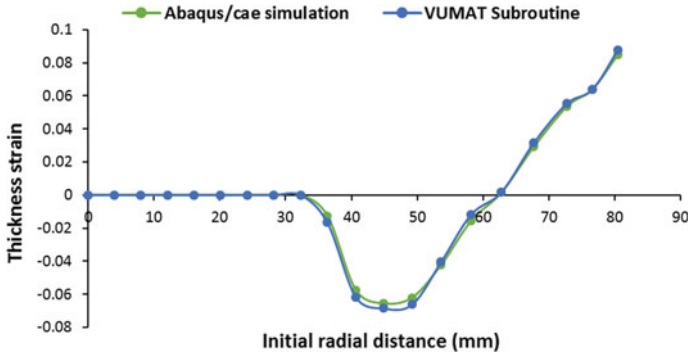
Fig. 41.7 Thickness strain distribution obtained from ABAQUS/CAE and VUMAT subroutine at $r_d = 12.7$ mm
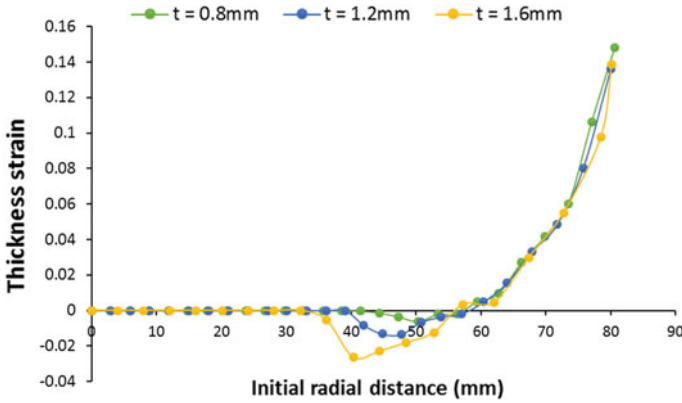
Fig. 41.8 Thickness strain distribution along 0° direction for different sheet thicknesses

simulation and simulation using VUMAT subroutine (along the rolling direction) was compared (Fig. 41.9), and both the curves match well. In addition, the effect of material properties on the thickness strain distribution was also obtained from ABAQUS simulations for AA6022-T4 sheet as shown in Fig. 41.10. AA6022-T4 shows larger thinning as compared to AA2090-T3, though the difference is not appreciable. Similar results are observed when VUMAT subroutine is implemented (Fig. 41.11).
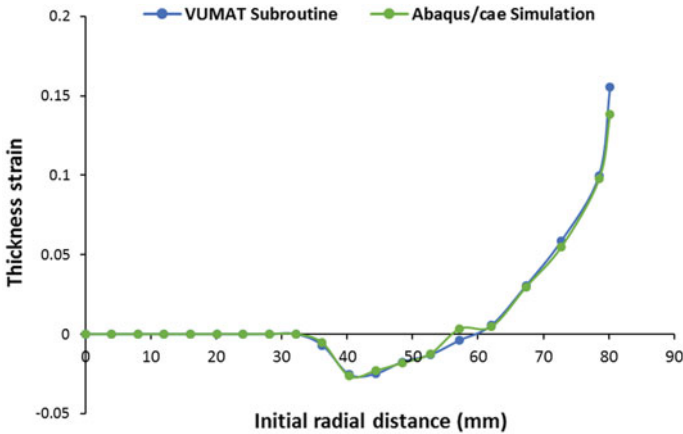
Fig. 41.9 Comparison between thickness strain distribution obtained from ABAQUS/CAE and VUMAT subroutine ($t = 1.6$ mm)
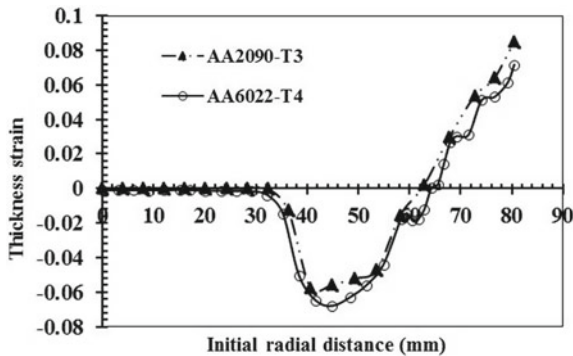
Fig. 41.10 Thickness strain distribution along 45° direction for AA2090-T3 and AA6022-T4 sheets from ABAQUS simulations

41.6   Conclusions

In the present work, two different yield functions were considered to simulate the cup deep drawing in ABAQUS/CAE. Hill's 48 and von Mises yield criteria were implemented in ABAQUS via UMAT/VUMAT subroutine. Thickness strain distributions were predicted and compared with existing results. The effect of rolling direction, die corner radius, initial sheet thickness, and material properties are also predicted. Results from ABAQUS simulation and from simulations after implementing the subroutines are compared. The following conclusions are drawn:
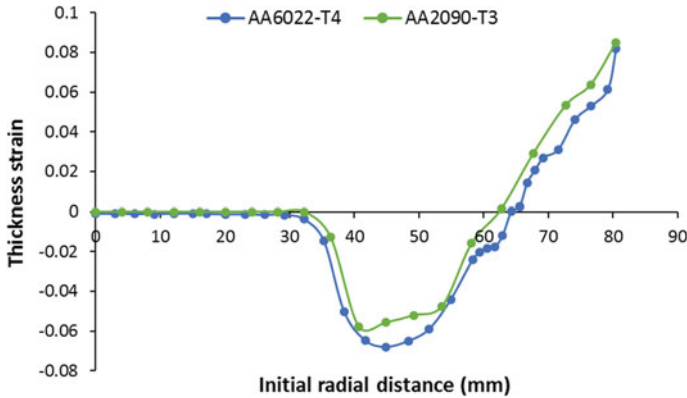
Fig. 41.11 Thickness strain distribution along 45° direction for AA2090-T3 and AA6022-T4 sheets by implementing VUMAT subroutine

(1) While performing isotropic analysis, no ear formation was observed in the final deformed configuration and the thickness strain distribution was exactly the same in all the rolling directions.

(2) While performing anisotropic analysis, ear formation was clearly observed in the final deformed configuration. In addition, thickness strain distributions were different for different directions, i.e., for 0°, 45°, and 90° directions.

(3) While comparing the results of thickness strain distribution obtained from user material subroutines and ABAQUS simulation, experimental results were nicely matching with the subroutine results.

(4) The maximum thickness strain decreases with the increase in the die profile radius and increases with an increase in sheet thickness.

(5) AA6022-T4 showed larger thinning as compared to AA2090-T3 showing the effect of material properties.

(6) Results from ABAQUS simulation and from simulation after implementing sub-routines match well when material properties, die corner radius, and initial sheet thickness are changed. Overall, the present work has ascertained the capability of VUMAT in ABAQUS for implementing the appropriate yield function for sheet forming simulations.

References[1]

1. Hu, W.: An orthotropic yield criterion in a 3-D general stress state. Int. J. Plasticity. **21**, 1771–1796 (2005)

---

[1]Note: Additional data can be provided on demand

2. Taherizadeh, A., Green, D.E., Ghaei, A., Yoon, J.W.: A non-associated constitutive model with mixed iso-kinematic hardening for finite element simulation of sheet metal forming. Int. J. Plasticity. **26**, 288–309 (2010)

3. Groover, M.P.: Fundamentals of Modern Manufacturing: Materials, Processes, and Systems, 3rd edn. Wiley (2007)

4. Kachanov, L.M.: Fundamentals of the Theory of Plasticity. Dover Publications. (2004)

5. Hill, R.: A theory of the yielding and plastic flow of anisotropic metals. Proc. R. Soc. Lond. **193**, 281–297 (1948)

6. Woodthorpe, J., Pearce, R.: The anomalous behaviour of aluminium sheet under balanced biaxial tension. Int. J. Mech. Sci. **12**, 341–347 (1970)

7. Dixit, P.M., Dixit, U.S.: Modeling of Metal Forming and Machining Processes-by Finite Element and Soft Computing Methods. Springer, London (2008)

8. Banabic, D.: Sheet Metal Forming Processes Constitutive Modeling and Numerical Simulation. Springer, Berlin, Heidelberg (2010)

9. Vrh, M., Halilovi, M., Starman, B., Štok, B., Comsa, D.S., Banabic, D.: Earing prediction in cup drawing using the BBC2008 yield criterion. In: The 8th International Conference and Workshop on Numerical Simulation of 3D Sheet Metal Forming Processes. AIP Conference Proceedings 1383, 142–149 (2011)

10. Barlat, F., Maeda, Y., Chung, K.: Yield function development for aluminum alloy sheets. J. Mech. Phys. Solids **45**, 1727–1763 (1997)

11. Butuc, M.C., Banabic, D., Barata, D.R.A., et al.: The performance of Yld96 and BBC2000 yield functions in forming limit prediction. J. Mater. Process. Technol. **125**, 281–286 (2002)

12. Banabic D., Comsa D.S., Balan T.: A new yield criterion for orthotropic sheet metals under plane-stress condition. In: Proceedings of the Cold Metal Forming Conference. Cluj-Napoca, p. 217 (2000)

13. Moreira, L.P., Ferron, G., Ferran, G.: Experimental and numerical analysis of the cup drawing test for orthotropic metal sheets. J. Mater. Process. Technol. **108**, 78–86 (2000)

14. Guner, A., Soyarslan, C., Brosius, A., Tekkaya, A.E.: Characterization of anisotropy of sheet metals employing inhomogeneous strain fields for Yld 2000–2D yield function. Int. J. Solids and Structures **49**, 3517–3527 (2012)

15. Banabic, D., Kuwabara, T., Balan, T., Comsa, D.S., Julean, D.: Non-quadratic yield criterion for orthotropic sheet metals under plane-stress conditions. Int. J. Mech. Sci. **45**, 797–811 (2003)

16. Laurent, H., Greze, R., Manach, P.Y., Thuillier, S.: Influence of constitutive model in springback prediction using the split-ring test. Int. J. Mech. Sci. **51**, 233–245 (2009)

17. Barlat, F., Lege, D.J., Brem, J.C.: A six-component yield function for anisotropic materials. Int. J. Plasticity **7**, 693–712 (1991)

18. Eggertsen, P.A., Mattiasson, K.: On constitutive modeling for springback analysis. Int. J. Mech. Sci. **52**, 804–818 (2010)

19. Soare, S., Yoon, J.W., Cazacu, O.: On the use of homogeneous polynomials to develop anisotropic yield functions with applications to sheet forming. Int. J. Plasticity **24**, 915–944 (2008)

20. Yoon, J.W., Hong, S.H.: Modeling of aluminum alloy sheets based on new anisotropic yield function. J. Mater. Process. Technol. **177**, 134–137 (2006)

21. Aretz, H.: A non-quadratic plane stress yield function for orthotropic sheet metals. J. Mater. Process. Technol. **168**, 1–9 (2005)

22. Xu, L., Barlat, F., Ahn, D.C.: Constitutive modelling of ferritic stainless steel sheets. Int. J. Mater. Form. 2, Springer/ESAFORM (2009)

23. Barlat, F., Aretz, H., Yoon, J.W., Karabin, M.E., Brem, J.C., Dick, R.E.: Linear transformation based anisotropic yield functions. Int. J. Plasticity **21**, 1009–1039 (2005)

24. Karafillis, A.P., Boyce, M.C.: A general anisotropic yield criterion using bounds and a transformation weighting tensor. J. Mech. Phys. Solids **41**, 1859–1886 (1993)

25. Banabic, D., Kuwabara, T., Balan, T., Comsa, D.S.: An anisotropic yield criterion for sheet metals. J. Mater. Process. Technol. **157**, 462–465 (2004)

26. Kuwabara, T., Ikeda, S., Kuroda, K.: Measurement and analysis of differential work hardening in cold-rolled steel sheet under biaxial tension. J. Mater. Process. Technol. **80**(8), 517–523 (1998)
27. Kuwabara, T., Bael, A.V.: Measurement and analysis of yield locus of sheet aluminum alloy 6XXX. In: Proceedings of the Fourth International Conference and Workshop on Numerical Simulation of 3D Sheet Forming Processes, Besanc, pp. 85–90 (1999)
28. Mattiasson, K., Sigvant, M.: An evaluation of some recent yield criteria for industrial simulations of sheet forming processes. Int. J. Mech. Sci. **50**, 774–787 (2008)
29. Barlat, F., Yoon, J.W., Cazacu, O.: On linear transformations of stress tensors for the description of plastic anisotropy. Int. J. Plasticity **23**, 876–896 (2007)
30. Barlat, F., Brem, J.C., Yoon, J.W., Chung, K., Dick, R.E., Choi, S.H., Pourboghrat, F., Chu, E., Lege, D.J.: Plane stress yield function for aluminum alloy sheets. Int. J. Plasticity **19**, 1297–1319 (2003)
31. Barlat, F., Lian, J.: Plastic behavior and stretchability of sheet metals, part I: a yield function for orthotropic sheets under plane stress conditions. Int. J. Plasticity **5**, 51–66 (1989)
32. Wu, H.C.: Anisotropic plasticity for sheet metals using the concept of combined isotropic-kinematic. Int. J. Plasticity. **18**, 1661–1682 (2002)
33. Dasappa, P., Inal, K., Mishra, R.: The effects of anisotropic yield functions and their material parameters on prediction of forming limit diagrams. Int. J. Solids and Structures **49**, 3528–3550 (2012)
34. Hill, R.: Constitutive modelling of orthotropic plasticity in sheet metals. J. Mech. Phys. Solids **38**, 405–417 (1990)
35. Hill, R.: A user-friendly theory of orthotropic plasticity in sheet metals. Int. J. Mech. Sci. **35**, 19–25 (1993)
36. Plunkett, B., Cazacu, O., Barlat, F.: Orthotropic yield criteria for description of the anisotropy in tension and compression of sheet metals. Int. J. Plasticity **24**, 847–866 (2008)
37. Marciniak, Z., Kuczynski, K.: Limit strains in the processes of stretch-forming sheet metal. Int. J. Mech. Sci. **9**, 609–620 (1967)
38. Choi, Y.: Modeling evolution of anisotropy and hardening for sheet metals. Ph.D. thesis. The Ohio State University (2003)
39. Yoon, J.W., Barlat, F., Chung, K., Pourboghrat, F., Yang, D.Y.: Earing predictions based on asymmetric nonquadratic yield function. Int. J. Plast **9**, 1075–1104 (2000)

Chapter 42
Multiphysics Simulation of ECM for the Machining of Al-SiC Composites

S. Venu, K. V. J. Bhargav, and P. S. Balaji

Abstract Al–Si composite is one of the widely used MMC in various application. It has some specific properties like high thermal conductivity and high strength-to-weight ratio which tend to use it in some high-end applications like microelectronics, aerospace, automobile, etc. In spite of its exceptional properties, Al-SiC is also one of the difficult composites to machine. So, machining of Al-SiC composite with a conventional process would face challenges. Unconventional process like electrochemical machining process offers a better alternative in generating accurate complex geometries in difficult to machine material. By varying the parameters of ECM process, the material removal of Al-SiC can be varied. Further, the material removal from ECM process is also influenced by the composition of Al-SiC. In this paper, multiphysics models have been developed in COMSOL to characterize the electrochemical process to study the material removal of Al-SiC. The parametric study is also performed to study the influence of machining parameters on material removal. This work can provide details on the ECM process for the machining of Al-SiC.

42.1 Introduction

42.1.1 Electrochemical Machining Process

The electrochemical machining process is an unconventional machining process. Faraday in 1833 has invented the principles of this process. The first controlled ECM

S. Venu (✉) · K. V. J. Bhargav · P. S. Balaji (✉)
Department of Mechanical Engineering, National Institute of Technology, Rourkela 769008, India
e-mail: mechvenu11@gmail.com

P. S. Balaji
e-mail: aerobala@gmail.com

is patented by Gussef in the year 1929 [1, 2]. The material removal in this process
is by the mechanism of anodic dissolution with high current density. The process
is carried out by passing a current through the electrolyte which is flowing through
the interelectrode gap. The process parameters are voltage (10–25 V), electrolyte
flow velocity (10–60 m/s) and interelectrode gap (0.01–0.6 mm) [3]. The theoretical
material removal rate is given by Faraday's law:

$$\frac{\Delta m}{\Delta t} = \frac{M \cdot I}{z \cdot F}$$

where $\frac{\Delta m}{\Delta t}$ is the material removal rate, M is the atomic weight, I is the current, z
is the valency of the dissolved metal and F is the Faraday constant. The material
removal rate can be controlled by varying the process parameters. Here, the tool is
considered as a cathode which is connected to negative potential, whereas workpiece
is connected with positive potential. Nature of the ECM process is non-contact type,
which results in the anodic profile prediction by modelling the process in COMSOL.
The dissolved material concentration and charge carriers within the machining gap
are affected by the electrolyte flow. During machining, fresh electrolyte needs to be
supplied steadily in the machining gap for dissolved material removal, to maintain
constant electrolyte conductivity and to ensure proper cooling (Fig. 42.1).
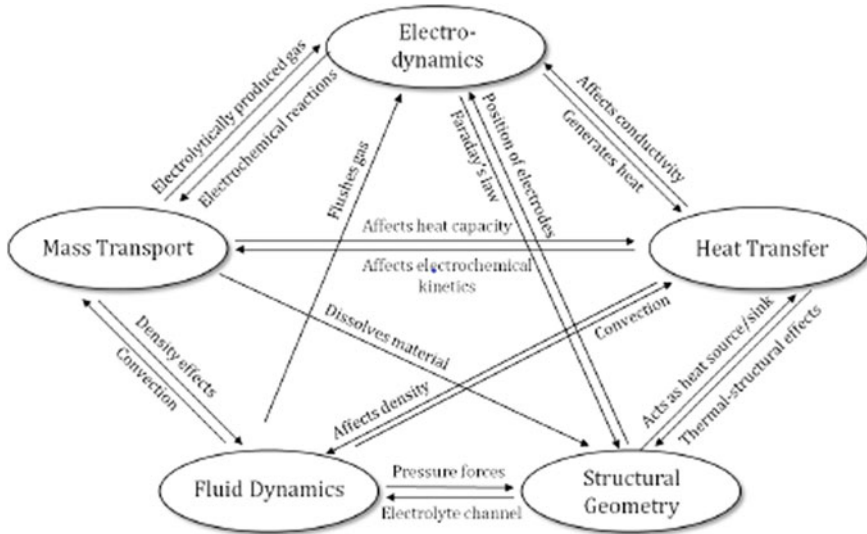
Fig. 42.1 Relevant physical phenomenon [4]

42.1.2   FEM

FEM simulation of the ECM process is carried out in COMSOL software, as the computing time is high. Proper geometric considerations and physical modules have to be taken into account for simulation. The principle procedure for FEM simulation of the ECM process is described in Fig. 42.2. A physical model equipped with multiphysical parameter is designed, meshing is done and then after calculation, the simulation gives the desired quantities. Computing time can be reduced by sequential simulation also.

COMSOL (known as FEMLAB) is a finite element analysis software package for solving partial differential equations (PDEs) for applications ranging from fluid dynamics, acoustics, structural mechanics and heat transfer to electrochemistry. Software flexibility allows the user to couple multiple PDEs using the single domain in addition to the adjoining model domain [6].
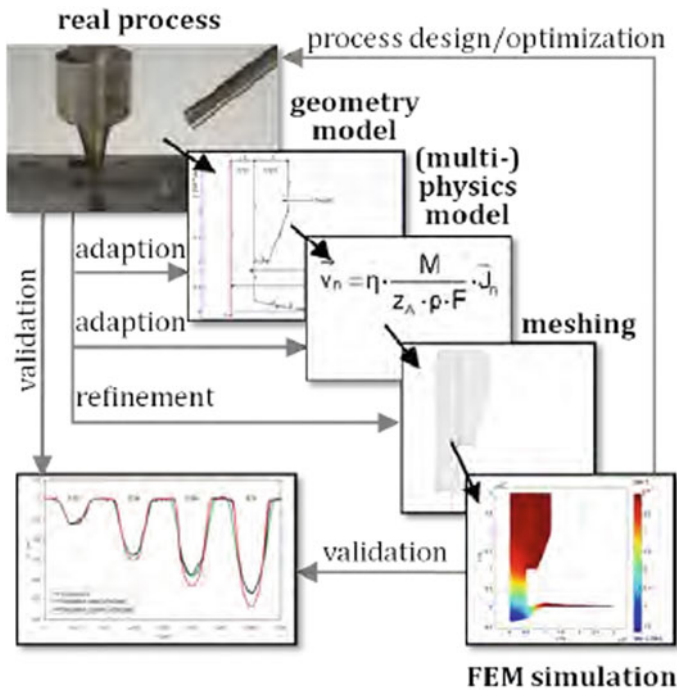
Fig. 42.2   Flow chart for FEM simulation of ECM process [5]

42.1.3 Importance of Al-SiC Composite

Material used in this simulation is Al-SiC composite with three different compositions. Aluminium-reinforced SiC has excellent thermo-physical properties such as high thermal conductivity, low coefficient of thermal expansion and enhanced mechanical properties, i.e. better wear resistance, high specific strength and improved specific modulus [7]. Because of these properties, Al-SiC has many potential applications:

- Packaging power devices—As aluminium has a high thermal expansion coefficient, it is used as heat sink or baseplate for attaching ceramic substrates. It acts as heat sinker or heat spreader, which increases the surface area for better heat removal by convection and conduction phenomenon [7].
- Aerospace industry—Most important application of Al-SiC is in the aerospace industry because of its high strength-to-weight ratio which is three times that of mild steel [8]. In addition to this, Al-SiC also has high modulus, wear resistance, less weight and high load-bearing capacity.
- Automobile industry—Al-SiC is used in making engine piston, engine cylinders, and brake pads because of its low thermal expansion coefficient, high thermal conductivity and improved properties at high temperature [9].
- Semiconductor equipment—It is used as a substrate in semiconductor because of its stability and high-dimensional accuracy when used practically [10].

42.2 Finite Elemental Modelling

42.2.1 Geometry

The geometry of the model consists of the workpiece (anode), insulation and tool (cathode) as shown in Fig. 42.3. Because of high metal conductivities and small potential gradients of the electrodes, the electrode domains are not included in the model. As the insulating layer is electrochemically inert, it is not included either. The electrolyte is the only modelled geometry in the simulation. The symmetrical geometry consists of four domains and those are an electrolyte, workpiece, cathode and insulation. The geometrical dimensions for modelling in COMSOL are shown in Fig. 42.3.

42.2.2 Al-SiC

Four multiphysics models were developed for four different studies as shown in Table 42.1. The material properties used are given in Table 42.2. In the first study,
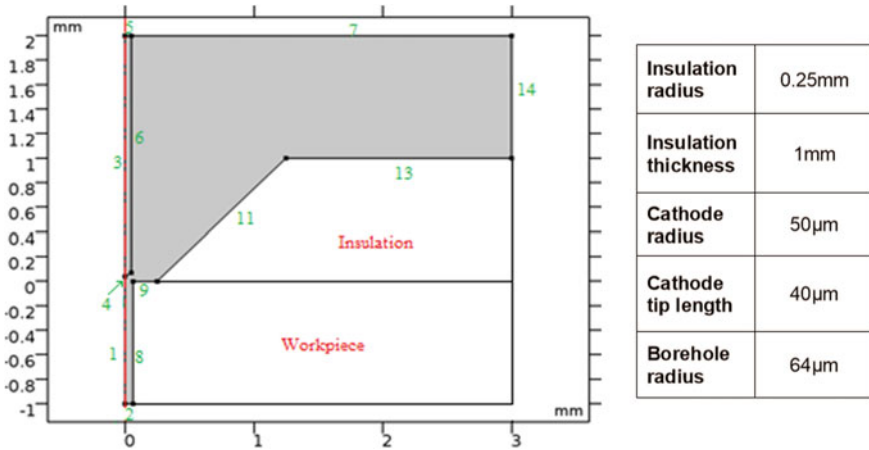
Fig. 42.3 ECM geometry 2D axial-symmetric

Table 42.1 Different parametric studies performed

	Input parameters		Output parameters		
	Variable	Constant	MR at each second		
Study 1	Composition	Voltage, electrolyte conductivity, interelectrode gap	MR_1	MR_2	MR_3
Study 2	Voltage	Composition, electrolyte conductivity, interelectrode gap	MR_1	MR_2	MR_3
Study 3	Interelectrode gap	Composition, electrolyte conductivity, voltage	MR_1	MR_2	MR_3
Study 4	Electrolyte conductivity	Voltage, composition, interelectrode gap	MR_1	MR_2	MR_3

Table 42.2 Material properties

Properties	Al	SiC
Molar mass (g/mol)	26.982	40.110
Molar density (g/cm^3)	2.70	3.21
No of participating electrons	3	6.5

three different compositions of Al-SiC were taken and the properties were found out using the rule of mixture given in Table 42.3. In other studies, the middle composition was taken. Using the rule of mixture, the physical properties of the materials have been found [11].

Applying rule of mixture for the first composite {Al(95%) + SiC(5%)}:

Table 42.3 Physical properties of the composition

Composition (%)		Molar mass (g/mol)	Molar density (g/cm³)	No. of participating electrons
Al	SiC			
95	5	27.638	2.730	3.175
90	10	28.294	2.751	3.350
85	15	28.951	2.777	3.525

- Molar mass$(M) = 0.95 \times 26.98 + 0.05 \times 40.11 = 27.638 \, \text{g/mol}$ (42.2)

- Molar density$(\rho) = 0.95 \times 2.7 + 0.05 \times 3.21 = 2.73 \, \text{g/cm}^3$ (42.3)

- No. of participating electrons $= 0.95 \times 3 + 0.05 \times 6.5 = 3.175$ (42.4)

The same procedure is followed to find the physical properties of other composites. The physical properties of the three different compositions considered in the studies are mentioned in Table 42.3.

42.2.3 Physics

The simulation of material removal was done in COMSOL Multiphysics by coupling the primary current distribution and deformed geometry. A time-dependent analysis was taken into account for the material removal. The electrolyte conductivity (sigma σ), molar mass (M), molar density (ρ) and no. of participating electrons (z) of the workpiece were given in the parameter section by assigning corresponding variables. These variables were called wherever they were required during the simulation. The boundary conditions considered for the simulation of the model shown in Fig. 42.2 have been tabulated in Table 42.4.

From Faraday's law, the relation between the volume of material removed and charge Q is given by [12]

$$V = \eta \cdot \frac{M}{\rho \cdot z \cdot F} \cdot Q \tag{42.5}$$

where η is the current efficiency, M is the molar mass, ρ is the mass denisity, z is the no. of participating electrons and F is Faraday's constant. The material removal also depends on the velocity vector in the normal direction $\overrightarrow{v_n}$ and the current density vector in the normal direction $\overrightarrow{j_n}$. The relation is given by [5]

$$\overrightarrow{v_n} = \frac{M}{\rho \cdot z \cdot F} \cdot \overrightarrow{j_n} \cdot \eta(J) \tag{42.6}$$

Table 42.4 Boundary conditions arrested in the model

Boundary	Definition
1	Axisymmetry
2	$\vec{n} \cdot \vec{j} = 0$
3	Axisymmetry
4	Continuity
5	$U_0 = 0\,\text{V}$
6	Continuity
7	$\vec{n} \cdot \vec{j} = 0$
8,9	$U_0 = 20\,\text{V}$
11–14	$\vec{n} \cdot \vec{j} = 0$

By implementing a condition for material removal,

$$\eta(J) = \begin{cases} 1 \text{ for } J > J \min \\ 0 \text{ for } J \leq J \min \end{cases} \tag{42.7}$$

From literature, $J_{\min}$ is considered to be 10 (A/cm^2) for optimum machining [13].

42.2.4 Meshing

Meshing is usually critical in the finite elements especially when diffusion at edges is involved is shown in Fig. 42.4. For lower computation times and accurate results, the effect of mesh refinements on electrode edges has been taken into account. The mesh
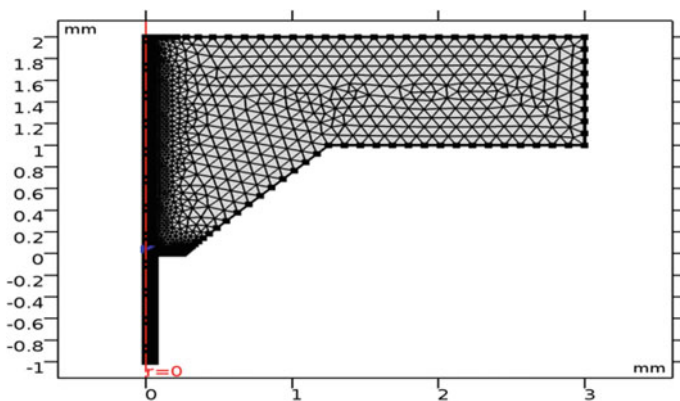

Fig. 42.4 Mesh for simulation

Table 42.5 Input parameters used in the study 1

Composition (%)		Voltage (V)	Electrolyte conductivity (S/m)	Interelectrode gap (mm)
Al	SiC			
95	5	14	7	0.04
90	10	14	7	0.04
85	15	14	7	0.04

used triangular element type, and number of elements are 5393. The above-mentioned element type supports re-meshing criteria.

42.3   Results and Discussion

The four different studies have been performed using COMSOL simulation for 3 s with a step size of 1 s to find material removal.

42.3.1   Study 1: Effect of Composition

In this study, three different compositions of Al-SiC have been varied by maintaining constant voltage, electrolyte conductivity and interelectrode gap to get material removal at each second of the simulation as shown in Table 42.5. The electrolyte used in this study is $NaNO_3$.

For the input parameters shown in Table 42.5, the material removal values at each second for three compositions were found and a plot between MR and time for each composite is shown in Fig. 42.5. It is observed that the MR is varying linearly in every composite and further the MR decreases with an increase in the composition of SiC.

42.3.2   Study 2: Effect of Voltage

In this study, three different voltages have been varied by maintaining constant composition, electrolyte conductivity and the interelectrode gap to get material removal at each second of the simulation as shown in Table 42.6. The electrolyte used in this study is $NaNO_3$.

For the input parameters shown in Table 42.6, the material removal values at each second for three different voltages were found and a plot between MR and time for
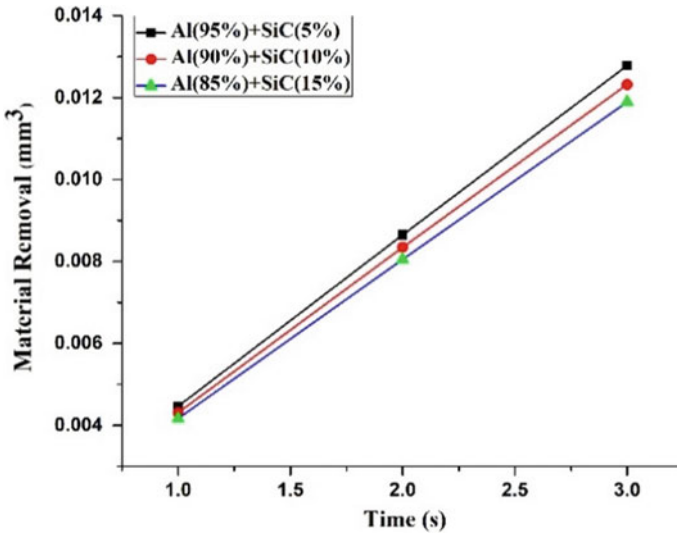
Fig. 42.5 Material removal for different compositions

Table 42.6 Input parameters used in the study 2

Composition (%)		Voltage (V)	Electrolyte conductivity (S/m)	Interelectrode gap (mm)
Al	SiC			
90	10	12	7	0.04
90	10	14	7	0.04
90	10	16	7	0.04

each voltage is shown in Fig. 42.6. It is observed that the MR is varying linearly for every voltage and MR increases with increase in the voltage.

42.3.3   Study 3: Effect of Interelectrode Gap

In this study, three different interelectrode gaps have been varied by maintaining constant composition, electrolyte conductivity and the voltage to get material removal at each second of the simulation as shown in Table 42.7. The electrolyte used in this study is $NaNO_3$.

For the input parameters shown in Table 42.7, the material removal values at each second for three interelectrode gaps were found and a plot between MR and time for each interelectrode gap has been drawn as shown in Fig. 42.7. It is observed
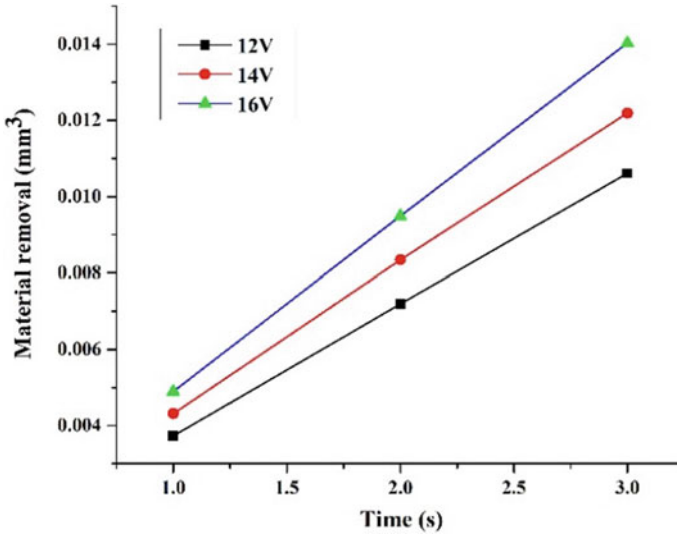
Fig. 42.6 Material removal for different voltages

Table 42.7 Input parameters used in the study 3

Composition (%)		Voltage (V)	Electrolyte conductivity (S/m)	Interelectrode gap (mm)
Al	SiC			
90	10	14	7	0.06
90	10	14	7	0.04
90	10	14	7	0.02

that the MR is varying linearly in each plot and MR decreases with increase in the interelectrode gap.

42.3.4 Study 4: Effect of Electrolyte

In this study, three different electrolytes with their corresponding electrolyte conductivities have been varied by maintaining constant composition, interelectrode gap and voltage to get material removal at 3 s of the simulation as shown in Table 42.8.

Here, in this analysis, the simulation time is increased to 3 s as there is no appreciable amount of material removal at 1 s.

For the input parameters shown in Table 42.8, the material removal values at 3 s for three electrolytes were found and a plot between MR and time for each electrolyte
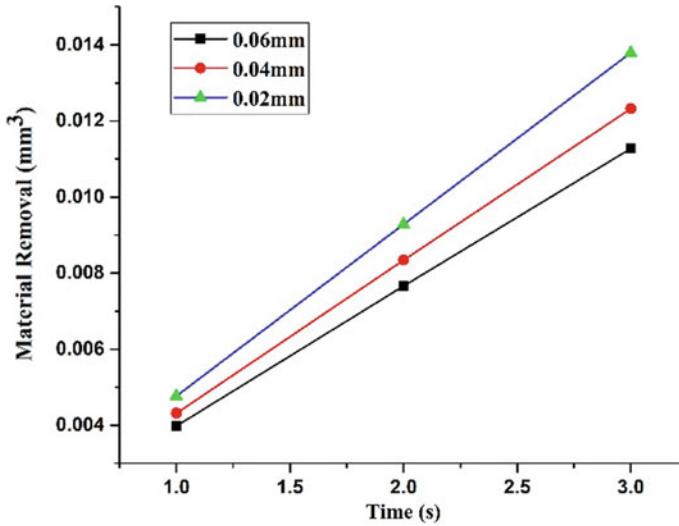
Fig. 42.7 Material removal for different interelectrode gaps

Table 42.8 Input parameters used in the study 4

Composition (%)		Voltage (V)	Electrolyte		Interelectrode gap (mm)
Al	SiC		Chemical name	Conductivity (S/m)	
90	10	14	Sea water	5	0.04
90	10	14	HCl	1.1	0.04
90	10	14	NaNO$_3$	7	0.04

has been drawn as shown in Fig. 42.8. It is observed that the MR is varying linearly in each plot and MR decreases with decrease in electrolytic conductivity.

42.4 Conclusion

These studies give detailed information about how the material removal varies with different input parameters and time. First three studies have shown that the material removal in each second of the machining has almost the same value. The fourth study shows completely different values in comparison with the other three. This variation is because of the variable parameter 'electrolyte conductivity' which used different electrolytes for the simulation. Hence, it can be concluded that electrolyte conductivity has more impact on material removal. This work can be further extended to optimize the process parameters for multiresponses.

Fig. 42.8 Material removal for different electrolytes
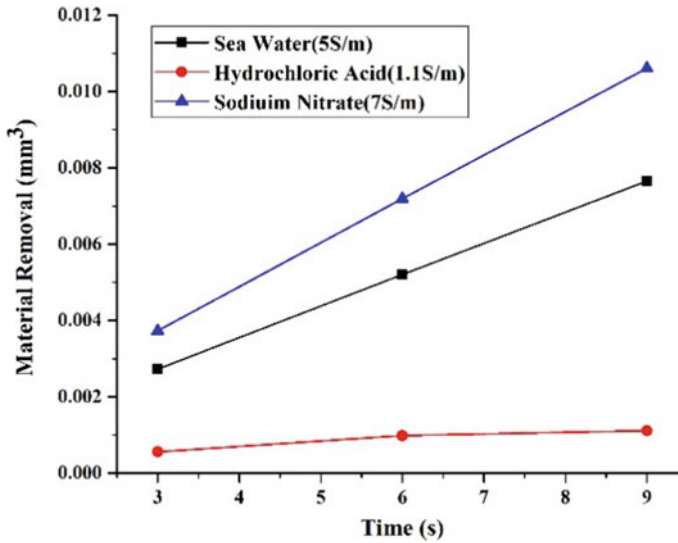
References

1. Senthilkumar, C., Ganesan, G., Karthikeyan, R.: Bi-performance optimization of electro-chemical machining characteristics of Al/20%SiCp composites using NSGA-II. **1**, 1–9 (2010)
2. Rajurkar, K.P., et al.: Modelling and monitoring interelectrode gap in pulse electrochemical machining. CIRP Ann. **44**(1), 177–180 (1995)
3. Rajurkar, K.P., et al.: New developments in electro-chemical machining. CIRP Ann. **48**(2), 567–579 (1999)
4. Van Tijum, R., Pajak, P.T.: Simulation of Production Processes Using the Multiphysics Approach: The Electrochemical Machining Process (2019)
5. Hackert-Oschätzchen, M., Jahn, S.F., Schubert, A.: Design of Electrochemical Machining Processes By Multiphysics Simulation (2019)
6. Li, Q., et al.: COMSOL multiphysics: a novel approach to ground water modeling. Groundwater **47**(4), 480–487 (2009)
7. Bukhari, M., Hashmi, M., Brabazon, D.: Application of metal matrix composite of CuSiC and AlSiC as electronics packaging materials. In: The 28 th International Manufacturing Conference (2011)
8. Suryanarayanan, K., Praveen, R., Srinivasan, R.: Silicon carbide reinforced aluminium metal matrix composites for aerospace applications: a literature review. Int. J. Innov. Res. Sci. **2**, 6336–6344 (2013)
9. Stojanovic, B., Ivanovic, L.: Application of aluminium hybrid composites in automotive industry. **22**, 247–251 (2015)
10. Occhionero, M., et al.: Aluminium silicon carbide (AlSiC) for advanced microelectronic packages. In: IMAPS May 1998 Boston Meeting, Ceramics Process Systems Corp. Citeseer (1998)
11. Senapaty, K.P., Balaji. P.: Numerical simulation of electric discharge machining of functionally graded material. In: IOP Conference Series: Materials Science and Engineering. IOP Publishing (2018)

12. McGeough, J.A.: Principles of Electrochemical Machining. Chapman & Hall (1974)
13. Haisch, T., Mittemeijer, E., Schultze, J.: Electrochemical machining of the steel 100Cr6 in aqueous NaCl and NaNO$_3$ solutions: microstructure of surface films formed by carbides. Electrochim. Acta **47**(1–2), 235–241 (2001)

Chapter 43
Corrosion Behavior of Microwave Clad Material Under Different Acidic Environment

Amit Kumar, Neeraj Kumar Bhoi, and Harpreet Singh

Abstract The requirement of better functional surface and enhanced product performance has always been thrust for the industrial and academia. The surface modification through microwave energy has been developed and relatively new innovative method for various coatings on the substrate material. The present study involves the hybrid microwave cladding of aluminum and silicon carbide composite in the mild steel substrate at lower cost and processing circumstances. In the present case, pure aluminum and pure Al + 5 wt%SiC were utilized for the cladding over the mild steel substrate material. To investigate the output response, corrosion behavior of the material is tested under two different acidic environments (i.e., sodium chloride and nitric acid). The weight loss measurement is done with the fixed interval of time to know the corrosion behavior of the material. The performance of the clad surface shows the better outcomes compared to the monolithic substrate material. The bonding between the clad and substrate is in excellent accord with the performance improvement as observed by the use of scanning electron microscope.

Keywords Microwave cladding · Composite material · Bonding strength · Corrosion behavior

43.1 Introduction

Mild steel is widely used in many engineering applications. However, there are some limitations which limit the applicability under highly corrosive environment. Corrosion may define as gradual or spontaneous deterioration of metals and metallic

A. Kumar · N. K. Bhoi · H. Singh (✉)
Department of Mechanical Engineering, PDPM IIITDM, Jabalpur 482005, India
e-mail: hps.dme@gmail.com

A. Kumar
e-mail: amit.sah1204@gmail.com

N. K. Bhoi
e-mail: neerajbitd@gmail.com

alloy [1, 2]. Deterioration of metal and metallic alloy occurred by chemical oxidization or electrochemical reaction in the presence of the surrounding environment [3, 4]. Deterioration has a term in corrosion show degradation of metallic properties in terms of appearance, strength, and resistive power to different exposed medium. The implantation of the new resistive surface over conventional material leads to possible remedies for the different functional application in aerospace, defence, automotive, industrial, and structural component [1–5]. The extensive use of cladding over the functional surface is a relatively old and developed method to protect the surface. Under the category of cladding, microwave cladding is a relatively new and better approach for the development of cladding over the substrate material [6, 7]. The use of microwave energy for the cladding process uses volumetric and rapid heating with low power consumption and enhanced material properties [8]. The use of microwave radiation for the different manufacturing process is well developed and used worldwide for their unique advantageous defined process limit [9]. In the stated context, several researchers tried various metallic powders for the cladding in the mild steel material for the enhancement in the wear resistance and hardness of the test sample [6, 10]. Cladding by the use of microwave radiation is a relatively new and developed method for the low-cost synthesis of different material under normal operating range. Reference can be made to the deposition of copper, nickel, WC10Co2Ni, and tungsten carbide in the austenitic steel material by the use of microwave radiation. It was revealed that the average hardness and bonding between the interface layers are significantly improved [11–13].

43.1.1   Benefits of Microwave Energy Over Conventional Heating

Microwave energy has enormous benefits, as compared to any other conventional heating process. In microwave heating process, there is a conversion of the electromagnetic wave into heat energy and the metallic material heat at molecular level. Microwave energy can be used in many manufacturing processes like casting of metals with microwave hybrid technique, joining of similar or dissimilar metals with the help of similar or dissimilar filler material, sintering of materials or ceramics, cladding of metals, ceramics or composition of both over the base material to improve surface properties mainly hardness, and corrosion and wear properties. Microwave heating takes less processing time and rapid heating of materials, uniform and volumetric heating of material, and no temperature gradient developed inside the material. However, conventional heating needs more time as compared to microwave heating and there is a thermal gradient present in the conventional heating process. Although it is intimidated that it takes 10–100 times less power consumption and 10–200 less processing time than conventional heating process [8].

43.2 Experimental Details

43.2.1 Material

In the present study for the cladding, powder material aluminum (325 mesh) and silicon carbide (420 mesh) were utilized and procured from Alpha Chemika Pvt. Ltd. Mumbai, India. For the corrosion, behavior study of nitric acid (HNO_3) and sodium chloride (NaCl) Assay>99% was purchased from Science Emporium Jabalpur, India. The powder sample and the acidic solution are used without any further purification and test. Aluminum metals have been widely used in many engineering materials due to their unique characterization: high corrosion resistance, high strength, light in weight, easily available, ductility strong, high reflectivity, and non-toxic [14, 15]. Silicon carbide is high microwave absorbing material. It helps to eliminate the possibility of cracks propagation due to non-uniform heating. Silicon carbide is a hard particle that may help to maintain the strength and hardness of the clad surface.

43.2.2 Procedure

For the cladding, mild steel (MS) plate of dimension $20 \times 20 \times 2.6$ mm^3 was used as substrate. Before the cladding, the substrate material was etched by ethanol and distilled water in the normal operating frequency range (i.e., 45–50 Hz) to remove the possible dirt and impurities from the surface. The powder materials were deposited by manually maintaining uniform thickness in etched substrate material in the temperature environment of 150–200 °C for the possible excitation of the molecule and for the better bonding between the substrate and raw powder material. The prepared samples were manually placed inside the microwave hybrid heating setup for the final clad formation between the material and substrate. In the present case, two different clad powders (i.e., aluminum and aluminum silicon carbide mixture) were utilized for the cladding in the mild steel substrate material. For the preparation of the aluminum and silicon carbide sample, mechanical-type ball mill was used at specified operating conditions which were previously reported by the researchers. For the microwave heating, conventional charcoal oven microwave is utilized at full operating power with the frequency level of 2.45 GHz [16]. The schematic representation of the developed microwave heating setup is illustrated in Fig. 43.1.

43.2.3 Development of Corrosion Environment

Two different corrosive media of nitric acid (HNO_3) and sodium chloride (NaCl) were developed for the determination of the corrosion rate of the clad sample. In the present case, 0.6 M of HNO_3 and 0.6 M of NaCl are diluted in 350 ml of distilled water for
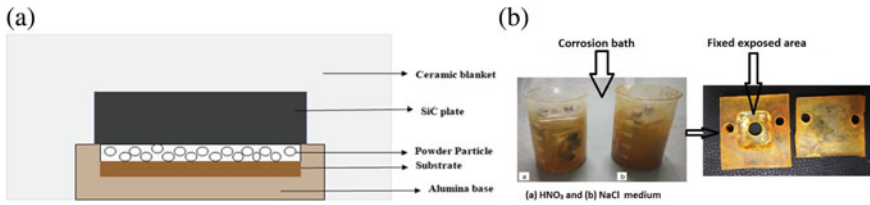
Fig. 43.1 Schematic representation of the developed **a** microwave cladding setup and developed, **b** corrosion bath

the corrosion behavior study. The diluted solution was maintained throughout the test and considered as equivalent to the sea environment. Figure 43.1b shows the pictorial representation of the developed corrosion bath for the study of corrosion test under the different acidic environment. The corrosion test was performed for a total duration of 168 h. The weight loss measurement technique was applied for the study of corrosion wear behavior of the different sample.

43.2.4 Metallurgical Characterization

For the material characterization, scanning electron microscope (SEM) equipped with energy-dispersive spectroscopy (EDAX) was utilized for the evaluation of surface morphology in the clad samples. The EDAX analysis in the interface zone of the clad part exhibits the different elements present in the sample after cladding.

43.3 Results and Discussion

43.3.1 Development and Formation of Clad Material

The raw powder material usually reflects the microwave energy at room temperatures so for the effective coupling between the microwave energy and powder material hybrid heating is employed. If the penetration depth of material is less than the particle size of material, then direct heating of material is not possible. In this condition, heating of process material has to be achieved using a combination of conduction and radiation heat transfer source. The skin depth of aluminum (Al) has to be calculated by the equation as mentioned below.

$$d = \sqrt{\frac{\rho}{\pi f \mu_r \mu_o}}$$

Table 43.1 Exposure time and observed phenomenon during the cladding process

Serial No.	Exposure time (s)	Remarks
1	400	Incomplete penetration of microwave energy
2	460	Powder heating only (low temperature)
3	520	Powder heating only
4	580	Partial semi-solid state of the clad powder
5	640	Partial melting of the clad powder
6	720	Formation of the bonding between the clad and substrate material
7	780	Overheating of the powder sample
8	840	Burning of the power and substrate material

where d = skin depth capacity (μm), ρ = resistivity = (2.65 μm cm), μ_r = relative permeability (1 H/m), μ_o = absolute permeability ($4\pi \times 10^{-7}$ H/m), and f = frequency of microwave (2.45 GHz).

The value of skin depth calculated through this equation has found approximately 1. 6 μm which is much lower than the size powder material particle. It has been concluded that the skin depth of aluminum is much less than the size of aluminum powder particles. The processing of aluminum cladding through microwave has occurred due to microwave hybrid heating technique. The use of hybrid heating provides the better and uniform coupling of the powder and substrate material with enhanced bonding between the interfaces. The silicon carbide block is effectively absorbing the microwave energy at room temperature and converts it into heat which enhances the coupling between the powder and substrate material. In the present study, silicon carbide block is used as a susceptor material for the cladding purpose. The use of susceptor heating enhances the coupling between the materials and enhances the bonding between the powder and substrate material [16]. For the experimentation, different exposure time was utilized for the cladding of the raw powder. The different experimental trails for the exposure time and the observed phenomenon are given in Table 43.1. The better and uniform cladding was observed at an exposure time of 720 s under 2.45 GHz frequency and 900 W microwave power level.

43.3.2   Corrosion Behavior

For the corrosion behavior study, the prepared clad sample was exposed to a fixed surface area to two different acidic media. Weight loss of the substrate and the clad sample is given in Fig. 43.2. From the observation, it is clear that the surface having clad material exhibits better corrosion resistance compared to that of the monolithic sample. The strong adhesion bonding between the clad and surface material reveals better corrosive surface under different exposure medium. A typical scanning electron microscopy image (SEM) is given in Fig. 43.3a. The morphology shows the interface
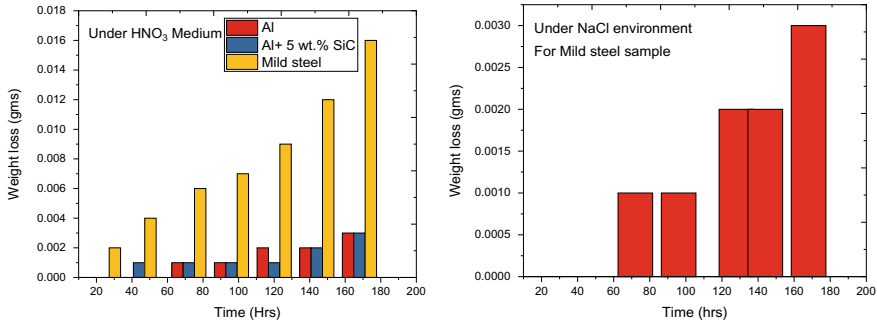
Fig. 43.2 Weight loss for the tested material with the time duration under nitric acid and sodium chloride medium
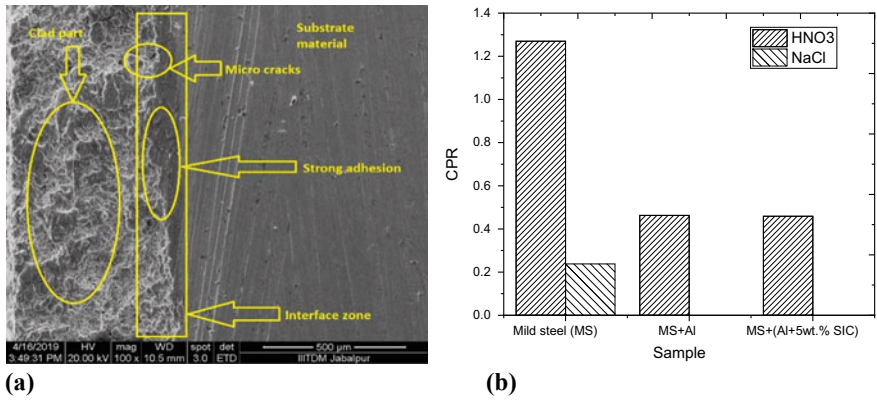
Fig. 43.3 **a** SEM morphology of the cladding surface and base material and **b** CPR of different sample

between the clad and substrate material. In the interfacial zone, small microcrack and porosity were observed which may be due to difference in the material behavior (i.e. ferrous and non-ferrous behavior). It can be seen that clad material is well bonded with the substrate material under the influence of microwave energy and diffusion between the molecule [10]. For the evaluation of the corrosion behavior, corrosion penetration rate (CPR) in terms of mils per year (mpy) is calculated through Eq. (43.1)

$$CPR = \frac{kW}{\rho at} \tag{43.1}$$

where ρ = density of materials grams per cubic centimeter, w = weight loss due to corrosion milligrams, a = exposed surface area in corrosion medium square inches, t = time in hrs, and k = is a constant depending on the system of the unit used and if

CPR in mm/year, then $k = 87.6$, and if CPR in mpy, then $k = 534$. The comparative assessment of CPR is given in Fig. 43.3b for the present study.

The corrosion behavior is an electrochemical phenomenon and can be explained through electrical as well as the chemical perspective of the material. Addition of the hard ceramic and formation of the oxide layer in the surface are in good agreement for the reduction in the corrosion rate under acidic environment. This fact can be judged by the theory behind the difference in the thermal conductivity of the created higher nobility in chemical perspectives which eventually lowers the corrosion rate. On the other hand, in the chloride medium, the decay in the clad sample is zero. This implies that the clad material protects the movement of the ion in the chloride solutions considerably leading the minimal decay and loss. The former argument is found to be well supported in the bonding between the clad and substrate material as observed in Fig. 43.3a. The corrosion proceeds much faster in aqueous solutions and can be seen in Fig. 43.2.

43.3.3   Energy-Dispersive Analysis

The characterization through energy-dispersive method finds the elemental analysis of any sample. In the present work, the EDS analysis validates the formation of metallurgical bonding between powder material and substrate material. The two different points in the sample were tested under EDS: one position of EDS analysis was at the interface and second position of EDS analysis was clad surface. The element distributions in two different positions are shown in Fig. 43.4. The element of iron is found at the outer surface region of all four clad samples. The presence of iron element revels the melting of the substrate material and metallurgical adhesion bond formation occurred in the cladding process [8]. A similar observation was also reported by the previous investigator for the cladding of the different sample with the use of microwave energy [6]. The presence of intermetallic compound and their functional percentage can be beautifully seen from Fig. 43.4.

43.4   Conclusion

A new processing method is adopted for the development of cladding over the substrate material. The present work demonstrates the clad of Al + SiC in the mild steel material under 2.45 GHz frequency. The major outcomes of the present study can be given as:

- It was found that the addition of aluminum and silicon carbide clad material over the substrate material reduces the tendency to corrosion under different aggressive environment.
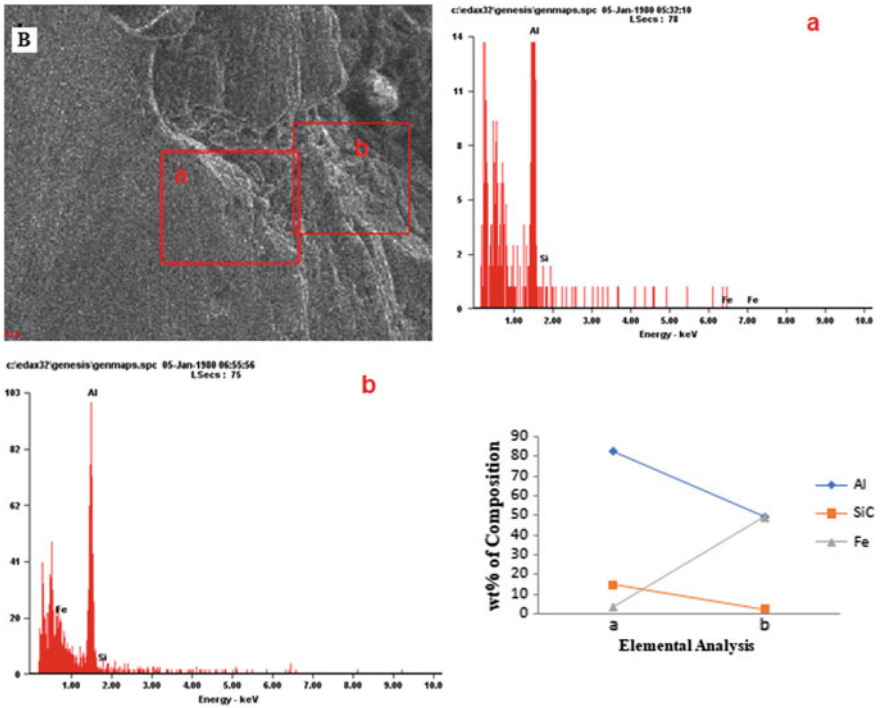
Fig. 43.4 EDS analysis of the clad medium Al + 5% SiC

- The benefits of the addition of the hard ceramics can be stated in terms of improvement in the hardness of the clad surface. In many cases, the hardness is the major concern along with the corrosion resistance surface line ship hull, naval structure, etc.
- No loss in terms of weight is found under sodium chloride medium for the clad surface. However, the decreasing amount of loss is observed with a nitric acid medium for the clad surface over the monolithic material.

43.5 Future Scope

In spite of the enormous advantages of microwave cladding, there are still challenges and limitation of microwave cladding. The limitation and problems listed below may in future find the solution to these problems:

- The mechanism of materials interaction with microwave is not investigated completely. Microwave cladding is limited for flat surfaces. The claddings of complex surfaces are still challenging task.

- Microwave has good absorber of silicon carbide (SiC) and aluminum oxide (Al_2O_3). The proper design of silicon carbide block casing the coating of tooltip may be potentially used in future.
- No efforts seem to have been made toward process modeling. Development of a mathematical model that counts the various input process conditions and output parameters required more research.

References

1. Liu, M., Guo, Y., Wang, J., Yergin, M.: Corrosion avoidance in lightweight materials for automotive applications. npj Mater. Degrad. **2** (2018). https://doi.org/10.1038/s41529-018-0045-2
2. Hassan, A., Elkady, H., Shaaban, I.G.: Effect of adding carbon nanotubes on corrosion rates and steel-concrete bond. Sci. Rep. 1–12 (2019)
3. Yan, J., Heckman, N.M., Velasco, L., Hodge, A.M.: Improve sensitization and corrosion resistance of an Al-Mg alloy by optimization of grain boundaries. Sci. Rep. **6**, 1–10 (2016). https://doi.org/10.1038/srep26870
4. Gateman, S.M., Stephens, L.I., Perry, S.C., et al.: The role of titanium in the initiation of localized corrosion of stainless steel 444. npj Mater. Degrad. **2**, 1–8 (2018). https://doi.org/10.1038/s41529-018-0026-5
5. Clauser, H.R.: Advanced composite materials. Sci. Am. **229**, 36–44 (2010). https://doi.org/10.1038/scientificamerican0773-36
6. Kaushal, S., Gupta, D., Bhowmick, H.: An approach for functionally graded cladding of composite material on austenitic stainless steel substrate through microwave heating. J. Compos. Mater (2017). 002199831770597. https://doi.org/10.1177/0021998317705977
7. Eli, J., Dikhtiar, V.: Method and device for drilling, cutting, nailing and joining solid non-conductive materials using microwave energy. US Patent 6,114,676 (2000)
8. Bhoi, N.K., Singh, H., Pratap, S., Jain, P.K.: Microwave material processing: a clean, green, and sustainable approach. In: Sustainable Engineering Products and Manufacturing Technologies, 1st edn. Academic Press, Elsevier, pp. 3–23 (2019)
9. Singh, H., Jain, P.K., Bhoi, N., Pratap, S.: Experimental study pertaining to microwave sintering (MWS) of Al-metal matrix composite—a review. Mater. Sci. Forum **928**, 150–155 (2018). https://doi.org/10.4028/www.scientific.net/MSF.928.150
10. Gupta, D., Sharma, A.K.: Development and microstructural characterization of microwave cladding on austenitic stainless steel. Surf. Coat. Technol **205**, 5147–5155 (2011). https://doi.org/10.1016/j.surfcoat.2011.05.018
11. Gupta, D., Sharma, A.K.: Microwave cladding: a new approach in surface engineering. J. Manuf. Process **16**, 176–182 (2014). https://doi.org/10.1016/j.jmapro.2014.01.001
12. Kaushal, S., Sirohi, V., Gupta, D., et al.: Processing and characterization of composite cladding through microwave heating on martensitic steel. Proc. Inst. Mech. Eng. Part L J. Mater. Des. Appl. **232**, 80–86 (2018). https://doi.org/10.1177/1464420715616139
13. Kaushal, S., Gupta, D., Bhowmick, H.: Investigation of dry sliding wear behavior of Ni–SiC microwave cladding. J. Tribol. **139**, 041603 (2016). https://doi.org/10.1115/1.4035147
14. Bhoi, N.K., Singh, H., Pratap, S.: Developments in the aluminum metal matrix composites reinforced by micro/nano particles—a review. J. Compos. Mater (2019). https://doi.org/10.1177/0021998319865307
15. Pattnaik, S.K., Bhoi, N.K., Padhi, S., Sarangi, S.K.: Dry machining of aluminum for proper selection of cutting tool: tool performance and tool wear. Int. J. Adv. Manuf. Technol. **98**, 55–65 (2018). https://doi.org/10.1007/s00170-017-0307-0

16. Bhoi, N.K., Singh, H., Pratap, S.: A study on microwave susceptor material for hybrid heating. J. Phys. Conf. Ser. 1240 (2019). https://doi.org/10.1088/1742-6596/1240/1/012097

Chapter 44
Numerical and Experimental Investigation on Heat Transfer Performance of Ferrofluid-Based Cooling System

Jaswinder Singh Mehta, Rajesh Kumar, Harmesh Kumar, and Harry Garg

Abstract The present study reports the experimental and numerical investigation of potential application of ferrofluid as a coolant for mini/microdevices. The kerosene-based ferrofluid was allowed to flow through a closed loop under the effect of a magnetic field generated by permanent magnet. Constant heat flux conditions varying from 0 to 10 W were applied and the temperature was measured using infrared thermography. The results of the simulation study were validated by performing experiments under the same test conditions, and a good agreement was found between the experimental observations and numerical results. Velocity and temperature profiles were plotted for the given heat load range, strengthening the candidature of ferrofluid as a potential coolant for mini/microdevices.

Keywords Numerical simulation · Heat transfer · Ferrofluid · Magnetic field · Kelvin body force

44.1 Introduction

With the size of electronic devices continually decreasing each passing day, a challenge is posed to the scientific community to find novel ways of dissipating the high heat flux generated by them. Thermal management of these devices is essential for their reliable and prolonged working else there is more likelihood of premature failure. Researchers are following different practices for tackling the heat transfer problem associated with them. Nanofluids, over a period of few years, have provided a satisfactory solution for convective heat transfer of micro- and miniscale devices, but there is a strong dependence on external means such as syringe pump or mechanical pumps for circulating the fluid. Thus, system reliability as a whole is lowered which might affect the efficiency and effectiveness of these devices. Ferrofluids in

J. S. Mehta (✉) · R. Kumar · H. Kumar
Department of Mechanical Engineering, UIET, PU, Chandigarh, India
e-mail: jsmehta@pu.ac.in

H. Garg
CSIR-CSIO, Chandigarh, India

such cases can provide a potential solution for cooling of such devices [1–8] with the added advantage that the system reliability is not affected.

Ferrofluid is a colloidal mixture consisting of monodomain magnetic particles of the size usually less than 10 nm in a non-magnetic carrier fluid. The nanoparticles are usually coated with a suitable surfactant layer of about 2–3 mm thickness so that they remain uniformly dispersed in the base fluid avoiding their agglomeration. Ferrofluid-driven heat exchangers work on the principle of thermo-magnetic convection [9], where the magnetic field generated by an external magnet provides the necessary pumping force to drive the fluid. Thus, the system is truly passive as there is no requirement of the pump or other devices for circulating the temperature-sensitive ferrofluid.

A numerical study to examine the hydrodynamic and thermal behavior of water-based ferrofluid in the presence of a non-uniform magnetic field with a sinusoidal corrugated wall was conducted using two-phase mixture method [10]. The effect of wavy amplitude, volume fraction, Reynolds number, and magnetic field differential on the Nusselt number and flow characteristics were presented. The Nusselt number was found to be an increasing function of wave amplitude, volume fraction of nanoparticles, and negative magnetic field gradient. The effect of magnetic field is more predominant at lower Reynolds numbers while a stronger magnetic field gradient is required at higher Reynolds number.

Three-dimensional forced convection heat transfer of water-based ferrofluid in a pipe subject to constant wall heat flux in the presence of permanent magnets or a current-carrying wire was investigated and compared [11]. Higher rate of heat transfer was observed when the magnetic field was generated by permanent magnets instead of electric current. The fluid mixing was intensified under the effect of the magnetic field leading to an increase in the Nusselt number along the pipe length.

The laminar forced convection heat transfer of ferrofluid in a uniformly heated parallel plate was experimentally studied under the influence of an alternating magnetic field generated by electromagnets [12]. The effect of electromagnets arrangement and locations on convection heat transfer was analyzed numerically and heat transfer was found to have a direct relation with the Reynolds number and ferrofluid concentration. It was observed that, in the presence of the alternating magnetic field, pressure drop rise was comparatively less than heat transfer enhancement.

The behavior of ferrofluids under the application of an external magnetic field to enhance heat transfer properties of laminar microfluidic channel flow was analyzed [13]. Heat transfer rate was enhanced with a volume concentration of magnetic nanoparticles while the reverse trend was observed with magnetic field strength. The effective thermal conductivity of the ferrofluid was also found to diminish experimentally and numerically due to the trapping of the magnetic particles.

The influence of non-uniform magnetic field on flow characteristics and laminar convective heat transfer of ferrofluid inside 90° elbow channel was numerically inspected [14]. Circulations were induced in the vicinity of the inner wall of the elbow in the presence of non-uniform magnetic field and mainstream flow is decelerated. Increasing the nanoparticles concentration enhances the heat transfer rate within the

channel. Also, heat transfer improved by approximately 18% as the Reynolds number was increased from 50 to 100.

The convective heat transfer behavior of Fe_3O_4/water (3 vol%) nanofluids was experimentally examined under a parallel constant and uniform magnetic field and temperatures [15]. The convective heat transfer coefficients of the fluid were observed to decrease with a parallel constant and uniform magnetic field and by increasing the intensity of the magnetic field strength. However, the heat transfer coefficients were enhanced with increasing temperature independent of the magnetic field.

A numerical study of enhancement of heat transfer coefficient in steady, laminar, and hydrodynamically fully developed flow of water-based ferrofluids under no magnetic field in parallel plate channels was reported [16]. Heat transfer coefficient was found to increase with nanoparticle concentration. A marginal increase in the enhancement factor was observed upon comparing thermally developing flow in microchannel and macrochannel of the same length in the heat flux range of 20–80 kW/m². However, a greater enhancement factor was found in microchannel compared to macrochannel of the same length for the thermally fully developed flow in the heat flux range of 1–4 kW/m².

The reported literature points out that the thermal and flow properties of a ferrofluid can be tuned under the application of an external magnetic field. Thus, the fluid can be stimulated by inducing temperature differential and non-uniform magnetic field by using a magnetic field, making it suitable for heat transfer applications. In this paper, numerical simulation along with the experimental investigation of convective heat dissipation of kerosene-based ferrofluid flowing through a closed loop has been performed. Permanent magnet NdFeB of strength 1000 Gauss is used for generation of magnetic field. Heat load of intensity varying from 0 to 10 W in steps of 2.5 was applied, and temperature measurements were done using infrared thermography technique. Results are plotted for different lengths of time for variation of temperature at different heat loads and the effectiveness of ferrofluid-based cooling system is judged from the fact that safe temperature limits were maintained in the system.

44.2 Mathematical Modeling and Numerical Simulation

44.2.1 Geometry Description

Figure 44.1 shows the schematic of 2D model used for the numerical study. Kerosene-based ferrofluid flows through the closed loop of dimensions 170 mm × 95 mm with an internal diameter as 2 mm. Permanent magnet of strength 1000 Gauss is being used for generation of the external magnetic field and rectangular fins of 1 mm (width) × 15 mm (height) with gap between them as 2 mm are employed in the lower loop for dissipation of heat flux to the surrounding air.
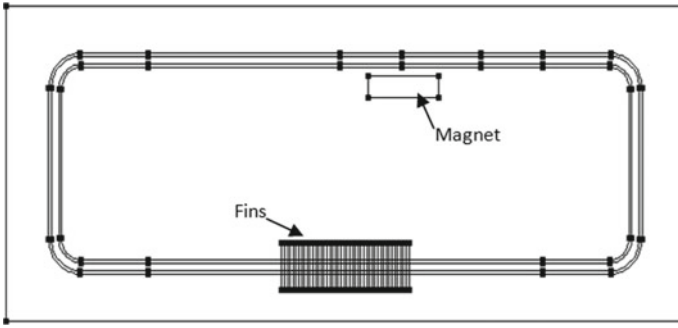
Fig. 44.1 Schematic of two-dimensional closed-loop model

44.2.2 Governing Equations

Following equations govern the flow of single-phase ferrofluid through the closed loop under consideration:

Continuity equation:

$$\frac{\partial \rho}{\partial t} + \nabla \cdot (\rho \vec{u}) = 0 \tag{2.1}$$

Momentum equation:

$$\rho \partial \vec{u} / \partial t + \rho \vec{u} \cdot \nabla \vec{u} = -\nabla p + \nabla \cdot \left(\mu \left(\nabla \vec{u} + (\nabla \vec{u})^{\mathrm{T}} \right) \right) + \vec{F} \tag{2.2}$$

Energy equation:

$$\rho c_p \left(\frac{\partial T}{\partial t} + \vec{u} \cdot \nabla T \right) = k \nabla^2 T \tag{2.3}$$

Magnetic induction:

$$\vec{B} = \mu_o \left(\vec{H} + \vec{M} \right) \tag{2.4}$$

Driving force (*Kelvin body force*):

$$\vec{F} = \left(\vec{M} \cdot \nabla \right) \vec{B} \tag{2.5}$$

Table 44.1 represents the characteristics of kerosene-based ferrofluid used for the numerical study.

A partial differential equation (PDE)-based multiphysics finite element software, COMSOL Multiphysics 5.0, is being used for modeling and solving the governing

Table 44.1 Kerosene-based ferrofluid properties

S. No.	Parameters	Value
1	Viscosity, μ	2 cP
2	Density, ρ	910 kg/m^3
3	Thermal conductivity, k	0.174 W/(m-K)
4	Curie temperature of the fluid	55 °C
5	Surrounding temperature	20 °C
6	Magnetic susceptibility	0.386
7	Relative permeability of fluid	1.386

equations. No-slip conditions were assumed for the flow at the inner wall surface. Initial temperature of the ferrofluid in the loop was considered at 273 K. A constant heat flux was provided and flow was assumed to be laminar and incompressible in nature.

44.2.3 Grid Study

Figure 44.2 represents the typical meshing in the computational domain, and Table 44.2 displays the variation in the results of ferrofluid temperature and velocity
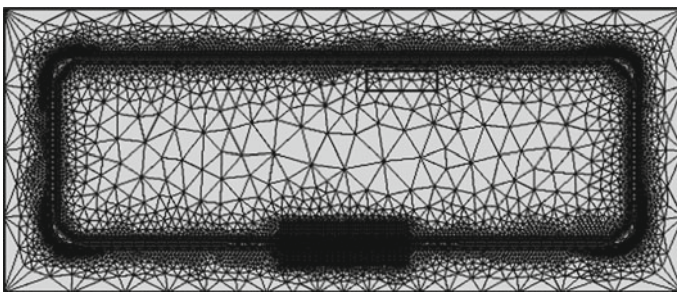

Fig. 44.2 Non-uniform grid distribution inside and around the closed loop

Table 44.2 Grid independency investigations for the selected domain

Grid size	Ferrofluid temperature (K)	Ferrofluid velocity (mm/s)
Normal	322.27	2.1455
Fine	322.83	2.1984
Finer	323.58	2.2575
Extra fine	323.66	2.2597
Extremely fine	323.62	2.2601

with different mesh settings. A grid independency check has been performed and it can be seen that on increasing the mesh density from finer to extremely fine, negligible changes in the two parameters were observed. Thus, physics-controlled finer mesh has been used in the fluid flow domain so as to envisage the temperature and velocity measurements accurately, while for the rest of the computational domain, the normal mesh is considered to be suitable.

44.3 Experimental Setup

The experimental setup for the ferrofluid-based cooling system is shown in Fig. 44.3. The test loop was constructed of a horizontal upper copper tube of internal diameter 2 mm, thickness 2 mm, and length 170 mm while the remaining length of the test loop was made of glass. A permanent magnet NdFeB of strength 1000 Gauss was used for generation of the magnetic field. Heat transfer section was heated electrically, and uniform heat flux condition was provided with the help of a DC power supply of power rating 0–30 V and 0–10 A (Make: ISO-TECH). Cold water was circulated in the lower loop and constant ferrofluid outlet temperature was maintained by varying the flow rate using Masterflex precision pump (Model 77200-60). Infrared thermal imager (Testo 875i) was used for measuring the temperature field of heated Cu tube and temperature at the outlet of heat sink section in the lower loop. The IR camera has a resolution of 160×120 pixels with an image refresh rate 33 Hz and thermal sensitivity of less than 50 mK at 30 °C.

The kerosene-based ferrofluid used in the experimentation was custom prepared, and the detailed specifications of which have been listed in Table 44.1.

The iron nanoparticles used in the kerosene-based ferrofluid have an average size of 30 nm as can be seen from Fig. 44.4.

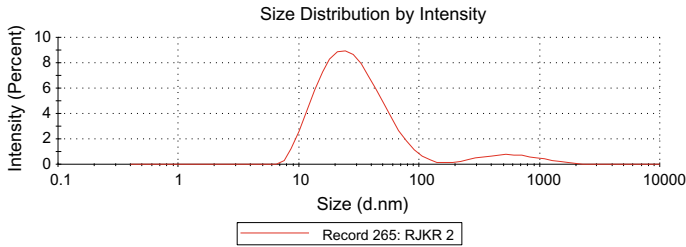**Fig. 44.3** Ferrofluid-based cooling system experimental setup

Fig. 44.4 Size distribution report of nanoparticles measured by DLS technique

44.4 Results and Discussions

Figure 44.5 displays the temperature contour at different point of time when the fluid was subjected to a constant heat flux of 5 W. As can be seen, with the passage of time, fluid temperature was increased and reaches in close vicinity to its Curie temperature. Thus, under the effect of magnetic field, due to spatially varying temperature distribution, fluid experiences Kelvin body force and it begins to flow in the direction of higher temperature section. The flow, therefore, establishes on its own under the application of a magnetic field only without the necessity of any mechanical pump.

Figure 44.6 demonstrates the velocity profile of ferrofluid at a varying length of time. The velocity builds up as the time progresses with an increase in magnitude of Kelvin Body Force and finally settles once the initial transient period is over. Maximum velocity is noticeable in the area when the fluid is about to enter the heated length.

The magnetic field distribution for the permanent magnet as shown in Fig. 44.7 clearly represents that the effect of magnetic field is felt only in a small region near the magnet location. At far-off locations, the magnetic field intensity is negligibly small so as the velocity.

Figure 44.8 displays the variation in average X-component of Kelvin body force that act on the ferrofluid at different instant of time.

Figure 44.9 demonstrates the variation of temperature recorded (*Y*-axis) at different points of time (*X*-axis) for the present experiment and numerical simulation performed using COMSOL MultiPhysics 5.0. A good agreement can be seen between the experimental and simulation results obtained for the present case when the heat load of 5 W was applied.

With the increase in heat load on the system, fluid velocity also tends to rise as depicted in Fig. 44.10. As the thermal input on the system is raised, higher temperature gradient is induced and is responsible for the generation of higher body force leading to higher velocity under the effect of the magnetic field.

The velocity profile at a cut section normal to fluid flow near the entrance to the heated length is also depicted in Fig. 44.11. Velocity is zero at the inner pipe surface due to prevailing of no-slip conditions and increases toward the center and is maximum along the center line of the pipe.
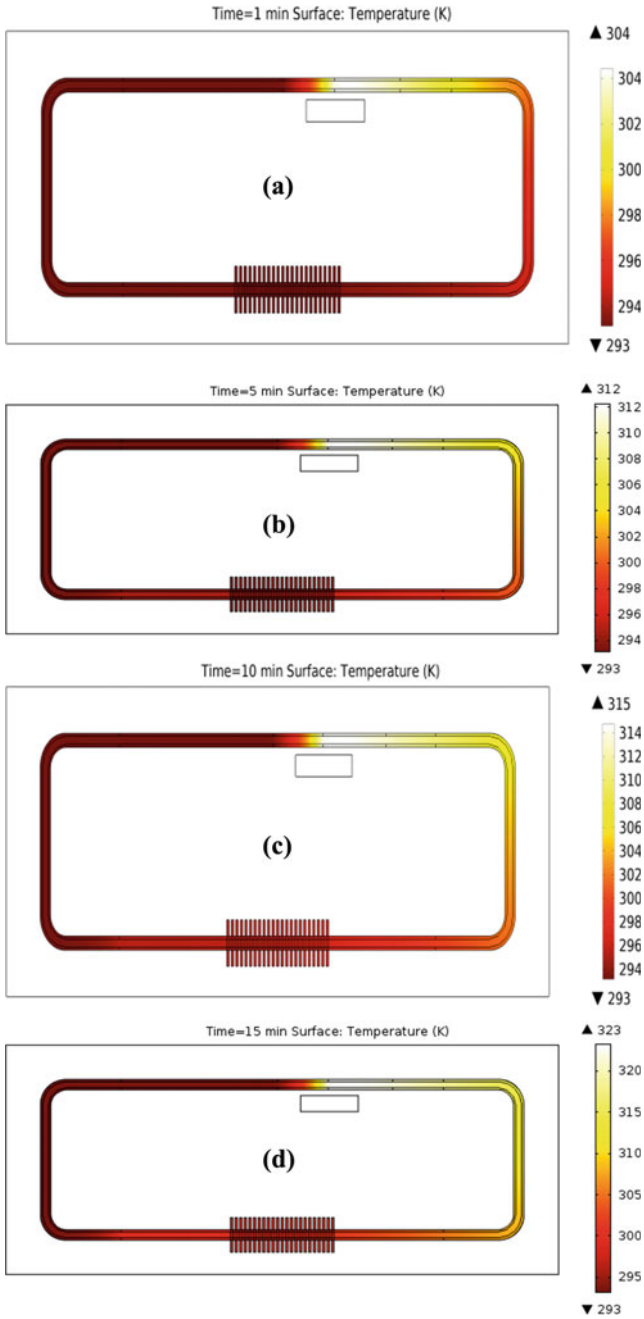
Fig. 44.5 Fluid temperature contour (K) generated at different length of time. **a** 1 min, **b** 5 min, **c** 10 min, **d** 15 min, **e** 25 min, **f** 35 min
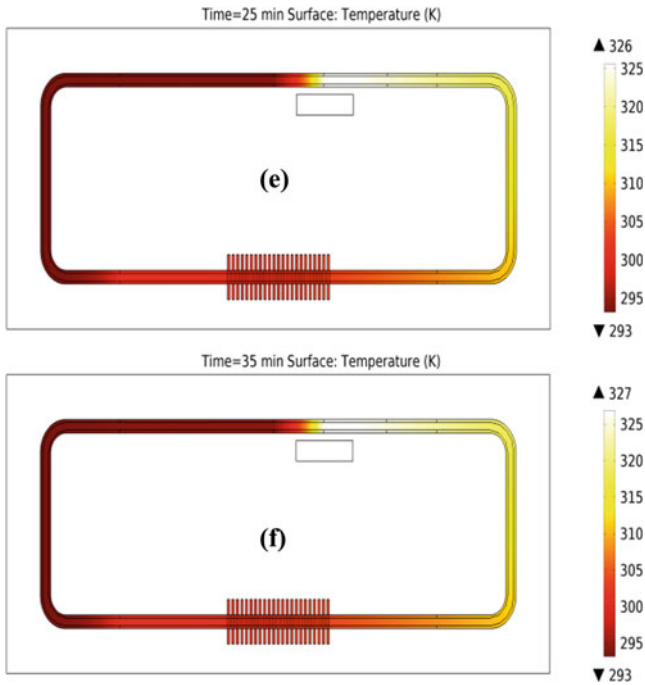
Time=25 min Surface: Temperature (K)

(e)

▲ 326
325
320
315
310
305
300
295
▼ 293

Time=35 min Surface: Temperature (K)

(f)

▲ 327
325
320
315
310
305
300
295
▼ 293

Fig. 44.5 (continued)

The temperature at the outer surface of the pipe is measured by infrared thermal imager (Testo 875i). It is based on the principle that every object above the absolute zero temperature emits infrared (IR) radiations. Based on the intensity of the IR radiation emitted by the object, the thermal imager displays the temperature of the object's surface. Thermogram as recorded by thermographic camera at an input heat load of 5 W has been presented in Fig. 44.12. The minimum and maximum temperature induced in the loop at a given instant of time is also represented in Fig. 44.13.

44.5 Conclusions

This paper is concerned with the numerical and experimental study of kerosene-based ferrofluid in a closed-loop shape under the effect of the constant magnetic field generated by a permanent magnet. Simulations were carried out using COMSOL MultiPhysics, and numerical results obtained were also validated by the experimental observations. Following inferences may be drawn from the study:

1. Ferrofluid-based cooling system was successful in dissipating the heat flux/load applied on the system. As the fluid temperature increases upon absorbing heat
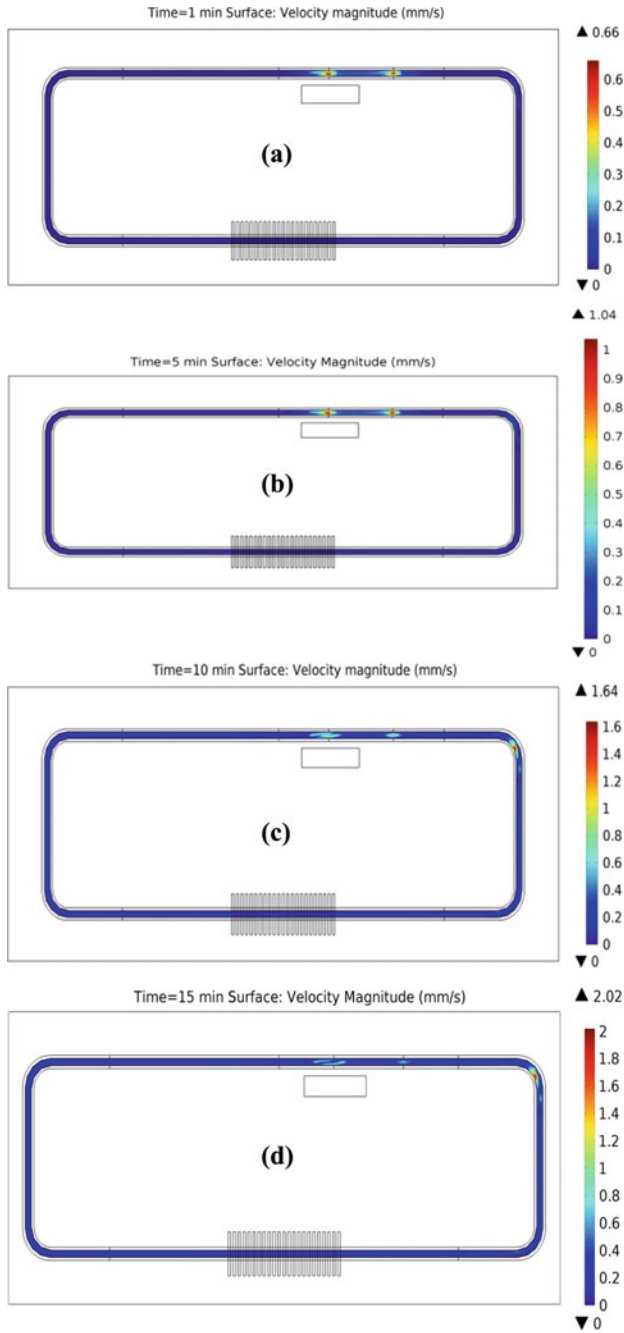
Fig. 44.6 Fluid velocity profile (mm/s) generated at different point of time. **a** 1 min, **b** 5 min, **c** 10 min, **d** 15 min, **e** 25 min, **f** 35 min
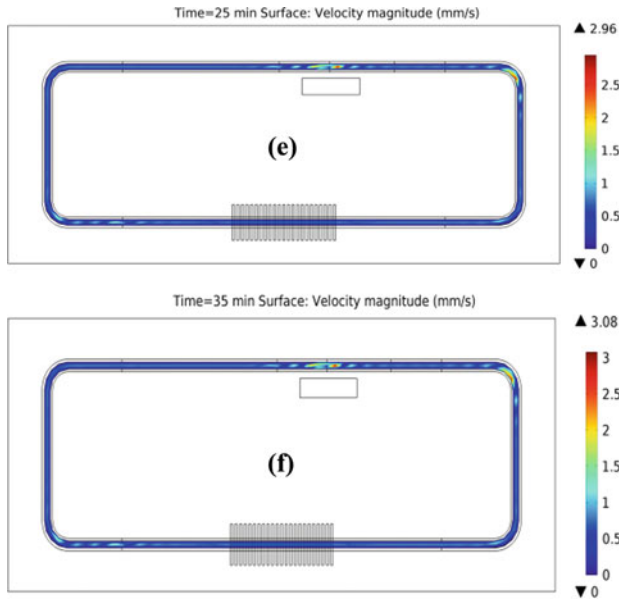
Fig. 44.6 (continued)
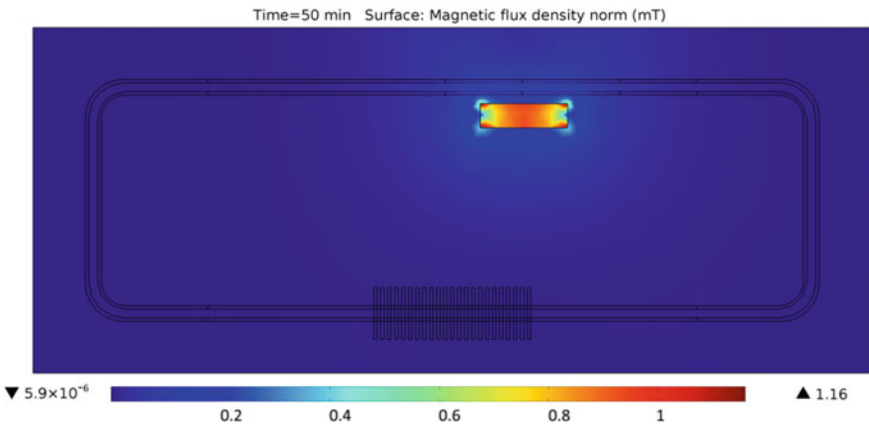
Fig. 44.7 Variation of magnetic flux density along the loop

from the heat source, due to thermal gradient along the x-axis near the magnet location, Kelvin body force begins to increase and as the fluid temperature reaches in close vicinity to the Curie temperature, driving force reaches its maximum value resulting in an increase in fluid velocity with the passage of time.

2. Maximum fluid velocity was observed near the section when the fluid was about to enter into the heated length. Due to existence of maximum temperature gradient
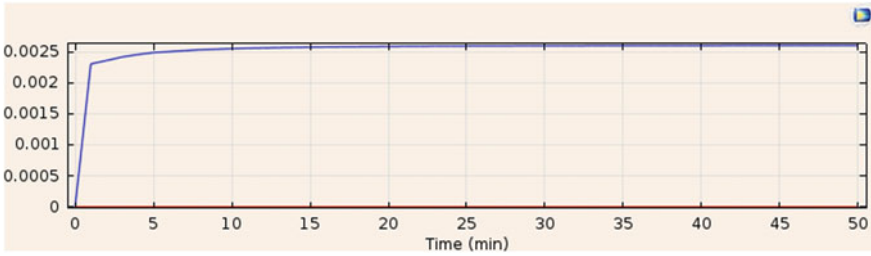
Fig. 44.8 Variation of average F_X (N/m^3) acting on the ferrofluid at different instant of time
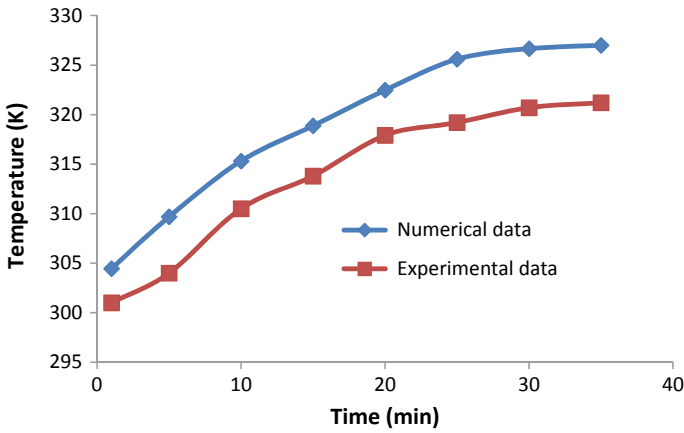
Fig. 44.9 Validation of simulation result with experimental data
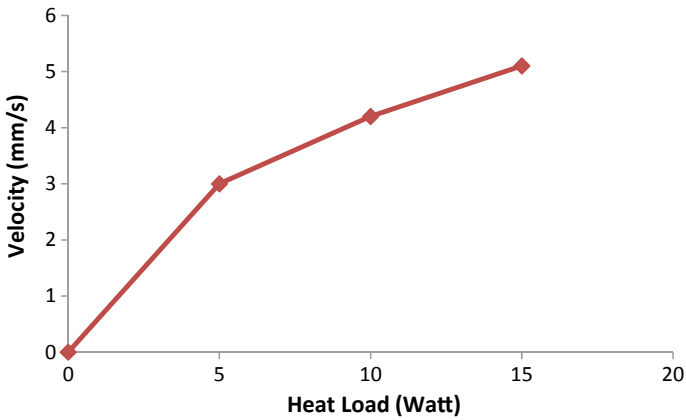
Fig. 44.10 Variation of fluid velocity with change in heat load
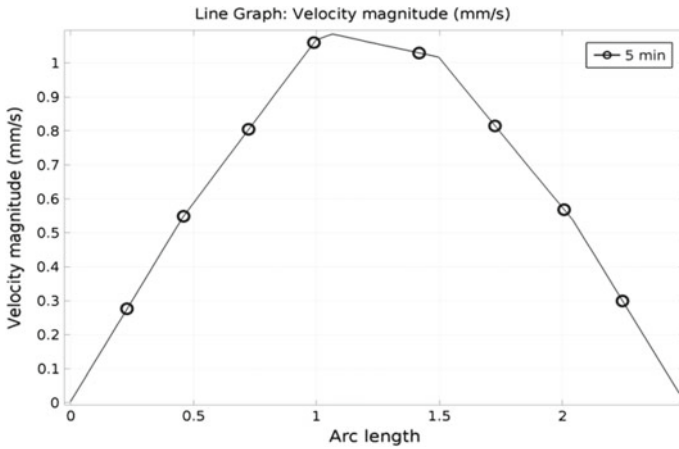
Fig. 44.11   Variation of fluid velocity at a perpendicular cut section
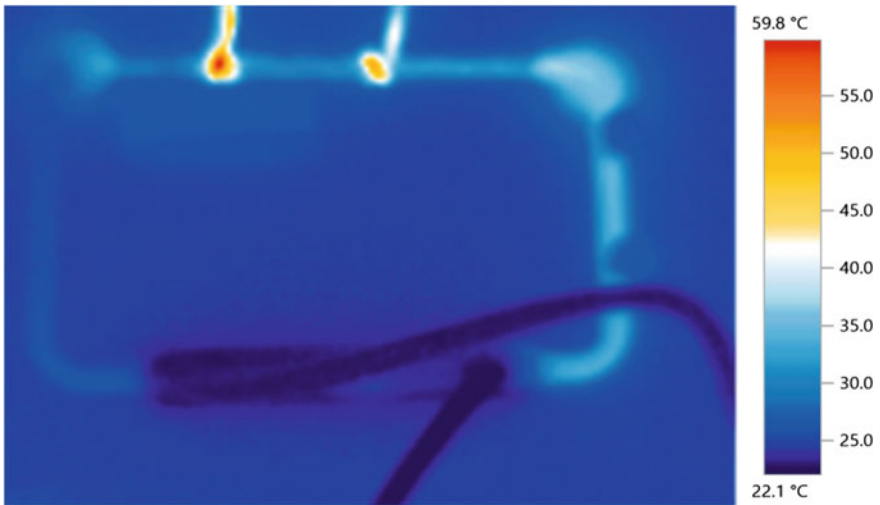
Fig. 44.12   Thermogram for the rectangular loop

at that location, fluid experiences maximum velocity near the heat source entrance section and it diminishes as the fluid moves to the other half of the loop in the lower limb.

Augmentation in the heat transfer with an increase in heat load was also observed, thus strengthening the candidature of ferrofluid as a coolant for mini/microdevices.
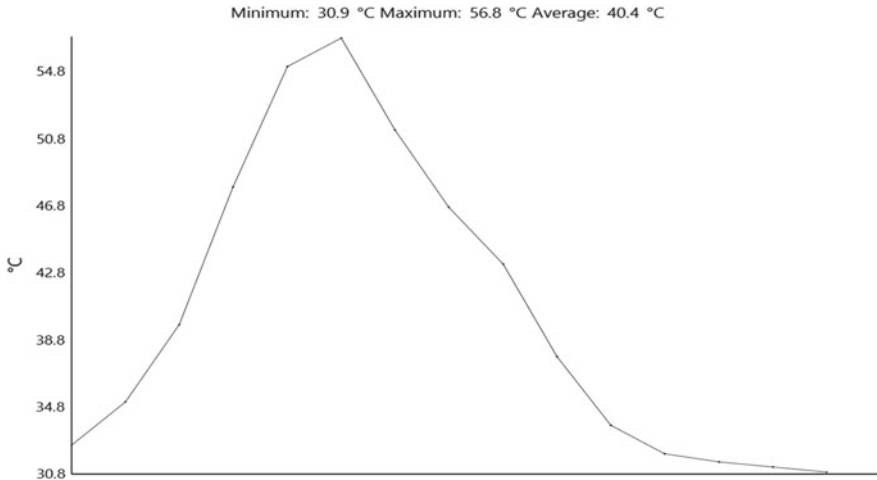
Fig. 44.13 Temperature variations in the loop as recorded by IR thermal imager

References

1. Aminfar, H., Mohammadpourfard, M., Zonouzi, S.A.: Numerical study of the ferrofluid flow and heat transfer through a rectangular duct in the presence of a non-uniform transverse magnetic field. J. Magn. Magn. Mater. **327**, 31–42 (2013)
2. Gavili, A., Zabihi, F., Isfahani, T.D., Sabbaghzadeh, J.: The thermal conductivity of water base ferrofluids under magnetic field. Exp. Therm. Fluid Sci. **41**, 94–98 (2012)
3. Goshayeshi, H.R., Goodarzi, M., Safaei, M.R., Dahari, M.: Experimental study on the effect of inclination angle on heat transfer enhancement of a ferrofluid in a closed loop oscillating heat pipe under magnetic field. Exp. Therm. Fluid Sci. **74**, 265–270 (2016)
4. Singh Mehta, J., Kumar, R., Kumar, H., Garg, H.: Convective heat transfer enhancement using ferrofluid: a review. ASME. J. Therm. Sci. Eng. Appl. **10**(2), 020801 (2017)
5. Cherief, W., Avenas, Y., Ferrouillat, S., Kedous-Lebouc, A., Jossic, L., Petit, M.: Parameters affecting forced convection enhancement in ferrofluid cooling systems. Appl. Therm. Eng. **123**, 156–166 (2017)
6. Yarahmadi, M., Moazami, H., Goudarzi, S.M.B.: Experimental investigation into laminar forced convective heat transfer of ferrofluids under constant and oscillating magnetic field with different magnetic field arrangements and oscillation modes. Exp. Therm. Fluid Sci. **68**, 601–611 (2015)
7. Aursand, E., Gjennestad, M.A., Yngve, Lervag K., Lund, H.: A multi-phase ferrofluid flow model with equation of state for thermomagnetic pumping and heat transfer. J. Magn. Magn. Mater. **402**, 8–19 (2016)
8. Sesen, M., Teksen, Y., Şendur, K., Pinar Mengüç, M., Öztürk, H., Yağc Acar, H.F., Koşar, A.: Heat transfer enhancement with actuation of magnetic nanoparticles suspended in a base fluid. J. Appl. Phys. **112**(6), 064320-1-6 (2012)
9. Rosensweig, R.E.: Ferrohydrodynamics. Cambridge University Press, New York (1985)
10. Asadi, A., Hossein, N.A., Sarhaddi, F., Keykha, T.: Laminar ferrofluid heat transfer in presence of non-uniform magnetic field in a channel with sinusoidal wall: a numerical study. J. Magn. Magn. Mater. **471**, 56–63 (2019)
11. Fadaei, F., Shahrokhi, M., Dehkordi, A.M., Abbasi, Z.: Heat transfer enhancement of Fe_3O_4 ferrofluids in the presence of magnetic field. J. Magn. Magn. Mater. **429**, 314–323 (2017)

12. Goharkhah, M., Ashjaee, M.: Effect of an alternating nonuniform magnetic field on ferrofluid flow and heat transfer in a channel. J. Magn. Magn. Mater. **362**, 80–89 (2014)
13. Gan Jia Gui, N., Stanley, C., Nguyen, N.-T., Rosengarten, G.: Ferrofluids for heat transfer enhancement under an external magnetic field. Int. J. Heat Mass Transf. **123**, 110–121 (2018)
14. Sheikholeslami, M., Gerdroodbary, M.B., Mousavi, S.V., Ganji, D.D., Moradi R.: Heat transfer enhancement of ferrofluid inside an 90° elbow channel by non-uniform magnetic field. J. Magn. Magn. Mater. **460**, 302–311 (2018)
15. Sha, L., Ju, Y., Zhang, H., Wang, J.: Experimental investigation on the convective heat transfer of Fe_3O_4/water nanofluids under constant magnetic field. Appl. Therm. Eng. **113**, 566–574 (2017)
16. Sengupta, A., Ghoshdastidar, P.S.: Heat transfer enhancement in ferrofluids flow in micro and macro parallel plate channels: a comparative numerical study. J. Therm. Sci. Eng. Appl. **10**(2), 021012 (2018)

Chapter 45
Fault Detection in Complex Mechanical Systems Using Wavelet Transforms and Autoregressive Coefficients

Amrinder Singh Minhas, Gurpreet Singh, P. K. Kankar, and Sukhjeet Singh

Abstract Vibration monitoring techniques have played a major role in the detection of faults in rotating machinery. In the present work, individual (healthy and faulty shafts, outer race fault in bearings) and combined faults (outer race fault of bearings and misalignment of shaft) have been detected using discrete wavelet transform (DWT). An autoregressive (AR) model is then constructed from the detailed coefficients of DWT to highlight the severity of the combined faults as compared to the healthy and individual faults in the system. The result shows greater fluctuations in the AR coefficients as the complexity of the faults rises in the system.

Keywords Bearing fault · Misalignment · Discrete wavelet transform · Autoregressive model

45.1 Introduction

Diagnosing bearing faults in the rotating machinery has been a challenging task in the condition monitoring especially when multiple faults are induced in a system.

Faults related to bearings are generally classified into distributed and discrete faults. Surface wear growth is a kind of distributed fault, whereas localized faults (point defects) comes under the category of discrete faults [1]. If the discrete faults

A. S. Minhas · S. Singh (✉)
Department of Mechanical Engineering, Guru Nanak Dev University, Amritsar, India
e-mail: sukhjeet.mech@gndu.ac.in

A. S. Minhas
e-mail: aminderminhas@gmail.com

G. Singh
Department of Electronics and Communication Engineering, Guru Nanak Dev University, Amritsar, India
e-mail: gurpreet.ece@gndu.ac.in

P. K. Kankar
Department of Mechanical Engineering, Indian Institute of Technology, Indore, India
e-mail: pkankar@iiti.ac.in

remain unattended, it will gradually lead to distributed faults and therefore it is important to detect the point defects in the bearings. Moreover, the fault magnitude increases at a faster pace if misalignment is present in the system. So it is crucial to examine the state of bearings with and without misalignment.

There is good literature available on the detection and diagnosis of bearing fault based on statistical parameters as well as analyzing time-domain signals [2–6]. Moreover, various frequency spectrum techniques are also employed for obtaining fault frequencies at various elements of bearings [7–9]. To extract the advantages of both time and frequency domains, many researchers have developed and efficiently applied the time-frequency techniques to analyze nonstationary nature of the bearing vibration signals [10, 11]. The peaks at these characteristic frequencies are calculated by observing the envelope spectrum of the damaged bearing. An effort has been made to improve the signal to noise ratio by combining a self-adaptive noise cancellation technique with an envelope detection method [12].

Wavelet analysis is a well-known technique and can be benignly used to investigate the bearing faults [13–16]. It is an extended time-frequency domain analysis method for identifying local features by decomposition of the time-domain signals on the basis of their frequencies by means of an adjustable window size [17]. Among various forms of wavelet transformation, one of the techniques that is extensively used is the discrete wavelet transform (DWT). This method is an effective tool for detecting single and multiple faults in the ball bearings. Impulses corresponding to characteristic defect frequencies are observed by Prabhakar and Mohanty [18] during the decomposition of signals. Similar experiments when conducted by DWT [19] capture the localized changes occurring in the signals proving the effectiveness of DWT.

On the other hand, Autoregressive (AR) is a time series based model to estimate the lagging condition of the machine due to the arrival of fault. AR model parameters are very sensitive to change in the condition of the machine and thus can act as an alert about the worsening condition of the system [20, 21]. The features extracted from the coefficients of AR model for the faulty bearing can also be fed to the classifier to automatically identify the bearing state [22].

In the present work, DWT is applied to the vibration signals extracted from the system and then AR model is constructed on the selected decomposition. The objective is to indicate the occurrence of bearing fault and to estimate the fault severity when the faulty bearing is accompanied by the misaligned shaft. To the best knowledge of the authors, there seems to be no previous work done in which ball bearing's fault severity combined with misalignment is predicted by the DWT based AR model.

45.2 Theoretical Description

45.2.1 Discrete Wavelet Transform

Discrete wavelet transform is required to discretely sample the wavelets for obtaining the components of a weak signal using decomposition at various scales of the actual signal

For a given time function $f(x)$:

$$Y(p, q) = \int\limits_{-\infty}^{+\infty} f(x)\tau_{p,q}^*(x)\mathrm{d}x \tag{45.1}$$

where * denotes complex conjugation, and $\tau_{p,q}(x) = \dfrac{\frac{1}{\sqrt{p}}\tau(x-p)}{p}$.

The scaling coefficients $A_{r,s}$ and the wavelet coefficients $D_{r,s}$ for resolutions of order greater than r can be achieved iteratively by

$$A_{r+1,s} = \sum_{n=-\infty}^{\infty} u(n-2s)A_{r,s} \tag{45.2}$$

$$D_{r+1,s} = \sum_{n=-\infty}^{\infty} v(n-2s)A_{r,s} \tag{45.3}$$

Here, u is a low-pass filter and v is a high pass filter which is obtained after analyzing original wavelet $\tau(x)$. The extraction of the original signals in the form of $A_{r,s}$ representing the lower frequency is called as approximation coefficients in the form $D_{r,s}$ representing the higher frequencies distribution is called as detailed coefficients.

The quality of wavelet analysis can be determined by adopting a suitable filter for the specific condition. Daubechies system of wavelets is chosen here for analyzing the signal because of its orthogonality, compact support in the time domain as well as the requirement of less computational effort [23].

45.2.2 Autoregressive Model

A linear combination of preceding signal values along with white noise $\chi(t)$ constitutes a linear autoregressive model signals $y(t)$ [24].

$$y(t) = \sum_{i=1}^{p} a(i)y(t-i) + \chi(t) \tag{45.4}$$

Here $a(i)$ is the model coefficients of ith AR model. As the model uses the previous output signals regressed onto itself, so it provides a forecast of the output signals. The model is able to predict the component of the signal by capturing an adequate linear relationship in the signal. Therefore, the model will execute "one-step-ahead" prediction of the vibration signal given to determine the consistency of the model.

$$y'(t) = \sum_{i=1}^{p} a(i)y(t-i) \tag{45.5}$$

The unpredictable component of the signal can be determined by computing the prediction error:

$$\chi(t) = y(t) - y'(t) \tag{45.6}$$

So a new signal will fit in a different AR model and have different AR coefficients depending upon the new model order which can provide the information on the condition of the system.

45.3 Experimental Setup and Methodology

The experimental setup consists of an induction motor of 0.75 kW, 50 Hz, 2-pole with rotor shaft coupled with a mild steel shaft using torsionally stiff spring coupling and aligned within 10 microns for recording normal state readings. The shaft is mounted on two deep groove ball bearings (make: SKF, 6204-2Z) each supported on a plummer block (refer [25] for further details). Sampling rate of 12,800 Hz is used for all the vibration signals and the data is acquired for two faulty conditions (only bearing fault and bearing fault with misalignment) besides for a healthy condition; the latter being used as baseline data for comparison with faulty conditions. The point hole of 2 mm is deliberately seeded in the outer race of bearing besides insuring 1 mm of shaft misalignment. The samples are collected for 35 Hz speed of the rotor.

Following methodology has been adopted for acquiring data from the test rig:

1. First, the time- domain and frequency spectrum of healthy and faulty system are extracted.
2. To further explore the fault-related information, the time-domain signals for healthy and faulty systems are decomposed into various approximation and detailed coefficient sub-bands using DWT.
3. Further, the energies of all sub-band for each system are calculated to select a sub-band signal for analysis.
4. To construct a suitable AR model, the model order is obtained using partial auto-correlation function (PACF) and verified by Akaike information criterion (AIC).

5. Finally, after determining model order, AR model is constructed for chosen sub-band signals of healthy and faulty system and AR coefficients are compared.

45.4 Results and Discussion

The time domain and frequency domain signals are shown in Fig. 45.1 for healthy and faulty systems respectively. The amplitude of the rotor system (i.e., faulty bearing and combination of faulty bearing and misaligned shaft) is on the higher side than the amplitude of the healthy system, which also otherwise is correct. At the same time, the fault frequencies are coming at the right places in the frequency domain of the rotor system with various faults which also gives a correct indication of the fault present in the system. In the case of a faulty bearing, as the ball rolls over the outer race (on which point defect is seeded), impulses are generated. These impulses are developed periodically according to bearing fault frequencies. The harmonics of bearing fault frequency can be observed in Fig. 45.1b.

Further, the outer race fault (ORF) amplitude increases sharply at outer race fault frequency. When the misalignment is added in the system, amplitude of sixth harmonic of shaft (at 210 Hz) coincides with 2nd harmonic of ORF frequency showing a significant rise in amplitude as observed in Fig. 45.1c. In actual operating conditions, the measured vibration signals are subdued due to the vibration coming from different sources like noise and vibrations of the other machinery operating in the vicinity of the test machine.

Localized changes of the test machine are lost in frequency spectrum because the results are averaged over the entire duration of the signal. So a time-frequency method DWT is used to analyze the transient signals that divide the signal into finer frequency ranges. The signals are decomposed into approximation and detailed coefficients. Daubechies 4 mother wavelet is used to decompose the signal up to six levels. The frequency bandwidths of approximation coefficients (A's) and detailed
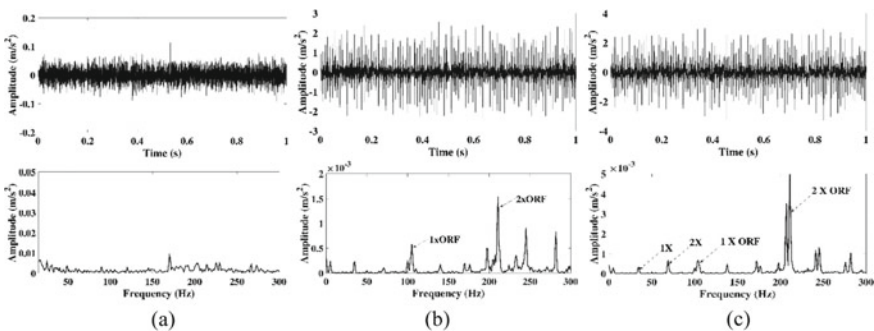

Fig. 45.1 Time domain and frequency spectrum **a** Healthy system **b** Faulty bearing system **c** Faulty bearing and misaligned system

coefficients (D's) of wavelet decompositions for a healthy system and various faulty systems are depicted in Fig. 45.2. It is important to select the signal which contains more information on the condition of the system under observation so that reliable AR model can be constructed at a later stage.

The decomposed signals are closely observed and it seems that maximum system information is captured in D2 coefficient which belongs to a higher frequency level. To confirm this, the energy level of all sub-bands for each system is calculated. When this approach is applied to every detailed coefficient of all the systems and compared as shown in Fig. 45.3 it is observed that the D2 sub-band is rich in information for all systems. So for further analysis, D2 sub-band is chosen for constructing the AR model.

AR model that represents the signal as a linear combination of its past values with an error term is proposed to the selected detailed coefficient signal for each condition (from Fig. 45.2). AR model order determined by PACF is tabulated in Table 45.1.
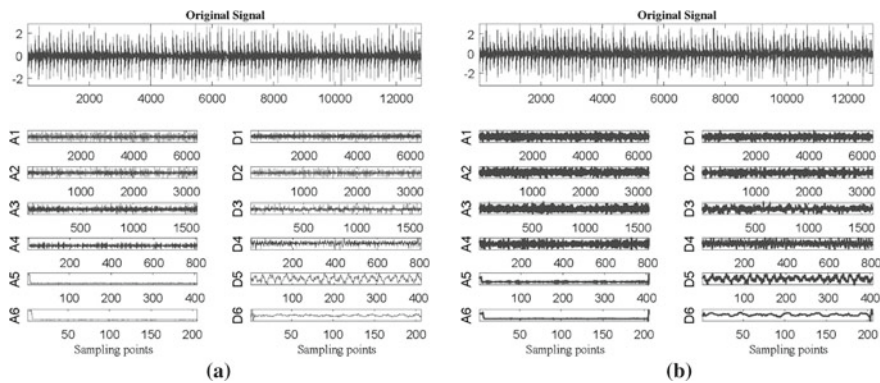
Fig. 45.2 Extraction of approximate and detailed coefficients by DWT method **a** Faulty bearing system **b** Faulty bearing and misaligned system

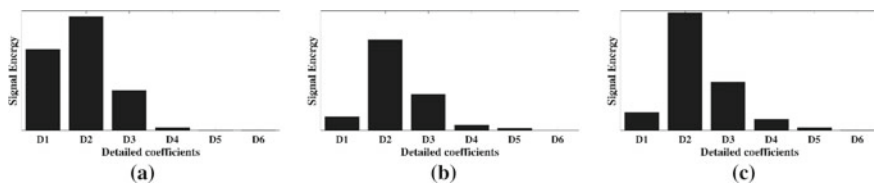**Fig. 45.3** Energy comparison of detailed coefficients **a** Healthy system **b** Faulty bearing system **c** Faulty bearing and misaligned system

Table 45.1 Estimated model order for healthy and faulty systems

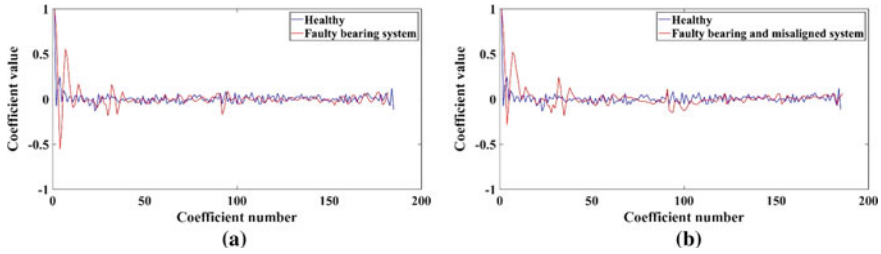| Healthy system	Fault bearing system	Faulty bearing with misaligned system
184	181	185

Fig. 45.4 AR coefficient comparison of healthy system with **a** Faulty bearing system **b** Faulty bearing with misaligned system

Table 45.2 Variance of model parameters for healthy and faulty system

Healthy system	Fault bearing system	Faulty bearing with misaligned system
0.0073	0.0167	0.0191

The determination of model order is an iterative process and needs to be determined in such a way that the both under-fitting and over-fitting of the model to the signal is avoided. So after determining the order from auto-correlation, the model order is also verified by determining the least value of AIC for the estimated model. The model order obtained in each state is compared to observe the variations in the state of the system. It is clearly noticeable from Fig. 45.4 that the variances of AR coefficients are increasing from the healthy case to the faulty case for vibration data. Moreover, the variation in coefficients seems to increase when both bearing and shaft misalignment exists in the system. The variance determined as shown in Table 45.2 verifies this observation. Thus, it can be concluded that variance of AR model parameters can be used as an indicator of a single as well as multiple faults in a system.

45.5 Conclusions

In this study, usefulness of autoregressive (AR) model is explored for indicating the severity of bearing fault with and without misalignment of shaft. AR models of vibration signals are determined for healthy and faulty systems which have 2 mm point defect on the outer race of the fault and also 1 mm shaft misalignment. Following conclusions can be inferred for the above study:

1. Time and frequency domain analysis of vibration signals does not give sufficient information to detect the severity of the damage in the acquired vibration signal.
2. The severity of the fault is well depicted from AR model coefficients extracted from the DWT signals. The fault aggravates when the combined fault (misaligned shaft + bearing fault) is acting simultaneously on the system and the same can

be determined from the variance of the AR model coefficients. Hence, AR model can be used as an efficient tool to predict the severity of the fault without much computational effort.

References

1. Antoni, J., Randall, R.: Unsupervised noise cancellation for vibration signals: part I -evaluation of adaptive algorithms. Mech. Syst. Signal Process. **18**, 89–101 (2004)
2. Gupta, P., Pradhan, M.: Fault detection analysis in rolling element bearing: a review. Mater. Today: Proceed. **4**, 2085–2094 (2017)
3. Rodriguez, P.H., Alonso, J.B., Ferrer, M.A., Travieso, C.M.: Application of the teager-kaiser energy operator in bearing fault diagnosis. ISA Trans. **52**, 278–284 (2013)
4. Paliwal, D., Choudhury, A., Tingarikar, G.: Wavelet and scalar indicator based fault assessment approach for rolling element bearings. Proced. Mater. Sci. **5**, 2347–2355 (2014)
5. Dron, J., Bolaers, F., et al.: Improvement of the sensitivity of the scalar indicators (crest factor, kurtosis) using a de-noising method by spectral subtraction: application to the detection of defects in ball bearings. J. Sound Vib. **270**, 61–73 (2004)
6. McInerny, S., Hardman, B., Sun, Q.: Investigation of fault detection algorithms applied to a helicopter input pinion bearing. Proceed. Comadem 2002 (2004)
7. Satyam, M., Rao, V.S., Devy, C.: Cepstrum analysis: An advanced technique in vibration analysis of defects in rotating machinery. Defence Sci. J. **44**, 53 (1994)
8. Tandon, N.: A comparison of some vibration parameters for the condition monitoring of rolling element bearings. Measurement **12**, 285–289 (1994)
9. Borghesani, P., Pennacchi, P., Randall, R., Sawalhi, N., Ricci, R.: Application of cepstrum pre-whitening for the diagnosis of bearing faults under variable speed conditions. Mech. Syst. Sig. Process. **36**, 370–384 (2013)
10. Guo, L., Chen, J., Li, X.: Rolling bearing fault classification based on envelope spectrum and support vector machine. J. Vib. Control **15**, 1349–1363 (2009)
11. Rai, V., Mohanty, A.: Bearing fault diagnosis using FFT of intrinsic mode functions in Hilbert-huang transform. Mech. Syst. Sig. Process. **21**, 2607–2615 (2007)
12. Mishra, C., Samantaray, A., Chakraborty, G.: Rolling element bearing defect diagnosis under variable speed operation through angle synchronous averaging of wavelet denoised estimate. Mech. Syst. Sig. Process. **72**, 206–222 (2016)
13. Raee, J., Raee, M., Tse, P.: Application of mother wavelet functions for automatic gear and bearing fault diagnosis. Expert Syst. Appl. **37**, 4568–4579 (2010)
14. Wu, J.-D., Liu, C.-H.: An expert system for fault diagnosis in internal combustion engines using wavelet packet transform and neural network. Expert Sys. Appl. 36:4278–4286 (2009)
15. Chen, H., Chua, P.S., Lim, G.: Adaptive wavelet transform for vibration signal modelling and application in fault diagnosis of water hydraulic motor. Mech. Syst. Sig. Process. **20**, 2022–2045 (2006)
16. Shi, J., Liang, M.: Intelligent bearing fault signature extraction via iterative oscillatory behavior based signal decomposition (IOBSD). Expert Syst. Appl. **45**, 40–55 (2016)
17. Daubechies, I., Grossmann, A., Meyer, Y.: Painless non-orthogonal expansions. J Math. Phys. **27**, 1271–1283 (1986)
18. Prabhakar, S., Mohanty, A., Sekhar, A.: Application of discrete wavelet transform for detection of ball bearing race faults. Tribol. Int. **35**, 793–800 (2002)
19. Mori, K., Kasashima, N., Yoshioka, T., Ueno, Y.: Prediction of spalling on a ball bearing by applying the discrete wavelet transform to vibration signals. Wear **195**, 162–168 (1996)
20. Wang, W., Wong, A.K.: Autoregressive model-based gear fault diagnosis. Trans-Am Soc Mech. Eng. J. Vib Acoust. **124**, 172–179 (2002)

21. Stack, J.R., Habetler, T.G., Harley, R.G.: Bearing fault detection via autoregressive stator current modeling. IEEE Trans. Ind. Appl. **40**, 740–747 (2004)
22. Kedadouche, M., Liu, Z., Thomas, M.: Bearing fault feature extraction using autoregressive coefficients, linear discriminant analysis and support vector machine under variable operating conditions. In: Advances in Condition Monitoring of Machinery in Nonstationary Operations, pp. 339–352. Springer (2018)
23. Mallat, S.G.: A theory for multiresolution signal decomposition: the wavelet representation. IEEE Trans. Pattern Anal. Mach. Intell. **11**, 674–693 (1989)
24. McCormick, A., Nandi, A., Jack, L.: Application of periodic time-varying autoregressive models to the detection of bearing faults, proceedings of the institution of mechanical engineers, part C. J. Mech. Eng. Sci. **212**, 417–428 (1998)
25. Singh, S., Kumar, N.: Detection of bearing faults in mechanical systems using stator current monitoring. IEEE Trans. Industr. Inf. **13**, 1341–1349 (2017)

Chapter 46
Designing of the PID and PI$^\lambda$ D$^\mu$ Controller for DC Motor

Check for updates

Parvendra Kumar and Degu Menna Eligo

Abstract In this paper, a novel approach has been proposed for consistent controller design. Engineers and scientists are often challenged with the design, analysis, and synthesis of actual problems. The development of a 'mathematical model' can be a feasible substitute for the actual problem. Here the construction of a mathematical model is from a process or plant. If the plant and the controller are described by a set of fractional differential equations then the fractional derivative and integral provide a wide range of applications for such dynamical systems. Here the stability of a DC motor is checked at a different level and it is found that, the existence of a large stability region in the complex plane with fractional-order system. Additional reliability and flexibility are obtained for system implementation in the control engineering with the large stability region. Instead of an analytically or experimentally approaches if a fractional-order controller design approach is used for a given process then the measured parameter gives the better result.

Keywords DC motor · Fractional-order system · Fractional-order calculus · Stability · MATLAB · Function under class · Ziegler–Nichols method

Nomenclature

PID	Proportional integral derivative
LTI	Linear time invariant
$G\mathrm{cl}_{ZN}$	Close-loop response of Ziegler–Nichols method
G_{Plant}	Plant transfer function
$G_{R1\mathrm{cl}}(s)$	Close-loop transfer function of plant

P. Kumar (✉) · D. M. Eligo
Department of Electrical and Computer Engineering, Wolaita Sodo University, Sodo, Ethiopia
e-mail: parvendraiitr@gmail.com

D. M. Eligo
e-mail: degmen11@gmail.com

46.1 Introduction

Model order reduction is a technique that is used in all fields of Aerospace, Chemical, Electrical, Mechanical, etc. To obtain the final product in mechanical and process control system, the role of model order reduction is important [1–3]. Usually, the analysis of large-scale systems is very complex and time-overriding [4]. For the stability checking purpose, first, a mathematical model is designed for the plant. In case, the implementing system model does not perform the desired performance, then to fulfill the requirement of the industry a controller is designed. The implementation and the order of the controller depend on the plant; it may be an integer or fractional-order. Analytical and experimental approaches are useful for the system which satisfies the Routh–Hurwitz stability criteria [5]. On the other hand, for the control system requires more flexibility and the stability region beyond the Routh–Hurwitz criteria [6–9], what an approach is suitable? A fractional-order approach [10] and [11] is used here to design the controller which has the ability to fulfill the stability condition beyond the Routh- Hurwitz criteria. Here a comparative approach provides the option to select a controller design method for the given process.

46.2 PID Controller Transfer Function

Figure 46.1 represents the block diagram for a PID controller. The representation of the PID controller in mathematical form is as,

$$u(t) = k_1 \left[e(t) + \frac{1}{T_i} \int_0^t e(t)d + T_d \frac{de(t)}{dt} \right] \tag{46.1}$$

In the block diagram, $u(s)$ denote command signal and $e(s)$ denote the error signals of the system. Here proportion gain is represented by k_1 and the integral and derivative time constants are representing by T_i, T_d, respectively. For the corresponding PID
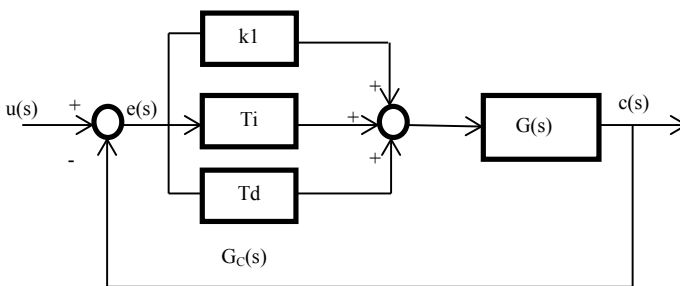

Fig. 46.1 Block diagram of a PID controller

controller, the transfer function $G_c(s)$ is given as

$$G_c(s) = k_1 \left[1 + \frac{1}{T_i s} + T_d s \right] \tag{46.2}$$

Equation (46.2) can be rewritten as

$$G_c(s) = k_1 + \frac{k_2}{s} + k_3 s \tag{46.3}$$

Here for the controller integral and derivative gain, values k_2 and k_3 are used, respectively.

To match the performance of the augmented process with the desired performance of the model, a controller is derived. A closed-loop control system should satisfy the desired performance [12, 13]. All these requirements are fulfilling by designing a PID controller in the form of full order and fractional-order.

46.3   Concept of Fractional-Order System

The addition of traditional integer order systems gives result in form of fractional-order system. Fractional-order system may be obtained from the fractional-order differential equations. A typical N-term linear fractional-order differential equation (FODE) is supposed by

$$\alpha_n D_t^{\beta_n} y(t) + \cdots + \alpha_1 D_t^{\beta_1} y(t) + \alpha_0 D_t^{\beta_0} y(t) = 0 \tag{46.4}$$

Let allowing for the control function on which input signal is applied to Fraction Order Differential Equation, Eq. (46.4) as follows:

$$\alpha_n D_t^{\beta_n} y(t) + \cdots + \alpha_1 D_t^{\beta_1} y(t) + \alpha_0 D_t^{\beta_0} y(t) = u(t) \tag{46.5}$$

After the Laplace transform of Eq. (46.5), we get

$$\alpha_n s_t^{\beta_n} Y(t) + \cdots + \alpha_1 s_t^{\beta_1} Y(t) + \alpha_0 s_t^{\beta_0} Y(t) = U(t) \tag{46.6}$$

A fractional-order transfer function obtains from Eq. (46.6) is as

$$G(s) = \frac{Y(s)}{U(s)} = \frac{1}{\alpha_0 s^{\beta_0} + \alpha_1 s^{\beta_1} + \cdots + \alpha_n s^{\beta_n}} \tag{46.7}$$

In comprehensive, for a single variable dynamic system the fractional-order transfer function of a system can be defined as

$$G(s) = \frac{b_0 s^{\gamma_0} + b_1 s^{\gamma_1} + \cdots + b_m s^{\gamma_m}}{a_0 s^{\beta_0} + a_1 s^{\beta_1} + \cdots + a_n s^{\beta_n}} \tag{46.8}$$

Here $b_i (i = 0, 1 \ldots m), a_i (i = 0, 1 \ldots n)$ are constant and $\gamma_i (i = 0, 1 \ldots m), \beta i (i = 0, 1 \ldots n)$ are random rational or real number and without missing generality, can be prescribed as $\gamma_m > \gamma_{m-1} > \cdots \gamma_0$ and $\beta_m > \beta_{m-1} > \cdots \beta_0$.

By the multi-valued transfer function, the incommensurable fractional-order system Eq. (46.8) can also be expressed incommensurable form as,

$$H(s) = \frac{b_0 s + b_1 s^{\frac{1}{v}} + \cdots + b_m s^{\frac{m}{v}}}{a_0 s + a_1 s^{\frac{1}{v}} + \cdots + a_n s^{\frac{n}{v}}}, (v > 1). \tag{46.9}$$

It is noted that Eq. (46.9) is a common representation of every fractional-order system.

46.4 Fractional-Order System Stability Conditions

Stability plays an important role in the literature to deal with the dynamical systems and their behaviors. In mathematical terminology, stability theory discourses the convergence clarifications of difference or differential equations. A linear time-invariant system is said to be stable if the roots of characteristics polynomial lie on the negative real axis. In the fractional-order system (LTI), the stability has different criteria as a comparison to integer one. Here the considerable point is that, for fractional-order system stability, the roots may lie on the right half or left half of the complex plane Figs. 46.2, 46.3, and 46.4 [14–16].

Fig. 46.2 Stability region for the corresponding fractional-order system with $0 < \alpha < 1$
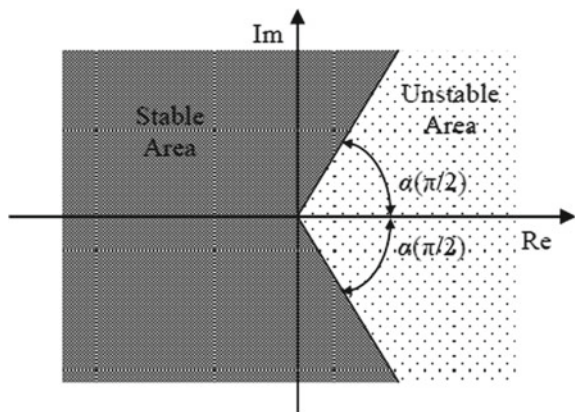
Fig. 46.3 Stability region for a corresponding fractional-order system with $\alpha = 1$
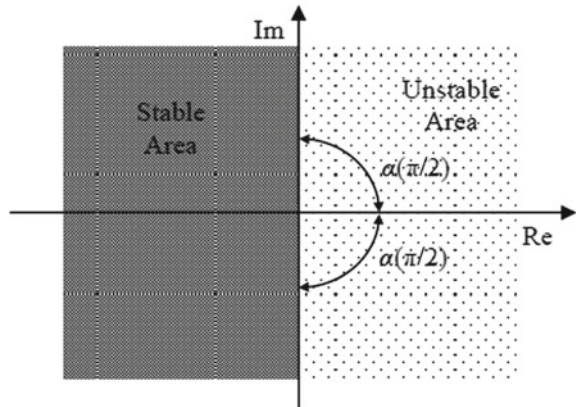

Fig. 46.4 Stability region for the corresponding fractional-order system with $1 < \alpha < 2$
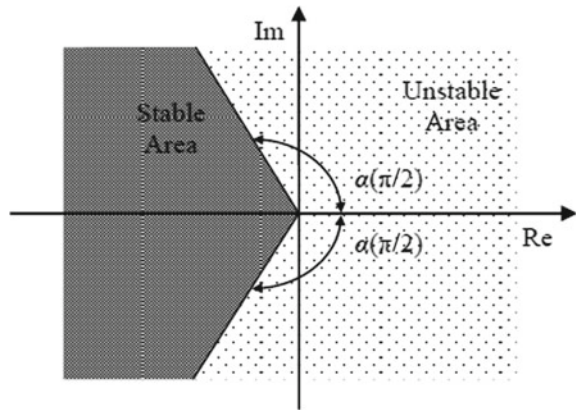
Theorem: The Matignon's stability theorem states the fractional-order transfer function $G(s) = \frac{N(s)}{D(s)}$ is stable if and only if $|\arg(\sigma_i)| = \alpha \frac{\pi}{2}$, where $\sigma = s^q$, $(0 < \alpha < 2)$ with $\forall \sigma_i \in C$, ith root of $D(\sigma) = 0$.

If $s = 0$, is a single root of $D(s)$ then the system is unstable.

This fact is demonstrated in Fig. 46.2 where the stability region for a corresponding fractional-order LTI system with order $0 < \alpha < 1$ is depicted [14–16]. For $\alpha = 1$ the stability is shown in Fig. 46.3. In this case, the region of stability corresponds to the classical s plane [15, 16]. Lastly, Fig. 46.4 shows the region of stability under the assumption of $1 < \alpha < 2$ [15, 16].

It is well known that only the poles play a significant role in the stability of a system. So, the stability intention is done by denominator part only and numerator does not have the role in stability of a FOTF. The analysis of fractional-order system stability can be done in another way also. Let us consider here, the characteristic equation of a general fractional-order system is

$$\alpha_0 s^{\beta_0} + \alpha_1 s^{\beta_1} + \cdots + \alpha_n s^{\beta_n} = \sum_{i=0}^{n} \alpha_i s^{\beta_i} = 0 \qquad (46.10)$$

For $\beta_i = \frac{v_i}{v}$, the transformation of the Eq. (46.10) into the σ-plane is,

$$\sum_{i=0}^{n} \alpha_i s^{\frac{v_i}{v}} = \sum_{i=o}^{n} \alpha_i \sigma^{v_i} = 0 \qquad (46.11)$$

Here $\sigma = s^{\frac{k}{m}}$ and m is the least common multiple of v. For a particular α_i, if the complete phase of all roots of transform Eq. (46.11) is $|\phi_\sigma| = |\arg(\sigma)|$, we can close the following points for the stability of fractional-order systems.

1. The stability condition is as $\frac{\pi}{2m} < |\arg(\sigma)| < \frac{\pi}{m}$.
2. The oscillation condition is as $|\arg(\sigma)| = \frac{\pi}{2m}$.

If any linear time-invariant fractional-order system satisfies the above two conditions then the system is stable otherwise not stable.

46.5 Fractional-Order Controller Design

For fractional-order control systems, most works are theoretical in nature. Till now, the application has no big coverage. In the main objective of this paper is to analyze the fractional-order control (FOC) system to examine the control performance. A PID controller may be converted into fractional-order $PI^\lambda D^\mu$ controller with integrator of real order λ and differentiator of real order μ. The transfer function of this type of controller in Laplace domain is

$$C(s) = K_P + \frac{K_I}{s^\lambda} + K_D s^\mu, (\lambda, \mu > 0) \qquad (46.12)$$

Here K_P, K_I, and K_D are the proportional gain constant, integral gain constant and the derivative gain constant respectively. For a classical PID controller $\lambda = 1$ and $\mu = 1$. If $\mu = 0$ and $\lambda = 0$, we obtained a PI^λ and PD^μ controller, respectively. These whole controllers are the case of $PI^\lambda D^\mu$ controller, which offers flexibility with a chance to change the dynamic property of fractional-order control systems. Basically, to design such a controller, two steps are used here.

Step 1: The design of K_P.

Overshoot [Pr], settling time [T_s], and static error [E_t] belong to the Proportional gain K_P. Broadly the K_P can be obtained by

$$K_P \geq \left(\frac{100}{E_t} \right) \qquad (46.13)$$

Here the selection of proportional gain K_P is for minimum static error.

Step 2: In this step, the parameters K_D, μ, K_I, and λ are designed.

To obtain the value of these parameters for Fractional-Order controller design, the analysis given below is necessary.

Let us assume the controller transfer function is $C(s)$, plant or process transfer function is $G(s)$ and the system has unity feedback. The formula for phase margin of controlled system [14, 17] is

$$\Phi_m = \arg\left[C(j\omega_g)G(j\omega_g)\right] + \pi \qquad (46.14)$$

Here $j\omega_g$ is the notation for crossover frequency. Phase margin is a constant phase or independent. This can be skilled by controller of the form

$$C(s) = k_1\frac{k_2 s + 1}{s^v}, k_1 = \frac{1}{K_{\text{plant}}}, k_2 = \tau \qquad (46.15)$$

Here the gain and time constant of plant are K_{plant} and τ, respectively.

Now from the Eqs. (46.14) and (46.15)

$$\begin{cases} \phi_m = \arg\left[C(j\omega_g)G(j\omega_g)\right] + \pi \\ \quad = \arg\left[\dfrac{k_1 k_{\text{plant}}}{j\omega^{(1+v)}}\right] + \pi \\ \quad = \arg\left[(j\omega)^{-(1+v)}\right] + \pi \\ \quad = \pi - (1+v)\dfrac{\pi}{2} \end{cases} \qquad (46.16)$$

We fix the gain margin for a given plant. After putting the value of gain in Eq. (46.16) one can find out the value of v and the values of k_1 and k_2 are obtained from Eq. (46.15). Now by using these constants in Eq. (46.15), a fractional I$^\lambda$D$^\mu$ controller obtained, which is a specific case of PI$^\lambda$D$^\mu$ controller, has the form

$$C(s) = k_1 k_2 s^{(1-v)} + k_1 s^{-v}; \ K_D = k_1 k_2 \text{ and } K_I = k_1 \qquad (46.17)$$

For the given value of K_P the full transfer function of fractional-order controller is

$$C(s) = K_P + K_D s^{(1-v)} + K_I s^{-v} \qquad (46.18)$$

After comparison with Eq. (46.12), we can say

$$\mu = (1 - v) \text{ and } \lambda = v$$
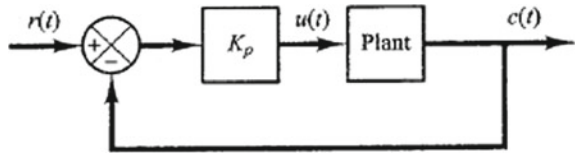
Type of controller	K_p	T_i	T_d
P	$0.5\,K_{cr}$	∞	0
PI	$0.45\,K_{cr}$	$1/1.2\,P_{cr}$	0
PID	$0.6\,K_{cr}$	$0.5\,P_{cr}$	$0.125\,P_{cr}$

46.6 Controller Design Using Ziegler–Nichols Second Method

The method allows us to set $T_i = \infty$ and $T_d = 0$. As the proportional control action increase K from 0 to a critical value K_{cr} at which the output shows sustained oscillations in the system Fig. 46.5.

Thus, the critical gain K_{cr} and the corresponding time period P_{cr} are obtained by experiment. By the Ziegler–Nichols second method, the values of the parameters K_p, T_i, and T_d can be obtained from Table 46.1.

The PID controllers tuned by the second method of Ziegler–Nichols rules give [18].

$$Gc(s) = K_p\left(1 + \frac{1}{T_i s} + T_d s\right) \tag{46.19}$$

$$= 0.6K_{cr}\left(1 + \frac{1}{0.5P_{cr}s} + 0.125P_{cr}s\right)$$

$$= 0.075K_{cr}P_{cr}\frac{\left(s + \frac{4}{P_{cr}}\right)^2}{s} \tag{46.20}$$

Equation (46.20) shows that the PID controller has a pole at the origin and double zeros at $s = \frac{-4}{P_{cr}}$.

46.7 Examples

Here we are conceding the general model [19] of DC motor as shown in Fig. 46.6. The angular velocity $\omega(t)$ is controlled by the applied voltage V_a

The mathematically model of DC motor is given as in Fig. 46.7.
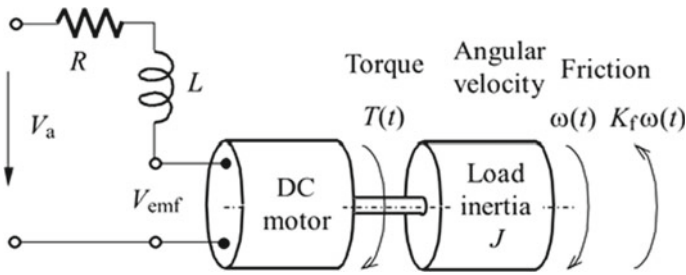
Fig. 46.6 General model of DC motor
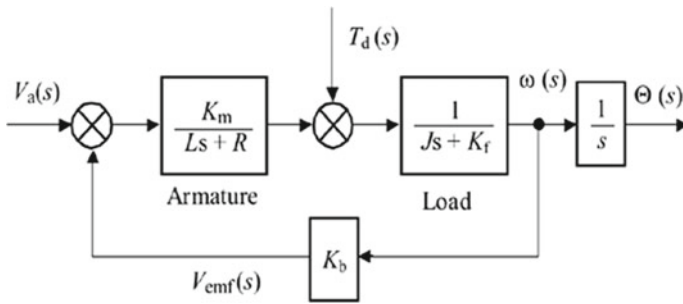
Fig. 46.7 Mathematical model of a DC motor

The obtained transfer function of the DC motor is

$$G_{\text{DCM}}(s) = \frac{\theta(s)}{V_a(s)} = \frac{K_m}{s[(Ls + R)(Js + K_f) + K_b K_m]} \tag{46.21}$$

In most application the time constant of DC motor is negligible therefore the simplified continuous mathematical model has the following form:

$$G_{\text{DCM}}(s) = \frac{\theta(s)}{V_a(s)} = \frac{K_m}{s[R(Js + K_f) + K_b K_m]}$$

$$= \frac{K_{\text{DCM}}}{\tau(\tau s + 1)} \tag{46.22}$$

where $\tau = \frac{RJ}{(RK_f + K_b K_m)}$ and $K_{\text{DCM}} = \frac{K_m}{(RK_f + K_b K_m)}$. It is also noted that $K_m = K_b$
For the give DC motor, the physical parameter is as

$$R = 6\,\Omega$$

$$K_m = K_b = 0.1$$

$$K_f = 0.2\,\text{N ms}$$

$$J = 0.01\,\text{kgm}^2/\text{s}^2$$

With the help of given constant, obtained transfer function is

$$G_{\text{DCM}}(s) = \frac{0.08}{s(0.05s + 1)} \tag{46.23}$$

46.7.1 Controller Design by Ziegler–Nichols Method with Stability and Sensitivity Analysis

The first requirement is to find out the starting point for K_p and double zeros.

Let start the tuning with considering the K_p only. Here, the closed-loop response is

$$G\text{cl}_{\text{ZN}} = \frac{C(s)}{R(s)} = \frac{0.08K_P}{s(0.05s + 1) + K_P} \tag{46.24}$$

By the help of Routh–Hurwitz criteria, the value of K_P for sustained oscillations is $K_P \geq 62.5$.

We set the value in MATLAB program with a hit and trial range.

After putting the values in $Gc_{\text{ZN}}(s) = K_p\left(1 + \frac{1}{T_i s} + T_d s\right)$, we find out the controller transfer function $Gc_{\text{ZN}}(s) = \frac{37.4s^2 + 523.6s + 1833}{s}$.

So here the initial values are obtained. According to the prerequisite of manufacture, one can set the value of maximum overshoot in programming. In general, permitting the better establishing of the system, the maximum overshoot should be between 10 and 40%. Using the MATLAB program, we vary the gain 120–30 with step size -0.2 and zeros as 7 to 0.3 with step size -0.2. Fine-tuning gives the following results:

Gain $(K) = 37.4$ and Zeros $(a) = 7$
Maximum overshoot $(m) = 1.05$.

The absolute close-loop transfer function of the given system is

$$Gcl_{ZN}(s) = \frac{2.992s^2 + 41.89s + 146.6}{0.05s^3 + 3.992s^2 + 41.89s + 146.6} \tag{46.25}$$

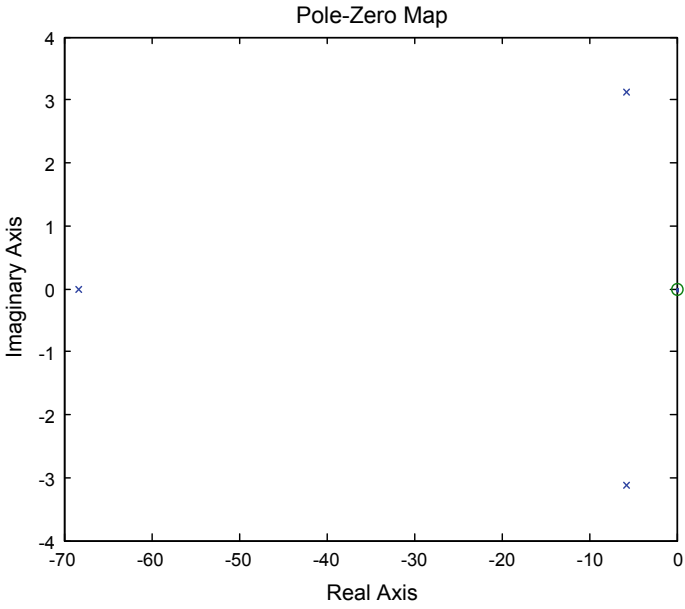Figure 46.8 shows the stability region and Fig. 46.9 Shows the step response of the system.

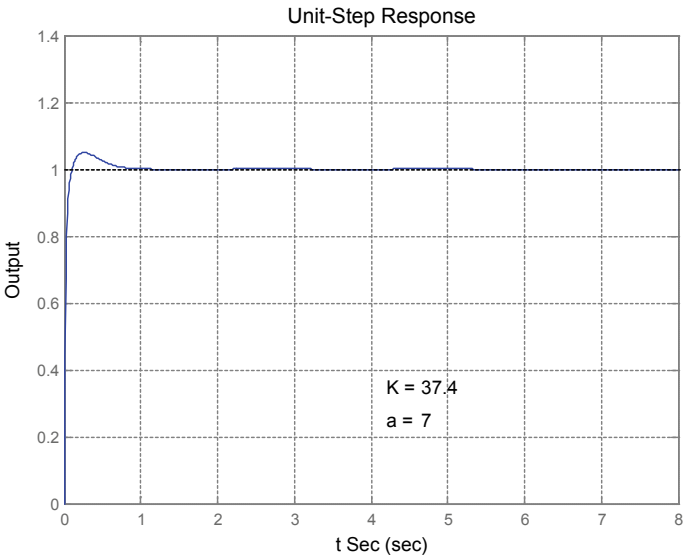**Fig. 46.8** Pole location on Pole-Zero Map of $Gcl_{ZN}(s)$

Fig. 46.9 Unit step response of the closed-loop $Gcl_{ZN}(s)$ system

46.7.2 Stability Check and Robust Controller Design by Fractional-Order Method

A robust controller is less sensitive to the parameter changes of the controlled system [20]. The uncertainty can be caused by non-precise identification. A controller with fractional-order is less sensitive to changes in controlled system parameters. The representation of FOPDT system with parameters uncertainty is

$$G(s) = \frac{[\underline{k}, \bar{k}]}{s([\underline{\tau}, \bar{\tau}]s + 1)} \tag{46.26}$$

where $\bar{k}$, $\bar{\tau}$, and $\underline{k}$, $\underline{\tau}$ are the upper and lower limits of the given parameters.

For maximum and minimum gain plot, the given system transfer function is shown respectively as

$$G_{R1}(s) = \frac{[\bar{k}]}{s([\underline{\tau}]s + 1)} \tag{46.27}$$

$$G_{R2}(s) = \frac{[\underline{k}]}{s([\bar{\tau}]s + 1)} \tag{46.28}$$

In the given example the transfer function of the DC motor is

$$G_{\text{Plant}} = \frac{0.08}{s(0.05s + 1)} \tag{46.29}$$

The technique proposed in Sect. 46.4 can be used here for fraction order controller design. According to this

Step 1: To design the K_P.

For least static error, the value of proportional gain $K_P = 10$, from Eq. (46.29)

Step 2: In this step, the parameters K_D, μ, K_I, and λ are designed.

The value of a time constant $\tau = 0.05$ and gain of Plant $K_{\text{Plant}} = 0.08$ respectively Eq. (46.29).

Let us fix the gain margin $\phi_m \geq 60°$ for the given system. Then we find out the value of $v = 0.3$ by Eq. (46.16). The other desired value $k_1 = 12.5$ and $k_2 = 0.05$ are obtained from Eq. (46.15). Now putting these values in Eq. (46.17), we got

$$C_{\text{FO}}(s) = 0.625s^{0.7} + \frac{12.5}{s^{0.3}} \tag{46.30}$$

Now after adding the value of $K_P = 10$ from step 1 into Eq. (46.30), we can obtain the final transfer function of fractional-order controller as

$$C_{\text{FO}}(s) = 10 + 0.625s^{0.7} + \frac{12.5}{s^{0.3}} \tag{46.31}$$

To make robust of the system an obtained controller transfer function is used with the transfer function obtained for maximum and minimum gain as given in Eq. (46.27) and Eq. (46.28). The open-loop control system for controller and plant $G_{R1}(s)$ is

$$G_{R1ol}(s) = \frac{0.0625s + s^{0.3} + 1.25}{0.04s^{2.3} + s^{1.3}} \tag{46.32}$$

For the given DC motor, the closed-loop transfer function with unity feedback is obtained as

$$G_{R1cl}(s) = \frac{C(s)G_{\text{Plant}}(s)}{1 + C(s)G_{\text{Plant}}(s)}$$

Or

$$G_{R1cl}(s) = \frac{0.0625s + s^{0.3} + 1.25}{0.04s^{2.3} + s^{1.3} + 0.0625s + s^{0.3} + 1.25} \tag{46.33}$$

The open-loop control system for controller and plant $G_{R2}(s)$ is

$$G_{R2ol}(s) = \frac{0.6s + 0.03750s^{0.3} + 0.750}{0.06s^{2.3} + s^{1.3}} \tag{46.34}$$

For the given DC motor, the close-loop transfer function with unity feedback is obtained as

$$G_{R2cl}(s) = \frac{0.3750s + 0.6s^{0.3} + 0.750}{0.06s^{2.3} + s^{1.3} + 0.03750s + 0.6s^{0.3} + 0.750} \tag{46.35}$$

The function *is stable* checked the denominator of $G_{R1cl}(s)$ and $G_{R2cl}(s)$, it is found that $K = 1$, indicate the system is stable. Here, Figs. 46.10 and 46.11 show that system controlled by fractional-order controller has more stability region and Fig. 46.12 Indicate that the complete designed system is stable.

Figure 46.12 shows that the closed-loop response of the system shown in both plants is almost the same. This means that due to the parameter variation there is no such effect on the stability and the system has a robust performance. The response for all three designed systems is shown in Fig. 46.13.
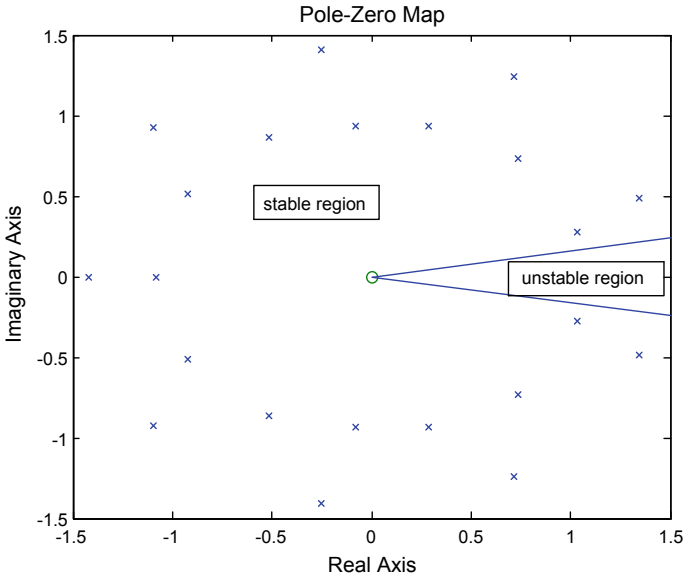
Fig. 46.10 Pole position of a closed-loop system $G_{R1cl}(s)$
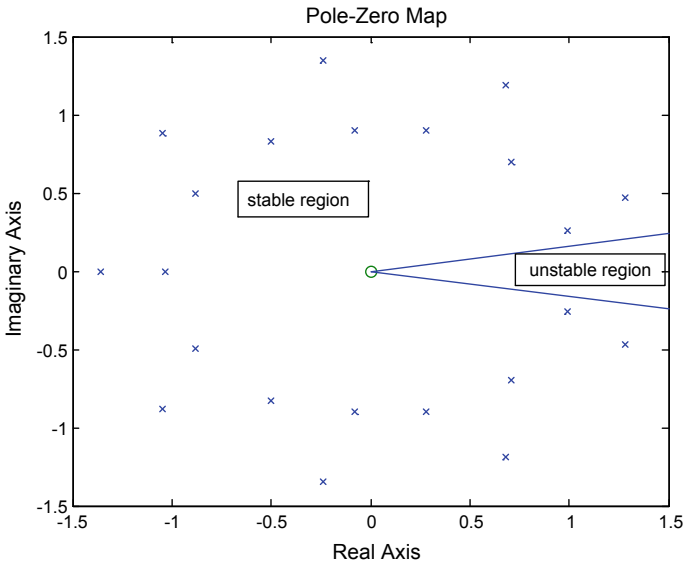

Fig. 46.11 Pole position of a closed-loop system $_{GR2cl}(s)$
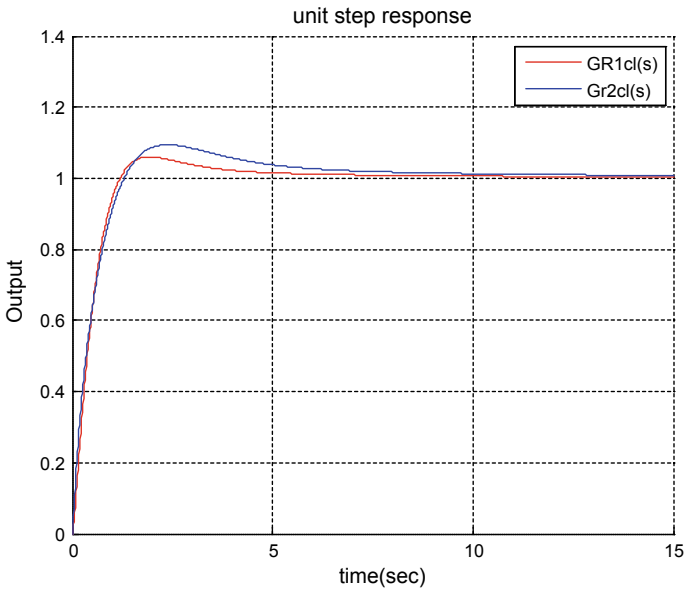
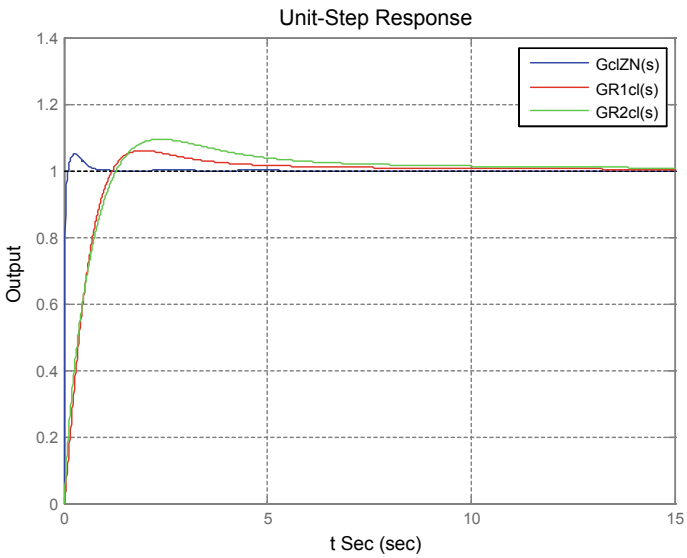**Fig. 46.12** Step response of closed-loop system $G_{R1cl}(s)$ and $G_{R2cl}(s)$

Fig. 46.13 Simultaneously unit step response of all designed systems

Table 46.2 Comparison for performance specification of designed controllers

Controller design	Ziegler–Nichols method	Fractional-order method	Fractional-order Method
Models	Full model	Full model	Full model
Specifications	$Gcl_{ZN}(s)$	$G_{R1cl}(s)$	$G_{R2cl}(s)$
Rise time (s)	0.0454	0.878	0.881
Settling time (s)	0.55	13.2	14
Peak amplitude	1.05	1.06	1.09
Overshoot (%)	5	6	9
At time (s)	0.26	1.87	2.32

46.8 Conclusions

On behalf of the result shown in Table 46.2, some important points may be described for the tuning of the controller. All basic ideas of fractional calculus, the stability of fractional-order system, robustness, and MATLAB function are presented here. The robustness analysis is investigated for the given real-time example. The core objective of the paper is to draw attention towards fractional-order system stability and analysis over a conservative way. Here a DC motor is controlled by a full order controller and fractional-order controller. It concludes here that the fractional-order system has more robustness and a large region for stability which improves the performance of the system. In Table 46.2 all transient parameters of fractional-order controller design system and conventional controller design are given. The conventional controller design has a better transient response over fractional-order controller design system. But in the fractional-order, the larger stability region provides more flexibility in the system. We trust that the relative approach used in this paper will provide the optimum method for designing the controller.

References

1. Gutman, P., Mannerfelt, C., Molander, P.: Contributions to the model reduction problem. IEEE Trans. Autom. Control **AC-27**(2), 454–455 (1982)
2. Bandyopadhyay, B., Rao, A., Singh, H.: On Pade approximation for multivariable systems. IEEE Trans. Circ. Syst. **36**(4), 638–639 (1989)
3. Smamash, Y.: "Truncation method of reduction: a viable alternative. Electron. Lett. **17**(2), 97–98 (1981)
4. Jamshidi, M.: An overview on the aggregation of large-scale systems, pp. 9–92 (1981)
5. Shamash, Y.: Model reduction using the Routh stability criterion and the Pade approximation technique. Int. J. Control **21**(3), 475–484 (1975)
6. Alfi, A., Tenreiro Machado, J.A.: Stabilization of fractional-order systems subject to saturation element using fractional dynamic output feedback sliding mode control. J. Comput. Nonlinear Dyn. **12**, 0310141–0310146 (2007)

7. Alfi, A., Khosravi, A., Lari, A.: Swarm-based structure-specified controller design for bilateral transparent teleoperation systems via synthesis. IMA J. Math. Control Inf. **31**, 111–136 (2014)
8. Mousavi, Y., Alfi, A.: A memetic algorithm applied to trajectory control by tuning of fractional order proportional-integral-derivative controllers. Appl. Soft Comput. **36**, 599–617 (2015)
9. Alfi, A., Fateh, M.M.: Intelligent identification and control using improved fuzzy particle swarm optimization. Expert Syst. Appl. **38**, 12312–12317 (2011)
10. Axtell, M., Bise, E.M.: Fractional calculus applications in control systems. In: Proceeding of the IEEE 1990 National Aerospace and Electronics Conference, New York, pp. 563–566 (1990)
11. Dorcak, L.: Numerical models for simulation the fractional-order control systems, pp. 62–68. UEF SAV, The Academy of Sciences Institute of Experimental Physics, Kosice, Slovak Republic (1994)
12. Hassanpour, H., Ghadi, A.R.: Image enhancement via reducing impairment effects on image components. Int. J. Eng.-Trans. B Appl. **26**(11), 1267–1274 (2013)
13. Soltani, J., Abjadi, N., Pahlavaninezhad, M.: An adaptive nonlinear controller for speed sensor less PMSM taking the iron loss resistance into account (research note). Int. J. Eng.-Trans. B: Appl. **21**(2), 151–160 (2008)
14. Chen, Y.Q., Petras, I., Xue, D.: Fractional order control—a tutorial. In: American Control conference, 10–12 June 2009
15. Petras, I.: Stability of fractional-order systems with rational orders: a survey. Fract. Calc. Appl. Anal. **12**(3), 269–298 (2009)
16. Petras, I.: Stability of fractional-order systems with rational orders. Mathematics—dynamical systems, pp. 1–25 (2008). arXiv: 0811.4102v2
17. Pilla, R., Tummala, A.S., Chintala, M.R.: Tuning of extended Kalman filter using self-adaptive differential evolution algorithm for sensorless permanent magnet synchronous motor drive. IJE Trans. B Appl. **29**(11), 1565–1573 (2016)
18. Oldham, K.B., Spanier, J.: The Fractional Calculus. Academic Press, New York (1974)
19. Vinagre, B.M. Podlubny, I., Dorcak, L., Feliu, V.: On fractional PID controllers: a frequency domain Approach. In: Proceeding of the IFAC Workshop on Digital Control PID'00, Terrassa, Spain, pp. 53–55 (2000)
20. Yan, Z., He, J., Li, Y., Li, K., Song, C.: Realization of fractional order controllers by using multiple tuning-rules. Int. J. Signal Process. Image Process. Pattern Recogn. **6**(6), 119–128 (2013)

Chapter 47
Sustainable Manufacturing-Related Aspects in Turning Operation: A Review Based Study

Ravi Pratap Singh, Ravinder Kataria, and Amit Kumar Tiwari

Abstract Subjected to natural concern and developing controls over pollution and contamination, the interest for sustainable and biodegradable cutting fluids rising. The continued use of conventional cutting fluid is being challenged to minimize the volume of fluids, reduce the health problems, and bio-certification. Cutting Fluids of different kinds are typically utilized to control the temperature in machining. As per the studies, 60% of companies are investing 20% more sum on their coolants/lubricants than on cutting tools. Functions like improving apparatus life and machining process proficiency, improve surface finishing and part accuracy, reducing cutting powers and vibrations get by using cutting fluids. Mineral, synthetic and semi-synthetic cutting fluids include in the environmental cycle with air, soil, water, and their danger impact harm the environment. In this paper, an attempt made concerning reducing the problems in machining and vegetable-based cutting fluids can also be used to optimize machining conditions.

Keywords Taguchi method · Tool life · Vegetable-based cutting fluids · Surface roughness

47.1 Introduction

In the present manufacturing industry, the interest is developing for ease, high profitability, and great item quality. High profitability that is naturally connected with high cutting velocity, feed rate and profundity of cut, essentially leads to a lot of warmth age and raise the temperature at the cutting zone [1]. In late decades, the negative effects of conventional cutting liquids are ending up increasingly noticeable. Traditional cutting fluids are viable in cooling, oil and carrying away chips during

R. P. Singh
Department of Industrial and Production Engineering, Dr B R Ambedkar National Institute of Technology, Jalandhar, India

R. Kataria (✉) · A. K. Tiwari
Lovely Professional University, Jalandhar, India
e-mail: kataria.ravinder07@gmail.com

machining tasks such as boring, turning and grinding [2]. In 2005, roughly 85% of the cutting liquids utilized far and wide are mineral-based cutting liquids, the most elevated interest among the others [3].

In this investigation, vegetable oils are utilized as the cutting liquid and are contrasted and customary oil and dry machining. Vegetable oils perform superior to different oils and the reasons are depicted as pursues:

(1) Vegetable oil has great lubricity properties.
(2) Vegetable oil has a higher blaze point, which lessens smoke development and flame danger. Higher blaze point esteem permits utilizing the cutting liquid in high-temperature cutting conditions.
(3) Vegetable oil atoms are very homogenous in size, be that as it may, mineral oil particles shift in size. Thusly, the properties of mineral oil, for example, consistency, bubbling temperature are progressively defenseless to variety.
(4) Vegetable oil has a higher breaking point and more noteworthy atomic weight and this outcome in less misfortune from vaporization and clouding [4].

47.2 Categories and Practices of Traditional Cutting Fluids in Machining Operation

For the most part, cutting liquids can be separated into three fundamental classes, for example, oil-based, watery-based, and gas-based (appeared in Fig. 47.1). Oil-based cutting liquids are utilized in tasks that require a decent greasing up property while watery-based cutting liquids are ideal where cooling and greasing up properties are
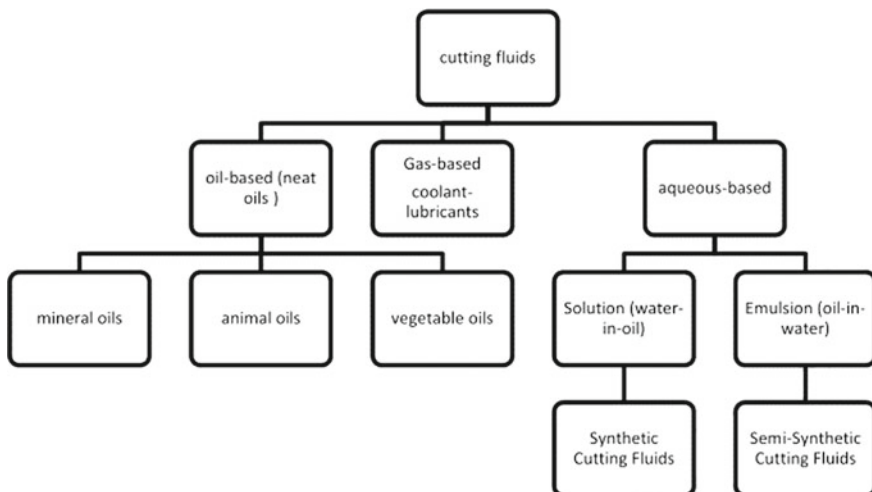

Fig. 47.1 Classification of Cutting Fluids [1]

Table 47.1 Various vegetable oils as lubricants [5]

Advantages	Disadvantages
Low pollution of the environment	Low thermal stability
High biodegradability	Oxidative stability
High flashpoints	High freezing points
Wide production possibilities	Poor corrosion protection
Low production cost	
Low toxicity	

basic. Watery-based cutting liquid can be additionally partitioned into emulsions and arrangements structure [1].

In summary, vegetable oils do show numerous alluring attributes, which make them appealing greases for some functional applications. Table 47.1 demonstrates the focal points and weaknesses of vegetable oils as metalworking liquids. In this investigation, the use of vegetable oil-based metalworking liquids in machining different evaluations of materials has been checked on and their applications as an option in contrast to mineral-based oil are featured.

47.3 Effect of Turning Process Parameter on Vegetable-Based Coolants

Ramana et al. [6] conducted examinations of three cutting conditions, for example, dry, palm oil, blend of palm oil and boric corrosive grease as far as surface roughness. The Taguchi strategy is utilized to discover the ideal cutting parameters for surface unpleasantness. The outcome showed that palm oil is higher in execution contrasted with dry and palm oil with boric corrosive blend as cutting fluid in this work. Khan et al. [7] displayed the impacts of least amount grease (MQL) by vegetable oil-based cutting liquid on the turning execution of low combination steel AISI 9310. It was additionally observed from the outcomes that the generous decrease in tool wears brought about upgraded the tool life and surface completion and improves the machinability qualities. Adithan et al. [8] examined the execution of coconut oil (vegetable-based) on the machining of AISI 304 material with a carbide instrument. They made sense of that coconut oil had improved the surface completion as well as diminished the instrument wear contrasted with mineral oils. Liu et al. [9] examined the impacts of air-cooling on the machinability of Ti–6Al–4V titanium compound in the hard-turning procedure. Results demonstrated that the compacted cooling air as gas altogether diminishes cutting temperature, instrument wear, and surface unpleasantness. Julie et al. [10] used L 9 Taguchi structure to think about an exploratory soybean-based cutting liquid against dry and mineral-based cutting liquids in turning activities. The exploratory information investigation uncovered

that soybean-based cutting liquid accomplished comparative execution in diminishing surface unpleasantness yet better with respect to on tool wear contrasted with oil-based cutting liquids (Table 47.2).

From the literature review, it is observed that various different types of vegetable-based cutting fluids used in machining. The list of are mentioned in below Table 47.3. Research work has been seen on vegetables-based coolants and that lubricant gives the positive results on machining.

Jayal et al. [1] reviewed some ongoing patterns and new ideas that are rising for assessing the maintainability substance at the item, procedure, and framework levels for empowering supportable assembling. It further features this requires improved item execution models, prescient procedure models and enhancement of individual assembling forms. Some ongoing patterns in creating improved and rearranged manageability scoring strategies for the item and procedure structure, and in creating prescient models and advancement systems for economical assembling. Khan et al. [2] shown the effects of least sum oil (MQL) by vegetable oil put together cutting oil with respect to the turning execution of low mix steel AISI 9310 when stood out from absolutely both machining in regards to chip–contraption interface temperature, chip course of action mode, instrument wear and surface unpleasantness. The base sum oil was outfitted with a shower of air and vegetable oil. MQL machining was performed much better about than the dry and wet machining. It was also seen from the results that the liberal abatement in device wears achieved updated the apparatus life and surface finish and improves the machinability characteristics. Adam et al. [3] concentrated on the investigation of surface harshness and chip arrangement amid processing activity of Mild Steel utilizing vegetable-based oil as an oil. Test set up structured by utilizing the processing machine. Taguchi Method of Symmetrical Array with a factorial plan of investigations is used to examine the reaction. Analysis of Variance (ANOVA) method was utilized to investigate the impact of procedure parameters and their connection amid machining. From the investigation, it is seen that cutting speed is the most noteworthy factor superficially harshness pursued by profundity of cut and feed rate. While Sunflower Oil gives the least surface harshness by setting of the best blend parameter. Biswojyothi et al. [4] researched the crushing of Titanium compound Ti–6Al–4V with MQL parameters. The investigations led permitted improvement of the innovative frameworks of ecologically well-disposed dry machining with remuneration of physical impacts of cutting liquids, which is wanted to be utilized to supplant customary machining advances with the utilization of cutting liquids [5]. The utilization of vegetable oils [6] may permit this blend, to make conceivable the advancement of another age of cutting liquids where elite in machining could be joined with great condition similarity. Enthusiasm for vegetable oil-based cutting liquids is developing. Contrasted with mineral oil, vegetable oil would overall be able to upgrade the cutting execution, expand the device life and improve the surface getting done with as indicated by some ongoing investigation from the industry. Xavior et al. [7] performed machining of AISI 304 material with a carbide instrument. They understand that coconut oil had improved the surface zenith similarly as diminished the instrument wear emerged from mineral oils Coconut oil, dissolvable oil and straight cutting oil were being considered at 0.5 mm

Table 47.2   A Summary of few studies reported on turning operation with different coolants

S. No.	Investigator	Work Material	Cutting condition	Results/Findings
1.	Marimuthu et al. [11]	Inconel 625	Dry Condition	Investigators reasoned that feed, profundity of cut and cutting rate as significant cutting parameters and it influences the MRR and Tool wear
2.	Kannnan, and Tony [12]	EN-8 steel	Veg-cutting fluid (Canola oil, Sesame oil, Sunflower oil, Palm oil and Rice bran oil)	Experimental study shows that the veg-oil-based sunflower oil can perform better than any other fluid. The sunflower and sesame oil gave better surface finish and lesser value of temperature at tool work interface. Sunflower oil is observed as the best possible alternative
3.	Yazid et al. [13]	Inconel 718	Dry Condition MQL 50 ml/h, and 100 ml/h	With the PVD coated carbide tool, MQL 50 ml produces enhanced surface roughness compare to MQL 100 ml and dry conditions
4.	Magri et al. [14]	Inconel 625 nickel-based alloy	High-pressure coolant	The utilization of high-pressure coolant hurts the tool wear advancement and, therefore, builds apparatus existence with synchronous improvement of workpiece surface harshness now and again

Table 47.2 (continued)

S. No.	Investigator	Work Material	Cutting condition	Results/Findings
5.	Ojolo et al. [15]	Mild Steel, Copper, and Aluminum	Straight biological oils	Bio-oils were reasonable for metalworking liquids but groundnut oil displayed the most elevated decrease in cutting power for the study conducted
6.	Lawal et al. [16]	Mild Steel	Vegetable oils and compared with soluble oil	Temperature was considered to assess the presentation of the cutting liquid
7.	Avila, and Abrao [17]	AISI 4340 steel	Emulsion synthetic, emulsion with and without mineral oil	The creators reasoned that the utilization of a cutting liquid dependent on an emulsion without mineral oil brought about longer instrument life contrasted with dry cutting

Table 47.3 Vegetable-based oil cutting fluids used in machining

Researchers	Type of vegetable oil fluids
Adithan et al. [8], Koshy et al. [18]	Coconut Oil
Kannnan et al. [12]	Canola oil, Sesame oil, Sunflower oil, Palm oil, and Rice bran oil
Ojolo et al. [15]	Coconut oil, shea butter oil, groundnut oil, and palm kernel oil
Lawal et al. [16]	Groundnut oil, palm oil, palm kernel oil, and olive oil
Talib et al. [19]	Jatropha oil
Zhang et al. [20]	Soybean oil, palm oil, and rapeseed oil
Emami et al. [21]	Palm oil
Wang et al. [22]	Peanut, Soybean, rapeseed, maize, palm, castor, and sunflower oil
Zareh et al. [23]	Soybean and rapeseed oils
Tazehkandi et al. [24]	Biodegradable vegetable oil
Srikant et al. [25]	Coconut-based emulsifier, and Sesame oil

of doc with varying feed rate. Coconut oil displayed an unrivaled outcome than the dissolvable oil and straight cutting oil. Ming Liu et al. [8] reviewed the impacts of air-cooling titanium compounds in the hard-turning framework. Results displayed that the compacted cooling air as gas all around decreases cutting temperature, instrument wear, and surface unpleasantness. Courbon et al. [9] found that HPJA was a skilled elective oil plan giving better chip deficiency, decreases in cutting powers and focal concentrations concerning oil and warm loads related to the mechanical get together. Devillez et al. [10] investigated on turning Inconel 718 with wet and dry turning tests were performed at different cutting conditions, with (0.5 mm doc and 0.1 mm/rev feed rate) and utilizing a verified carbide device. For every test, cutting power was evaluated. Sayuti et al. [12] used immaterial entire oil (MQL) mixed with a nanoparticle with SiO_2 in turning of set AISI4140 steel to improve the machining process. Conclusion demonstrated that the base instrument wear is verified with a 0.5% wt. nanoparticle center in the mineral oil. The exploratory data assessment concluded that soybean-based cutting fluid achieved similar execution in decreasing surface roughness yet better stressed on mechanical gathering wear rose up out of oil-based cutting fluids [13]. Krishna et al. [14] researched the execution of nano-boric dangerous with molecule size of 50 nm suspensions in SAE-40 and coconut oil with 10 ml/min flow rate amidst turning of AISI 1040 steel with developed carbide contraption (SNMG 120408). The starters were composed under changing cutting rate (60, 80 and 100 m/min), feed rate (0.14, 0.16 and 0.2 mm/rev) and hugeness of cut (1.0 mm). Overall with nanobalms showed up diversely in connection to base oil and that in the majority of the cases, coconut oil-based nano-iota suspensions demonstrated better execution wandered from SAE-40 based oil. Kirby et al. [15] studied the control parameters for this activity included axle speed, feed rate, profundity of cut, and device nose span. By utilizing the Taguchi parameter plan strategy streamlined the surface completion in a turning activity. The outcomes found that the control components effect affected the reaction variable, with feed rate and device nose span having the most noteworthy impacts. The estimation of the workpieces in this affirmation run prompted the end that the chose parameter esteems from this procedure created a surface harshness that was much lower than different mixes tried in this examination. Kushwaha et al. [16] looked at the impact of cutting parameters and workpiece surface when turning Inconel 625 Solid rod by utilizing PVD covered (TiAlN/TiN) carbide tool. CNC Turning was led under two cutting conditions, to be specific Dry and Wet. CNC turning process parameters dictated by utilizing Taguchi L9 symmetrical exhibits and impact of turning process parameters, i.e., cutting rate, feed rate and profundity of cut are analyzed for two yield points, i.e., Surface Roughness and MRR. In this examination, it is begun that the cutting condition, feed pursued by the profundity of cut, and cutting pace plays more critical assignment on the chosen reaction parameters. Jiang et al. [17] conducted a study on the oil supply pace of MQL and the means to recognize the effects of the base sum oil. The examinations were coordinated by replacing the oil supply rate from 2 ml/h to 14 ml/h, and cutting force. The results demonstrate that the extension of the oil supply rate satisfactorily lessens cutting force and surface obnoxiousness, anyway after 10 ml/h the abatement is never again significant. Kamata [18] attempted the machining by selecting cutting

speeds at modestly higher characteristics: 1 and 1.5 m/s. The longest instrument life was practiced by TiCN/Al$_2$O$_3$/TiN covering in wet cutting. As the slicing pace was extended to 1.5 m/s, the gadget lives were unquestionably shortened while turning of Inconel 718 with MQL. Nageswaran [19] researched and observed a changed cutting supplement with constrained coolant application. Through an arrangement of tests, a channel configuration embeds with constrained coolant application, has appeared around 24–33% diminishing in apparatus wear contrasted with just a finished embed. Half and half embed with its cooling and channel highlights have even extended the operational cutting area with essentially less tool wear. Yazid et al. [20] conducted the turning of Inconel 718, a profoundly destructive safe, nickel-based super combination. The microstructure examination by SEM on the machined surface suggests that genuine changes happened, provoking microstructure change at subsurface level assessing from a couple to a couple of micron in thickness. The outcomes of this assessment show that MQL may possibly improve surface trustworthiness characteristics. Shokrani [21] presented one of the plain first examinations on cryogenic CNC end milling of the Inconel 718 nickel-based composite utilizing TiAlN covered strong carbide tools. Notwithstanding surface roughness, control utilization and tool wear have likewise been checked in this investigation. Ramana et al. [22] attempted test examinations of the execution of three cutting conditions, for example, dry, palm oil, blend of palm oil and boric corrosive grease as far as surface roughness. The outcome moreover showed that palm oil is higher in execution contrasted with dry and palm oil with boric corrosive blend as cutting liquid in this work because of this warm and oxidative solidness which is being practically identical to other vegetable cutting liquids utilized in machining. Rahim et al. [23] portrayed the aftereffects of an examination on the impacts of utilizing distinctive MQL oils (manufactured ester and palm oil) on the penetrating of Ti–6Al–4V. It was discovered that penetrating under dry conditions brought about the briefest device life because of serious chipping. The introduced outcomes showed the significant advantage of utilizing palm oil as far as smaller scale hardness, surface harshness, and subsurface distortion. This work demonstrates that palm oil can be utilized as a feasible option in contrast to an engineered ester as an MQL lubricant. Reddy et al. [24] stated that with the assistance of practical assembling Eco-accommodating machining procedures are picking up significance to stay away from natural contamination. To stay away from these issues, the advancement of nanomaterial by nanotechnology procedures, the adequacy of the cutting liquids can be expanded by scattering them. In the present work, a vegetable oil-based MQL with various volume parts of Al$_2$O$_3$ (aluminum oxide) nanoparticles is utilized as the cutting liquid for machining Inconel 600 composite. Trial results for three distinct conditions—dry, MQL, MQL + Al$_2$O$_3$ nanoparticles are plotted. It is seen that surface completion and temperature scattering of the workpiece increment with various volume divisions of Al$_2$O$_3$ nanoparticle expansion.

47.4   Conclusion

In this work, the ecological and wellbeing impacts because of the utilization, upkeep, and transfer of cutting liquids are portrayed toward the start. The point by point writing recommended that the green assembling strategies, for example, vegetable-based cutting liquids, dry cutting, least amount grease (MQL), and cryogenic cutting are a portion of the manageable arrangements of these issues.

The significant focal points of the new created vegetable-based cutting liquids are high biodegradability and naturally well-disposed while giving the equivalent or better execution than mineral-based cutting liquids. The vegetable oils are potential cutting liquids as an option in contrast to mineral-based or customary cutting liquids. Nonetheless, the detriments of vegetable oils are low warm and oxidative steadiness, high solidifying focuses, and poor erosion assurance.

Another compelling method to limit ecological issues from the utilization of cutting liquids is to limit the amount with a blend of vegetable-based cutting liquids. From the examinations, MQL is best when dry cutting isn't relevant and flood cooling isn't attractive. Likewise, the examination demonstrates that the lower feed rate, high cutting velocity, and high pivotal profundity of cut improves surface completion. Additionally, cutting liquids are as significant as the cutting parameters in machining since cutting liquid lessens the instrument wear and grating among instrument and workpiece extensively contributing improved surface unpleasantness and instrument life.

In an end, the vegetable-based cutting liquids are accepted as the earth's cognizant machining that could decrease the environmental and medical issues brought about by the ecofriendly regular cutting liquids and application techniques. Future research should focus on the answers to conquer the downsides of the vegetable-based cutting liquids, for example, low thermal and oxidative stability. In outline, future research should concentrate on the chemical composition, choice, application techniques, amount optimization and reusability of the vegetable-based cutting liquids for Sustainability of cutting fluids.

47.5   Future Scope

In spite of the fact that bio-based (vegetables) cutting liquids are not impeccable in all perspectives, it has the least negative impacts on nature contrasted with other cutting liquids. Without a doubt, vegetable-based cutting liquids have effectively prompted monetary benefits by method for minimizing the cleaning process duration and transfer cost. In light of the insights, the interest for bio-based greases is relied upon to increment around 58% or 0.29 Mt in 2018 contrasted with 2011. In this manner, future research should focus more on the answers to defeat the disadvantages of the vegetable-based cutting liquids, for example, low thermal and oxidative soundness to fulfill the need.

In outline, future research should concentrate on the chemical composition, choice, application techniques, amount optimization and reusability of the vegetable-based cutting liquids for the Sustainability of cutting fluids. Besides, this from the review of different journal papers it is seen that not so much research has been done on 'Inconel Alloys' with vegetable-based cutting oil which will create a boom in the machining industries. Inconel materials are very hard and tough working load capacitive material. With this cutting fluid uses we can achieve great success in sustainable manufacturing and save the environment for upcoming generations.

References

1. Vieira, J.M., Machado, A.R., Ezugwu, E.O.: Performance of cutting fluids during face milling of steels. J. Mater. Process Tech. **116**, 244–251 (2001)
2. Shah, M., Rawat, U., Potdar, V.V.: A study of vegetable based oils as cutting fluid in machining of alloys. Int. J. Innovative Res. Adv. Eng. **1**, 47–49 (2014)
3. Debnath, S., Reddy, M.M, Yi, Q.S.: Environmental friendly cutting fluids and cooling techniques in machining: A Review. J. Cleaner Prod. 0959–6526 (2014)
4. Kannnan, A., Gim, K.T.: Study of new vegetable oil based eco-friendly cutting fluid for machining operation. Int. J. Sci. Res. (IJSR) **6**, 289–294 (2017)
5. Shashidhara, Y.M., Jayaram, S.R.: Vegetable oils as a potential cutting fluid—an evolution. Tribol. Int. **43**, 1073–1081 (2010)
6. Ramana, M.V, Rao, K.G, Rao, H.D.: Effect of process parameters on surface roughness in turning of titanium alloy under different conditions of lubrication. Recent Adv. Robot. Aeronaut. Mech. Eng. 83–91 (2014)
7. Khan, M.M.A, Mithu, M.A.Z, Ranjan, N.: Effects of minimum quantity lubrication on turning AISI 9310 alloy steel using vegetable oil based cutting fluid. J. Mater. Process. Technol. **209**, 5573–5583 (2009)
8. Xavior, M., Adithan, M.: Determining the influence of cutting fluids on tool wear and surface roughness during turning of AISI 304 austenitic stainless steel. J. Mater. Process. Technol. **209**, 900–909 (2008)
9. Liu, N.M., Chiang, K.T., Hung, C.M.: Modeling and analyzing the effects of air- cooled turning on the machinability of Ti–6Al–4V titanium alloy using the cold air gun coolant system. Int. J. Adv. Manuf. Techno. **67**, 1053–1066 (2013)
10. Julie, Z.Z., Rao, P.N., Eckman, M.: Experimental evaluation of a bio-based cutting fluid using multiple machining characteristics. Int. J. Mod. Eng. **12**, 35–44 (2012)
11. Marimuthu, P., Baskaran, R., Chandrasekaran, K., Bensamraj, J.: Effect of cutting parameters on super alloy in turning operation under dry condition. Int. J. Eng. Technol. **6**, 2573–2578 (2014)
12. Kannnan, A., Tony Gim, K.: Study of new vegetable oil based eco-friendly cutting fluid for machining operation. Int. J. Sci. Res. (IJSR), ISSN, 2319–7064 (2015)
13. Yazid, M.Z.A., Ibrahim, G.A., Said, A.Y.M., CheHaron, C.H., Ghani, J.A.: Surface integrity of Inconel 718 when finish turning with the PVD coated carbide tool under MQL. Procedia Eng. **19**, 396–401 (2011)
14. Magri, A., Diniz, E.A., Suyama, I.D.: Evaluating the use of high-pressure coolant in turning process of Inconel 625 nickel-based alloy. J. Eng. Manuf. 1–11 (2016)
15. Ojolo, S.J, Amuda, M.O.H, Ogunmola, O.Y., Ononiwu, C.U.: Experimental determination of the effect of some straight biological oils on cutting force during cylindrical turning. Rev. Mater. **13**(4) 650–663 (2008)
16. Lawal, S.A., Abolarin, M.S., Ugheoke, B.I., Onche, E.O.: Performance evaluation of cutting fluids developed from fixed oils. LEJPT **10**, 137–144 (2007)

17. Avila, R.F., Abrao, A.M.: The effect of cutting fluids on the machining of hardened AISI 4340 steel. J. Mater. Process. Technol. **119**, 21–26 (2001)
18. Koshy, P.C., Krishnan, P., Kumar, R., Thottackkad, V.M.: Evaluation of the tribological and thermo-physical properties of coconut oil added with MoS 2 nanoparticles at elevated temperatures. Wear **330**, 288–308 (2015)
19. Talib, N., Rahim, A.E.: The effect of tribology behavior on machining performances when using bio-based lubricant as a sustainable metalworking fluid. Proc. CIRP **40**, 504–508 (2016)
20. Zhang, Y., Li, C., Jia, D., Zhang, D., Zhang, X.: Experimental evaluation of MoS_2 nanoparticles in jet MQL grinding with different types of vegetable oil as base oil. J. Clean. Prod. **87**, 930–940 (2015)
21. Emami, M., Sadeghi, H.M., Sarhan, D.A.A., Hasani, F.: Investigating the minimum quantity lubrication in grinding of Al_2O_3 engineering ceramic. J. Clean. Prod. **66**, 632–643 (2014)
22. Wang, Y., Li, C., Zhang, Y., Yang, M., Li, B., Jia, D., Hou, Y., Mao, C.: Experimental evaluation of the lubrication properties of the wheel/workpiece interface in minimum quantity lubrication (MQL) grinding using different types of vegetable oils. J. Clean. Prod. **127**, 487–499 (2016)
23. Desari, Z.B., Davoodi, B.: Assessing the lubrication performance of vegetable oil-based nano-lubricants for environmentally conscious metal forming processes. J. Clean. Prod. **135**, 1198–1209 (2016)
24. Tazehkandi, H.A., Shabgard, M., Farid, P.: Application of liquid nitrogen and spray mode of biodegradable vegetable cutting fluid with compressed air in order to reduce cutting fluid consumption in turning Inconel 740. J. Clean. Prod. **108**, 90–103 (2015)
25. Srikant, R.R., Ramana, V.S.N.V.: Performance evaluation of vegetable emulsifier based green cutting fluid in turning of American Iron and Steel Institute (AISI) 1040 steel–an initiative towards sustainable manufacturing. J. Clean. Prod. **108**, 104–109 (2015)